GEOTECHNICAL PROPERTIES OF DEEP-OCEAN SEDIMENTS : A CRITICAL STATE APPROACH

by

Edmond Wai Leung Ho

B.Sc.,M.Sc.,D.I.C.

A thesis submitted to the City University
for the degree of Doctor of Philosophy
in Civil Engineering

Geotechnical Engineering Research Centre
Department of Civil Engineering
The City University, London
EC1V 0HB

Nov., 1988

List of Contents

	Page
Title Page	i
List of Contents	ii
List of Plates	vii
List of Tables	vii
List of Figures	viii
List of Symbols	xiv
Acknowledgement	xviii
Declaration	ixx
Synopsis	xx
Chapter 1 : Introduction	1
1.1 Current Knowledge on the Behaviour of Deep-Ocean sediments	1
1.2 Objectives of Research	2
1.3 Testing and Analysis	3
Chapter 2 : Stress-Strain Behaviour of Soils	4
2.1 Stress and Strain Parameters	6
2.1.1 Stress Diagrams and Stress Paths	6
2.1.2 Stress and Strain Invariants	7
2.2 Relationships between Effective Stress and Specific Volume	9
2.2.1 Normal Compression and Swelling	9
2.2.2 Critical States and Peak Strength Envelopes	13
2.2.3 The State Boundary Surface	16
2.3 Stress-Strain Behaviour of Soils	17
2.3.1 Elastic Constitutive Equations	19
2.3.2 Elasto-Plastic Constitutive Equations	21
2.4 Cam-Clay and Modified Cam-Clay Constitutive Equations	24
2.4.1 Some Characteristics of the Incremental Elasto-Plastic Models	26
2.4.2 Determination of the Compliance Parameters from Triaxial Tests	29

Page

2.5 A Model for the Behaviour of Anisotropic Soils 32
2.5.1 Some Aspects of the Behaviour of Anisotropically Compressed Soils 33
2.5.2 The Development of Constitutive Equations 35
2.5.2.1 The Cross Anisotropic Elastic Constitutive Equations 35
2.5.2.2 Elasto-Plastic Constitutive Equations 38
2.5.4 Discussion 45

Chapter 3 : Marine Geology 47

3.1 The Ocean Basin 47
3.2 Types and Distributions of Ocean Sediments 49
3.2.1 Pelagic Deposits 49
3.2.2 Terrigeneous Deposits 49
3.3 The Great Meteor East (GME) Study Area 50
3.3.1 The Regional Setting 50
3.3.2 Sedimentology 51
3.3.3 Sediment Properties 52
3.4 The Nares Abyssal Plain (NAP) Study Area 53
3.4.1 The Regional Setting 53
3.4.2 Sedimentology 53
3.4.3 Sediment Properties 54

Chapter 4 : Review of the Behaviour of Deep-Ocean Sediments 56

4.1 Index Properties 57
4.2 Consolidation and Compression Characteristics 58
4.3 Stress-Strain Behaviour 62
4.4 Strength Characteristics 63

Chapter 5 : Procedures for Trimming and Classification Tests 66

5.1 The Sub-Sample Cores 66

Page

5.2 Trimming of the Sub-Sample Cores 66
5.2.1 The IOS Tubed Specimens 67
5.2.2 The GME Tubed Specimens 67
5.2.3 The NAP Tubed Specimens 68
5.2.4 The GME C-6 Tubed Specimens 69
5.3 Procedures for Classification Tests 70
5.3.1 Salt-Water Content Determinations 70
5.3.2 Atterberg Limits 71
5.3.3 Specific Gravity Tests 71
5.3.4 Particle Size Analysis 72
5.3.5 Calcium Carbonate Content Determinations 72
5.3.6 Particle Shapes and Arrangements 72

Chapter 6 : Microcomputer Controlled Triaxial Stress Path Cells 73

6.1 The Triaxial Stress Path Apparatus 74
6.2 Intrumentations and Calibrations 75
6.2.1 Axial Load Cell 75
6.2.2 Pressure Transducers 76
6.2.3 Volume Change Transducer 76
6.2.4 Axial Displacement Transducer 76
6.3 Pressure Control and Power Supply System 77
6.4 The 'Spectra' Microcomputer Control System 78
6.4.1 The Main Components 79
6.4.2 Operations 79
6.5 The 'BBC' Microcomputer Control System 80
6.5.1 The Main Components 81
6.5.2 Operations 81
6.6 The Option Menu 82
6.7 Calculations of Stresses and Strains 85
6.7.1 The Current States 85
6.7.2 The Required Stresses and Strains 87
6.8 Accuracy of the System 88
6.8.1 Accuracy of the Measurements 88

Page

6.8.1.1 Resolutions 88
6.8.1.2 The Calibration Constants 88
6.8.1.3 Noise and Drift 89
6.8.1.4 System Compliance 90
6.8.2 Accuracy of the Controller 91
6.8.3 Discussion 92

Chapter 7 : Procedures for Triaxial Stress Path Testing 94

7.1 Sample Preparations 94
7.1.1 Preparation for the Tubed Triaxial Specimens 94
7.1.2 Preparation for the Reconstituted Triaxial Specimens 94
7.2 Setting Up in the Triaxial Apparatus 96
7.2.1 Preparing the Triaxial Apparatus 96
7.2.2 Preparing the Triaxial Specimen 97
7.2.3 Setting the Initial Isotropic Stresses 98
7.2.4 Initial Isotropic Consolidation 99
7.2.5 Flushing of the Drainage System 99
7.2.6 Joining the Specimen Top Platen to the Load Cell 100
7.3 Stress Path Testing Procedures 101
7.3.1 Isotropic and Anisotropic Compression Tests 101
7.3.2 Undrained Shearing Tests 102
7.3.3 Drained Shearing Tests 103
7.3.4 Unloading the Apparatus 104
7.3.5 Rate of Loading 104

Chapter 8 : Test Results 107

8.1 Classification Test Results 107
8.2 Triaxial Test Results 108

Chapter 9 : Analyses and Discussions 109

9.1 Soil Classifications 109

		Page
9.2	Consolidation	112
9.3	Compression Behaviour	113
9.4	Strength Characteristics	118
	9.4.1 Limiting States	118
	9.4.2 Undrained Shear Strength	122
	9.4.3 Angle of Shearing Resistance	125
9.5	State Boundary Surface	126
9.6	Stress-Strain Behaviour	130
	9.6.1 Stress-Strain Curves	130
	9.6.2 Stiffness Parameters	131
	9.6.3 Compliance Parameters	136
Chapter 10 : Conclusion		138
10.1	The Carbonate Sediments	139
10.2	The Non-carbonate Sediments	141
10.3	Critical State model	142
Appendix A :	Derivation of Constitutive Equations for Modified Cam-Clay	146
Appendix B :	Procedures for the Calculations of the Required Amount of Salt for Reconstituted Specimens	150
Appendix C :	The Constitutive Equations for City-Clay	152
Appendix D :	Non-uniformity of Triaxial Samples due to Consolidation with radial drainage	153
References		155

List of Plates

5.1 The IOS sub-sample core.
5.2 Trimming of the IOS sub-sample on a wire-saw frame.
5.3 Trimming of the GME sub-sample using a thin wall tube.
5.4 Trimming of the NAP sub-sample using a thin wall tube.
5.5 Trimming of the GME C-6 sub-sample using three thin wall tubes.
6.1 The triaxial stress path apparatus.
6.2 The inner salt-water chamber.
6.3 The 'Spectra' microcomputer control system.
6.4 The 'BBC' microcomputer control system.
7.1 Equipments for preparing triaxial test specimens.
8.1 Micrographs of the specimens

List of Tables

3.1 Classifications of ocean sediments.
4.1 Details of the North Pacific deep-ocean sediments.
4.2 Details of the North Atlantic deep-ocean sediments.
4.3 Correlations between compression index and index properties.
4.4 Summary of the K_o values for deep-ocean sediments.
5.1 Details of the sub-sample cores.
6.1 Resolutions of the instruments.
6.2 Summary of the accuracies of the measurements.
7.1 Summary of the rates of loading for triaxial stress path testing.
8.1 Summary of results of the index properties.
8.2 Summary of test results and loading history of the tubed specimen.
8.3 Summary of test results and loading history of the reconstituted Specimens.
9.1 Summary of the compression parameters for deep-ocean sediments.
9.2 Summary of test results for IOS tubed specimens.
9.3 Summary of test results for GME tubed specimens.
9.4 Summary of test results for NAP tubed specimens.
9.5 Summary of test results for GME C-6 tubed specimens.
9.6 Summary of test results for GME reconstituted specimens.

9.7 Summary of test results for NAP reconstituted specimens.
9.8 Summary of the critical state parameters for deep-ocean sediments.
9.9 The predicted undrained shear strength ratios for K_o normally consolidated deep-ocean sediments.
9.10 Summary of the undrained stiffnesses for deep-ocean sediments.

List of Figures

2.1 Elasto-plastic stress-strain behaviour.
2.2 The three dimensional stress space.
2.3 The Mohr circle state of stress.
2.4 One dimensional compression behaviour of soils.
2.5 Isotropic and one dimensional compression and swelling lines.
2.6 Behaviour of normally consolidated soil.
2.7 Relationships between M and ϕ'_{cs}.
2.8 Behaviour of overconsolidated soils.
2.9 Three dimensional state boundary surface and the elastic wall.
2.10 Normalised sections of the state boundary surface.
2.11 Normality condition.
2.12 Hardening and softening.
2.13 Patterns of the individual compliance for Cam-Clay and Modified Cam-Clay models.
2.14 Behaviour of heavily overconsolidated and lightly overconsolidated soils.
2.15 Behaviour of normally consolidated soils.
2.16 Yield curve for a natural soft clay.
2.17 Yield curves for natural soft clay.
2.18 Normalised effective stress paths for an 'undisturbed' marine soft clay.
2.19 Normalised effective stress paths of reconstituted Speswhite kaolin.
2.20 Normalised effective stress paths of reconstituted Cowden Till.
2.21 Normalised effective stress paths of reconstituted Kawasaki clays
2.22 An idealised constant volume section of an anisotropic state boundary surface.

2.23 The predicted undrained effective stress paths for an elastic soil.
2.24 A flow rule for an anisotropic yield locus.
2.25 The predicted constant volume section of the state boundary surface.
2.26 Patterns of the individual compliance for K_o compressed Speswhite kaolin clay.
2.27 The predicted and the experimental tangent shear stiffness for K_o normally compresed Speswhite kaolin.
3.1 An idealised section of the ocean floor.
3.2 North Atlantic study areas.
3.3 Regional setting of the Greater Meteor East.
3.4 Regional setting of the Nares Abyssal Plain.
3.5 Engineering properties of GME core D10695.
3.6 Engineering properties of GME core 82 PCM 29.
3.7 Engineering properties of NAP core 84 PCM 17 and 84 PCM 39.
3.8 Engineering properties of NAP cores (motor-vane strength)
4.1 Geotechnical properties (MPG-1 , North Pacific).
4.2 Geotechnical properties (MPG-1 , North Pacific).
4.3 Deep sea drilling project, hole 576A (North Pacific).
4.4 Geotechnical properties (KNORR-31 , North Atlantic).
4.5 Geotechnical properties (KNORR-31 , North Atlantic).
4.6 Geotechnical properties (KNORR-31 , North Atlantic).
4.7 Geotechnical properties (KNORR-51 , North Pacific).
4.8 Geotechnical properties (KNORR-51 , North Pacific).
4.9 Geotechnical properties (North Atlantic).
4.10 Geotechnical properties (North Atlantic).
4.11 Plasticity chart for North Pacific and North Atlantic deep-ocean sediments.
4.12 One dimensional consolidation test results (Gulf of Mexico).
4.13 One dimensional consolidation test results (North Atlantic).
4.14 One dimensional consolidation test results (North Atlantic).
4.15 One dimensional consolidation test results (North Atlantic).
4.16 One dimensional consolidation test results (North Atlantic).
4.17 Relationship between compression index and plastic index.

4.18 Relationship between compression index and liquid limit.
4.19 Variation of compression index with carbonate content.
4.20 Variation of compression index with carbonate content.
4.21 Profiles of OCR versus depth.
4.22 Profiles of OCR versus depth.
4.23 Variation of OCR with carbonate content.
4.24 Permeability test results.
4.25 Permeability test results.
4.26 Permeability test results.
4.27 Relationship between Poisson's Ratios and density.
4.28 Stress-strain response and tangent modulus.
4.29 Stress-strain and pore pressure response of triaxial compression tests.
4.30 Stress-strain and pore pressure response of triaxial compression tests.
4.31 Stress-strain and pore pressure response of triaxial compression tests.
4.32 Stress-strain and pore pressure response of triaxial compression tests.
4.33 Relationship between c_u / σ_v' and plasticity index.
4.34 Relationship between c_u / σ_v' and plasticity index.
4.35 Stress paths of triaxial compression tests.
4.36 Undrained triaxial compression test results at maximum effective stress ratio.
4.37 Relationship between $\sin \phi'$ and plasticity index.
4.38 Triaxial compression test results.
4.39 Undrained triaxial compression test results.
6.1 Microcomputer controlled triaxial stress path system.
6.2 A typical load cell calibration curve.
6.3 The axial compliance of the load cell.
6.4 A typical pressure transducer calibration curve.
6.5 A typical volume gauge calibration curve.
6.6 A typical displacement transducer calibration curve.
6.7 Drainage connections between the sample and the volume gauge.
6.8 The main control loop program : Flow Chart.

6.9 The option menu for the control program.
6.10 The choice of a calibration constant.
6.11 Noise and drift of the measuring device.
6.12 Recorded and controlled stresses in a stress path cell with feed-back control.
7.1 The floating ring type oedometer for preparing reconstituted triaxial specimens.
7.2 The inner salt-water chamber on the triaxial cell pedestal.
7.3 Stress paths for isotropic and anisotropic compression.
7.4 Examples of the directions of stress paths in relation to the principal stress increments.
7.5 Stress paths for constant p´ and q´ loading and unloading tests
8.1 Plasticity chart.
8.2 Grading curves.
8.3 K_o compression of the IOS tubed specimens.
8.4 K_o compression of the GME tubed specimens.
8.5 K_o compression of the GME C-6 tubed specimens.
8.6 K_o compression of the NAP tubed specimens.
8.7 K_o compression of the GME reconstituted specimens.
8.8 K_o compression of the NAP reconstituted specimens.
8.9 The basic shearing test results of the IOS tubed specimens.
8.10 The basic shearing test results of the GME tubed specimens.
8.11 The basic shearing test results of the GME C-6 tubed specimens.
8.12 The basic shearing test results of the NAP tubed specimens.
8.13 The basic shearing test results of the GME reconstituted specimens.
8.14 The basic shearing test results of the NAP reconstituted specimens.
8.15 Undrained effective stress paths for IOS tubed specimens.
8.16 Undrained effective stress paths for GME tubed specimens.
8.17 Undrained effective stress paths for GME C-6 tubed specimens.
8.18 Undrained effective stress paths for NAP tubed specimens.
8.19 Undrained effective stress paths for GME reconstituted specimens.
8.20 Undrained effective stress paths for NAP reconstituted specimens
8.21 Stress -strain curves for IOS tubed specimens.

8.22 Stress-strain curves for GME tubed specimens.
8.23 Stress-strain curves for GME C-6 soecimens.
8.24 Stress-strain curves NAP tubed specimens.
8.25 Stress-strain curves for GME reconstituted specimens.
8.26 Stress-strain curves for NAP reconstituted specimens
9.1 K_o normally consolidated states for IOS tubed specimens.
9.2 K_o and isotropic normally consolidated states for GME tubed and reconstituted specimens.
9.3 K_o normally consolidated states for GME C-6 tubed specimens.
9.4 K_o normally consolidated states for NAP tubed and reconstituted specimens.
9.5 A comparison of the normal compression lines between tubed and reconstituted specimens.
9.6 Relationship between N_o and λ_o for deep-ocean sediments
9.7 Relationships between K_o and ϕ_c' for the North Atlantic deep-ocean sediments.
9.8 Relationships between λ_o and index properties.
9.9 Critical states for IOS tubed specimens.
9.10 Critical states for GME tubed specimens.
9.11 Critical states for GME C-6 specimens.
9.12 Critical states for NAP tubed specimens.
9.13 Critical states for GME reconstituted specimens.
9.14 Critical states for NAP reconstituted specimens.
9.15 Critical states for GME tubed specimens.
9.16 Critical states for GME C-6 tubed specimens.
9.17 Critical states for NAP tubed specimens.
9.18 Critical states for GME reconstituted specimens.
9.19 Critical states for NAP reconstituted specimens.
9.20a Undrained shear strength with vertical effective stress for the GME specimens.
9.20b Undrained shear strength with vertical effective stress for the NAP specimens.
9.21 Relationships between the undrained shear strength ratio and plasticity index for deep-ocean sediments.
9.22 Relationship between SIN ϕ_c' and plasticity index.

9.23 Normalised stress paths for IOS tubed specimens.
9.24 Normalised state paths for GME tubed specimens.
9.25 Normalised state paths for GME C-6 specimens.
9.26 Normalised state paths for NAP specmens.
9.27 Normalised state paths for GME reconstituted specimens.
9.28 Normalised state paths for NAP reconstituted specimens.
9.29 State boundary surfaces for deep-ocean sediments.
9.30 Normalised stress-strain curves for IOS tubed specimens.
9.31 Normalised stress-strain curves for GME tubed specimens.
9.32 Normalised stress-strain curves for GME C-6 specimens.
9.33 Normalised stress-strain curves for NAP tubed specimens.
9.34 Normalised stress-strain curves for GME reconstituted specimens.
9.35 Normalised stress-strain curves for NAP reconstituted specimens.
9.36 Normalised shear stiffness for IOS tubed specimens.
9.37 Normalised shear stiffness for GME tubed specimens.
9.38 Normalised shear stiffness for GME C-6 specimens.
9.39 Normalised shear stiffness for NAP tubed specimens.
9.40 Normalised shear stiffness for GME reconstituted specimens.
9.41 Normalised shear stiffness for NAP reconstituted specimens.
9.42 A comparison of the undrained shear stiffnesses between different tubed sediments.
9.43 A comparison of the undrained shear stiffnesses between tubed and reconstituted GME sediments.
9.44 A comparison of the undrained shear stiffnesses between tubed and reconstituted NAP sediments.
9.45 The normalised compliance parameters for the NAP tubed specimens.
9.46 The normalised compliance parameters for the NAP tubed specimens.
9.47 The normalised compliance parameters for the NAP reconstituted specimens.
9.48 A comparison of the normalised compliance parameters between theoretical and experimental results for NAP tubed specimens.
9.49 A comparison of the normalised compliance parameters between theoretical and experimental results for NAP reconstituted specmens.

List of Symbols

A : activity
A : area
A : the shear compliance parameter
B : Skempton´s pore pressure parameter
B : the coupling compliance parameter
C : the coupling compliance parameter
C´ : the general compliance matrix in terms of effective stress
C_c : compression index
C_s : swelling index
D : the bulk compliance parameter
E : work done by external load
E´ : effective Young´s modulus
E'_h : the value of E´ in horizontal direction
E'_v : the value of E´ in vertical direction
E_u : equivalent undrained Young´s modulus
F : flow parameter
G´ : elastic shear modulus
G_s : specific gravity of soil grains
G_u : equivalent undrained shear modulus
J´ : elastic coupling modulus
K´ : elastic bulk modulus
K_o : coefficient of earth pressure at rest
LL : liquid limit
LI : liquidity index
M : effective stress ratio at critical state
OCR : overconsolidation ratio ($\sigma'_{vc}/\sigma'_{vi}$)
PL : plastic limit
PI : plasticity index
V : voltage
V : volume
W : work done by internal load
a : axial direction
c´ : intercept of peak envelope in q´ - p´ space

c_u : undrained shear strength

c_v : coefficient of consolidation

d : depth below sea-floor

e : voids ratio

h : height

h : horizontal direction

k : coefficient of permeability

ln : natural logarithm

m : water content

$\bar{m}$: salt-water content

m_i : initial salt-water content

m_v : coefficient of volume compressibility

n : porosity

p' : mean effective stress $= (\sigma_1' + 2\sigma_3') / 3$

p'_c : past maximum mean effective stress

p'_e : equivalent effective pressure : value of p' at the point on the normal compression line at the same specific volume

p'_{en}: value of p' at the end of a shearing test

p'_o : value of p' at the start of a shearing test

p'_{cs}: value of p' at critical state

p'_p : value of p' at the point on the normal compression line projected from the swelling line

p'_u : value of p' at critical state for undrained loading

q' : deviatoric stress $= (\sigma_1' - \sigma_3')$

q'_{en}: value of q' at the end of a shearing test

q'_o : value of q' at the start of shearing test

q'_p : peak deviator stress for undrained test

q'_u : value of q' at critical state for undrained loading

r : radial direction

r : salt content

s' : $= (\sigma_1' + \sigma_3') / 2$

t' : $= (\sigma_1' - \sigma_3') / 2$

t : time

u : pore pressure

u_b : back pressure

u : mean excess pore pressure

v : vertical direction

v : specific volume

v_o : value of v at the start of shearing test

v_o^* : value of v at the start of a shearing test (corresponding to the the value on the selected NCL at p'_o)

v_{en} : value of v measured at the end of a shearing test

v_{cs} : value of v at critical state

v_κ : specific volume swelled to $p' = 1$ kPa

v_λ : $= v + \lambda \ln p'$, on reference p' section

$'$: effective stress (eg. σ')

Γ : specific volume at critical state with $p' = 1$ kPa

Γ_c : value of Γ in compression

Γ_e : value of Γ in extension

Δ : large increment of.....

M : slope of critical state line in $q' - p'$ space

M_c : value of M for triaxial compression

M_e : value of M for triaxial extension

N : specific volume of isotropic normally consolidated soil at $p' = 1$ kPa

N_o : specific volume of K_o normally consolidated soil at $p' = 1$ kPa

α : degree of elastic anisotropy

γ : bulk unit weight

γ' : effective unit weight

δ : small increment of.....

ε : natural strain

ε^e : elastic natural strain

ε^p : plastic natural strain

ε_o : ordinary strain

ε_v : natural volumetric strain

ε_s : natural shear strain

κ : slope of isotropic swelling line in $v - \ln p'$ space

κ_o : slope of K_o swelling line in $v - \ln p'$ space

λ : slope of isotropic normally consolidated line in $v - \ln p'$ space

λ_o : slope of K_o normally consolidated line in $v - \ln p'$ space

ν' : Poisson's ratio for an isotropic elastic material

ν'_{vh}: Poisson's ratio for a transversely isotropic elastic material

ν'_{vv}: Poisson's ratio for a transversely isotropic elastic material

$\bar{\nu}'$: modified Poisson's ratio

η'_o : effective stress ratio at K_o condition

σ : stress

$\dot{\sigma}$: rate of change of stress

σ_1 : major principal stress

σ_2 : intermediate principal stress

σ_3 : minor principal stress

σ'_v : vertical effective stress

σ'_{vc}: past maximum vertical effective stress

σ'_{vi}: in-situ vertical effective stress

σ'_{vo} : value of σ'_v at the start of a shearing test

σ'_{oct} : octahedral effective stress

τ' : shear stress

τ'_{oct} : octahedral shear stress

ϕ' : angle of internal friction in terms of effective stress

ϕ'_{cs}: value of ϕ' at critical state

ϕ'_c : value of ϕ'_{cs} in triaxial compression test

ϕ'_e : value of ϕ'_{cs} in triaxial extension test

Acknowledgement

I am indebted to Professor J.H. Atkinson and Mr. J.S. Evans for their constructive guidance and encouragement throughout my research. I would like to thank other research staff ,particularly D[redacted], and also other research students at the Geotechnical Engineering Research Centre for the advice they gave me and for the useful discussions we had over tea-time.

My thanks also go to the technicians for their help on making special testing equipment and to [redacted] in the Physics Department for his help on the X-ray diffraction techniques and on using the electron microscope.

I should like to thank Building Research Establishment, the Institute of Oceanographic Science and the ESOPE* Research Party for providing me with sediment samples and in particular, [redacted] of Building Research Establishment for his helpful discussions.

I am extremely grateful to the Department of the Environment, City University and the Committee of Vice-Chancellors and Principals of the Universities of the United Kingdom for their financial support.

Finally, I would like to thank [redacted] for carrying out some of the triaxial tests and [redacted] for typing part of the thesis.

* ESOPE (Etude des Sediments Oceaniques par Penetration) is an international investigation primarily organised by C.E.A. (Commissiat A l Energie Atomique) to obtain 30m long piston core in the deep-ocean.

Declaration

I grant powers of discretion to the University Librarian to allow the thesis to be copied in whole or in part without further reference to the author. This permission covers only single copies made for study purposes, subject to normal conditions of acknowledgement.

Synopsis

The problem of disposal of high-level radioactive waste has led to consideration of using the sediments of the deep-ocean floor as repositories and to the initiation of research to establish an understanding of the fundamental behaviour of deep-ocean sediments.

Previous work to establish the mechanical behaviour of these anisotropically (K_o), normally consolidated sediments has consisted generally of conventional testing (eg. strained controlled triaxial tests) on mainly isotropically consolidated specimens of various qualities of samples.

The work described in this thesis consisted of a series of triaxial stress path tests using microcomputer controlled hydraulic triaxial cells (Atkinson et al. 1985), to investigate the strength and stress-strain behaviour for mainly K_o consolidated 'undisturbed' (tubed) and reconstituted specimens of deep-ocean sediments taken from two study areas in the North Atlantic Ocean.

The test results have been analysed within the framework of critical state soil mechanics to investigate sediment characteristics such as the state boundary surface, drained and undrained strength and stress-strain behaviour. While marked anisotropic behaviour is found in a number of respects, the results indicate that analysis in a critical state framework is as valid as for terrestrial sediments. Differences in behaviour between tubed and reconstituted specimens have been observed and the effect of the presence of carbonate has been investigated.

An attempt has been made to develop an elasto-plastic constitutive K_o model based on critical state concepts. This model has been found to agree reasonably well with experimental data for kaolin and deep-ocean sediments.

Chapter 1 : Introduction

The research described in this thesis forms part of a programme of research undertaken by the UK Department of the Environment on the engineering aspects of ocean disposal of high-level (heat generating) radioactive waste. The main objective of their research programme was to assess the practicality and the environmental impact of the ocean disposal by the free-fall penetrator (Freeman 1983). In this method a stream-lined projectile encasing the canister of solidified waste is allowed to fall freely through the water column to bury itself at a depth of a few tens of metres in the ocean seabed. A knowledge of the geotechnical properties of the deep-ocean sediments is essential in evaluating problems such as,

i) depth of burial ;
ii) hole closure behind the free-fall penetrator ;
iii) the effects of the waste on the surrounding sediments during the burial process.

1.1 Current Knowledge on the Behaviour of Deep-Ocean Sediments

Certain areas in the North Atlantic have been designated as study areas for the purpose of disposing radioactive waste and two of these areas are currently under consideration: Great Meteor East (GME) and Nares Abyssal Plain (NAP) (Anderson 1983). Sediments in both these areas are made up largely of turbidites which are comprised of clay and silt

sized particles. One significant difference between the sediments at the two sites is the amount of carbonate present: at GME carbonate contents of up to 60% are not uncommon whereas 5 to 10% carbonate contents are typically found at NAP.

A large amount of information is available on the basic physical properties of deep-ocean sediments (eg. Deep-sea drilling projects) but little is known of their mechanical behaviour. The limited geotechnical information is largely based on results of conventional testing techniques using oedometers, shear vanes and conventional triaxial equipment (eg. Carchedi, 1979 ; Demars, 1975 ; Silva and Jordan, 1984 ; Valent, 1979) and there are practically no good quality geotechnical data (eg. stress-strain and strength properties) available particularly for the North Atlantic deep-ocean sediments.

1.2 Objectives of Research

The main objectives of the research are :

i) to investigate the fundamental properties (constitutive stress-strain relationships and strength properties) of deep-ocean sediments from the GME and the NAP study areas;

ii) to investigate differences in behaviour between the 'undisturbed' (tubed) and reconstituted samples of deep-ocean sediment ;

iii) to compare the behaviour of deep-ocean sediments with that predicted by current soil mechanics theories, and if necessary, extend these theories to take account of anisotropic (K_o) behaviour.

1.3 Testing and Analysis

The main research programme consisted of triaxial tests on 38mm diameter samples of deep-ocean sediment using standard hydraulic stress path cells (Bishop and Wesley, 1975) with automatic controlling and logging equipment (Atkinson et al., 1985 ; Clinton, 1985). The testing programme involved drained and undrained tests, loading (compression) or unloading (extension) following different stress paths on predominantly K_o compressed 'undisturbed' (tubed) and reconstituted (reconsolidated from slurry) samples. Test results are analysed within the framework of critical state soil mechanics (Schofield and Wroth, 1968 ; Atkinson and Bransby, 1978), primarily investigating soil characteristics such as state boundary surface and elasto-plastic stress-strain behaviour and to see how well the behaviour of deep-ocean sediments corresponds to theoretical models of soil behaviour such as Modified Cam-Clay (Roscoe and Burland, 1968). The test data can also be used to provide a basis from which to develop and to calibrate the constitutive equations for anisotropic (K_o) soils such as the soil model (City-Clay) developed in this thesis.

Chapter 2 : Stress-Strain Behaviour of Soils

The fundamental theories of classical soil mechanics are based on Terzaghi's principle of effective stress (Terzaghi, 1936), theory for one dimensional consolidation and Mohr-Coulomb's failure criterion. The stress-strain behaviour of soil before failure is taken as elastic: usually linear, homogeneous and isotropic, occasionally soil elastic behaviour can be taken as non-linear, inhomogeneous and anisotropic. The simplicity of this approach has led to its application in many practical problems. It has, however, some shortcomings. It does not predict permanent deformations which invariably arise on unloading.

Recent modern theories of soil mechanics recognise that stress-strain behaviour of soil before failure is likely to contain both elastic and plastic components of strains. These theories adopt the ideas of plasticity theory originally developed for metals and their application can take account of the frictional response and the volume change characteristics of soils. The advantages of using these theories are that they can be developed to a complete mathematical model of soil within the assumptions made for a particular theory and allow the general form of constitutive equations to be obtained, such as the incremental stress-strain relationship (eg. Naylor et al., 1981). ie.

$$[\,\delta\varepsilon\,] = [\,C'\,]\,[\,\delta\sigma'\,] \qquad (2.1)$$

These constitutive equations are particularly useful for modern

numerical analyses (eg. the finite element method) using computers. Eqn (2.1) relates the increment of strain to the increment of effective stress by a compliance matrix [C′]. This matrix contains a number of material parameters which take into account elastic (recoverable) and plastic (irrecoverable) strains associated with the general requirements for elasticity and for plasticity such as yielding, strain hardening or softening and flow (see Fig. 2.1).

One of the well known theories of soil mechanics which adopts the ideas of plasticity is critical state soil mechanics (Schofield and Wroth, 1968). The main feature of the theory is the existence of a state boundary surface which limits all the possible states for soil. The exact constitutive equations depend on the exact shape of the state boundary surface, for example Cam-Clay (Schofield and Wroth, 1968) and Modified Cam-Clay (Roscoe and Burland, 1968) which were derived theoretically from the considerations of energy(work) dissipation. Recently some theories have been developed which attempt to account for additional effects such as anisotropy, non-associated flow rule and kinematic hardening, mainly to give a better fit to experimental data. These form an associated family of elasto-plastic stress-strain models which are, however, mathematically more complex than but conceptually similar to the original framework of critical state theory (Schofield and Wroth, 1968).

2.1 Stress and Strain Parameters

2.1.1 Stress Diagrams and Stress Paths

Throughout this thesis we will consider only saturated soils and stress within the soil skeleton is controlled by effective stress, σ' which is related to the total stress and pore pressure by the equation $\sigma' = \sigma - u$ (Terzaghi, 1936). Soil behaviour depends not only on the change of effective stresses but also on the way in which the states of soil change and on the previous history of loading. It is therefore necessary to record the loading history in which one or more stresses are varied and to present these stress paths graphically in a stress diagram.

In general, the three dimensional stress system of a cubical element contains six independent stress components (ie. three normal stresses and three shear stresses). It is more convenient to think in terms of principal stress space (see Fig 2.2). The plane normal to the space diagonal, the locus of all points for which $\sigma'_1 = \sigma'_2 = \sigma'_3$ is called the octahedral plane and the octahedral normal stress, $(\sigma'_1 + \sigma'_2 + \sigma'_3)/3$ is constant on that plane. For the condition of axial symmetry ($\sigma_2' = \sigma_3'$) all the axi-symmetric triaxial test data will lie on a particular plane (the axi-symmetric plane), see Fig 2.2. The method of plotting stress paths in three dimensional stress space may be cumbersome and is not easy to follow. Under certain circumstances a simpler picture of stress paths can be presented by selecting different

axes. For example Henkel (1960) used axes σ_1' and $\sqrt{2} \cdot \sigma_3'$ for stress paths under triaxial (axial-symmetry) conditions. A common practice for a number of ground engineering problems takes the vertical and horizontal stresses as the principal stresses (ie. $\sigma_1' = \sigma_v'$ and $\sigma_3' = \sigma_h'$). This is also true for most soil testing equipment (eg. triaxial and oedometer tests on vertical specimens). It is therefore convenient to trace the loading history of a soil element in the stress diagram with axes of $\sigma_1' = \sigma_v'$ and $\sigma_3' = \sigma_h'$, where the intermediate principal stress σ_2' is ignored. Although these axes for stress paths are simple and easy to construct, for analysis of test data it is more convenient to separate shear or deviator stress from normal or mean effective stress and this leads to the construction of a Mohr's circle state of stress in which the stress path is plotted by tracing the path of the apex of the Mohr's circle with axes $t' = (\sigma_1' - \sigma_3')/2$ and $s' = (\sigma_1' + \sigma_3')/2$ (see Fig. 2.3).

2.1.2 Stress and Strain Invariants

Stress invariants are defined as the magnitude of stress parameters which are unaffected by the choice of reference axes (Atkinson and Bransby, 1978). The parameters s' and t' as described in section 2.1.1 are a rather special case as their values are independent of the arbitrary choice of the orientation of the reference axes. However the term 'stress invariants' is strictly reserved for parameters appropriate to general state of stress and the use of parameters s' and t' for two dimensional analysis is only convenient when the

intermediate principal stress is not known. The general form of stress invariants for condition of axial symmetry ($\sigma_2' = \sigma_3'$) are the octahedral normal stress, σ'_{oct} and the octahedral shear stress, τ'_{oct} and they are defined in terms of principal effective stresses as,

$$\sigma_{oct}' = (\sigma_1' + 2\sigma_3')/3 \tag{2.2}$$

$$\tau_{oct}' = \sqrt{2}(\sigma_1' - \sigma_3')/3 \tag{2.3}$$

For simplicity stress parameters are chosen as(Schofield andWroth, 1968),

$$p' = \sigma_{oct}' = (\sigma_1' + 2\sigma_3')/3 \tag{2.4}$$

$$q' = 3\tau_{oct}'/\sqrt{2} = (\sigma_1' - \sigma_3') \tag{2.5}$$

Having chosen the appropriate stress parameters, the strain parameters must be carefully selected by considering the work done by external loads, E which must be equal to the internal work done , W . Assuming coaxiality condition holds, the work done per unit volume by external loads is,

$$E = \sigma_1'\varepsilon_1 + \sigma_2'\varepsilon_2 + \sigma_3'\varepsilon_3 \tag{2.6}$$

The internal work done per unit volume can be written as the sum of the product of the appropriate stress and strain parameters, such that for the condition of plane strain where $\varepsilon_2 = 0$,

$$W = t' \varepsilon_\gamma + s' \varepsilon_v \qquad (2.7)$$

The corresponding strain parameters are (Atkinson and Bransby, 1978),

$$\varepsilon_\gamma = \varepsilon_1 - \varepsilon_3 \qquad (2.8)$$

$$\varepsilon_v = \varepsilon_1 + \varepsilon_3 \qquad (2.9)$$

For the condition of axial-symmetry, where $\sigma_2' = \sigma_3'$ and $\varepsilon_2 = \varepsilon_3$,

$$W = q' \varepsilon_s + p' \varepsilon_v \qquad (2.10)$$

The corresponding strain parameters are (Atkinson and Bransby, 1978)

$$\varepsilon_s = 2(\varepsilon_1 - \varepsilon_3)/3 \qquad (2.11)$$

$$\varepsilon_v = \varepsilon_1 + 2\varepsilon_3 \qquad (2.12)$$

2.2 Relationships between Effective Stress and Specific volume

2.2.1 Normal Compression and Swelling

It is common both in research and in engineering practice to perform one-dimensional compression tests in the oedometer and results are usually presented in e - $\log_{10} \sigma_v'$ diagram. A typical set of results

in Fig. 2.4 shows the sample was loaded from A to B, unloaded to C and reloaded from C to D. By ignoring the small hysterisis due to unloading and reloading cycle, this behaviour can be idealised to straight lines shown in Fig. 2.4. The slope C_c of the normal compression line (ABD) is known as the compression index and the slope C_s of the swelling line (BC) is known as the swelling index, where

$$- C_c = de / d(\log_{10} \sigma'_v) \tag{2.13}$$

$$- C_s = de / d(\log_{10} \sigma'_v) \tag{2.14}$$

For one dimensional compression ($\varepsilon_r = 0$), the vertical effective stress varies linearly with the horizontal effective stress and the relationship is given by

$$K_o = \sigma'_h / \sigma'_v \tag{2.15}$$

where K_o is the coefficient of earth pressure at rest. The value of K_o is a constant during normal compression for a particular soil type but varies with overconsolidation ratio, OCR (see Fig. 2.4) which is given by,

$$OCR = \sigma'_{vm} / \sigma'_v \tag{2.16}$$

where σ'_{vm} and σ'_v are the past maximum and the current vertical effective stresses respectively. Assuming σ_v' and σ_h' are the major and minor principal stresses, the appropriate stress parameters

(see section 2.1.2) for the conditions of axial symmetry are written as,

$$q' = \sigma'_v - \sigma'_h = \sigma'_v (1 - K_o) \qquad (2.17)$$

$$p' = \sigma'_v (1 + 2 K_o) / 3 \qquad (2.18)$$

Equations (2.17) and (2.18) show that q' and p' can only be found if the value of K_o of the soil is known or if the horizontal stress is measured in the special oedometer in which the horizontal force is measured by means of a force transducer (Brooker and Ireland, 1965). In the case of triaxial stress path cells (Bishop and Wesley, 1975) from which both σ_v' and σ_h' are measured during K_o compression tests, it is more convenient to present results in terms of the stress parameters, q' and p' together with v - ln p' diagram (see Fig. 2.5) in which the slope of q' - p' diagram is given by,

$$\eta'_o = 3(1-K_o)/(1+2K_o) \qquad (2.19)$$

where η_o' is a soil constant.

The slope λ_o of the normal compression line and the slope, κ_o of the swelling line are given by

$$-\lambda_o = dv / d(\ln p') \qquad (2.20)$$

$$-\kappa_o = dv / d(\ln p') \qquad (2.21)$$

It should be noted that there is a relationship between eqns (2.13) and (2.14), (2.20) and(2.21), that is

$$2.303\ \lambda_o = C_c \tag{2.22}$$

$$2.303\ \kappa_o = C_s \tag{2.23}$$

The equations for the anisotropic (K_o) normal compression line and the swelling line are given by (see Fig. 2.5),

$$v = N_o - \lambda_o \ln p' \tag{2.24}$$

$$v = v_{\kappa o} - \kappa_o \ln p' \tag{2.25}$$

where N_o, λ_o and κ_o are soil constants.

In conventional practice where samples are isotropically compressed and swelled in the triaxial cell, the value of K_o is unity (ie $q' = 0$: see Fig 2.5) throughout the loading history. The slope of the isotropic compression and swelling lines in e - ln p′ space are taken as parallel to the one dimensional compression and swelling lines (see Fig. 2.5). That is for isotropic compression,

$$v = N - \lambda \ln p' \tag{2.26}$$

for isotropic swelling,

$$v = v_{\kappa} - \kappa \ln p' \qquad (2.27)$$

where N, λ and κ are soil constants.

The normal compression line is unique for a particular soil type and loading history (ie. K_o or isotropic) and it also has a special significance which represents a boundary between the possible states and the impossible states (Atkinson and Bransby, 1978).

2.2.2 Critical States and Peak Strength Envelopes

Schofield and Wroth (1968), Atkinson and Bransby (1978) have shown that for a particular isotropic normally consolidated or lightly overconsolidated soil ($1 < OCR < 2$), the ultimate failure points of all undrained and drained compression tests can be defined by a single straight line through the origin in $q' - p'$ space and by a single curve line in $v - p'$ space whose shape is similar to that of the isotropic normal compression line. This unique failure line is known as the critical state line at which ultimate failure will occur and is however, independent of stress path followed by the sample. Critical state failure is therefore defined as the state at which soil continues to distort in shear at constant effective stresses (ie $\delta q'$, $\delta p' = 0$) and at constant volume ($\delta v = 0$) and is usually reached at modest shear strains of up to about 15 % (see Fig. 2.6c).

It will be helpful to think of the critical state line in three dimensional space ($q' - p' - v$). The projection of the line on the $q' - p'$ plane shown in Fig. 2.6.a is written as

$$q' = M\, p' \tag{2.28}$$

where M is the slope of the critical state line and can be related to the Mohr- Coulomb failure criterion (Atkinson and Bransby, 1978) such that,

in compression $$\sin \phi_c' = 3 M_c / (6 + M_c) \tag{2.29}$$

in extension $$\sin \phi_e' = 3|M_e| / (6 - |M_e|) \tag{2.30}$$

where subscripts c and e refer to compression and extension respectively. It should be noted that for $M = M_c = |M_e|$; $\phi_c' < \phi_e'$ and for $\phi_{cs}' = \phi_c' = \phi_e'$; $M_c > |M_e|$ or $M_e = -3M_c/(3+M_c)$.

The relationships between ϕ_{cs}' and M in compression and extension are given in Fig. 2.7 which shows that when ϕ_c' and ϕ_e' are small ($\phi_{cs}' < 15°$), M_c can be taken approximately equal to $|M_e|$.

The projection of the critical state line on the $v - \ln p'$ space is conveniently defined by a straight line parallel to the normal compression line (see Fig. 2.6b) and can be written as,

$$v = \Gamma + \lambda \ln p' \tag{2.31}$$

where M, λ and κ are soil constants.

The uniqueness of the critical state line for a particular soil type is an important concept for the development of the theory of critical state soil mechanics. It represents a unique relationship between effective stresses and volumes similar to the normal compression line as described earlier and also serves as a boundary for all possible ultimate failure states.

The behaviour of a heavily overconsolidated soil (OCR > 2) is rather different from that of a normally consolidated soil. It contains a series of peak strength envelopes which expand with decreasing specific volume and each of these envelopes is limited by the critical state line on the right and also by a broken line to the left which represents zero minor effective principal stress (no tension cut - off) as indicated in Fig. 2.8a. A typical set of drained compression test results given in Figs. 2.8 b & c which shows that the sample reaches a peak deviator stress at B and then drops to a value close to critical state at C as shear strain increases. This drop of deviator stress from peak to ultimate value (softening) is associated with the dilating response of the sample (see Fig. 2.8c). It may be difficult to locate the exact value of critical state particularly the critical state specific volume as the strains in the sample become non-uniform or discontinuous due to the formation of slip planes (Atkinson and Richardson, 1987). Nevertheless the peak strength envelope shown in Fig. 2.8a can be defined as (Atkinson and Bransby, 1978),

$$q' = c' + H\,p' \qquad (2.32)$$

where c' is the intercept on q' axis whose value depends on the specific volume,

H is the slope of the peak strength envelope and is taken to be a soil constant.

Although recent research (Atkinson and Farrar, 1984) shows that the peak envelope may not be straight and is curved towards the origin particularly at low effective stresses, the simple straight line (eqn 2.32) is sufficient to represent the peak envelope of a heavily overconsolidated soil for the purpose of this thesis.

2.2.3 The State Boundary Surface

The idea of the existence of a state boundary surface for soil was based on the experimental work of Rendulic (1936) and later of Henkel (1960), and was the main feature in the development of critical state soil mechanics. It provides a conceptual model for soil behaviour known as the critical state model (Schofield and Wroth, 1968). The state boundary surface represents a boundary which limits all possible states for a particular soil in q'-p'-v space. It assumes that the behaviour of soil is purely elastic for states lying within the state boundary surface while plastic (irrecoverable) strain will occur as the state of the sample traverses the state boundary surface. The differences between theories which depend on the existence of the state boundary surface are mainly on the exact shape of the surface, for example the Cam-Clay model (Schofield and Wroth, 1968) and the

Modified Cam-Clay model (Roscoe and Burland, 1968), which are derived theoretically by the consideration of work dissipation or developed from experimental data (Atkinson and Bransby, 1978). Fig. 2.9 shows the three dimensional state boundary surface in compression proposed by Atkinson and Bransby(1978) which shows a surface containing lines of constant volume, joining the isotropic compression line, the critical state line and the no tension cut off line. The surface between the isotropic compression line and the critical state line represents yielding and hardening of normally consolidated and lightly overconsolidated soils, called the Roscoe surface, while the surface between the critical state line and the no tension line represents yielding and softening of heavily overconsolidated soils, called the Hvorslev surface (Atkinson and Bransby, 1978).

The swelling line given by equation (2.27) is inside the state boundary surface where soil behaviour is elastic. For an isotropic elastic soil, the state of soil can only move on a vertical plane for a particular swelling line called the isotropic elastic wall (see Fig. 2.9). It should be noted that the intersection between the elastic wall and the state boundary (A B′C′) is a yield curve (Calladine, 1963) which represents the limit for elastic soil behaviour. The state boundary surface contains an infinite number of these yield curves which expand (harden) or contract (soften) in sizes depending on the initial state of the soil and can be conveniently normalised by the parameter $p_e' = \exp [(N - v)/\lambda]$ for the constant volume section (Atkinson and Bransby, 1978), by $p_p' = \exp [(N - v_\kappa)/(\lambda - \kappa)]$ for

the yield locus section and by $v_\lambda = v + \lambda \ln p'$ for the reference p' section of the state boundary surface (see Fig. 2.10 ; Atkinson, 1984c).

2.3 Stress-Strain Behaviour of Soils

The stress-strain behaviour of soils can be described in incremental form (Atkinson and Bransby, 1978 ; Naylor et al., 1981) and expressed as

$$[\delta\sigma'] = [D'][\delta\varepsilon] \tag{2.33}$$

where [D′] is a stiffness matrix associated with effective stress soil parameters.

If the determinant of [D′] is not zero, equation (2.33) can be inversed and expressed as

$$[\delta\varepsilon] = [C'][\delta\sigma'] \tag{2.34}$$

where [C′] is a compliance matrix which contains a number of material properties and are constants only for infinitesimal loading. Assuming the total strain is the sum of the elastic and plastic component of strain, ie.

$$[\delta\varepsilon] = [\delta\varepsilon]^e + [\delta\varepsilon]^p \tag{2.35}$$

where superscripts e and p represent elastic and plastic respectively. Equation (2.34) can be written as

$$[\ \delta\varepsilon\ ] = \{[\ C'\ ]^{e} + [\ C'\ ]^{p}\}\ [\ \delta\sigma'\ ] \qquad (2.36)$$

By using the appropriate stress and strain parameters as described in sections 2.1, the complete constitutive equations for an elasto-plastic incremental model can be written as (Atkinson and Richardson, 1985),

$$\begin{bmatrix} \delta\varepsilon_s \\ \delta\varepsilon_v \end{bmatrix} = \begin{bmatrix} A & B \\ C & D \end{bmatrix} \begin{bmatrix} \delta q' \\ \delta p' \end{bmatrix} \qquad (2.37)$$

It remains to determine the values of $[C']^{e}$ and/or $[C']^{p}$ to describe the behaviour of soil. For soil states which lie within the state boundary surface, soil behaviour is elastic, ie. $[C']^{p} = 0$ and the parameters in $[C']^{e}$ are associated with elastic soil parameters. For states which traverse the state boundary surface, soil behaviour is elasto-plastic, ie. $[C']^{e}$, $[C']^{p} > 0$, and the parameters in $[C']^{p}$ are associated with the shape of the state boundary surface and with a flow rule.

2.3.1 Elastic Constitutive Equations

If soil states are inside the state boundary surface the soil behaviour is taken to be elastic and strains are recoverable. The complete incremental cross-anisotropic elastic constitutive equations for the condition of axial symmetry (Graham and Houlsby, 1983) are given by,

$$\begin{bmatrix} \delta q' \\ \delta p' \end{bmatrix} = \begin{bmatrix} 3G' & -J' \\ -J' & K' \end{bmatrix} \begin{bmatrix} \delta\varepsilon_s^{e} \\ \delta\varepsilon_v^{e} \end{bmatrix} \qquad (2.38)$$

where G' is the elastic shear modulus

K' is the elastic bulk modulus

J' is the elastic coupling modulus.

If the determinant of the stiffness matrix in eqn (2.38) is not equal to zero, it can be inverted to give,

$$\begin{bmatrix} \delta\varepsilon_s^e \\ \delta\varepsilon_v^e \end{bmatrix} = \begin{bmatrix} A^e & B^e \\ C^e & D^e \end{bmatrix} \begin{bmatrix} \delta q' \\ \delta p' \end{bmatrix} \qquad (2.39)$$

where

$$A^e = K' / (3G'K' - J'^2)$$

$$B^e = C^e = -J' / (3G'K' - J'^2)$$

$$D^e = 3G' / (3G'K' - J'^2)$$

For an isotropic elastic soil, the shear and volumetric deformation are decoupled (ie. $J' = 0$ or $B^e = C^e = 0$) and the elastic wall lies on a vertical plane (see Fig. 2.9). The values of G' and K' are given by,

$$G' = E' / 2(1+\nu') \qquad (2.40)$$

$$K' = E' / 3(1-2\nu') \qquad (2.41)$$

and

$$\mu' = K'/3G' = 2(1+\nu') / 9(1-2\nu') \qquad (2.42)$$

The elastic bulk modulus, K' can be related to the slope of the swelling line (eqn 2.27), where

$$1/K' = \delta\varepsilon_v^e / \delta p' = -\frac{\delta v^e}{v} / \delta p' = \kappa / vp' \qquad (2.43)$$

Therefore the complete constitutive equations for an isotropic elastic soil are given by Atkinson (1984c),

$$\begin{bmatrix} \delta\varepsilon_s^e \\ \delta\varepsilon_v^e \end{bmatrix} = \begin{bmatrix} \frac{2(1+\nu')}{3E'} & 0 \\ 0 & \frac{3(1-2\nu')}{E'} \end{bmatrix} \begin{bmatrix} \delta q' \\ \delta p' \end{bmatrix}$$

or

$$= \frac{1}{vp'} \begin{bmatrix} \mu'\kappa & 0 \\ 0 & \kappa \end{bmatrix} \begin{bmatrix} \delta q' \\ \delta p' \end{bmatrix} \qquad (2.44)$$

Eqn (2.44) shows that the isotropic elastic soil behaviour is non-linear and that μ' and κ are soil constants and the stiffnesses depend on the current state of the sample (ie. vp').

2.3.2 Elasto-Plastic Constitutive Equations

Soil behaviour is elasto-plastic if the soil traverses the state boundary surface. The total strain is the sum of the elastic and plastic components. The elastic component of strain can be determined by eqn (2.44) while the plastic component of strain can be determined by plasticity theory associated with yielding and flow. The shape of the state boundary surface can be described mathematically in the form given by Atkinson (1984c),

$$v = F(q', p') \qquad (2.45)$$

differentiating eqn (2.45), we have

$$\delta\varepsilon_v = -\frac{\delta v}{v} = -\frac{1}{v}\frac{\partial F}{\partial q'}\cdot\delta q' - \frac{1}{v}\frac{\partial F}{\partial p'}\cdot\delta p' \qquad (2.46)$$

The plastic component of volumetric strain can be determined from eqn (2.35) and combines with eqns (2.43) and (2.46), we have

$$\delta\varepsilon_v^p = -\left(\frac{1}{v}\cdot\frac{\partial F}{\partial q'}\right)\delta q' - \left(\frac{1}{v}\cdot\frac{\partial F}{\partial p'} + \frac{\kappa}{vp'}\right)\delta p'$$

or

$$= Q\,\delta q' + P\,\delta p' \qquad (2.47)$$

where Q and P are the hardening parameters which depend on the exact equation of the state boundary surface.

In the theory of plasticity ,the gradient $\delta\varepsilon_s^p/\ \delta\varepsilon_v^p$ of the plastic strain increment $\delta\varepsilon^p$ is controlled by the current state of stress and is independent of the increment of stress causing yield. The precise relationship between the vector of plastic strain increment and stress is known as a flow rule and is written as

$$F = \delta\varepsilon_s^p \big/ \delta\varepsilon_v^p \qquad (2.48)$$

where F is the flow parameter which depends only on the current state of stress.

It may be convenient to define a plastic potential such that the vector of the plastic strain increment is perpendicular to the plastic potential (see Fig. 2.11). The flow rule is said to be associated and the normality condition applied if the plastic potential and yield curve coincide. When the state of a sample traverses the state boundary surface the yield curve will expand (harden) or contract (soften) in sizes as indicated in Fig. 2.12 depending on the initial state of the sample. From eqns (2.47) and (2.48) and eliminating $\delta\varepsilon_v^p$, we have,

$$\delta\varepsilon_s^p = FQ\,\delta q' + FP\,\delta p' \tag{2.49}$$

From eqns (2.37) and (2.39), combine with eqns (2.47) and (2.49), the complete general form of incremental constitutive equations for a cross-anisotropic elasto-plastic soil model can be written as

$$\begin{bmatrix} \delta\varepsilon_s \\ \delta\varepsilon_v \end{bmatrix} = \begin{bmatrix} \dfrac{K'}{3G'K'-J'^2} + FQ & \dfrac{-J'}{3G'K'-J'^2} + FP \\ \dfrac{-J'}{3G'K'-J'^2} + Q & \dfrac{3G'}{3G'K'-J'^2} + P \end{bmatrix} \begin{bmatrix} \delta q' \\ \delta p' \end{bmatrix} \tag{2.50}$$

For soils where the elastic behaviour is isotropic ($J' = 0$; Graham and Houlsby, 1983) and the flow rule is associated ($FP = Q$; Atkinson and Bransby, 1978 ; Naylor et al., 1981), eqn (2.50) can be simplified and is given by,

$$\begin{bmatrix} \delta\varepsilon_s \\ \delta\varepsilon_v \end{bmatrix} = \begin{bmatrix} \dfrac{1}{3G'} + FQ & Q \\ Q & \dfrac{1}{K'} + \dfrac{Q}{F} \end{bmatrix} \begin{bmatrix} \delta q' \\ \delta p' \end{bmatrix} \tag{2.51}$$

where the compliance matrix is symmetrical, the values of G' and K' are related to μ', κ and the current state in eqn (2.44), while the values of F and Q can be determined from the state boundary surface (eqn 2.45). Eqn (2.50) or (2.51) is only valid for soil whose state remains on the state boundary surface and the behaviour is elasto-plastic but becomes elastic when soil state moves inside the state boundary surface, where Q and $P = 0$.

2.4 Cam-Clay and Modified Cam-Clay Constitutive Equations

The complete incremental elasto-plastic constitutive equations for Cam-Clay (Schofield and Wroth, 1968) in the form of eqn (2.51) are given by Atkinson (1984c),

$$\begin{bmatrix} \delta\varepsilon_s \\ \delta\varepsilon_v \end{bmatrix} = \left[\frac{1}{vp'}\right] \begin{bmatrix} \frac{\lambda-\kappa}{M-\eta'} + \mu'\kappa & \frac{\lambda-\kappa}{M} \\ \frac{\lambda-\kappa}{M} & \kappa + \frac{(M-\eta')(\lambda-\kappa)}{M} \end{bmatrix} \begin{bmatrix} \delta q' \\ \delta p' \end{bmatrix} \qquad (2.52)$$

where μ' is defined by eqn (2.42) and M, λ, κ are soil constants. Following similar approaches, the complete incremental elasto-plastic constitutive equations for Modified Cam-Clay (Roscoe and Burland, 1968) can be obtained (see Appendix A) and is given by,

$$\begin{bmatrix} \delta\varepsilon_s \\ \delta\varepsilon_v \end{bmatrix} = \left[\frac{1}{vp'}\right] \begin{bmatrix} \mu'\kappa + \frac{4\eta'^2(\lambda-\kappa)}{M^4-\eta'^4} & \frac{2\eta'(\lambda-\kappa)}{M^2+\eta'^2} \\ \frac{2\eta'(\lambda-\kappa)}{M^2+\eta'^2} & \kappa + \frac{(\lambda-\kappa)(M^2-\eta'^2)}{M^2+\eta'^2} \end{bmatrix} \begin{bmatrix} \delta q' \\ \delta p' \end{bmatrix} \qquad (2.53)$$

The major difference between Cam-Clay and Modified Cam-Clay models is the shape of the state boundary surface. It can be seen from eqn (2.53) that the Modified Cam-Clay matrix is slightly more complex but similar to that of the Cam-Clay (eqn 2.52). Their compliance matrices are symmetrical and $1/vp'$ is a common factor of the matrices. It is interesting to note that eqns(2.52) and (2.53) can be rewritten as (Atkinson, 1984c),

$$\begin{bmatrix} v\delta\varepsilon_s \\ v\delta\varepsilon_v \end{bmatrix} = \begin{bmatrix} A & B \\ C & D \end{bmatrix} \begin{bmatrix} \delta q'/p' \\ \delta p'/p' \end{bmatrix} \qquad (2.54)$$

where the compliances A to D depend only on the four soil constants M, λ, κ, μ' and principally on the current effective stress ratio, η' hence as the state changes during loading, values of A to D will also change. The compliance matrix is symmetric (ie. B = C) for conditions of coaxiality, cross-anisotropy and associated flow rule (Atkinson and Bransby, 1978), while the factor $1/vp'$ exists for soils for which the shape of the state boundary surface is independent of its size. Fig. 2.13 shows the patterns of the individual compliance in eqn (2.54) of the two soil models using soil parameters for Speswhite kaolin (after Ho, 1985) and it suggests that the exact shape of the state boundary surface may have a significant effect on the subsequent stress-strain behaviour of soils.

2.4.1 Some Characteristics of the Incremental Elasto-Plastic Model

Any mathematical model which can be expressed in the form of eqn (2.54) is characterised as an associated family of critical state models in which the compliance matrix may or may not be symmetrical (Naylor et al., 1981), depending on the flow rule and the precise shape of the state boundary surface. Eqn (2.54) can be expanded and expressed as

$$v\,\delta\varepsilon_s = A\frac{\delta q'}{p'} + B\frac{\delta p'}{p'} \tag{2.55}$$

$$v\,\delta\varepsilon_v = C\frac{\delta q'}{p'} + D\frac{\delta p'}{p'} \tag{2.56}$$

Differentiating η' where $\eta' = q'/p'$, we have

$$\delta\eta' = \frac{\delta q'}{p'} - \frac{\eta'\,\delta p'}{p'} \tag{2.57}$$

Combine eqn (2.57) with eqns (2.55) and (2.56) and eliminate $\delta q'/p'$, we have

$$v\,\delta\varepsilon_s = A\,\delta\eta' + (A\eta' + B)\frac{\delta p'}{p'} \tag{2.58}$$

$$v\,\delta\varepsilon_v = C\,\delta\eta' + (C\eta' + D)\frac{\delta p'}{p'} \tag{2.59}$$

Re-arranging eqn (2.57), we have

$$\frac{\delta p'}{p'} = \frac{\delta\eta'}{\left(\frac{\delta q'}{\delta p'} - \eta'\right)} \tag{2.60}$$

Eliminating $\delta p'/p'$ in eqns (2.58) and (2.59), and using eqn (2.60), we have

$$v\,\delta\varepsilon_s = \left[A + \frac{(A\eta' + B)}{(\frac{\delta q'}{\delta p'} - \eta')} \right] \delta\eta' \qquad (2.61)$$

$$v\,\delta\varepsilon_v = \left[C + \frac{(C\eta' + D)}{(\frac{\delta q'}{\delta p'} - \eta')} \right] \delta\eta' \qquad (2.62)$$

Atkinson(1984c & 1985a) has suggested some normalising procedures for soil test data in which results should be plotted with η' against $v\varepsilon_s$. Eqns(2.61) and (2.62) have demonstrated that the normalised stress-strain curves are path dependent (dq'/dp') except for isotropic elastic soil (ie. $B = B^e = C = C^e = 0$).

Figs. 2.14 a and b illustrate the idealised state paths for lightly and heavily overconsolidated soils (states below state boundary surface) for which elastic behaviour (paths O_1A_1 and O_2A_2) is isotropic (ie. $A = A^e$; $B = B^e = 0$; $C = C^e = 0$; $D = D^e$) and is path independent until yielding occurs beyond A_1 and A_2 (see Fig. 2.14 c and d) and behaviour becomes elasto-plastic as defined by eqn (2.61). The behaviour of normally consolidated soil is elasto-plastic (paths OA_1 and OA_2 in Fig. 2.15) the soil starts to yield and harden as loading begins and the behaviour is governed by eqns (2.61) and (2.62). For conventional undrained loading (path OA_1 in Fig. 2.15), $\delta\varepsilon_v = 0$

eqn (2.56) becomes,

$$\frac{\delta q'}{\delta p'} = - \frac{D}{C} \tag{2.63}$$

sub. eqn(2.63) to (2.61), we have

$$v\,\delta\varepsilon_s = \left[A - \frac{(A\eta' + B)}{(\frac{D}{C} + \eta')} \right] \delta\eta' \tag{2.64}$$

For constant p′ loading (ie. $\delta p' = 0$), eqns(2.61) and (2.62) become

$$v\,\delta\varepsilon_s = A\ \delta\eta' \tag{2.65}$$

$$v\,\delta\varepsilon_v = C\ \delta\eta' \tag{2.66}$$

Comparing eqns (2.64) and (2.65), it clearly demonstrates the path dependency stress-strain behaviour of normally consolidated soil (see Fig. 2.15 d).

By re-arranging eqns(2.55) and (2.56), the normalised stiffnesses of soils (Atkinson, 1985a) can also be examined, ie.

$$\frac{\delta q'}{\delta\varepsilon_s}\Big/(vp') = \frac{1}{(A + B/\frac{\delta q'}{\delta p'})} \tag{2.67}$$

$$\frac{\delta p'}{\delta\varepsilon_v}\Big/(vp') = \frac{1}{(C\frac{\delta q'}{\delta p'} + D)} \tag{2.68}$$

It can be seen that the normalised stiffness parameters are also path dependent except for isotropic elastic materials (ie. $B = B^e = C = C^e = 0$). For undrained tests, where $\delta v = 0$ and $\delta q'/\delta p' = - D/C$ and eqn (2.67) becomes

$$\frac{\delta q'}{\delta \varepsilon_s}\Big/(v p') = \frac{1}{\left(A - \frac{BC}{D} \right)} \tag{2.69}$$

For constant p' test where $\delta q'/\delta p' = \infty$ eqn (2.67) becomes

$$\frac{\delta q'}{\delta \varepsilon_s}\Big/(v p') = \frac{1}{A} \tag{2.70}$$

Comparing eqn (2.69) with (2.70) it shows that the normalised shear stiffness parameter for undrained loading is higher than that for the drained loading at the same effective stress ratio, η' for a normally consolidated soils since all the compliances and also the products of the compliances (B & C) are likely to be positive (see Fig. 2.13).

2.4.2 Determination of the Compliance Parameters from Triaxial Tests

The normalised compliance parameters given in eqn (2.54) can be determined directly from results of special triaxial stress path tests (Atkinson and Richardson, 1985).

For constant p' test ($\delta p' = 0$), eqns (2.55) and (2.56) become

$$\frac{\delta q'}{\delta \varepsilon_s}\Big/(v p') = \frac{1}{A} \tag{2.71}$$

$$\frac{\delta q'}{\delta \varepsilon_v}\Big/(vp') = \frac{1}{C} \qquad (2.72)$$

respectively. Whilst for constant q′ test (δq′=0), eqn(2.55) and (2.66) become

$$\frac{\delta p'}{\delta \varepsilon_s}\Big/(vp') = \frac{1}{B} \qquad (2.73)$$

$$\frac{\delta p'}{\delta \varepsilon_v}\Big/(vp') = \frac{1}{D} \qquad (2.74)$$

Atkinson and Richardson (1985) adopted a successive constant p′ and q′ loading/unloading path approach from which all four compliances can be examined in a single test. The advantage of their approach is that it does not require the separation of the elastic and plastic components of strain for the examination of elasticity and normality (ie. if B = C). Alternatively, separate constant p′ and q′ tests with loading and unloading cycles (see section 7.3.3) can be conducted on identical specimens, from which the complete history of the individual compliance parameter can be examined. The latter approach has the advantage that test specimens do not suffer excessive changes of stress path directions, so that threshold effect (Richardson, 1988) can be avoided except in the early parts of the unloading and reloading cycles. However, this early threshold effect may have little affect on the results during yielding.

It should be noted that the compliance parameters can also be determined indirectly from results of a pair of different triaxial test paths (eg. undrained and drained test paths). However, this will

require further mathematical manipulations in order to examine the compliance parameters. In laboratory where advanced stress path equipment is not available, conventional triaxial test paths (ie. drained and undrained tests) are usually carried out on identical specimens. The following describes how the results from the conventional triaxial test paths can be used to obtain the compliance parameters.

For undrained test ($\delta v = 0$), sub. eqn(2.56) into eqns (2.67) & (2.68)

$$\frac{\delta q'}{\delta \varepsilon_s}\Big/(vp') = \frac{1}{(A - \frac{B.C}{D})} \tag{2.75}$$

$$\frac{\delta p'}{\delta \varepsilon_v}\Big/(vp') = \frac{1}{(\frac{-A.D}{C} + B)} \tag{2.76}$$

For conventional drained test ($dq'/dp' = 3$), eqns (2.67) and (2.68) become

$$\frac{\delta q'}{\delta \varepsilon_s}\Big/(vp') = \frac{1}{(A + \frac{B}{3})} \tag{2.77}$$

$$\frac{\delta p'}{\delta \varepsilon_v}\ (vp') = \frac{1}{(3C + D)} \tag{2.78}$$

respectively.

The compliance parameters can be obtained by normalising results as indicated in eqns (2.75) to (2.78) and by solving these four equations simultaneously with the four compliance parameters as unknowns at the same effective stress ratio, η'. A number of solutions

should be evaluated at different η' in order to obtain the complete history of these parameters.

2.5 A Model for the Behaviour of Anisotropic Soils

The critical state approach provides a conceptual framework for which some aspects of soil behaviour can be explained. In the preceeding sections it has been shown that the critical state theory recognised the existence of a state boundary which separates possible states from impossible states : behaviour below the surface is elastic while on the state boundary surface, elasto-plastic deformations will occur. The critical state model provides a single framework which accommodates the familiar Mohr-Coulomb strength criterion and the Terzaghi theory for one-dimensional consolidation. It also allows constitutive equations relating stress and strain to be developed for solutions to boundary value problems using computer based analytical methods (eg. the finite element method).

The original critical state models were developed for isotropically compressed soil, with symmetrical stress-strain behaviour about the mean effective stress, p′ axis (Schofield and Wroth, 1968 ; Roscoe and Burland, 1968 ; Atkinson and Bransby, 1978). Real soils are usually anisotropic and non-homogeneous. A number of tests results show that although the concept of a state boundary surface may be valid, the shape is unlikely to be symmetrical about either the isotropic or the η_o' axes. Moreover, the elastic behaviour is likely to be anisotropic

and plastic yielding may not be associated.

In order to improve the prediction of stress-strain behaviour of real soils, a number of mathematical models have been developed from the original critical state Cam-Clay model to attempt to account for such factors as anisotropy, non-associated flow and kinematic hardening (eg. Ohta and Wroth, 1976 ; Banerjee and Stipho, 1978 ; Pender, 1977 and 1978 ; Morz et al, 1981 ; Banerjee and Pan, 1986). These models are ,however, mathematically complex and remain to be calibrated with high quality experimental data. The author proposes a model named the City-Clay model to include anisotropy for both elastic and plastic deformations based on critical state concepts as well as from a number of high quality test data of anisotropically (K_o) compressed specimens under the axially symmetrical conditions provided by the micro-computer controlled Bishop and Wesley triaxial cells.

2.5.1 Some Aspects of the Behaviour of Anisotropically Compressed Soils

Experimental results show that there is strong evidence of the existence of state boundary surfaces for nominally 'undisturbed' natural clays (eg. Wong and Mitchell, 1975 ; Pender et al., 1975 ; Graham et al., 1983) and for anisotropically (K_o) compressed reconstituted and natural clay samples (eg. Parry and Nadarajah, 1973; Koustofas, 1980 ; Nakase and Kamei, 1983 ; Gens, 1983 ; Atkinson et al., 1986 ; Ng, 1985) whose shapes are not symmetrical about the isotropic p'-axis (see Figs. 2.16 to 2.21) and their results also

show significant anisotropic behaviour in a number of important respects, so that the Cam-Clay (Schofield and Wroth, 1968) and the Modified Cam-Clay (Roscoe and Burland, 1968) may not be able to predict adequately the behaviour of these soils.

The constant volume section of the state boundary surface for K_o normally consolidated soils (ie. on the wet side of the critical state : Roscoe Surface, Atkinson and Bransby, 1978) show a peak deviator stress in compression (see Figs. 2.18 to 2.21) which usually occurs at about 1/2 % shear strain (Jardine et al., 1985 ; Ho, 1985 ; Atkinson et al., 1986 ; Koustofas, 1981) before reaching a critical state value at large shear strain ($\varepsilon_s > 15$ %). The reasons for the drop from the peak deviator stress to critical state at constant volume during shear in compression while the effective stress ratio, q'/p' is increasing (hardening), are not clear. This may be attributed to the structural collapse characteristics of K_o normally compressed soils which is similar to the characteristics of aged sensitive soft clays (Mitchell, 1976). It is therefore necessary to identify this peak deviator stress and to distinguish it from the peak state of an overconsolidated soil as described in section 2.3.2 and also from the critical state which occurs at large shear strain (see Fig. 2.22).

Limited experimental data show that the elastic behaviour of soils (behaviour below state boundary surface) is anisotropic (eg. Graham and Houlsby, 1983 ; Ho, 1985 ; Koustofas, 1981 ; Ng, 1985 ; Richardson, 1985). The normalised tangent shear stiffness in compression is

significantly lower than that in extension test for K_o normally compressed soils (Ho, 1985 ; Ng, 1985).

2.5.2 The Development of Constitutive Equations

A complete general incremental form of elasto-plastic constitutive equations for anisotropic soils is developed based on approaches as described in section 2.3.2. The soil behaviour is taken to be cross-anisotropic for states within the state boundary surface and elasto-plastic when the soil state traverses the state boundary surface from which the plastic strain is calculated from a non-associated flow rule. The proposed model (the City-Clay) is simple to use and requires the usual critical state soil parameters to describe the complete incremental stress-strain behaviour of anisotropic soils.

2.5.2.1 The Cross-Anisotropic Elastic Constitutive Equations

The complete cross-anisotropic elastic incremental constitutive equation (Graham and Houlsby, 1983) is given by :

$$\begin{bmatrix} \delta\varepsilon_s^e \\ \delta\varepsilon_v^e \end{bmatrix} = \frac{1}{3G'K'-J'^2} \begin{bmatrix} K' & -J' \\ -J' & 3G' \end{bmatrix} \begin{bmatrix} \delta q' \\ \delta p' \end{bmatrix} \qquad (2.79)$$

By following the procedures given by Graham and Houlsby (1983), the

elastic compliance parameters can be written in the form of :

$$\frac{K'}{3G'} = \frac{2(1-\bar{\nu}'+4\alpha\bar{\nu}'+2\alpha^2)}{9(2(1-\bar{\nu}')-4\alpha\bar{\nu}'+\alpha^2)} \tag{2.80}$$

$$\frac{3G'}{J'} = \frac{3(2(1-\bar{\nu}')-4\alpha\bar{\nu}'+\alpha^2)}{2(1-\bar{\nu}'+\alpha\bar{\nu}'-\alpha^2)} \tag{2.81}$$

$$\frac{K'}{J'} = \frac{(1-\bar{\nu}'+4\alpha\bar{\nu}'+2\alpha^2)}{3(1-\bar{\nu}'+\alpha\bar{\nu}'-\alpha^2)} \tag{2.82}$$

$$\alpha^2 = \frac{E_h'}{E_v'} \tag{2.83}$$

$$\bar{\nu}' = \alpha\nu_{vv}' = \nu_{vh}' \tag{2.84}$$

where subcripts v and h in eqn(2.84) refer to vertical and horizontal directions respectively. From eqn (2.43), where $1/K' = \kappa/vp'$ and combines with eqn (2.84) and we have

$$\frac{1}{J'} = \frac{(1-\bar{\nu}'+4\alpha\bar{\nu}'+2\alpha^2)}{3(1-\bar{\nu}'+\alpha\bar{\nu}'-\alpha^2)} \cdot \frac{\kappa}{vp'} \tag{2.85}$$

$$\frac{1}{3G'} = \frac{(1-\bar{\nu}'+4\alpha\bar{\nu}'+2\alpha^2)}{9(1-\bar{\nu}'-2\alpha\bar{\nu}'+\alpha^2/2)} \cdot \frac{\kappa}{vp'} \tag{2.86}$$

substitute eqns (2.85), (2.86) and (2.80) into eqn (2.79), we have

$$\begin{bmatrix} \delta\varepsilon_s^e \\ \delta\varepsilon_v^e \end{bmatrix} = \begin{bmatrix} \frac{1}{vp'} \end{bmatrix} \begin{bmatrix} A^e = f(\alpha,\bar{\nu}') & B^e = f(\alpha,\bar{\nu}') \\ C^e = f(\alpha,\bar{\nu}') & D^e = f(\alpha,\bar{\nu}') \end{bmatrix} \begin{bmatrix} \delta q' \\ \delta p' \end{bmatrix} \qquad (2.87)$$

where the elastic compliance parameters A^e to D^e are given in Appendix C. It remains to determine the values of $\bar{\nu}'$ and κ, and also α (see eqn 2.83) in order to describe the complete cross-anisotropic elastic stress-strain behaviour of a soil. For undrained tests (ie. $\delta\varepsilon_v = 0$), rearranging eqn (2.79), we have

$$\frac{\delta q'}{\delta p'} = \frac{3G'}{J'} \qquad (2.88)$$

From eqns (2.81) and (2.88), the slope of the undrained effective stress path is governed only by α and $\bar{\nu}'$. For $\alpha = 1$ (ie $E_h' = E_v'$, isotropic soil), the undrained effective stress path is vertical ($dq'/dp' = \infty$) and eqn (2.44) recovers from eqn (2.87). For $\alpha < 1$ (vertically stiffer : $E_h' < E_v'$) and $\alpha > 1$ (horizontally stiffer : $E_h' > E_v'$), the estimated directions of the undrained effective stress paths are given in Fig. 2.23. A single value of α can be chosen for soil by determining the average slope of the undrained effective stress path (ie. straight stress path for a value of $\bar{\nu}'$ (say 0.25) using eqns (2.81) and (2.88). For paths which are highly non-linear, it is necessary to determine a number of values of α along that path for analysis.

2.5.2.2 The Elasto-Plastic Constitutive Equations

Using similar approaches as described in section 2.3.2, the exact equations for the state boundary surface (eqn 2.45) and for the flow rule (eqn 2.48) are required to describe the complete elasto-plastic stress-strain behaviour for anisotropic soils (ie. eqn 2.50).

To date no theoretical model (ie. with the consideration of energy dissipation) has been developed to account for anisotropy due to anisotropic compression. It may be necessary, at present, to consider the anisotropic state boundary surface and the flow rule independently and to derive the constitutive equations semi-empirically from experimental data (eg. Atkinson and Bransby, 1978) so that some assessments on the prediction of the behaviour of anisotropic soil can be made.

The equations for the anisotropic state boundary surface have been investigated by a number of researchers (eg, Ohta, 1973 ; Pender, 1977 and 1978 ; Mroz et al., 1981) and more recently by Atkinson et al. (1986). The predicted shapes of the state boundary surface given by Pender (1977 and 1978) and Atkinson et al.(1986) provide better fits to the wet side of the state boundary surface (Atkinson and Bransby, 1978) of a number of different K_o compressed soils (comparing Fig. 2.19 with Fig. 2.25 for Speswhite kaolin and Fig. 2.20 with Fig. 2.26 for Cowden Till). Although similar shapes of the anisotropic state boundary surface can be predicted using these

two equations (see Figs. 2.25 and 2.26) Pender's equation is slightly advantageous due to its flexibility in choosing the exact position of the critical state at constant volume (p_u'/p_e'). Whereas Atkinson et al.(1986) fix $p_u'/p_e' = (1/2)^{1-\frac{\kappa_o}{\lambda_o}}$ which is an extended version of Modified Cam-Clay (see Appendix A). For the purpose of this thesis, the proposed model (the City-Clay) was developed based on Pender's equation for the state boundary surface, although similar approaches can be used to develop models using different state boundary surfaces (eg. Atkinson et al., 1986).

The original equation for the undrained effective stress path (Pender, 1977 and 1978) is written as

$$\left[\frac{\eta' - \eta_o'}{M - \eta_o'}\right]^2 = \frac{p_u'}{p'} \cdot \frac{(1 - \frac{p_o'}{p'})}{(1 - \frac{p_o'}{p_u'})} \qquad (2.89)$$

where η' = q'/p' , the current effective stress ratio

η_o' = effective stress ratio at K_o state

p'_o = initial mean effective stress before undrained loading

p'_u = mean effective stress at critical state for undrained loading.

Re-arranging eqn (2.89), we have

$$\left(\frac{\eta' - \eta_o'}{M - \eta_o'}\right)^2 = \frac{p_u' \cdot p_o'}{p_o' \cdot p'} \cdot \frac{(1 - \frac{p_o'}{p'})}{(1 - \frac{p_o'}{p_u'})}$$

or

$$\left(\frac{p_o'}{p'}\right)^2 - \frac{p_o'}{p'} + C' = 0 \qquad (2.90)$$

where $C' = \left(\frac{\eta' - \eta'_o}{M - \eta'_o} \right)^2 \cdot \frac{p'_o}{p'_u} \left(1 - \frac{p'_o}{p'_u} \right)$ (2.91)

Eqn (2.90) is a quadratic equation containing two roots, ie,

$$\frac{p'_o}{p'} = \frac{1 \pm \sqrt{1 - 4C'}}{2}$$

or

$$\frac{p'}{p'_o} = \frac{2}{1 \pm \sqrt{1 - 4C'}} \qquad (2.92)$$

Eqn (2.92) represents the locus of the roots of eqn (2.90) which relate p'/p_o' and η' directly. For state boundary surface (wet side of the critical), $0 < p'/p_o' < 1$, the true root of eqn (2.92) is

$$\frac{p'}{p'_o} = \frac{2}{1 + \sqrt{1 - 4C'}} \qquad (2.93)$$

Eqn (2.93) is the simplified Pender's equation (ie. eqn 2.89) and can be taken as the normalised constant volume section of the state boundary surface.

Where $p_o' = p_e'$ (Atkinson and Bransby, 1978) eqn (2.93) becomes

$$\frac{p'}{p'_e} = \frac{2}{1 + \sqrt{1 - 4C'}} \qquad (2.94)$$

normalised section of the yield locus. Where $p_o' = p_p'$ (Atkinson 1984c), eqn(2.93) can be written as

$$\frac{p'}{p'_p} = \left[\frac{2}{1 + \sqrt{1 - 4C'}} \right]^{\lambda/(\lambda_o - \kappa_o)} \qquad (2.95)$$

From the derivation of the constitutive equations for Modified Cam-Clay (see Appendix A), the state boundary surface can be written as

$$v = \Gamma - \kappa_o \ln p' - (\lambda_o - \kappa_o) \ln p'_x \qquad (2.96)$$

At critical state, $p' = p'_x$: $\eta' = M$: eqn (2.95) becomes

$$\frac{p'_x}{p'_p} = \left[\frac{p'_u}{p'_o} \right]^{\lambda_o / (\lambda_o - \kappa_o)} \qquad (2.97)$$

sub. eqn(2.95) into eqn (2.97), we have

$$\frac{p'_x}{p'} = \left[\frac{p'_u}{2 p'_o} \cdot \left(1 + \sqrt{1 - 4C'} \right) \right]^{\lambda_o / (\lambda_o - \kappa_o)} \qquad (2.98)$$

sub. eqn (2.98) into eqn (2.96) and eliminate p_x', we have the state boundary surface, ie.

$$v = \Gamma - \lambda_o \ln p' - \lambda_o \ln \left(\frac{p'_u}{2 p'_o} \right) - \lambda_o \ln \left(1 + \sqrt{1 - 4C'} \right) \qquad (2.99)$$

For $v = N_o$, $\eta' = \eta'_o$ and $\Gamma = \Gamma_o$ at $p' = 1$, eqn(2.99) becomes

$$N_o - \Gamma_o = -\lambda_o \ln \left(\frac{p'_u}{p'_o} \right) \qquad (2.100)$$

For constant p' section, where $v_\lambda = v + \lambda_o \ln p'$ (Atkinson and Bransby, 1978), eqn (2.99) can be written as

$$v_\lambda = \Gamma_o - \lambda_o \ln \left(\frac{p'_u}{2 p'_o} \right) - \lambda_o \ln \left(1 + \sqrt{1 - 4C'} \right) \qquad (2.101)$$

From eqn (2.99), the constitutive equation such as eqn (2.47) can be obtained and is given by

$$\delta\varepsilon_v^p = \frac{1}{vp'}\left\{\left[\frac{-4\lambda_o C'}{(\eta'-\eta_o')(1-4C'+\sqrt{1-4C'})}\right]\delta q' + \left[(\lambda_o-\kappa_o)+\frac{4\lambda_o C'\eta'}{(\eta'-\eta_o')(1-4C'+\sqrt{1-4C'})}\right]\delta p'\right\} \quad (2.102)$$

The constitutive equation for plastic shear strain increment $\delta\varepsilon_s^p$ (eqn 2.49) can now be obtained by relating an appropriate flow rule, F to eqn (2.102).

The precise requirements for a particular flow rule for an anisotropic state boundary surface are not known. However, from the shape of the constant volume section of the anisotropic state boundary surface of a number of different soils reported previously (see Figs 2.16 to 2.21) and assuming that κ_o/λ_o is small (ie. the yield locus section becomes similar in shape with the constant volume section of the state boundary surface), it can be seen that associated flow rule can not be applied. Normality conditions on anisotropic state boundary surfaces do not meet the requirements of critical state theory (ie. at constant volume $\delta v = 0$; see Fig. 2.24). Therefore it may be necessary, at present, to derive a suitable flow rule $F = \delta\varepsilon_s^p/\delta\varepsilon_v^p$ such that it depends only on the current state of stress, η' causing yield which also satisfies consistent boundary conditions in both compression and extension at critical state.

Under the condition of axial symmetry ($\delta\varepsilon_2 = \delta\varepsilon_3 = 0$),

$$\frac{\delta\varepsilon_s}{\delta\varepsilon_v} = \frac{2}{3} \tag{2.103}$$

$$F = \frac{\delta\varepsilon_s^p}{\delta\varepsilon_v^p} = \frac{\delta\varepsilon_s - \delta\varepsilon_s^e}{\delta\varepsilon_v - \delta\varepsilon_v^e} = \frac{\frac{\delta\varepsilon_s}{\delta\varepsilon_v} - \frac{\delta\varepsilon_s^e}{\delta\varepsilon_v}}{1 - \frac{\delta\varepsilon_v^e}{\delta\varepsilon_v}} \tag{2.104}$$

Differentiating eqn(2.43) and combine with eqns (2.103) and (2.24), we have the flow rule at K_o conditions, ie.

$$\left[\frac{\delta\varepsilon_s^p}{\delta\varepsilon_v^p}\right]_{\eta'_o} = \frac{(2/3 - \frac{\delta\varepsilon_s^e}{\delta\varepsilon_v})}{(1 - \kappa_o/\lambda_o)}$$

or

$$\approx \frac{2/3}{(1 - \kappa_o/\lambda_o)} \tag{2.105}$$

For the conditions at critical state,

$$\left[\frac{\delta\varepsilon_s^p}{\delta\varepsilon_v^p}\right]_M = \infty \tag{2.106}$$

For the conditions at $q' = 0$, Graham et al. (1983) indicated that

$$\left[\frac{\delta\varepsilon_s^p}{\delta\varepsilon_v^p}\right]_{\eta'=0} = -ve \tag{2.107}$$

However, some uncertainties regarding to the flow rule arise between $\eta' = \eta'_o$ and $\eta' = 0$, eg. the value of F at $\eta' = 0$ (see Fig 2.24a). Fig. 2.24b illustrates two possibilities for the flow rule linking compression and extension. The first possibility has a step change at $\eta' = \eta'_o$ from which F = 0 for extension and $F=(2/3)/(1-\frac{\kappa_o}{\lambda_o})$ for compression. The second possibility contains a smooth curve

joining the compression and extension flow rule with $F < 0$ at $\eta' = 0$. The latter one has been chosen to develop an expression for a flow rule which satisfies eqns (2.105), (2.106) and (2.107) and is given by

$$F = \frac{\eta' - \eta'_o}{(M - \eta')^2} + \frac{2/3}{(1 - \kappa_o/\lambda_o)} \qquad (2.108)$$

Eqn (2.108) is a non-associated flow rule in that $F = \delta\varepsilon_s^p / \delta\varepsilon_v^p \neq \delta q'/\delta p'$ where $\delta q'/\delta p'$ is the derivative of eqn (2.95).

By combining eqn (2.108) with (2.102) and with eqn (2.87), the complete elasto-plastic constitutive equations in the form of eqn (2.37) can be written as,

$$\begin{bmatrix} \delta\varepsilon_s \\ \delta\varepsilon_v \end{bmatrix} = \left[\frac{1}{vp'}\right] \left\{ \begin{bmatrix} A & B \\ C & D \end{bmatrix}^e + \begin{bmatrix} A & B \\ C & D \end{bmatrix}^p \right\} \begin{bmatrix} \delta q' \\ \delta p' \end{bmatrix} \qquad (2.109)$$

where the elastic compliance parameters $[A, B, C, D]^e$ are defined by eqn (2.87) and the plastic compliance parameters $[A, B, C, D]^p$ are defined by eqns (2.102) and (2.108), and $1/vp'$ is a common factor of the compliance matrix (see Appendix C) which is similar to those of Cam-Clay (eqn 2.52) and Modified Cam-Clay (eqn 2.53). The use of eqn(2.102) will require the knowledge of the critical state parameters (M, λ_o, κ_o, μ') and will also require the ratio, p_{cs}'/p_o' and the slope of the undrained effective stress path to be

specified ($\delta q'/\delta p'$) for an overconsolidated soil in order to describe the complete incremental stress-strain behaviour of an anisotropic elasto-plastic soil.

2.5.4 Discussion

The previous sections have described the necessity of a constitutive model for anisotropic soil due to K_o compression. Such a model has been proposed (the City-Clay) and was developed within the framework of critical state concepts that the state boundary surface is not symmetrical about the isotropic p′ stress axis and the flow rule which governs the plastic strain increments is non-associated.

The patterns of the individual compliance parameters (eqn 2.54) of the City-Clay model using soil constants for Speswhite kaolin clay (Ho, 1985) are given in Fig. 2.26, which show great differences in behaviour compared with those of Cam-Clay and Modified Cam-Clay models given in Fig. 2.13. The predicted undrained tangent shear stiffnesses using eqn (2.67) and assume that soil elastic behaviour is isotropic (ie. $J' = 0$; $B^e = 0$ $C^e = 0$) with a constant Poisson's ratio ν' of 0.25 are given in Fig 2.27. It can be seen that good agreement is found between the predicted and the experimental derived compression tangent shear stiffness. However, the extension stiffness has been underestimated at small strain ($|v. \varepsilon_s| < 0.2\%$). The reason for this may be partly due to the anisotropic elastic response of the K_o kaolin clay which has not been incorporated in the analysis and the

possibility of the plastic threshold effects (Atkinson 1987). However, the assumptions made for the present analysis do give promising predictions of K_o soil behaviour in compression and extension.

The advantage of using the City-Clay model is that it does offer some insight into the differences between the compression and the extension behaviour of anisotropic soils. Its constitutive equations, whose derivation is based on critical state concepts only require the usual critical state soil constants (Schofield and Wroth, 1968 ; Roscoe and Burland, 1968) to describe the complete incremental stress-strain behaviour of anisotropic soils. However, the suitability of this soil model must be assessed by calibration against data from tests on a range of K_o compressed soils and this is reported and discussed in sections 9.5 and 9.6.

Chapter 3 : Marine Geology

3.1 The Ocean Basins

The earth is about 4,600 million years old. At present 80% of its surface is covered by water, so only 20% is available for direct observation. The features of the submarine topography were not even suspected at the beginning of the present century. It is largely through the use of geophysical techniques that we are now able to describe the great submerged basins, mountains etc.(eg. Houtz and Ewing, 1963 ; Hamilton, 1967).

There are two hypotheses explaining the formation of the ocean basins, i) sea floor spreading, ii) plate tectonics. The sea floor spreading hypothesis (Heirtzler, 1968) is largely based on the observation from the geophysical techniques that two oceanic crustal blocks move away from one another. The plate tectonics hypothesis (Dewey, 1972) is that the continental and the oceanic crust of the earth are made up by six major tectonic plates which move over and beneath one another as a single unit. Details of the mechanism of the two hypotheses involved are outside the scope of this thesis.

An idealised section of the ocean floor is given Fig. 3.1. It is divided into four major parts, i) continental shelves, ii) continental slopes, iii) continental rises, iv) abyssal plains.

The continental shelves extend from the edges of the continental land mass to a depth of a few hundred metres. The shelves extend up to about 50 to 80 km wide and at about 1:2000 slope inclination. They were above sea level during the Pleistocene glaciation when much of their erosion and sedimentation characteristics were formed and their surfaces modified by wave and tidal currents.

Beyond the shelves, the ocean floor is marked by a sudden increase in slope to about 1:20 for a distance of about 15 km and is called the continental slope. The sediments on these slopes are mostly muds and silty sands derived from the continental erosion and which have been carried across the shelves and draped over the edges (Demars and Anderson, 1971). As the sediments accumulate they slump and slide down the slope as "turbidity currents". A turbidity current is able to transport large quantities of sedimentary material introduced with the original slump and picked up by the current as it flows over the seabed.

The lower part of the slope becomes gentler (1:100) and is called the continental rise and extends much further (about 200 to 400 km from the land mass) at water depths of about 4 km. It is on the continental rise that turbidity currents start to lose speed and produce single graded beds of sand, silt and clay called turbidites. The extent of turbidites may reach beyond the rises to the flat deep sea bottom called the abyssal plain with water depths in excess 5 km .

3.2 Types and Distributions of Ocean Sediments

Ocean sediments can be divided into two main groups, comprising pelagic and terrigeneous deposits. The main basis for classifications appears to be source and origin of deposition (see Table 3).

3.2.1 Pelagic Deposits

These are materials comprised largely of the remains of marine organism, volcanic ashes and wind-borne dust etc. which settle out from the water column (Longwell and Flint, 1962). The deposition rate is very slow, about 0.1 to 30 mm per 1000 years (see Table 3.1). Pelagic sediments cover almost 3/4 of the world's ocean floor at water depths in excess of 4.5 km (48 % calcareous; 14 % siliceous; 38 % brown clay; Ewing et al., 1973) and are found predominantly in the Pacific Ocean (Horn et al., 1974).

3.2.2 Terrigeneous Deposits

These deposits are comprised of various proportions of clay, silt, sand and gravel size (Davie et al., 1978). Their properties depend on the morphological constraints, such as the slope gradient of the ocean floor. The depositional mechanisms (eg. turbidity currents) can give the terrigeneous deposits a heterogenous nature. The coarse materials transported by a turbidity current or flow slide will be deposited on the steeper continental slope to form " proxal turbidites ",while silts

and clays will be deposited on the flatter slope of the continental rise or even reaching the flat abyssal plain as " distal turbidites " depending on the speed and the density of the turbidity current (Embly and Jacobi, 1977).

The turbidite layers are generally between a few centimetres to metres thick as they were deposited in a single geological event. The average period of occurrence of a single turbidity current is not known exactly, probably about the same order as interglacial periods of 10,000 years. Therefore above each turbidite layer , pelagic deposits can build up to form a bed of hemi-pelagic deposits. The terrigeneous deposits occur more frequently in the North Atlantic than the North Pacific Ocean. This is mainly due to the presence of the tectonic boundary which acts as a barrier round the perimeter of the Pacific and also a smaller catchment area supplying river sediments to the Pacific Ocean (Hornet al., 1974).

3.3 The Great Meteor East (GME) Study Area

3.3.1 Regional Setting

The principal area of the Great Meteor East (GME) is situated between 30.5^{o}N and 32.5^{o}N, 23^{o}W and 26^{o}W (see Fig.3.2) on the western margin of the Madeira Abyssal Plain (MAP) in the centre of the Canary Basin. Immediately to the west of GME the abyssal plain abuts against the lower flank of the Mid-Atlantic Ridge which is

characterised by numerous abyssal hills and seamounts. The central and deepest part of the Canary Basin is occupied by the MAP, a narrow strip of flat seafloor about 200 km wide. It's eastern edge includes the lowermost part of the Madeira-Tore Rise, the Canary Rise and the North-Western African Continental Rise (see Fig. 3.3). Water depths in most areas at GME vary between 5 and 5.5 km (Searle et al., 1985).

3.3.2 Sedimentology

Sediment thickness within the GME varies from zero to over 2 km. The greatest thickness occurs in the narrow basement valleys in the centre of the area and in the fracture zone. Sediment thicknesses in excess of 250 metres characterises most of the area, including almost all of the area beneath the abyssal plain (Searle et al., 1985).

Sediments fall into two basic types : turbidites and pelagic deposits (see section 3.2). These two types of sediments alternate generally with thick turbidite layers (0.5 to 5 metres thick) separated by thin layers of pelagic deposits. Sedimentation in this area is cyclical with the pelagic units being deposited very slowly and the turbidites rapidly. The rate of deposition for the pelagic unit varies from about 0.25 to 0.6 centimetres per 1000 years. The period of deposition of a single turbidite is not known but is likely to be less than one year (Bowen et al., 1984). Studies on some recovered core samples show that the mean sedimentation rate varies from 4.6 to 10 centimetres per 1000 years (Searle et al., 1985).

It has been shown by Searle et al. (1985) that the turbidites originate from the upper continental slope of north-west Africa or possibly from the Madeira Rise (see Fig.3.3). The large scale sediment mass movement on the upper continental slope off north-west Africa seems to be triggered during major sea level rises and falls (ie. at the beginning or the end of an ice-age), but not during the quiet intervals between them (Embly, 1976 ; Searle et al., 1985).

3.3.3 Sediment Properties

Extensive laboratory tests (eg. index, oedometer, strength tests etc). have been carried out on a number of recovered core samples. Results of these tests show that these sediments are very soft in their natural states with natural water content above the liquid limit. Generally they contain about 60% calcium carbonate and clay fraction ($< 2\,\mu m$) varies between 40% and 60% (see Fig. 3.5a). Results also show that these sediments are highly compressible with the compression index, C_c varying between 0.5 and 1.5 (Fugro, 1982) and the measured permeability within the turbidite layers being in the order of 10^{-7} to 10^{-8} m/s (Searle et al., 1985). The undrained shear strength ratio, c_u / σ_v' obtained from triaxial compression tests on the same sample core is found to be approximately 0.25 for unconsolidated undrained tests and 0.35 for consolidated undrained tests (Freeman, 1984 ; see Fig. 3.5c). Results of the motor-vane tests on other core samples reported by RGD (1982) show that the vane strength increases with depth with an average sensitivity of about 4

(Fig. 3.6b). The sudden increase in strength at depths of 4.5 metres and 8.5 metres corresponds to thin layers of hemi-pelagic and pelagic clays (see section 3.2). It is not clear whether the pelagic clays are stronger than the turbidites or whether this is only a result of sample disturbance (Freeman, 1982).

3.4 The Nares Abyssal Plain (NAP) Study Area

3.4.1 Regional Setting

The Nares Abyssal Plain (NAP) site is situated between 22^{O} N and $24^{O}10'$N, $60^{O}50'$W and 66^{O}W (see Fig. 3.2), and is bounded in the south by the Greater Antilles Ridge, in the west by the Vema Gap and by the edge of the Southern Bermuda Rise in the north (see Fig. 3.4 ; Duin, 1984). The NAP site is an essentially flat area, dipping gently to the north and east (gradient ~1:2000) and is interrupted only by isolated volcanic peaks and basement highs. Water depths in most of the area vary between 5.5 and 6 km.

3.4.2 Sedimentology

Generally the NAP sediment thickness lie between 300 and 700 metres, the average thickness is being approximately 500 metres Duin, 1984). Studies show that the upper stratified sediments are deposited partly by turbidity currents (see section 3.2), thus the sediment column is rather variable (Kuijper, 1984). It may contain

predominantly pelagic sediments laminated with turbidite silts or a few tens of metres of turbidites interbedded with pelagic deposits. In general the sediment column can be characterised by a number of more or less consistent sedimentary units (pelagic and turbidite deposits). These consist of interbedded limestones and cherts, together with consolidated and unconsolidated silts, clays and microfossil oozes.

The average sedimentation rate for the pelagic clays is about 2 to 3 centimetres per 1000 years and about 10 to 50 centimetres per 1000 year for turbidites in the area (Kuijper, 1984). At present turbidites enter the NAP area only through the Vema Gap in the west after they have traversed the Southern Hatteras Abyssal Plain (Duin, 1984 ; see Fig. 3.4).

3.4.3 Sediment properties

Results of laboratory tests on some recovered core samples (see Table 3.2 for core details) show that these sediments are very soft and contain not more than 10 % calcium carbonate with clay fraction varying between 70% and 80% for pelagic clays and between 20% and 40% for turbidites (RGD, 1984 ; see Fig. 3.7). The fine grain portions of the turbidites are found to be very compressible with the compression index lying between 0.5 and 1.0 (Fugro, 1985) and the permeablility between 10^{-9} and 10^{-10} m/s (Shepard, 1984). The undrained shear strength generally increases with depth (Shepard, 1984 ; see Fig. 3.8) with the maximum strength occurring immediately adjacent to

the silt rich base of the turbidite interval, which is almost twice the strength determined from the overlying more clay rich sediment.

In the absence of any major geological event such as erosion and glaciation taking place in the deep-ocean seabed, the sediments should be normally consolidated soils (ie. the current vertical effective stresses should not have been exceeded; Terzaghi and Peck, 1967). Results reported by other researchers showed that deep-ocean sediments are overconsolidated (OCR > 1) particularly over the top few metres of the seafloor (eg. Demars, 1975; Carchedi, 1979; Silva et al., 1984) and underconsolidated at deeper depths (eg. Silva and Jordan, 1984). Their results also showed that deep-ocean sediments are aged, cemented in-situ (Nacci et al., 1975; Kelly et al.,1974) and may show a grain crushing phenomenon (Valent, 1979 and Valent et al., 1982).

Most of the deep-ocean sediment information reported in the literature has been obtained from tube sampling and the geotechnical data for these sediments were mostly obtained from the results of conventional shear strength tests (eg. motor-vane and fall-cone tests) and from oedometer tests on specimens taken from tubed samples (eg Buchan et al., 1971; RGD, 1982). These testing techniques are at best approximate methods of measuring the geotechnical properties of fine grain soils and when performed on recovered samples there are additional effects of samples disturbance due to pore water expansion. To-date extensive laboratory strength measurements (eg. triaxial testing) have been performed on recovered deep-ocean

sediments tubed samples and most of these tests are either unconsolidated or isotropic consolidated undrained compression tests (eg. Demars,1975; Valent et al., 1982; Silva et al , 1984). Little information is available on the behaviour of K_o consolidated deep-ocean sediment samples. Nevertheless the conventional triaxial test will improve the credibility of both stress-strain stiffnesses and strength profiles, although the uncertainties concerning the effects of sampling disturbance and pore water expansion due to the excessive total stress release (~ 50 MPa) will remain.

A summary of the available published basic geotechnical properties (eg. m , LL , PL , particle size , vane strength profiles) of some North Pacific and North Atlantic deep-ocean sediments taken along the recovered sample cores is given in Figs. 4.1 to 4.10 (see Tables 4.1 and 4.2 for core details).

4.1 Index Properties

The basic index properties of deep-ocean sediments are mostly available in the literature. Plasticity charts for some of the North Atlantic and North Pacific deep-ocean sediments have been summarised by OAP (1982), see Figs.4.11 (a) and (b). It can be seen that all the results plot adjacent to the A-line except for the high carbonate clayey silts reported by Nacci et al.(1975) which are below the A-line. This may reflect the presence of water trapped within the calcareous soil skeleton.

Index test results are obtained from tests based on experience on terrestrial soils. To-date no standard method of preparation and testing for deep-ocean sediments has been published. Richards (1974) suggested some standardised methods of index tests for deep-ocean sediments regarding the presence of salt in the sediments, while Noorany (1982) introduced a simplified equation for the calculation of salt-water content. Demars et al. (1976) suggested carbonate content as an index property for ocean calcareous sediments since the results of the index properties obtained by conventional testing techniques may be questionable due to the high water-holding capacity and the susceptibility to crushing of the calcareous particles.

4.2 Consolidation and Compression Characteristics

A large number of laboratory consolidation tests have been performed on samples of deep-ocean sediments mainly recovered from shallow depths (top 8 metres). Most of these tests have been performed either in conventional oedometers or in back pressured type of consolidometers to ensure full saturation during testing. No significant difference has been found on the evaluation of the consolidation characteristics by these two methods (Clukey and Silva, 1981 ; Valent, 1979 ; Nickerson, 1978).

The shape of the void ratio versus log σ_v' curve for a normally consolidated soil will be straight with pre-consolidation vertical effective stress, σ_{vc}' equals to in-situ vertical effective stress,

σ_{VO}' (ie. OCR =1). Results presented by Bryant et al.(1974) for some deep-ocean carbonate sediments from the Gulf of Mexico show concave upward e-log σ_V' curves (see Fig.4.12) which make the determination of value of σ_{VC}' and the compression index, C_C very difficult. These concave upward e-log σ_V' curves may be associated with sensitive clay fabric (Terzaghi and Peck, 1967), but other deep-ocean carbonate and non-carbonate sediments do not show sigificant concave e-log σ_V' curves (eg. Demars,1975 ; Valent et al., 1982 ; Silva and Hollister, 1979 ; Silva and Jordan, 1984 ; see Figs. 4.13 to 4.16).

A number of empirical correlations between the compression index and some index properties have been developed for terrestrial and shallow marine soft clays (see Table 4.3). They provided a framework from which to compare the results of deep-ocean sediments. Nacci et al. (1975) suggested that, on average, marine clays were more compressible than terrestrial clays with the same liquid limit. It was suggested that these higher compressibilities for marine clays could probably be attributed to the more highly flocculated microstructure of the clays deposited in a saline environment. A new empirical correlation between the compression index and plasticity index (see Fig. 4.17) based on results of a large number of tests on two types of North Atlantic deep-ocean biogenic oozes was then developed. A comprehensive study on the prediction of the compression index using these empirical correlations, (Valent et al., 1982) led to the conclusion that none of these correlations could accurately predict the compression indices of the types of North Atlantic calcareous

oozes they tested. Demars et al.(1976) showed that the compression index decreased with increasing carbonate content (see Fig. 4.18) which also agreed well with the investigations by Poulos (1980), see Figs. 4.19 and 4.20.

The reasons for the overconsolidated behaviour particularly over the top few metres of the seabed (see Figs. 4.21 and 4.22) , is not clear. Experiences based on terrestrial soils and near shore marine clays suggested that this behaviour may be attributed to ageing and delayed consolidation (Bjerrum, 1967 and 1973). Cementation of deep-ocean carbonates (Kelly et al., 1974; Nacci et al., 1975) is also a likely contributory factor. The effects of carbonates on overconsolidaton ratio has been investigated by Demars, 1975 on some North Atlantic carbonate sediments. His results are plotted in Fig. 4.23 which indicate that overconsolidation ratio increases with calcium carbonate content. At shallow depth, all above reasons for the overconsolidated behaviour are possible whereas gravitational consolidation due to the increasing sediment overburden may exceed these effects (ie. pre-consolidation pressure, σ_{vc}') at depths below about five metres of the seabed and this suggests that ageing and cementation bonds may be fairly weak in these sediments. Due to the slow rate of sedimentation of these sediments the reason for the underconsolidation at deeper depth is not clear, except it may be a result of sampling disturbance (Hvorslev, 1949).

Results of consolidation tests yield coefficient of consolidation,

c_v and the coefficient of volume compressibility, m_v from which the permeability, k can be calculated from the equation, $k = \gamma_w \cdot c_v \cdot m_v$ (Terzaghi, 1943). Very little information can be found in the literature on the values of c_v for deep-ocean sediments (for limited published data, see Table 4.4). The permeability can also be calculated directly by imposing a hydraulic gradient across the sample and measuring the flow rate. Clukey and Silva (1981) have compared permeability values derived by these two methods and found reasonable agreement between them. Silva et al.(1984) and Bryant et al. (1975) present results of the coefficient of permeability of a number of deep-ocean sediments with a range of void ratios (see Figs. 4.24 to 4.26). It can be seen that the Atlantic calcareous sediments are more permeable than the Pacific clays. The typical values of permeability vary from 10^{-8} to 10^{-10} m/s at low effective stresses and high void ratios.

Under the condition of deposition in the deep-ocean, the sediments are consolidated under K_o conditions ie. no lateral strain . K_o values can be measured either by laboratory equipment eg. instrumented oedometers (Brooker and Ireland, 1965) , triaxial apparatus (Bishop and Henkel, 1962) or by in-situ equipment eg. pressuremeters (Wroth, 1984). There is little information in the literature on the values of K_o of deep-ocean sediments. The available K_o values are mostly determined by conventional laboratory triaxial testing equipment (eg. Herrmann and Houston, 1976 ; Sicilliano, 1984 ; Marine Geotechnical Consortium, 1985) and their results are summarised in Table 4.4 . It

can be seen that the K_o values of the Atlantic silts and clays are lower than those of the Pacific pelagic clays.

4.3 Stress-Strain Behaviour

Very little detailed published data can be found on the stress-strain stiffnesses of deep-ocean sediments. Some geophysical studies have been made on the elastic properties of seafloor sediments (Hamilton, 1971), indicating values of Poisson's ratio for some marine sediments between 0.44 and 0.49 with a wide range of wet density (see Fig. 4.27). Other researchers (eg. Nacci et al. 1975 ; Davie et al., 1978 ; Akers, 1980 ; Silva et al., 1983 ; Nambiar, 1985) used conventional strain controlled triaxial apparatus (Bishop and Henkel, 1962) to measure the stress-strain-pore pressure response of deep-ocean sediments (see Figs. 4.28 to 4.32). Modulus of elasticity, E is usually expressed as E_{50}/ c_u where c_u is the undrained shear strength and E_{50} is the secant modulus at 50 % peak shear stress (Davie et al., 1978 ; Poulos, 1980), while others (eg. Akers, 1980 ; Silva et al., 1983) expressed tangent modulus as a function of deviator stress and compared with the hyperbolic model (Konder, 1963 ; see Fig. 4.28).

The range of the stress-strain stiffnesses of deep-ocean sediments is not known. Soil stiffnesses depend on the current effective stresses, water content and on the stress history of the soil, type of test conditions (eg. isotropic or anisotropic

consolidated) as well as on the type of interpretation used for analyses (secant or tangent stiffness, Atkinson et al., 1985c). Generally the modulus of elasticity values obtained by the geophysical methods are higher than those obtained by the conventional static laboratory tests (ie. triaxial tests) because the former methods measure elastic moduli at extremely low strain amplitudes (Morris and Abbiss, 1979).

4.5 Strength Characteristics

The strength characteristics are usually expressed either in terms of undrained shear strength c_u or in terms of effective stress parameters (ie. c' and ϕ'). Most available undrained strength data with depth of deep-ocean sediments have been obtained by laboratory motor vane shear apparatus (eg. Keller and Lambert, 1980 ; Kelly et al., 1974 ; Silva, 1979 ; see Figs. 4.33 and 4.34), while further undrained shear strength data and the angle of internal friction, ϕ' have been determined from conventional triaxial compression tests (Bishop and Henkel, 1962) on isotropically consolidated samples (eg. Demars, 1975 ; Akers, 1980 ; Valent et al., 1982). Very little information is available on the behaviour of anisotropically (ie. K_o) consolidated deep-ocean sediments and no previous work has been carried out using advanced triaxial testing equipment (eg. Atkinson et al, 1985b ; Clinton and Woods, 1986). The undrained shear strength profiles of deep-ocean sediments have also been determined by in-situ measurements eg. in-situ vane apparatus (

Silva, 1985); free-fall penetrator (Freeman et al., 1984). These allow comparisons to be made between laboratory and in-situ measured data.

The range of the undrained shear strength profile of a number of different deep-ocean sediments have been summarised by Davie et al. (1978) and OAP (1982) which show large variations of the strength profiles (c_u / d) and this probably reflects the heterogenous nature of the sediments, different testing conditions and different degrees of sampling disturbance. In general the deep-ocean calcareous oozes exhibit higher strength data (ie. c_u / d and ϕ') than the non-calcareous deep-ocean sediments and terrestrial soils at the same plastic index . This can probably be attributed to the presence of cementation bonds and interlocking between the calcareous particles (Damars et al., 1976 ; Kelly et al., 1974).

Sicilliano (1984) investigated the effects due to the test conditions (ie. isotropic and K_o normally consolidated) on the behaviour of deep - ocean sediments using conventional strain controlled triaxial apparatus (Bishop and Henkel, 1962). His results showed significant different undrained effective stress paths between them (see Fig. 4.35), whereas very similar strength data were obtained at maximum effective stress ratio, σ_1' / σ_3' (see Fig. 4.36).

The effective angle of internal friction, ϕ' for some North Atlantic

deep-ocean sediments have been reported by Demars etal., 1976 and are found to be higher than the terrestrial soils (see Fig. 4.37). Grain crushing phenomena on some calcareous oozes have been reported by Valent (1979) from which the angle of internal friction, ϕ' decreased with increasing effective stress level (see Fig. 4.38) Nambiar et al. (1985) investigated the effect of calcium carbonate on the strength properties of a fine grained carbonate sediments. No grain crushing phenomenon was observed with increasing effective stress level and on the removal of calcium carbonate the angle of internal friction decreased from 36.9^{o} to 32.5^{o} (see Fig. 4.39).

Chapter 5 : Procedures for Sample Trimming and Classification Tests

5.1 The Sub-Sample Cores

Deep-ocean sediment samples were provided by the Institute of Oceanographic science (IOS) and the Building Research Establishment (BRE). These samples were recovered by gravity corers (Schultheiss, 1982) at different locations (mainly within the GME and NAP sites; see chapter 3) in the North Atlantic Ocean. They were contained in plastic tubes of different diameters and lengths depending on the type of sampling method used. The original long sample cores were cut to short lengths (sub-sample cores) and sealed with plastic end caps before transporting to the soils laboratory at the City University. These sub-sample cores were then stored in the refrigerator of about 5^{o} C to await testing. Details of these sample cores are given in Table 5.1.

5.2 Trimming of the Sub Sample Cores

The sub-sample cores were carefully extruded and trimmed to nominal 38 mm diameter triaxial specimens with equipment which will be described in the following sections. The trimmed triaxial specimens and the trimmings were examined for evidence of layering and were then covered with cling-film, placed in labelled plastic bags (with marks to distinguish between the top and bottom of the samples) and then restored in the refrigerator. For the purpose of

this thesis all trimmed triaxial specimens were named " tubed " specimens. The trimmings of the samples were then kept separately for classification tests (see later sections).

5.2.1 The IOS Tubed Specimens

A number of sub-sample cores (core no. 10406) were provided by the Institute of Oceanographic Science (IOS). Their locations are just outside the GME study area (see chapter 3) and are referred as the IOS-samples. They were contained in transparent plastic tubes of about 2.5 mm wall thickness and sealed with end caps (see plate 5.1 ; Table 5.1 for details). These samples were extruded by simply pushing at one end using a piston and were then trimmed to nominally 38 mm diameter by 100 mm long on a wire-saw frame (see Plate 5.2). In the process of trimming the sample and the wire-saw were charged with a 12 volts DC supply. It is believed that the electric current passing through the pore water (salt-water) of the sediments could reduce further sample disturbance during the trimming process (Atkinson, 1984a). The trimmed triaxial specimens were then restored in the refrigerator to await for testing.

5.2.2 The GME Tubed Specimens

A number of sub-sample cores (D11172-6 and D11174-10) were provided by the Building Research Establishment (BRE) and their locations are within the GME study area (see Chapter 3) and are

referred as the GME - samples. They were contained in transparent plastic tubes, sealed with end caps (similar to those of the IOS-samples; see Table 5.1 for details).

These sub-sample cores were trimmed to triaxial specimens by using a 38 mm internal diameter by 120 mm long thin wall tube. Plate 5.3 illustrates the tubing equipment for these samples in which the core sample was extruded by pushing a piston at one end of the core at the same time the sample was trimmed by the thin wall tube which has been fixed in position at the other end. The speed of the piston for extruding the sample was kept to a continuous motion of about 1mm per second until the tube was filled. The filled tube was then covered with cling-film and placed in plastic bag and restored in the refrigerator awaiting for testing. The trimmings of the samples were examined and described before transferring to a separate plastic bag for later classification tests.

5.2.3 The NAP Tubed Specimens

A number of sub-sample cores (84 PCM 19 and 33) recovered by gravity piston corers (Schultheiss,1982) from the NAP study area (see Chapter 3) in the North Atlantic Ocean were provided by the Institute of Oceanographic Science (IOS) and were named the NAP-samples. Only two of these cores were taken for testing (see Table 5.1 for core details). These samples were contained in 83 mm internal diameter by 700 mm long plastic tubes with 5 mm wall thickness and

sealed with plastic end caps. These samples were extruded and trimmed to triaxial specimens using a 38 mm internal diameter by 120 mm long thin wall tube. Plate 5.4 illustrates the tubing operation of a sub-sample core in which the sample was extruded vertically upwards by pushing a piston at constant speed (~ 1 mm per second) from the bottom end of the sample, and at the same time the sample was trimmed by the thin wall tube which has been fixed in position at the top. The top 5 mm of the core samples were removed before the tubing operation began. After the tube was filled, it was then covered with cling-film and placed in plastic bag before restoring in the refrigerator for future testing, whereas the trimmings were kept separately for later classification tests. The remainder of sub-sample cores were then resealed with end caps and restored in the refrigerator to await further tests.

5.2.4 The GME C6 Tubed Specimens

Four sub-sample cores were provided by the ESOPE Research Party via the Building Research Establishment. These samples were recovered by a Stacor large-sized fixed piston corer (Fay et al., 1985) at a location within the GME study area (see Chapter 3) and were named the GME-C6 samples (see Table 5.1 for core details). These samples were contained in plastic tubes of 10 mm wall thickness and sealed with plastic end caps. These samples were extruded and trimmed to 38 mm diameter triaxial specimens by thin wall tubes using procedures similar to those for the NAP-samples, except that three triaxial specimens

were obtained at the same level of the sub-sample core (see Plate 5.5). The cores and/or trimmed triaxial specimens were then resealed with end caps and restored in the refrigerator for future testing.

5.3 Procedures for Classification Tests

All the classification tests were carried out on the trimmimgs of the sub-sample cores. Procedures for these tests were performed in accordance with BS 1377:1975 but with slight modifications due to the presence of salt in the sediment.

5.3.1 Salt Water Content Determinations

The water content was determined by oven-drying at 105^{O} C over a period of 24 hours and is defined as the proportion of liquid phase to solid phase by weight in %. The actual water content (salt-water content) due to the presence of soluble salt in the liquid phase can be calculated by using an expression given by Noorany (1984), ie.

$$\bar{m} = m / (1 - r - r.m / 100) \qquad (5\text{-}1)$$

where $\bar{m}$ is the salt water content in %,

m is the uncorrected water content determined by conventional method in %,

r is the proportion of salt in salt water by weight and is assumed to be 0.035.

5.3.2 Atterberg Limits

A standard cone penetrometer was used to determined the liquid limits of the sediments. A cone test was first carried out on a specimen at natural water content according to procedures as described by BS 1377:1975 Test 2A for air dried soils. If the natural state of the sample was below the liquid limit (ie. penetration below 20 mm), three more cone tests were carried out at higher water content by adding salt-water (r = 0.035) to the sample as recommended by Richards (1974). If the natural state of the sample was above or equal to liquid limit, the sample was then allowed to air-dry at room temperature before carrying out the next three cone tests as described above. Water contents were calculated as described in section 5.3.1.

The plastic limit was determined according to procedures as described by BS 1377:1975 Test 3A on air-dried samples. Water contents were calculated as decribed in section 5.3.1.

5.3.3 Specific Gravity Tests

The Density Bottle Method as described by BS 1377:1975 clauses 2.6.23 to 2.6.24 was used to determine the specific gravity of the sediment. Samples were first prepared by washing with distilled water through filter paper for three times in order to leach out dissolved salt. The washed samples were allowed to air-dry and then were broken down into powder form using a rubber pestle before carrying out the

specific gravity tests.

5.3.4 Particle Size Analysis

The hydrometer method as described by BS 1377:1975 was used to determine the particle size distribution of the sediments.

5.3.5 Calcium Carbonate Content Determinations

The gravimetric method for the loss of carbon dioxide (Chaney et al., 1982) was used to determine the calcium carbonate content of the sediments.

5.3.6 Particle Shapes

Electro-micrographs from a scanning electron microscope were obtained and these discussed in Chapter 8 (see Plate 8.1).

Chapter 6 : Microcomputer Controlled Triaxial Stress Path Cells

Two types of microcomputer based automatic control systems for triaxial stress path testing were developed at the City University. The first type has been described by Atkinson et al. (1983), which operates six hydraulic triaxial stress path cells (Bishop and Wesley, 1975) logged and controlled by a central microcomputer named the 'Spectra' system. This was later linked with a second microcomputer for permanent data storage and analysis (Woods, 1985). The second triaxial stress path control system was developed on the basis of the 'Spectra' system but operates a single triaxial cell with a dedicated BBC Acorn B type microcomputer (Clinton, 1985 & 1986). Both systems are operated with feed-back control and have the same type of instrumentation but experience has shown that the 'BBC' automatic control system is more versatile than the 'Spectra' control system. The 'BBC' control system can easily be converted to manual control by replacing the microcomputer with cyclic relay timers and a digital voltmeter (Atkinson, 1985b). It also has the advantage that an accident (eg. operator's error) involved in one cell cannot affect any other apparatus. There is also the added flexibility in being able to develop the basic programme to carry out special testing requirements.

The majority of the tests reported in this thesis have been carried out in the 'Spectra' control system.

6.1 The Triaxial Stress Path Apparatus

The triaxial apparatus was used to test 38 mm diameter soil samples. In this apparatus the sample is placed vertically in the apparatus between two rigid end platens and encased in a rubber membrane. The radial and pore pressures are controlled by fluid pressure, while the axial load is supplied by hydraulic pressure to the base ram of the apparatus (Fig. 6.1). This type of hydraulic triaxial stress path cell was developed by Bishop and Wesley (1975). A slightly modified version of this apparatus has been developed at Imperial college recently and is used at the City University (see Plate 6.1) where a drainage connection block has been added and the cell body has been enlarged to 200 mm diameter to accommodate larger samples and internal instrumentation.

Since the liquid phase of the soil sample is sea-water, salt-water was used as cell fluid to avoid building up osmotic pressure across the sample membrane which would cause a migration of water through it. An internal salt water chamber (Atkinson and Lewin, 1984) which allows the sample to be completely surrounded by salt water while using de-aired main tap water for the bulk of the cell fluid (see Plate 6.2) was made for the standard aluminium cell body. A complete stainless steel triaxial cell operated with a 'BBC' control system which allows de-aired salt-water to be used as the cell fluid was also used.

6.2 Instrumentation and Calibration

The instrumentation in the Bishop and Wesley triaxial cells consists of standard triaxial electrical instruments which measure the axial force, cell pressure, pore pressure, axial displacement and volume change. The principle that the measuring instruments should be positioned as close as possible to the sample is for accurate measurement and also for ensuring accurate feed-back control. The general arrangement of the instruments on the triaxial apparatus is shown in Fig. 6.1. The electrical instrumentation is based on a full Wheatstone Bridge arrangement of strain gauges powered by a maximum nominal voltage of 10 volts.

6.2.1 Axial Load Cell

A standard 450 kgf Imperial College type internal load cell was used to measure axial force. This device makes all measurements inside the cell body and close to the sample so as to measure axial load without friction lossess and also unaffected by changes of cell pressure. This device was calibrated by dead weight method and the detailed calibration procedures have been described by Atkinson et al. (1983) for the 'Spectra' control system and by Clinton (1985) for the 'BBC' control system. A typical calibration curve for the load cell is given in Fig. 6.2.

6.2.2 Pressure Transducers

Both cell and pore pressures are measured by Druck type pressure transducers with a range of 0-1000 kPa. The cell pressure transducer is mounted at the base of the cell body and the pore pressure transducer is mounted in the drainage block measuring pore pressure at the base of the sample via a drainage lead (see Fig. 6.7). A standard pressure transducer calibrator was used to calibrate the transducer characteristics and a typical calibration curve is given in Fig. 6.4.

6.2.3 Volume Change Transducers

The volume change is measured via a second drainge lead at the sample base through the drainage block to a 50 cc capacity Imperial College volume gauge adjacent to the triaxial apparatus. The change in volume in the volume gauge is measured by monitoring the movement of the floating frictionless piston with a displacement transducer (see Fig. 6.7). A typical calibration curve for the volume gauge is shown in Fig. 6.5.

6.2.4 Axial Displacement Transducer

The axial displacement of the sample is measured externally by monitoring the upward movement of the axial ram piston with a displacement transducer and a dial gauge mounted at the top of the cell body (see Fig. 6.1). The displacement transducer was

calibrated using a micrometer and a typical calibration curve is shown in Fig. 6.6.

6.3 Pressure Control and Power Supply System

The pressure supplied to the hydraulic stress path cells is from the cell pressure, back pressure and the axial ram pressure. These pressures are supplied by a central air compressor operating at about 800 kPa, which is stepped down through an air-pressure control valve allowing a maximum operating pressure of about 700 kPa to the triaxial apparatus. This supply pressure passes through three air-pressure control valves, one regulates pressure directly to the back pressure in the volume gauge and the others to the cell and the axial ram pressures through air and water interfaces. Axial strain control can be operated by linking a Bishop-type screw jack ram into the the axial ram hydraulic system and closing the lead to the air and water interface (see Fig. 6.1). The control of the pressures to the triaxial apparatus can be done by air-pressure control valves driven by electric motors acting through suitable reduction gear-boxes. Two types of motor system were used. One operated in the 'Spectra' control system which uses 240 volts AC motors acting through gear boxes and controlled by switching the motors on or off as required. The other type of motor operates in the 'BBC' control system which uses 12 Volts DC stepper motor acting through gear boxes. Opening and closing a switch will cause the motor to step through a small fixed rotation. Thus it is controlled by opening and closing a switch a number of times.

The axial strain control can be achieved by connecting a motor with a suitable reduction gear box directly onto the Bishop-type ram drive to the axial ram hydraulic system (see Fig. 6.1). The combination of the motor and the gear box provided a maximum axial strain rate in the 'Spectra' system of about 0.5 % per hour and a maximum of about 3 % per hour in the 'BBC' system for a 76 mm long sample.

Both the 'Spectra' and the 'BBC' control systems are powered by a 240 volts mains power supply through filters to remove spikes and to avoid external interferences. Precautions have also been made to protect the systems against mains power failure. In the event of a mains power supply failure the main components of the systems (ie. instrumentation) are immediately supplied by an emergency back-up power pack which lasts for about an hour. Later(within half an hour after power failure) a back-up generator is automatically switched on to supply power to both the air compressors and the main components of the control system until the mains power supply resumes.

6.4 The 'Spectra' Microcomputer Control System

The details of the arrangements of this system and its operation have been described by Atkinson et al.(1983), see Plate 6.3. This system was subsequently linked with a second microcomputer mainly for data storage and analysis (Woods, 1985). For the purpose of this thesis, only the main components of the system and its main operation will be described.

6.4.1 The Main Components of the System

The 'Spectra' control system comprises six Bishop and Wesley type triaxial cells which are controlled and monitored by a central Intercole Spectra X-b system (see Plate 6.3) which consists of

a) a 32 K words memory microcomputer for control operation and data storage;
b) a single cartridge tape drive for the operating programme;
c) a VDU with keyboard for control console;
d) a 48 input and output channel interface unit for analogue to digital and digital to analogue conversion;
e) an Epson RX-80 printer for hard copies;
f) CM 62 relay boxes for switching the electric motors;
g) a 192 k Epson QX-10 microcomputer with VDU and keyboard for permament data storage transferred from the 'Spectra' microcomuter.

6.4.2 Operations

The control software of this system is written in high-level Basic language and is named 'Spectra'. The main control loop of the programme is shown in Fig. 6.8. The transducers of each operating triaxial cell are scanned every ten seconds and the current states of stresses and strains are computed. These are then compared with the required states of stresses and strains according to the pre-defined stress or strain path. Corrections will be made if any current state lies outside the

limits specified by the operator. These limits are usually ± 1 kPa for all stresses and ± 0.01 % for all strains.

The computed current stresses and strains are recorded and stored hourly in the 'Spectra' computer. These records can be displayed or printed at any time during a test stage by interrupting the main control loop programme through the 'Option-Call' switch. At the beginning of each day the records stored for the previous 24 hours for each cell are transferred and stored in the Epson microcomputer leaving sufficient memory in the 'Spectra' computer for storing data in the succeeding day. At the same time all these records are printed as hard copies. When the test stage is stopped through the option menu (see section 6.6) all the current day's records are printed and all records since the start of the test stage are stored permanently on a floppy disc through the Epson microcomputer (Woods, 1985a).

6.5 The 'BBC' Microcomputer Control System

The details of the arrangements of this system and its operation have been described by Atkinson and Clinton (1984) and Clinton (1985 & 1986). The system is similar to that of the 'Spectra' system except that it operates a single Bishop and Wesley-type triaxial cell (see Plate 6.4). For the purpose of this thesis, only the main hardware of this system and its main operation will be described.

6.5.1 The Main Components of the System

The main components of the system (see Plate 6.4) consist of

a) a 32 k memory Acorn BBC model B microcomputer and a 32 k sideways ram with a disc filing system for control operation and storage;
b) a Cumania single 80 track disc drive for the operating programme;
c) an Intercole Spectra Micro-ms interface unit for analogue to digital and digital to analogue conversion;
d) a CM 62 relay box for switching the motors;
e) an Epson RX-80 printer for hard copies;
f) a monochrome monitor screen for control console.

6.5.2 Operations

The control program of the 'BBC' microcomputer is written in modular form to enable simple adaptations (eg. to operate with a different interface unit). More specialised stress or strain paths can also be accommodated by a simple alteration to the appropriate program module.

The main control program has a feed-back control loop (Fig. 6.8) similar to that of the 'spectra' system. Signals from each intrument are read at a predetermined interval (typically every 10 seconds) and are transferred to the computer through the analogue-digital interface unit. The current values of stress and strain are computed and then compared with the required values calculated from the

predefined stress or strain path. Any required corrections can be made by the command of the computer to the appropriate motor via the digital-analogue interface unit. A set of current values of stress and strain is recorded at a predetermined time interval (typically every one hour but will depend on the duration of test and loading rate) and stored in the sideways ram. These records can be displayed or printed at any time by interrupting the main control program by pressing the ´ Option-Call´ switch (see later section). All records are printed and stored on a floppy disc after the test stage is stopped.

6.6 The Option Menu

The main control loop program (Fig. 6.8) can be interrupted once the ´Option-Call´ switch is pressed. The option menu (see Fig. 6.9) is then be displayed on screen, allowing the operator to command any other function corresponds to the option number. The function of each option is described as follows:

Option A : Return control

The computer returns to automatic control by rejoining the main control loop program.

Option B : Enter test data

Test data are required for the computer to calculate and to control stresses and strains. Data are entered at the start of a test stage and these are,

a) Job title

b) Test and Stage No

c) Initial length and diameter

d) Control time interval : (fixed at 10 seconds in the 'Spectra' system)

e) Record time interval : (fixed at one hour in the 'Spectra' system)

f) File name

g) Stress or strain path input specifications :

Control code -1 : no control

0 : stress control

1 : strain control

Starting values (kPa or % strain)

Increment (kPa per hour or % strain per hour)

Final values (kPa or % strain)

The controller applies the required stress or strain path and, on completion of loading, it holds the stresses or strains constant at their finishing values until the test stage is stopped.

For the 'Spectra' system the control limits for stresses and strains are also required and these are usually specified as 1 kPa for all stress and 0.01% for all strains.

Option C : Zero stress tranducers

The stresses are set to zero at the stage when preparing the apparatus (see chapter 7). These zeros are then

recorded as references to calculate the current stresses (see section 6.7).

Option D : Set initial pressures

This option enables a check on the current state of the specimens at the start of a test stage and also allows the required stresses to be set by controlling the air-pressure control valve manually.

Option E : Zero strain transducers

This enables strains to be set to zero and this should be done at the start of a test stage after the initial dimensions of the sample have been entered through option B. Strains can be re-set to zero again between test stages if accumulated strains are not required. In this case new dimensions (ie. the final dimensions of the previous stage) must be entered.

Option F : Start a test stage

The apparatus is completely under computer control according to the input test data in option B. A hard copy of the entered test data is obtained.

Option G : Stop a test stage

The test is stopped. All records are then printed and stored on a floppy disc.

Option H : Display current state

The current state of the sample is displayed on screen.

Option I : Print record in store

Record is printed as hard copies.

Option J : Display records in store

Records are displayed on the screen.

Option K : Calibrate transducers

This enables the transducers' output range to be calibrated from which a suitable gain value can be chosen to give the best resolution of each measuring device.

Option L : Enter calibration data

The appropriate calibration constants are entered according to the allocated channel number for each instrument.

Option M : Check time

This enables the computer time to be checked on screen.

Option N : Transfer data to disc

This allows data stored in the computer to be transferred to a floppy disc while a test is running. This option is not available in the 'Spectra' system.

6.7 Calculations of Stresses and Strains

6.7.1 The Current States

The current values of the five independent measurements through the transducers (section 6.2) in terms of engineering units are calculated using the equation, $R = C (V - V_o)$, where R is the current value, C is the calibration constant, V is the current output of the transducer and V_o is the initial value (ie. zero) of the transducer.

Thus the current value of

a) the axial force, $F_a = C_a (V_a - V_{ao})$ kN (6.1)

b) the radial pressure, $\sigma_r = C_r (V_r - V_{ro})$ kPa (6.2)

c) the pore pressure, $u = C_u (V_u - V_{uo})$ kPa (6.3)

d) axial displacement, $\Delta h = C_h (V_h - V_{ho})$ mm (6.4)

e) volume change, $\Delta V = C_v (V_v - V_{vo})$ cm^3 (6.5)

It should be noted that compressive stresses and strains are taken as positive. The strains are calculated in terms of ordinary strains in which axial strain is $\varepsilon_{ao} = \Delta h/h_o$ % and volumetric strain is $\varepsilon_{vo} = \Delta V/V_o$ %, where h_o and V_o are respectively the values of the initial height and volume of the sample entered in Option B. The axial force is measured by an internal load cell which is not affected by the change of cell pressure and the axial stress, σ_a is given by

$$F_a = (\sigma_a - \sigma_r). A \qquad (6.6)$$

where A is the current area of the sample. The current area is calculated assuming that the sample deforms as a right cylinder (Bishop and Henkel, 1962) :

$$A = A_o \cdot \frac{(1 - \varepsilon_{vo} /100)}{(1 - \varepsilon_{ao} /100)} \qquad (6-7)$$

where A_o is the initial sample area. The axial stress, σ_a can then

be calculated from equations (6.1),(6.2),(6.4),(6.5),(6.6) and (6.7) and is written as,

$$\sigma_a = \frac{F_a \cdot (1 - \varepsilon_{vo} /100)}{A_o \cdot (1 - \varepsilon_{ao} /100)} \qquad (6.8)$$

6.7.2 The Required Stresses and Strains

The required values for the controlled stress and strain paths are calculated assuming that the stresses or strains vary linearly with time. Thus the required value after an elapsed time, t ,is given by,

$$R(t) = \text{starting value} + (t \times \text{increment per hour }) \qquad (6.9)$$

It is relatively simple to add or to alter a small subroutine to the control program to allow for other loading functions (eg. non-linear paths).

6.8 Accuracy of the System

The accuracy of the system can be divided into two parts, i) the accuracy of the measurement which depends on the measuring devices, ii) the accuracy of the controller (ie. the ability to follow closely the required values of stresses snd strains) which depends on the controlling equipment such as the speed of the motors and the characteristics of the pressure regulators.

6.8.1 Accuracy of the Measurements

6.8.1.1 Resolutions

Five individual measurements are made by instruments close to the sample in the triaxial apparatus (see section 6.2). Signals from these instruments pass through the analogue-digital interface unit before passing to the micro-computer. The conversion of the signal for each input channel of the interface unit should be pre-selected to give the maximum resolution of the measuring signal. Thus the choice of the interface unit is important as it controls the accuracy and the resolution of the measuring system. The resolution depends on the number of bits in the interface unit. An n-bit interface unit will have a resolution of $1/(2)^n$ of the full range. The resolution of the individual instruments for the 'Spectra' and the 'BBC' control system is summarised in Table 6.1.

6.8.1.2 The Calibration Constants

The choice of the calibration constants for the instruments is an important factor governing the accuracy of the measurement. The methods of calibration have been described in some detail by Atkinson et al.(1983) and Clinton (1985). As a result of this calibration it is found that the measuring devices are non-linear over the full range of the calibration, particular at low stress range and near the end of the travel of the displacement transducers. Hystereses of the

instruments is also found on reversal of load and displacement. Since the control system allows only one calibration constant for each device except for the load cell which has one for compression and one for extension the calibration curve is linear. Thus the calibration constants should be chosen such that they represent the relevant range of stresses and displacements for a particular test, so that errors involved due to non-linearity and hysteresis will be kept to a mininum. This is illustrated diagrammetrically in Fig. 6.10 using an exaggerated calibration curve for a pressure transducer. The calibration constant is chosen such that the best measurement will be made if the pressure is between 200 kPa and 300 kPa.

6.8.1.3 Noise and Drift

Fig. 6.11 illustrates the definitions of noise and drift of the instrument output which produce variations of signals with time. Drift is caused by the change of resistance of the transducer at constant strain and its magnitude can be assessed by comparing the initial zero readings of the transducer with the final zero readings after the transducer is loaded. Noise is caused by the change of resistance due to interference induced by other devices. The magnitude of noise of the instrument can be assessed by observing the variation of readings over a short period of time. The magnitude of noise and drift of individual instrument in terms of engineering units are summarised in Table 6.2.

6.8.1.4 System Compliance

There are errors in the measurement of volume change and axial displacement of the sample. The errors occur in the volume gauge due to the expansion of the volume gauge bellofram as the back pressure changes and the hysteresis response of the volume gauge. Clinton (1985) has described methods of calibrating the magnitude of volume expansion. The typical value for a 50 cc volume gauge is about 0.2 cc per 100 kPa change in back pressure. Correction for a small change of back pressure is not significant, while corrections for hysteresis, eg. on swelling , can be avoided by carefully opening and closing the air-bleed valve of the volume gauge (see Fig. 6.7) to allow a small reversal of the volume transducer to take place before testing.

Errors in the measurement of axial displacement occur mainly due to the compressibility in the axial loading system such as the compliance of the load cell and the loose fitting between the load cell and the triaxial cell body (Atkinson and Evans, 1985). The method for calibrating these errors has been described in details by Atkinson et al. (1983) and Clinton (1985). A typical curve for the compressibility in the axial loading system is given in Fig. 6.3. The axial compliance of the system is the slope of the calibration curve, which can be seen to be approximately linear over a range of stresses. The axial compliance in compression is usually found to be lower than that in extension. The horizontal portion of the calibration curve (see Fig. 6.3) is the gap G in the axial loading system as the load cell is

unloaded from compression to extension due to the loose fitting in the loading system . The typical values for the axial compliance of the system in compression and in extension are respectively about 0.05 % ε_a and 0.08 % ε_a per 100 kPa change in axial stress respectively for a 76 mm long sample and the gap G is about 0.1 mm.

6.8.2 Accuracy of the Controller

The accuracy of the controller is defined as its ability to follow closely the required stresses and strains. The controlling accuracies have been discussed by Atkinson et al.(1985b) and are illustrated diagrammatically in Fig. 6.12 which shows a stress path cell, a controller and VDU. The actual stress σ_s on the sample is sensed by a transducer and the computed stress through the use of a calibration constant and displayed on the VDU is σ_r . The microcomputer commands the controller to supply a pressure, p_c ,and the actual supplied pressure , p_s ,which gives rise to a sample stress, σ_s . The accuracy of the measurement ($\sigma_s - \sigma_r$) is governed by the characteristics of the measuring system and has been discussed in section 6.8.1. The accuracy of the control is ($p_s - p_c$) which is governed by the pressure control system such as the speed of the motor and the characteristic of the air pressure regulator valve. The control equipment is all commercially available and its accuracy is usually within ± 0.5 kPa. The error in ($\sigma_s - p_s$) is mainly due to the friction in the loading ram and losses in the pipe work. The computer should continue to adjust the command pressure , p_c, until the

recorded stress, σ_r , is the same as the required stress irrespective of the errors in the controller, ($p_s - p_c$), and the friction losses , ($\sigma_s - p_s$).

6.8.3 Discussion

From the above, it seems that the greatest error occurs in the measurement of the axial stress. This is partly due to the friction in the loading ram. Also the axial stress as calculated in eqn(6.8) involves the errors in the other measurements. The overall accuracies of the individual measurements are summarised in Table 6.2 which are better or as good as those for the conventional triaxial testing equipment. Clearly errors in the derived parameters such as the mean effective stress p' which involves a number of independent measurements, may be worse than a single independent measurement but the worst possible error can be assessed using Table 6.2.

There are also errors associated with the triaxial test sample itself such as non-uniform straining, the effects of membrane and filter-paper side drain stiffnesses. These cause problems in assessing the actual state of stress and strain of the sample. Non-uniform straining of the sample refers to barrelling or necking particularly near to failure due to end restraints. This error may be reduced either by using free ends (Barden and McDermott, 1965) or by making sure that test samples are close to the height to diameter ratio of two to one

before shearing (Bishop and Green, 1975) as reported here. A number of research workers (eg. Henkel and Gilbert, 1952 ; Duncan and Seed, 1967 ; Richardson, 1985) have investigated the effects of membrane and filter-paper stiffnesses. Their results indicate that while errors are not significant in compression tests they are more severe in extension tests. The effect due to side drains may be greatly reduced by using a 'fish-net' shape radial side drain (see Plate 7.1 ; Lewin, 1984), while errors in strength due to the rubber membrane alone are usually within 5 kPa using the Bishop and Henkel (1962) type of corrections. These corrections were orginally made for results of unconsolidated undrained tests but for consolidated drained or undrained tests the sample membrane buckles during the consolidation stage, particularly under K_o conditions for soft clay, and the subsequent effects of a buckled membrane on the stress-strain and strength properties may not be as significant as those in unconsolidated shear tests.

Results presented in this thesis are for tests which were carried out mainly on K_o compressed soft samples surrounded with 'fish-net' type filter paper side drains and thin rubber membranes. The volume changes due to consolidation are mostly in excess of 10 % and the membranes were observed to buckle after consolidation stages. Thus corrections for the filter paper side drain and membrane stiffnesses have not been applied.

Chapter 7 : Procedures for Triaxial Stress Path Testing

Details of the procedures for the triaxial stress path testing using the microcomputer controlled systems (see chapter 6) have been described by Atkinson et al. (1983) and Clinton (1985). These testing procedures were slightly modified to suit this particular project on the properties of deep-ocean sediments and will be described in the following sections.

7.1 Sample Preparations

7.1.1 Preparation for the Tubed Triaxial Specimens

Details of the trimming procedures for the sub-sample cores have been described in Chapter 5. The trimmed samples were taken out from the refrigerator and placed on the sample cradle. Samples which were kept inside the thin wall tubes were pushed out by a piston directly onto the sample cradle. The samples were then cut to nominally 80 mm in length and the sample diameter was assumed to be the same as the internal diameter of the thin wall tube (ie. 38 mm). The weights of the triaxial specimens were then recorded. The salt-water contents of the trimmed ends were determined according to section 5.2.

7.1.2 Preparation for the Reconstituted Triaxial Specimens

The main objective of the technique for preparing reconstituted soil

specimens is to produce cylindrical 38 mm diameter samples efficiently (usually within 24 hours) in which water content distribution is uniform and the sample should also be stiff enough to be handled routinely in the soil laboratory with minimum amount of disturbance.

Each reconstituted soil specimen was formed by re-using materials of a tested 'tubed' triaxial specimen. These materials, after oven-drying at 105^{o} C for at least 24 hours, were mixed thoroughly with de-aired distilled water to form a slurry of about 110 % water content and salt (NaCl) was added to the slurry to maintain the salt content of the slurry at 3.5 % by dry weight (see Appendix B for detailed calculation procedures). The slurry was transferred to a dessicator and maintained under a partial vacuum of about one atmosphere for at least an hour before pouring into a 38 mm internal diameter Perspex tubular sample former (see Fig. 7.1). The slurry was then left in the sample former unloaded for at least half an hour before it was compressed vertically via the top piston with a maximum dead weight of 2 kg over a period of 24 hours with increments of 0.5, 0.5, and 1 kg. The final increment of 1 kg (ie. at 2 kg) was usually applied within five hours after the loading began and at this time the long Perspex sample tube was pulled upward slightly along the slurry and the vertical pistons and hung freely in the water bath to form a long floating ring type of oedometer (see Fig. 7.1). The initial weight of the slurry had been estimated in order to achieve a final length of about 80 mm specimen under the maximum vertical load of 2 kg. After 24 hours the reconstituted specimen was then unloaded and extruded to

the sample cradle from the sample tube by pushing a piston from one end (it was necessary to note the top and the bottom end of the specimen). The weight of the specimen was recorded and the exact dimensions of the specimen were then measured to the nearest 0.1 mm using vernier calipers.

7.2 Setting Up in the Triaxial Apparatus

The setting up procedures were followed by choosing the appropriate options in the option menu list (see section 6.6). This option menu list was displayed on screen once the "option-call" switch was pressed. Before preparing the triaxial apparatus the appropriate calibration constants for the measuring devices must be entered.

7.2.1 Preparing the Triaxial Apparatus

The triaxial apparatus was first prepared by entering nominal dimensions (38 mm diameter, 76 mm length) and with all manual control on the air-pressure regulator valves (control code -1 for all functions, see section 6.6). The cell was then half-filled with de-aired water preferably covering the load cell by controlling the cell pressure regulator. The drainage system (Fig. 6.7) was flushed by opening and closing the air-bleed valve in the drainage block and then opening and closing the drainage valve and at the same time the volume gauge was centred. All the transducer readings were set to zero. The cell was completely filled with water, to check that suffi-

cient was available, before emptying it.The sides of the sample top and bottom platens were slightly greased with silicone grease to ensure a good seal for the membrane and the 'O' rings. Before preparing the triaxial test specimen the following items were assembled (see Plate 7.1) :

i) a porous stone saturated with salt water (r=0.035)

ii) two 38 mm diameter filter paper discs

iii) a 'fish-net' type filter paper radial side drain (Lewin, 1984)

iv) a rubber tension cap and top sample platen

v) a thin rubber membrane, 'O' rings, a membrane stretcher.

7.2.2 Preparing the Triaxial Specimen

The triaxial specimen was prepared as described in section 7.1. the saturated porous stone with a filter paper disc (wetted with salt water) on its top was placed on the bottom platen (pedestal) of the triaxial apparatus. The triaxial specimen was carefully assembled on the porous stone , a wet filter paper disc and then a rigid sample top platen was placed on the top of the specimen. The specimen was then enclosed by a wet 'fish-net' shaped filter paper side drain before encasing with a rubber membrane and two 'O' ring seals at each end. The tension cap platen was then fitted onto the sample top platen. For tests in the conventional aluminium triaxial cell body in which the inner salt-water chamber was used (see section 6.3), the bottom chamber disc was first fitted on the bottom platen of the apparatus before assembling the specimen.

The cylindrical chamber was assembled over the triaxial specimen on the bottom chamber disc before sealing with 'O' rings and the tension cap platen was fitted onto the sample top platen (Fig. 7.2). The inner chamber was then filled by injecting salt-water (r=0.035) through the gap between the sample top platen and the flexible chamber membrane using a wash bottle (see Plate 6.2).

7.2.3 Setting the Initial Isotropic Stresses

The triaxial cell body was fixed in place and then filled with de-aired water for the aluminium cell body and with de-aired salt water for the stainless steel cell body. The cell pressure was raised manually to about 50 kPa with the drainage valve closed (ie. undrained) by controlling the air-pressure regulator. The sample was then left for about half an hour to reach equilibrium under the constant cell pressure. The cell pressure was then raised at constant rate (10 kPa/hour) using the automatic control systems (chapter 6) to 200 kPa. The Skempton pore pressure coefficient, B (Skempton, 1954) of the specimen was assessed by calculating the ratio between the increments of pore pressure response and the cell pressure ($B = \Delta u / \Delta p$) particularly near to the end of the loading stages (ie. 180 to 200 kPa). If the B value was below 96 %, the flushing procedure was required (see section 7.2.5).

7.2.4 Initial Isotropic Consolidation

The cell pressure was raised slowly undrained by controlling the air pressure valve manually until the observed pore pressure response was 210 kPa. At a convenient time the drainage valve was opened allowing the specimen to consolidate against a preset constant back pressure of 200 kPa and a constant cell pressure (ie. p'=10 kPa). The observed volumetric strains were recorded at root time intervals (ie. 1/4, 1/2, 1, 4, 9, 16 minutes etc) until no further volume change was observed (ie. complete consolidation).

When consolidation was complete, the drainage valve was closed. The current dimensions of the specimen were calculated from the observed final ordinary volumetric strain, ε_{vo} by assuming $\varepsilon_{ao} = \varepsilon_{ro} = \varepsilon_{vo}/3$. Thus the approximate current height, h and diameter, d of the specimen is $h_o(1 - \varepsilon_{vo}/3)$ and $d_o(1 - \varepsilon_{vo}/3)$ respectively, where h_o is the initial height and d_o is the initial diameter of the specimen.

7.2.5 Flushing of the Drainage System

The Bishop-type ram was first connected to the air-bleed valve in the drainage block (see Fig. 6.7) and was then wound in slightly to increase pressure in the ram. The drainage valve was opened (the drainage system should be at equilibrium because the pore and the back pressure are the same, ie. 200 kPa) and then the air-bleed valve, so that the whole system was under the same back pressure of 200 kPa. The

Bishop-type ram was then wound out slowly drawing water from the volume gauge (not from the specimen), flushing out any air bubbles in the system. The flushing continued until no air bubbles were observed in the drainage leads. The drainage valve and the air bleed valve were closed and the Bishop-type ram was then disconnected from the apparatus.

7.2.6 Joining the Specimen Top Platen to the Load Cell

The top suction release valve was first connected and opened to the Bishop-type ram, the axial ram pressure was then raised manually by controlling the air-pressure regulator until a slow continuous upward movememt of the axial ram was observed by the movement of the vertical dial gauge. This upward motion was stopped when the rim of the rubber tension cap was in contact with the load cell. At this time the Bishop-type ram was wound out very slowly until no further movement of the dial gauge (ie. upward movement) was observed indicating that the top cap and the load cell were in contact. The Bishop-type ram was then disconnected leaving the suction release valve opened. The current state of the specimen was checked and both axial ram and cell air pressure regulator adjusted to achieve the required isotropic stress state (ie. $\sigma_a = \sigma_r$). Some excess pore pressure would build up during this operation but it was usually not significant (within 3 kPa). The dimensions of the specimen were assumed to be unchanged (ie. to be the same as the dimensions after initial isotropic consolidation stage).

7.3 Stress Path Testing Procedures

After the top cap of the specimen and the load cell had been connected, the specimens were subjected to either isotropic or anisotropic compression to the required effective stresses (Fig. 7.3) before shearing to failure. Details of the loading history of each specimen are given in Table 7.1 . All the stress path tests were carried out using the microcomputer controlled systems as described in Chapter 6.

7.3.1 Isotropic and Anisotropic Compression Tests

These tests were carried out with the drainage valve open and with a constant back pressure of 200 kPa. For isotropic compression tests the total axial and radial stresses were raised at the same rates to the required stress state (see Fig. 7.4), while for anisotropic compression tests total axial and radial stresses were raised at different rates. The ratio of the stress increments, $\dot{\sigma}_a / \dot{\sigma}_r$ governed the direction of the stress path followed. Examples of the directions of the stress paths which relate to the ratio of the principal stress increments are given in Fig. 7.4 .

One form of anisotropic compression was K_o compression which was carried out by first compressing the specimen from the isotropic stress state to the anisotropic stress state , assuming K_o = 0.5, (A to B in Fig. 7.3) at a slightly higher effective stress. It was then

followed by K_o compression (B to C in Fig. 7.3) which was carried out by raising the total axial stress in small increments (range between 2 to 6 kPa per hour) and at the same time controlling the total radial stress so as to maintain zero radial strain within 0.01 %. The same procedures in principle was followed for K_o swelling in which the total axial stress was reduced in small increments (C to D in Fig. 7.3). At the end of the loading (compression) or unloading (swelling) stage, the specimen was allowed to reach equilibrium state under the constant total stresses and back pressure. This stage was judged to be complete when the volumetric strain had been observed to be constant for at least three hours.

7.3.2 Undrained Shearing Tests

After being compressed to the required effective stress levels, the drainage valve was closed. The undrained tests to failure were carried out at constant total radial stress in two stages (Atkinson and Evans, 1985) :

Stage i , stress control : increase (compression) or decrease (extension) the total axial stress in small increments.

Stage ii , strain control : at a suitable time, stop stage (i) above and start a new stage by controlling axial strain as described in section 6.3 . The axial strain rate was chosen so that it would approximately equal the strain rate at the end of the previous stage. The specimen was then strained to at least 15 % ε_a .

7.3.3 Drained Shearing Tests

Drained tests to failure were also carried out in two stages as described in section 7.3.2 but with the drainage valve open and with a constant back pressure of 200 kPa. Three types of drained stress paths were investigated (see Fig. 7.4),

a) Conventional drained tests to failure

b) Constant p´ tests to failure

c) Constant q´ tests.

The conventional drained test to failure was carried out by increasing total axial stress and then axial strain (compression) or decreasing total axial stress and then axial strain (extension) with constant radial stress and back pressure (path OB in Fig. 7.4).

The constant p´ stress control test was carried out by increasing the total axial stress and decreasing the total radial stress (compression) or by decreasing total axial stress and increasing total radial stress (extension) in a ratio of $\dot{\sigma}_a/\dot{\sigma}_r = -2$ (Fig.7.4.) In some tests the stress paths were reversed after reaching point B (see Fig. 7.5). This was done by unloading to the initial state (path BO) and then reloading along the same path passing through the point B before switching over from stress to strain control to failure (path BCD). The strain controlled constant p´ test was carried out by increasing axial strain (compression) or decreasing axial strain (extension) and at the same time controlling total radial

stress to vary according to the change of total axial stress so as to maintain $\dot{\sigma}_a / \dot{\sigma}_r = -2$. This test stage required some modifications to the main control program (Clinton 1985) and these tests were only carried out in the 'BBC' control system (see section 6.5).

7.3.4 Unloading the Apparatus

After the specimen had reached end state (ie. at least 15 % ε_a) the test stage was stopped and the drainage valve closed if it was a drained test. The suction release valve was connected to a Bishop-type ram (the same one used for flushing) and the axial ram pressure opened to the pressure supply. The axial ram pressure was slowly decreased by operating the air-pressure regulator until the axial stress was about 5 kPa to 10 kPa below the radial stress (this step was not required for tests in extension). The Bishop-type ram was wound in until the specimen top platen separated from the load cell. The axial ram and cell pressure were then reduced to zero and all the cell water drained from the apparatus. The specimen was then removed and the water content was determined by oven-drying as described in section 5.2.

7.3.5 Rate of Loading

Tests should be carried out in a reasonable time and without causing errors due to incomplete drainage or incomplete equalisation of pore pressures. The current conventional method for determining loading rate

is that described by Bishop and Henkel (1962). However, this leads to very slow rates of loading. Alternative methods for calculating an acceptable rate of loading have been suggested by Atkinson (1984b) in which the loading rate is related to the magnitude of errors due to incomplete drainage, or equalisation based on the steady rate at which the rate of dissipation equals the rate of generation of pore pressure. Test error is simply related to the magnitude of excess pore pressure. The estimated mean excess pore pressure, $\bar{u}$ can be expressed as,

$$\bar{u} = \mu\, t_1 \, (\dot{p} + \bar{\alpha}\, \dot{q}) \qquad (7.1)$$

$$\text{or} \quad \bar{u} = v \,.\, p' \,.\, \Delta\varepsilon_v \,/\, \lambda \qquad (7.2)$$

where μ depends on the drainage conditions

t_1 is the time for consolidation in a root-time plot

$\bar{\alpha}$ is the slope of the undrained effective stress path

$\Delta\varepsilon_v$ is the change of volumetric strain after loading is stopped (ie. when total stresses are held constant).

The loading rates used during the compression and swelling stages were in the range of 2 to 6 kPa per hour, applied automatically in small increments of not less than 1.5 kPa. On completion of loading and unloading, observations of volume change were continued for at least 6 hours before proceeding to the next stage of the test. These observations are recorded in Table 7.1 as $\Delta\varepsilon_v$ % and they provide an

indication of excess pore pressures set up by the chosen rate of loading : it was considered that the small values of $\Delta\varepsilon_v$ listed in Table 7.1 indicated that these excess pore pressures were small and tolerable. Thus on one hand, the chosen rates of loading enabled tests to be completed in a reasonable time without signific-ant errors compared to the accuracies of the measurements. On the other hand, the loading rates were also slow enough to avoid the build up of non-uniform pore pressures which could cause a non-uniform redistribution of water content across the radius of the triaxial specimen (Atkinson et al. 1985a). The loading rates during the shearing stages for both drained and undrained tests are also listed in Table 7.1. The loading was applied in small increments of not less than 1.5 kPa during the initial stress controlled stage and in small increments of not less than .02% ε_a during the final strain controlled stage (see section 7.3.2).

Chapter 8 : Test Results

8.1 Classification Test Results

The Atterberg limits (LL , PL) of the sediments are plotted in a Plasticity chart (see Fig. 8.1) and the grading curves are given in Figs 8.2 (a to d). Results of the index properties are summarised in Table 8.1. The micrographs of the sediments are shown in Plates 8.1 (a to d).

8.2 Triaxial Test Results

The triaxial test results are presented in terms of the critical state soil parameters (Schofield and Wroth, 1968). The current state of a sample is given by the deviator stress, q' , the mean effective stress p' and the specific volume, v. For the condition of axial symmetry in compression and extension, $q' = (\sigma_a' - \sigma_r')$, $p' = (\sigma_a' + 2.\sigma_r') / 3$ where subscripts a and r refer to the axial and radial directions respectively (Wood, 1984). For saturated soils $v = 1 + \bar{m} G_s$ where $\bar{m}$ is the salt-water content as discussed in section 5.3. The corresponding strain parameters are the deviatoric shear strain $\varepsilon_s = 2(\varepsilon_a - \varepsilon_r)/3$ and the volumetric strain $\varepsilon_v = \varepsilon_a + 2. \varepsilon_r$ where ε_a and ε_r are the axial and the radial strains respectively which relate to the current dimensions of the sample (ie. natural strain $\varepsilon = - \ln(1 - \varepsilon_o)$ and ε_o is the ordinary strain which relates to the initial dimensions of the sample ; see Richardson, 1985). The

relationships between these stress and strain parameters are discussed in section 2.1.

Figs. 8.3 to 8.8 show the compression and/or swelling of the specimens to different effective stresses in v - ln p' space. The current specific volume, v of the sample during loading was calculated from the final measured salt-water content (see section 5.3.1) using the equation $v = v_i (1 - \varepsilon_{vo})$ where v and v_i are the current and the initial specific volumes respectively, and ε_{vo} is the observed ordinary volumetric strain. The loading history of the tests are summarised in Tables 8.2 to 8.3 . Also given are the results of the initial isotropic consolidation and the states at the start of shearing. It should be noted that the values of v_o are back-calculated from the final salt-water content, whilst the values of v_o^* are interpreted from a selected normal compression line for a particular group of sediment (see a later section).

The basic shearing test results presented in terms of the total stresses and ordinary strains are given Figs. 8.9 to 8.14. The undrained effective stress paths during shearing are shown in Figs. 8.15 to 8.20 and the corresponding deviatoric stress-strain curves are shown in Figs. 8.21 to 8.26 .

Chapter 9 : Analyses and Discussions

9.1 Soil Classifications

Results plotted in the plasticity chart (see Fig.8.1) indicate that the North Atlantic deep-ocean sediments are of high to extremely high plasticities which lie fairly close to the A-line. The particle size ranges from poorly graded clayey silts to silty clays (see Fig. 8.2 a to d). While the grading curves of the carbonate sediments (see Fig. 8.2 a, b & c) are within the same envelope with clay fraction ranges between 15% to 35% , the GME curves (see Fig. 8.2 b) lie towards the upper part of the envelope. Fig. 8.3 d indicates that the NAP (non-carbonate) sediments are in general finer than those carbonate sediments from in and around GME area.

The micrographs given in Plate 8.1 (a to d) show the particle shapes of the sediments. It can be seen that the IOS, GME and the GME C-6 specimens contain particles which are similar to those containing predominantly hollow and disc form of Coccolithic (Nannofossils) reported by Chaney et al. (1982) and this may account for their high calcium carbonate content (see Table 8.1). The sediments from NAP which contain practically no calcium carbonate (see Table 8.1) are rather different from the GME sediments in terms of their plasticities (see Fig. 8.1), gradings (see Fig. 8.2) as well as their particle shapes (see plate 8.1).

The activity, A (Skempton, 1953) which relates to the mineralogy and the pore water chemistry of these sediments are summarised in Table 8.1. The high activity (A>1.5) of the carbonate sediments may reflect the high water holding capacity of the carbonate particles (Demars et al., 1976), while the lower activity (A<1.0) of the non-carbonate NAP sediments indicates the presence of illite rich clay particles (Skempton, 1953).

From the results of the index properties given in Table 8.1 and Figs. 8.1 and 8.2, these North Atlantic sediments can be classified as,

The IOS specimen : very high plasticity carbonate clayey silt.
The GME specimen : extremely high plasticity carbonate clayey silt.
The GME C-6 specimen : extremely high plasticity carbonate clayey silt.
The NAP specimen : high to very high plasticity silty clay.

The range of plasticity of the GME sediments shown in Fig. 8.1 is similar to that of the other North Atlantic carbonate clayey silts given in the literature (eg. see Fig. 4.11b). The plasticities of NAP sediments are found to be lower than those of the sediments from other locations in the NAP site (see Fig. 4.11 b) but similar to those of the North Pacific illite rich sediments (see Fig. 4.11a).

9.2 Consolidation

The coefficients of consolidation, c_v and volume compressibility, m_v were determined from the initial isotropic consolidation stages using Bishop and Henkel (1962) method and the coefficient of permeability, k was calculated from $k = \gamma_w . c_v . m_v$ (Terzaghi, 1943). The results are summarised in Tables 8.2 and 8.3 for tubed and reconstituted specimens respectively. The results obtained in these earlier stages of isotropic consolidation tests may not be representative due to sample disturbance (this is discussed further in the next paragragh). The c_v values of the tubed specimens (see Table 8.2) are in general higher than those of reconstituted specimens (see Table 8.3). Very little published c_v data is available in the literature to allow for any comparison. However, the range of the calculated permeability for the GME and the IOS specimens is in general agreement with those of the other sediments obtained at the same site (see Fig. 3.5b) and also similar to the type of North Atlantic calcareous silty clay reported by Herrmann and Houston (1976) , see Table 4.4 . While the permeability of the NAP sediment is similar to that of a Pacific smectite sediment obtained from permeameter tests (Silva et al. 1984 , see Fig. 4.26). The results indicate that the IOS and the GME specimens are in general more permeable than the NAP specimens by about an order of magnitude. This may be due to the more porous and silty nature of the carbonate GME and IOS sediments as discussed in section 9.1. However, no significant difference in permeability is found between the tubed and the reconstituted specimens from GME material and from NAP material.

9.3 Compression Behaviour

The states of K_o compression can be defined by eqns (2.19) (2.24) & (2.25), and the states of isotropic compression by eqns (2.26 & 2.27), where N, λ, κ are soil constants and the subscripts o for these constants are for K_o states. Figs 8.3 to 8.8 show the states during compression and/or swelling in v - ln p′ space. The initial scatters during loading are results of disturbance during sampling and preparation as the test specimens were trimmed and then transferred to the triaxial cells for recompression. The vertical portions of the compression lines at the end of loading (ie. when total stresses are held constant) represent the dissipation of residual excess pore pressures (Atkinson, 1984). Since the loading rates and the observed changes of volumetric strain $\Delta\varepsilon_v$ at the end of loading are small (see Table 7.1), thus the possibility of sample non-uniformity due to radial drainage (Atkinson et al., 1985a) has been avoided and the slope of the normal compression line during loading may be regarded as the representative value (Atkinson, 1984b).

The test specimens were recompressed in the triaxial stress path cell to at least twice the estimated in-situ vertical effective stresses (except for specimen B of the GME C-6 sediments, see Table 8.2) and the applied vertical effective stresses in oedometers for tubed and reconstituted specimens respectively. Therefore the effects of sample disturbance on the subsequent strength and stress-strain behaviour may be considered to be negligible (Hight et al., 1985 ; Baligh et al., 1987).

The compression lines given in Figs. 8.3 to 8.8 have been interpreted so that variations within a particular type of sediment can be identified. This was done by examining the slopes of the normal compression lines and comparing them with the corresponding gradings (see Figs. 8.2 a to d) and plasticities (see Table 8.1 and Fig. 8.1). As a result, two groups of IOS and NAP tubed specimens have been identified. The IOS group A contains specimens IOS-3 and 4 of similar index properties (see Table 8.1 and Fig. 8.3). This group of sediment has a higher λ value than that of the group B sediment which contains IOS-1 , 2 , 5 and 6 . The NAP group A contains specimens in cores 84PCM33/3 and 84PCM33/4 of similar index properties and are more compressible than the group B sediment in cores 84PCM19/1 and 84PCM19/4. There are , however, some doubts about the accuracies of the final specific volumes, v_{en} from which the states of compression and/or swelling are calculated (see section 8.2). This would explain why the normal compression lines lie parallel to but only close to each other for a particular type of sediment although similar rates of loading were used (see Table 7.1). An average normal compression line for a particular type of sediment is selected (see Figs. 9.1 to 9.4) and the specific volumes, v_o calculated from the end of the tests are then corrected to give v_o^* at the same p'_o (see Tables 9.2 to 9.7) and the corresponding compression parameters are summarised in Table 9.1.

Since most specimens have been normally compressed (ie. normally consolidated soils), little is known of their swelling behaviour (ie.

κ) except for the lightly overconsolidated reconstituted specimens(GME specimens GR-11 & 12 ; NAP specimens NR-5 & 6). However, the swelling parameters for the tubed specimens can be estimated from the initial recompression stages and this is done on the GME C-6 specimens (see Fig. 9.3). The κ_o values are summarised in Table 9.1. The estimated p_c' in Fig. 8.5 using the method suggested by Graham and Houlsby (1983) indicates that the GME C-6 tubed specimens are indeed overconsolidated in-situ. This was done by comparing the estimated, σ_{vi}' with σ_{vc}', where $\sigma_{vi}' = \gamma' d$ and $\sigma_{vc}' = 3\, p_c'/(1+2\, K_o)$ are the in-situ and the past maximum vertical effective stress respectively. The corresponding OCR values (= $\sigma_{vc}'/\sigma_{vi}'$) appear to decrease with depth as shown in Table 8.2 for GME C-6 specimens. For those specimens which have been recompressed to at least twice their in-situ vertical effective stresses are assumed to be normally consolidated soils (ie. OCR=1). The decrease in OCR with depth has also been observed in other types of deep-ocean sediments tested in oedometers (see Fig. 4.21) and the reason for the apparent overconsolidation may be attributable to ageing and cementation (Bjerrum, 1972 ; Demars, 1975).

Results given in Figs. 8.4 b and 8.7 a indicate that the isotropic normal compression line is approximately parallel to the K_o normal compression line in $v - \ln p'$ space for tubed and reconstituted specimens respectively. It can also be seen that the states for isotropic and K_o compression of the GME tubed specimens coincide, in $v - \ln p'$ space , whilst the isotropic compression states lie above the K_o compression states for the GME reconstituted specimens which appear

to agree with that predicted by critical state theory (see Fig. 2.5). Results given in Table 9.2 and Figs. 9.2 and 9.4 show that the κ_o and κ values of the GME tubed specimens are higher than those of the GME reconstituted specimens.

A comparison of the K_o normal compression lines between different types of tubed and reconstituted specimens is shown in Fig. 9.5. The results show that the tubed specimens are generally more compressible and initially looser than the reconstituted specimens at the same mean effective stress. The carbonate tubed specimens (ie.IOS, GME and GME C-6) appear to be more compressible than the non-carbonate NAP tubed specimens and this effect is reversed after reconstitution. Each normal compression line has been extended beyond the range of experimental data (see Fig. 9.5) and it can be seen that the compression lines do not consistently pass through a single point as suggested by Schofield and Wroth (1968). However, results given in Fig. 9.6 indicate that for both tubed and reconstituted specimens N_o increase linearly with increasing λ_o .

Fig. 9.7 shows the average K_o values interpretated from η'_o given in Table 9.1 using eqn (2.19) for each type of sediments and the results are plotted against the corresponding angle of shearing resistance at critical state in compression, ϕ'_c (see Table 9.8). It can be seen that the results do not seem to be consistent with that proposed by Jaky (1944) but Jaky's relationship appears to be a lower bound of the experimental data. It should be noted that the K_o values for the

GME carbonate sediments (including C-6 carbonate specimens) are of similar magnitude with the values for the tubed carbonate specimens only being slightly lower than those for the reconstituted specimens, although the λ_o values have been greatly reduced after reconstitution (see Table 9.1). However, the low K_o values of the GME sediments are consistent with those of the other Atlantic calcareous sediments reported by Herrmann and Houston (1976), while the high K_o values of the NAP sediments are similar to those of the Pacific pelagic clay (see Table 4.4).

An investigation has been carried out in order to assess the effect of the carbonate content on the behaviour of the reconstituted GME sediments. This was done by comparing the test results (see Figs 8.7e and 9.2) of the reconstituted carbonate specimens (GR-1 to 12) with those of the reconstituted non-carbonate specimens (GR-13 & 14). It is seen that after the carbonate materials have been removed by diluted hydrochloric acid the sediments become slightly more compressible than the original reconstituted carbonate specimens. However, no significant difference in K_o value is found between the carbonate and non-carbonate reconstituted GME sediments (see Figs. 9.2a and 9.7).

Fig. 9.8 (a, b & c) shows the correlation between the interpreted λ_o values and index properties, and the results are compared with both the empirical and theoretical relationships as given in Table 4.3. Although fairly large scatters of data are obtained , the predictions based on plasticity index and liquid limit appear to represent lower bounds of

the experimental data for the tubed specimens. No correlation is found for the reconstituted specimens and neither the results of the tubed nor of the reconstituted specimens correlate with carbonate content as proposed by Poulos (1980)

9.4 Strength Characteristics

9.4.1 Limiting States

The limiting states for soils have been discussed in section 2.2.2. For normally consolidated and lightly over-consolidated soils, limiting states are governed by ultimate or critical states. The critical state is said to have been reached when a specimen is strained continuously at constant states (ie. $\delta q'$, $\delta p'$ and $\delta v = 0$). It is important to identify critical state of a specimen by examining both the effective stress ratio, η', and volumetric straining, $\delta \varepsilon_v$, as well as deviatoric stress, q', because in some cases, a specimen may reach peak shear stress or may be strained at constant shear stress before reaching the critical state. The critical state parameters can be expressed as follows :

in compression $$q' = M_c \; p' \tag{9.1}$$

$$v = \Gamma_c - \lambda_c \ln p' \tag{9.2}$$

in extension $$q' = M_e \; p' \tag{9.3}$$

$$v = \Gamma_e - \lambda_e \ln p' \tag{9.4}$$

where M, λ and Γ are soil constants and subscripts c and e refer to compression and extension respectively.

Results presented in this thesis (see Figs. 8.9 to 8.14) have been examined carefully in order to identify the critical states (see Tables 9.2 to 9.7 and Figs. 9.9 to 9.14) in view of the problems associated with indentification of the critical states. Fig. 8.21 shows the stress-strain curves for the IOS specimens in which specimens IOS-4 & 5 failed during stress control loading stages and the recorded maximum deviatoric stresses may represent or be close to the peak deviatoric stress, whilst the recorded end states (see Table 9.2) for these two specimens may not be as representative of the critical states as those specimens tested under slow strain control loading, although fairly high shear strains had been reached. Therefore the critical state values of these two specimens, as well as those specimens which have not reached the constant effective stress ratios at large shear strains (eg. NAP specimens , NT-11 & 13 in Figs. 8.24b and 9.33 c) have been omitted in Tables 9.2 to 9.7. Furthermore, there are problems that the recorded end state may not represent the actual critical state values even when the specimen has been strained at constant effective stress ratio. This is partly due to the inaccurate measurement of sample dimensions at large strain, non-

uniform straining, as well as the effects of membrane stiffness. This effect is particularly severe in extension tests when "necking" occurs as shear strain in extension increases. In addition,this may give rise to non-uniform pore pressures within the sample : higher pore pressure may be generated at the centres of normally consolidated samples due to the localised shear stresses at the sample ends with consequent migration of water away from the centres of the samples (Atkinson, 1987). As a result, the specimen becomes stiffer in the central portion and the critical state calculated from the measured boundary stresses may not correspond to the specific volume calculated from the overall water content of the specimen at the end of the test. The method which has been adopted in this thesis to estimate the values of critical state stresses (q'_{cs} , p'_{cs}) is by examining the undrained effective stress paths for undrained tests (see Figs. 8.15 to 8.20) and the normalised paths in q'/p'_e - p'/p'_e space for drained tests (see Figs. 9.23 to 9.28). These stress paths may exhibit sudden changes in direction before straining at constant effective stress ratio (ie. at critical state) due to the equalisation of non-uniform pore pressures . This sudden change in stress path direction near the critical state has also been observed by Coop and Cherrill (1987) in investigations of the behaviour of a calcareous silty sand. The estimated critical state stresses (q'_{cs}, p'_{cs}) are taken as the point of intersection between the line extended from the stress path before changing its direction and the line of constant effective stress ratio at critical state and the results are indicated by arrows in Figs. 8.15 , 8.16, 8.19 & 8.20 for

undrained tests and Figs. 9.23 & 9.24 for drained tests. However, for those specimens whose paths do not show such sudden change of stress path direction , the end stress states (q_{en}', p_{en}') are taken as the critical state stresses (ie. q_{cs}', p_{cs}'). The critical state values for different types of sediments are summarised in Tables 9.2 to 9.7 and plotted in Figs. 9.9 to 9.14.

From the limited number of tests carried out on the IOS sediments, it is not possible to define clearly the critical state line in terms of their specific volumes (see Fig. 9.9). Nevertheless the parameters M_c and M_e are tentatively obtained and summarised in Table 9.8. Figs. 9.10 to 9.14 show that well defined critical state lines for other types of sediments can be inferred. Also given are the corresponding normal compression lines (NCL) which are found to be parallel to the critical state lines (CSL) in v - ln p' space in both compression and extension (ie. $\lambda_o = \lambda_c = \lambda_e$). The critical state parameters as defined by eqns (9.1) to (9.4) for each type of sediment are summarised in Table 9.8. Figs 9.15 to 9.19 show the unique critical state points obtained by using the normalising parameters p'_e and v_λ as described in section 2.2.3.

Figs. 9.10 and 9.15 show that the critical states for K_o and isotropically compressed GME specimens coincide in q' - p' space and are approximately parallel in v - ln p' space. However, the isotropic critical state is somewhat denser than the K_o critical state line at the same mean effective stress. This is similar to the results of

the other type of deep-ocean sediments reported by Sicilliano (1984), see Fig. 4.36. Table 9.8 shows that the M_c values of the carbonate specimens (ie. IOS, GME, GME C-6) are in general higher than those of the non-carbonate NAP specimens. It can also be seen that in each case the critical state line is not symmetrical about the isotropic p′-axis and the M_c value is consistently higher than the M_e value for the same type of sediments. This is , however, in contrast with that of K_o kaolin clay reported by Atkinson et al.,(1986). Results also show that the critical state line in compression do not coincide with that in extension in v - ln p′ space (see Figs. 9.12 to 9.14) except for the GME tubed specimens (see Fig. 9.10).

The critical states of the two groups of NAP tubed specimens (see section 9.3) are given in Figs. 9.12 and 9.17. Similar values of M are found for the two groups of specimens in compression and in extension regardless of the marked differences in their densities (see Fig. 9.5) and plasticities (see Fig. 8.1). Fig. 9.13 shows that the two non-carbonate GME reconstituted specimens of higher compressibilities (GR-13 & 14) lie close to the other carbonate GME reconstituted specimens in q′ - p′ space which indicates that carbonate content has little effect on the strength properties of the reconstituted GME specimens.

9.4.2 Undrained Shear Strength

The undrained shear strength, c_u is taken as half the deviatoric

stress at critical state for undrained tests(ie. $q_u'/2$). However , the peak undrained shear strength (ie. $q_p'/2$) which typically occurs far from critical state at a shear strain of about 0.5 to 1 % for K_o normally consolidated soils (Koustofas, 1981 ; Atkinson et al., 1986) has also been identified (see Tables 9.2 to 9.7). It should be noted that only the results for GME C-6 tubed specimens show significant peak deviatoric stresses before reaching the critical states (see Fig. 8.23 and Table 9.5) and this is associated with the particular shapes of their undrained effective stress paths (see Fig. 8.17). Neither the results of the other tubed specimens (GME and NAP) nor of the reconstituted specimens presented in this thesis show this marked post peak drop in deviatoric stress behaviour.

The undrained shear strength c_u is often expressed as a function of vertical effective overburden pressure, σ_{vo}' . The c_u/σ_{vo}' ratio is a constant for a particular normally consolidated soil and can be predicted using the critical state parameters defined in section 2.2. By using eqns (2.28 and 2.31) with $q' = q_{cs}' = q'_u$; $p' = p_{cs}' = p'_u$ for the condition at critical state, eqn (2.24) with $p' = p_o'$ for K_o normally consolidated condition and $v_o = v_{cs} = v_u$ for undrained test condition, we have

$$q'_u = M\ p'_o\ \exp.^{-(N_o - \Gamma)/\lambda_o} \qquad (9.5)$$

Using eqns (2.18) and (2.19), eliminating K_o with $\sigma_v' = \sigma_{vo}'$; $q_{cs}' =$

2 c_u and the undrained shear strength ratio is given by

For compression $$\left(\frac{c_u}{\sigma'_{vo}}\right)_c = \frac{3M_c}{2(3+2\eta'_o)} \exp^{-(N_o-\Gamma_c)/\lambda_o} \quad (9.6)$$

For extension $$\left(\frac{c_u}{\sigma'_{vo}}\right)_e = \frac{3M_e}{2(3+2\eta'_o)} \exp^{-(N_o-\Gamma_e)/\lambda_o} \quad (9.7)$$

where M , η'_o, λ_o and Γ are soil constants and subscripts c and e refer to compression and extension respectively.

The c_u values plotted against σ_{vo}' for K_o normally consolidated GME and NAP specimens are given in Figs. 9.20a and 9.20b respectively. The experimental data show good agreement with those predicted by eqns (9.6 & 9.7) using the appropriate soil parameters given in Tables 9.1 and 9.8. It can be seen that the predicted c_u/σ_{vo}' ratios in compression are higher than those in extension for both tubed and reconstituted specimens (see Table 9.9) and the results illustrate the undrained strength anisotropy of K_o soils. The higher compressive shear strength is mainly due to the higher M values in compression than in extension. Similar values of c_u/σ'_{vo} are found between the tubed and the reconstituted specimens although marked differences are found in their λ_o and M values (see Table 9.8). It should also be noted that the c_u/σ_{vo}' ratios of the GME specimens are higher than, but of similar values, to the peak deviatoric stress ratios ($q_p'/2\sigma_{vo}'$) of the GME C-6 tubed specimens. It can also be seen that little difference in c_u/σ'_{vo} is found between the GME carbonate and non-

carbonate reconstituted specimens. The experimental c_u/σ'_{vo} ratios in compression given in Fig. 9.21 agree well with those of a number other deep-ocean sediments (see Fig. 4.34) and also show reasonably good agreement with the plasticity index as compared with the empirical correlation given by Skempton (1957).

The c_u/σ'_{vo} value can be related to the c_u/d by assuming that $\sigma'_{vo} = \gamma' d$, where γ' is the effective unit weight and d is the depth below seafloor. From the results given in Table 9.9, the c_u/d in compression for the GME and GME C-6 specimens are found to be 1.71 and 1.12 respectively, which are similar to those obtained from the same area tested using motor-vane (RGD, 1982 ; see Fig. 3.6), triaxial tests (Freeman, 1988) and model free-fall penetrator tests (Freeman, 1984 ; see Fig. 3.5c). However, the c_u/d of 1.35 in compression calculated for the NAP sediments (average of group A and B) from Table 9.9 is lower than those obtained from triaxial tests (Freeman, 1988) but generally higher than those obtained from motor-vane tests (RGD, 1984 ; see Fig. 3.8).

9.4.3 Angle of Shearing Resistance

The Mohr-Coulomb angles of shearing resistance at critical states , ϕ'_{cs} , calculated from eqn(2.29) and eqn(2.30) for compression and extension respectively are summarised in Table 9.8 . The higher values of ϕ_{cs}' in compression measured for the IOS, GME and GME C-6 carbonate specimens compared with those of the NAP non-carbonate specimens can probably be attributed to the irregular shape and the

more silty nature of the carbonate sediments (see Plate 8.1 and Fig. 8.2). High angles of shearing resistance in compression measured for carbonate sediments (in excess of 35^{o}) have also been reported by Demars (1975), Poulos (1980) and Nambiar et al. (1985). Results also show that ϕ_{cs}' values in compression of the reconstituted GME specimens are lower than those of the tubed GME specimens, while the value of ϕ_{cs}' in extension has increased slightly after reconstitution. The reason for the drop in ϕ_{cs}' in compression may be attributable to the removal of cementing and the possibility of breaking down of the carbonate particles during preparation of reconstituted specimens is also likely (Nambiar et al. 1985). These effects may have modified the original macrofabric and grading of the sediments. This is supported by the results of the reconstituted non-carbonate GME specimens (GR-13 & 14 : carbonate removed by dilute hydrochloric acid before reconstitution) which are found to be similar to those of the carbonate reconstituted specimens (see Figs. 9.7 and 9.13). However, the reason for the increase of ϕ_{e}' after reconstitution for both NAP and GME specimens is not clear. It is also interesting to note that no significant difference in the values of ϕ_{c}' and ϕ_{e}' is found between the tubed and the reconstituted NAP specimens which contain virtually no calcium carbonate.

From the results given in Table 9.8 , it appears that ϕ_{c}' is not equal to ϕ_{e}' for the types of tubed and reconstituted specimens tested. In general, it is found that $\phi'_{c} > \phi'_{e}$ and $\phi'_{c} < \phi'_{e}$ for carbonate GME and non-carbonate NAP specimens respectively.

Fig. 9.22 shows the correlation between ϕ'_c and plasticity index, and compared with those of the other North Atlantic sediments reported by Demars et al. (1976). It can be seen that ϕ'_c values of the carbonate GME and IOS sediments ($CaCO_3$>40%) are in general higher than Demars et al (1976) data at the same plasticity index. While the ϕ'_c value of the non-carbonate NAP sediment lie toward the upper part of Demars et al, (1976) data. The ϕ'_c values do not appear to correlate with plasticity index as proposed either by Kenny (1959) or Demars et al (1976).

9.5 The State Boundary Surface

The existence of a state boundary surface for soil has been discussed in some detail in section 2.2.3. Since most test specimens were predominantly normally consolidated (see OCR values in Tables 8.2 and 8.3) and then sheared under different loading paths in either drained or undrained conditions toward their critical states, the soil states are therefore likely to traverse the state boundary surface on the wet side of the critical state (ie. the Roscoe surface, Atkinson and Bransby, 1978). The resulting state paths can then be normalised to account for different effective stresses and specific volumes to examine both the existence and the geometry of the state boundary surface for a particular soil type. The appropriate normalising parameters required to account for different initial states and stress paths are the equivalent pressure p_e' and the equivalent specific volume, v_λ (see section 2.2.3). It should be

noted that the resulting geometries normalising by p_e' and v_λ are the constant volume (Atkinson and Bransby. 1978) and the reference p' (Atkinson, 1984c) sections of the state boundary surface respectively.

The undrained effective stress paths of each type of sediment are shown in Figs. 8.15 to 8.20. It can be seen that the shapes of the undrained effective stress paths are typical of the behaviour of K_o normally consolidated soils, for example kaolin clay (Atkinson et al. 1986 , see Fig. 2.19), a marine soft clay (Koustofas, 1981, see Fig.2.18) and a deep-ocean sediment (Sicilliano, 1984, see Fig. 4.35).

The normalised state paths (including those of conventional drained and constant p' tests) are given in Figs. 9.23 to 9.28. However, since the compression parameters of the IOS specimens have not been well established, the reference p' section of the state boundary surface has been omitted in Fig. 9.23. It can be seen that the normalised state paths lie fairly close within narrow bands for normally consolidated specimens (OCR =1, see Figs. 9.23 to 9.28). These normalised paths serve as a boundary for lightly over consolidated reconstituted specimens (see Figs. 9.27a and 9.28a). It is also clear from Fig. 9.25 (a to h) that by carefully identifying the initial states of the GME C-6 tubed specimens after K_o recompression (ie. normally or overconsolidated ,see Table 8.2), the existence of a state boundary surface for these nominally undisturbed (obtained by a larger diameter "Stacor" piston sampler) specimens

becomes apparent. However, in the case in Fig. 9.25(g & h) the state paths of the lightly overconsolidated specimen C-6 1B/B cross the state boundary surface (ie. the normalised state paths for truly normally consolidated specimens). This may be attributable to the inaccurate estimation of the p'_c value of this specimen (ie. p'_c value being underestimated).

Results given in Fig. 9.24 a for K_o and Fig.9.24c for isotropically compressed GME specimens clearly indicate that the geometry of the state boundary surface depends on the past loading history (ie. K_o or isotropically compressed ; Gens 1979 ; Sicilliano, 1984). The geometry of the K_o state boundary surface is found to be of similar trend to those reported by Parry and Nadarajah (1973) and Atkinson et al.,(1986) in that the surface is not symmetrical about the isotropic p' axis. The differences in geometry of the state boundary surface are found between the tubed and the reconstituted specimens (eg. see Figs. 9.24 a and 9.27a for GME specimens) may be due to the differences in both the compression parameters (see Table 9.1) and the parameters at critical state (see Table 9.8).

An attempt has been made to compare the normalised experimental data with the predicted K_o state boundary surface of the proposed soil model (City-Clay, see eqns. 2.94 & 2.101) using the determined soil parameters given in Tables 9.1 and 9.8. The predicted K_o state boundary surfaces are found to be in good agreement with the experimental data for both tubed specimens (see Figs. 9.24a , 9.25 a

to d and 9.26 a, b & d) and reconstituted specimens (see Figs. 9.27 a & b and 9.28 a to c) except for the conventional drained extension test data (see Figs. 9.26c , 9.27b and 9.28b). This may be due to the fact that the loading path for the conventional drained extension test ($\delta q'/\delta p' = 3$) is likely to move inside the state boundary surface rather than traversing it. Consequently, the normalised experimental data derived from the conventional drained extension tests may not represent the state boundary surface.

Fig. 9.29 shows the predicted geometry of the state boundary surface for different types of sediments in $q'/p'_e - p'/p'_e$ space using Modified Cam-Clay (eqn A9 in Appendix A) and these are compared with those predicted using City-Clay (eqn. 2.94). It can be seen that the Modified Cam-Clay and City-Clay state boundary surfaces are very different and, with reference to Figs. 9.23 to 9.28, it is apparent that conventional Modified Cam-Clay is not adequate for the present data.

9.6 Stress-Strain Behaviour

9.6.1 Stress-Strain Curves

The deviatoric stress-strain data ($q' - \varepsilon_s$) given in Figs. 8.21 to 8.26 are normalised by plotting q'/p' against $v\varepsilon_s$ in Figs. 9.30 to 9.35 (Atkinson 1984c). It can be seen that the normalised data lie closely within narrow band for a particular type of test path with the

maximum effective stress ratios, η' coinciding with the values at critical state. However, some scatter of data is obtained particularly for the tubed specimens, probably a result of sample disturbance. Figs. 9.34b and 9.35b show a somewhat stiffer and more brittle stress-strain response of the lightly overconsolidated reconstituted specimens (OCR=2) compared to those of normally consolidated specimens (OCR=1). This is due to the fact that the behaviour for lightly overconsolidated specimens is elastic ,whilst the behaviour for truly normally consolidated specimens is elasto-plastic (see section 2.4)

Little difference in the normalised undrained stress-strain behaviour is found between the group A (Fig. 9.33a) and group B (Fig. 9.33 b) of the NAP tubed specimens despite of the differences in their plasticities (see Fig.8.1) and the critical state parameters (see Table 9.8). It should be noted that in Figs. 9.33 c and d for NAP tubed specimens and Figs. 9.34c and 9.35 (c & d) for reconstituted specimens the undrained compression tests show somewhat stiffer behaviour than those of the conventional drained and constant p' tests. This stress path dependent stress-strain behaviour appears to agree well with that predicted by the incremental soil model as described in section 2.4.1. However, the behaviour in extension is difficult to assess at this stage and will be dealt with in the next section.

9.6.2 Stiffness Parameters

The deviatoric stress-strain data were analysed in terms of tangent stiffness following the method described by Atkinson et al.(1986). In this method, a straight line is fitted to a group of data points (usually taken to be a group of four consecutive data points thoughout the analysis) using the least square method (Woods, 1985a) and the corresponding stiffness is calculated and assigned to these data points. The same analysis is continued to the next group of data points in which the first three points overlapped with the previous analysis. The procedure is then repeated until the end point is reached. Average values of stiffness are to be taken for those overlapped points (ie. those have been analysed more than once).

Since the analysed test data are mainly of those obtained during stress control test stages, the applied stress rate, $\dot{\sigma}$ and the recorded strain rate, $\dot{\varepsilon}$ are both very small. Therefore in the limit of $\Delta q' \to 0$ and $\Delta\varepsilon_s \to 0$, the average stiffness ($\Delta q'/\Delta\varepsilon_s$) calculated in this way can be approximately taken to be the tangent stiffness ($dq'/d\varepsilon_s$). The tangent shear stiffnesses were normalised by the current states of the specimens as discussed in section 2.4.1 and the results are plotted against ln ($v.\varepsilon_s$) in Figs. 9.36 to 9.41 in order to expose the small strain response. It can be seen that the normalised experimental data of a particular type of sediments lie within narrow bands for a particular type of loading path and in all cases the normalised shear stiffnesses in extension are higher than those in compression at strain

($v.\varepsilon_s$) up to about 2% except for the lightly overconsolidated specimens (see Figs. 9.40b and 9.41b). It is also seen that the normalised stress-strain stiffnesses are non-linear (ie. stiffness decreases with strain level), particularly in extension.

Figs. 9.40b and 9.41b show the normalised stiffness with strain level for the lightly overconsolidated (OCR=2) GME and NAP reconstituted specimens respectively. The higher compression stiffness response at small strain may be associated with the 'threshold effect' (Richardson, 1985) in which soil stiffness depends on the amount of deviation between the previous and the current loading paths. The higher the deviation from the original loading path, the higher the stiffness can be obtained. Results given in Figs 8.19b and 8.20b for GME and NAP reconstituted specimens respectively clearly show a more severe change of loading path in compression compared to that in extension after K_o swelling. It can also be seen that the elastic soil behaviour of the K_o lightly overconsolidated specimens is likely to be anisotropic. This means that the value of α which relates to the slope of the undrained effective stress path (see eqns. 2.81 and 2.88) are likely to be less than unity (ie. vertically stiffer, $E'_v > E'_h$, see section 2.5.2.1). Comparisons of the normalised undrained stiffnesses are also made between normally and lightly overconsolidated reconstituted specimens (see Figs. 9.40b and 9.41b). It can be seen that the normalised compression stiffnesses of the lightly overconsolidated specimens are three to four times higher than those of the normally consolidated specimens at strain level ($v\varepsilon_s$) up to about

1%, whilst little difference is found in the normalised extension stiffnesses. In the case of the GME C-6 specimens (see Figs. 9.38) the stiffer stress-strain response of the specimens B at small strain confirm that these specimens are indeed overconsolidated (see Table 8.2).

Fig. 9.37 b shows that the normalised undrained shear stiffness for isotropic normally consolidated specimens is approximately twice that for K_o normally consolidated specimens. This illustrates the effect of stress history on the subsequent stress-strain behaviour of soils. Fig. 9.40d shows that little difference is found in the undrained shear stiffness as of the carbonate and the non-carbonate reconstituted GME specimens.

Figs. 9.39(a, b & c), 9.40(a & c) and 9.41 (a & c) show the comparisons of the normalised shear stiffnesses from undrained tests with those of conventional drained and constant p´ tests for NAP tubed, GME reconstituted and NAP reconstituted normally consolidated specimens respectively. In all cases, the undrained stiffnesses are found to be the highest at small strain. However, these differences are less significant in extension tests. This is probably due to the fact that differences in the applied test path directions in extension are not as severe as those in compression tests and consequently differences in the extension stiffnesses are small. Nevertheless, the observed stress path dependent stiffness response agrees qualitatively with that predicted by the incremental soil model as discussed in section 2.4.1.

A comparison is made of the normalised undrained stiffness response between the K_o normally consolidated tubed specimens from the four source areas (see Fig. 9.42). It shows a little difference in the compression behaviour whilst somewhat larger scatter is found in extension but the results become fairly indistinguishable as strains ($v.\varepsilon_s$) reach about 0.5% for compression and -0.2% for extension.

Figs. 9.43 and 9.44 show the differences in the normalised undrained shear stiffnesses between the tubed and the reconstituted specimens of GME and NAP sediments respectively. Results show that the stiffnesses for the reconstituted specimens are higher than those for tubed specimens except for the NAP specimens in compression where there is little difference. The difference in the stiffness response is particularly severe for the GME specimens which contain about 50% of calcium carbonate (see Table 8.1). The reason for this may be attributable to the differences in the critical state parameters between the GME tubed and reconstituted specimens (see Table 9.8).

Table 9.10 summarises the undrained stiffnesses of both tubed and reconstituted specimens in Figs. 9.42 to 9.44 at strain levels, $v.\varepsilon_s$ of 0.05% and 0.5%. It should be noted that soil stiffness is not only stress path and history dependent, it also depends on the current states of the specimens (vp′). In calculating the current states, a depth (d = 20m) below seabed is assumed (ie. $\sigma'_v = \gamma' d$) where γ' is the effective unit weight of the specimens ($\gamma' = 5\ kN/m^3$). With these values the mean effective stresses, p′ and the specific volumes, v can

be calculated using eqns (2.18) and (2.24), and the corresponding compression parameters given in Table 9.1 . The tangent stiffnesses are then evaluated. It should be noted that in a conventional undrained test path in which $\delta\sigma_r = 0$ with σ_a varying , the stiffness, $dq'/d\varepsilon_s = 3G_u = E_u$, where G_u and E_u are the equivalent undrained shear and Young's moduli respectively. However, in this case the values presented in Table 9.10 do not represent the elastic parameters. It is only a convenient way to present a more familiar set of stiffness data at this stage. The E_u/c_u values are also interpreted in Table 9.10 in which the c_u values are calculated using data given in Table 9.9 at the same depth (ie. 20m). The results show that the E_u/c_u values in compression are as much as five to six times less than those in extension. This is mainly due to the lower c_u and the higher E_u values in extension at the same vertical effective stress. It is also found that these values given in compression at small strain (ε_s = 0.02%) are of similar magnitudes compared to those of the terrestrial soft clays given by Duncan and Duchigiani (1976) but higher than those of the deep-ocean sediments reported by Silva et al. (1983), see Fig. 4.28.

9.6.3 Compliance Parameters

Special triaxial stress path tests were carried out in order to evaluate the compliance parameters [A , B , C , D] directly following the method as described in section 2.4.2 . This method requires separate constant p' and q' tests with loading/unloading/reloading

cycles (see Fig. 7.5) on identical specimens. However, due to the lack of the GME tubed specimens and the length of time involved these tests were performed only on the NAP specimens. The compliance data are derived from the basic test data using the method as described in section 9.4.2 and the results are normalised by the current state of the test specimens in accordance with eqns.(2.71 & 2.74).

Figs. 9.45 and 9.47 show the variation of two sets of normalised compliance parameters with the current effective stress ratio, η' for the tubed NAP specimens normally consolidated at different effective stresses (see Table 8.2). The similarities of these two sets of data indicate the uniqueness of these compliance parameters in both compression ($\eta' > \eta'_o$) and extension ($\eta' < \eta'_o$). However, it has not been possible to examine the compliance parameters B and D in compression from these tests. The scatters of the results during the earlier part of the unloading and reloading cycles (states within state boundary surface : the compliance parameters are elastic) may be due to hysteresis and/or threshold effect and possibly creep. Nevertheless, the results do illustrate that the sediment behaviour becomes elasto-plastic once yielding occurs and this is also found to be consistent to that of the reconstituted specimens (see Fig. 9.47). It can also be seen from these figures that the compliance parameters vary asymmetrically either about η'_o or the isotropic p' axis (ie. η' = 0). The pattern of the variations of the compliance parameters with η' are somewhat different from those predicted by either Cam-Clay or Modified Cam-Clay models (see Fig. 2.13) in which the compliances are

symmetrical about $\eta' = 0$ with B = C but consistent to those predicted by City-Clay model (see Fig. 2.26).

Attempts have been made to compare the normalised compliance parameters between the experimental derived data and the theoretical predictions based on City-Clay (see Appendix C) for both tubed and reconstituted NAP specimens. However, although the elastic behaviour of the specimens is likely to be anisotropic (see section 9.4.2), for simplicity of the comparisons in which the variations of the total compliances (ie. the sum of the elastic and the plastic components of the compliance parameters ; see eqn 2.36) are being considered, the elastic behaviour of City-Clay is taken to be isotropic (ie. $\propto = 1$, $B^e = C^e = 0$) with a Poisson's ratio of 0.3. Whilst the plastic components of the compliance parameters are calculated using values provided in Tables 9.1 and 9.8. The results are shown in Figs. 9.48 and 9.49 for tubed and reconstituted specimens respectively and it can be seen that reasonable agreement is found between the experimental and theoretical compliances A and C. However, the predictions compared with the compliances B and D are not quite as convincing.

Much further detailed research, both experimental and theoretical is required to evaluate these compliance parameters and to examine the consequence of the development of the constitutive models for anisotropic soils. However, the results based on the constitutive equations derived for City-Clay are encouraging.

Chapter 10 : Conclusions

Extensive triaxial stress path tests have been carried out on both tubed and reconstituted specimens of the North Atlantic deep-ocean sediments. These specimens were predominantly one dimensional (K_o) normally consolidated to different effective stresses and sheared in compression and extension, drained and undrained following different loading paths using microcomputer controlled hydraulic stress path cells (Atkinson et al. 1985 ; Atkinson and Clinton, 1986).

Test results are analysed and presented within the framework of critical state soil mechanics in order to examine sediment characteristics such as the state boundary surface, critical states and elasto-plastic stress-strain parameters. The test data were obtained from specimens consolidated by slow drained compression rather than by conventional undrained loading followed by consolidation and sheared in compression and extension. Therefore the test specimens were not subject to radial non-uniformities (Atkinson et al. 1985) and the rates of loading in both stress and strain control were not excessive as compared to those in conventional method using a single stage of strain control loading (Atkinson and Evans, 1985). In addition special measures have been taken to avoid test errors such as application of corrections due to the system compressibility, use of "fish net" shaped radial side drains etc. Thus the test data presented in this thesis can be considered to be more reliable than many earlier published data and also form a basis from which to develop an appropriate constitutive

model for deep-ocean sediments.

10.1 The Carbonate Sediments

The sediments taken from in and around the GME site were of very high to extremely high plasticity clayey silts with clay fraction ranges from 15% to 35% , and with carbonate content in excess of 45%. The particle shapes were typical of hollow and disc form of Coccolithic (Nannofossils) origins (Chaney et al. 1982).

The compression parameters for each type of sediment were determined and were given in Table 9.1. Among those tubed sediments, the GME C-6 specimens which were recovered using a large diameter gravity corer were of the highest compressibility. The tubed specimens were found to be more compressible than the reconstituted specimens at the same mean effective stress. The compression indices determined for these sediments did not correlate well with index properties as predicted by either empirical or theoretical relationships. Little difference in K_o values was found between tubed and reconstituted specimens and the values were also found to be similar to those of the other carbonate sediments given in the literature but inconsistent with that predicted by Jaky (1944) relationship.

The undrained shear strength ratios, c_u/σ'_{vo} in compression were higher than those in extension for both tubed and reconstituted specimens, and little difference was found between tubed and reconstituted specimens.

The c_u/δ'_{vo} in compression agreed reasonably well with plasticity index as proposed by Skempton (1957) and the corresponding c_u/d values were found to be in good agreement with data obtained from conventional laboratory tests on specimens taken from the same site, and also with data derived from model free-fall penetrator tests.

High ϕ' values in both compression and extension (in excess of 35°) were found for both tubed and reconstituted specimens. The ϕ'_c for tubed specimen was found higher than that for reconstituted specimen, whilst ϕ'_e was increased after reconstitution. The ϕ'_c values were also found to be higher than those of the other North Atlantic carbonate sediments reported by Demars et al. (1976).

The sediments from in and around GME site exhibited both non-linear and stress path dependant stress-strain behaviour. The compression stiffnesses were found lower than those in extension up to shear strain of about 0.5% for both tubed and reconstituted specimens. The undrained stiffnesses for the reconstituted specimens were higher than those for tubed specimens in both compression and extension. The undrained tangent stiffnesses were determined and values at shear strains of 0.02% and 0.2% were tabulated in Table 9.9. The undrained stiffnesses in compression at 0.02% shear strains were found to be similar to the initial undrained tangent stiffnesses of terrestrial soft soils given by Duncan and Duchigiani (1976) but higher than those of the other deep-ocean sediments reported by Silva et al. (1983).

10.2 The Non-carbonate Sediments

The sediments taken from the NAP site were of high to very high plasticity silty clay with clay fraction ranges from 45% to 65% and with no carbonate content.

Two groups of tubed specimens were identified and their compression parameters were determined (see Table 9.1). The compression indices determined for these sediments did not correlate well with index properties as predicted by either empirical and theoretical relationships. The reconstituted specimens were found to be less compressible than the tubed specimens at the same mean effective stress. The K_o values for the reconstituted specimens were lower than those for the tubed specimens and these values were also found to be inconsistent with that predicted by Jaky (1944).

The c_u/δ'_{vo} in compression were higher than those in extension for both tubed and reconstituted specimens and little difference was found between tubed and reconstituted specimens. The c_u/δ'_{vo} in compression agreed well with plasticity index as proposed by Skempton (1957). However, the corresponding c_u/d values were inconsistent with data obtained from conventional laboratory tests on specimens taken from the same site.

The ϕ' values in both compression and extension were obtained. The ϕ'_c were lower than the ϕ'_e for both tubed and reconstituted specimens and

the ϕ' values were increased after reconstitution in both compression and extension.

The sediments taken from the NAP site exhibited both non-linear and stress path dependant stress-strain behaviour. The normalised undrained compression stiffnesses were found lower than the extension stiffnesses up to shear strains of about 0.5% for both tubed and reconstituted specimens. The undrained extension stiffness for the tubed specimens were lower than those for the reconstituted specimens, whilst similar compression stiffnesses were found between tubed and reconstituted specimens. The undrained tangent stiffnesses were determined and the values at shear strains of 0.02% and 0.2% were tabulated in Table 9.9. The values at 0.02% shear strain were similar to the initial tangent undrained stiffnesses for terrestrial soft soils (Duncan and Duchigiani (1976) but higher than those of the other deep-ocean sediments reported by Silva et al. (1983).

10.3 Critical State Model

The results obtained from the present tests conformed reasonably well within the framework of critical state soil mechanics. The compression parameters during one dimensional (K_o) and isotropic drained loading for the carbonate sediments were summarised in Table 9.1. The value for λ_o was found to be approximately the same as the value for λ found for isotropic normal compression.

Reasonably well defined critical state lines were inferred for each type of sediment being investigated. However, it was necessary to examine stress ratio, volumetric strain, pore pressure changes, as well as deviatoric stress in order to identify critical states from peak deviatoric stress states for K_o normally consolidated and lightly over-consolidated soils. The critical state soil parameters given in Table 9.8 were not symmetrical about the isotropic p´ axis. The slope of the critical state line was found to be the same as in extension in v - ln p´ space (ie. $\lambda_c = \lambda_e$) and the critical state line was also found to be parallel to the one dimensional and isotropic normal compression lines (ie. $\lambda = \lambda_o = \lambda_c = \lambda_e$). It was found that neither $M_c = |M_e|$ nor $\phi'_c = \phi'_e$ for the types of the sediments being examined.

State boundary surfaces were obtained from results normalised to take account of different effective stresses and specific volumes and results showed that such a surface was unique for a particular type of sediment. The resulting geometry of the K_o state boundary surface was asymmetrical about the isotropic p´ axis which was similar to those reported for reconstituted soft clay (eg. Parry and Nadarajah, 1971 ; Atkinson et al, 1986). The geometry of the experimental state boundary surface was found to be substantially different from either the surface for the isotropic normally consolidated specimens or the surface for the equivalent isotropic Modified Cam-Clay model. However, such a surface can simply be modelled by the normalised version of Pender (1977) equation using soil parameters corresponded to the compression and the critical state lines.

Significant path dependant stress-strain behaviour was found for both tubed and reconstituted specimens. After normalisation to take account of different stresses and volumes, the tangent stiffness parameters varied within narrow bands with strain level for a particular loading path. Results also illustrated an anisotropic elastic behaviour when soil states were within the state boundary surface and soil behaviour became elasto-plastic once yielding ocurred. The tangent stiffness parameters in extension were in general higher than those in compression at small strain. The compliance parameters obtained from the results of special stress path tests were found to be in reasonable agreement with those predicted using a simple elasto-plastic model (City-Clay) derived in this thesis. The reason for the greater differences of behaviour between the tubed and the reconstituted GME carbonate specimens than the NAP non-carbonate specimens can be attributed to the breaking down of the cementation bonds between the carbonate particles after reconstitution.

The test data presented in this thesis are of particular interest to those who are concerned with engineering problems in deep-ocean sediments such as the free-fall penetrator (Freeman, 1984) and the knowledge of the sediment behaviour may also be applicable to problems such as construction in soft clay in general. The data comprises a reliable and consistent set of stress path tests in compression and extension on specimens of deep-ocean sediments taken from two North Atlantic sites. Results indicate that although the behaviour of one dimensionally (K_o) consolidated sediments conformed well within the

critical state framework, it is necessary to extend the simple isotropic model (eg. Modified Cam-Clay) in order to account for the effect due to one dimensional compression and such a model (City-Clay) has been proposed and the comparisons with data of kaolin and deep-ocean sediments are encouraging. However, much further work , both experimental and theoretical is required to examine how well the other types of deep-ocean sediments can be adapted to the critical state theory such as the effects due to overconsolidation etc. and the consequence of the development of an appropriate constitutive model, in particular to incorporate soil characteristics such as creep which may also have a significant effect on the behaviour of deep-ocean sediment.

Appendix A : Derivation of Constitutive Equations for Modified Cam-Clay

The equation of yield locus for Modified Cam-Clay (Roscoe and Burland 1968) is given by

$$\frac{p'}{p'_p} = \frac{M^2}{M^2 + \eta'^2} \tag{A.1}$$

On critical state line (see Fig. A1), E(v_x , p_x'), where $\eta' = M$, $p' = p_x'$

$$\frac{p'_x}{p'_p} = \frac{1}{2} \tag{A.2}$$

At B(v_u , p_p') on the normal compression line

$$v_u = N - \lambda \cdot \ln p'_p \tag{A.3}$$

At E(v_x , p_x') on the swelling line and the critical state line

$$v_\kappa = v + \kappa \cdot \ln p' = v_x + \kappa \cdot \ln p'_x \tag{A.4}$$

$$v = \Gamma - \lambda \cdot \ln p'_x \tag{A.5}$$

From eqns (A.3),(A.4) and (A.5) and eliminating p_p' , we have

$$v = \Gamma - \kappa \cdot \ln p' - (\lambda - \kappa) \cdot \ln p'_x \tag{A.6}$$

Sub. eqns (A.1) and (A.2) into eqn (A.6), we have the three dimensional

state boundary surface for Modified Cam-Clay, ie.

$$v = \Gamma - \lambda \ln p' - (\lambda - \kappa)\left[\ln \frac{1}{2}\left(1 + \frac{\eta'^2}{M^2}\right)\right] \qquad (A.7)$$

For $\eta' = 0$; $v = N$ and $p' = 1$, on the isotropic compression line , eqn (A.7) becomes

$$N - \Gamma = (\lambda - \kappa) \ln 2 \qquad (A.8)$$

The constant volume section of the state boundary surface is given by

$$\frac{p'}{p_e'} = \left[\frac{M^2}{M^2 + \eta'^2}\right]^{\left(1 - \frac{\kappa}{\lambda}\right)} \qquad (A.9)$$

For $p' = p_x'$; $\eta' = M$, we have

$$\frac{p_x'}{p_e'} = (2)^{1 - \frac{\kappa}{\lambda}} \qquad (A.10)$$

From eqn (2.46) in section 2.3.2 , eqn (A.6) becomes

$$\delta \varepsilon_v^p = Q \ \delta q' + P \ \delta p' \qquad (A.11)$$

where

$$Q = \frac{1}{v.p'}\left[\frac{2\eta'(\lambda - \kappa)}{(M^2 + \eta'^2)}\right]$$

$$P = \frac{1}{v p'}\left[\frac{(\lambda - \kappa)(M^2 - \eta'^2)}{(M^2 + \eta'^2)}\right]$$

The flow rule, F for Modified Cam-Clay (Roscoe and Burland, 1968)

is given by

$$F = \frac{\delta \varepsilon_s^p}{\delta \varepsilon_v^p} = \frac{2\eta'}{(M^2 - \eta'^2)} \qquad (A.12)$$

and combines eqns (A.11) and (A.12) and with P F = Q for the normality condition to be applied (Atkinson and Bransby, 1978), we have

$$\delta \varepsilon_s^p = Q F \ \delta q' + P F \ \delta p' \qquad (A.13)$$

By using eqn (2.35) in section 2.3 to include elastic and plastic component of strains, we have the complete constitutive equations for Modified Cam-Clay, ie.

$$\begin{bmatrix} \delta \varepsilon_s \\ \delta \varepsilon_v \end{bmatrix} = \frac{1}{v p'} \begin{bmatrix} \mu' \kappa + \frac{4\eta'^2(\lambda-\kappa)}{(M^4 - \eta'^4)} & \frac{2\eta'(\lambda-\kappa)}{(M^2 + \eta'^2)} \\ \frac{2\eta'(\lambda-\kappa)}{(M^2+\eta'^2)} & \kappa + \frac{(\lambda-\kappa)(M^2-\eta'^2)}{(M^2+\eta'^2)} \end{bmatrix} \begin{bmatrix} \delta q' \\ \delta p' \end{bmatrix} \qquad (A.14)$$

where $\mu' = K'/(3G') = 2(1 - \nu')/9(1 - 2\nu')$ for an isotropic elastic materal (see section 2.3.1).

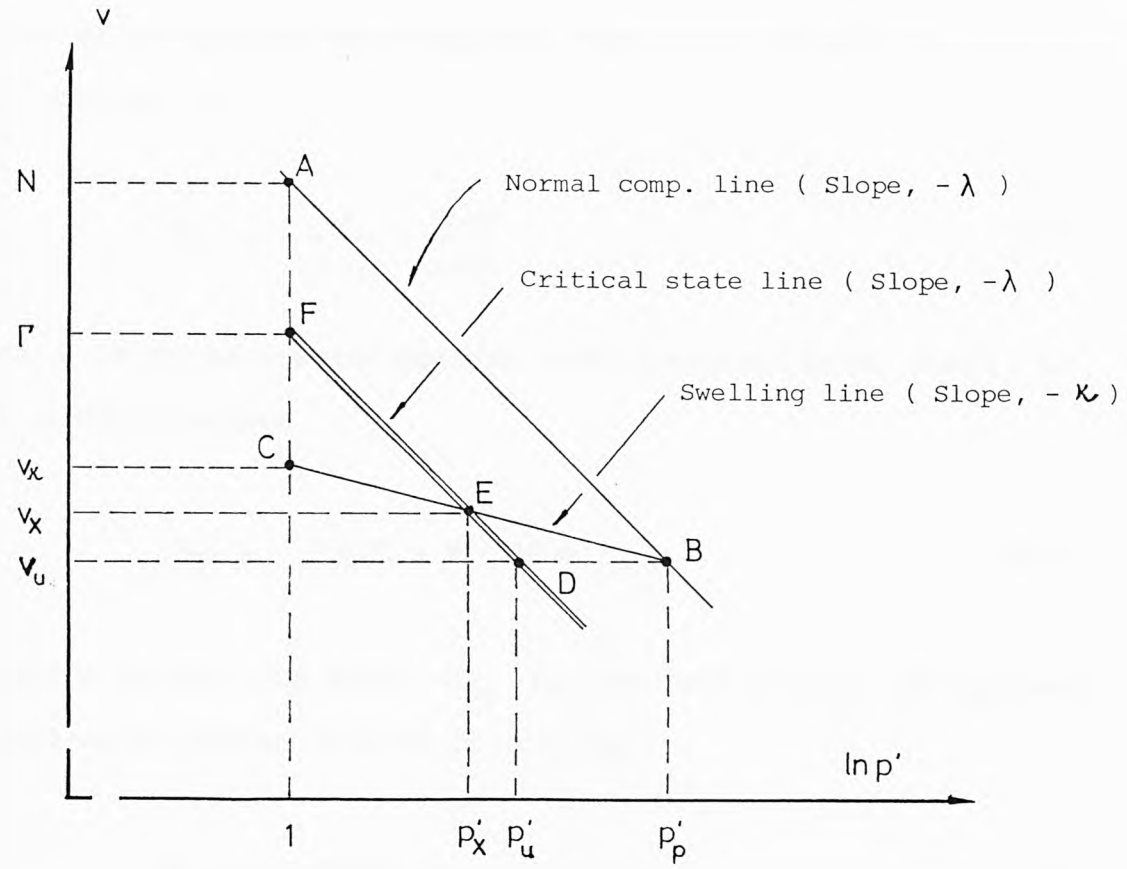

Fig. A1 Derivations of constitutive equations for Modified Cam-Clay.

Appendix B : Procedures for the Calculations of the Required Amount of Salt for Reconstituted Specimens

The origin uncorrected water content m (%) and the weight W (g.) of an oven dried specimen were recored. The amount of salt S_1 (g.) in this specimen is

$$S_1 = \frac{r}{(1-r)} \cdot \frac{W.m}{100} \tag{B.1}$$

where r is the salt-water content and is assumed to be 0.035 , so that eqn(B.1) becomes

$$S_1 = 3.627 \times 10^{-4}.W.m \tag{B.2}$$

The amount of distilled water W_{w1} (g.) required to bring the specimen to salt-water content of 0.035 is given by

$$W_{w1} = 27.57 \cdot S_1 \tag{B.3}$$

For a slurry of salt-water content $\bar{m}$, the required amount of salt-water W_{sw} (g.) is

$$W_{sw} = 1.096 \left(\frac{W.\bar{m}}{100} - W_w\right) \tag{B.4}$$

Therefore the required amount of salt S_2 (g.) and distilled water W_{w2} (g.) for the original dried specimen to produce a slurry of salt-

water content $\overline{m}$ are

$$S_2 = W_{sw} \cdot 0.035 \tag{B.5}$$

$$W_{w2} = W_{w1} + W_{sw} - S_2 \tag{B.6}$$

Appendix C : The Constitutive Equations for City-Clay

$$\begin{bmatrix} \delta\varepsilon_s \\ \delta\varepsilon_v \end{bmatrix} = \frac{1}{vp'} \left\{ \begin{bmatrix} A & B \\ C & D \end{bmatrix}^e + \begin{bmatrix} A & B \\ C & D \end{bmatrix}^p \right\} \begin{bmatrix} \delta q' \\ \delta p' \end{bmatrix} \tag{C1}$$

where

$$A^e = (\kappa_o / 9) \Big/ \left[\frac{(1-\bar{\nu}'-2\alpha\bar{\nu}'+\alpha^2/2)}{(1-\bar{\nu}'+4\alpha\bar{\nu}'+2\alpha^2)} - \frac{(1-\bar{\nu}'+\alpha\bar{\nu}'-\alpha^2)^2}{(1-\bar{\nu}'+4\alpha\bar{\nu}'+2\alpha^2)^2} \right] \tag{C2}$$

$$B^e = (-\kappa_o / 3) \Big/ \left[\frac{(2-2\bar{\nu}'-4\alpha\bar{\nu}'+\alpha^2)}{2(1-\bar{\nu}'+\alpha\bar{\nu}'-\alpha^2)} - \frac{(1-\bar{\nu}'+\alpha\bar{\nu}'-\alpha^2)}{(1-\bar{\nu}'+4\alpha\bar{\nu}'+2\alpha^2)} \right] \tag{C3}$$

$$C^e = B^e \tag{C4}$$

$$D^e = (\kappa_o) \Big/ \left[1 - \frac{(1-\bar{\nu}'+\alpha\bar{\nu}'-\alpha^2)^2}{(1-\bar{\nu}'+4\alpha\bar{\nu}'+2\alpha^2)(2-2\bar{\nu}'-4\alpha\bar{\nu}'+\alpha^2)} \right] \tag{C5}$$

$$A^p = \left[\frac{-4\lambda_o C'}{(\eta'-\eta'_o)(1-4C'+\sqrt{1-4C'})} \right] \left[\frac{\eta'-\eta'_o}{(M-\eta')^2} + \frac{2/3}{(1-\kappa_o/\lambda_o)} \right] \tag{C6}$$

$$B^p = \left[(\lambda_o-\kappa_o) + \frac{4\lambda_o C'\eta'}{(\eta'-\eta'_o)(1-4C'+\sqrt{1-4C'})} \right] \left[\frac{\eta'-\eta'_o}{(M-\eta')^2} + \frac{2/3}{(1-\kappa_o/\lambda_o)} \right] \tag{C7}$$

$$C^p = \frac{-4\lambda_o C'}{(\eta'-\eta'_o)(1-4C'+\sqrt{1-4C'})} \tag{C8}$$

$$D^p = (\lambda_o-\kappa_o) + \frac{4\lambda_o C'\eta'}{(\eta'-\eta'_o)(1-4C'+\sqrt{1-4C'})} \tag{C9}$$

Appendix D: Non-uniformity of Triaxial Samples due to Consolidation with Radial Drainage

Consolidation of triaxial specimens with radial drainage using conventional filter paper trips (Bishop and Henkel, 1962) have long been accepted in routine commercial and research laboratory mainly to minimize the time for consolidation. A series of triaxial tests have been carried out on reconstituted specimens of Speswhite kaolin using equipment as described by Atkinson (1985b) in order to examine the effect due to radial drainage and the results have been reported by Atkinson, Evans and Ho (1985). The results showed that significant non-uniformities of water content occur in specimens with radial drainage when subjected to undrained loading followed by consolidation or when subjected to rapid drained loading. These non-uniformities occur when early consolidation at radial boundary causes concentrations of total stresses and subsequently variations in the final water content, strength and stiffness across the sample diameter. The result is that the final water content is greatest at the centre and the specimen has a soft core surrounded by a relatively stiff shell (see Figs.D1 & D2). These non-uniform water contents imply sustantial variations in effective stresses and 20 % of these variations were estimated for normally consolidated Speswhite kaolin clay. However, this non-uniformity can be avoided by removing radial drainage or it can be minimized by slow drained loading if radial drainage is necessary.

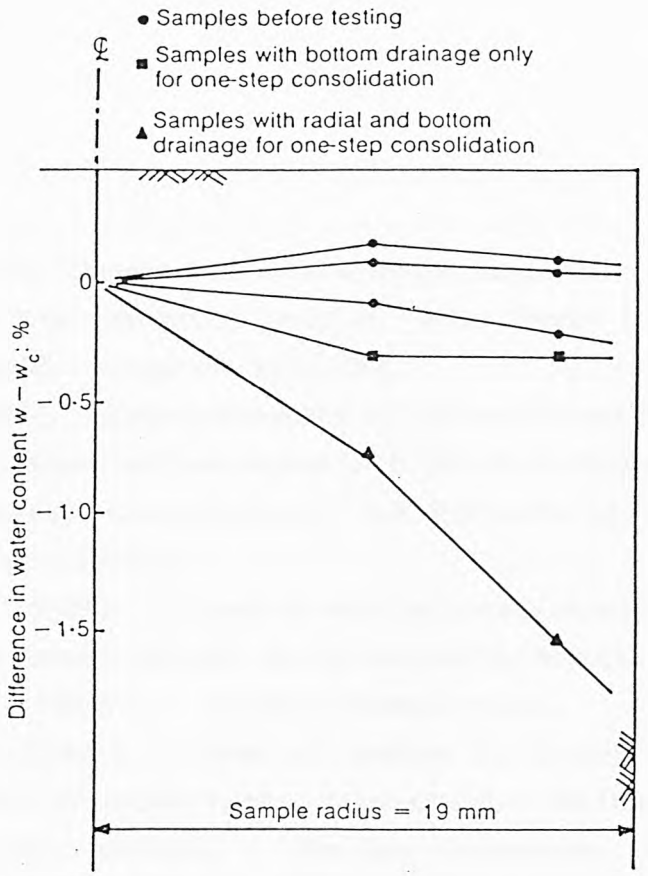

Fig. D1 Radial variation in water content across triaxial samples.

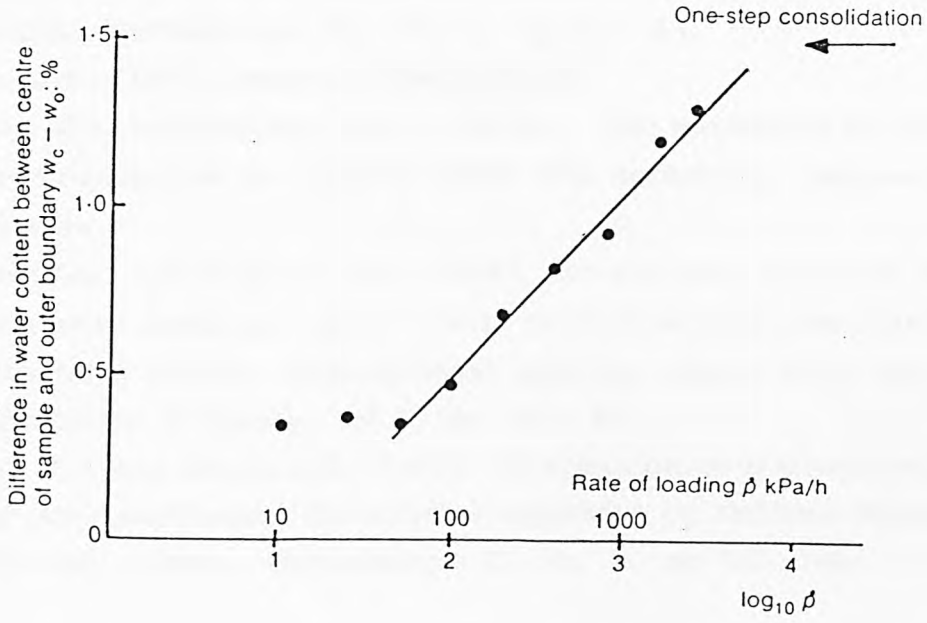

Fig. D2 Variation in water content across triaxial samples with radial drainage with rate of drained loading.

References

Akers, S.A. (1980). Stress-strain and strength properties of marine sediments from the north pacific. M.Sc Thesis : University of Rhode Island, Kingston, R.I., USA.

Algomar, G. (1967). Interpretation of strength and consolidation data from some bottom cores off Tel-Aviv-Palmakhim Coast, Isreal. Marine Geotechnique, A.F. Richards ed. University of Illinois, pp 131-153.

Anderson, D.R. (1981). Seabed working group meeting. Proceeding of the 6th Annual Nuclear Energy Authority Report, Paris.

Atkinson, J.H. (1984a). Private communication.

Atkinson, J.H. (1984b). Rate of loading in drained and undrained stress path triaxial tests. Geotechnical Engineering Research Centre Report, GE/84/1. The City University, London.

Atkinson, J.H. (1984c). Some procedures for normalising soil test results. Geotechnical Engineering Research Centre Report, GE/84/3. The City University, London.

Atkinson, J.H. (1985a). Analysis of soil test data. Geotechnical Engineering Research Centre Report, GE/85/6. The City University, London.

Atkinson, J.H. (1985b). Simple and inexpensive pressure control equipment for conventional and stress path triaxial testing of soils. Geotechnique 35, No. 1, pp 61 - 63.

Atkinson, J.H. (1987). Private communication.

Atkinson, J.H. and Bransby, P.L. (1978). The mechanics of soils - an introduction to critical state soil mechanics. McGraw-Hill, London.

Atkinson, J.H. and Clinton, D.B. (1984). Stress path tests on 100mm diameter samples. Proc. Conf. Site Investigation Practice, Assessing BS5390, 20th Regional meeting, Engng. Geol. Society, University of Surrey, Vol.1, pp. 33 - 43.

Atkinson, J.H. and Evans, J.S. (1985). Discussion on the measurement of soil stiffnesses in triaxial apparatus by Jardine, Symes and Burland (1984). Geotechnique 35, No. 3. pp 323 -340.

Atkinson, J.H. and Farrar, D.M. (1984). Stress path tests to measure soil strength parameters for shallow landslips. Geotechnical Engineering Research Centre Report, GE/84/12. The City University, London.

Atkinson, J.H. and Lewin, P.I. (1984). Private Communication.

Atkinson, J.H. and Richardson, D. (1985). Elasticity and normality in soil - experimental examinations. Geotechnique 35, No. 4, pp 443-449.

Atkinson, J.H. and Richardson, D. (1987). The effect of local dainage in shear zones on the undrained strength of overconsolidated clay. Geotechnique 37, No.3 , pp. 393-403.

Atkinson, J.H., Evans, J.S. and Ho, E. W. L. (1985a). Non-uniformity of triaxial samples due to consolidation with radial drainage. Geotechnique 35, No.3, pp 353-355.

Atkinson, J.H. , Evans, J.S. and Scott, C.R. (1983). Stress path testing equipment, Spectra System - Operation Manual. Geotechnical Engineering Research Centre Report GE/83/1, The City University, London.

Atkinson, J.H. , Evans, J. S. and Scott, C. R. (1985b). Developments in microcomputer controlled stress path testing equipment for measurement of soil parameters. Ground Engineering, Vol. 18, No. 1, pp. 15 - 22.

Atkinson, J.H., Richarson, D. and Woods, R.I. (1985c). Technical note on determination of tangent stiffness parameters from soil test data. Computer and Geotechnics , Vol. 2 , pp. 131-140.

Atkinson, J.H., Richardson, D. and Robinson, P.J. (1986). Compression and extension of K_o normally consolidated kaolin clay. Journal of Geotechnical Engineering , ASCE , Vol. 113, pp. 1468-1482.

Baligh, M. M., Azzouz, A.S. and Chung-Tien Chin (1987). Disturbance due to "ideal" tube sampling. Journal of geotechnical engineering. Proceeding of A.S.C.E. Vol.113, No.7, July, 1987.

Banerjee, P.K. and Stipho, A.S. (1978). Associated and non-associated constitutive relationships for undrained behaviour of isotropic soft clays. International Journal for Numerical and

Analytical Methods in Geomechanics, Vol. 2, pp 35-56.

Banerjee, S. and Pan, Y.W. (1986). Transitional yielding model for clay. Journal of Geotechnical Engineering, Vol. 112, No. 2, pp 170-186.

Barden, L. and McDermott, R.J. (1965). Use of free ends in triaxial testing of clays. Journal of Soil Mechanics and Foundations Div., Proc. of A.S.C.E., SM6, pp 1 - 23.

Bishop, A.W. and Green, G.E. (1965). The influence of end restraint on the compression strength of a cohesionless soil. Geotechnique, 15, No. 2, pp 243 - 264.

Bishop, A.W. and Henkel, D.J. (1962). The measurement of soil properties in triaxial test. Edward Arnold, London, 228 pp.

Bishop, A.W. and Wesley, L.D. (1975). A hydraulic triaxial apparatus for controlled stress path testing. Geotechnique 25, No. 4, pp 657 - 670.

Bjerrum, L, (1967). Engineering geology of Norwegian normally consolidated marine clays as related to settlement of buildings. 7th Rankine Lecture, Geotechnique, 17, No. 1 , pp 81-118.

Bjerrum, L. (1973). Problems of soil mechanics and construction on soft clays. Proceedings. 8th ICSMFE, Moscow, Vol. 3, pp 111-159.

Bowen, A.J., Normark, W.R. and Piper, W.J. (1984). Modelling of turbidity currents on Navy submarine fan, California continent borderland. Sedimentology 31, pp169-185.

Bryant, W.R., Hhottman, W and Trabant, P (1979). Permeability of unconsolidated and consolidated sediments,Gulf of Mexico. Marine Geotechnology, Vol. 1, No. 1 , pp. 1-14.

Brooker, E.Q. and Ireland, H.D. (1965). Earth pressure at rest related to stress history. Canadian Geotechnical Journal, Vol. 2, No. 1, pp 1-15.

B.S. 1377 (1975). Methods of test for soils for civil engineering purposes. British Standard Institution, London.

Buchan, S., Dewes, F.C.D., Jones, A.S.G., McCann, D.M. and Taylor Smith, D. (1971). The accoustic and geotechnical properties of North Atlantic cores. Geological Report No. 71-1, Marine

Science Laboratories, University College of North Wales, Bangor.

Calladine, C.R. (1963). Correspondence on the yielding of clay. Geotechnique 13, No.3, pp 250-255.

Chaney, R.C., Slonim, S.M. and Slomin, S.M. (1982). Determination of calcium carbonate content in soils. In geotechnical properties, behaviour and performance of calcareous soils, K.R. Demars and R.C. Chaney, Eds., American Society for Testing and Materials. STP 777, pp 3-15.

Clinton, D.B. (1985). Determination of soil parameters for design from stress path tests. Geotechnique Engineering Research Centre Report GE/85/29. The City University, London.

Clinton, D.B. (1986). User manual for 'Triax' and 'Triax+' for BBC microcomputer controlled stress path testing. Geotechnical Engineering Research Centre Report GE/86/14. The City University, London.

Clinton, D.B. and Woods, R.I. (1985). An application of microcomputer to the laboratory testing of soils. Geotechnical Engineering Research Centre Report GE/85/24. The City University, London.

Clukey, E.C. and Silva, A.J. (1981). Permeability of deep - sea clays : Northwestern Atlantic. Marine Geotechnology, Vol. 5, No. 1, pp 1-25.

Coop, M. C. and Cherrill, H. E. (1987). Private communication.

Costa Filho, L.M. (1980). A laboratory Investigation of the small strain behaviour of London clay. Ph.D thesis, Imperial College, The University of London.

Davie, J.R. Feuske, C.W. and Serocki, S.J. (1978). Geotechnical properties of deep continental margin soils. Marine Geotechnology, Vol. 3, No. 1, pp 85-119.

Demars, K. R., (1975). Strength and stress-strain behaviour of deep-ocean carbonate soils. Ph.D thesis, University of Rhode Island, Kingston, R.I., USA.

Demars, K.R. and Anderson, D.G. (1971). Environmental factors affecting the emplacement of seafloor installation. Naval Civil Engineering Lab. Tech. Report R -744, 83 pp.

Demars, K.R., Nacci, V.A., Kelly, W.E. and Wang, M.C. (1976). Carbonate content : an index properties for ocean sediments. Proc. 6th Offshore Technology Conference, Paper No. OTC 2627, pp 97-106.

Dewey, J.F. (1972). "Plate Tectonics." Scientific American (Off print No. 900).

Duin, E.J. Th. (1984). Geophysics of the Southern Nares Abyssal Plain, Western North - Atlantic. Contribution to the Seabed Working Group Programmes, A . Kuipers, Ed., Rijks Geologische Dienst, pp. 5-38.

Duncan, J. M. and Duchigiani, A. L. (1976). An engineering manual for settlement studies. Berkeley : University of California.

Duncan, J.M. and Seed, H.B. (1967). Corrections for strength test data. Journal of Soil Mechanics and Foundations Div. Proc. of ASCE, SM5, pp 121- 137.

Embly, R.W. and Jacobi, R.D. (1977). Distribution and morphology of large submarine sediment slides and slumps on Atlantic continental margins. Marine Geotechnology, Vol. 2, pp 205-228.

Ewing, M. (1973). Sediments distribution in the oceans. The Atlantic Geological Society of America, Bulletin Vol. 84, pp 71 - 88.

Fay, J.B., Montarges, P. le Tirant and Brucy, F.(1985). Use of the self - boring pressuremeter and the Stacor large - size fixed piston corer for deep seabed surveying. Advances in Underwater Technology and Offshore Engineering. Offshore Site Investigation Volume 3, pp 187-201.

Freeman, T.J. (1983) . Ocean disposal of high level waste - deep ocean model penetrator experiments - phase 1 report. Building Research Establishment Note, September 1983.

Freeman, T. J. (1988). The use of penetrator for the measurement of the undrained shear strength of soft marine clays. In penetration testing in the UK. Thomas Telford, London , pp. 105-109.

Freeman, T.J., Murry, C.N., Francis, T.J.G., McPhail, S.D. and Schultheiss, J. (1984). "Nature." Vol. 310, pp 130-133.

Fugro (1985). Laboratory testing report for soil samples from Nares Abyssal Plain Atlantic Ocean. A report submitted to the Department of the Environment.

Gens, A. (1979). Discussion on the design parameters for soft clays. In 7th European Conference on Soil Mechanics and Foundation Engineering. Vol. 4 , Brighton, pp. 25-27.

Gens, A. (1983). Stress-strain and strength characteristics of a low plasticity clay. Ph.D. Thesis, Universitiy of London.

Graham, J. and Houlsby, G.T. (1983). Anisotropic elasticity of a natural clay. Geotechnique 33, No.2, pp 165-180.

Graham, J., Noonan, J.L. and Lew, K.V. (1983). Yield states and stress - strain relationships in a natural plastic clay. Canadian Geotechnical Journal, 20, pp 502-516.

Hamilton, E.L. (1971). Elastic properties of marine sediments. Journal of Geophysical Research, Vol. 76, No. 2, pp 579-603.

Hamilton, E.L. (1967). Marine geology of abyssal plains in Gulf of Alaska. Journal of Geophys. Research, Vol. 72, No. 16, pp 4189 - 4213.

Heirtzler, J.R. (1968) Sea-floor Spreading. Scientific American (Off print No. 875).

Henkel, D.J. (1960). The shear strength of saturated remoulded clay. Proceedings of research conference on shear strength of cohesive soils, Boulder, Colorado. pp 533-540.

Henkel, D.J. and Gilbert, G.D. (1952). The effect of the rubber membrane on the measured triaxial compression strength of clay samples. Geotechnique 2, No. 1, pp 20 - 29.

Herrmann, H.G. and Houston, W.N. (1976). Response of seafloor soils to combined static and cyclic loading. Proc. 8th OTC Conference, Houston, Paper No. OTC 2428, pp 53-60.

Herrmann, H.G., Rocker, K.Jr., and Babinean, P.H. (1972). Lobster and FMS : Devices for monitoring lone-term seafloor foundation behaviour. Technical Report R-775, Naval Civil Engineering Laboratory, Port Hueneme, California.

Hight, D. W., Gens, A. and Jardine, R. J. (1985). Evaluation of geotechnical parameters from triaxial tests on off-shore clays. Advan-

ced Underwater Technology and Offshore Engineering. Vol. 3 , pp. 253-268.

Ho, E.W.L. (1985). Undrained compression and extension tests on reconstituted Speswhite kaolin consolidated under K_o conditions with particular reference to the effect of perfect sampling. Geotechnical Engineering Research Centre Report, GE/85/17. The City University, London.

Horn, D.R., Delach, M.N. and Horn, B.M. (1974). Physical properties of sedimentary provinces, North Pacific and North Atlantic oceans. Deep-sea sediments, Physical and Mechanical Properties, Inderblitzen Al Ed. Plenum Press. pp 417-442.

Houtz, R.E., and Ewing, J. (1963). Detailed sedimentary velocities from seismic refraction profiles in the Western North Atlantic. Journal of Geophys. Research, Vol. 68, pp 5233-5258.

Hvorslev, M.J. (1949). Subsurface exploration and sampling of soils for civil engineering purposes. Reports on Soil Sampling, US Waterways Experiment Station, Vicksburg, 521 pp.

Jaky, J. (1944). The coefficient of earth pressure at rest. Journal of the society of Hungarian Architects and engineers. Budapest, pp. 335-348.

Jardine, R.J. Symes, N. J. and Burland, J. B. (1984). The measurement of soil stiffness in triaxial apparatus. Geotechnique 34, No. 3, pp 323 - 340.

Keller, G.H. and Lambert, D.N. (1980). Variation of sediment geotechnicalproperties between the Greater Antilles Outer Ridge and the Nares Abyssal Plain. Marine Geotechnology, Vol. 4, No. 2, pp 125-143.

Kelly, W.E., Nacci, V.A., Wang, M.C. and Demars, K.R. (1974). Carbonate cementation in deep-ocean sediments. Proceedings of A.S.C.E., Vol. 100, GT3, pp 383-386.

Kenny, T. C. (1959). Discussion, Proceeding of ASCE , Vol. 85, No.SM 3, pp.67-79.

Konder, R.L. (1963). Hyperbolic stress-strain response : cohesive soils. Journal of Soil Mechanics and Foundations Division, ASCE, Vol. 89, No. SM1, pp 115-143.

Koustofas, D.C. (1981). Undrained behaviour of a marine clay. American Society for testing and Materials, SPT 740. Laboratory Shear Strength of Soils, pp 254-276.

Kuijper, A. (1984). A sedimentation model for the Southern Nares Abyssal Plain, Western North - Atlantic. Contribution to the Seabed Working Group. A. Kuijper, Ed., Rijks Geologische Dienst, pp 75-80.

Lewin, P.I. (1984). Private Communication.

Longwell, C.R. and Flint, R.F. (1962). Introduction to Physical geology. 2nd ed. John Wiley, New York.

Marine Geotechnical Consortium, (1985). Geotechnical properties of Northwest Pacific pelagic clays : Deep Sea Drilling Project Leg 86, Hole 576A. Initial Reports of the Deep Sea Drilling Project, Vol. 86, US Government Printing Office, Washington.

McClelland, B. (1967). Progress of consolidation in delta front and prodelta clays of the Mississippi River. Marine Geotechnique A.F.Richards ed., University of Illinois, pp 22-40.

Mitchell, J.K. (1976). Fundamentals of soil behaviour. John Wiley and Sons, New York.

Morgenstern, N. R. (1967). Submarine slumping and the imitation of turbidity currents. Marine Geotechnique, A.F. Richards ed., Universtiy of Illinois Press, Urbana.

Morris, D.V. and Abbiss, C.P. (1979). Static modulus of Gault Clay predicted from seismic tests. Ground Engineering, Vol. 12, No. 8, pp 44-50.

Mroz, Z., Norris, V.A., Zienkiewicz, O.C. (1981). An anisotropic critical state model for soils subject to cyclic loading. Geotechnique 23, No. 3, pp 450 -453.

Nacci, V.A., Wang, M.C. and Demars, K.R. (1975). Engineering behaviour of calcareous soils ASCE conference on Civil Engineering in the Ocean III, University of Delaware, Newark, Vol. 1 pp 380-400.

Nakase, A. and Kamei, T. (1983). Undrained shear strength anisotropy of normally consolidated cohesive soils. Soils and Foundations 23, No.1, pp 81-101.

Nambier, M.R.M., Venkatappa Rao, G. and Gulhati, S.K. (1985). The nature and engineering behaviour of fine grained carbonate soil from off the West Coast of India, Marine Geotechnology, Vol. 6, No. 2, pp 145-171.

Naval Facilities Engineering Command (1971). Design Manual : Soil Mechanics, Foundations and Earth Structures. Washington : Department of Navy.

Naylor, D.J., Pande, G.N. , Simpson, B. and Tadd, R (1981). Finite elements in geotechnical engineering. Pineridge Press.

Ng, C. (1985). Report of progress in first year of research on strength and deformation characteristics of Cowden Till. Geotechnical Engineering Research Centre Report, GE/85/7. The City University, London.

Nickerson, C.R. (1978). Consolidation and permeability characteristics of deep-sea sediments. M.Sc Thesis: Worchester Polytechnic Institute, Worchester. Massachusetts, USA.

Noorany, I. (1984). Phase relations in marine soils. Proceedings of A.S.C.E. GT. 4, Vol. 110, pp 539-543.

OAP (1982), Penetrator option - studies relevant to emplacement in deep ocean sediments. A report submitted to the Department of Environment by Ove Arup and Partners, DoE Report No. DoE/RW/82.102.

Ohta, H. and Wroth, C.P. (1976). Anisotropy and stress reorientation in clay. Numerical Method in Geomechanics. Proc. of American Society of Civil Engineers, 1, pp 320-328.

Parry, R.H.G. and Nadarajah, V. (1973). A volumetric yield locus for lightly overconsolidated clay. Geotechnique 23, No.3, pp 450-453.

Poulos, H.G. (1980). A review of the behaviour and engineering properties of carbonate soils. Research Report No. 381, Civil Engineering Laboratories, The University of Sydney, Sydney, Australia.

Pender, M.J. (1977). A unified model for soil stress- strain behaviour. Proc. of 9th International Conference on Soil Mechanics and Foundation Engineering, Tokyo . Speciality

session No.9, Constit utive Equations for Soils. pp 213-222.

Pender, M.J. (1978). A model for the behaviour of overconsolidated clay. Geotechnique 28, No.1, pp 1-25.

Pender, M.J., Parry, R.H.G. and George, P.J. (1975). The response of a soft clay layer to embankment loading. Proc. of Second Australian, New Zealand Conference on Geomechnaics. Brisbane, pp 169-173.

Rendulic, L. (1938). A Consideration of the question of plastic limiting states. Bauingenieur, 19, pp 159-164.

RGD (1984). Rijks Geologische Dienst. Contribution to the Seabed Working Group. Netherland Progress report 1984.

Richards, A.F. (1974). Standardisation of marine geotechnics symbols, definitions, units and test proceedures. Deep Sea Sediment. Physical and Mechanical Properties, A.L. Inderblitzen eds., Plenum Press, pp 271 -292.

Richardson, D (1985). Report on progress in second year of research on threshold effects in soil mechanics. Geotechnical Engineering Research Centre Report , GE/85/23 . The City University, London.

Richardson, D. (1986). Effect of membrane and filter paper stiffnesses on the stress-strain behaviour of triaxial samples. Geotechnical Engineering Research Centre Report, GE/86/4. The City University, London.

Rijks Geologische Dienst (1982). Geological studies on abyssal plains in the North Atlantic. Progress Report. Contribution to the Seabed Working Group Programme. Progress Report, 1982.

Roscoe, K.H. and Burland, J.B. (1968). On the generalised stress strain behaviour of 'wet clay'. Engineering Plasticity Ed. J. Heyman, F. A Leckie. Cambridge University Press. pp 535 - 609.

Schofield, A.N. and Wroth, C.P. (1968). Critical state soil mechanics. McGraw - Hill.

Schultheiss, P.J. (1982). Geotechnical properties of deep-sea sediments : A critical review of measuring techniques. IOS report 134. The Institute of Oceanographic Science.

Searle, R.C., Schulthe s, P.J., Weaver, P.P.E., Noel, R.B., Jacobs,

C.L. and Hugget, Q.J. (1985). Great Meteor East : geological studies of its suitability for disposal of heating - emitting radioactive wastes. Institute of Oceanographic Science Report, 193.

Sherpard, L.E. (1984). Geotechnical property characteristics of Nares Abyssal Plain sediments : A summary report. Contribution to the Seabed Working Group Programmes, A. Kuiper, Ed., Rijks Geolgische Dienst, pp 107-112.

Sicilliano, R.J. (1984). Constitutive behaviour of isotropically and K_o consolidatd marine sediments in undrained shear. M.Sc Thesis: University of Rhode Island, R.I., USA.

Silva, A.J. (1979). Geotechnical properties of deepsea clays : A brief-discussion. 1st Canadian Conference on Marine Geot. Engineering Calgary.

Silva, A.J. (1985). Comparison of in-situ and ship-board vane measurements of a deep-sea clay. Proc, Int. Conf. on Off-Shore Site Investigation, The Society for Underwater Technology, London, pp 219-230.

Silva, A. J. and Calnan, D.I.(1982). Geotechnical aspects of subsurface seabed disposal of high level radioactive waste. Annual Report no. 6 , DOE/SLA Contract nos. 13-1256 and 13-9927.

Silva, A.J. and Hollister, C (1979). Geotechnical properties of ocean-sediments recovered with the giant piston corer : Blake- Bahama OuterRidge. Marine Geology, 29 , pp. 1-22

Silva, A.J. and Jordan, S.A. (1984). Consolidation properties and stress history of some deep sea sediments. Symposium on Seabed Mechanics, University of Newcastle upon Tyne. England.

Silva, A.J., Moran, K. and Akers, S.A. (1983). Stress-strain-time behaviour of deep sea clays. Canadian Geotechnical Journal Vol. 20, pp. 517-531.

Skempton, A,W. (1953). The colloidal activity of clays. Proceedings of the 3rd International Conference on Soil Mechanics and Foundation Engineering. Vol. 1, pp. 57-61.

Skempton, A.W. (1954). The pore pressure coefficients A and B. Geotechnique 4, No.2, pp 143-147.

Terzaghi, K. (1936). The shearing resistance of saturated soil and the angle between the planes of shear. Proc. 1st Int. Conf. Soil Mech. and Foundation Engineering 1, pp 54-56. Harvard. Mass.

Terzaghi, K. (1943). Theoretical Soil Mechanics. New York. John Wiley and son. 510 pp.

Terzaghi, K. and Peck, R.B. (1967). Soil Mechanics in Engineering Practice. John Wiley and Son, Inc.

Valent, P.J. (1979). Engineering behaviour of two deep ocean calcareous sediments, including influence on the performance of the propellant driven anchor. Ph.D Thesis: Purdue University, West Lafayette, Indiania, USA.

Valent, P.J., Altschaeff, A.G. and Lee, H.J. (1982). Geotechnical properties of two calcareous oozes. In Geotechnical Properties, Behaviour and Performance of Calcareous Soils. ASTM,STP 777, K.R. Demars and R.C. Chaney, Ed., pp 79-95.

Wong, P.K.K. and Mitchell, R.J. (1975). Yielding and plastic flow of sensitive cemented clay. Geotechnique 25, No. 4, pp 763-782.

Wood, D. M. (1984). On stress parameters. Geotechnique 34, No. 2, pp 282-287.

Woods, R. I. (1985a). Link-Epson-Spectra data capture program user manual. Geotechnical Engineering Research Centre Report GE/85/10. The City University, London.

Woods, R.I. (1985b). Evaluation of soil stiffness from triaxial test data. Geotechnical Engineering Research Centre Report : GE/85/12 The City University , London.

Woods, R.I. and Clinton, D.B. (1986). A microcomputer stress path testing and data analysis system for research and practice. Symposium on Computer Applications in Geotechnical Engineering, Univers y of Birmingham, England.

Wroth, C.P. (1984). The interpretation of in-situ soil tests. Geotechnique 34, No. 4, pp 449-489.

Wroth, C.P. and Wood, D.M. (1978). The correlation of index properties with some basic engineering properties of soils. Canadian Geotechnical Journal 15, No. 2, pp 137-145.

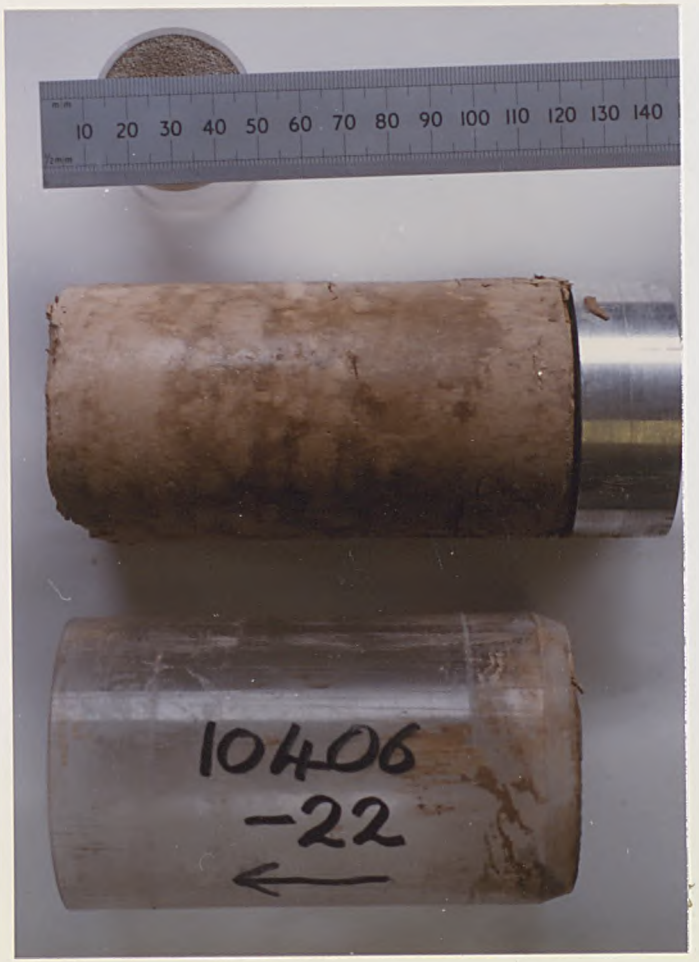

Plate 5.1 The IOS sub-sample core.

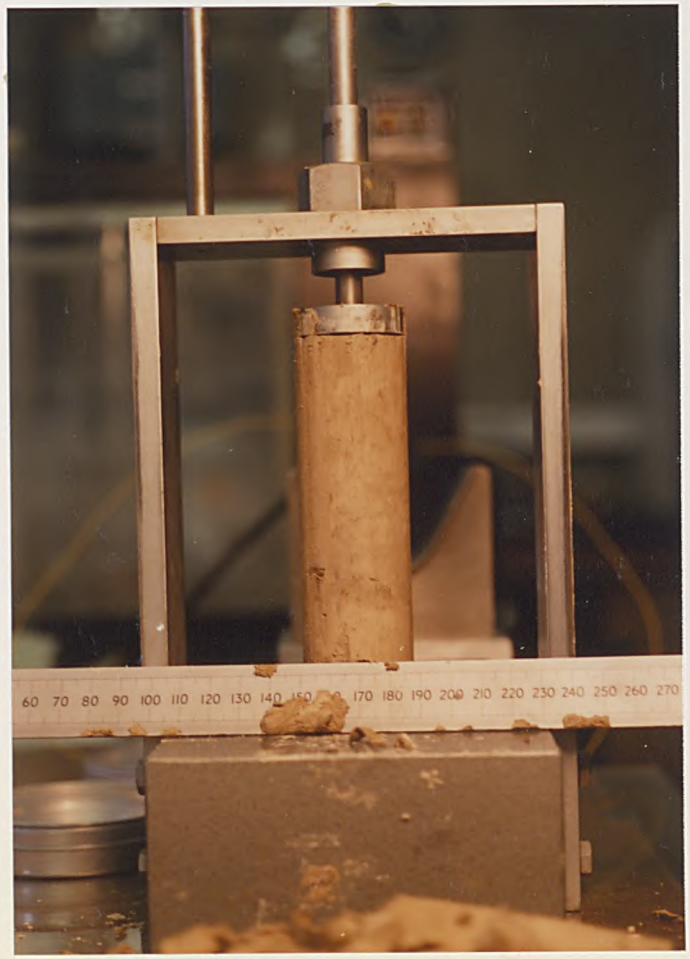

Plate 5.2 Trimming of the IOS sample core.

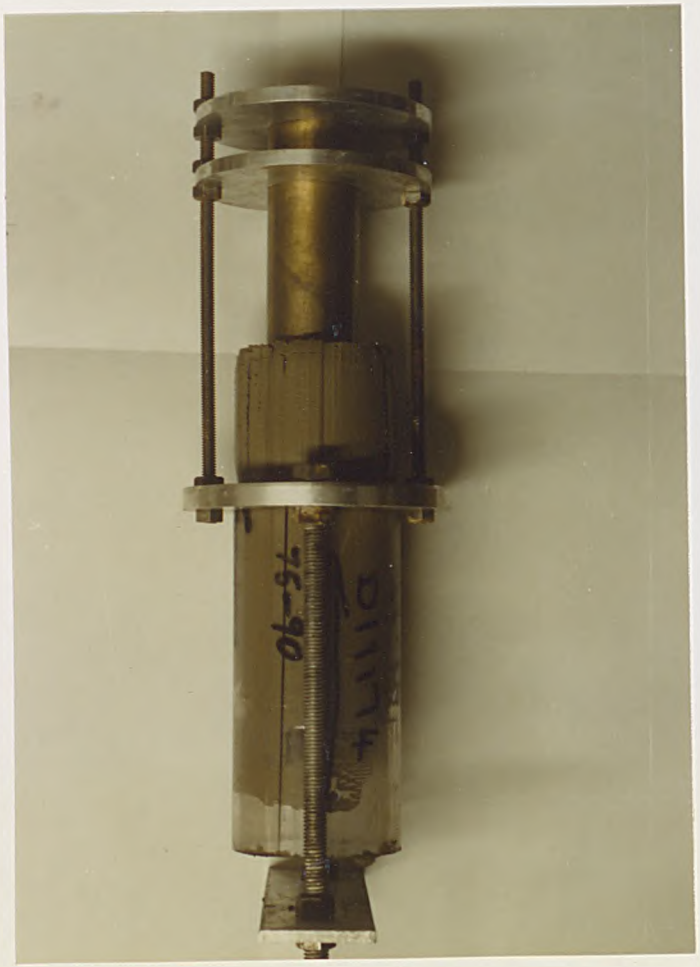

Plate 5.3 Trimming of the GME sub-sample core.

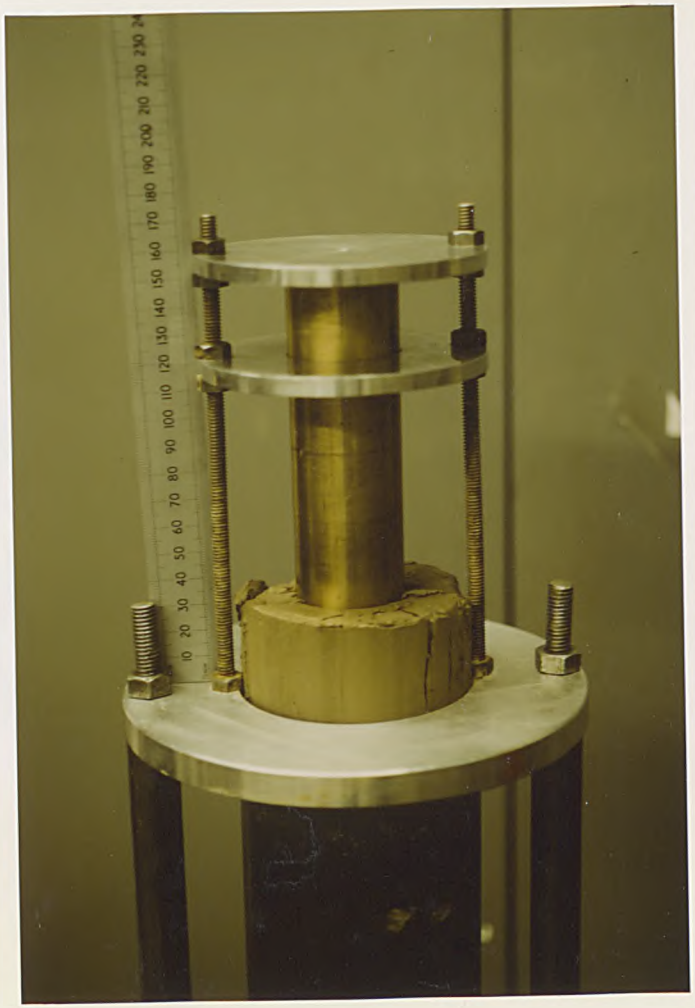

Plate 5.4 Trimming of the NAP sub-sample core.

Plate 5.5 Trimming of the GME C-6 sub-sample core.

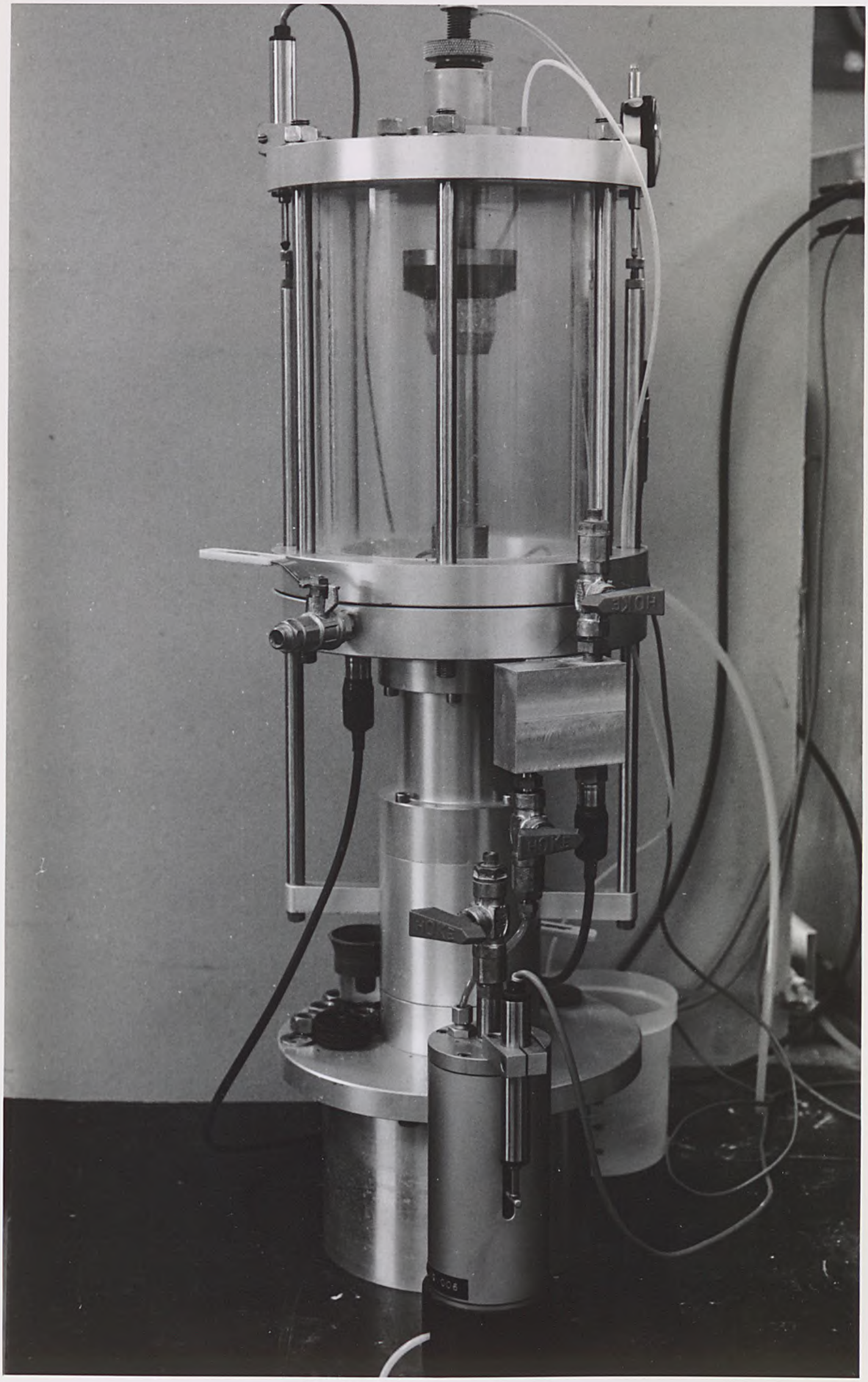

Plate 6.1 The triaxial stress path apparatus.
(after Bishop and Wesley, 1975)

Plate 6.2 The inner salt-water Chamber.

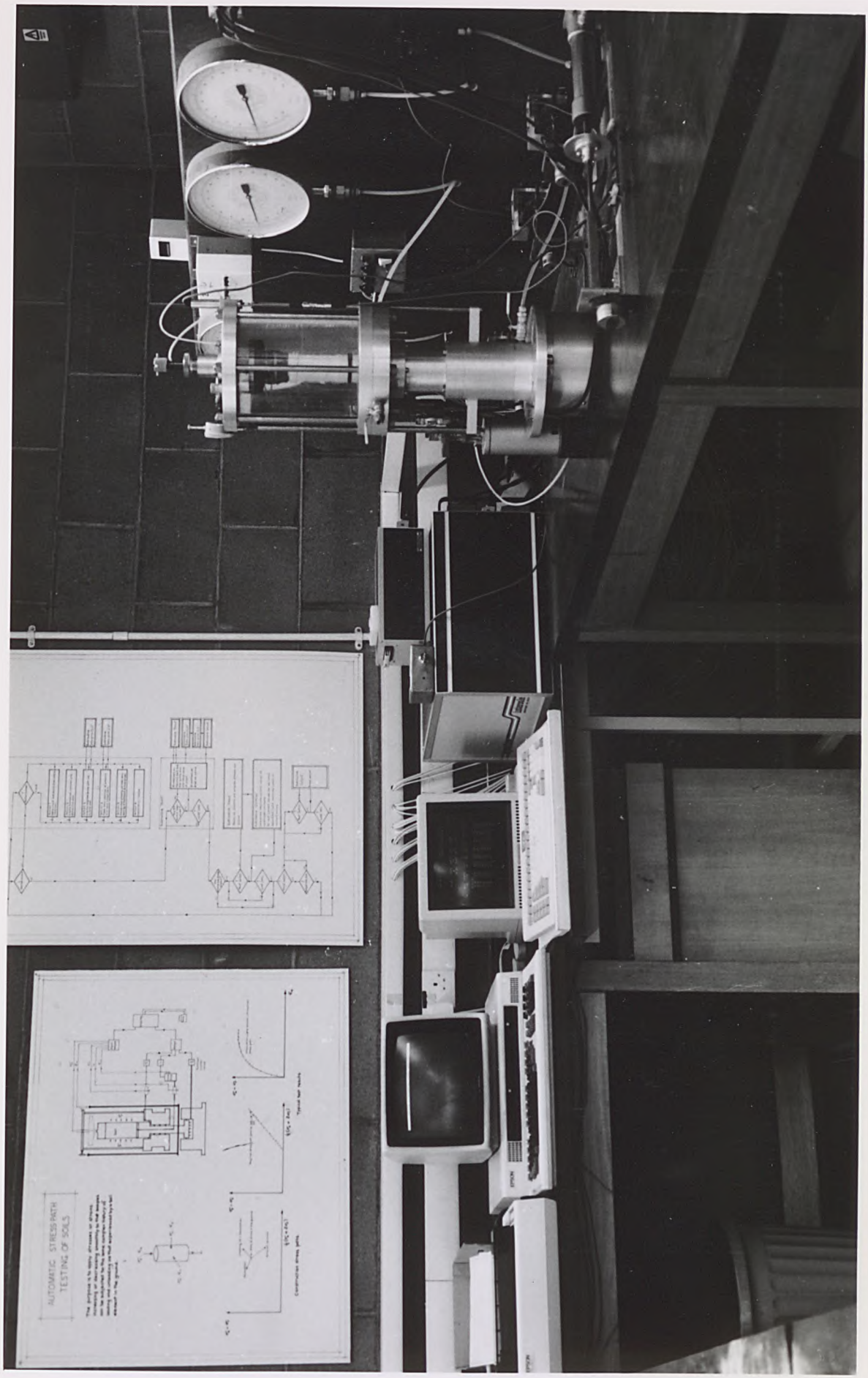

Plate 6.3 The 'Spectra' microcomputer control system.

(after Atkinson et al., 1985)

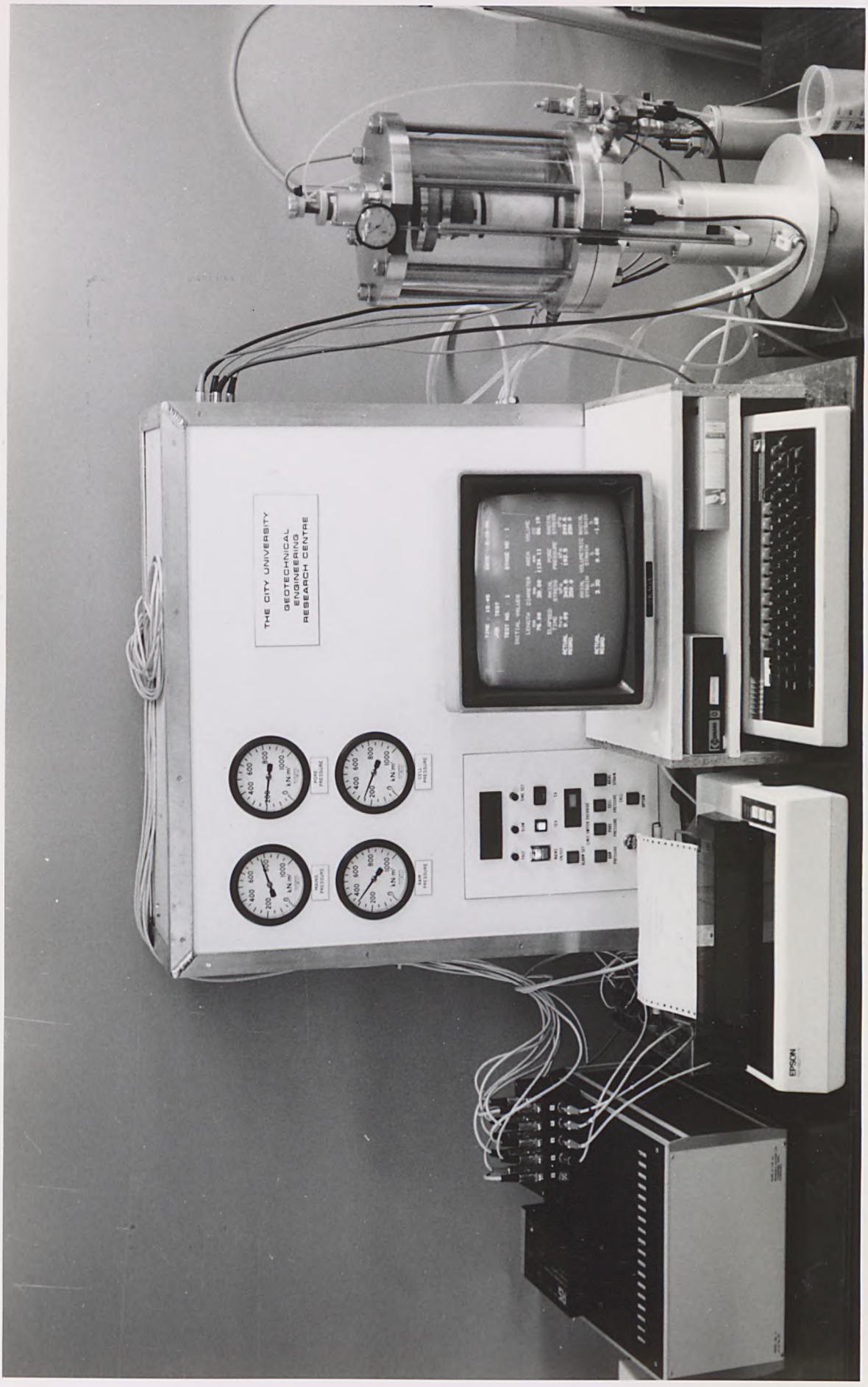

Plate 6.4 The 'BBC' microcomputer control system.

(after Clinton, 1985)

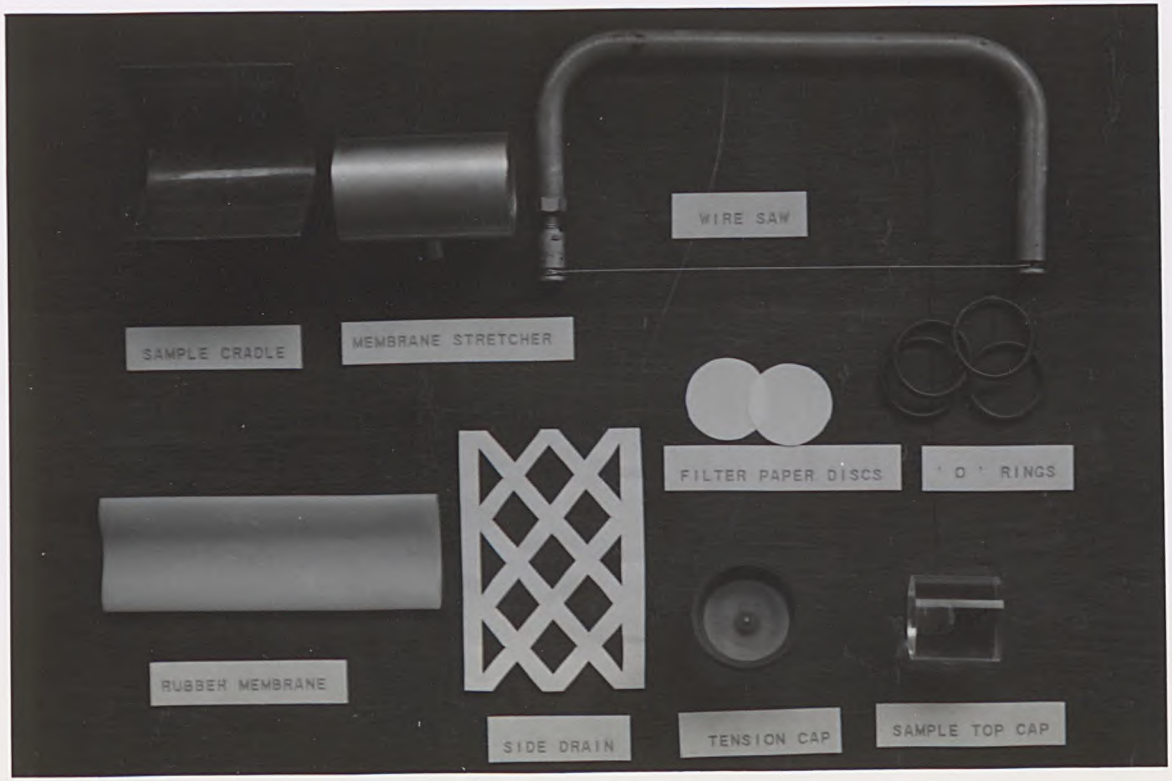

Plate 7.1 Equipments for preparing triaxial test specimens.

(a) The IOS specimens (x 3000)

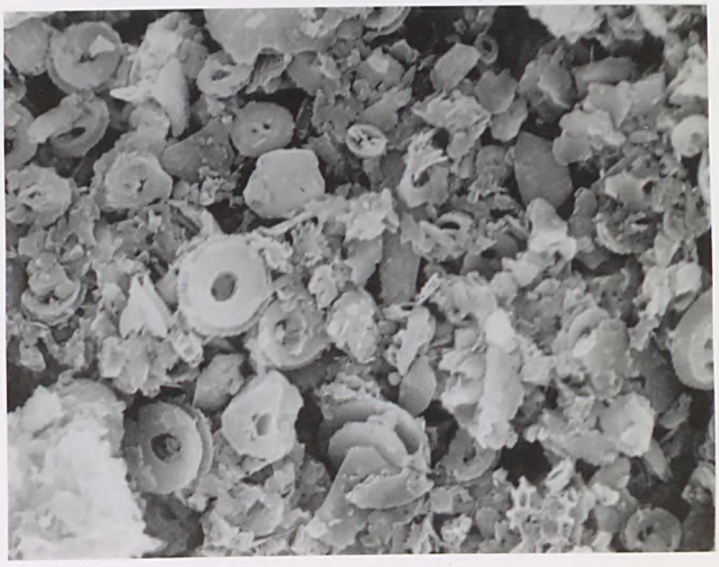

(b) The GME specimens. (x 3000)

Plate 8.1 Micrographs of the specimens.

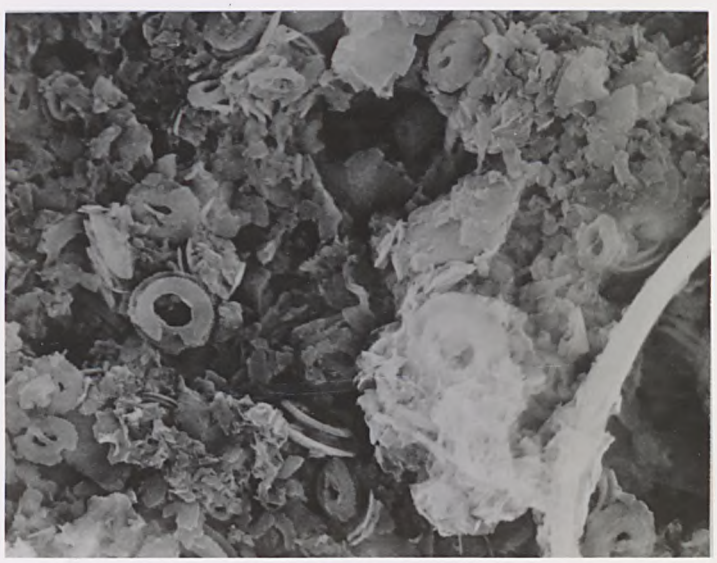

(c) The GME C-6 specimens. (x 3000)

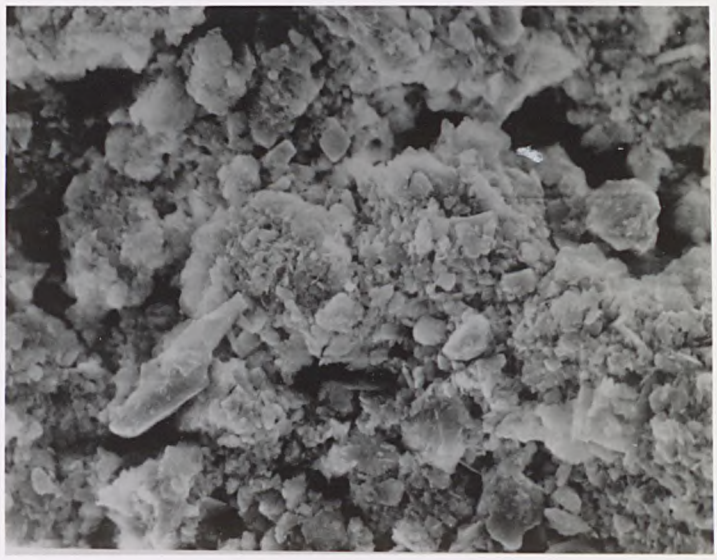

(d) The NAP specimens. (x 1000)

Plate 8.1 Micrographs of the specimens.

	Types		Origins	Water depths (m)	Mean particle size	Rate of deposition mm/ 1000 yrs.
Pelagic clays	Red clays		Wind-borne dust	4000-8000	1 μm	0.1 to 1
	Volcanic		Volcanic dust	4000-8000	20 μm	0.1 to 1
	Authigenic		Nodular	2000-3000	1-3 μm	0.1 to 1
	Biogeneous oozes	Calcareous >30% $CaCO_3$	Nanofossils	4000-5000	< 4 μm	10 to 30
			Foraminifera	3000-4000	> 4 μm	
			Pteropod	2000-3000	1-2 mm	
			Corals	<35	> 2 mm	
		Siliceous >30% SiO_2	Silica	2000-6000	2 μm	10 to 20
			Planktonic	2000-6000		
Terrigeneous deposits	Turbidites	Proxal	water deposited	800-3000	3-10 μm	50 to 1000
		Distal	water deposited	3000-5000	2-5 μm	50 to 1000
Hemi-pelagic clays	Distal turbidites		interbedded with pelagic clays	3000-5000	2-4 μm	-
	Biogeneous		transported by turbidity currents.	3000-5000	2-4 μm	-

Table 3.1 Classifications of Ocean Sediments

Site	Cruise	Core no	Core length (cm)	Locations	water depths (cm)	soil type	test type	reference
* MPG-1	MARA-02	GC-04	2.6	30.1°N/157.9°W	5868	Illite	Index-depth Triaxial	Akers, 1980
	VEMA-32 (1975)	PC-115	10.04	31°5´N/158°31´W	5500	Illite	Index-depth Triaxial Oedometer	Silva et al.,1983 Silva et al.,1982
	LL-44 (1976)	GPC-3	24.4	30°19.9´N/157°49.4´W	5705	Smectite	Index-depth Triaxial Oedometer	Silva et al.,1984 Akers, 1980 Silva et al.,1983
	DS1208-81 (1981)	GC-10 GC-11 Dredge	- - -	30°20´N/157°50´W 30°23´N/157°50´W 30°20´N/119°49´W	5860 5860 5800	Illite Illite Illite	Triaxial Triaxial Triaxial	Siciliano, 1983
-	DSDP-576A (1982)	Drilling	65.9	32°21.4´N/164°16.5´E (outside MPG-1)	6217	Illite	Index-depth Oedometer Triaxial	Marine Geotechnical Consortim, 1985 Siciliano, 1983

*(MPG-1) Lat. 29°40´N to 31°40´N : Long. 156°40´W to 160°40´W

Table 4.1 Details of the North Pacific deep-ocean sediments.

Site	Cruise	Core no	Core length (m)	Locations	Water depths (m)	Soil type	Test type	Reference
Bermuda Rise	KNORR-31	GPC-3	22.9	33°51´N / 57°2.6´W	5090	Calcareous	Index-depth Oedometer	Silva et al, 1976
		GPC-5	31.9	33°41.2´N / 57°36.9´W	4583	Calcareous	Index-depth Oedometer Permeability	Silva et al, 1976 Clukey and Silva, 1982
		GPC-6	14.0	33°56.9´N / 57°21.3´W	4672	Calcareous	Index-depth Oedometer	Silva et al, 1976
		GPC-7	41.6	28°17.9´N / 72°17.8´W	4935	Calcareous	Index-depth Oedometer	Silva and Hollister, 1979
		GPC-8	29.5	28°41.7´N / 75°16´W	4962	Calcareous	Index-depth Oedometer	Silva and Hollister, 1979
		GPC-9	36.9	28°14.7´N / 74°26.4´W	4758	Calcareous	Permeability Index-depth	Clukey and Silva, 1982
		GPC-11	24.6	28°38´N / 72°21.5´W	4967	Calcareous	Permeability Index-depth Oedometer	Clukey and Silva, 1982
Rockall Trough	KNORR-51	GPC-17 GPC-19 GPC-21 GPC-34	10.0 14.9 2.8 2.6	56°17´N/12°30´W 56°18´N/12°31´W 56°18´N/12°31´W 55°24´N/13°12´W	2505 2535 2567 2807	Calcareous	Index-depth	Carchedi, 1979

Table 4.2 Details of the North Atlantic Deep-Ocean Sediments.

To be continued....

Continue to Table 4.2

Site	Core no	Core length (m)	Locations	Water depths (m)	Soil type	Test type	Reference
East Thulean Rise	G-1 G-2 G-3 G-4	4.6 4.4 3.5 3.0	44° N-56° N 0° W-23° W	4115 4267 4572 4572	Calcareous clay	Index-depth oedometer Triaxial	Demars, 1975
Canary Basin	BS-1 BS-2 BS-3 BS-4	5.2 6.0 4.7 4.6	20° N-40° N 10° W-30° W	4877 4877 5486 4572	Calcareous clay	Index-depth oedometer Triaxial	Demars,1975 Nacci, 1975
Venezue-lan Basin	Box-corer	.46	15°N/69°20´W	3939	Calcareous silty-clay	Index Oedometer Triaxial	Valent, 1979 & 1982
Blake Plateau	Piston corer	-	77°12´W/28°N	1130	Calcareous silty-sand	Index Oedometer Triaxial	Valent, 1979 & 1982
-	GC-1 GC-2 GC-3	1.8 2.2 2.2	22°44´N/66°28´W 22°17´N/67°26´W 21°52´N/67°38´W	5800 5450 5250	Silty-clay	-	Keller and Lambert, 1979
Gulf of Mexico	-	-	-	-	varies	Permeability	Bryant et al, 1975

Compression index	Reference	Remark
$C_c = .009\ (LL - 10)$	Terzaghi and Peck, 1967	Empirical formula on terrestrial soils
$C_c = .54\ (e_o - .35)$	NAVFAC, 1971	Empirical formula on terrestrial soils
$C_c = .011\ (LL - 12)$	Herrmann et al., 1972	Empirical formula on marine soils
$C_c = .02 + .014\ PI$	Demars, 1975	Empirical formula on deep-ocean calcareous sediments
$C_c = G_s\ PI\ /\ 200$	Wroth and Wood, 1978	Critical state theory

Table 4.3 Correlations between compression index and index properties.

Soil	PI(%)	Clay(%)	k(m/s)	K_o	Testing equipment	Reference
Atlantic calcareous silty clay	14-37	33-40	$1x10^{-9}$	0.45	Triaxial apparatus	Herrmann and Houston, 1976
Atlantic calcareous silty sand	NP	NP	$3x10^{-9}$	0.36	Triaxial apparatus	Herrmann and Houston, 1976
Pacific pelagic clay	48	75	-	0.52	Triaxial apparatus	Sicilliano, 1985
Pacific pelagic clay	138	78	-	0.55	Triaxial apparatus	M.G.C.* ,1985
	130	88	-	0.56	Triaxial apparatus	

* Marine Geotechnical Consortium

Table 4.4 Summary of the K_o values of deep-ocean sediments.

Sample Core No	Locations	Site	Water depth (m)	Gravity corer	Core dia./length (mm / m)
Core-10406	Long. 32 34.7´N Lat. 22 27.5´W	IOS*	5268	Kastenlot	65 / -
D11172-6	Long. 24 48.2´N Lat. 31 26.7´W	GME	5438	Piston	65 / -
D11174-10	Long. 24 49.6´N Lat. 31 26.5´W	GME	5439	Piston	65 / -
C -6	Long. 31 16.5´N Lat. 25 22.1´W	GME	5360	Stacor	108 / 33.42
84 PCM 19	Long. 22 40.6´N Lat. 63 28.6´W	NAP	5772	Piston	83 / 7.57
84 PCM 33	Long. 22 13.9´N Lat. 63 16.1´W	NAP	5715	Piston	83 / 7.38

* a site just outside GME site

Table 5.1 Details of the sub-sample cores.

Measurement	Instrument	Working range	Channel range	Resolutions*	Resolutions+
Deviator load	Load cell	0 - 600 kPa	40 mV	0.03 kPa	0.4 kPa
Cell and pore pressure	pressure transducers	400 kPa	20 mV	0.03 kPa	0.4 kPa
Axial strain	Linear displacement transducer	0 - 40 %	80 mV	0.001 %	0.01 %
Volumetric strain	Volume gauge transducer	0 - 40 %	80 mV	0.001 %	0.01 %

* For the 'Spectra' control system.

\+ For the 'BBC' control system.

Table 6.1 Resolutions of the instruments.

Measurement	Instrument	Individual accuracy			Overall accuracies
		Noise	Drift	Hysteresis	
σ_a kPa	Load cell	± 0.5	± 2	± 1	± 4
u , σ_r kPa	Pressure transducers	± 0.5	± 1	± 1	± 2
ε_a %	Linear displacement transducer	± 0.01	± 0.01	± 0.01	± 0.02
ε_v %	Volume gauge transducer	± 0.01	± 0.01	-	± 0.02

Table 6.2 Summary of the accuracies of the measurements.

Test no	Sample no	Compression stage			Shearing stage		
		$\dot{\sigma}_a$ kPa/hr	ε_v* %	$\Delta\varepsilon_v$+ %	$\dot{\sigma}_a$ kPa/hr	$\dot{\sigma}_r$ kPa/hr	$\dot{\varepsilon}_a$ %/hr
T2301	IOS-1	4	4.30	0.15	5	0	0.50
T3202	IOS-2	4	8.33	0.42	-10	0	-0.30
T3203	IOS-3	4	18.82	0.46	-20	0	-0.30
T3204	IOS-4	6	17.14	-	5	0	-
T2205	IOS-5	6	10.38	0.22	5	0	-
T2206	IOS-6	4	10.22	0.44	-10	0	-0.20
T2211	GT-1	6	16.50	0.45	5	0	0.40
T2212	GT-2	6	23.53	-	-15	0	-0.50
T2213	GT-3	5	13.78	0.45	5	0	0.50
T3214	GT-4	3	15.96	2.18	4	0	0.25
T3215	GT-5	2	14.65	0.90	-10	0	-0.25
T2216	GT-6	3	18.45	0.88	4	0	0.25
T2301	GT-7	3	7.81	0.89	2	0	0.15
T2303	GT-8	5	14.62	0.73	4	0	0.50
T2305	GT-9	1	12.25	0.37	1.5	0	0.30
N9501	NT-1	1	27.48	0.26	-4	0	0.75
N9502	NT-2	3.5	28.43	0.12	-3	0	-0.75
N2503	NT-3	2.5	20.79	0.77	-4	0	-0.50
N2504	NT-4	1	13.62	1.17	3	0	0.50
N9511	NT-5	1	11.75	0.73	2	0	0.50
N2512	NT-6	1	11.24	0.53	2	0	0.30
N9513	NT-7	1.5	13.95	0.61	3	0	0.35
N9514	NT-8	2	18.82	0.60	2	0	0.25

* Total volumetric strain

\+ The observed change of volumetric strain at the end of loading

Table 7.1 Summary of the rates of loading for triaxial stress path testing.

To be continued...

Continue to Table 7.1

Test No	Sample No	$\dot{\sigma}_a$ kPa/hr	ε_v* %	$\Delta\varepsilon_v$+ %	$\dot{\sigma}_a$ kPa/hr	$\dot{\sigma}_r$ kPa/hr	$\dot{\varepsilon}_a$ %/hr
N2515	NT-9	2	16.79	0.58	-3	0	-0.50
N2521	NT-10	2	18.85	0.88	-4	0	-0.40
N9522	NT-11	1	12.97	0.81	2	0	1.00
N2523	NT-12	2.5	17.65	0.93	-2	0	-0.25
N9524	NT-13	2	16.04	0.83	2	0	1.00
N2531	NT-14	1.5	12.58	0.62	0.5	-0.25	1.50
N9532	NT-15	1.5	11.48	1.04	1	1	-
N9533	NT-16	2	12.75	0.47	-0.8	0.4	-0.30
N2534	NT-17	2	15.69	0.67	1	1	-
N9535	NT-18	1.5	15.78	0.67	0.4	-0.2	0.20
N9536	NT-19	1	11.98	0.80	-0.5	0.25	-1.00
T9801	11C/A	4	10.18	0.81	4	0	0.20
T9802	11C/B	4	3.28	0.29	4	0	0.60
T9803	11C/C	5	13.16	0.42	8	0	1.00
T9811	22A/A	2	10.24	0.95	4	0	0.40
T9812	22A/B	1	3.28	0.21	2	0	0.60
T9813	22A/C	2	16.77	0.71	4	0	0.40
T9821	30A/A	1	3.47	0.45	2	0	0.40
T9822	30A/B	2	1.26	0.13	2	0	0.50
T9823	30A/C	2	9.02	0.53	4	0	1.00
T9831	1B/A	3	12.21	0.94	4	0	0.40
T9832	1B/B	5	1.96	0.35	4	0	0.40
T9833	1B/C	12	18.99	0.91	8	0	0.50
T3221	GR-1	6	10.92	0.41	5	0	0.20
T2222	GR-2	5	11.83	0.20	-10	0	-0.25
T2223	GR-3	4	8.05	0.53	5	0	0.10
T2224	GR-4	3	4.68	0.47	4	0	0.40
T2225	GR-5	1.5	6.87	0.41	-10	0	-0.5
T2226	GR-6	6	12.91	0.60	5	0	0.25

To be continued....

Continue to Table 7.1

Test No	Sample No	$\dot{\sigma}_a$ kPa/hr	ε_v* %	$\Delta\varepsilon_v$+ %	$\dot{\sigma}_a$ kPa/hr	$\dot{\sigma}_r$ kPa/hr	$\dot{\varepsilon}_a$ %/hr
T2234	GR-7	4	6.39	0.77	4	0	0.10
T2235	GR-8	4	9.33	0.43	-15	0	-0.10
T9302	GR-9	1	8.13	0.26	- 1.5	0	-0.10
T2304	GR-10	5	12.94	0.46	4	0	0.30
T2401	GR-11	3.5	11.21	0.42	1.5	0	0.15
T2402	GR-12	5.5	10.18	0.40	-2	0	-0.20
T2701	GR-13	2.5	10.29	0.33	2	0	0.15
T9703	GR-14	4	14.92	0.45	2	0	0.15
T9253	GR-15	3	9.42	0.43	3	0	0.15
T2255	GR-16	4	12.90	0.35	-3	0	-0.05
T9256	GR-17	2	6.14	0.28	2	0	0.20
T9261	GR-18	2.5	10.17	0.26	2	0	0.15
T9262	GR-19	3	10.08	0.35	-6	0	-0.20
T2272	GR-20	3	8.73	0.50	-3	0	-0.05
T2284	GR-21	2	8.55	0.11	3	0	0.15
T2601	GR-22	3	7.98	0.46	1.2	1.2	-
T2602	GR-23	2	7.54	0.23	0.8	-0.4	0.25
N1541	NR-1	1.5	10.93	0.37	2.5	0	0.40
N3542	NR-2	3	18.13	0.57	3	0	0.30
N3543	NR-3	4	15.34	0.39	-4	0	-0.25
N1544	NR-4	1.5	13.09	0.62	-2.5	0	-0.30
N2561	NR-5	1	16.88	1.50	-2	0	-0.75
N9562	NR-6	1	13.70	0.33	2	0	0.75
N1571	NR-7	5	10.88	0.49	1	0	0.30
N3572	NR-8	8	17.22	0.32	2	0	0.40
N3573	NR-9	5	14.23	0.49	-2	0	-0.30
N3574	NR-10	7.5	13.74	0.43	-3	0	-0.30
N2551	NR-11	2	12.22	0.90	1	1	-
N9553	NR-12	2.75	13.36	0.18	0.6	-0.3	0.50
N9554	NR-13	3	14.39	0.61	-1.4	0.7	-0.20

Core No.		Sample No.	G_s	LL %	PL %	PI %	Clay %	Silt %	Sand %	$CaCO_3$ %	Activity
D10406	5	10S-1	2.72	71	38	33	28	56	14	-	1.18
	8	10S-2	2.72	70	33	38	-	-	-	-	-
	10	10S-3	2.68	74	29	45	35	58	7	-	1.29
	15	10S-4	2.74	83	31	52	44	49	7	-	1.18
	18	10S-5	2.68	72	36	37	-	-	-	-	-
	22	10S-6	2.73	74	38	37	-	-	-	-	-
D11172-6	0-15	GT-1	2.66	107	43	64	40	53	7	50	1.60
	60-75	GT-2	2.67	104	42	61	40	54	6	-	1.53
	105-120	GT-3	2.66	98	41	57	-	-	-	50	-
D11174-10	30-45	GT-4	2.69	103	41	62	43	50	7	54	1.44
	75-90	GT-5	2.66	106	41	65	41	51	8	-	1.59
	105-120	GT-6	2.67	106	42	64	-	-	-	45	-
C-6		6-11C	-	130	58	72	30	61	19	58	2.40
		6-22A	-	106	46	60	35	45	20	52	1.71
		6-30A	-	93	57	48	36	54	10	50	1.33
		6-1B	-	104	51	53	38	49	13	66	1.39
84PCM33/4		NT-1	-	-	-	-	65	27	8	-	-
		NT-3	2.76	87	41	46	56	32	12	0	0.82
84PCM19/4		NT-10	2.76	71	30	41	46	30	24	0	0.89

Table 8.1 Summary of results of the index properties.

Core no.	Sub. core no.	Samples				Initial Isotropic consolidation		Loading history				Initial State (Start of shearing)			
		No.	depths (m)	$\bar{m}_i$ %	γ KN/m^3	$C_v \times 10^{-9}$ m^2/s	$k \times 10^{-9}$ m/s	Comp	OCR	Shearing †	(C/E)	q_o' kPa	p_o' kPa	v_o	v_o*
IOS D10406	5	10S-1	0.76	82	15.4	205	5.3	K_o	1	undrained	C	57	77	2.92	-
	8	10S-2	1.32	77	15.1	374	4.0	"	"	"	E	76	100	2.86	-
	10	10S-3	1.72	96	14.9	150	3.9	"	"	"	E	123	142	2.84	-
	15	10S-4	2.36	93	14.6	179	3.4	"	"	"	C	112	121	2.95	-
	18	10S-5	2.81	78	15.5	297	2.4	"	"	"	C	158	193	2.72	-
	22	10S-6	3.23	73	15.4	445	2.5	"	"	"	E	149	195	2.77	-
GME D11172-6	105-120	GT-1	8.20	122	14.1	24.3	1.1	"	"	"	C	135	135	3.29	3.26
	0-15	GT-2	7.60	120	13.8	55.3	2.9	"	"	"	E	126	180	3.06	3.15
	60-75	GT-3	8.60	120	13.4	84.9	4.0	"	"	"	C	84	92	3.44	3.40
	90-105	GT-9	8.50	117	14.1	12.0	1.1	Iso.	"	"	C	0	120	3.34	3.30
GME D11174-10	30-45	GT-4	13.90	122	13.5	20.7	1.4	K_o	"	"	C	60	84	3.32	3.44
	75-90	GT-5	14.30	121	13.7	20.0	1.3	K_o	"	"	E	62	80	3.38	3.46
	105-120	GT-6	14.60	120	14.0	25.6	1.5	K_o	"	"	C	105	113	3.25	3.32
	0-15	GT-7	13.60	118	13.9	14.5	1.0	Iso.	"	"	C	0	72	3.48	3.48
	135-147	GT-8	14.90	118	14.4	17.0	1.0	Iso.	"	"	C	0	93	3.40	3.39

† C - Compression
E - Extension

Table 8.2 Summary of test results and loading history of the tubed specimens.

To be continued....

Continue to Table 8.2

GME		Sample				Initial isotropic consolidation		Loading history			Initial state (Start of shearing)			
Core	Sub-core no.	No	depth (m)	$\bar{m}_i$ %	γ kN/m^3	$C_v \times 10^{-9}$ m2/s	$k \times 10^{-9}$ m/s	Comp	OCR	Shearing + (C/E)	q_o' kPa	p_o' kPa	v_o	v_o*
C-6	11C	A	23.67	118	14.5	189.2	3.5		1.0	" C	119	128	3.78	3.54
		B	23.67	121	14.6	188.5	1.7	K_o	1.1	undrained C	60	63	4.00	3.81
		C	23.67	116	14.3	208.7	1.9		1.0	" C	192	210	3.48	3.24
	22A	A	12.17	108	14.4	133.7	1.3		1.0	" C	60	71	3.49	3.89
		B	12.17	106	14.5	83.4	1.4	K_o	1.3	undrained C	31	35	3.74	4.22
		C	12.17	108	14.5	138.9	1.6		1.0	" C	79	106	3.28	3.66
	30A	A	4.17	132	13.8	94.7	2.2		1.1	" C	29	30	4.25	4.20
		B	4.17	127	13.9	80.2	1.8	K_o	2.1	undrained C	15	15	4.36	4.30
		C	4.17	128	14.1	27.8	0.6		1.0	" C	57	64	3.99	3.96
	1B	A	33.47	97	14.8	85.7	0.5		1.0	" C	162	192	3.22	3.30
		B	33.47	98	15.0	77.3	0.4	K_o	1.2	undrained C	93	90	3.56	3.65
		C	33.47	97	14.9	77.3	0.4		1.0	" C	250	284	2.97	3.06

+ C - Compression
E - Extension

TO be continued....

Continue to Table 8.2

Core no	Sample NAP				Initial isotropic consolidation		Loading history			Initial state (Start of shearing)			
	No	depth m	γ kN/m^3	$\bar{m}_i$ %	$C_v x10^{-9}$ m^2/s	$k x10^{-9}$ m/s	Comp.	OCR	shearing + (C/E)	q_o' kPa	p_o' kPa	v_o	v_o*
84 PCM 33/4	NT-1	3.60	14.2	105.8	9.2	0.5	K_o	1	undrained E	56	63	3.17	3.24
	NT-2	3.80	14.3	108.9	12.7	0.7	"	"	undrained E	45	52	3.09	3.33
	NT-3	4.00	14.3	111.4	10.8	0.5	"	"	undrained E	47	72	3.11	3.18
	NT-4	4.20	14.6	109.9	11.8	0.5	"	"	undrained C	30	43	3.27	3.42
84 PCM 19 / 4	NT-5	3.60	15.0	85.5	9.1	0.4	"	"	undrained C	31	49	2.84	3.01
	NT-6	3.80	15.4	78.1	9.8	0.4	"	"	undrained C	39	59	2.81	2.96
	NT-7	4.00	15.5	93.3	12.9	0.6	"	"	undrained C	46	74	2.72	2.89
	NT-8	4.20	15.0	85.2	9.2	0.4	"	"	undrained C	59	95	2.84	2.82
	NT-9	4.40	15.6	80.4	10.4	0.4	"	"	undrained E	68	103	2.83	2.79

+ C - Compression
E - Extension

To be continued....

Continue to Table 8.2

Core no	Sample NAP				Initial isotropic consolidation		Loading history			Initial state (Start of shearing)			
NAP	No	depth m	γ kN/m^3	$\bar{m}_i$ %	$C_v x10^{-9}$ m^2/s	$kx10^{-9}$ m/s	Comp.	OCR	shearing + (C/E)	q_o' kPa	p_o' kPa	v_o	v_o*
84 PCM 33/3	NT-10	4.60	14.6	109.1	15.3	0.5	K_o	1	drained E	60	85	3.12	3.11
	NT-11	4.80	14.6	108.1	18.8	0.6	"	"	drained C	36	51	3.41	3.34
	NT-12	5.00	14.5	107.0	15.0	0.6	"	"	drained E	46	70	3.19	3.20
	NT-13	5.20	14.8	100.9	12.5	0.5	"	"	drained C	46	70	3.09	3.20
84 PCM 33/1	NT-14	6.60	14.7	86.9	12.0	0.4	"	"	const.q'	36	51	3.10	3.00
	NT-15	6.80	14.9	94.5	13.1	0.4	"	"	const.p'C	32	55	3.03	2.98
	NT-16	6.90	15.2	88.0	13.7	0.4	"	"	const.p'E	54	88	2.87	2.84
	NT-17	7.10	15.2	89.5	11.3	0.4	"	"	const.q'	57	87	2.91	2.84
	NT-18	7.30	14.9	95.0	8.8	0.4	"	"	const.p'C	46	70	2.87	2.91
	NT-19	7.40	14.8	96.7	8.5	0.4	"	"	const.p'E	33	54	3.10	2.98

+ C - Compression
E - Extension

Sample GME		Initial isotropic consolidation		Loading history				Initial state (Start of shearing)			
No.	γ kN/m^3	$C_v x10^{-9}$ m^2/s	$k x10^{-9}$ m/s	Comp.	OCR	Shearing †	(C/E)	q_o' kPa	p_o' kPa	v_o	v_o*
GR-1	15.6	57.0	1.0	K_o	1	undrained	C	133	136	2.73	2.73
GR-2	15.6	57.5	1.2	"	"	"	E	145	177	2.64	2.69
GR-3	15.0	17.0	1.8	"	"	"	C	130	136	2.76	2.73
GR-4	15.4	22.5	0.2	"	"	"	C	68	74	2.84	2.82
GR-5	15.2	58.0	1.0	"	"	"	E	71	72	2.91	2.83
GR-6	15.4	194.0	5.9	"	"	"	C	102	100	2.79	2.78
GR-7	15.4	37.2	0.9	"	"	"	C	70	72	2.74	2.83
GR-8	15.3	34.0	0.7	"	"	"	E	140	142	2.74	2.73
GR-9	15.5	194.0	5.9	Iso.	"	"	E	0	150	3.01	3.02
GR-10	14.9	15.0	0.5	"	"	"	C	0	173	2.89	2.99

† C - Compression
E - Extension

Table 8.3 Summary of test results and loading history of the reconstituted specimens.

To be continued....

Continue to Table 8.3 .

GME Sample		Initial isotropic consolidation		Loading history				Initial state (Start of shearing)			
No.	kN/m^3	$C_v x10^{-9}$ m^2/s	$k x10^{-9}$ m/s	Comp.	OCR	Shearing	(C/E)	q_o' kPa	p_o' kPa	v_o	v_o^*
GR-11	15.7	18.7	0.8	K_o	2	undrained	C	56	81	2.73	2.80
GR-12	15.7	22.5	0.5	"	"	"	E	59	78	2.71	2.80
GR-13†	15.0	14.7	0.7	"	1	"	C	87	89	2.96	2.90
GR-14+	15.4	16.8	0.6	"	"	"	C	143	152	2.72	2.80
GR-15	15.4	36.8	0.8	"	"	drained	C	109	104	2.77	2.77
GR-16	15.4	36.7	1.1	"	"	"	E	187	190	2.66	2.68
GR-17	15.5	25.8	0.8	"	"	"	C	68	75	2.78	2.82
GR-18	15.1	26.5	0.9	"	"	"	C	137	145	2.63	2.72
GR-19	15.5	37.0	1.2	"	"	"	E	150	145	2.61	2.72
GR-20	15.6	35.7	1.0	"	"	"	E	100	93	2.70	2.79
GR-21	15.9	31.2	1.2	"	"	"	C	116	124	2.65	2.75
GR-22	15.1	31.6	1.1	"	"	constant q'	C	73	74	2.78	2.82
GR-23	15.6	28.4	1.3	"	"	Constant p'	C	73	76	2.73	2.82

† Carbonate removed by HCL.

To be continued....

Continue to Table 8.3 .

NAP Sample		Initial isotropic consolidation		Loading history				Initial state (Start of shearing)			
No.	kN/m^3	$C_v x10^{-9}$ m^2/s	$kx10^{-9}$ m/s	Comp.	OCR	Shearing +	(C/E)	q_o' kPa	p_o' kPa	v_o	v_o^*
NR-1	16.1	-	-	K_o	1	undrained	C	57	62	2.38	2.41
NR-2	15.7	-	-	"	"	"	C	78	92	2.32	2.33
NR-3	16.2	30.2	1.1	"	"	"	C	83	94	2.32	2.32
NR-4	16.1	21.0	0.5	"	"	"	E	54	64	2.34	2.40
NR-5	16.2	13.9	0.5	"	2	"	E	17	62	2.31	2.38
NR-6	15.8	13.1	0.5	"	"	"	C	20	61	2.36	2.38
NR-7	16.3	21.0	0.5	"	1	drained	C	55	63	2.39	2.40
NR-8	15.8	16.3	0.6	"	"	"	C	81	100	2.28	2.31
NR-9	15.9	-	-	"	"	"	E	54	65	2.40	2.40
NR-10	16.2	-	-	"	"	"	E	84	94	2.33	2.32
NR-11	15.8	9.9	0.4	"	"	constant q´	C	51	71	2.49	2.38
NR-12	15.9	19.1	0.7	"	"	constant p´	C	65	82	2.45	2.35
NR-13	16.1	13.3	0.6	"	"	constant p´	E	63	82	2.38	2.35

+ C - Compression
E - Extension

	Specimens	K_o compression					Isotropic compression		
		N_o	λ_o	κ_o	η'_o	K_o	N	λ	κ
Tubed	IOS A	4.71	0.37	-	0.90	0.44	-	-	-
	IOS B	3.69	0.18	-	0.78	0.48	-	-	-
	GME	5.12	0.38	-	0.90	0.44	5.02	0.36	-
	GME C-6	6.45	0.60	0.04	0.95	0.42	-	-	-
	NAP A	5.15	0.46	-	0.64	0.55	-	-	-
	NAP B	4.18	0.30	-	0.64	0.55	-	-	-
Recon-stituted	GME	3.47	0.15	0.04	0.95	0.42	3.87	0.17	-
	NAP	3.23	0.20	0.04	0.80	0.48	-	-	-

Table 9.1 Summary of the compression parameters for deep-ocean sediments.

Group	Sample no.	Initial State (Start of shearing)			End State (End of shearing)			Peak deviator Stress	Critical State		
		q_o' kPa	p_o' kPa	v_o*	q_{en}' kPa	p_{en}' kPa	v_{en}	q_p' kPa	q_{cs}' kPa	p_{cs}' kPa	v_{cs}
A	IOS-1	57	77	2.91	150	96	2.92	84	84	54	2.91
A	IOS-2	76	100	2.86	-65	63	2.86	-52	-52	50	2.86
B	IOS-3	123	142	2.88	-77	84	2.84	-72	-72	78	2.88
B	IOS-4*	112	121	2.94	85	64	2.95	118	-	-	-
A	IOS-5*	158	193	2.74	113	82	2.72	186	-	-	-
A	IOS-6	149	195	2.74	-90	102	2.77	-82	-82	92	2.74

* Failed in stress control

Table 9.2 Summary of test results for IOS tubed specimens.

Sample No	Initial state (Start of shearing)			End state (End of shearing)			Peak deviator stress	Critical state		
	q_o' kPa	p_o' kPa	v_o*	q_{en}' kPa	p_{en}' kPa	v_{en}	q_p' kPa	q_{cs}' kPa	p_{cs}' kPa	v_{cs}
GT-1	135	135	3.26	170	90	3.29	170	170	90	3.16
GT-2	126	180	3.15	-115	130	3.06	-115	-115	120	3.15
GT-3	84	92	3.40	110	60	3.44	110	110	60	3.40
GT-4	60	84	3.44	91	60	3.32	91	-	-	-
GT-5	62	80	3.46	- 60	60	3.38	-50	- 50	50	3.46
GT-6	105	113	3.32	121	70	3.25	124	121	70	3.32
GT-7	0	72	3.48	86	48	3.48	68	68	38	3.48
GT-8	0	93	3.39	88	49	3.41	88	88	49	3.39
GT-9	0	120	3.30	130	70	3.25	110	110	60	3.30

Table 9.3 Summary of test results for the GME tubed specimens.

	Sample No	q_o' kPa	p_o' kPa	v_o*	q_{en}' kPa	p_{en}' kPa	v_{en}	q_p' kPa	q_{cs}' kPa	p_{cs}' kPa	v_{cs}
Group A	NT-1	63	63	3.24	-52	48	3.17	-52	-52	48	3.24
	NT-2	45	52	3.33	-43	43	3.09	-63	-43	43	3.33
	NT-3	47	72	3.18	-51	52	3.11	-51	-51	52	3.18
	NT-4	30	43	3.42	36	26	3.27	42	36	26	3.42
Group B	NT-5	31	49	3.01	40	29	2.84	41	40	29	3.01
	NT-6	39	59	2.96	52	37	2.81	52	52	37	2.96
	NT-7	46	74	2.89	62	45	2.72	63	62	45	2.89
	NT-8	59	95	2.81	76	58	2.84	82	76	58	2.81
	NT-9	68	103	2.79	-70	74	2.53	-70	-70	74	2.79
Group A	NT-10	60	85	3.11	-49	48	3.16	-	-49	48	3.15
	NT-11	36	51	3.34	84	68	3.14	-	-	-	-
	NT-12	46	70	3.20	-42	40	3.25	-	-42	40	3.26
	NT-13	46	70	3.20	98	83	3.00	-	-	-	-
Group B	NT-14	36	51	3.00	36	110	2.88	-	-	-	-
	NT-15	32	55	2.98	69	55	2.88	-	-	-	-
	NT-16	54	88	2.84	-85	88	2.76	-	-85	88	2.73
	NT-17	57	87	2.84	57	190	2.68	-	-	-	-
	NT-18	46	70	2.91	87	70	2.72	-	-	-	-
	NT-19	33	54	2.98	-57	54	3.01	-	-57	54	2.89

Table 9.4 Summary of test results for the NAP tubed specimens.

Sample No.	Initial state (Start of shearing)			End state (End of shearing)			Peak deviator stress	Critical state		
	q_o' kPa	p_o' kPa	v_o*	q_{en}' kPa	p_{en}' kPa	v_{en}	q_p' kPa	q_{cs}' kPa	p_{cs}' kPa	v_{cs}
6-11C/A	119	128	3.54	110	61	3.78	146	110	61	3.54
6-11C/B	60	63	3.81	67	36	4.00	85	67	36	3.81
6-11C/C	192	210	3.24	160	93	3.48	232	160	93	3.24
6-22A/A	60	71	3.89	62	35	3.49	75	62	35	3.89
6-22A/B	31	35	4.22	38	20	3.74	45	38	20	4.22
6-22A/C	79	106	3.66	94	56	3.28	105	94	56	3.66
6-30A/A	29	30	4.20	39	20	4.25	45	39	20	4.20
6-30A/B	15	15	4.30	26	14	4.36	33	27	14	4.30
6-30A/C	57	64	3.96	52	30	3.99	76	52	30	3.96
6-1B/A	162	192	3.30	142	85	3.22	202	143	85	3.30
6-1B/B	93	90	3.66	82	47	3.56	128	82	47	3.65
6-1B/C	250	284	3.06	229	143	2.97	285	229	143	3.06

Table 9.5 Summary of test results for GME-C6 tubed specimens.

Sample no	Initial state (Start of shearing)			End state (End of shearing)			Peak deviator stress	Critical state		
	q_o' kPa	p_o' kPa	v_o*	q_{en}' kPa	p_{en}' kPa	v_{en}	q_p' kPa	q_{cs}' kPa	p_{cs}' kPa	v_{cs}
GR-1	133	136	2.73	177	112	2.73	172	172	108	2.73
GR-2	145	177	2.69	-121	126	2.64	- 86	- 86	90	2.69
GR-3	130	136	2.73	160	101	2.76	160	160	101	2.73
GR-4	68	74	2.82	100	62	2.84	95	95	60	2.82
GR-5	71	72	2.83	- 70	60	2.91	- 45	- 45	40	2.83
GR-6	102	100	2.78	130	82	2.79	130	130	82	2.78
GR-7	70	72	2.83	110	69	2.74	96	96	60	2.83
GR-8	140	142	2.72	-108	98	2.74	- 76	- 76	70	2.72
GR-9	0	150	3.02	-115	110	3.01	-115	-115	110	2.97
GR-10	0	173	2.99	120	80	2.65	120	120	80	2.73
GR-11	56	81	2.80	161	102	2.67	161	161	102	2.73
GR-12	59	78	2.81	- 80	80	2.65	- 65	- 65	65	2.73
GR-13+	87	89	-	95	60	2.96	100	95	60	2.90

+ Carbonate removed by HCL.

Table 9.6 Summary of test results for the GME reconstituted specimens.

To be continued ....

Continue to Table 9.6

Sample no	Initial state (Start of shearing)			End state (End of shearing)			Peak deviator stress	Critical state		
	q_o' kPa	p_o' kPa	v_o*	q_{en}' kPa	p_{en}' kPa	v_{en}	q_p' kPa	q_{cs}' kPa	p_{cs}' kPa	v_{cs}
GR-14+	143	152	2.80	158	107	2.72	178	158	107	2.80
GR-15	109	104	2.77	220	141	2.69	-	220	141	2.69
GR-16	187	190	2.68	-105	95	2.68	-	-105	95	2.70
GR-17	68	75	2.82	174	110	2.69	-	174	110	2.73
GR-18	137	145	2.72	302	200	2.54	-	302	200	2.63
GR-19	150	145	2.72	- 80	69	2.64	-	- 77	70	2.75
GR-20	100	93	2.79	- 50	40	2.77	-	- 47	40	2.86
GR-21	116	124	2.75	256	170	2.58	-	256	170	2.68
GR-22	73	74	2.82	73	136	2.80	-	-	-	-
GR-23	73	76	2.82	122	77	2.70	-	122	77	2.79

+ Carbonate removed by HCl.

Sample No.	Initial state (Start of shearing)			End state (End of shearing)			Peak deviator stress	Critical state		
	q_o' kPa	p_o' kPa	v_o*	q_{en}' kPa	p_{en}' kPa	v_{en}	q_p' kPa	q_{cs}' kPa	p_{cs}' kPa	v_{cs}
NR-1	57	62	2.41	74	53	2.38	68	68	49	2.41
NR-2	80	92	2.33	95	68	2.32	95	95	68	2.32
NR-3	83	94	2.32	-79	74	2.32	-60	-60	57	2.32
NR-4	54	64	2.40	-54	44	2.34	-43	-43	38	2.40
NR-5	17	62	2.38	-74	72	2.31	-	-67	65	2.33
NR-6	20	61	2.38	100	73	2.46	-	100	73	2.33
NR-7	55	63	2.40	111	81	2.31	-	106	77	2.32
NR-8	81	100	2.31	154	124	2.21	-	154	124	2.24
NR-9	54	65	2.40	-44	38	2.44	-	-40	35	2.44
NR-10	84	95	2.32	-59	48	2.37	-	-55	45	2.36
NR-11	47	71	2.38	47	130	2.38	-	-	-	-
NR-12	65	82	2.35	109	82	2.39	-	109	82	2.29
NR-13	63	82	2.35	-82	82	2.30	-	-82	82	2.27

Table 9.7 Summary of test results for NAP reconstituted specimens

Specimens		Ko								ISOTROPIC							
		M_c	Γ_c	λ_c	ϕ'°_c	M_e	Γ_e	λ_e	ϕ'°_e	M_c	Γ_c	λ_c	ϕ'°_c	M_e	Γ_e	λ_e	ϕ'°_e
Tubed	IOS A	1.54	-	-	37.8	-0.91	-	-	32.4	-	-	-	-	-	-	-	-
	IOS B	-	-	-	-	-0.91	-	-	32.4	-	-	-	-	-	-	-	-
	GME	1.80	4.97	0.38	43.8	-0.95	4.96	0.38	34.4	1.80	4.78	0.36	43.8	-	-	-	-
	GME C-6	1.75	5.99	0.60	42.6	-	-	-	-	-	-	-	-	-	-	-	-
	NAP A	1.36	4.96	0.46	33.7	-1.00	5.00	0.46	36.9	-	-	-	-	-	-	-	-
	NAP B	1.36	4.02	0.30	33.7	-1.00	4.08	0.30	36.9	-	-	-	-	-	-	-	-
Recon-stituted	GME	1.55	3.43	0.15	38.0	-1.05	3.37	0.15	39.5	1.52	3.71	0.17	37.3	-1.05	3.81	0.17	39.5
	NAP	1.38	3.17	0.20	34.1	-1.06	3.14	0.20	40.1	-	-	-	-	-	-	-	-

Table 9.8 Summary of the critical state parameters for deep-ocean sediments.

Specimen		Compression	Extension
		$(c_u/\sigma_{vo}')_c$	$(c_u/\sigma_{vo}')_e$
Tubed	IOS	-	-
	GME	0.378	-0.195
	GME C-6	0.249	-
	NAP A	0.315	-0.253
	NAP B	0.280	-0.250
Reconstituted	GME	0.365	-0.165
	NAP	0.333	-0.220

Table 9.9 The predicted undrained shear strength ratios for K_o normally consolidated deep-ocean sediments.

Specimen		Compression v.ε_s*						Extension v.ε_s*					
		0.05%			0.5%			-0.05%			-0.5%		
		$\frac{dq'/d\varepsilon_s}{vp'}$	E_u+ (MPa)	$\frac{E_u}{c_u}$$	$\frac{dq'/d\varepsilon_s}{vp'}$	E_u+ (MPa)	$\frac{E_u}{c_u}$$	$\frac{dq'/d\varepsilon_s}{vp'}$	E_u+ (MPa)	$\frac{E_u}{c_u}$$	$\frac{dq'/d\varepsilon_s}{vp'}$	E_u+ (MPa)	$\frac{E_u}{c_u}$$
Tubed	IOS	20	4.0	-	15	3.0	-	145	29.0	-	75	15.0	-
	GME	40	9.0	238	15	3.4	90	75	16.8	862	40	9.0	462
	GME C-6	30	7.3	292	15	3.6	146	-	-	-	-	-	-
	NAP	45	10.0	320	15	3.4	107	90	20.0	797	45	10.1	398
Recon-stituted	GME	60	10.4	286	20	3.5	95	155	26.9	1633	75	13.0	790
	NAP	40	6.1	182	15	2.3	68	150	22.7	1030	60	9.1	412

* v.ε_s = 0.05% and 0.5% represent approximately 0.02% and 0.2% ε_s respectively.

\+ E_u = $dq'/d\varepsilon_s$ at 20m depth below seabed (σ'_v = 100 kPa).

\$ c_u = values estimated from Table 9.9.

Table 9.10 Summary of the undrained stiffnesses for deep-ocean sediments from Figs. 9.42 to 9.44 .

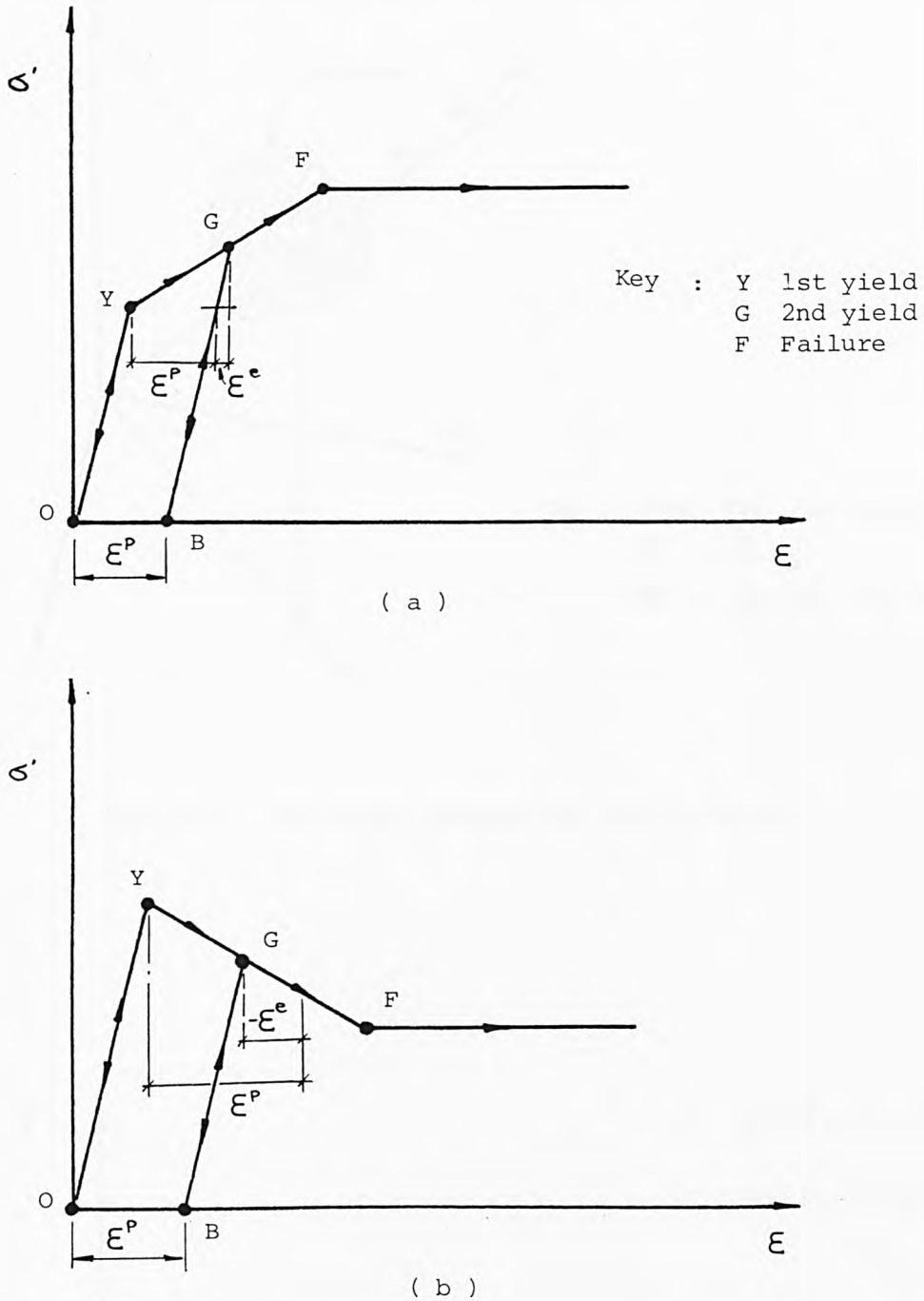

Fig. 2.1 Elasto-plastic stress-strain behaviour, a) strain hardening b) strain softening (after Atkinson and Bransby, 1978).

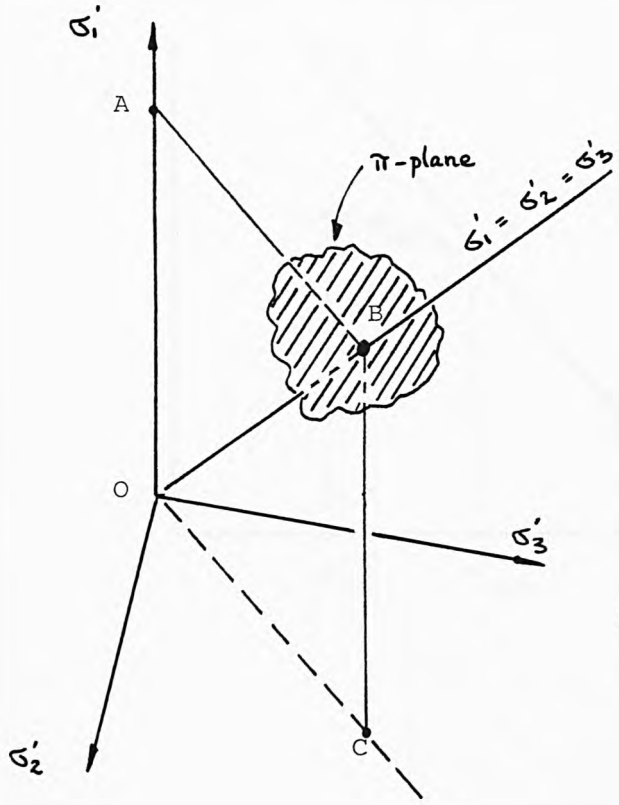

Key : OABC , The axi-symmetric plane

$\overrightarrow{OC} = \sqrt{2}.\sigma'_3$

$\overrightarrow{OB} = \frac{1}{\sqrt{3}}(\sigma'_1 + \sigma'_2 + \sigma'_3)$

Fig. 2.2 The three dimensional stress space.

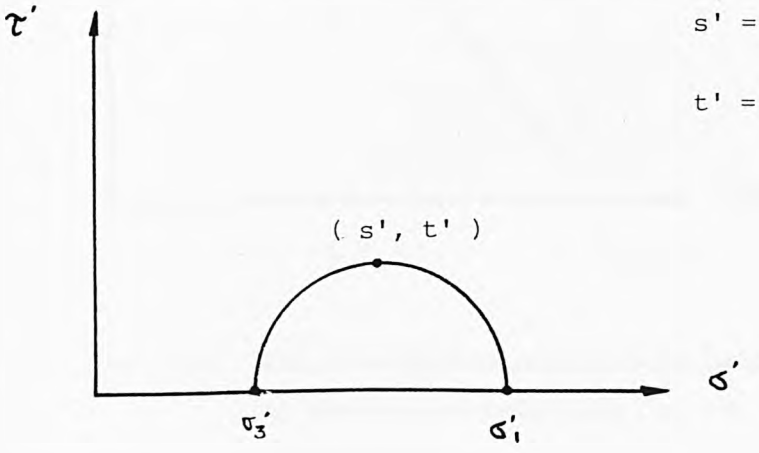

$s' = \frac{1}{2}(\sigma'_1 + \sigma'_3)$

$t' = \frac{1}{2}(\sigma'_1 - \sigma'_3)$

Fig. 2.3 The Mohr circle state of stress.

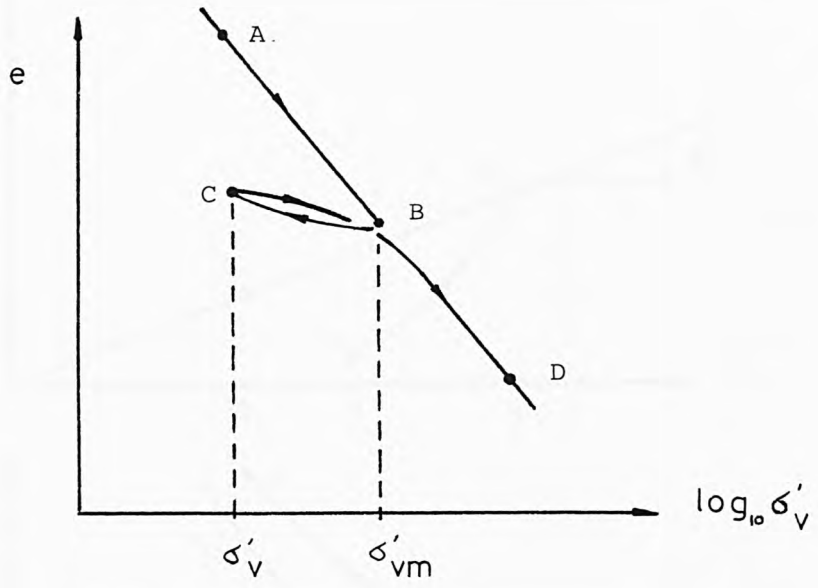

(a)

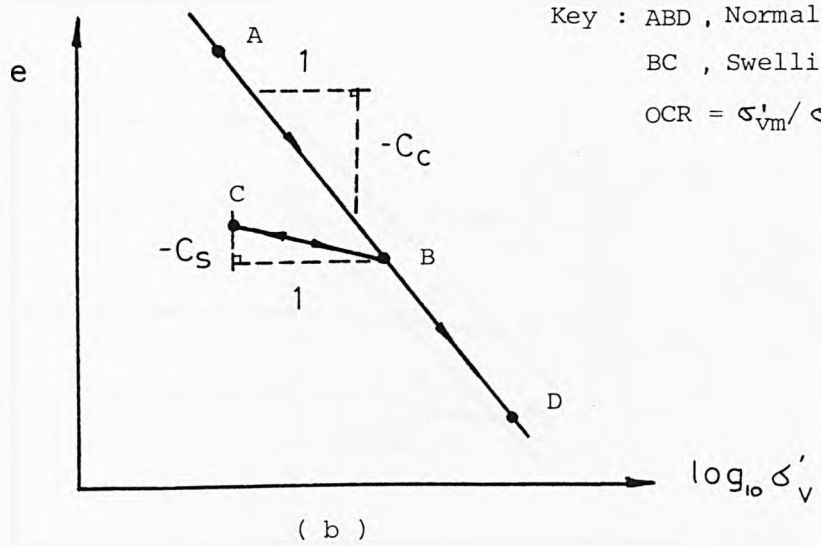

Key : ABD , Normal comp. line
BC , Swelling line
OCR = $\sigma'_{vm}/\sigma'_{vo}$

(b)

Fig. 2.4 One dimensional compression behaviour of soils ,
a) the actual behaviour b) the idealised behaviour.

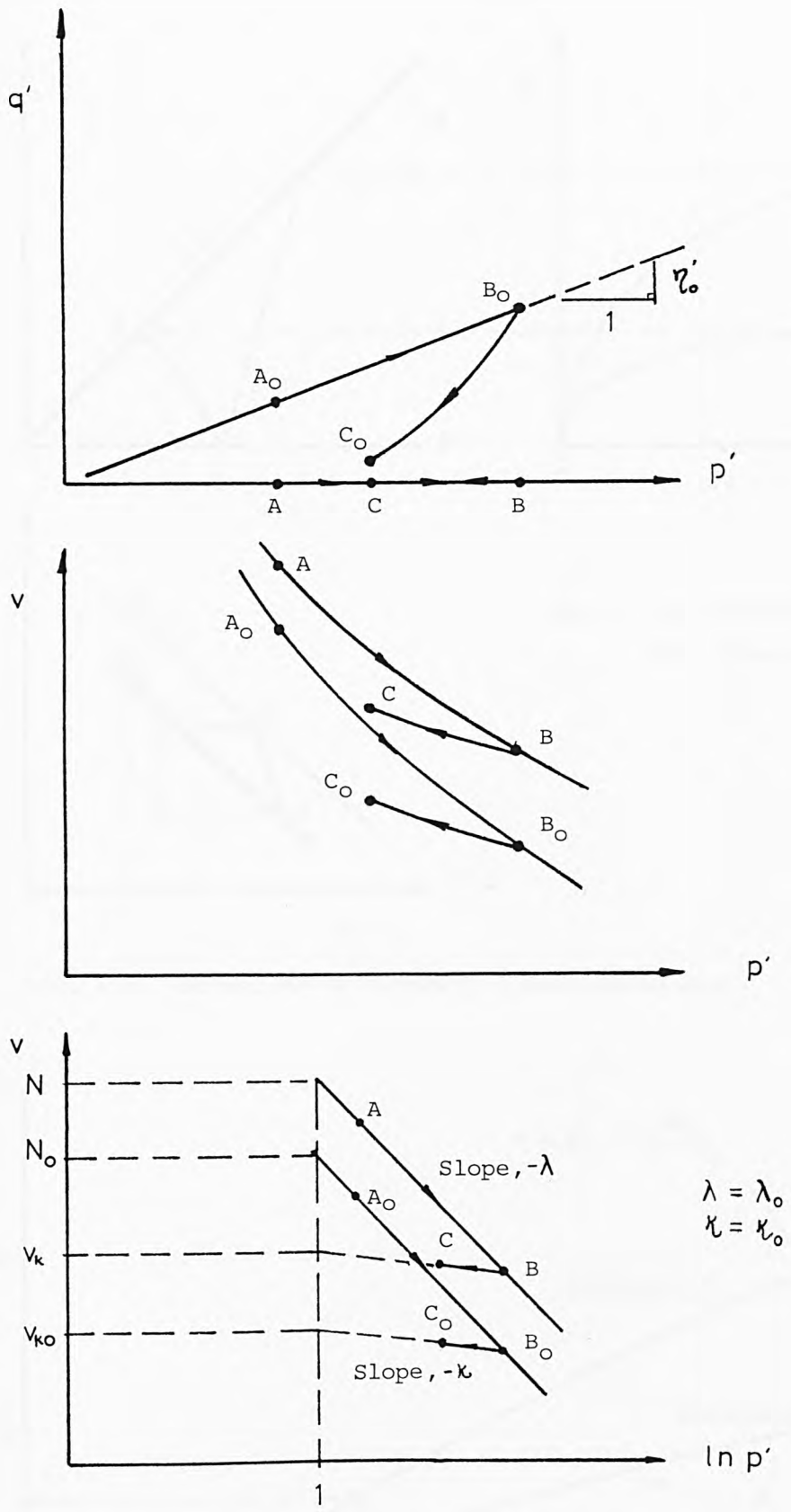

Fig. 2.5 Isotropic (ABC) and One dimensional ($A_OB_OC_O$) compression and swelling lines.

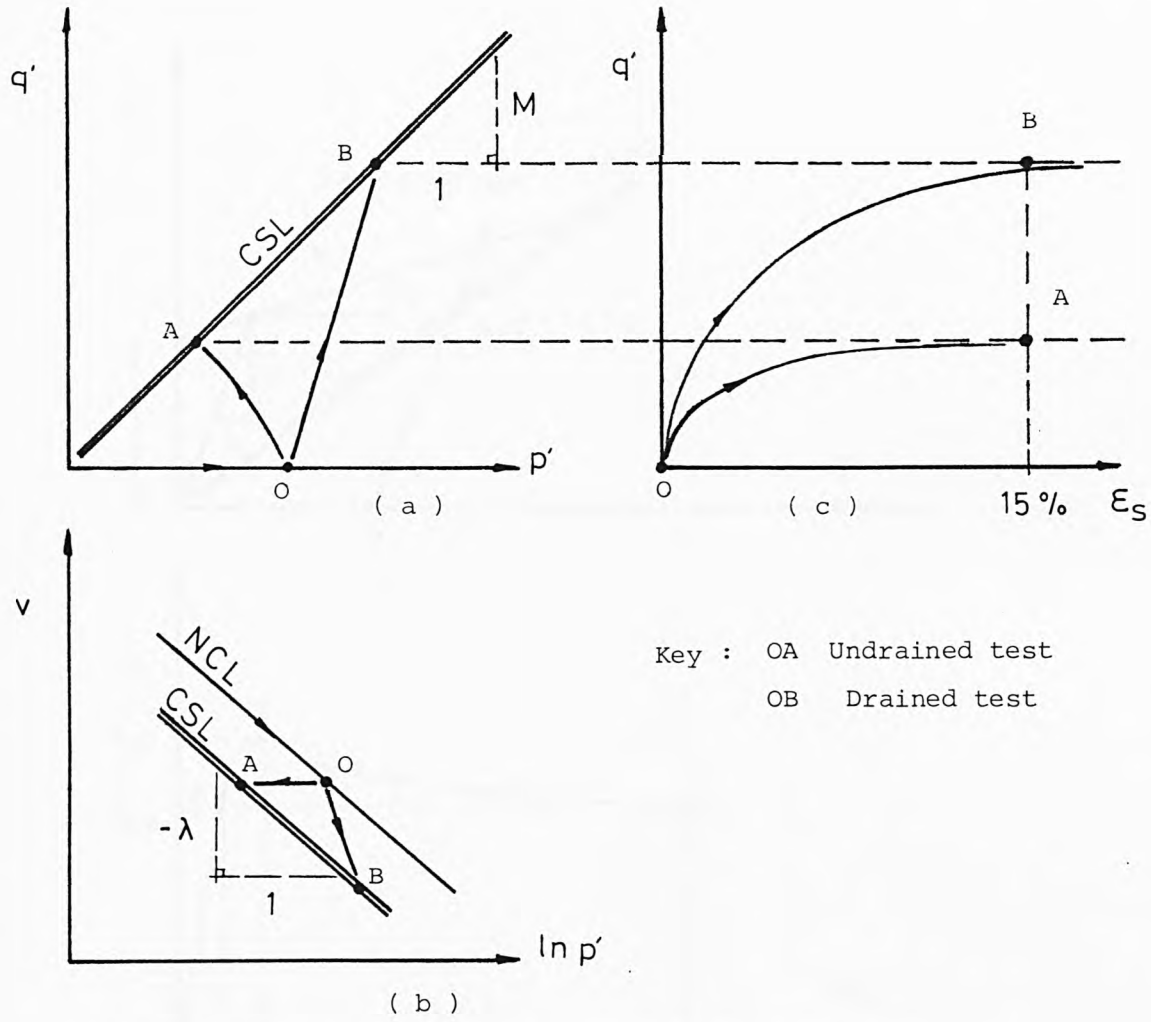

Fig. 2.6 Behaviour of normally consolidated soil.

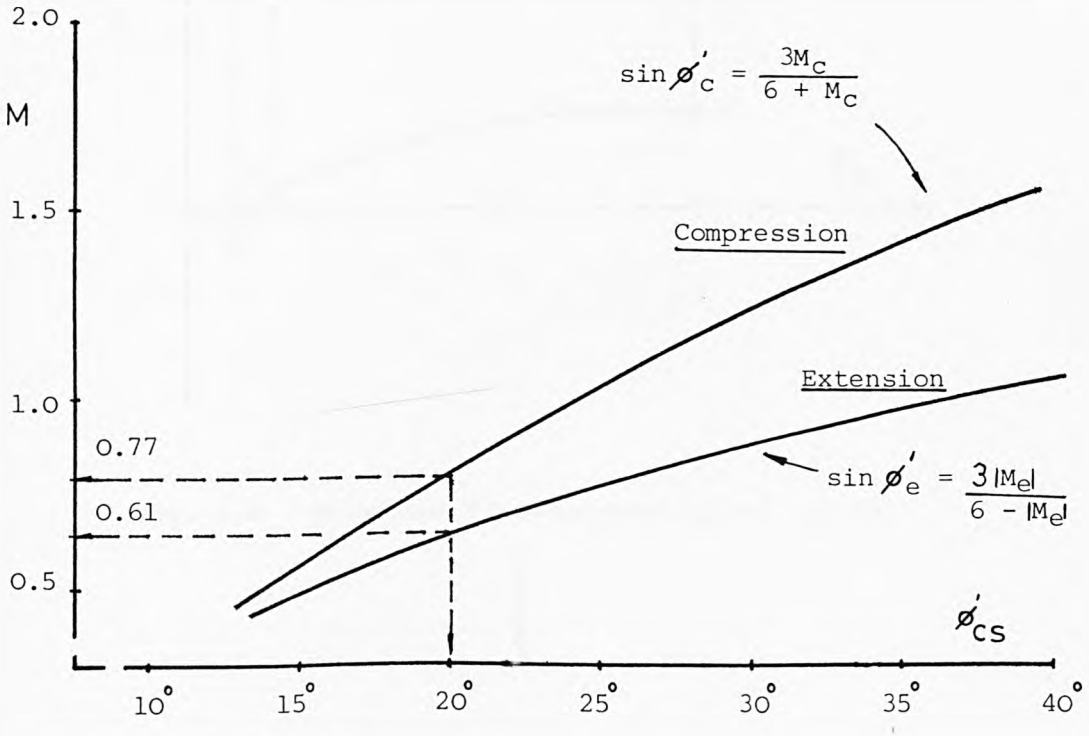

Fig. 2.7 Relationships between M and ϕ'_{cs}.

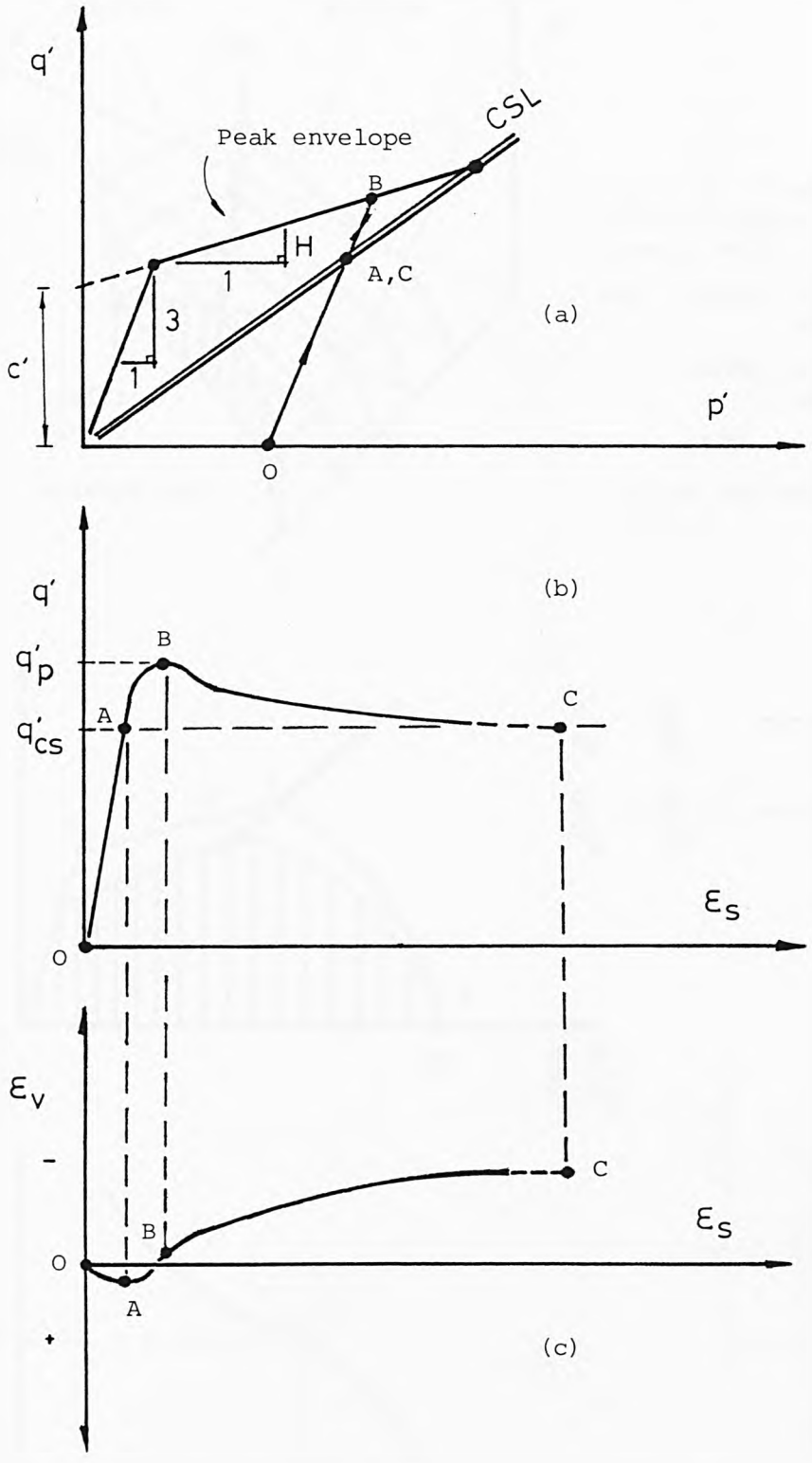

Fig. 2.8 Behaviour of overconsolidated soils.

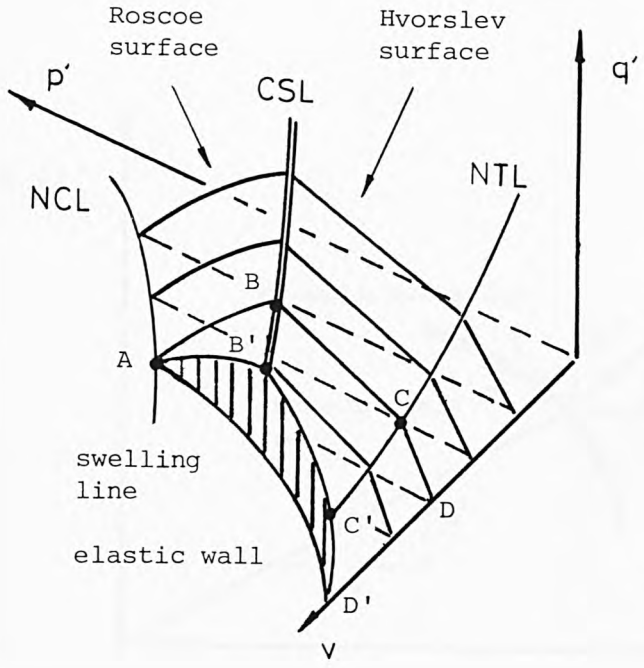

Fig. 2.9 Three dimensional state boundary surface and a elastic wall.

Key : ABCDA constant volume section

$A\acute{B}\acute{C}\acute{D}A$ elastic wall section

$A\acute{B}\acute{C}\acute{D}$ yield curve

(after Atkinson and Bransby, 1978)

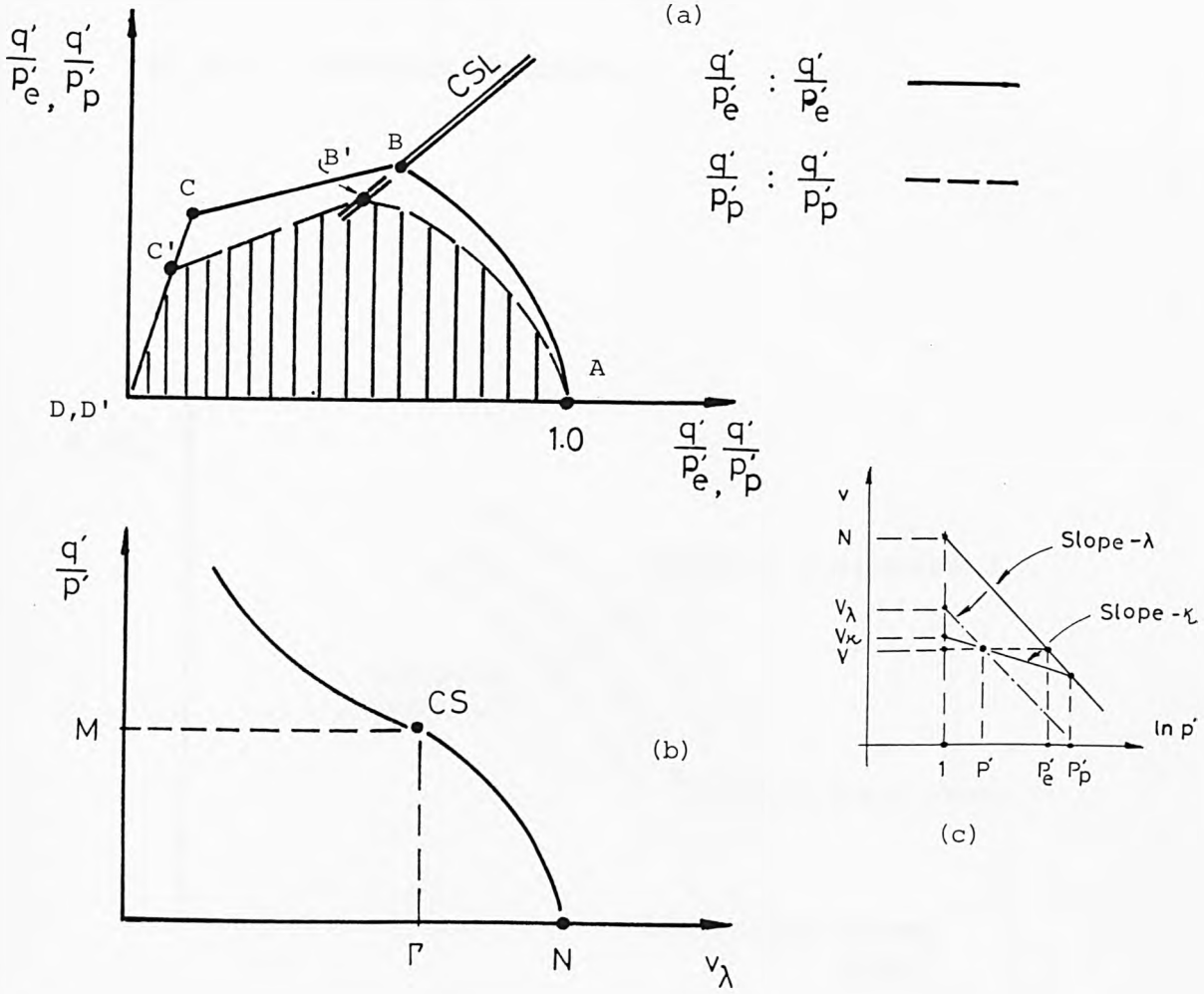

Fig. 2.10 Normalised sections of the state boundary surface a) with respect to p'_e and p'_p , b) with respect to v_λ , c) definitions of the normalising parameters (after Atkinson, 1984c).

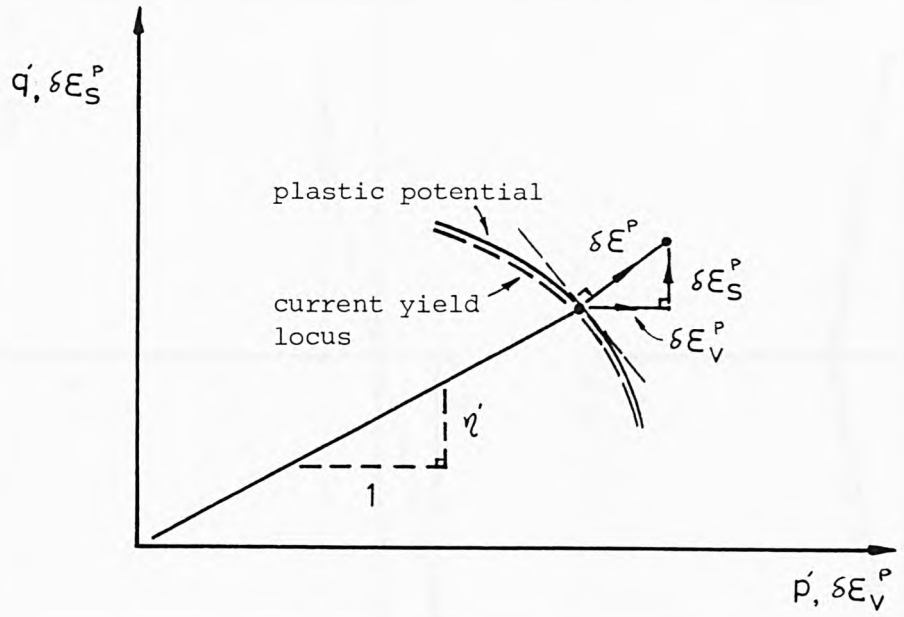

Fig. 2.11 Normality condition.

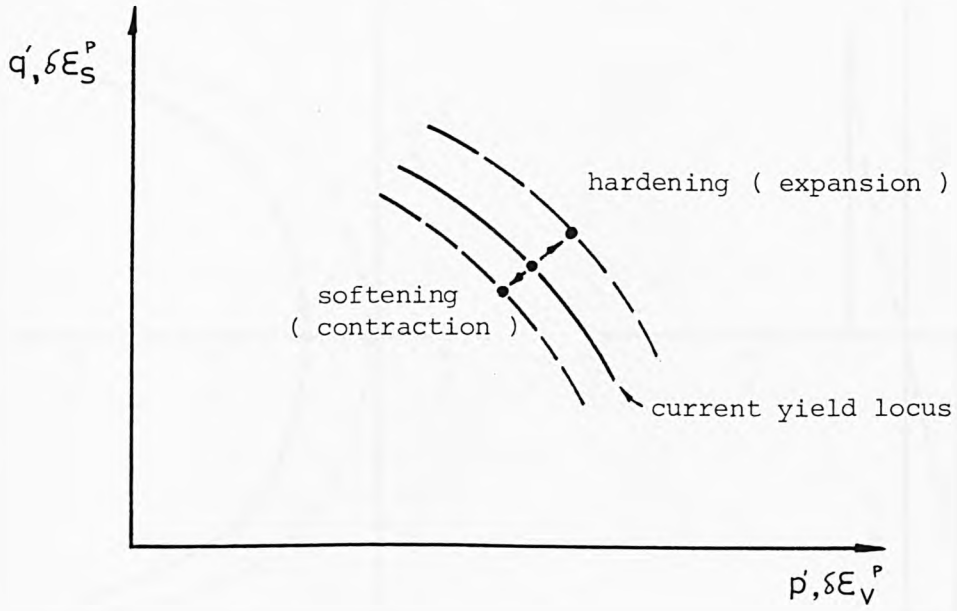

Fig. 2.12 Hardening and softening.

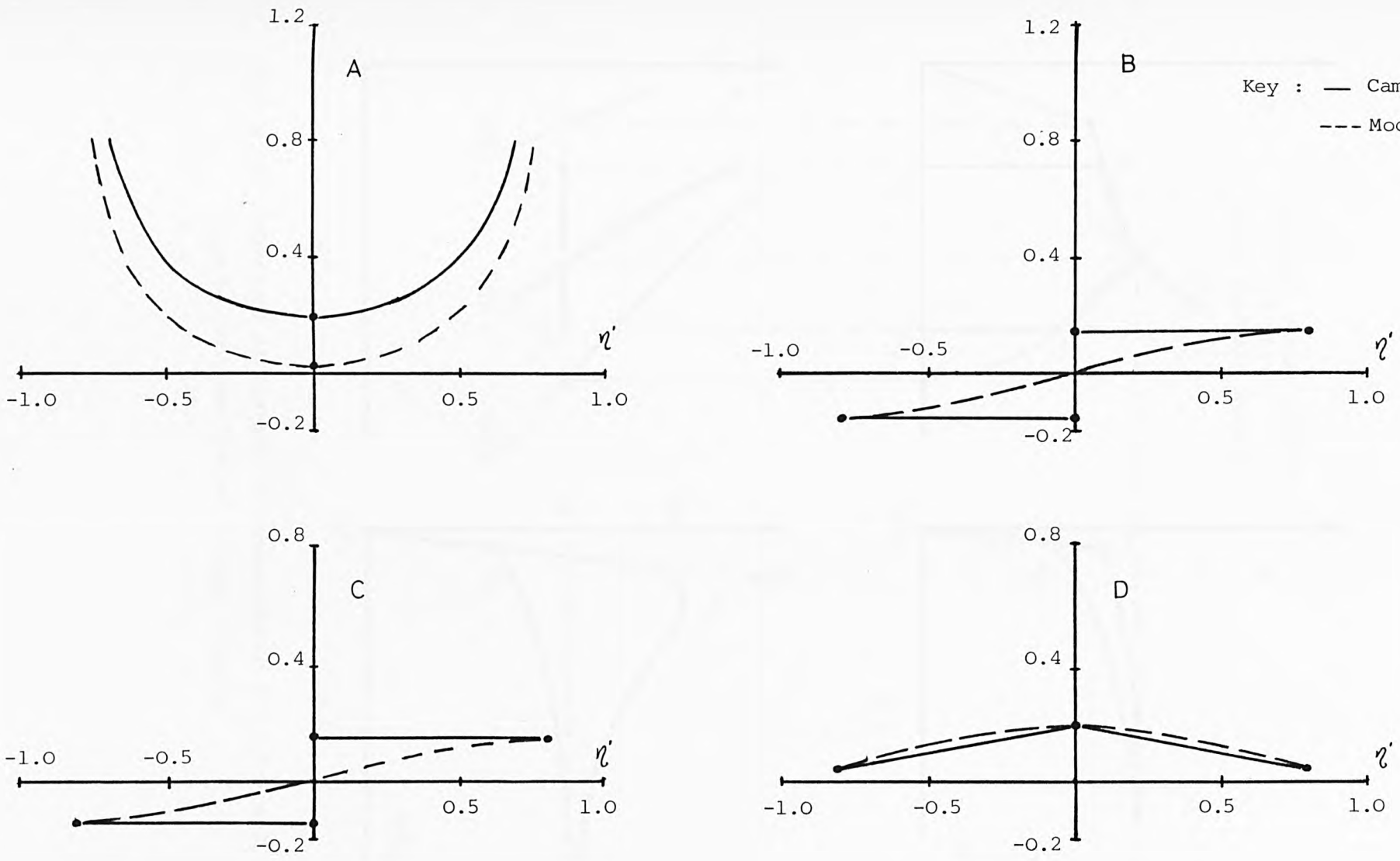

Fig. 2.13 Patterns of the individual compliance for Cam-Clay and Modified Cam-Clay models.

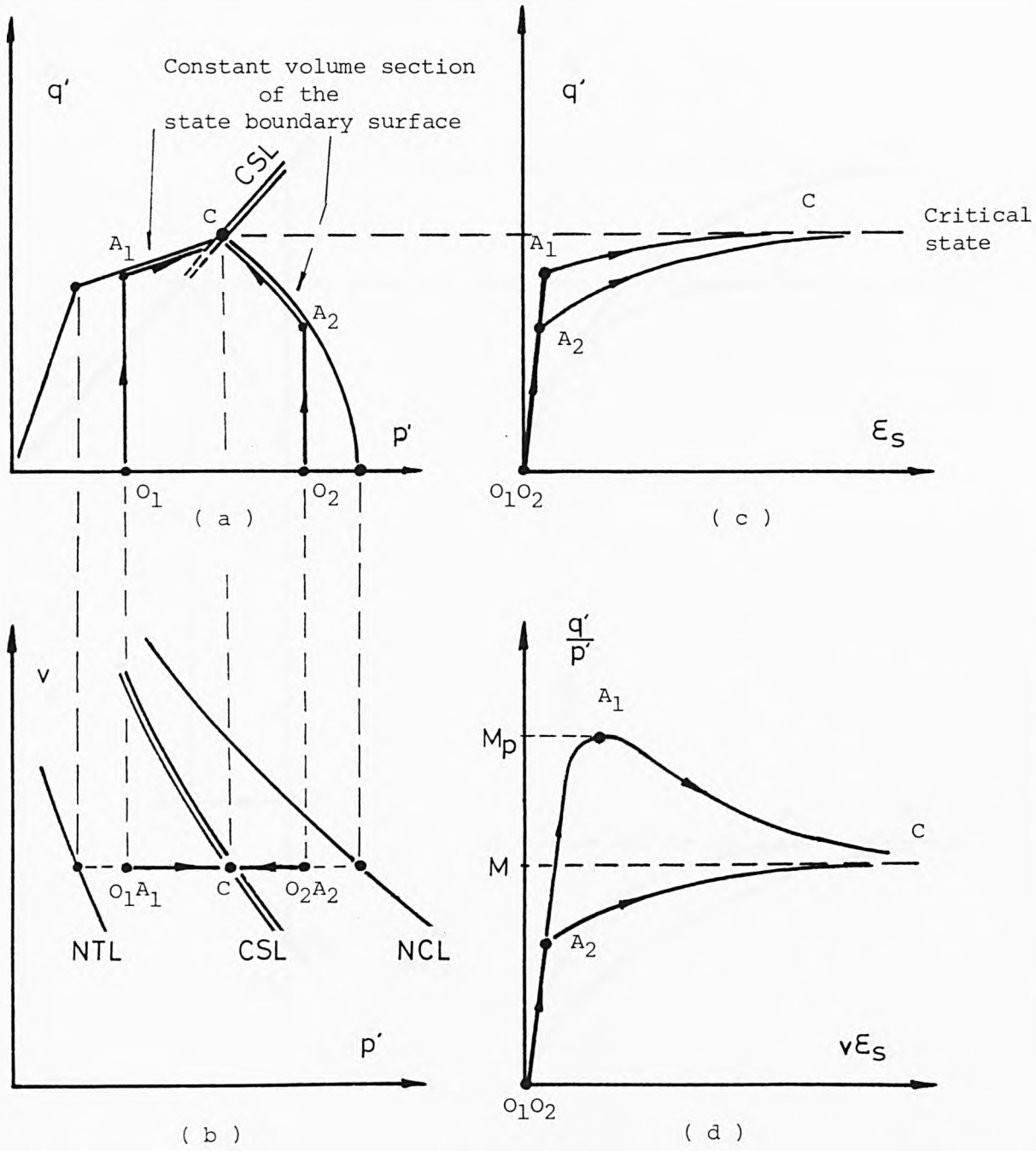

Fig. 2.14 Behaviour of heavily overconsolidated (O_1A_1C) and lightly overconsolidated (O_2A_2C) soils.

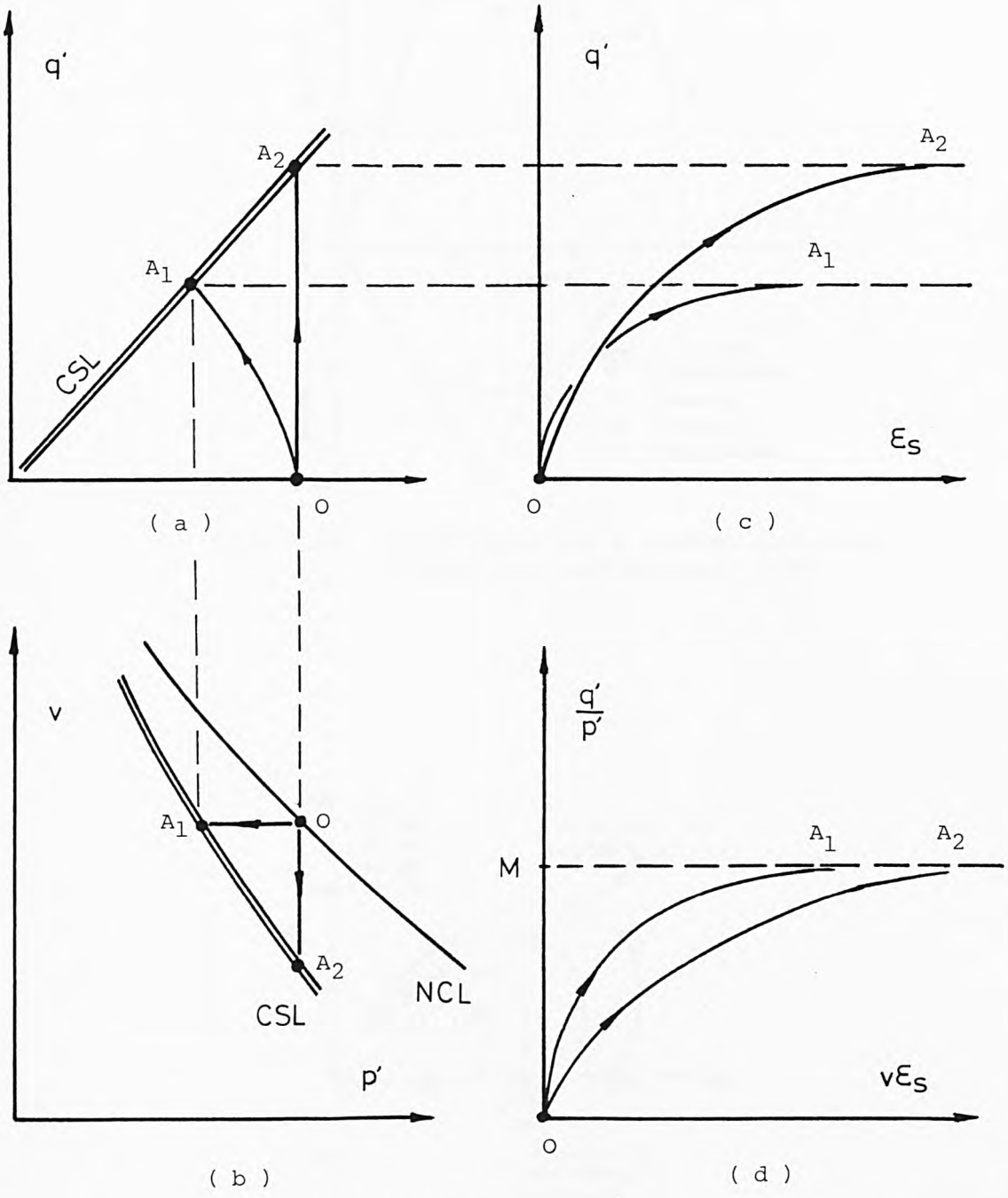

Fig. 2.15 Behaviour of normally consolidated soils.

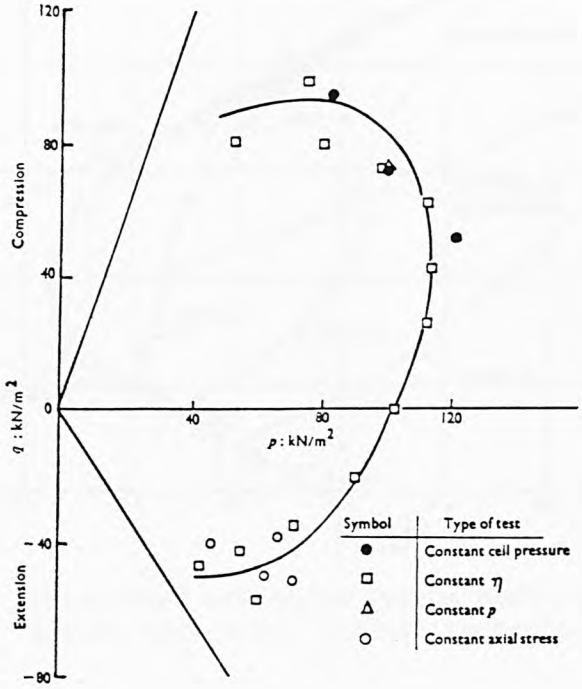

Fig. 2.16 Yield curve for a natural soft clay.
(after Wong and Mitchell, 1975)

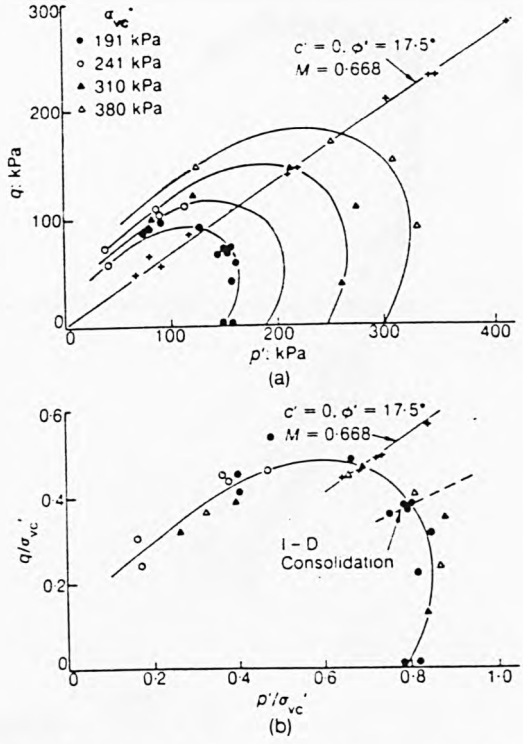

Fig. 2.17 Yield curves for natural soft clay.
(after Graham et al., 1983)

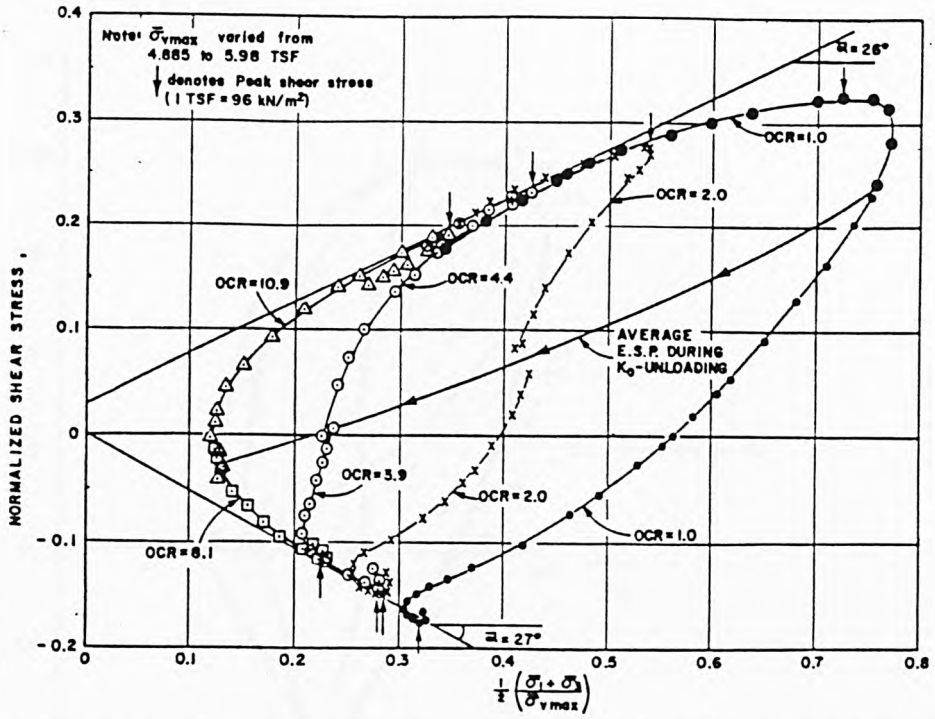

Fig. 2.18 Normalised effective stress path for a 'undisturbed' marine soft clay. (after Koutsofas , 1981)

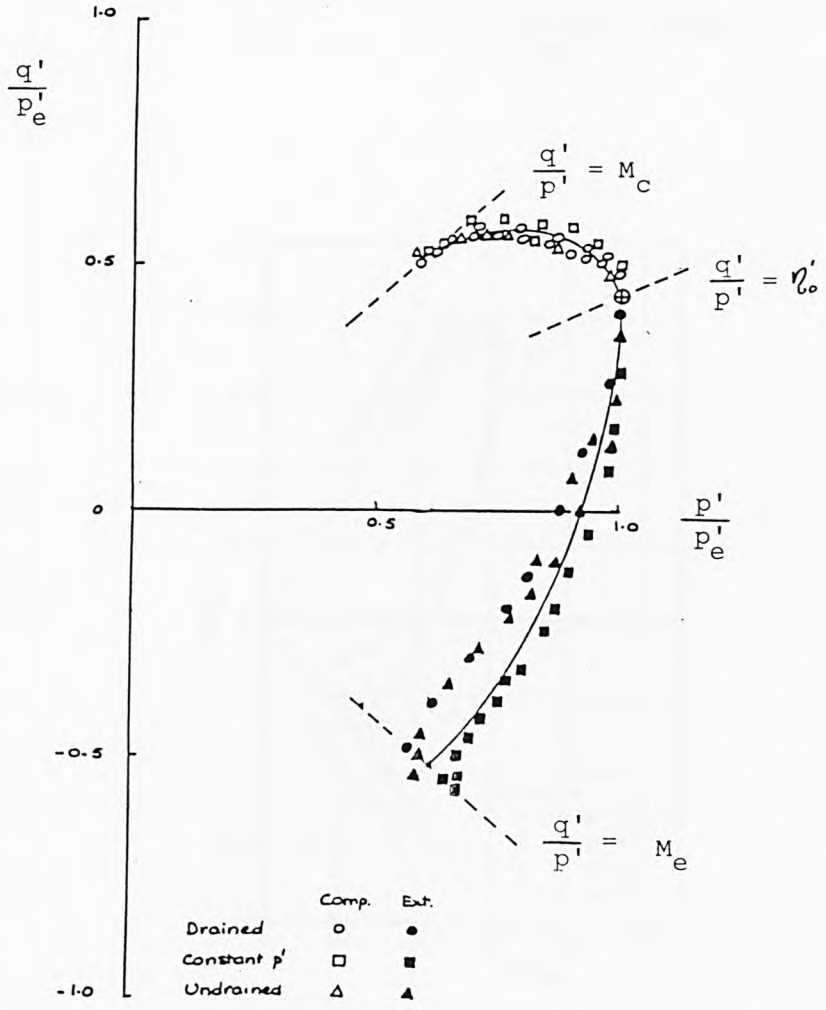

Fig. 2.19 Normalised effective stress path of 'reconstituted' Speswhite kaolin. (after Atkinson et al., 1986)

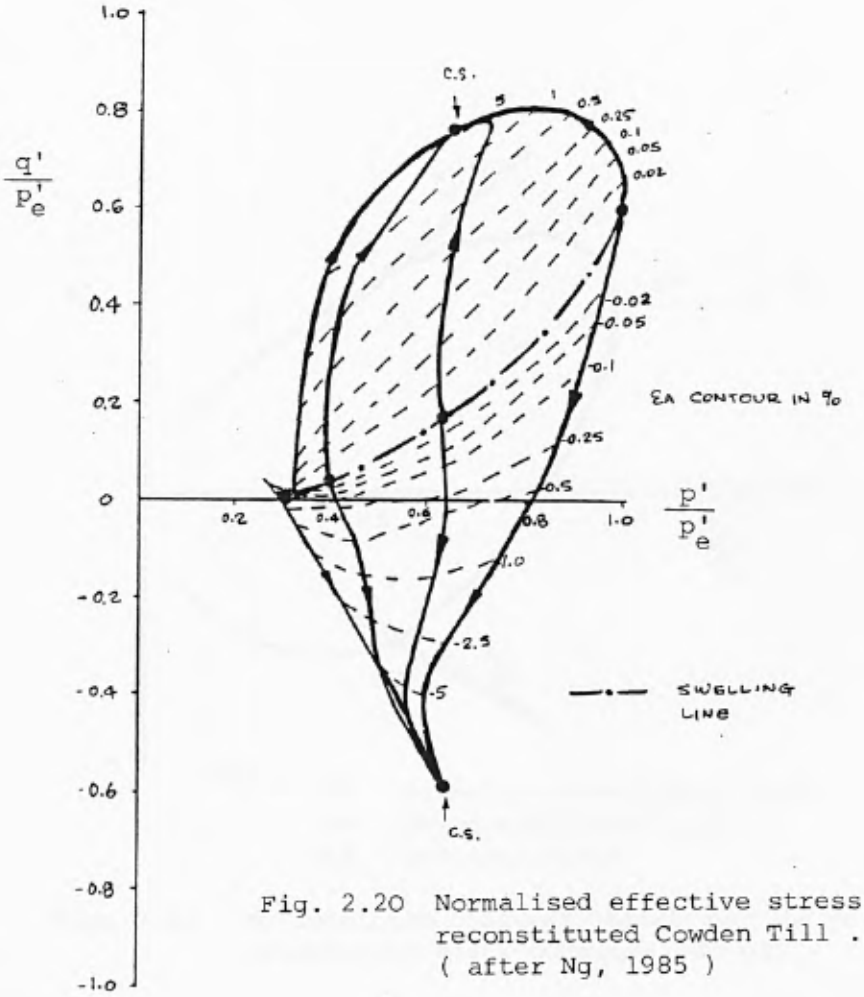

Fig. 2.20 Normalised effective stress paths of reconstituted Cowden Till .
(after Ng, 1985)

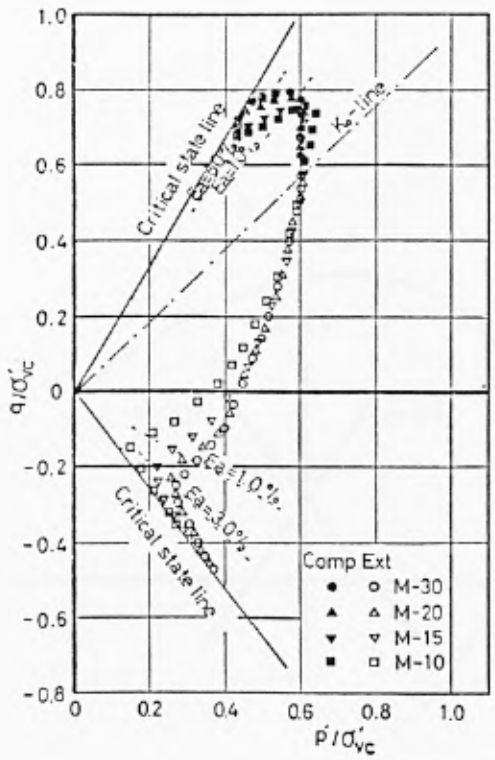

Fig. 2.21 Normalised effective stress paths of reconstituted Kawasaki clays.
(Nakase and Kamei, 1983)

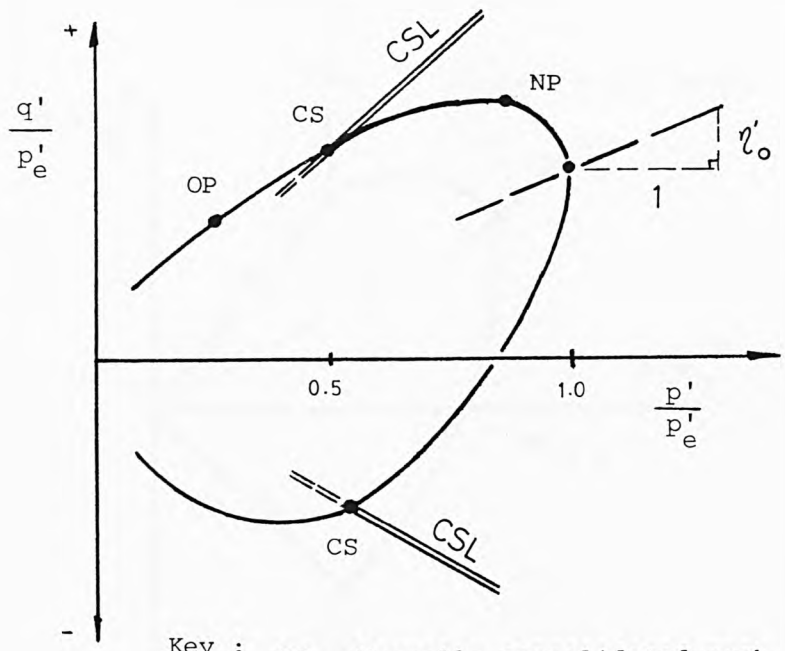

Key :
NP Normally consolidated peak
OP Overconsolidated peak
CS Critical state

Fig. 2.22 An idealised constant volume section of an anisotropic state boundary surface.

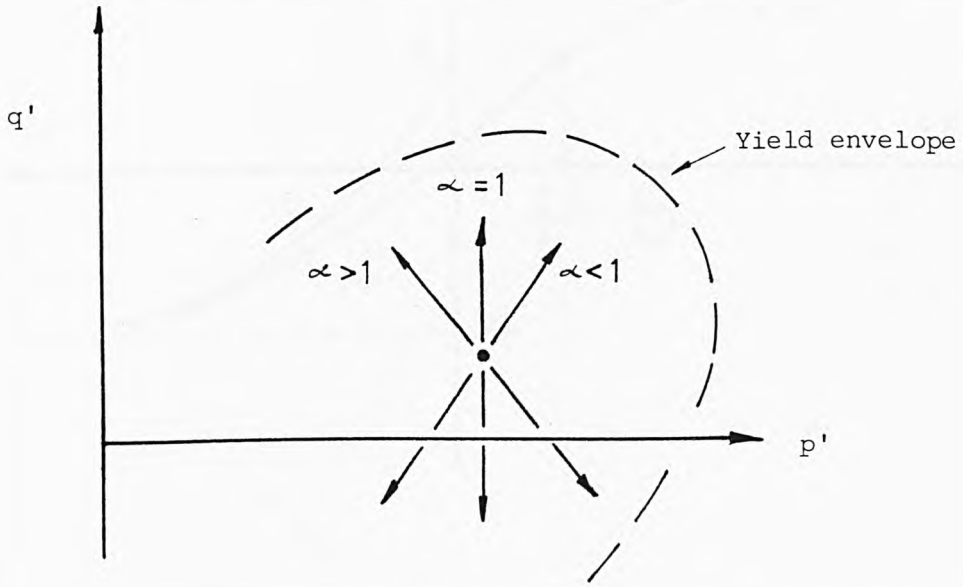

Fig. 2.23 The predicted undrained effective stress paths for an elastic soil. (after Graham and Houlsby,1983)

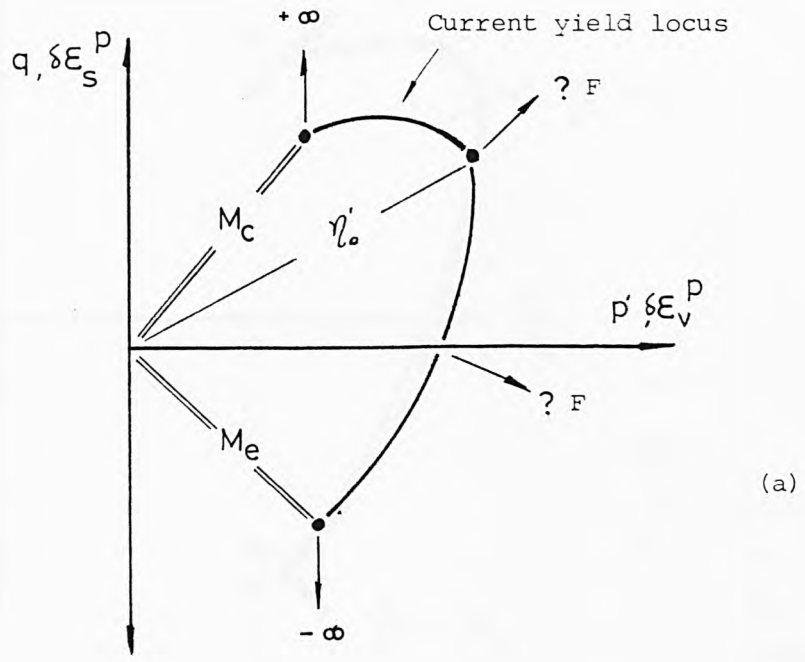

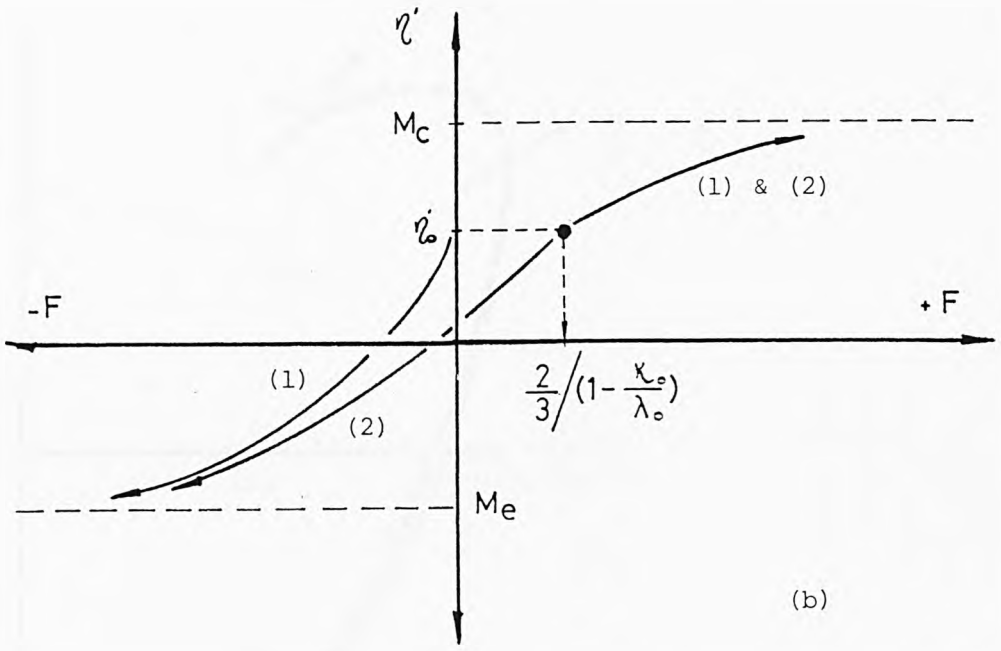

Fig. 2.24 A flow rule for an anisotropic yield locus.

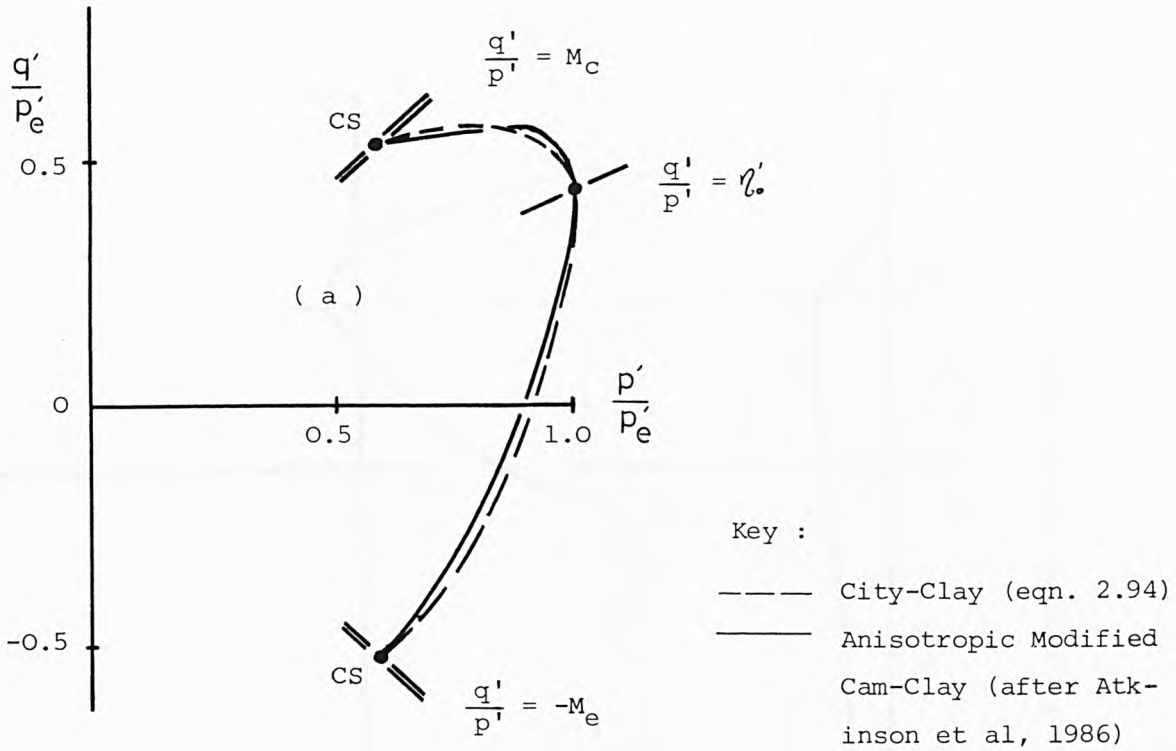

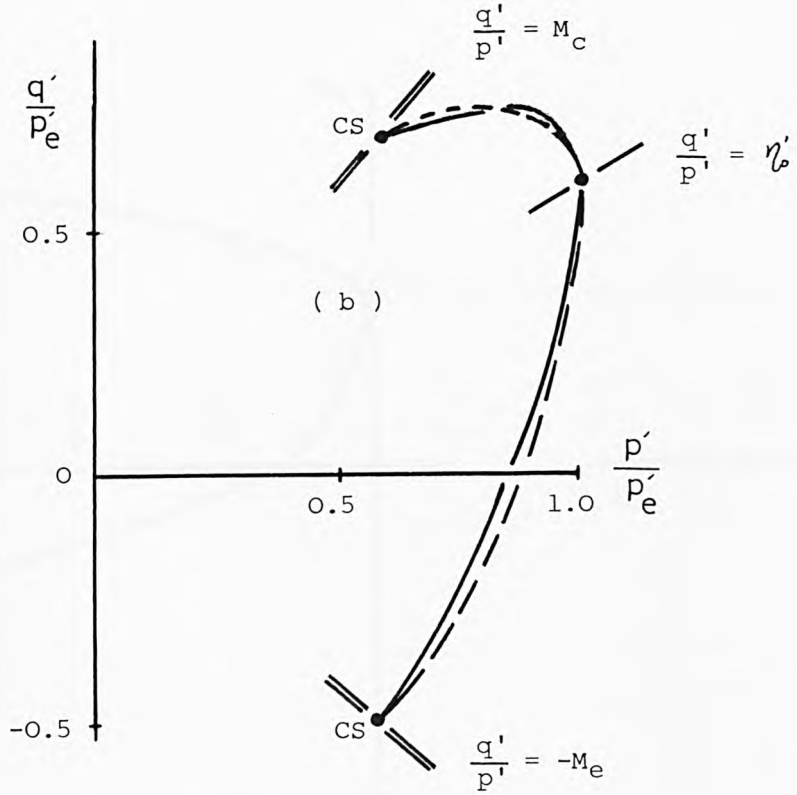

Fig. 2.25 The predicted constant volume section of the state boundary surface for a) Speswhite kaolin clay b) Cowden Till.

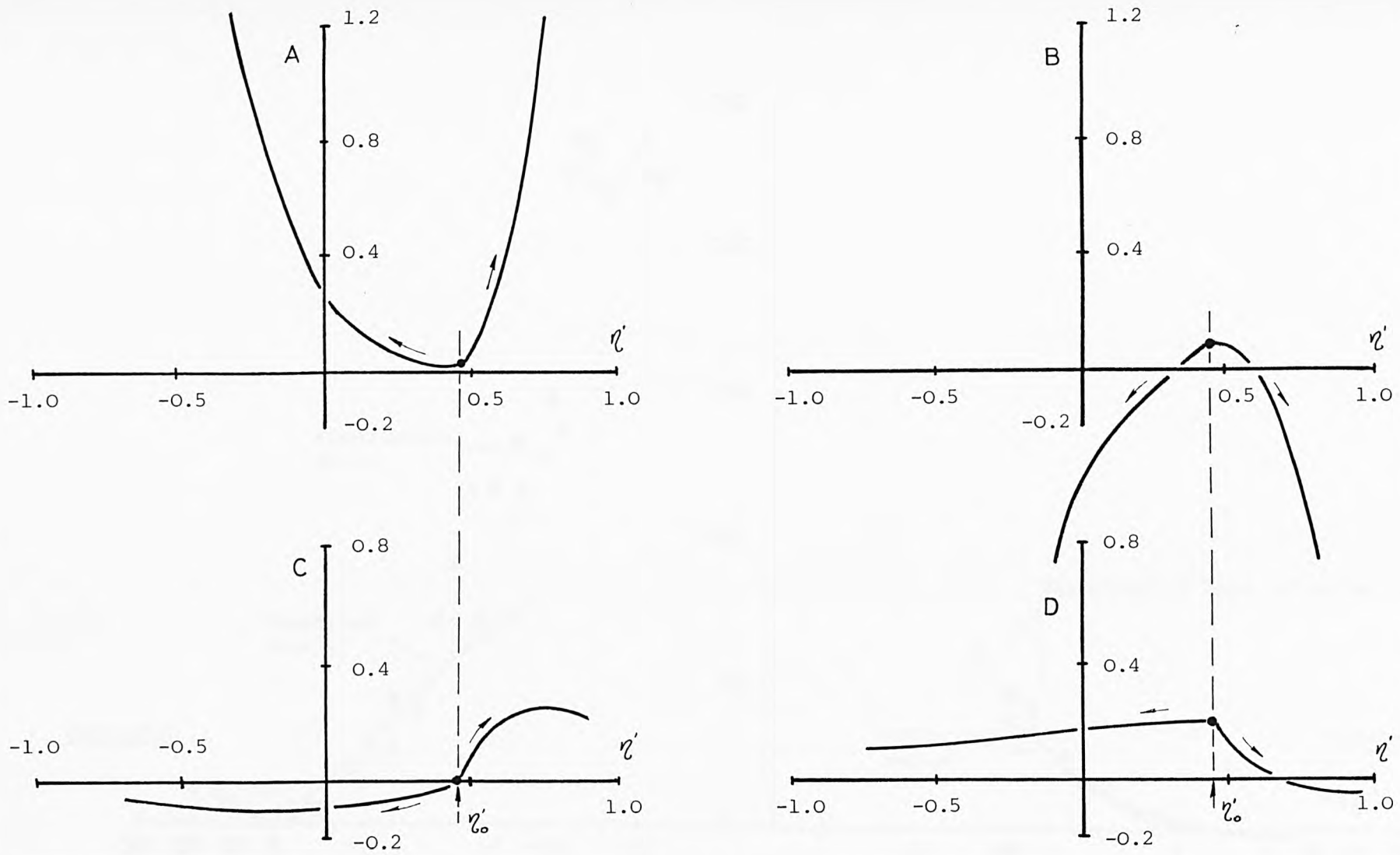

Fig. 2.26 Patterns of the individual compliance for K_o compressed Speswhite kaolin clay.

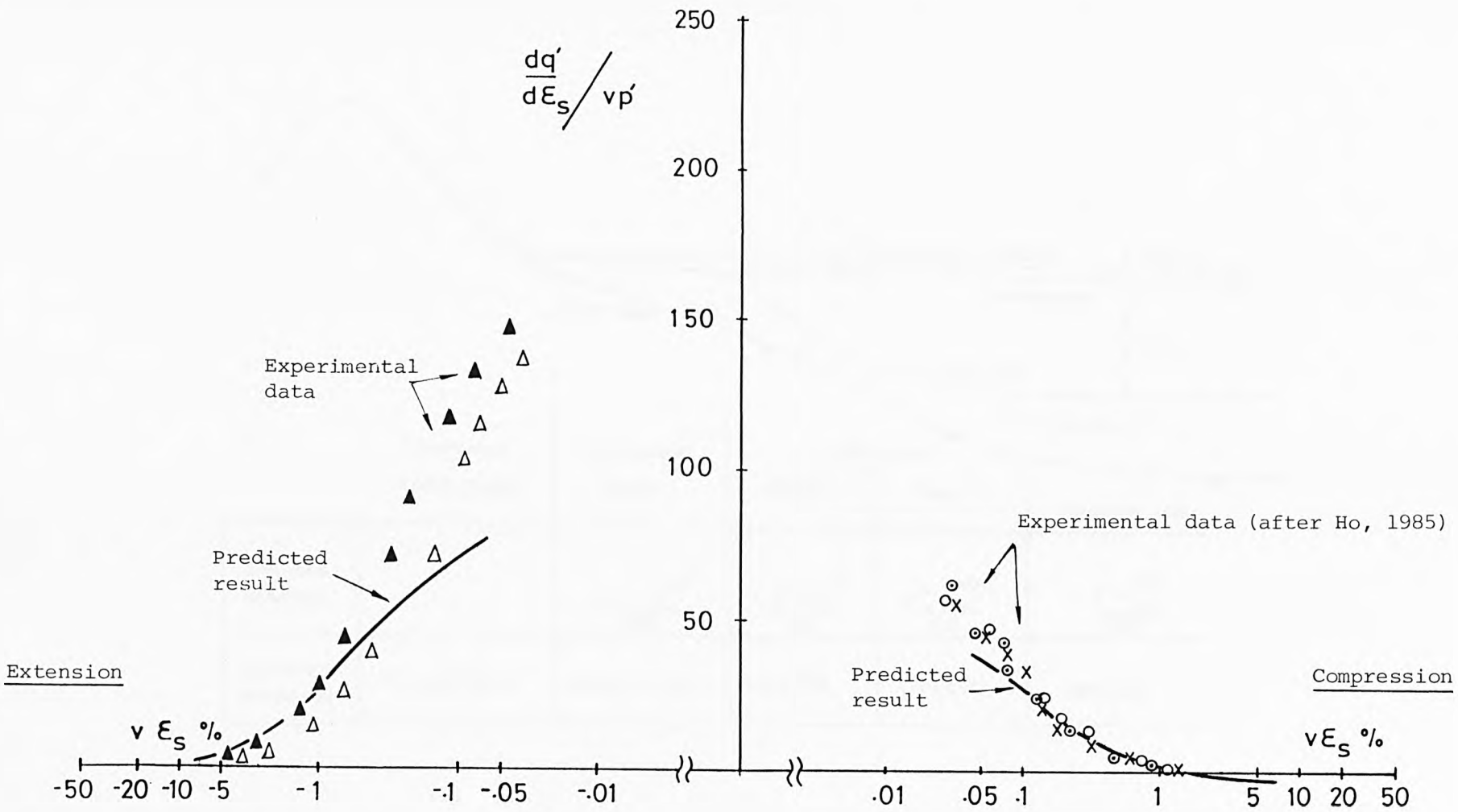

Fig. 2.27 The predicted and the experimental tangent shear stiffness for K_o normally compressed Speswhite kaolin.

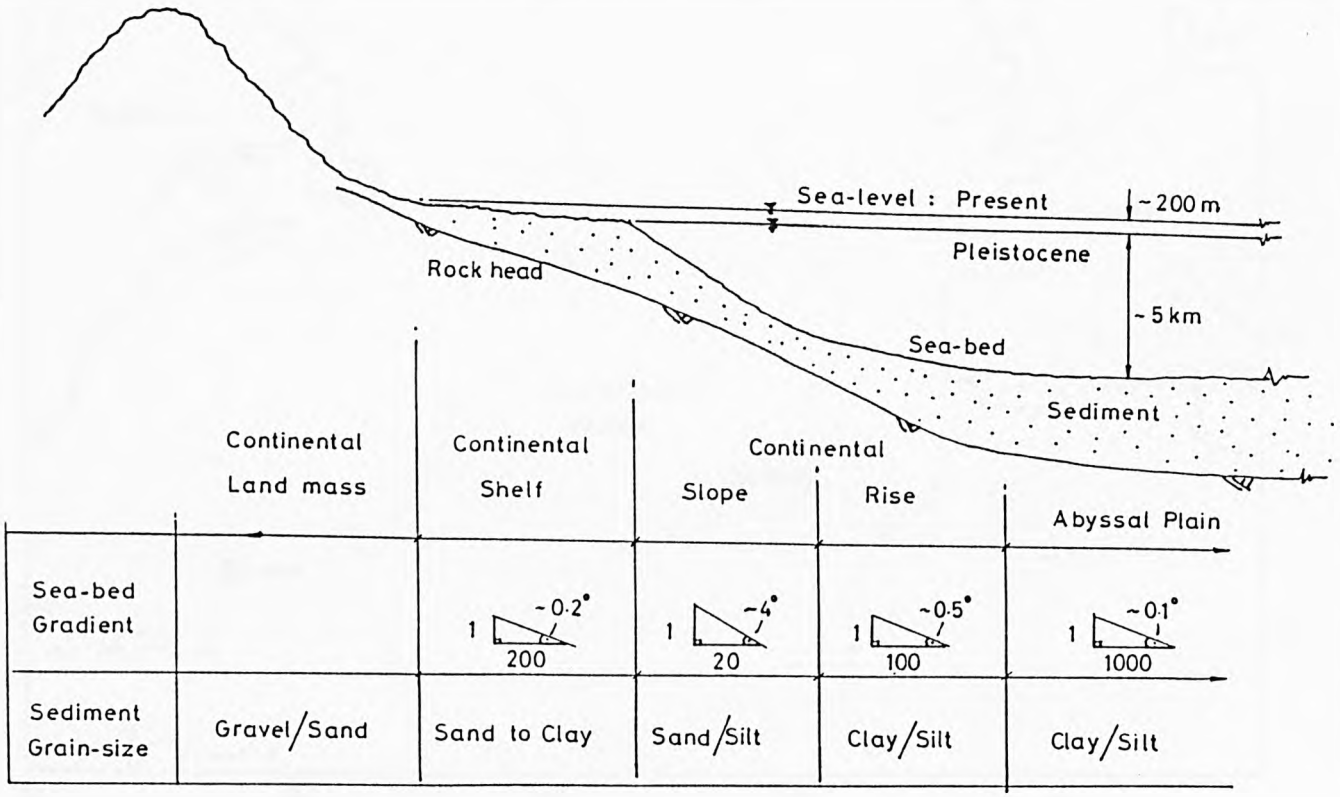

Fig. 3.1 An idealised section of the ocean floor.

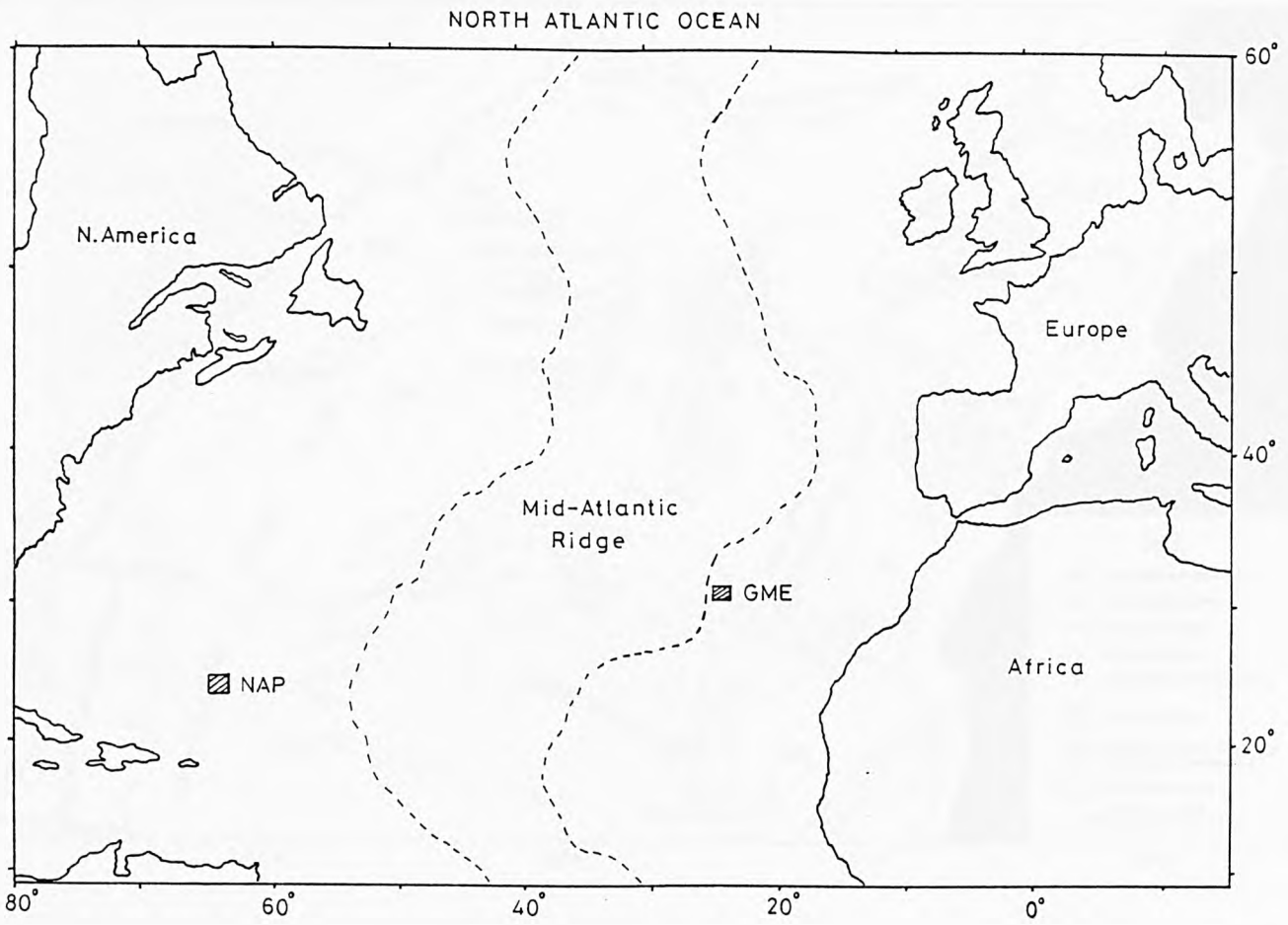

Fig. 3.2 North Atlantic study areas : Great Meteor East (GME)
Nares Abyssal Plain (NAP)

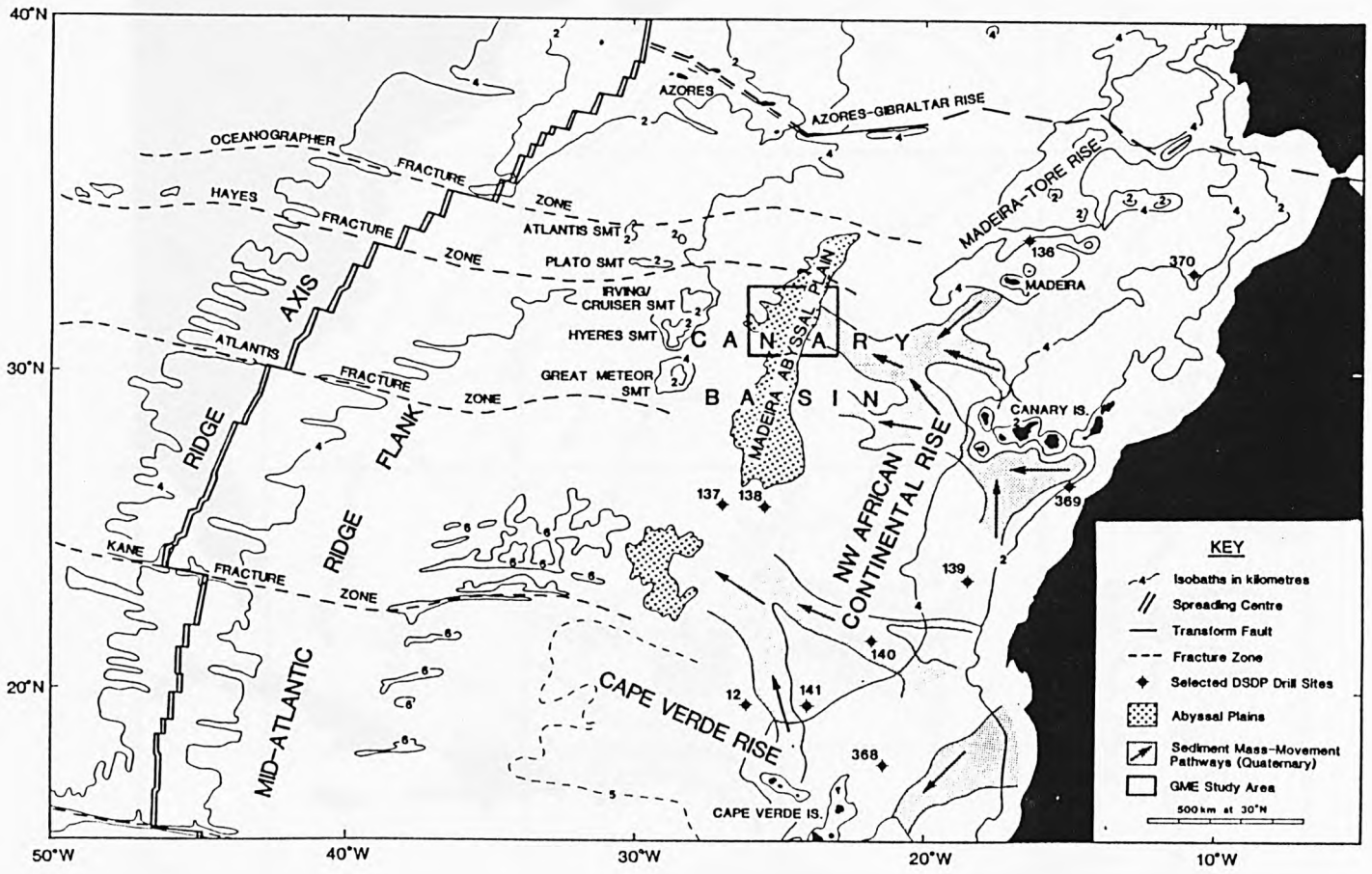

Fig. 3.3 Regional setting of the Great Meteor East (GME).
(after Searle et al, 1985)

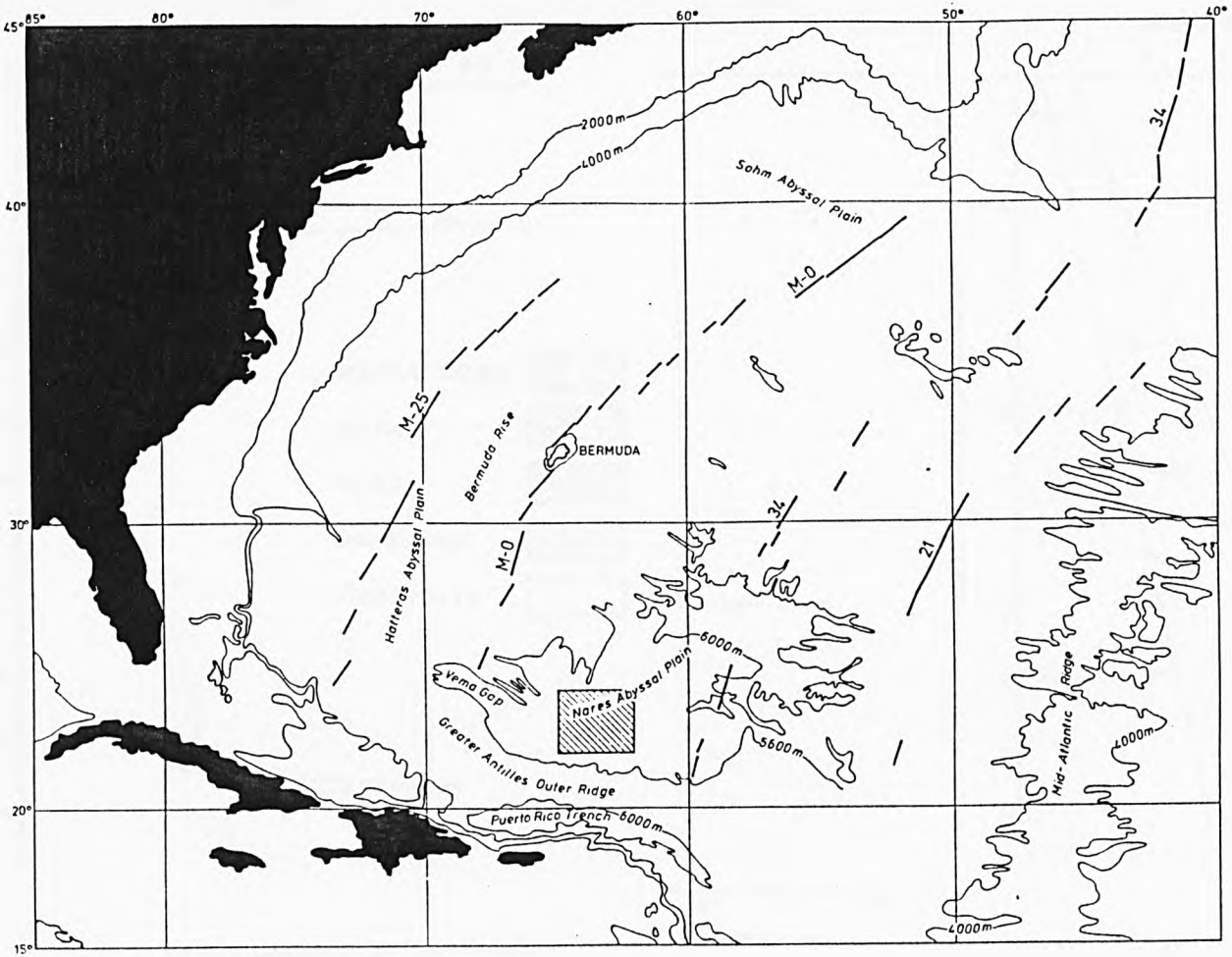

Fig. 3.4 Regional setting of the Nares Abyssal Plain (NAP).

(after RGD , 1984)

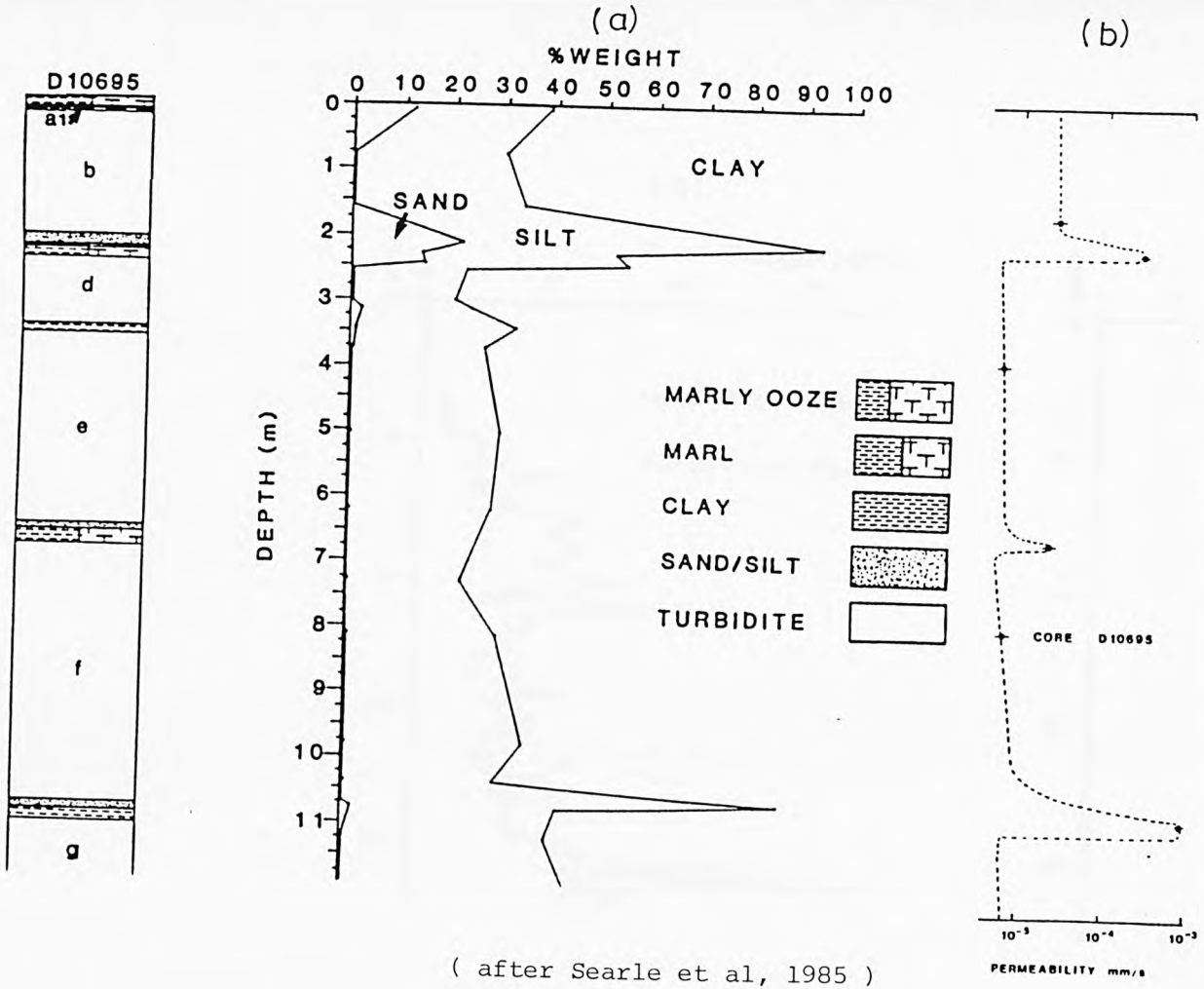

(after Searle et al, 1985)

(after Freeman, 1984)

Fig. 3.5 Engineering properties of GME core D10695.

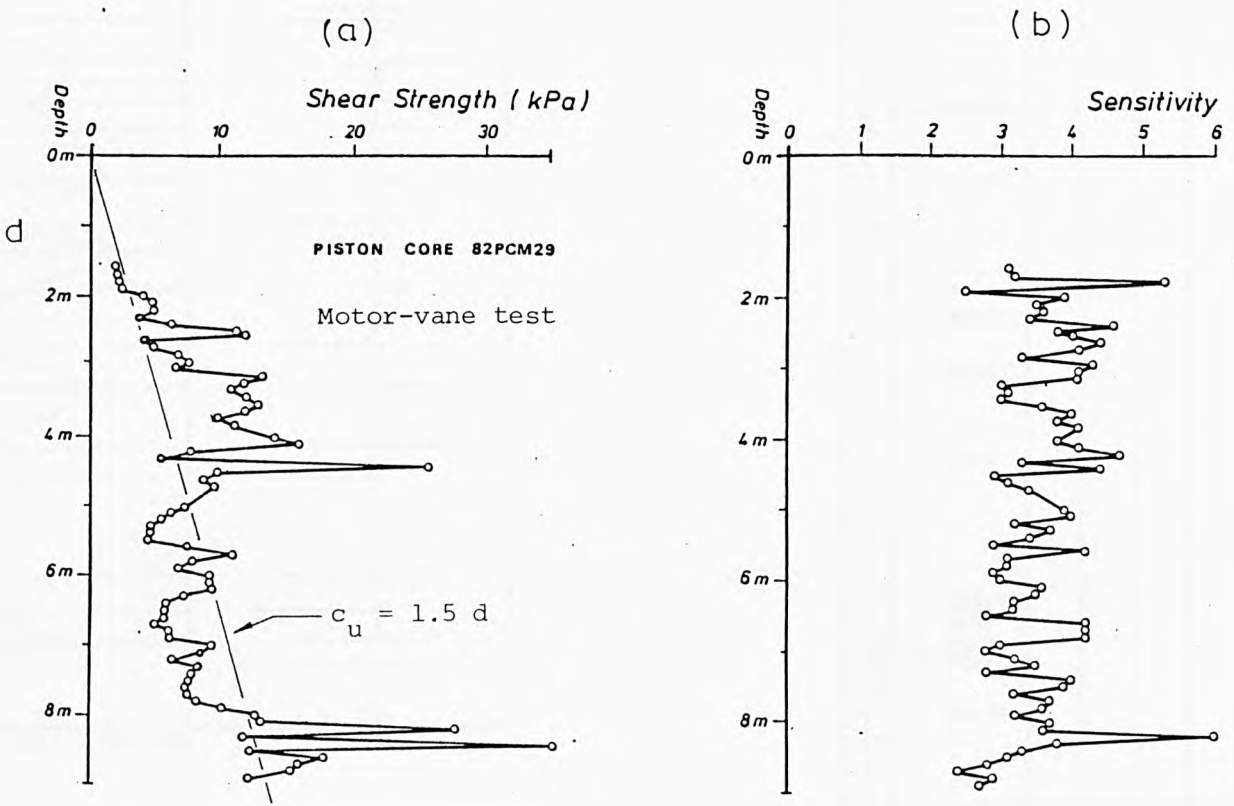

Fig. 3.6 Engineering properties of GME core 82 PCM 29 (after RGD, 1982).

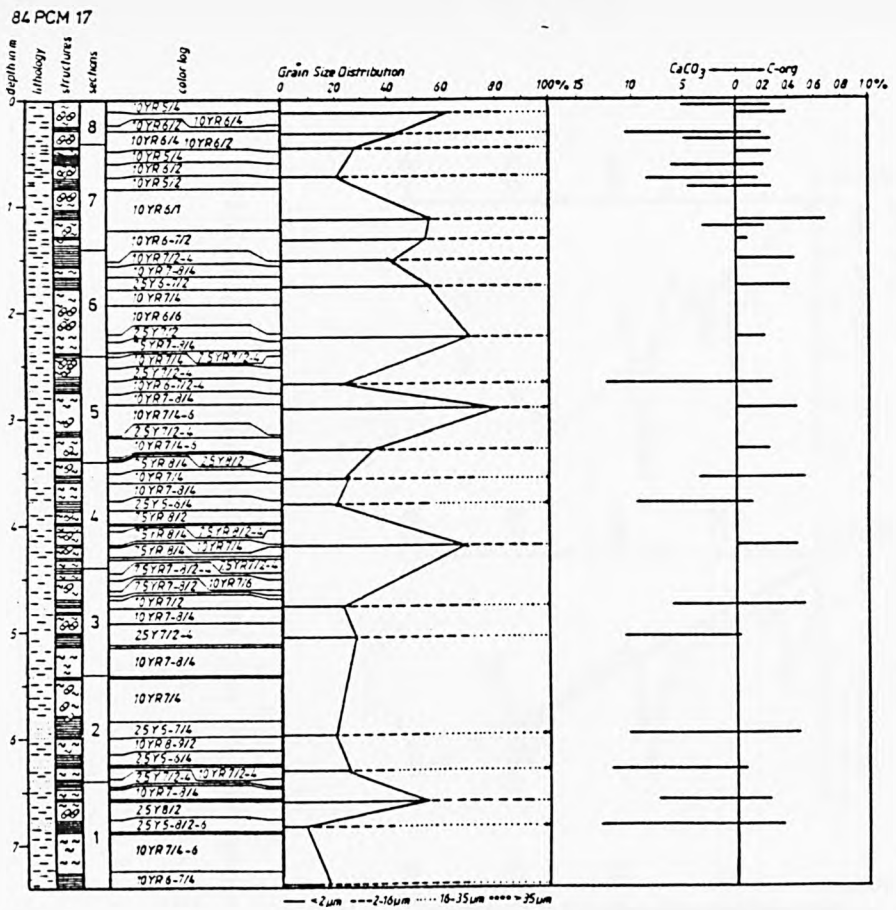

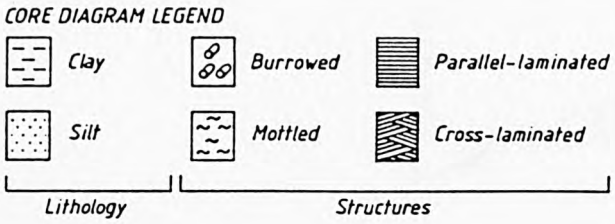

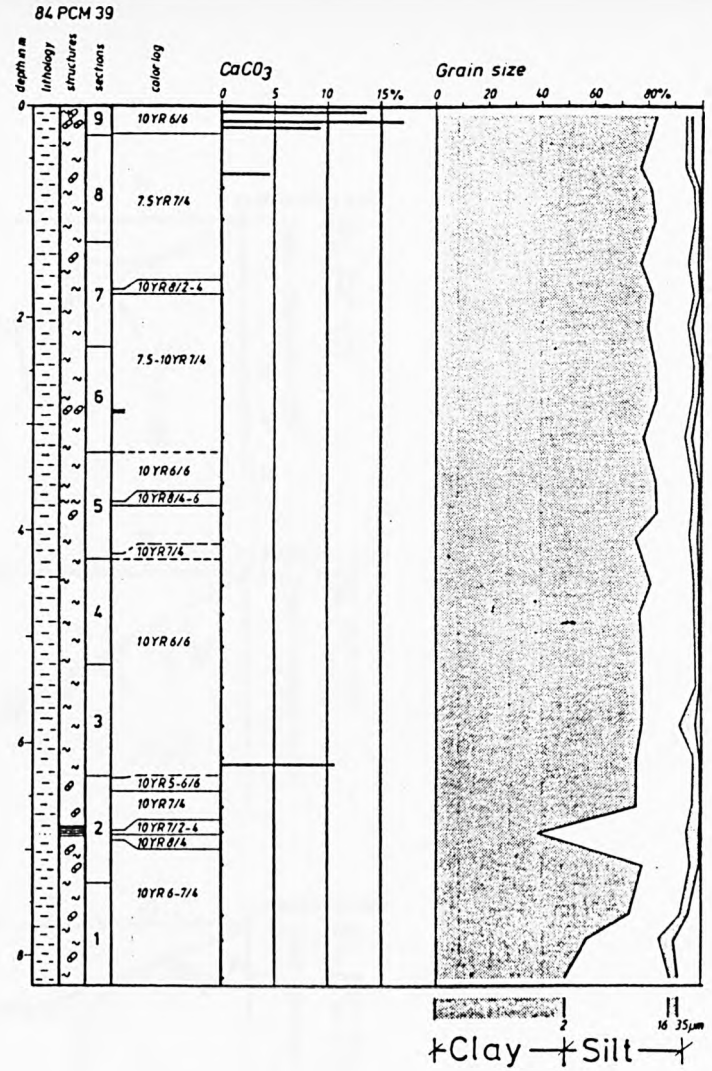

Fig. 3.7 Engineering properties of NAP cores 84 PCM 17 and 84 PCM 39 (after RGD, 1984).

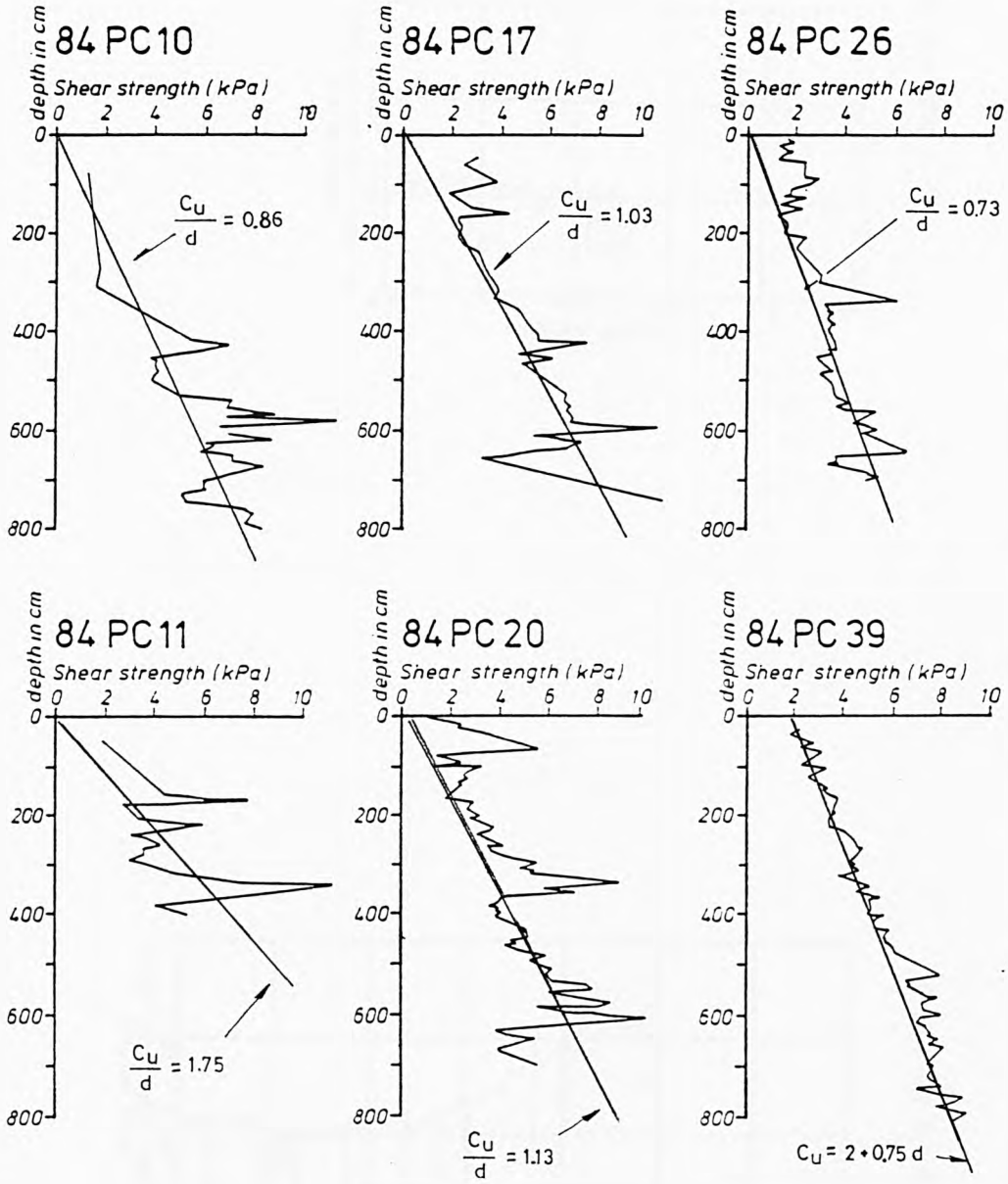

Fig. 3.8 Engineering properties of NAP cores.

(Motor-vane strength, after RGD, 1984)

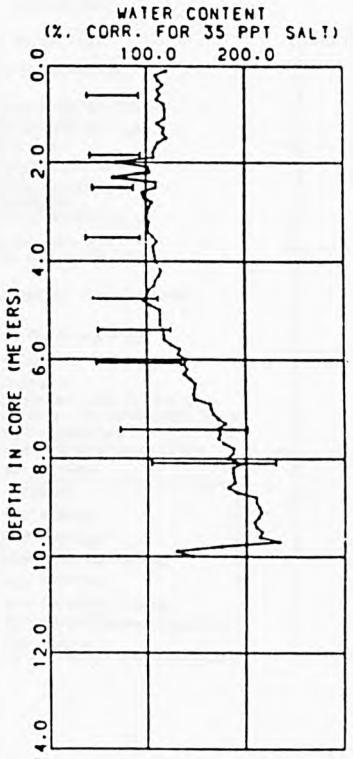

a, (VEMA-32 PC-115)

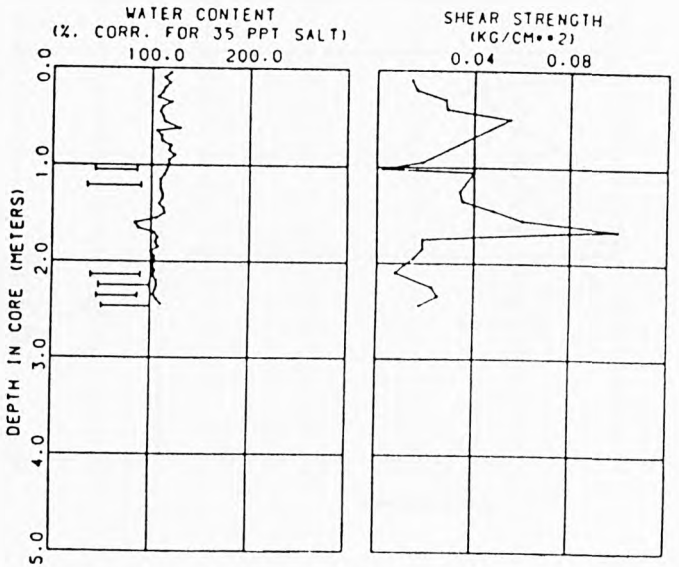

b, (MARA-02 GC-04)

Fig. 4.1 Geotechnical Properties (MPG-1 North Pacific)
(after Akers, 1980)

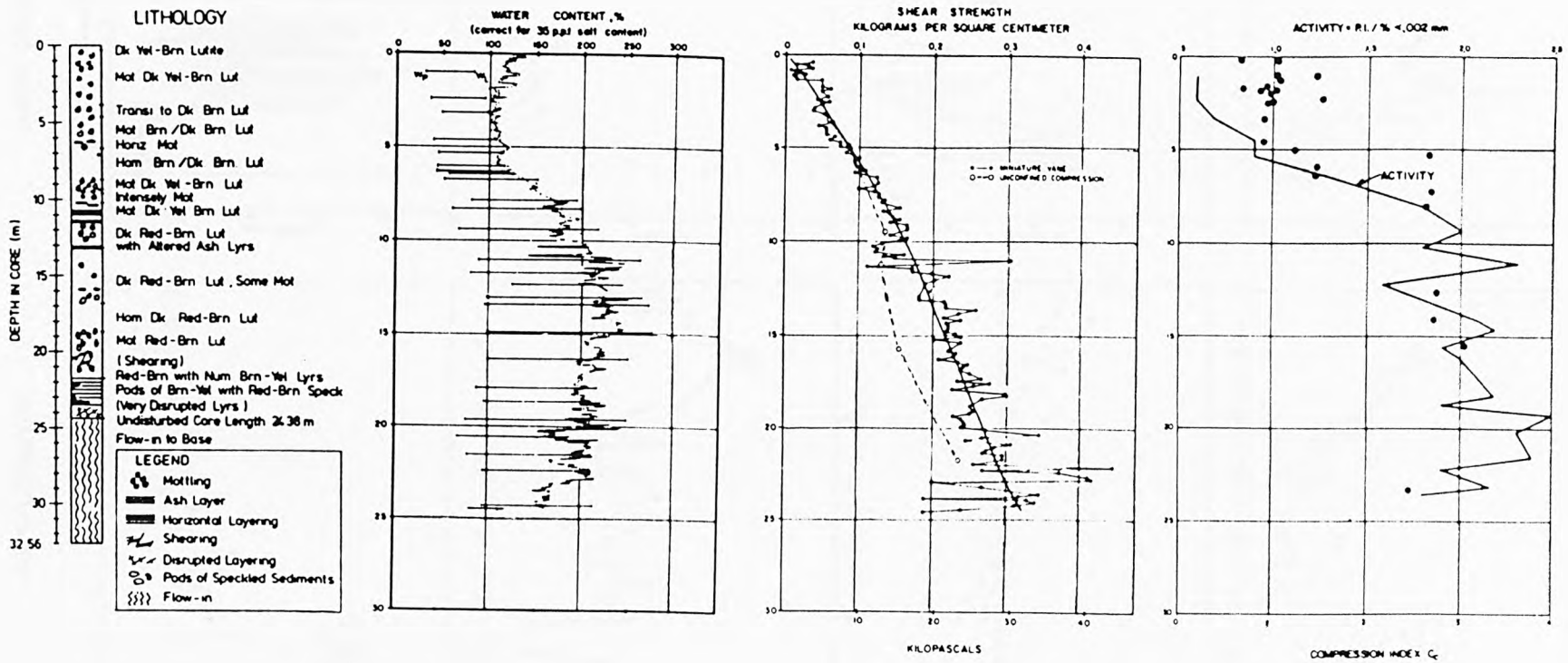

Fig. 4.2 : Geotechnical Properties (LL-44 GPC-3), (after Silva et al, 1984)
(MPG-1 North Pacific)

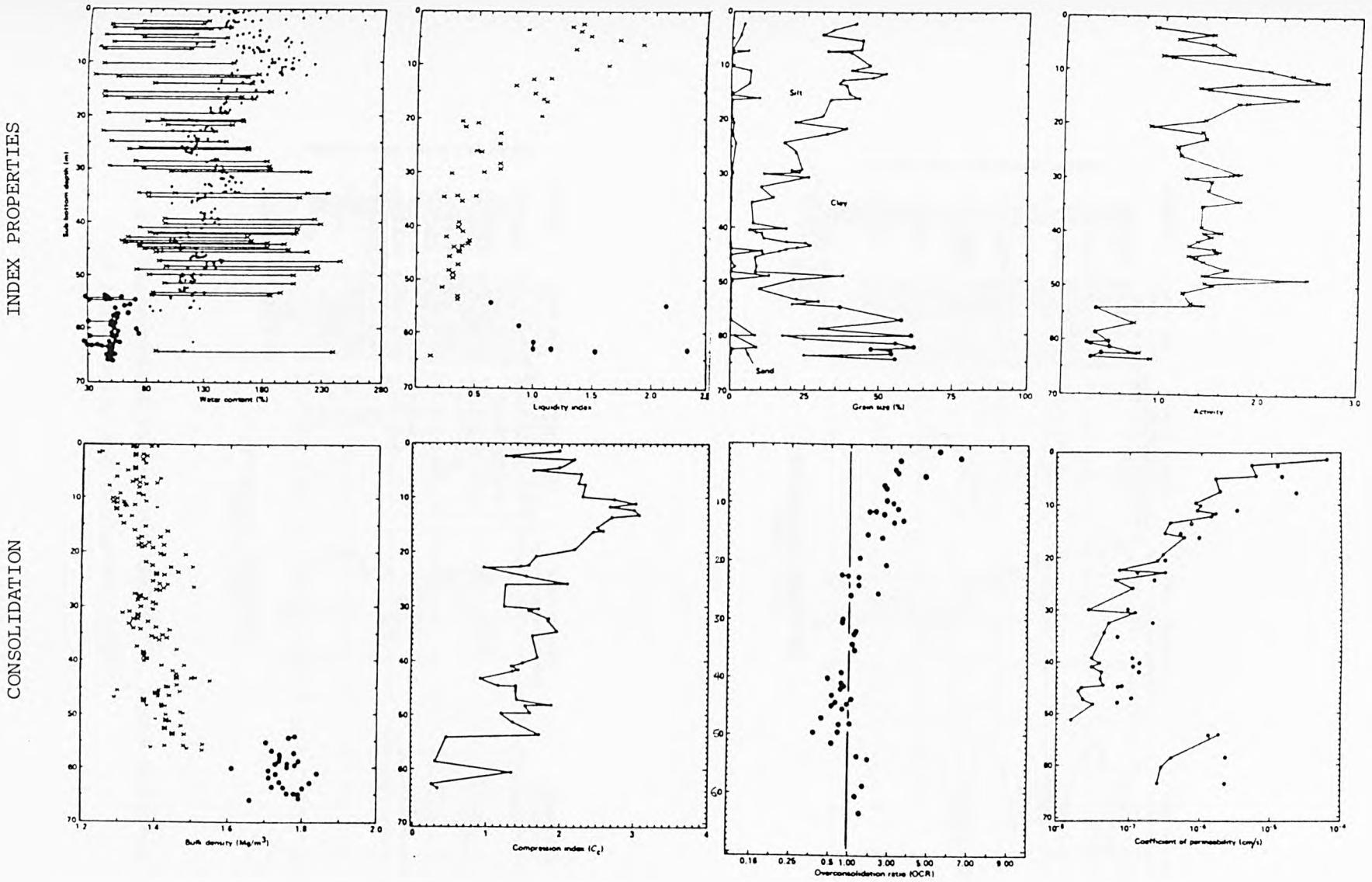

Fig. 4.3 Deep Sea Drilling Project(DSDP) Hole 576A (North Pacific)
(after marine Geotechnical Consortium, 1985)

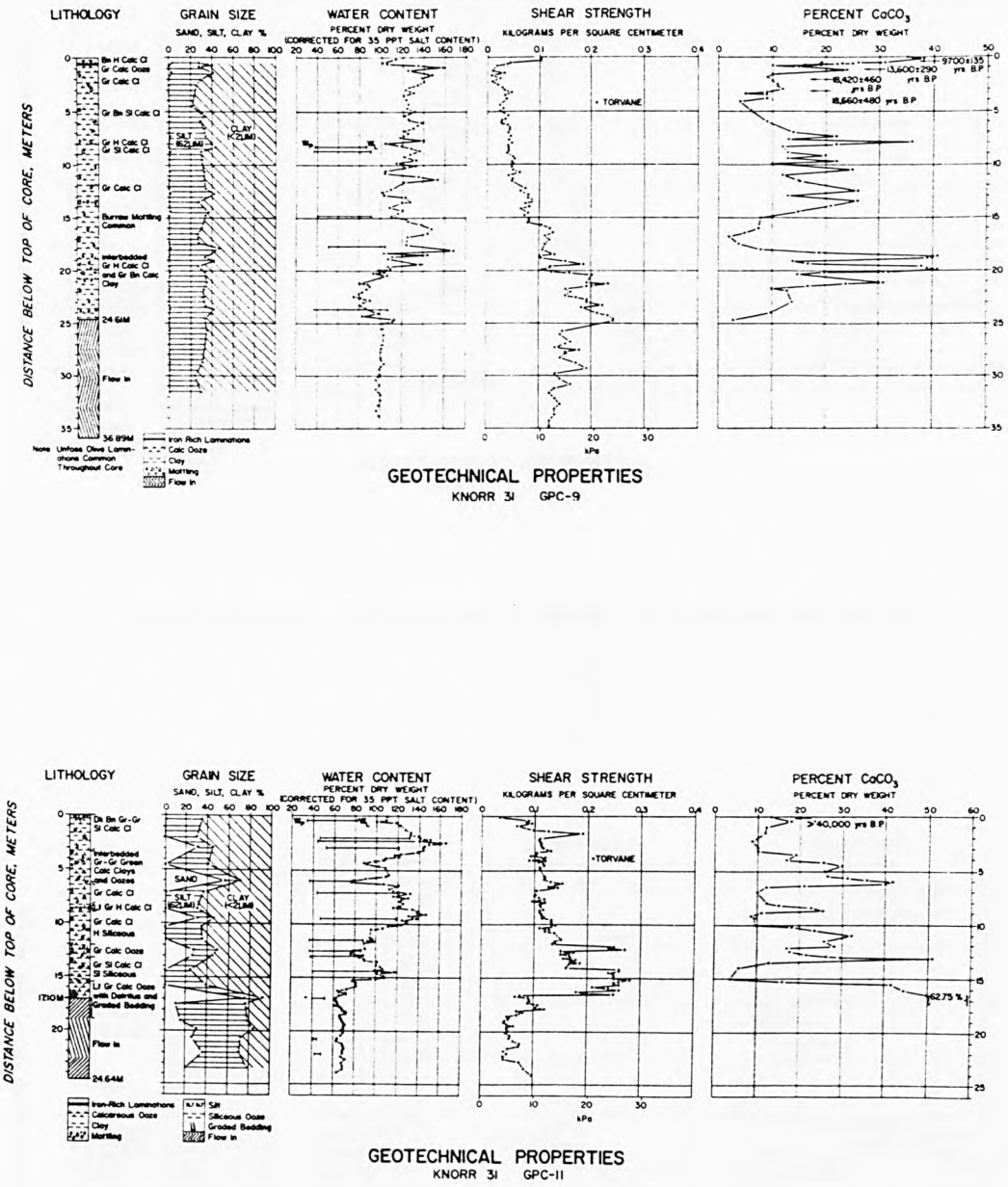

Fig. 4.4 Geotechnical Properties (KNORR-31, North Atlantic)
(after Silva and Hollister, 1979)

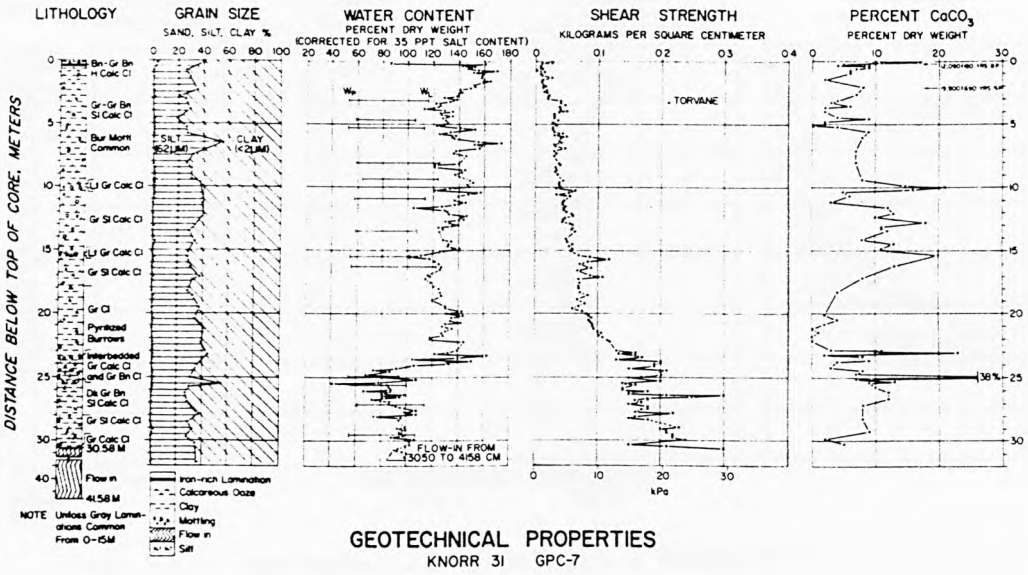

Fig. 4.5 Geotechnical Properties (KNORR-31 , North Atlantic)

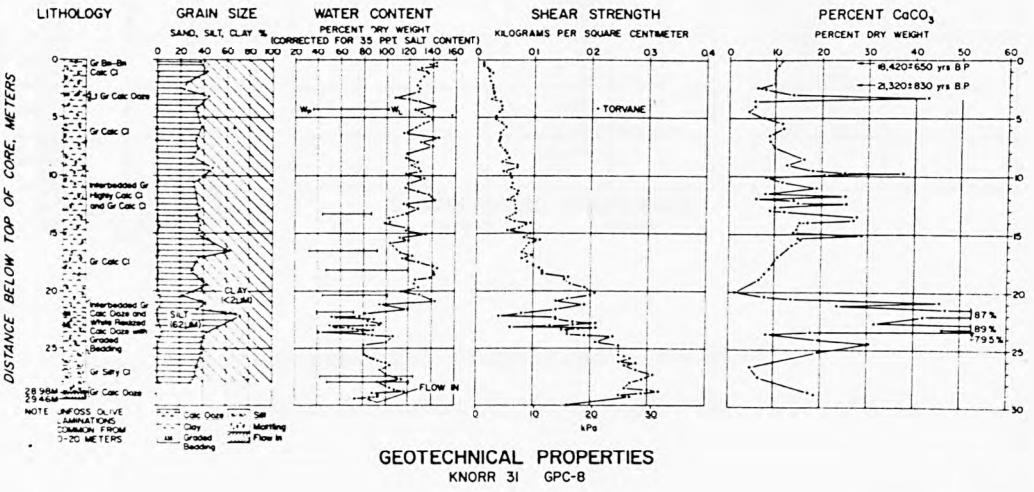

Fig. 4.6 Geotechnical Properties (KNORR-31 , North Atlantic)

(after Silva and Hollister, 1979)

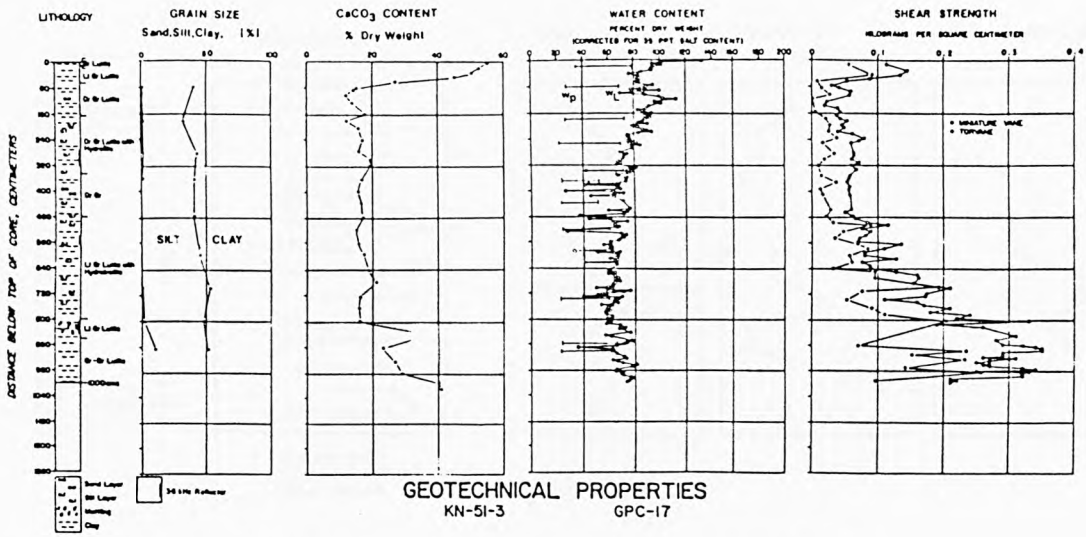

Fig. 4.7 Geotechnical Properties (KNORR-51)

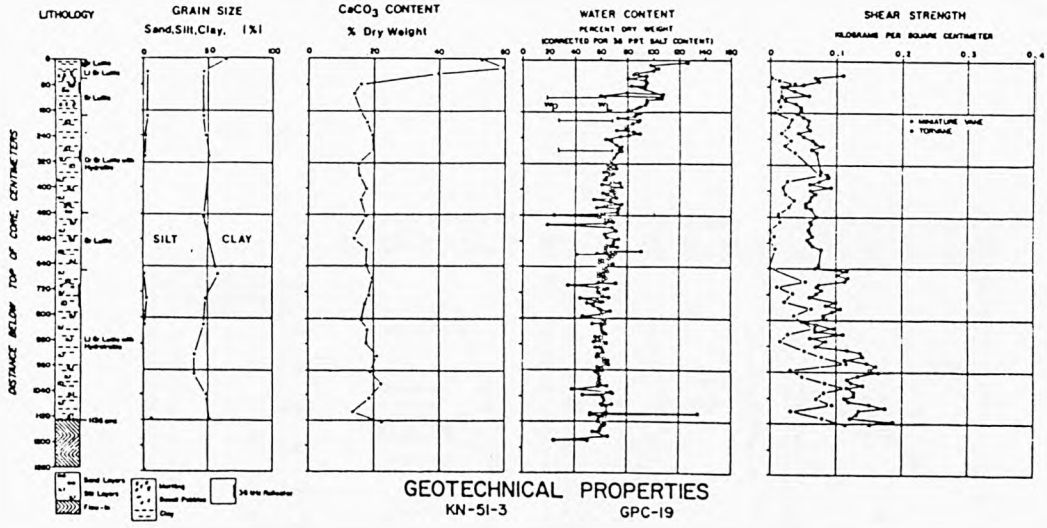

Fig. 4.8 Geotechnical Properties (KNORR-51)
North Atlantic (after Carchedi, 1979)

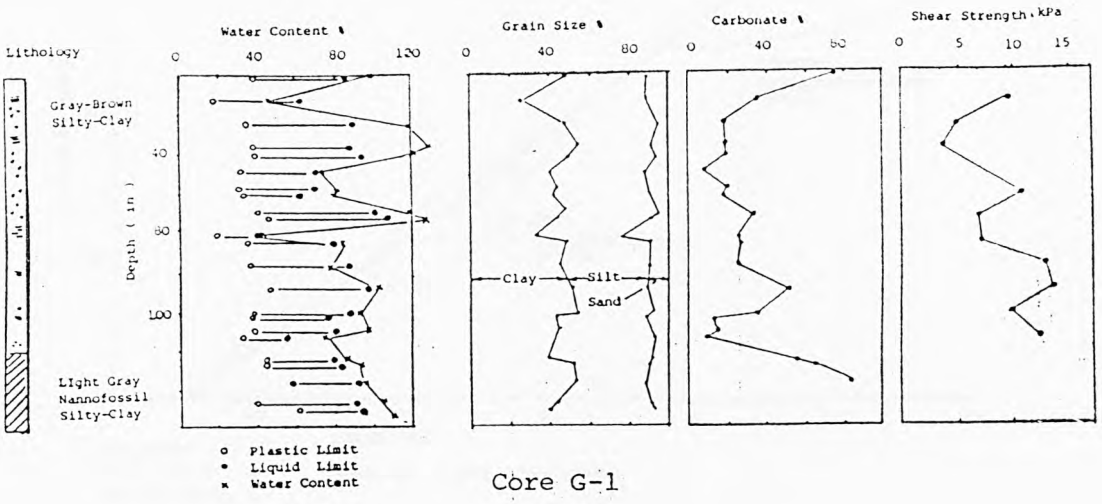

Fig. 4.9 Geotechnical Properties (North Atlantic, after Demars, 1975)

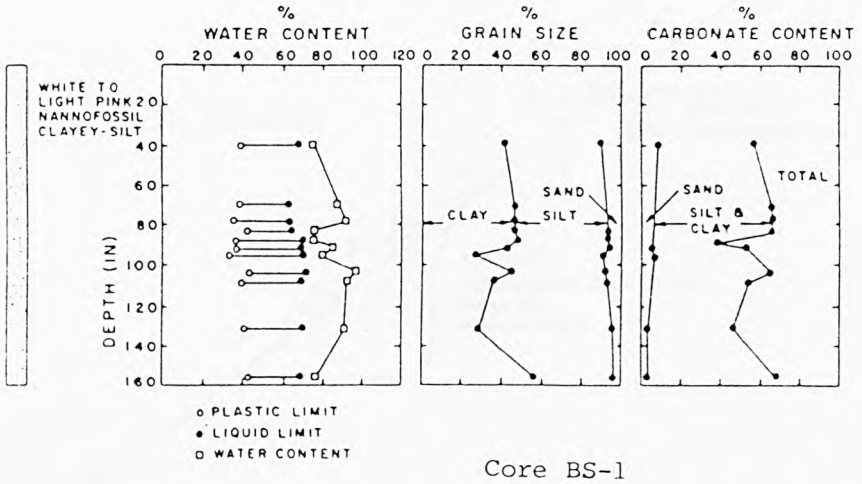

Fig. 4.10 Geotechnical Properties (North Atlantic, after Demars, 1975)

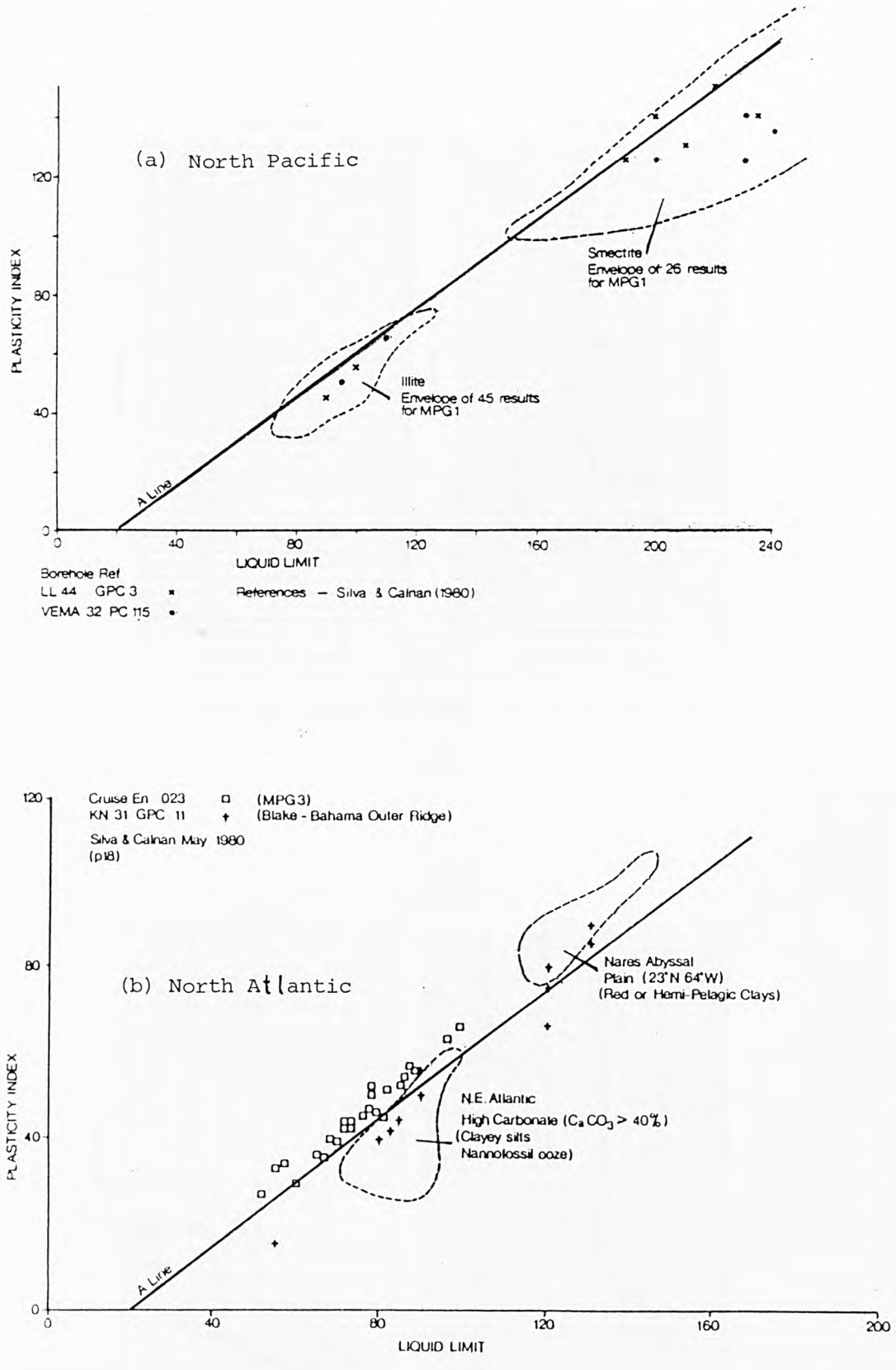

Fig. 4.11 Plasticity Charts for North Pacific and North Atlantic Deep-ocean Sediments (after OAP, 1982).

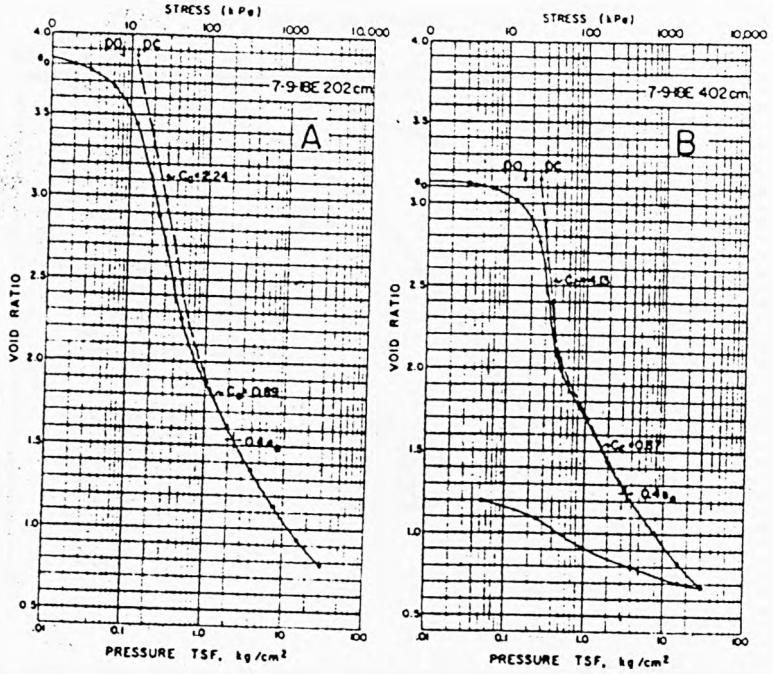

(a) Core 7-9-18E

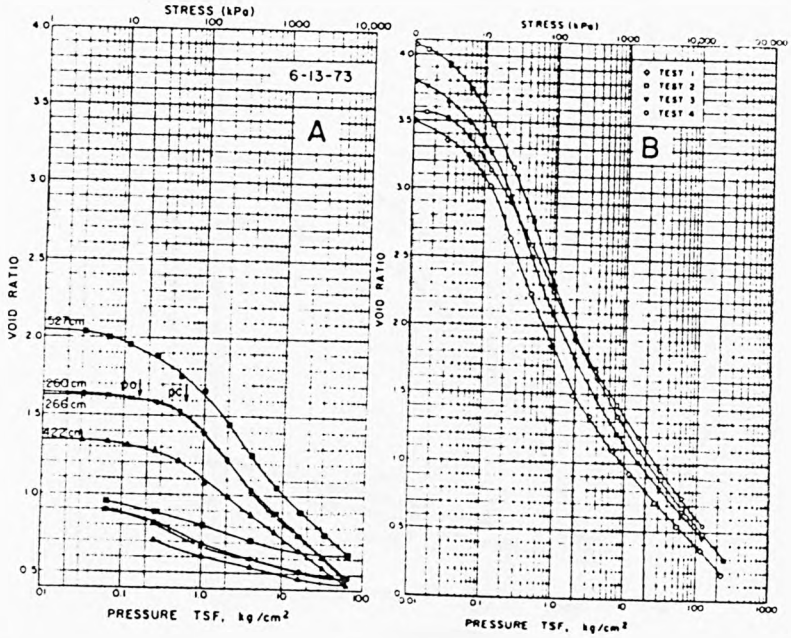

(b) Core 6-13-73

Fig. 4.12 One Dimensional Consolidation Test Results
(Gulf of Mexico, after Bryant et al., 1974)

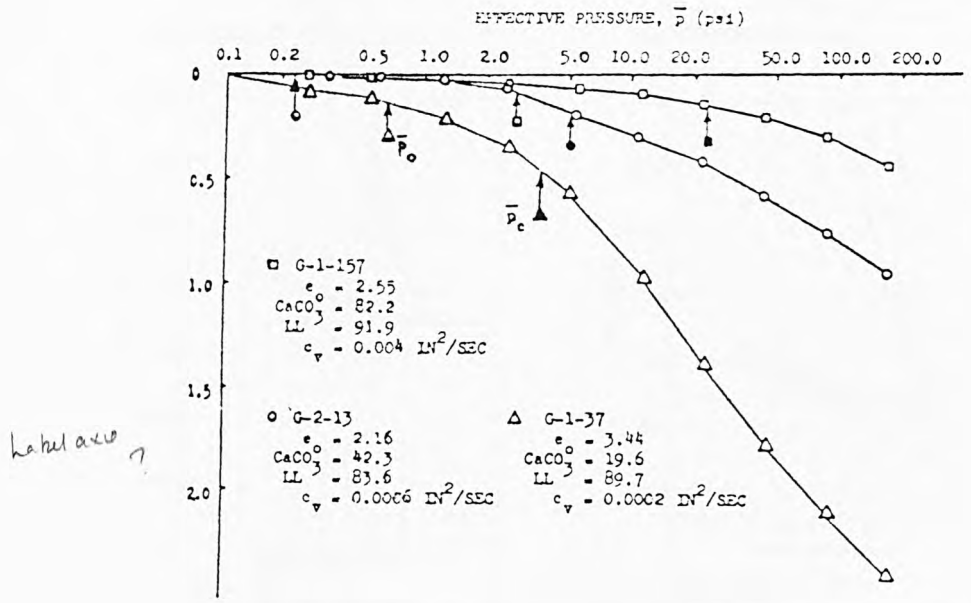

Fig. 4.13 One Dimensional Consolidation Test Results
(North Atlantic, after Nacci et al, 1975)

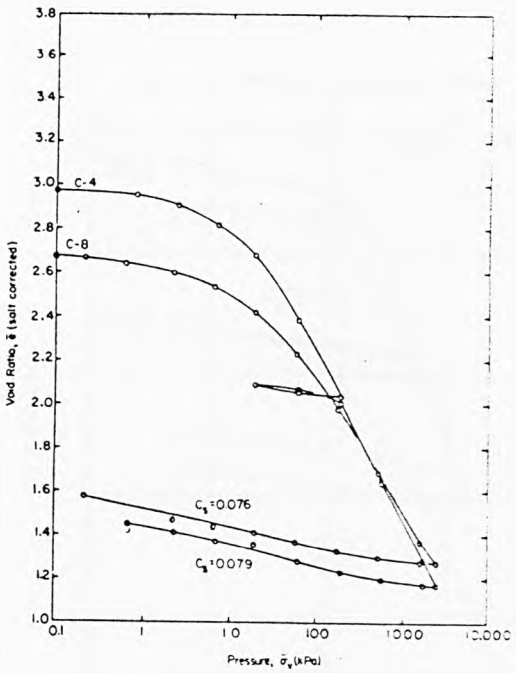

Fig. 4.14 One Dimensional Consolidation Test Results
(North Atlantic, after Valent et al., 1982)

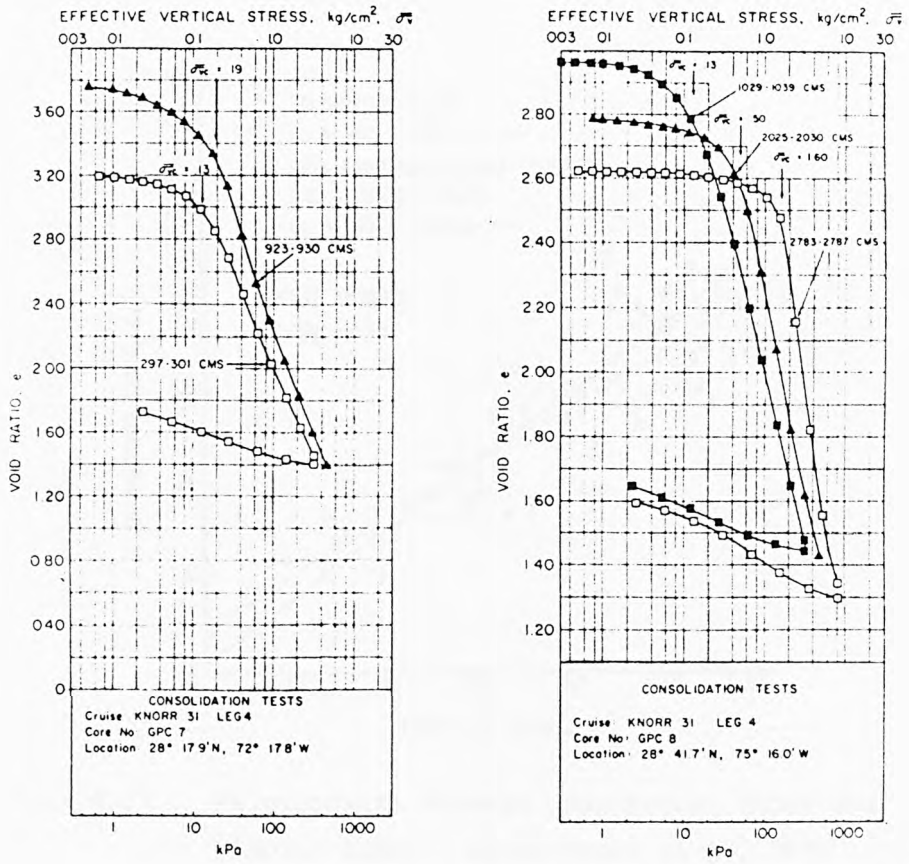

(North Atlantic, after Silva and Hollister, 1979)

Fig. 4.15 One dimension consolidation test results.

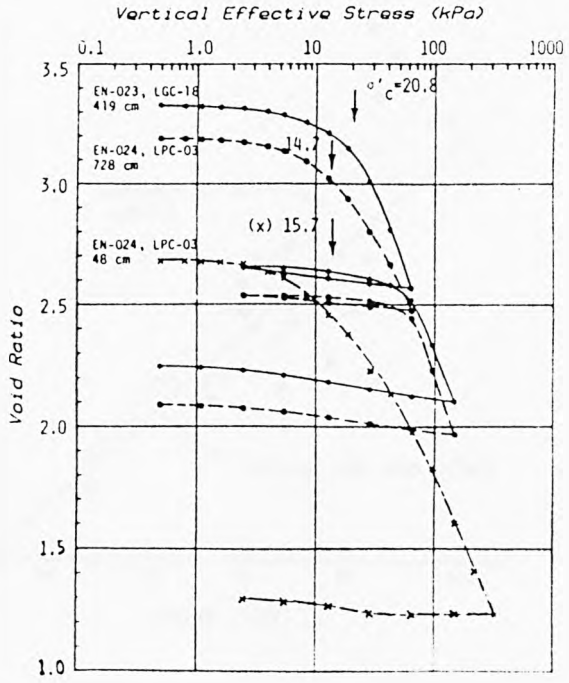

(North Atlantic, after Silva and Jordan, 1984)

Fig. 4.16 One Dimensional Consolidation Test Results

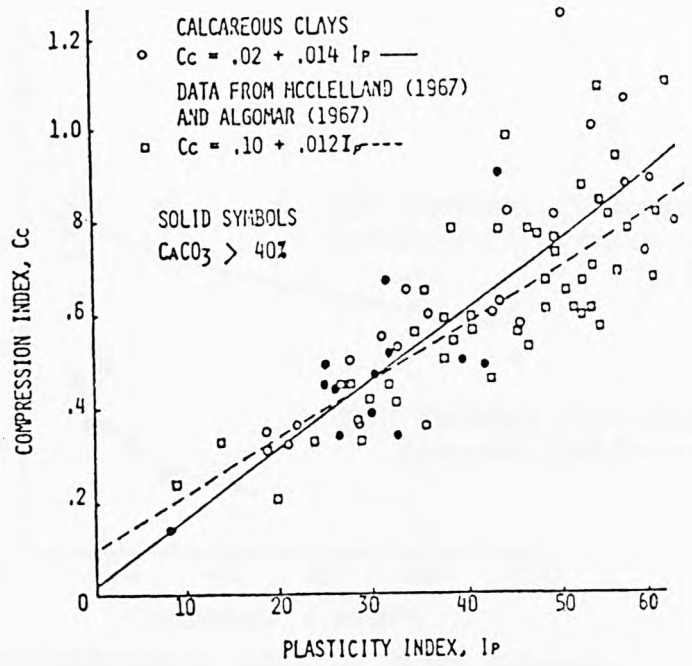

Fig. 4.17 Relationship between Compression Index and Plastic Index (after Nacci et al, 1975)

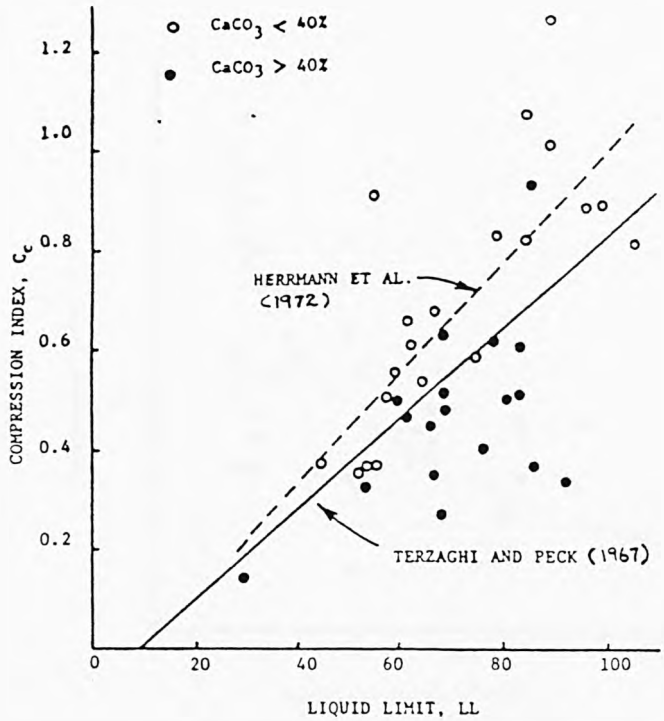

Fig. 4.18 Relationship between Compression Index and Liquid Limit (after Demars etal, 1976)

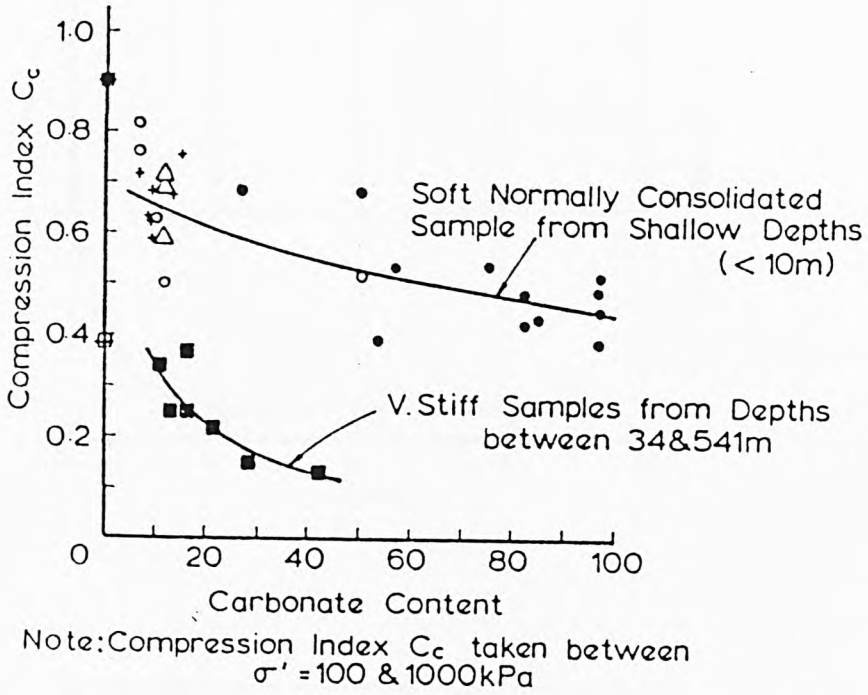

Fig. 4.19 Variation of Compression Index with Carbonate Content
(after Poulos, 1980)

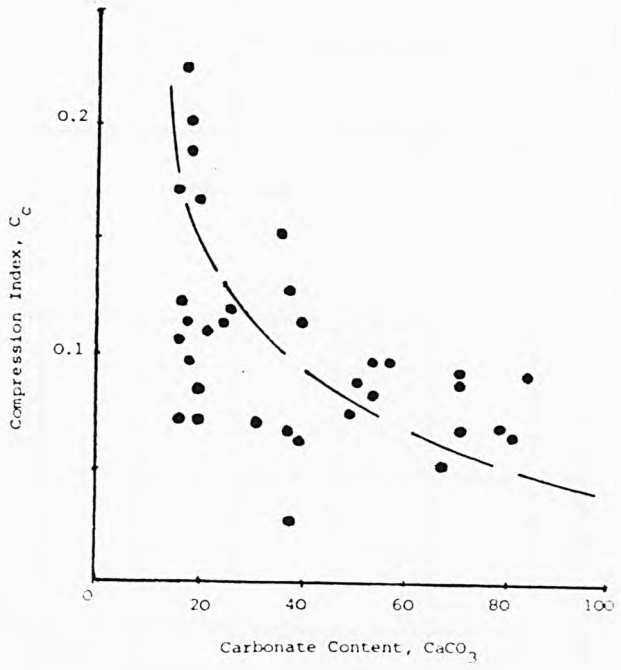

Fig. 4.20 Variation of Compression Index with Carbonate Content
(after Demars, 1975)

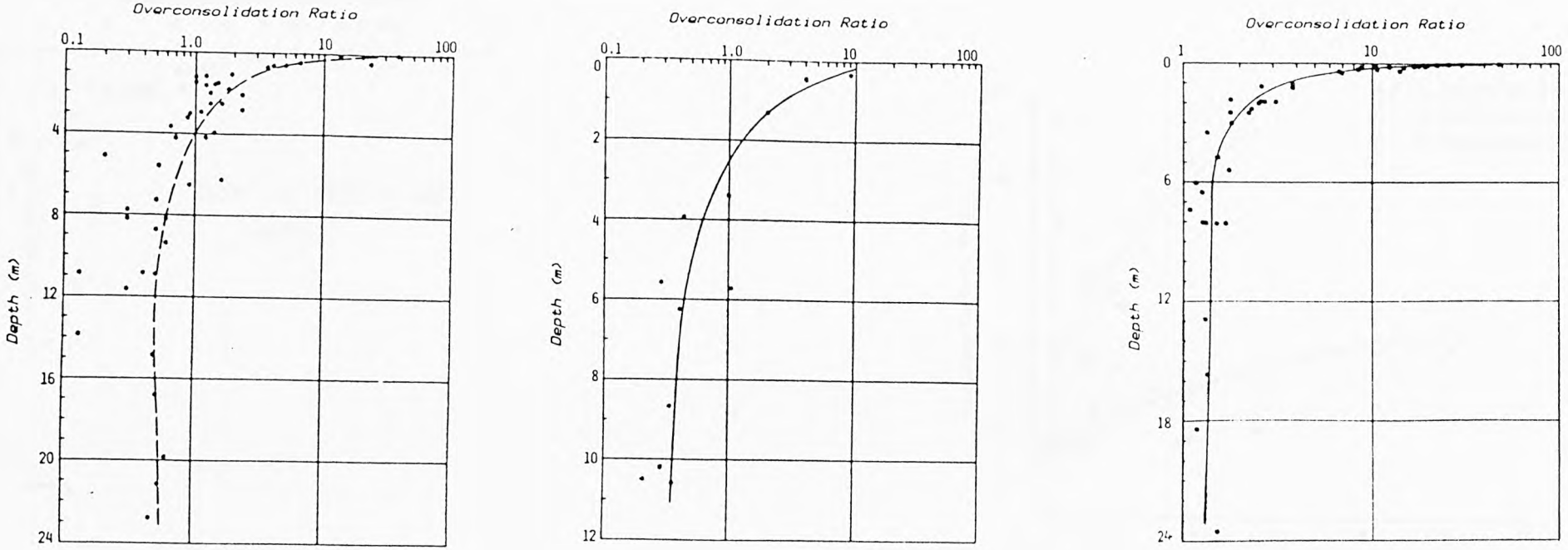

a, (North Atlantic)

b, (North Atlantic)

c, (North Pacific)

Fig. 4.21 Profile of OCR versus depth (after Silva and Jordan, 1984)

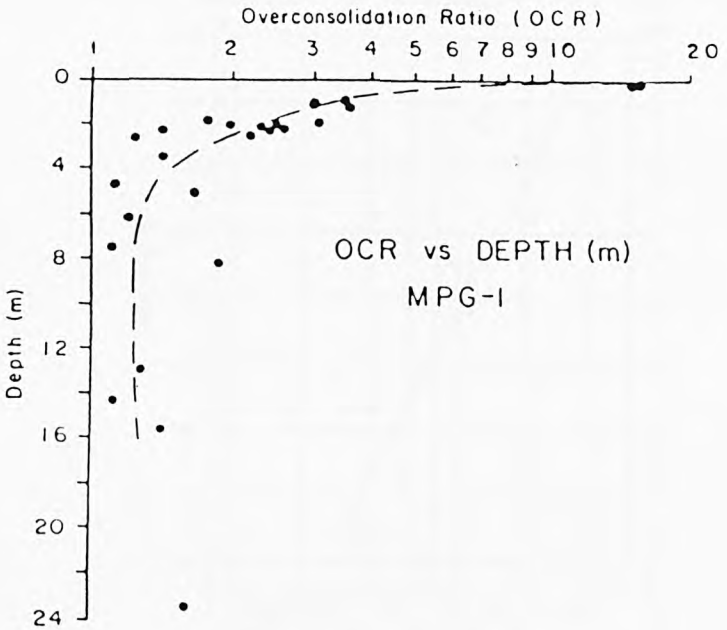

Fig. 4.22 Variation of OCR with Depth
(North Pacific, after Silva etal, 1984)

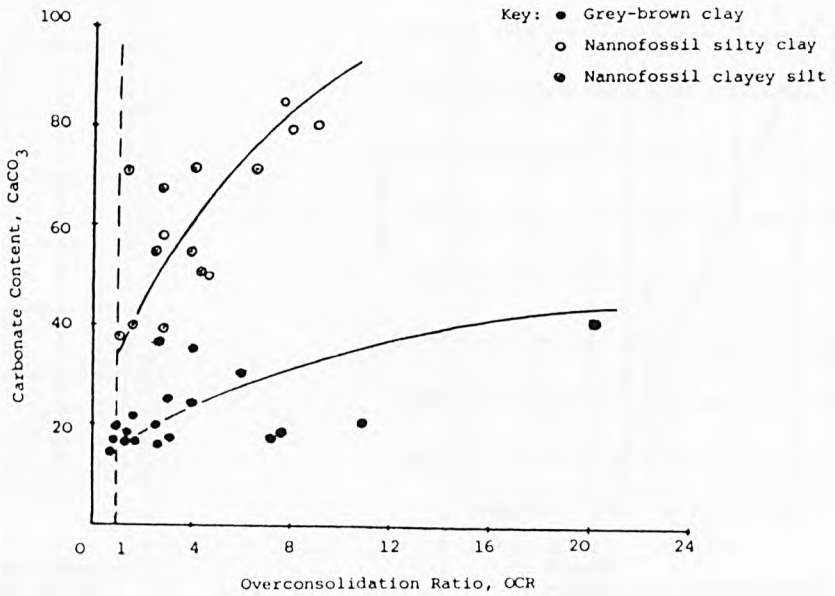

Fig. 4.23 Variation of OCR with Carbonate Content
(Data from Demars, 197)

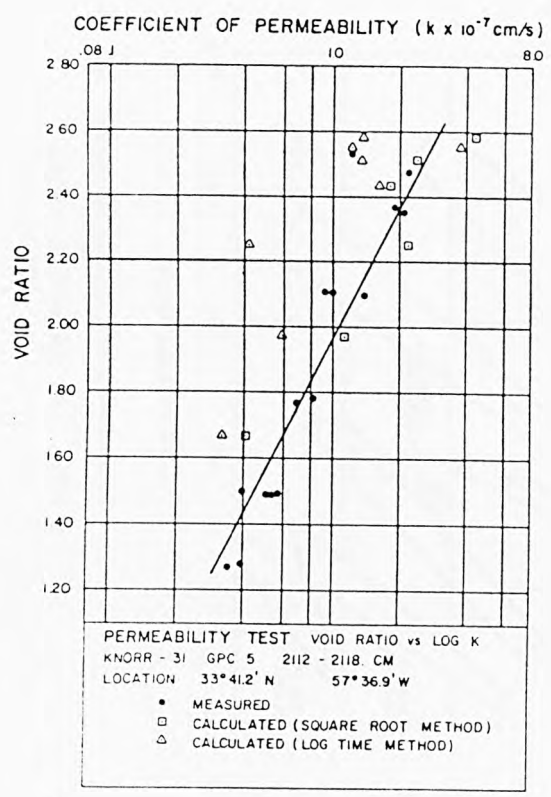

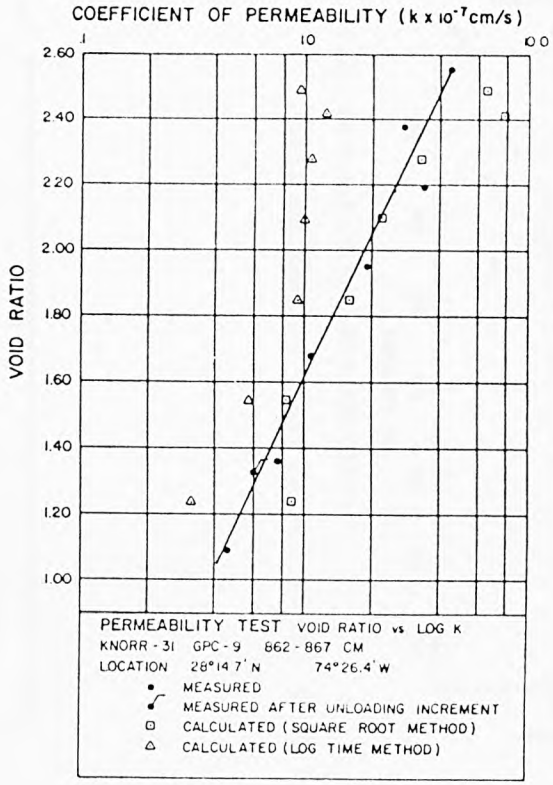

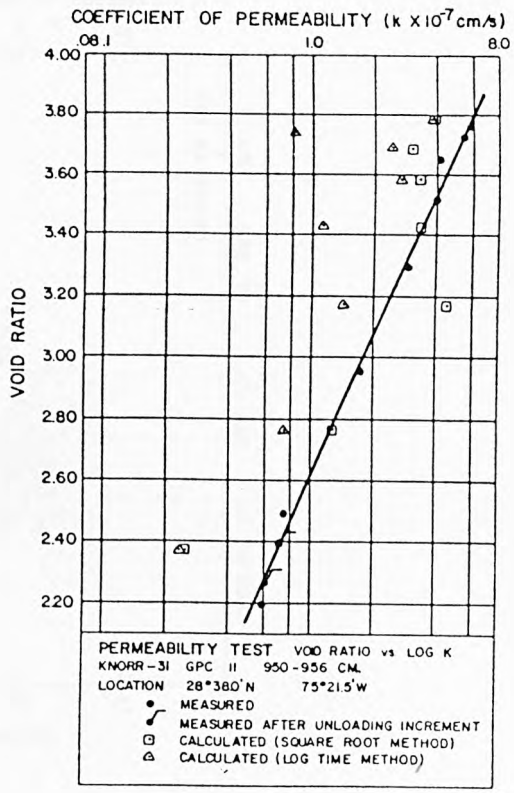

Fig. 4.24 Permeability Test Results (e Vs k), (after Clukey and Silva, 1982)

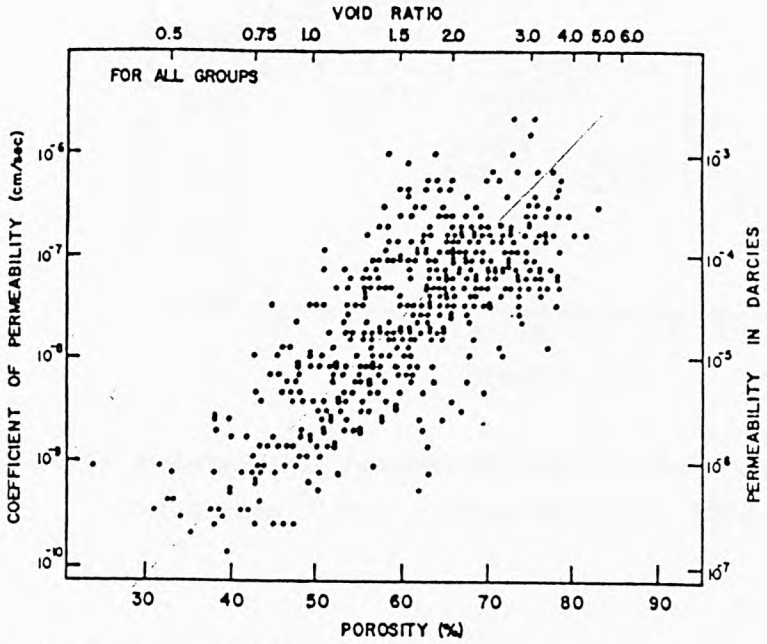

Fig. 4.25 Permeability Test Results

(GUlf of Mexico, after Bryant et al, 1975)

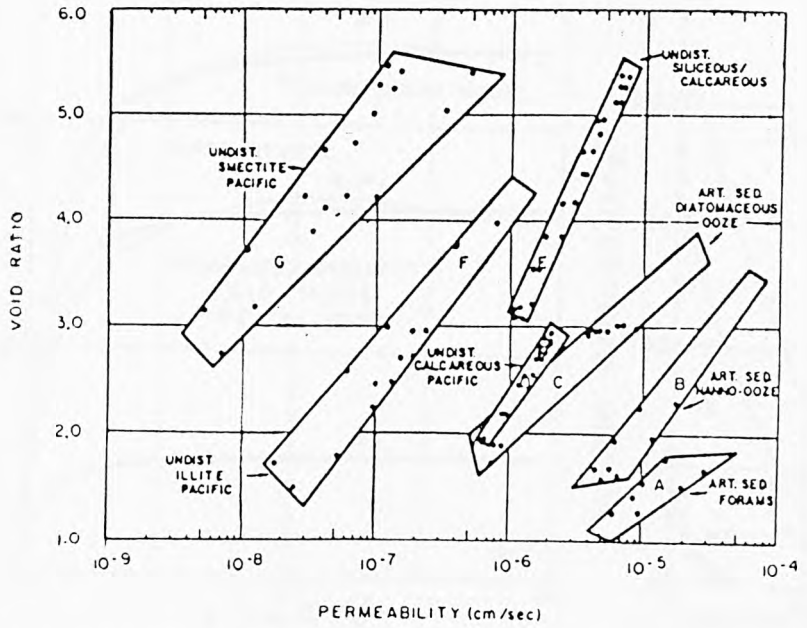

Fig. 4.26 Permeability Test Results

(after Silva et al, 1984)

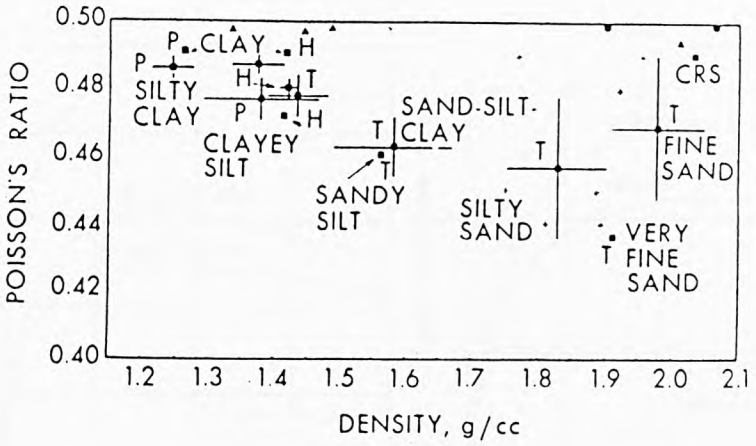

Fig. 4.27 Relationship between Poisson's Ratios and Density of Marine Clays. (after Hamilton, 1971)

Sample	E_u (kPa)	$\frac{E_u}{c_u}$
*1	160	4.0
*4	220	3.8
*5	40	3.3

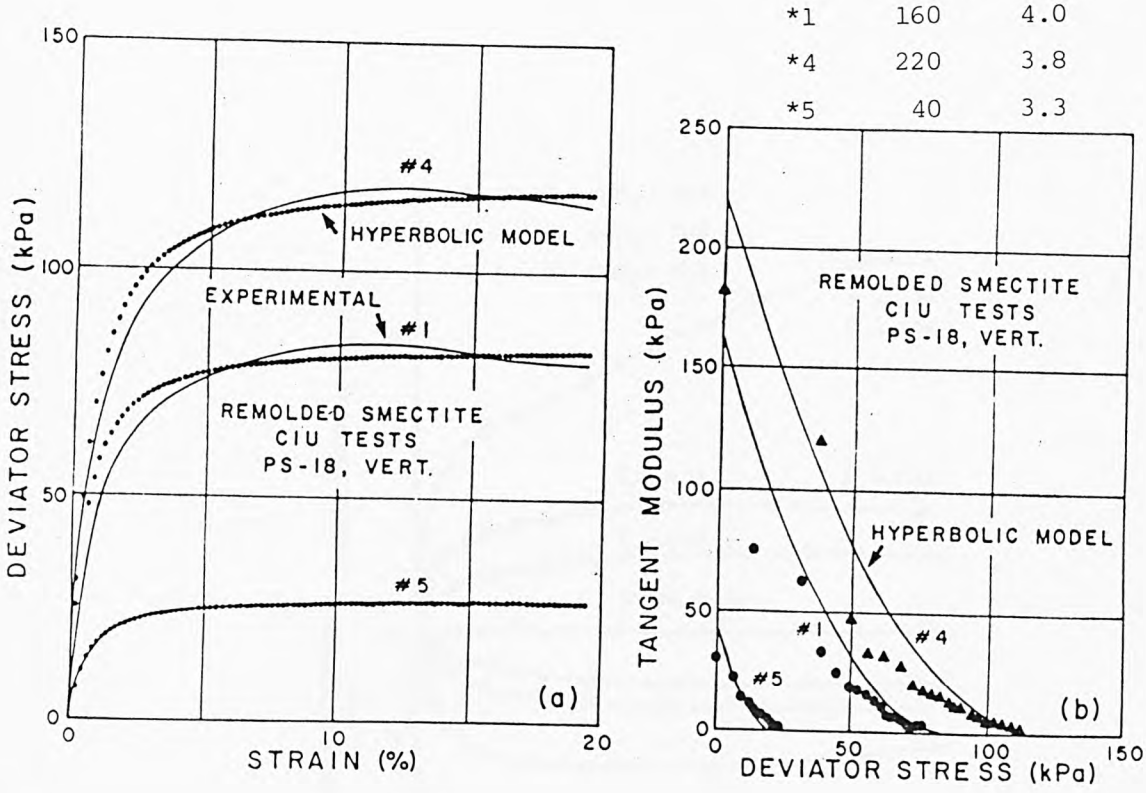

Fig. 4.28 Stress-Strain Response and Tangent Modulus (after Silva et al, 1983)

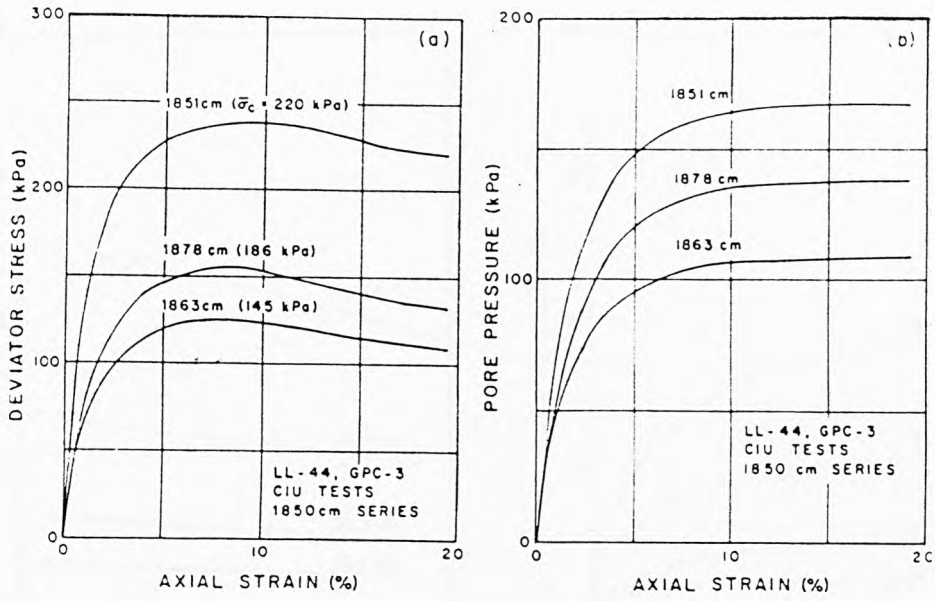

Fig. 4.29 Stress-Strain and Pore Pressure Response of Triaxial Compression Tests. (after Akers, 1980)

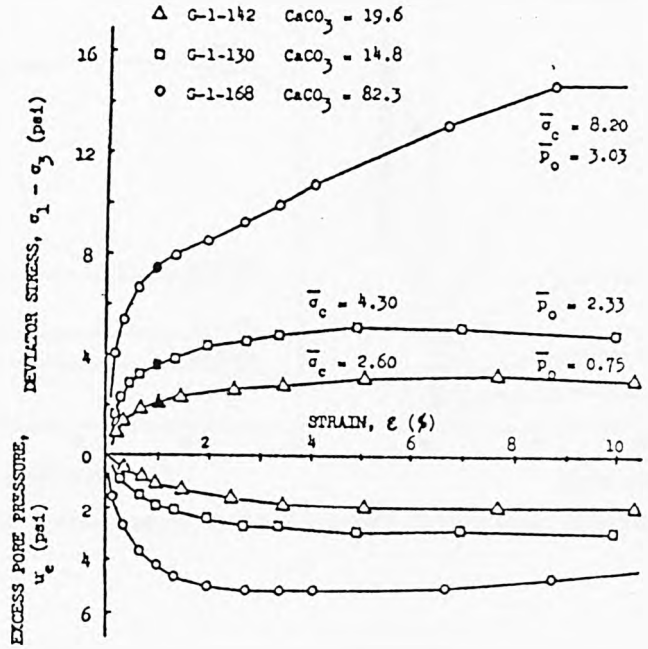

Fig. 4.30 Stress-Strain and Pore Pressure Response of Triaxial Compression Tests. (after Nacci etal, 1975)

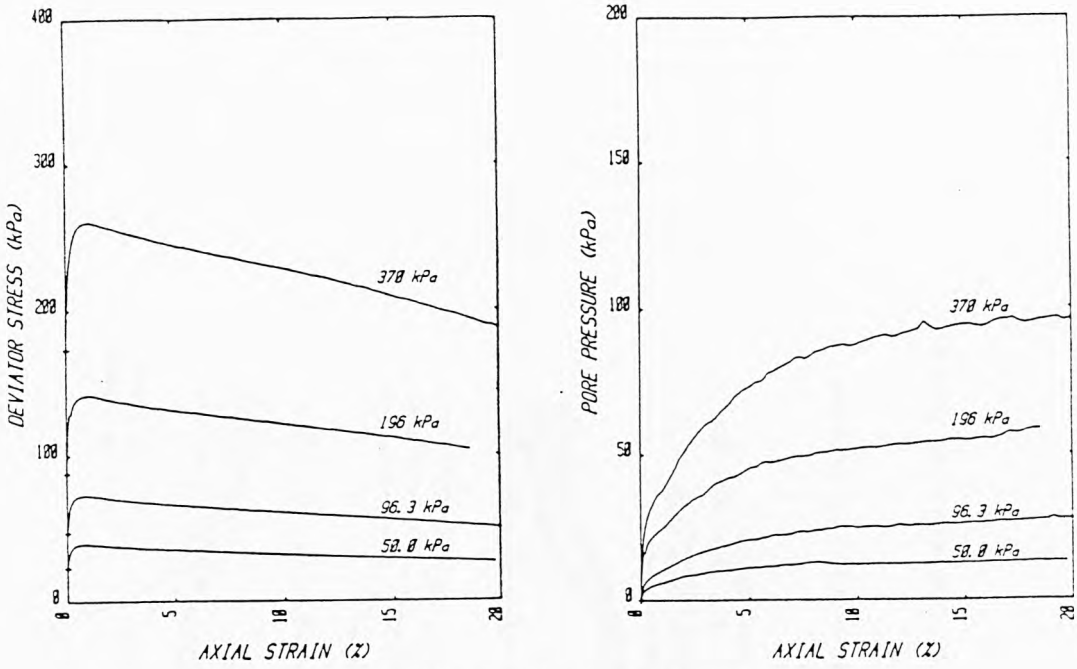

(a) K_o Consolidated Undrained Compression

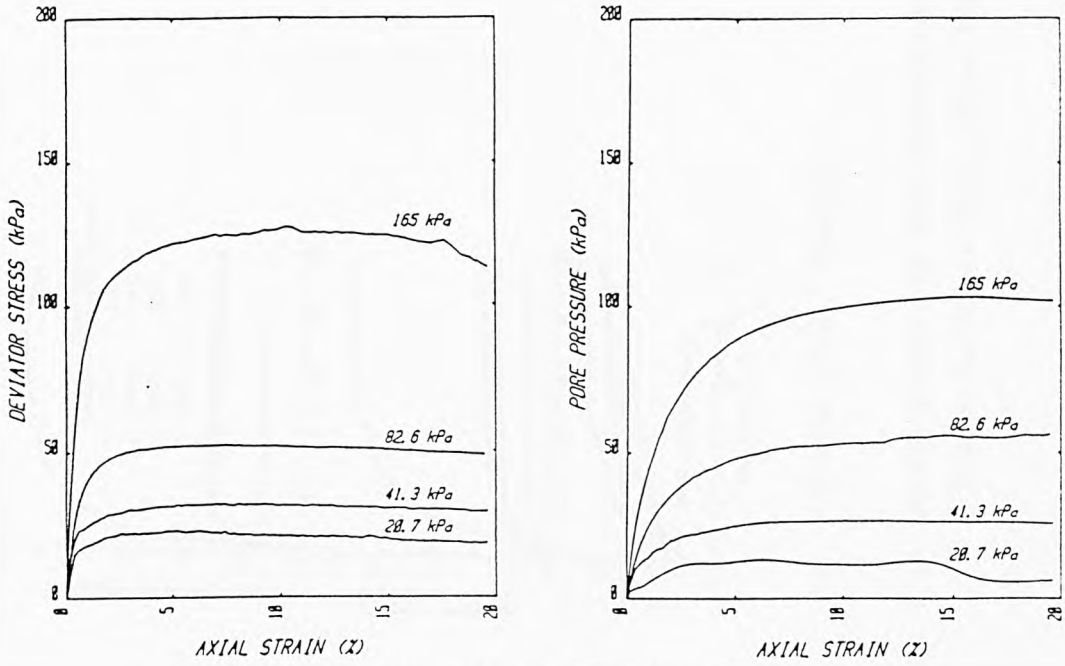

(b) Isotropic Consolidated Undrained Compression

Fig. 4.31 Stress-Strain and Pore Pressure Response of Triaxial Compression Tests. (after Siciliano, 1984)

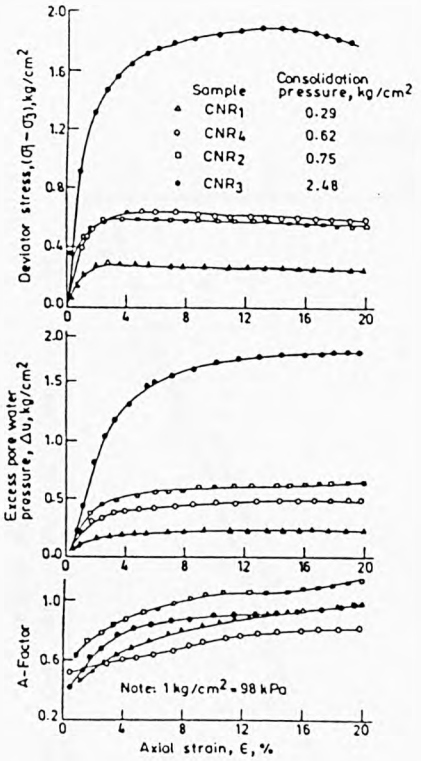

(a) " Undisturbed " Samples

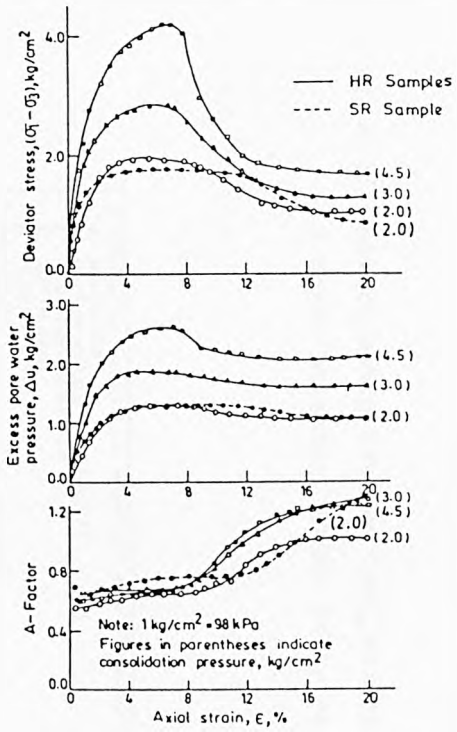

(b) " Remoulded " Samples

Fig. 4.32 Stress-Strain and Pore Pressure Response of Triaxial Compression Tests.
(Indian Carbonate Soil, after Nambiar et al, 1985)

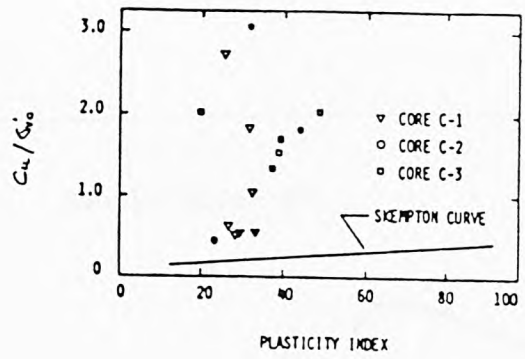

Fig. 4.33 Relationship Between Cu/σ'_{vo} and Plasticity Index
(North Atlantic, after Kelly et al, 1974)

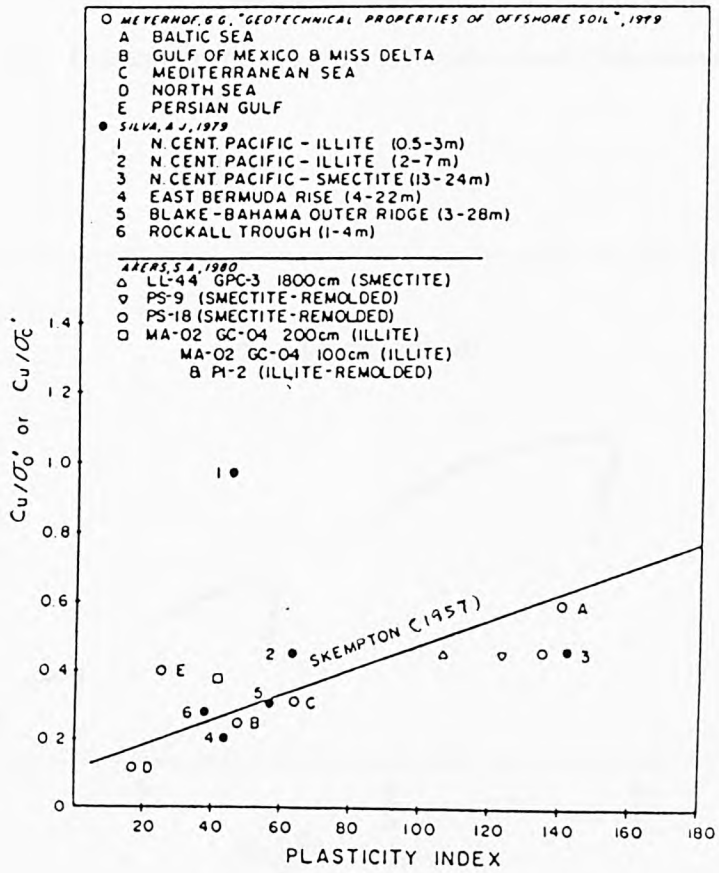

Fig. 4.34 Relationship Between Cu/σ'_v and Plasticity Index
(after Silva, 1979)

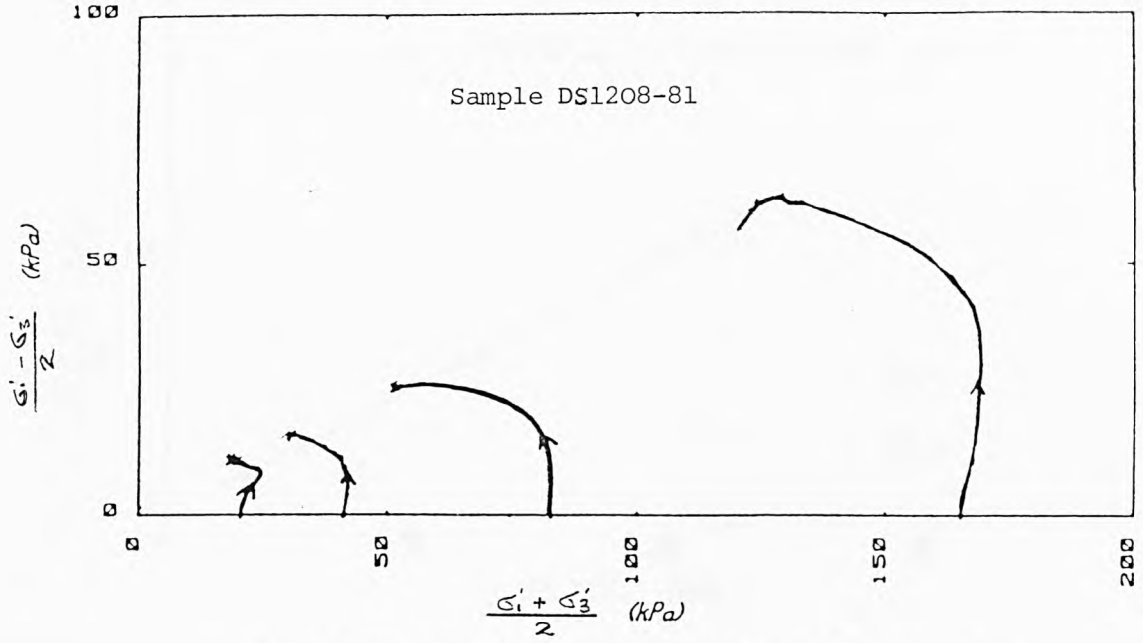

(a) Isotropic Consolidated Undrained Compression

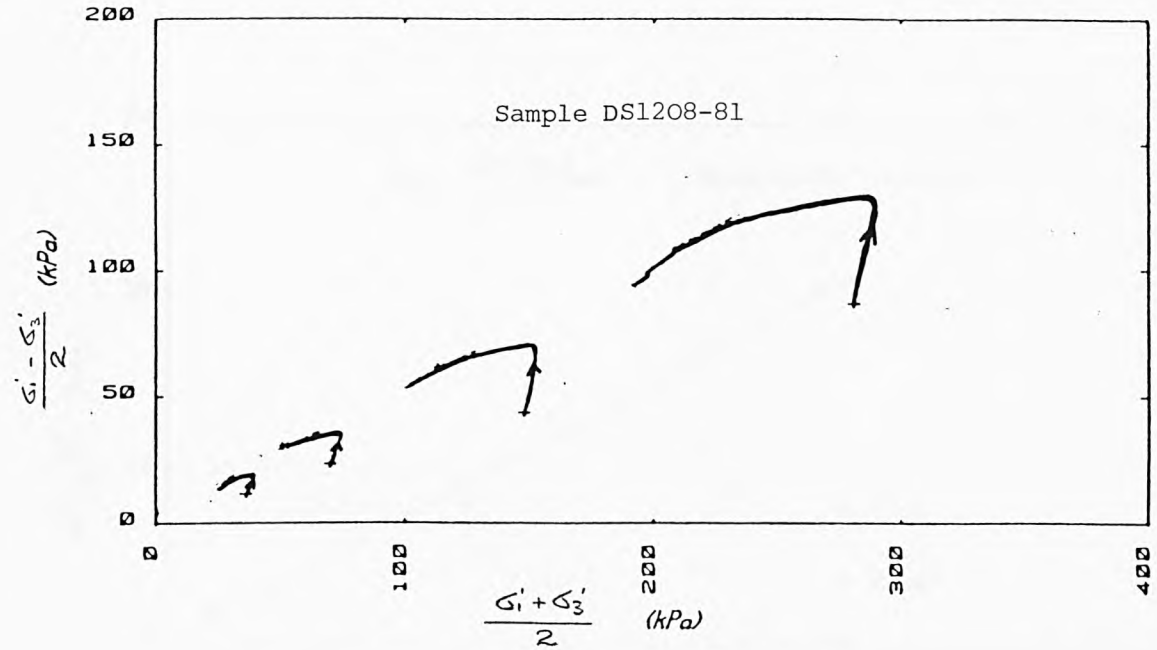

(b) K_o Consolidated Undrained Compression

Fig. 4.35 Stress Paths of Triaxial Compression Tests.
(North Pacific, after Siciliano, 1984)

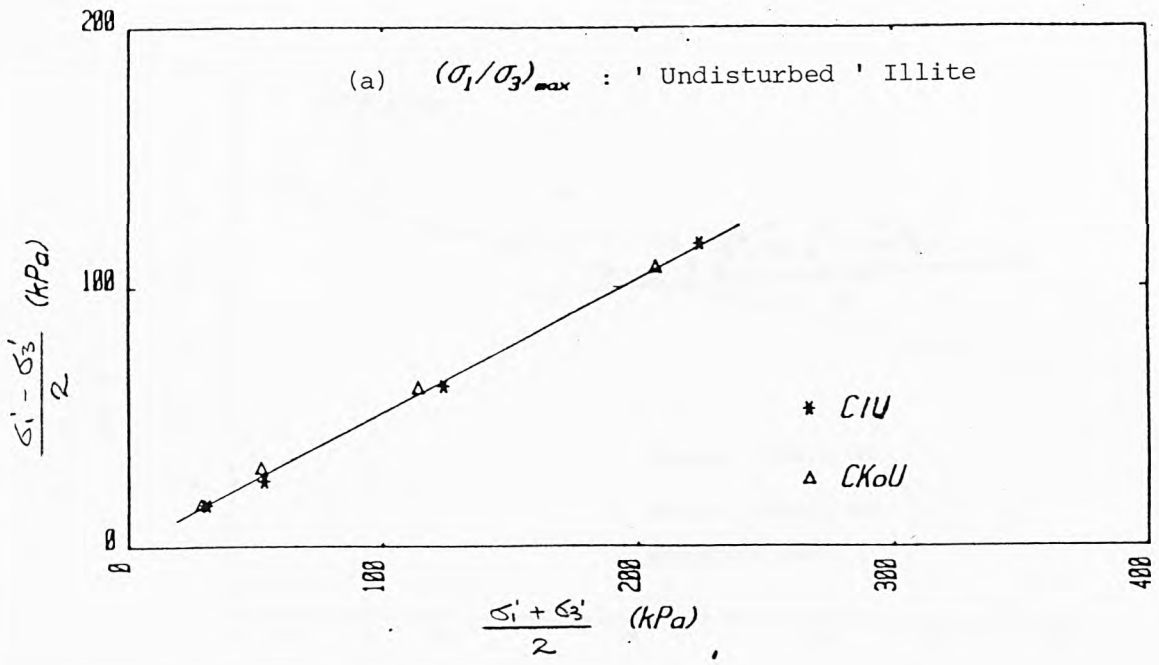

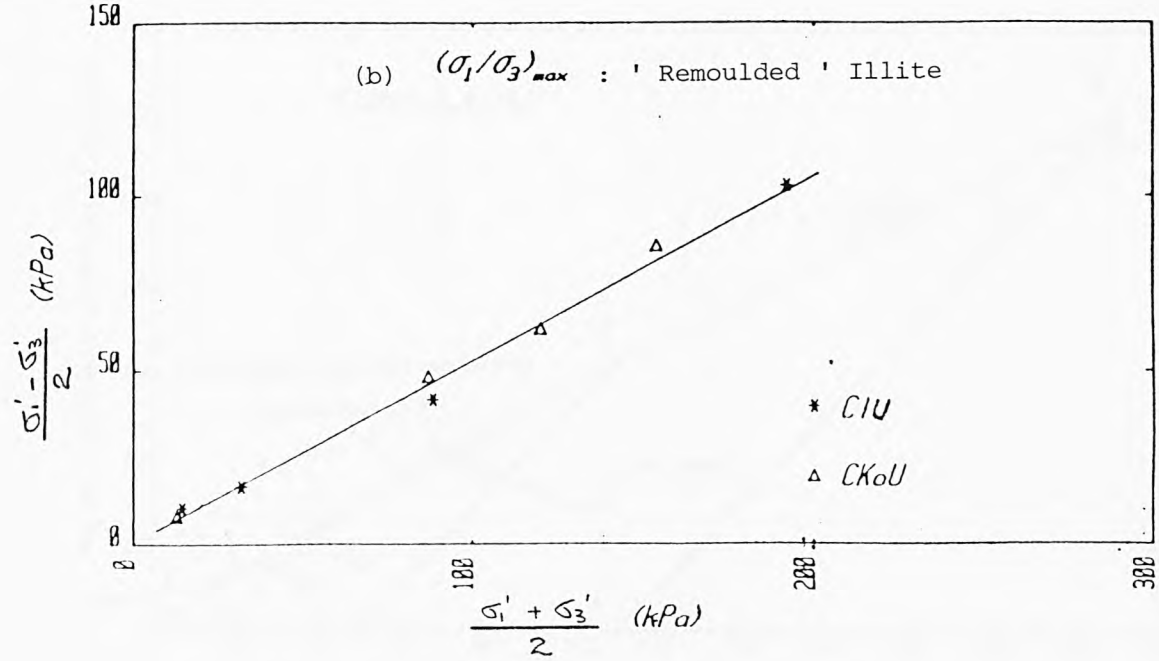

Fig. 4.36 Undrained Triaxial Compression Test Results at Maximum Stress Ratio (after Siciliano, 1984)

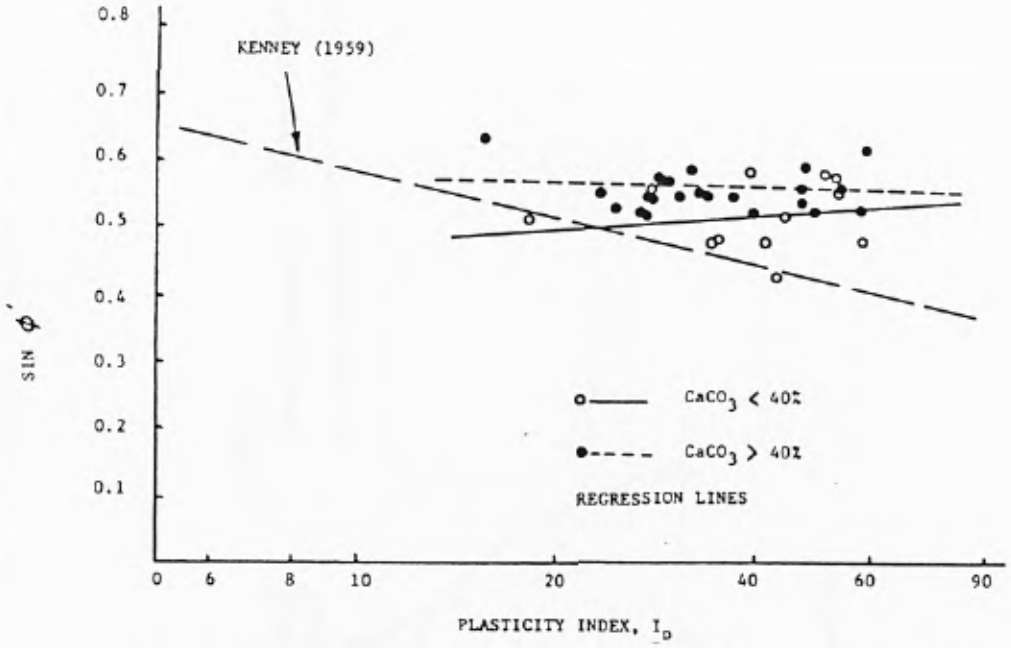

Fig. 4.37 Relationship between SIN ϕ' and Plasticity Index
(North Atlantic, after Demars et al, 1976)

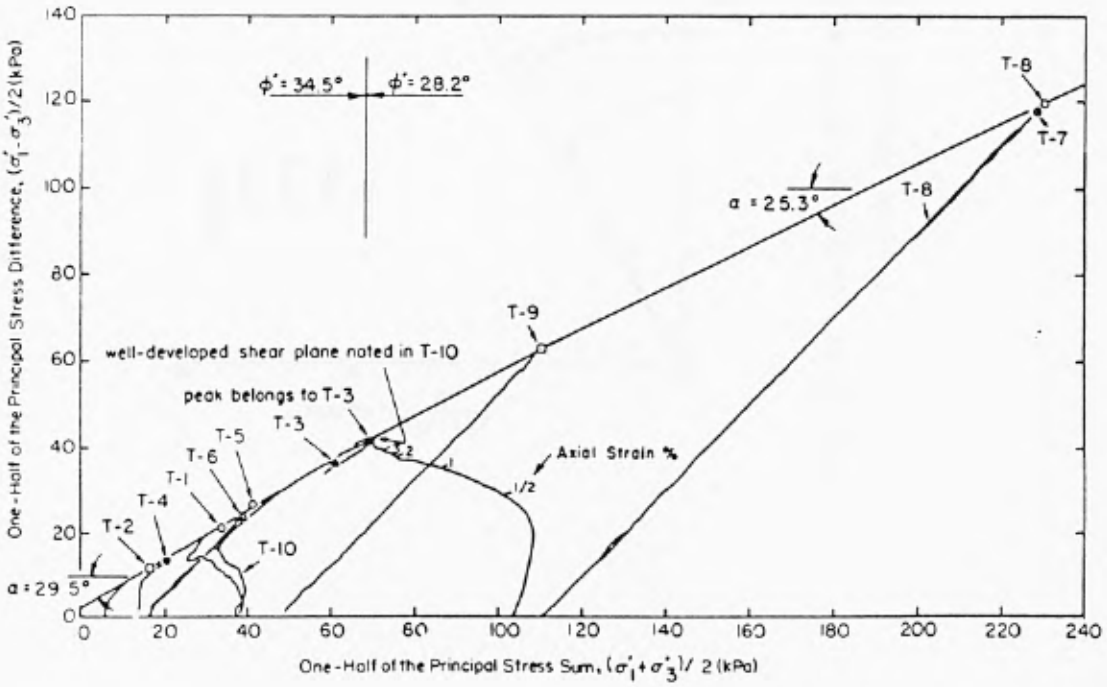

Fig. 4.38 Triaxial Compression Tests Results
(after Valent et al, 1982)

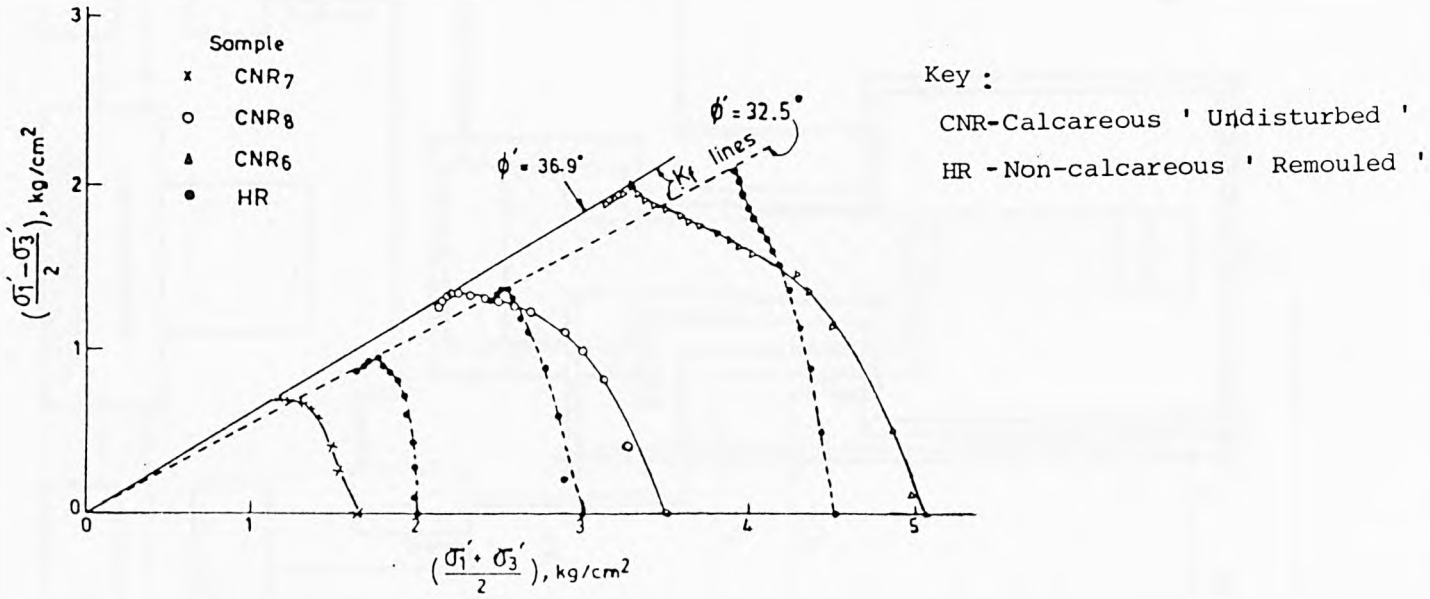

Fig. 4.39 Undrained Triaxial Compression Test Results
(after Nambiar et al, 1985)

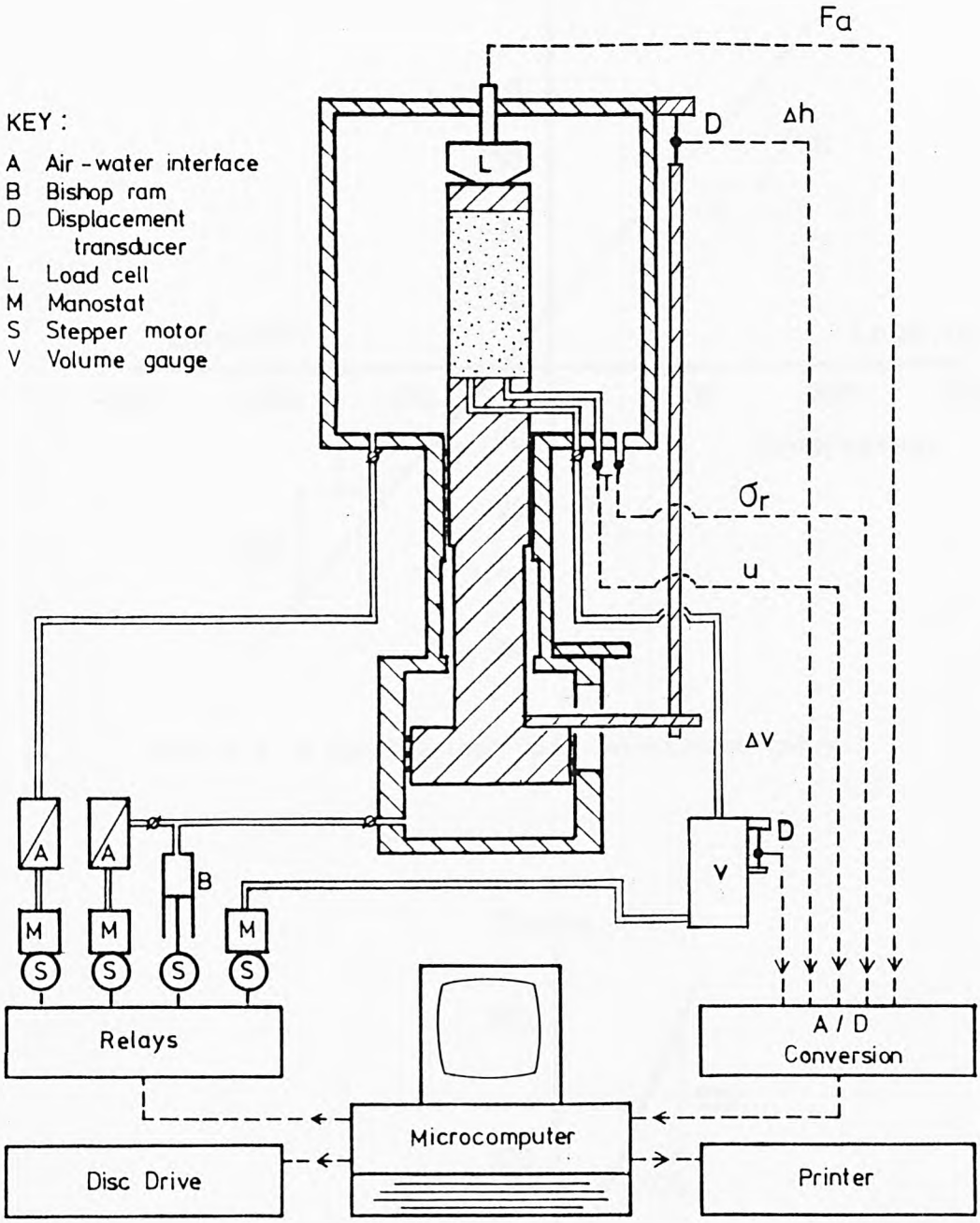

Fig. 6.1 Microcomputer controlled triaxial stress path system.
(after Atkinson et al., 1985 and Clinton 1985)

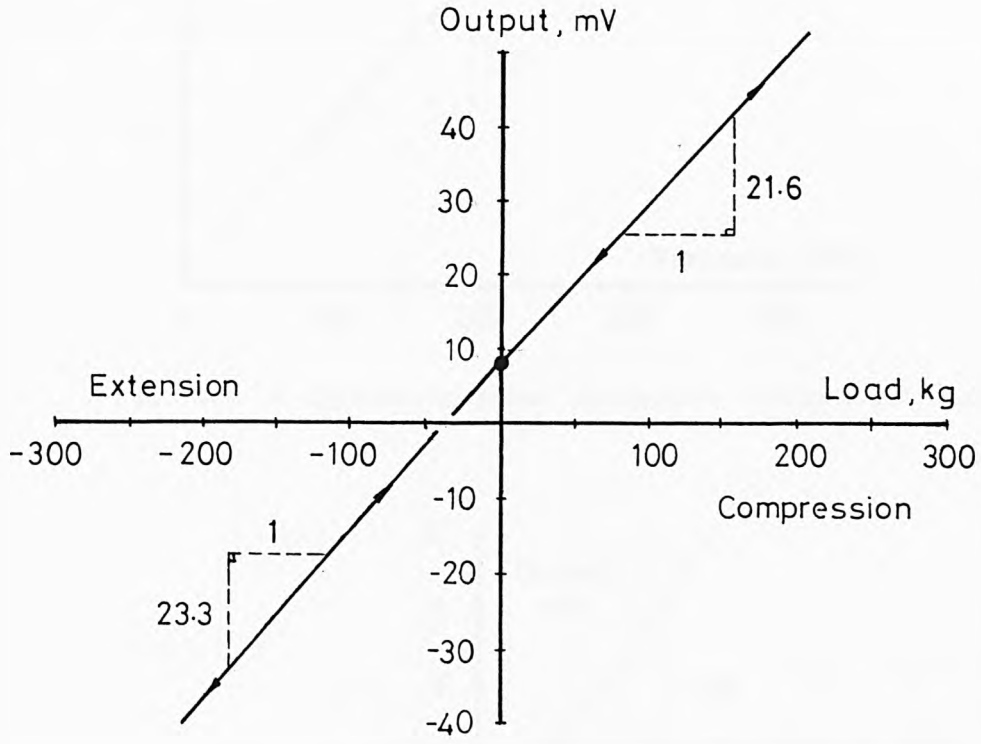

Fig. 6.2 A typical load cell calibration curve.

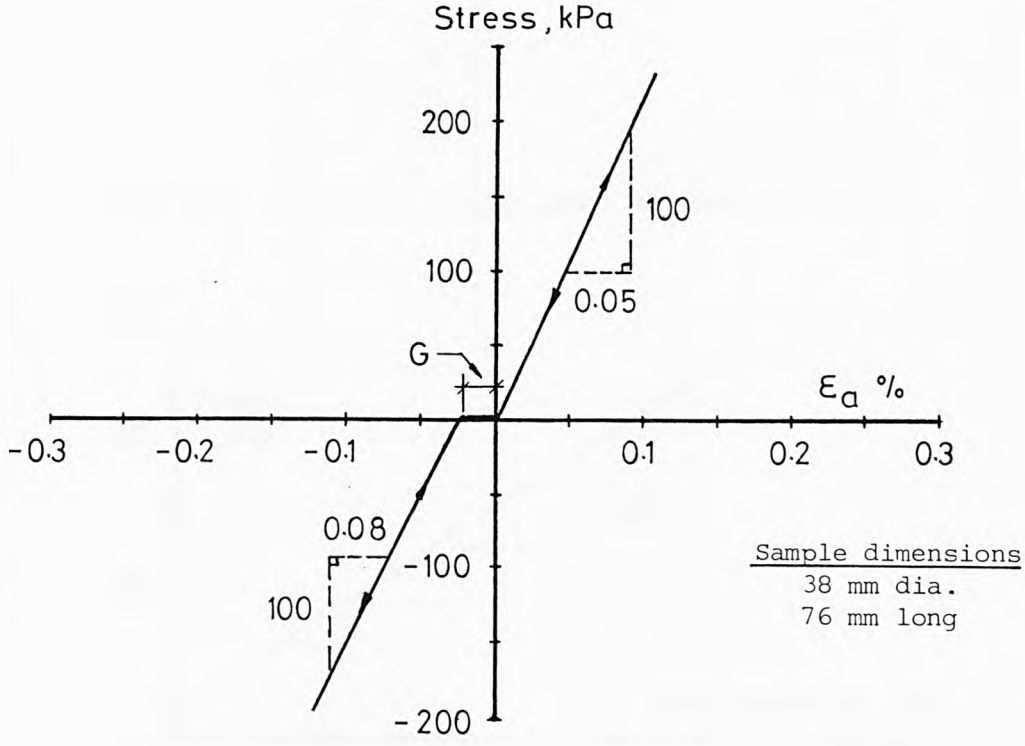

Fig. 6.3 The axial compliance of the load cell.

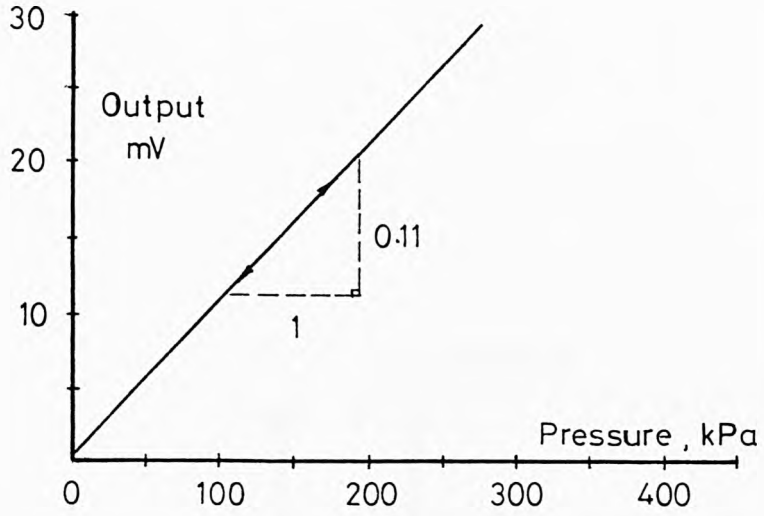

Fig. 6.4 A typical pressure transducer calibration curve.

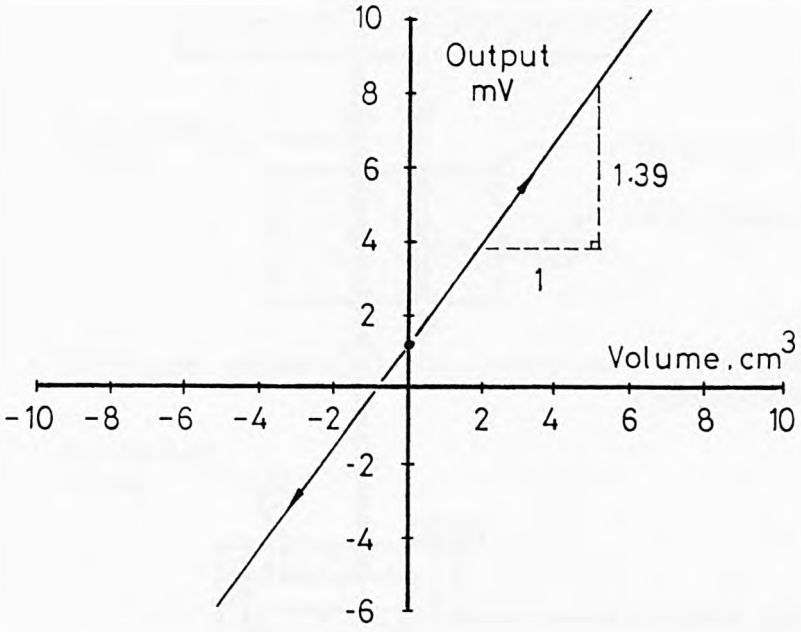

Fig. 6.5 A typical volume gauge calibration curve.

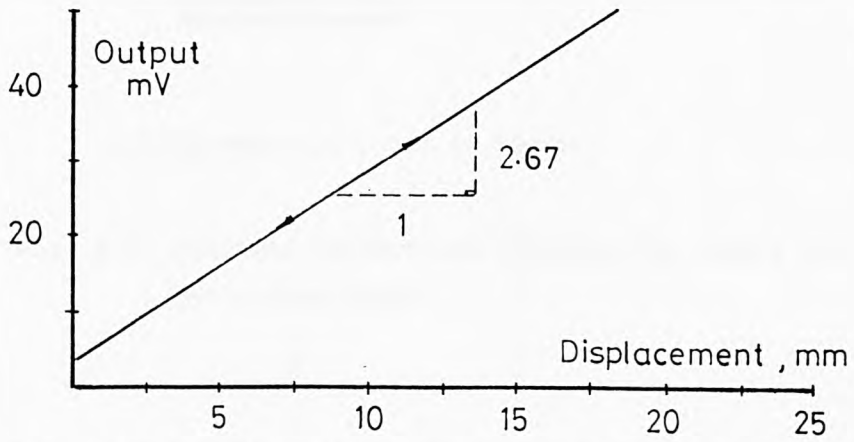

Fig. 6.6 A typical displacement transducer calibration curve.

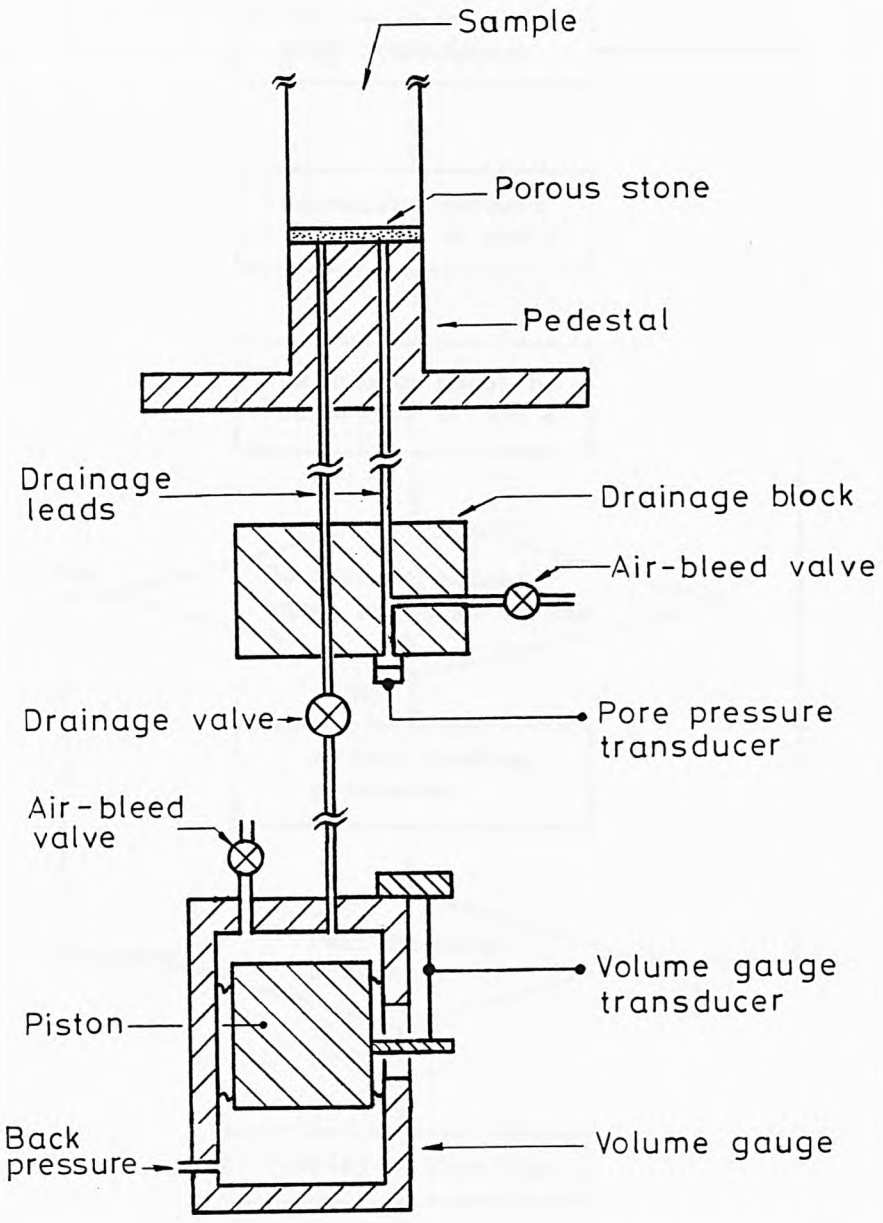

(Diagrammatric , not to scale)

Fig. 6.7 Drainage connections between the sample and the volume gauge.

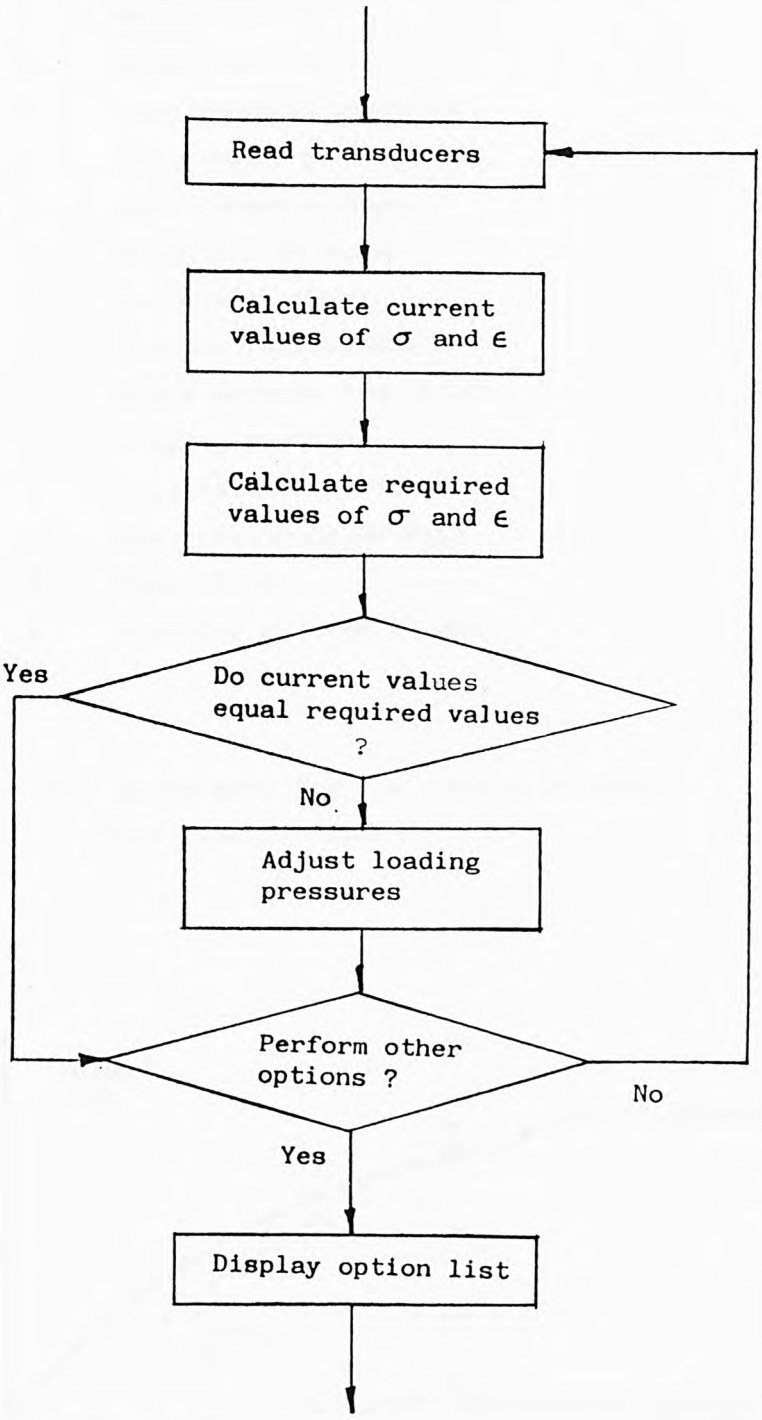

Fig. 6.8 The main control loop program : Flow Chart.

(after Atkinson et al., 1985)

Option	
A	Return control
B	Enter test data
C	Zero pressure readings
D	Set initial pressures
E	Zero strain readings
F	Start a test stage
G	End a test stage
H	Display current state
I	Print records from store
J	Display records
K	Calibrate transducers
L	Enter calibration data
M	Time check
N	Transfer records to disc

Fig. 6.9 The option menu for the control program.
(after Clinton, 1985)

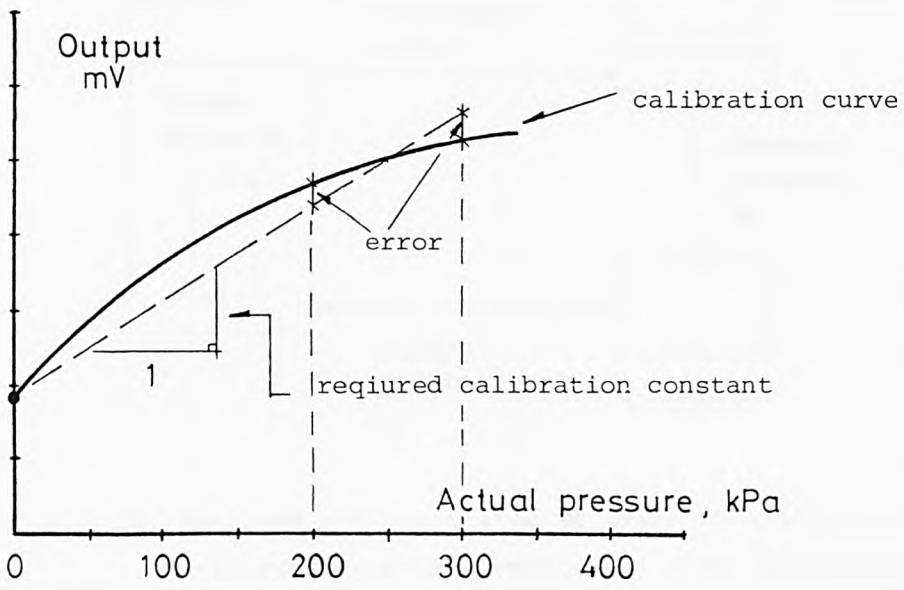

Fig. 6.10 The choice of a calibration constant.

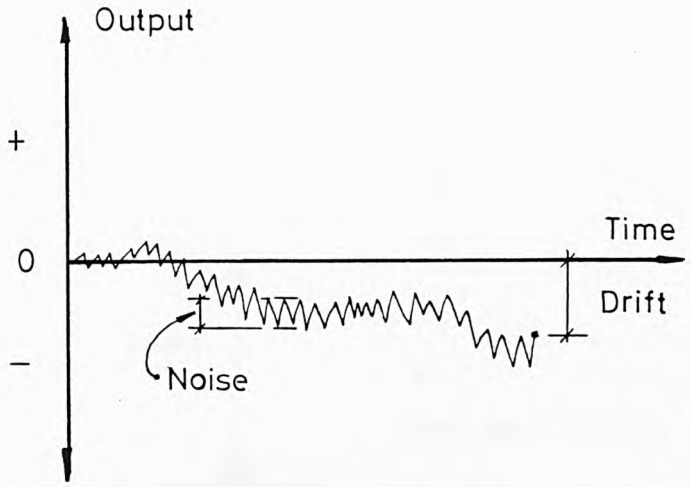

Fig. 6.11 Noise and drift of the measuring device.

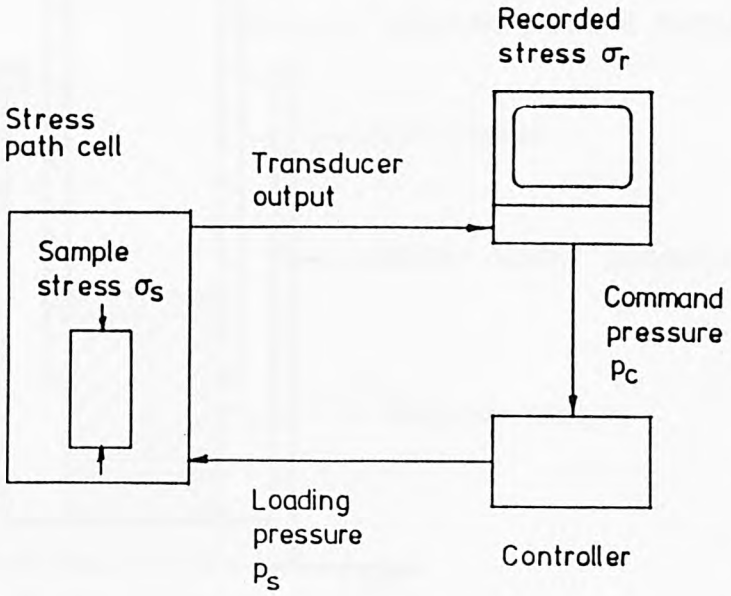

Fig. 6.12 Recorded and controlled stresses in a stress path cell with feed-back control. (after Atkinson et al., 1985)

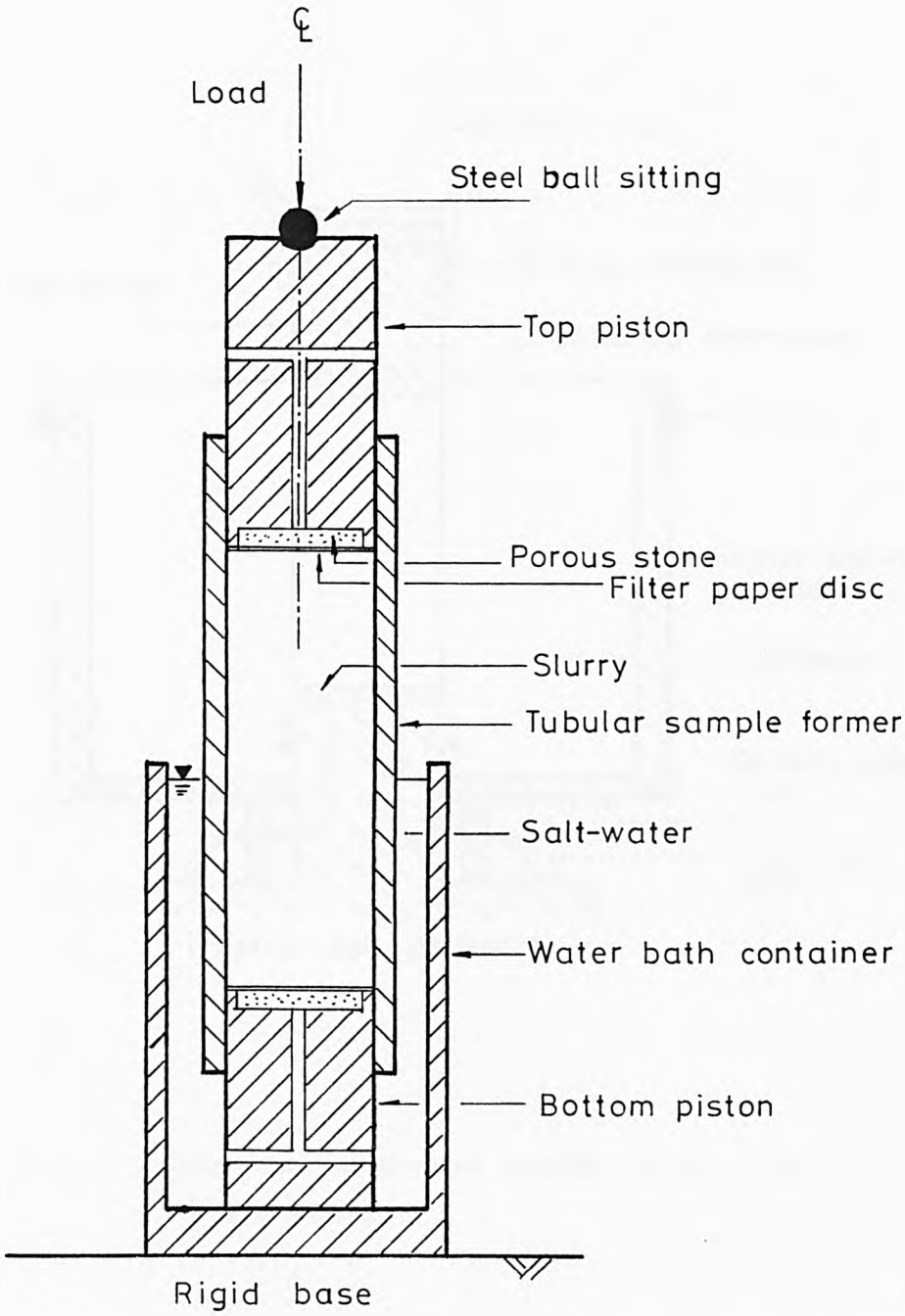

Fig. 7.1 The floating ring type oedometer for preparing reconstituted triaxial specimen.

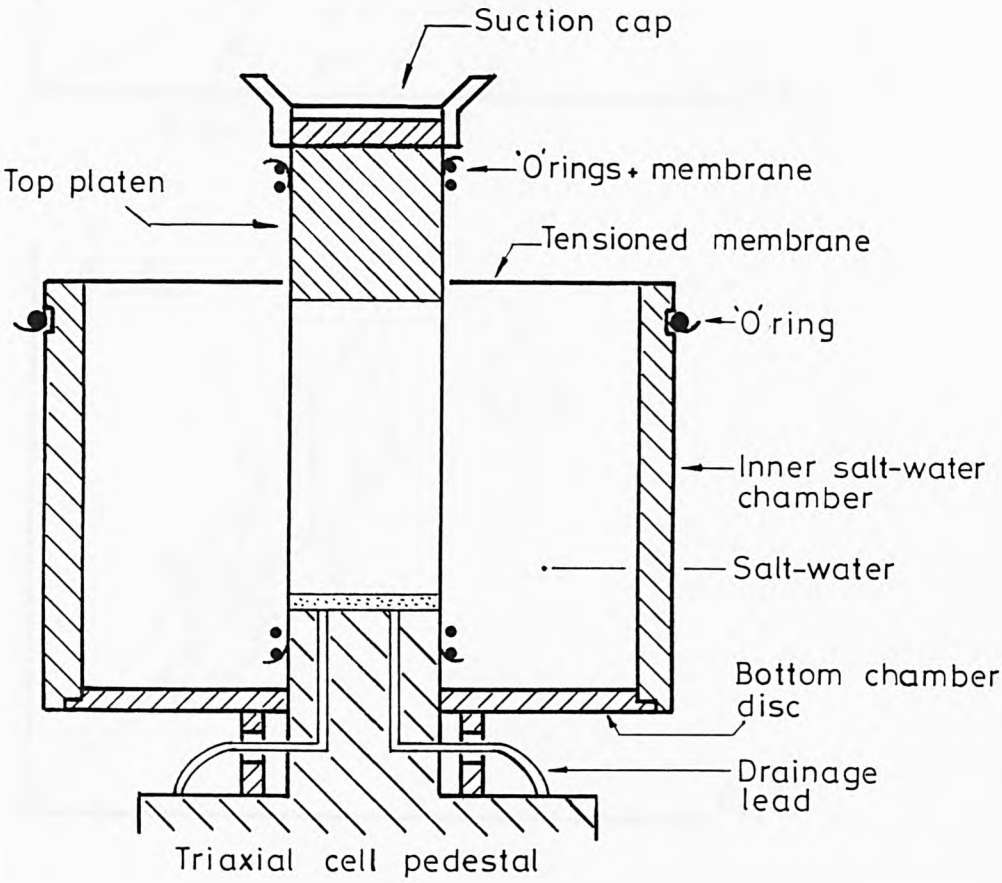

Fig. 7.2 The inner salt-water chamber on the triaxial cell pedestal.

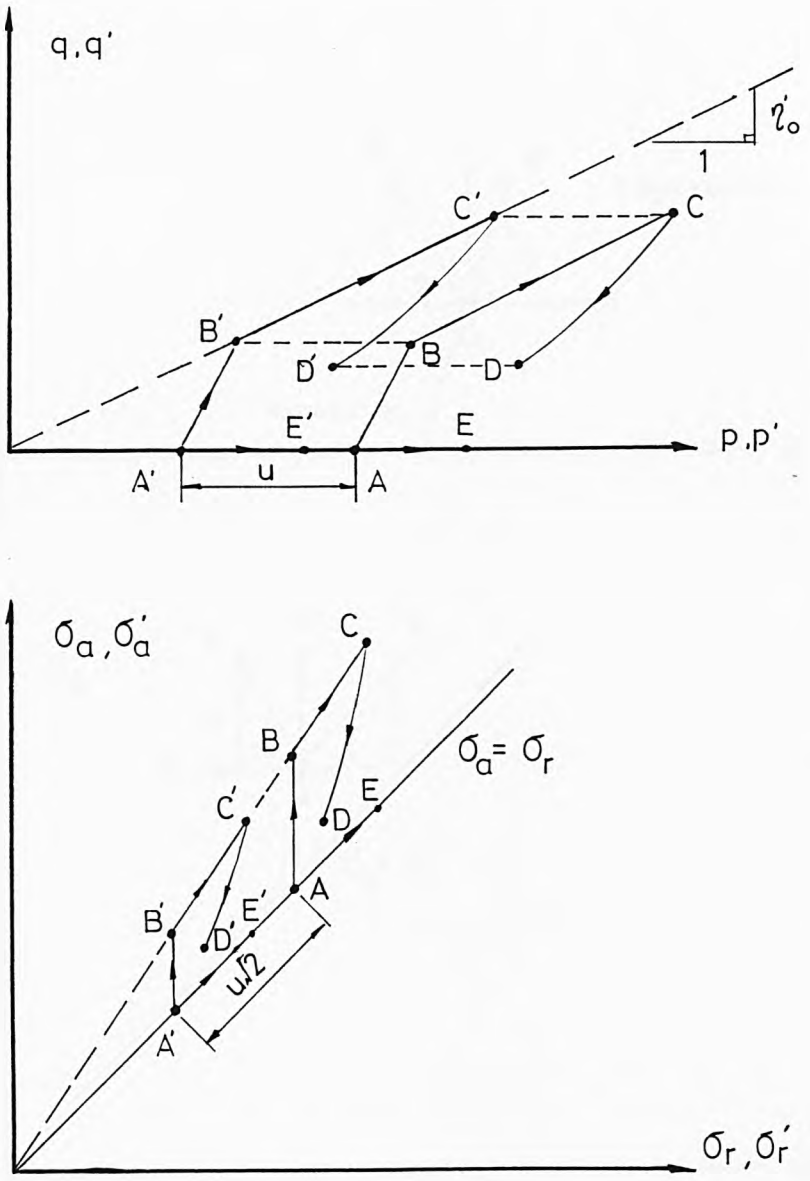

Key : A' , initial isotropic stress state
A'-E' , isotropic compression
A'-B' , anisotropic compression
B'-C' , K_o compression
C'-D' , K_o swelling

Fig. 7.3 Stress paths for isotropic and anisotropic compression.

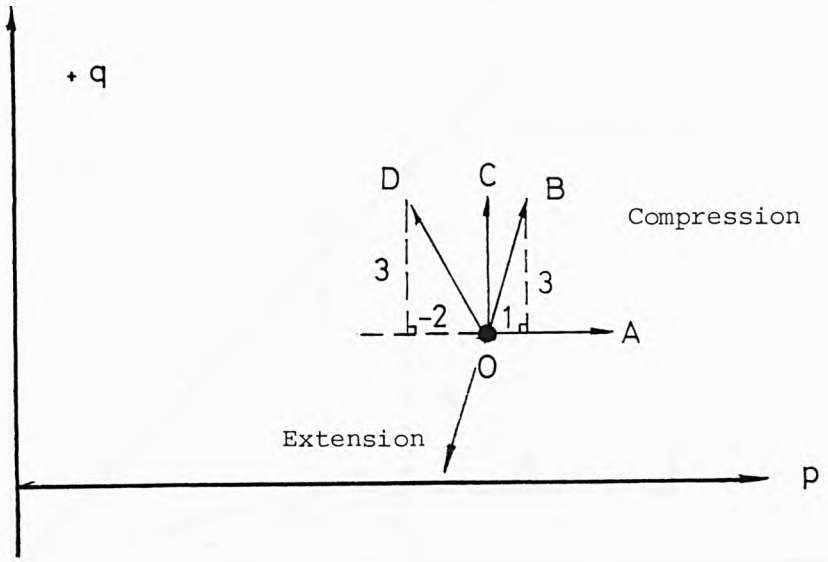

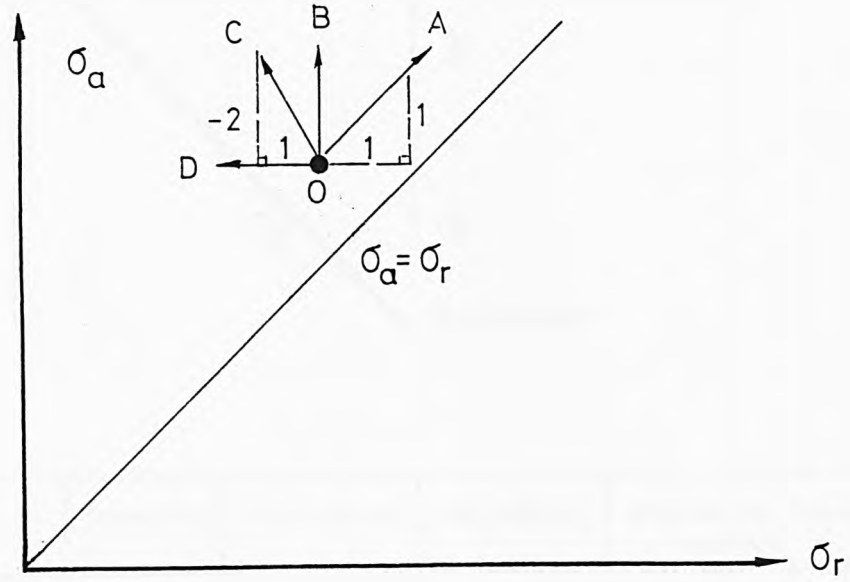

Path	Test	$\frac{\dot{q}}{\dot{p}}$	$\frac{\dot{\sigma}_a}{\dot{\sigma}_r}$
OA	Const. q'	0	1
OB	Drained	3	∞
OC	Const. p'	∞	-2
OD	Unloadung	-3/2	0

Fig. 7.4 Examples of the directions of stress paths in relation to the principal stress increments.

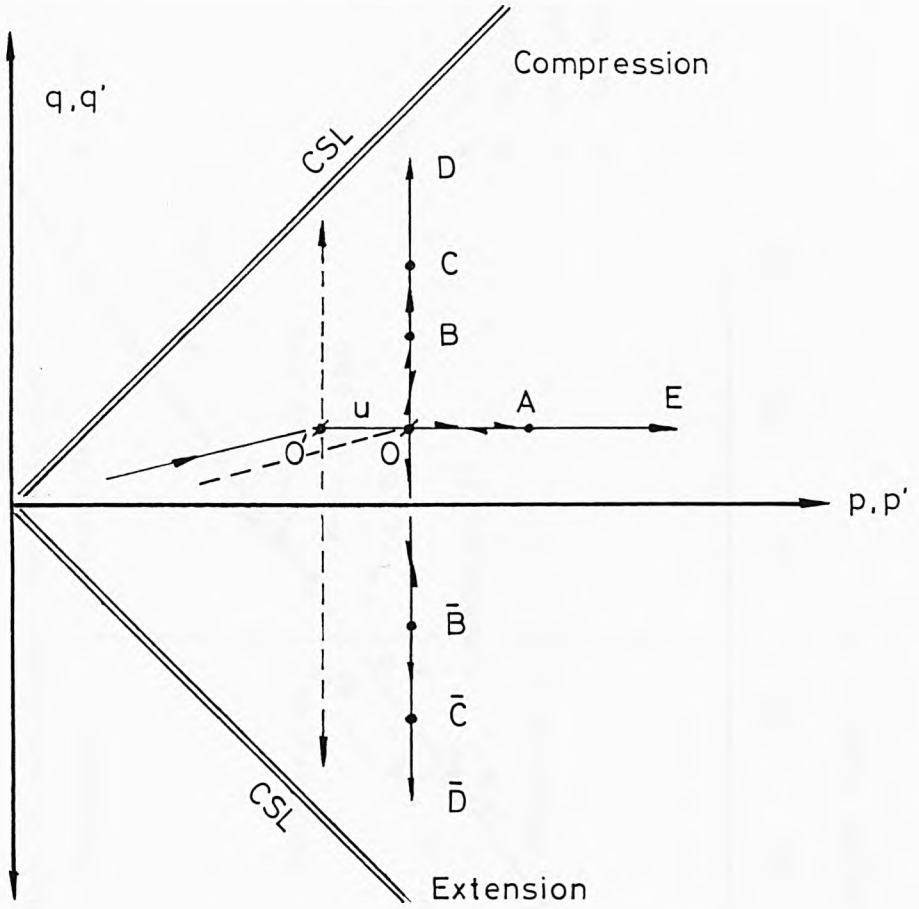

Test	Loading	Unloading	Reloading	Stress to strain control	Failure
Const. q	OA	AO	OAE	-	-
Const. p (comp.)	OB	BO	OBC	C	CD
Const. p (ext.)	$\bar{OB}$	$\bar{BO}$	$\bar{\bar{OBC}}$	$\bar{C}$	$\bar{\bar{CD}}$

Fig. 7.5 Stress paths for constant p and q loading and unloading tests.

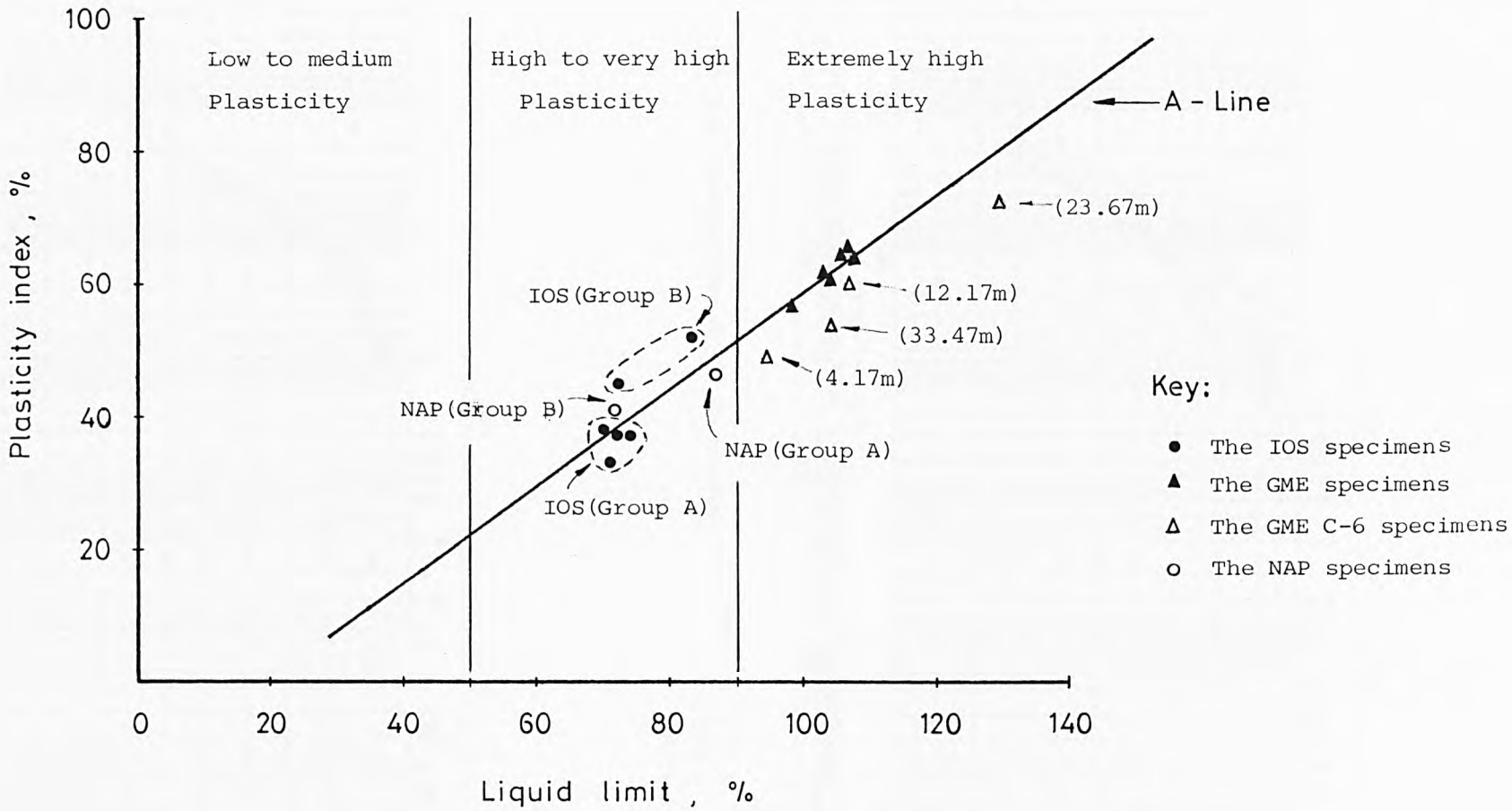

Fig. 8.1 Plasticity chart.

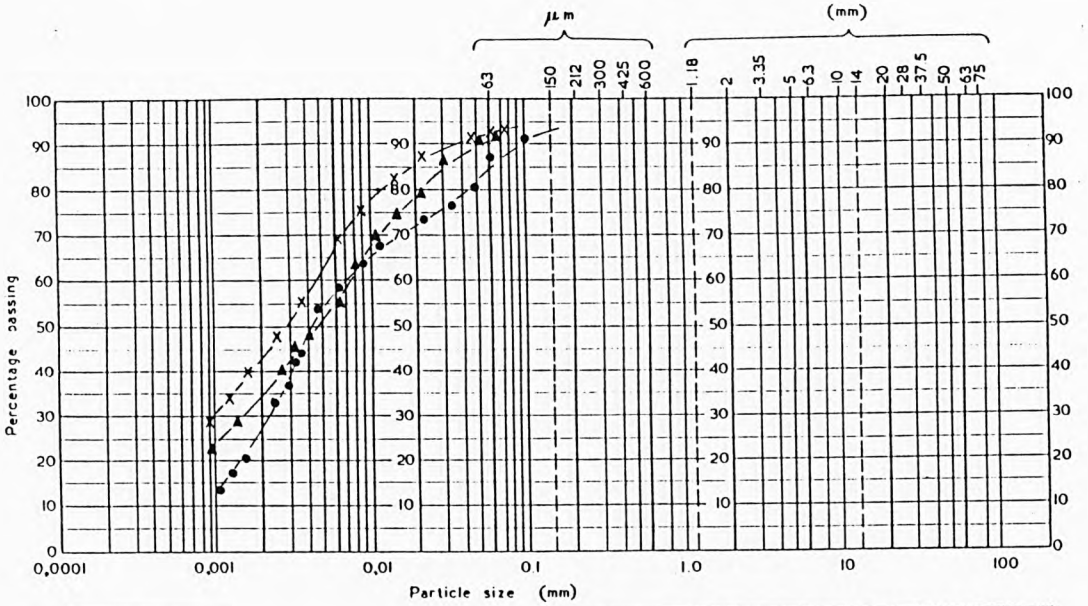

Group

Key: • IOS-1 A
▲ IOS-3 B
x IOS-4 B

Fig. 8.2a Grading curves for the IOS specimens.

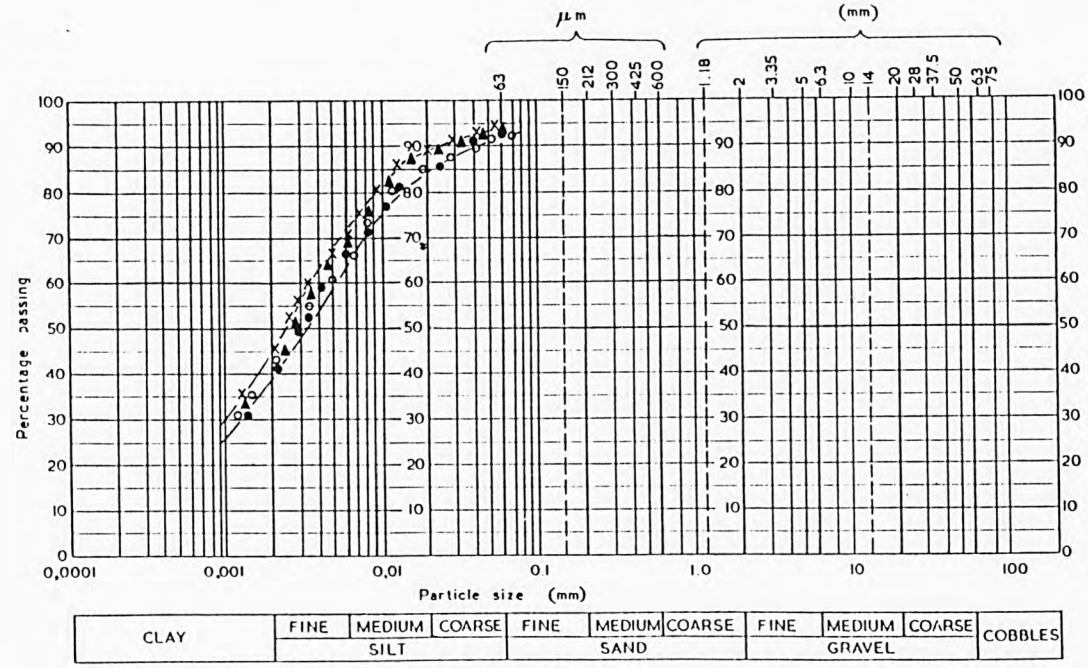

Key: ▲ GT-1 } Core D11172/6
• GT-2 }
x GT-4 } Core D11174/10
o GT-5 }

Fig. 8.2b Grading curves for the GME specimens.

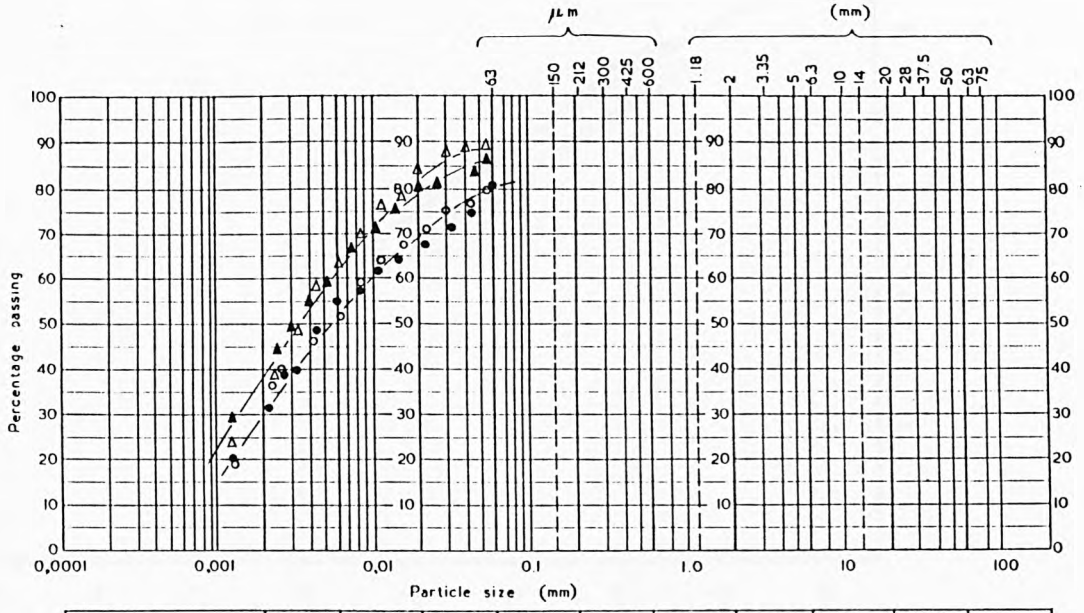

Key: Depth

- • 6-11C (23.67m)
- ○ 6-22A (12.17m)
- △ 6-30A (4.17m)
- ▲ 6-1B (33.47m)

Fig. 8.2c Grading curves for the GME C-6 specimens.

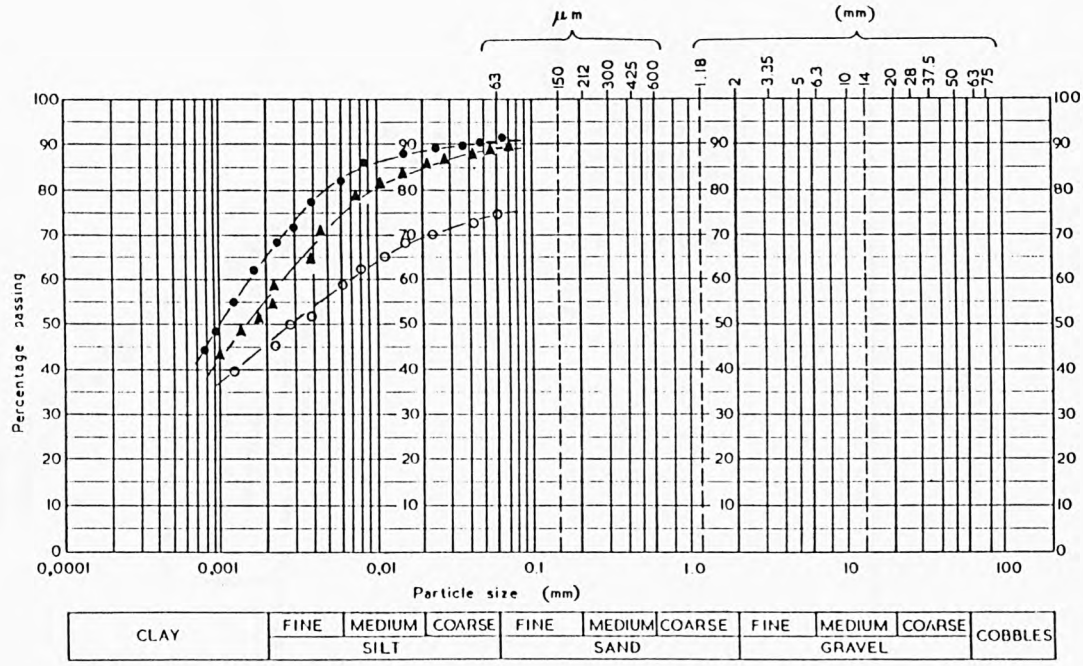

Key:

- • NT-1 } Group B
- ▲ NT-3
- ○ NT-10 Group A

Fig. 8.2d Grading curves for the NAP specimens.

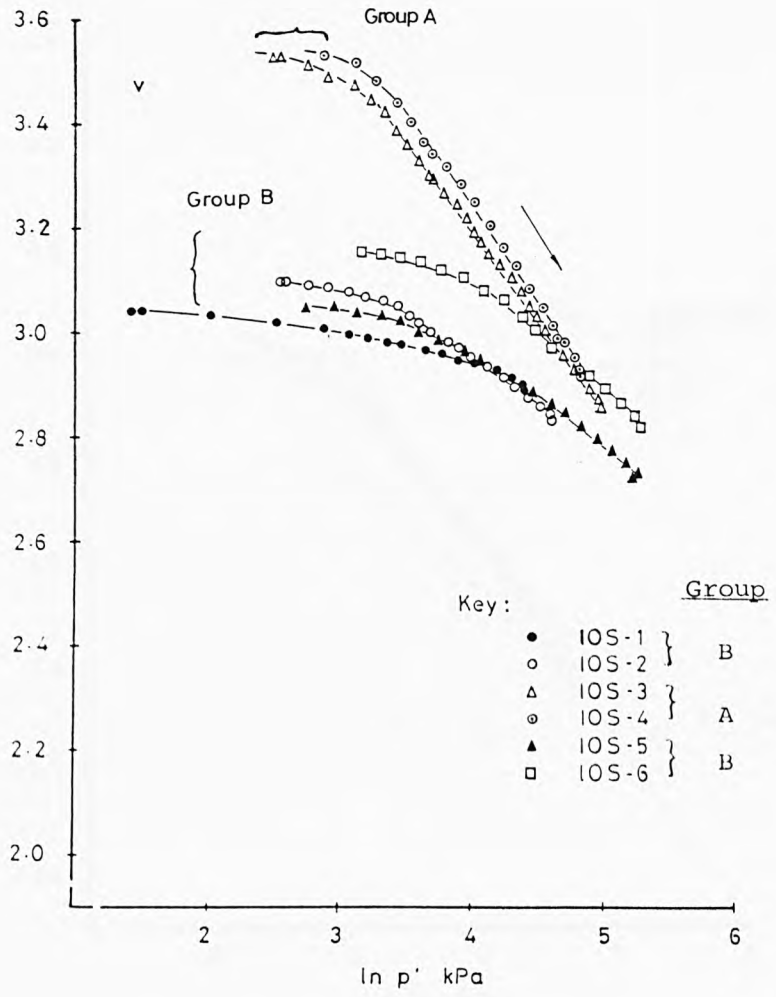

Fig. 8.3 K_o compression of the IOS tubed specimens.

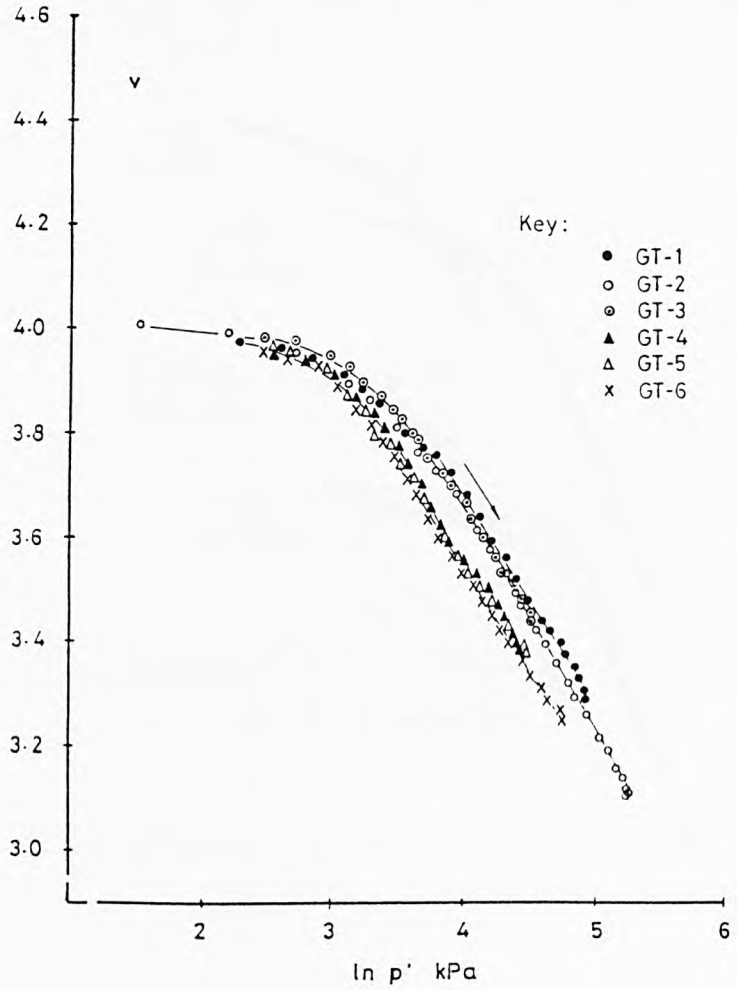

Fig. 8.4a K_o compression of the GME tubed specimens.

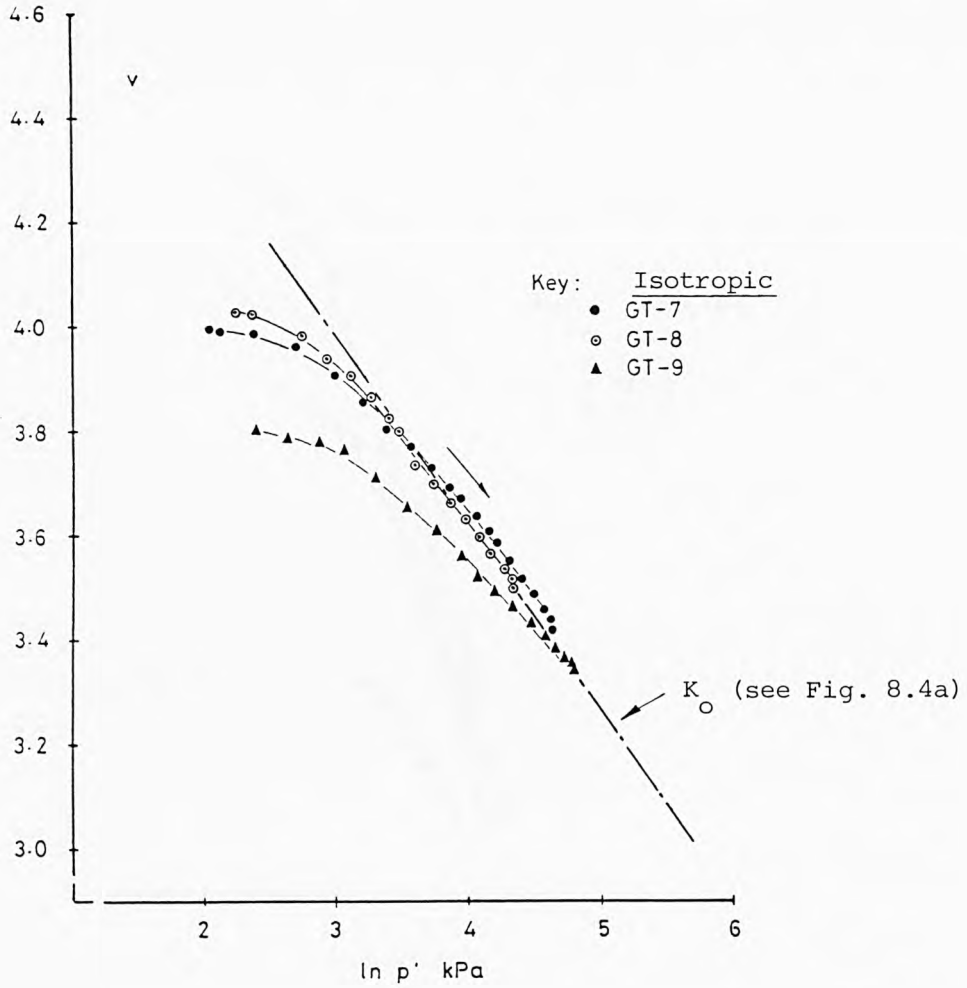

Fig. 8.4b Isotropic compression of the GME tubed specimens.

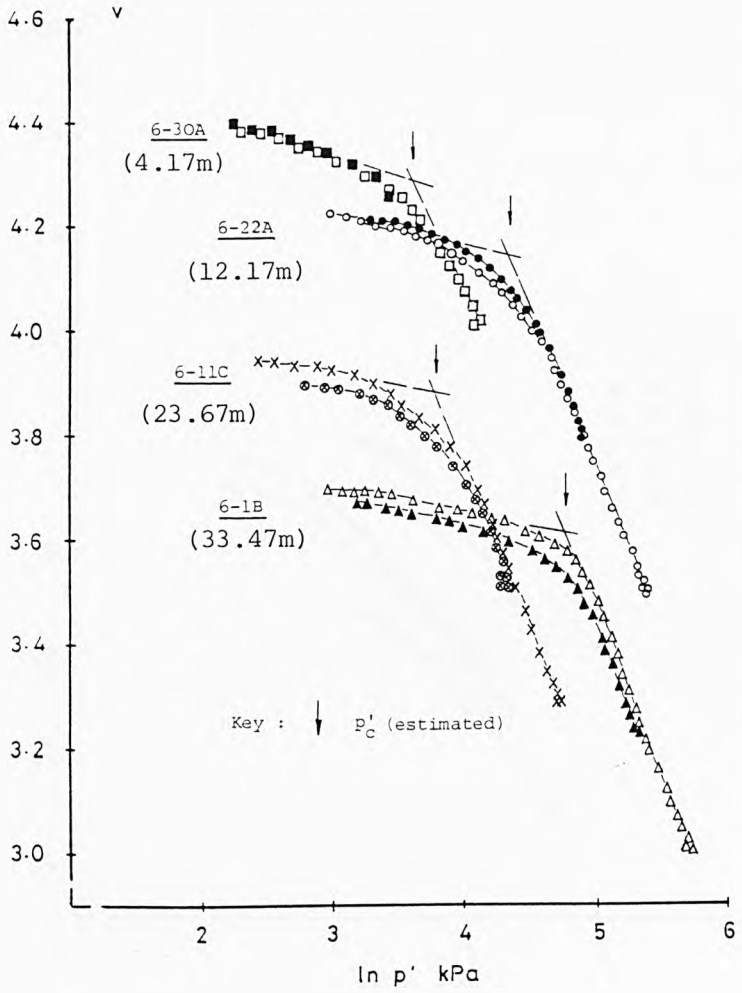

Fig. 8.5 K_o compression of the GME-C6 tubed specimens.

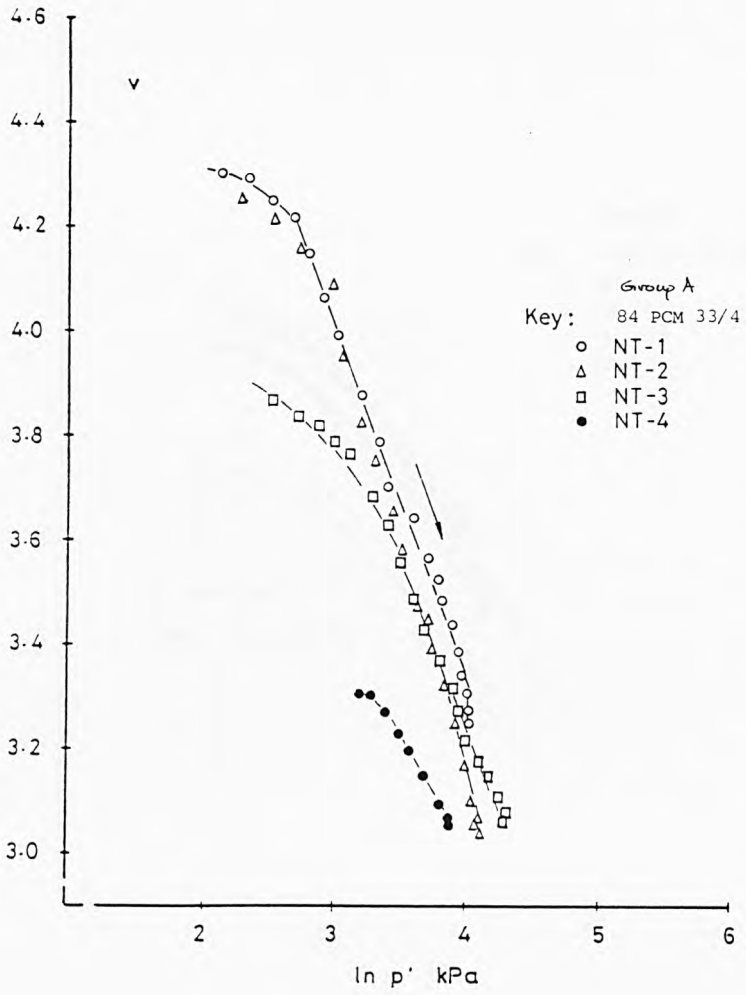

Fig. 8.6a K_o compression of the NAP tubed specimens.

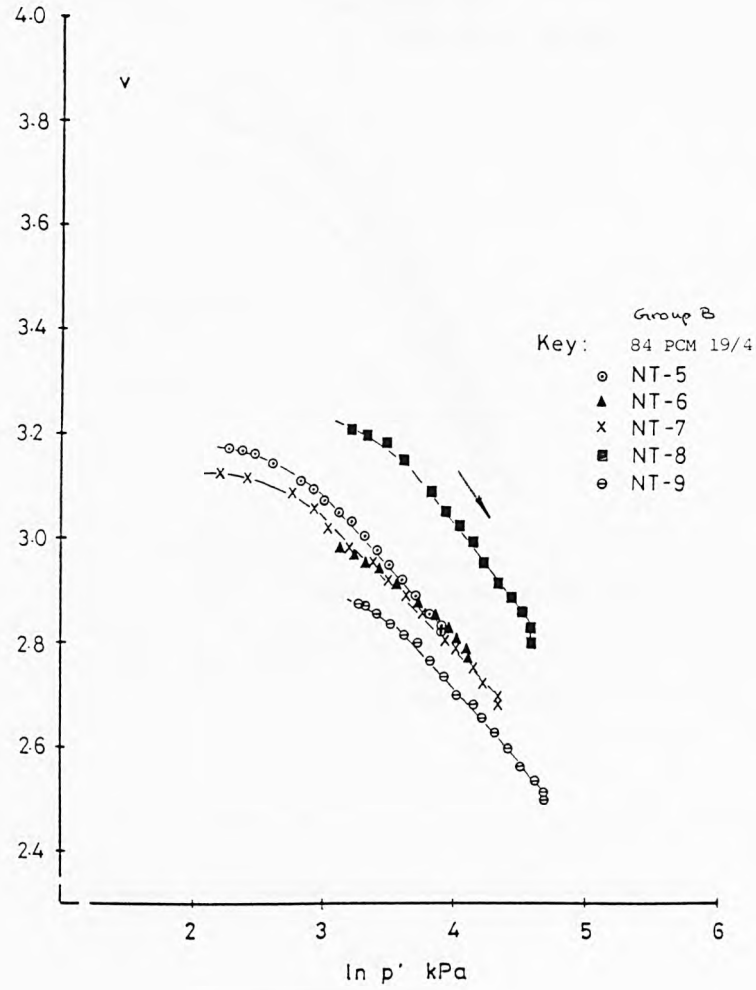

Fig. 8.6b K_o compression of the NAP tubed specimens.

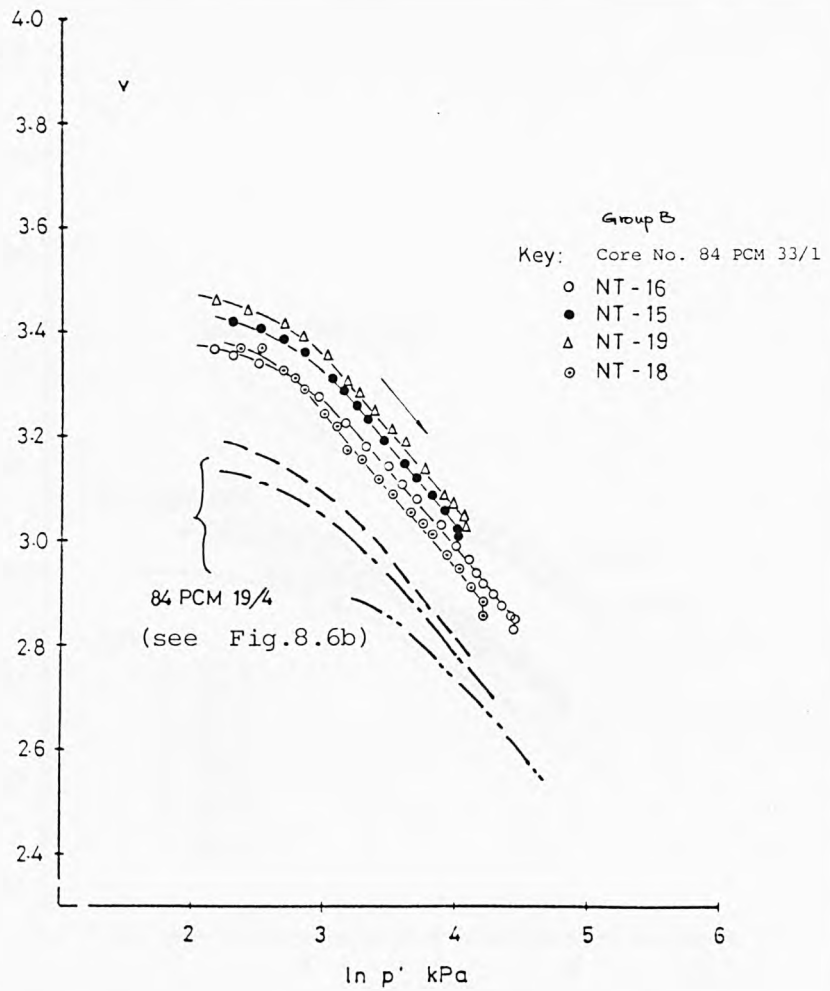

Fig. 8.6c K_o compression of the NAP tubed specimens.

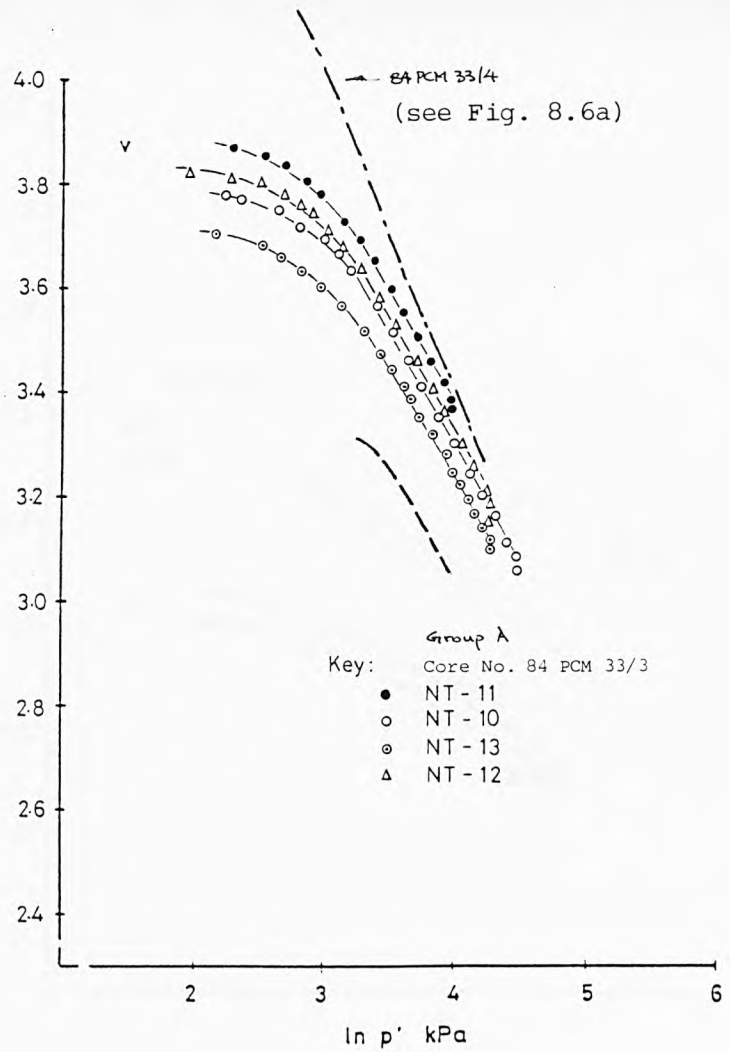

Fig. 8.6d K_o compression of the NAP tubed specimens.

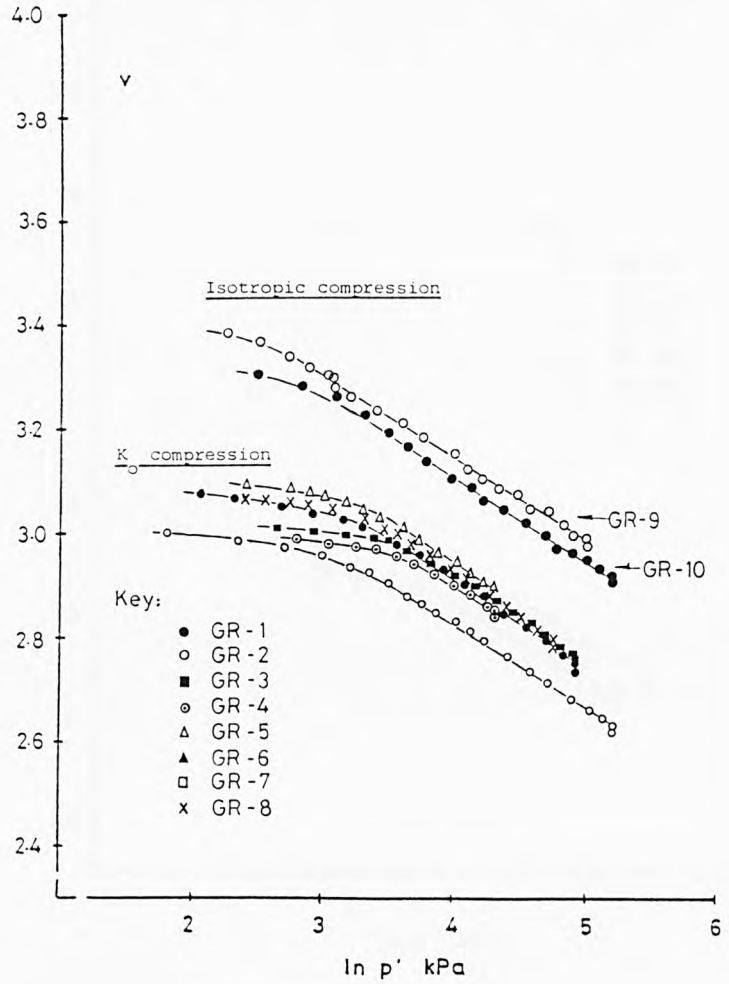

Fig. 8.7a K_o and isotropic compression of the GME reconstituted specimens.

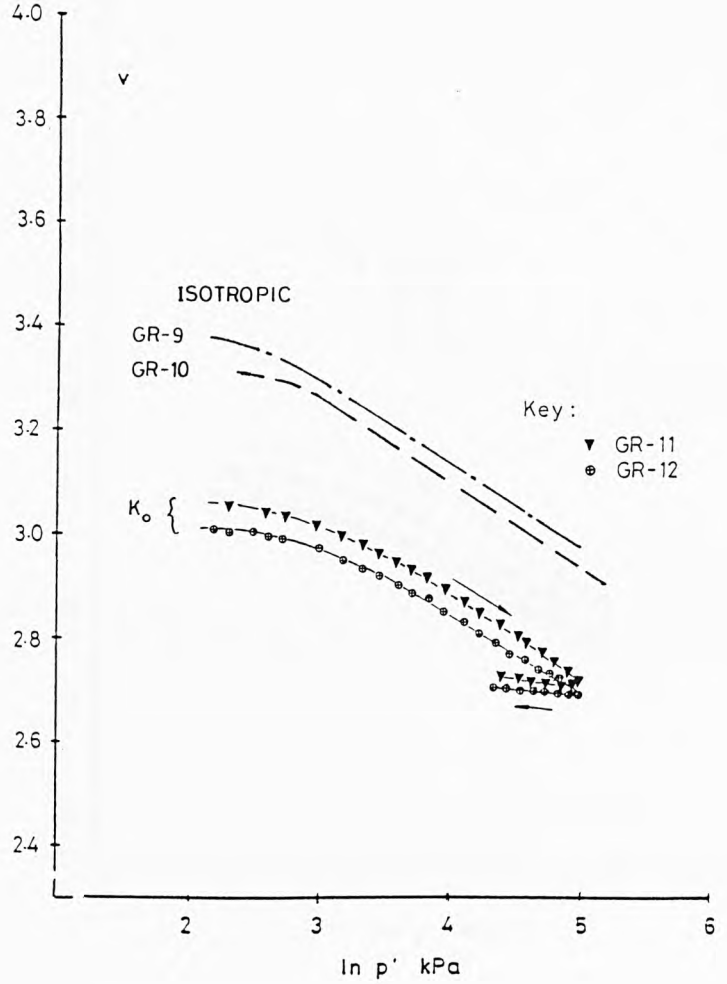

Fig. 8.7b K_o compression and swelling of the GME reconstituted specimens.

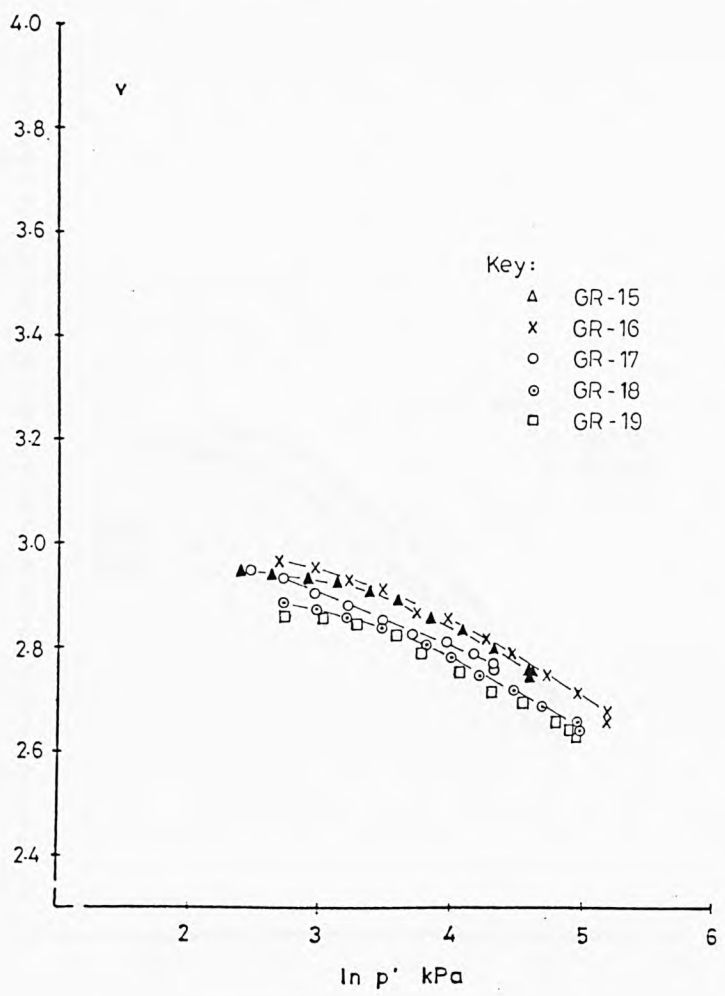

Fig. 8.7c K_o compression of GME reconstituted specimens.

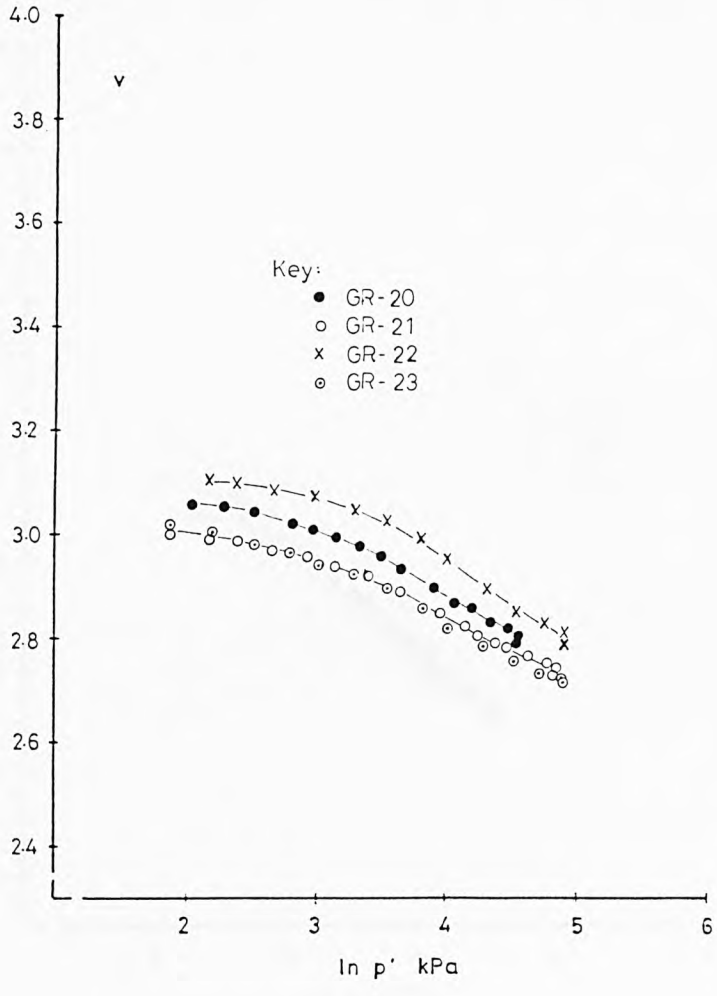

Fig. 8.7 d K_o compression of GME reconstituted specimens.

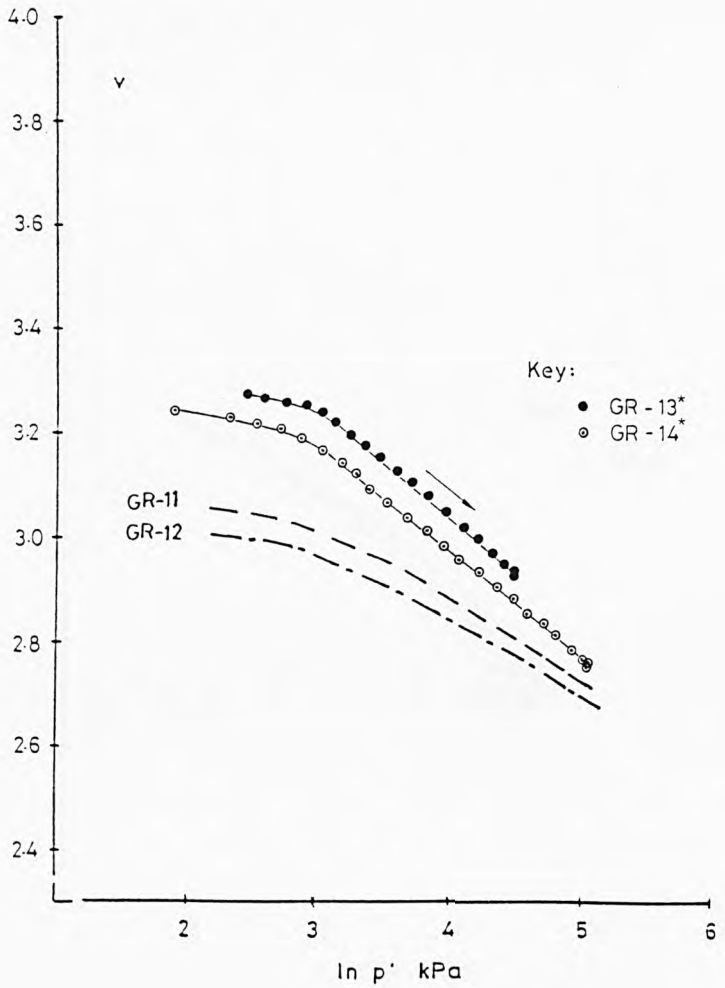

* Carbonates removed by HCL.

Fig. 8.7e K_o compression of the GME reconstituted specimens.

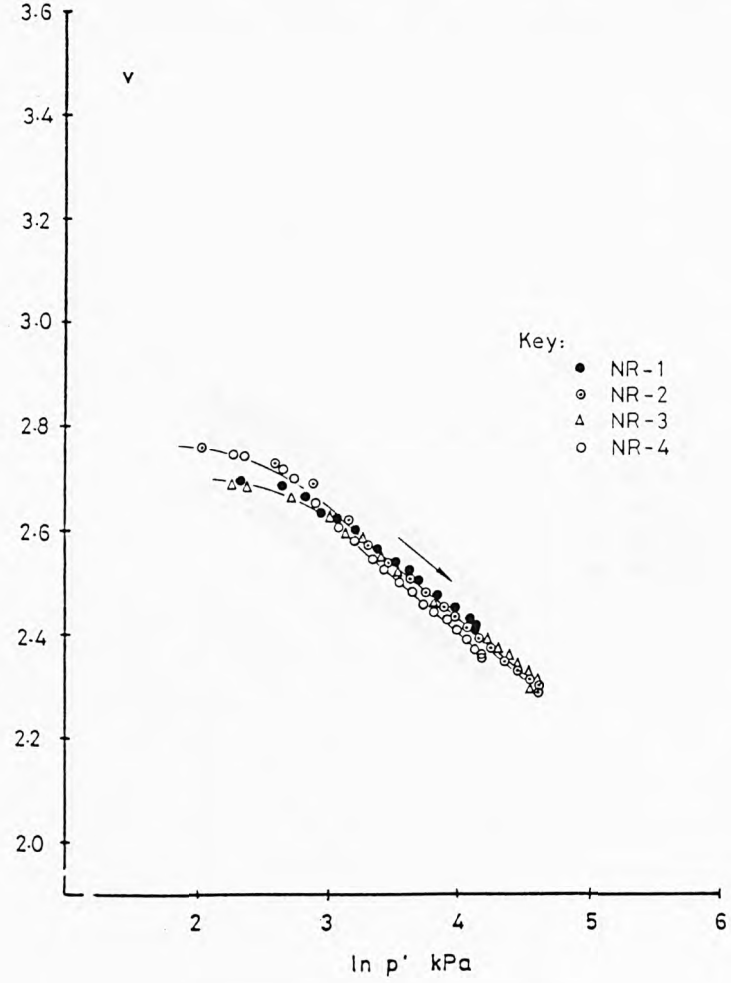

Fig. 8.8a K_o compression of the NAP reconstituted specimens.

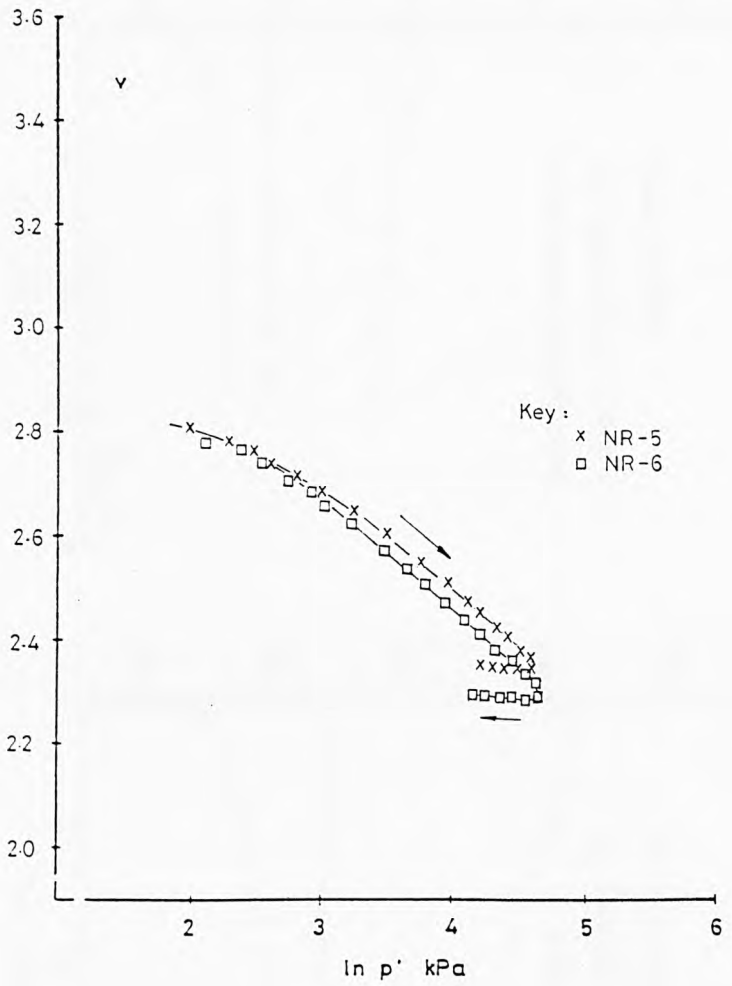

Fig. 8.8b K_o compression and swelling of the NAP reconstituted specimens.

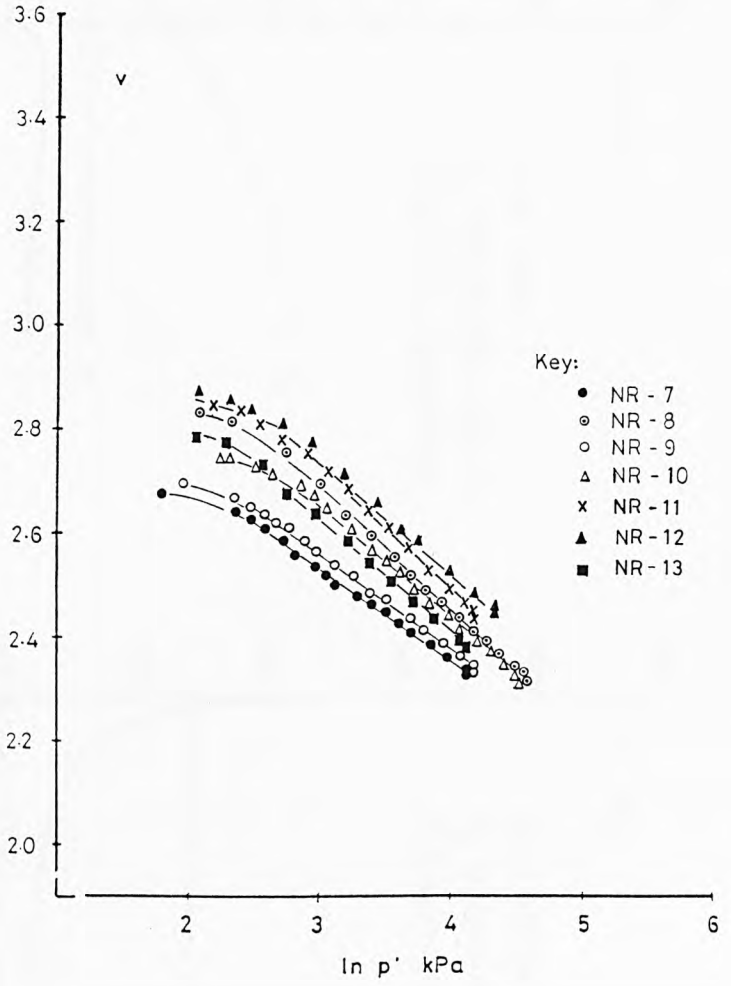

Fig. 8.8c K_o compression of the NAP reconstituted specimens.

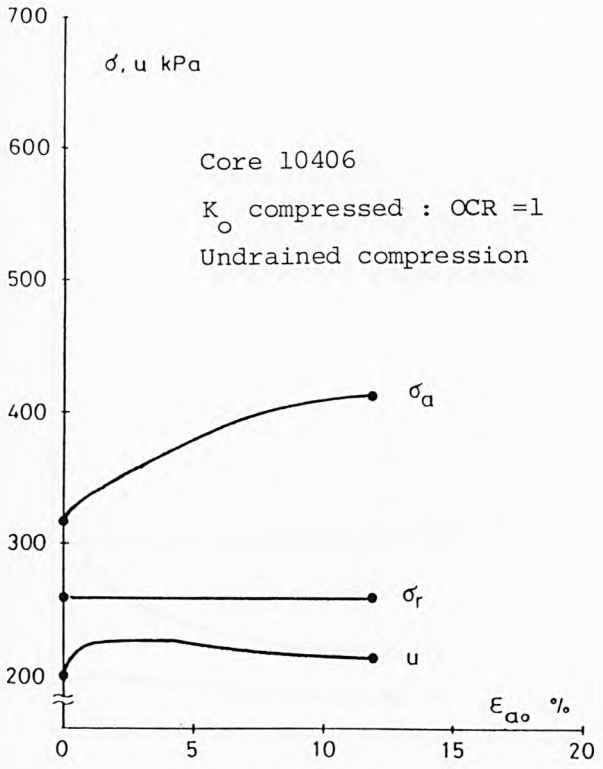

(a) IOS-1

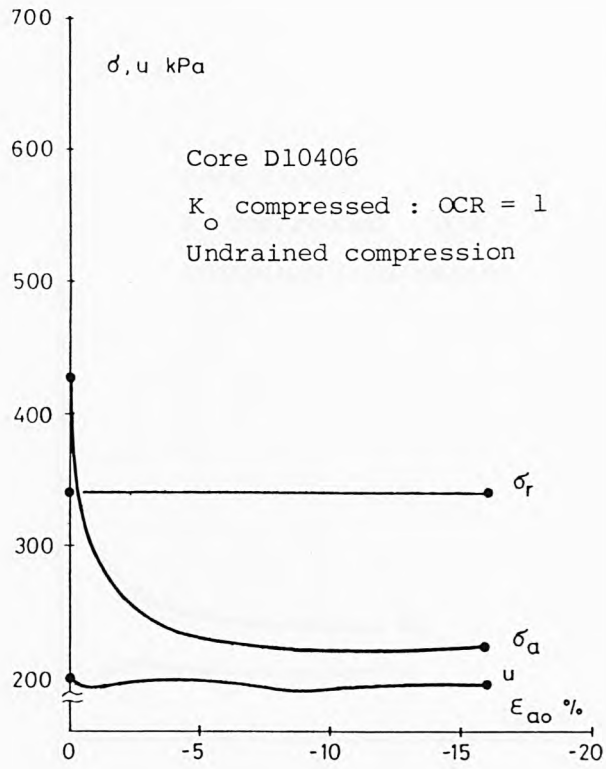

(b) IOS- 3

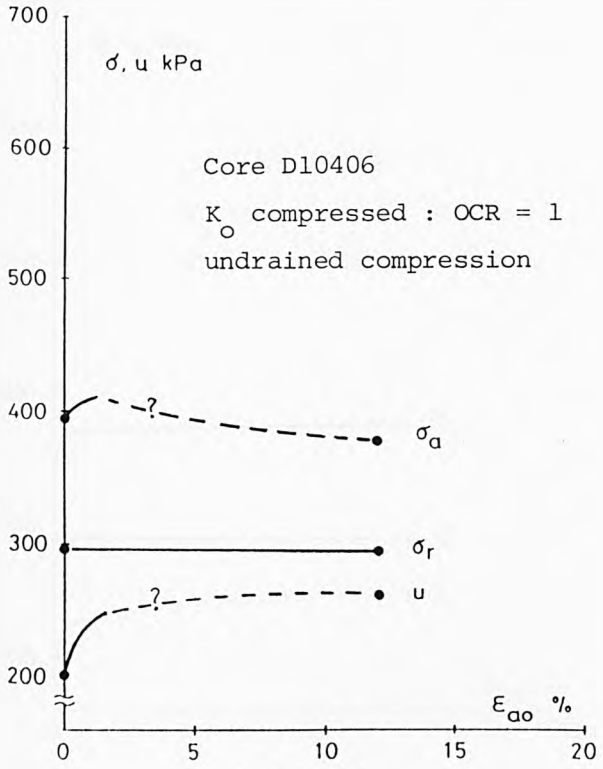

(c) IOS-4

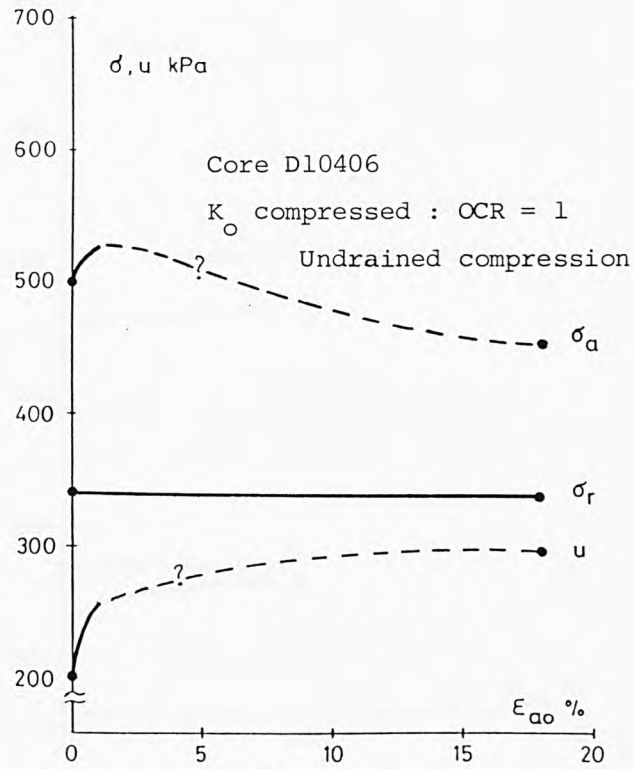

(d) IOS-5

Fig. 8.9 The basic shearing test results of the IOS tubed specimens.

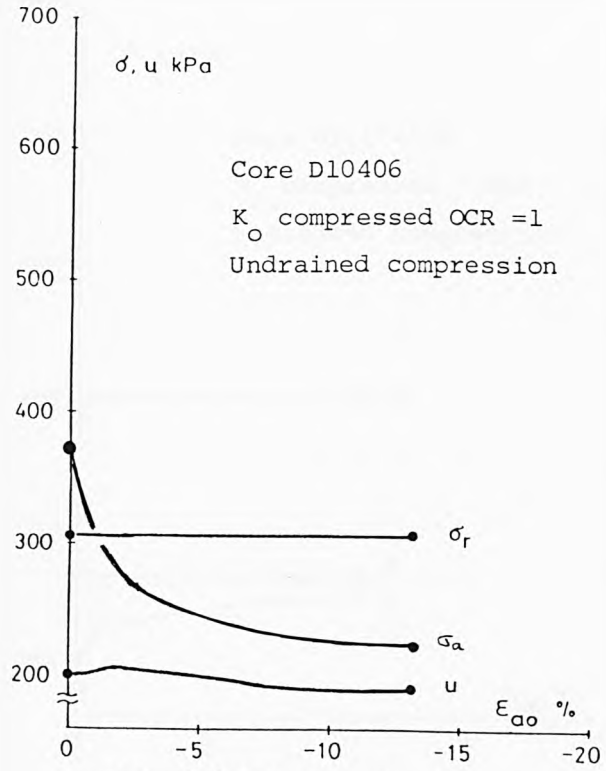

Fig. 8.9 (e) IOS- 2

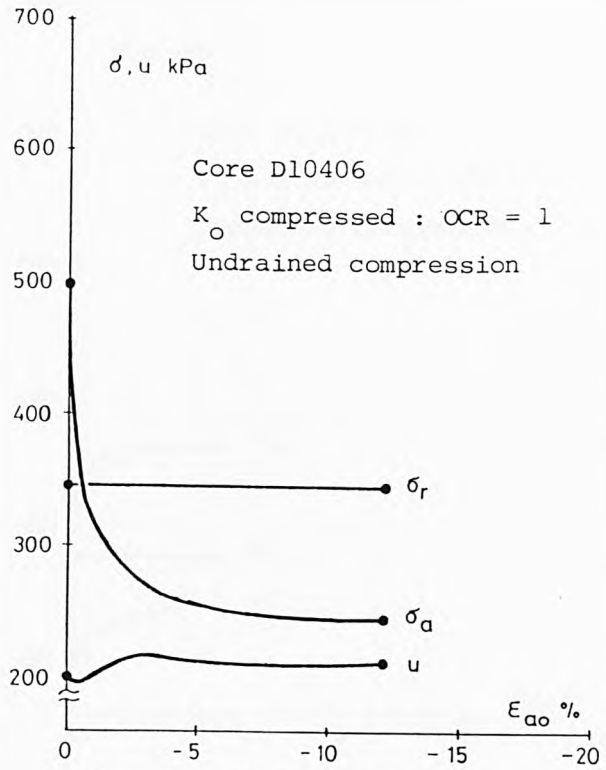

Fig. 8.9 (f) IOS-6

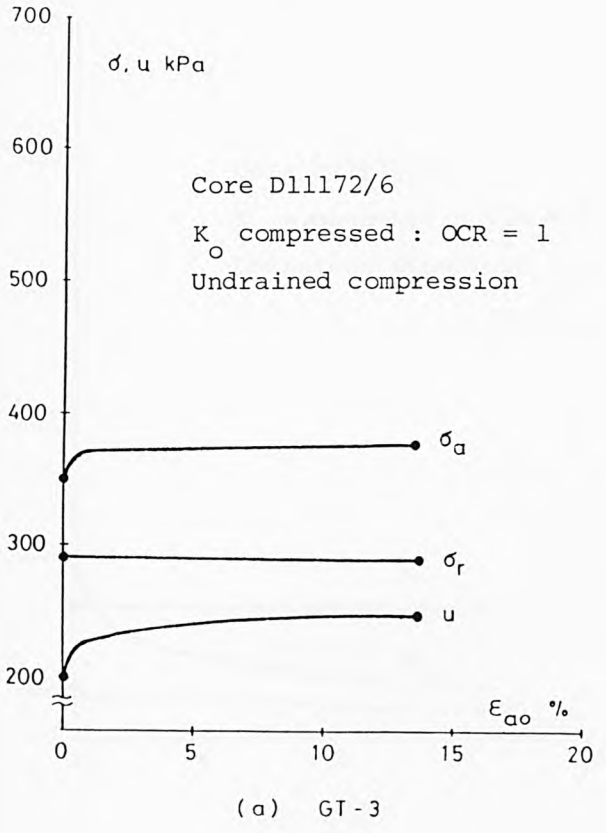

(a) GT - 3

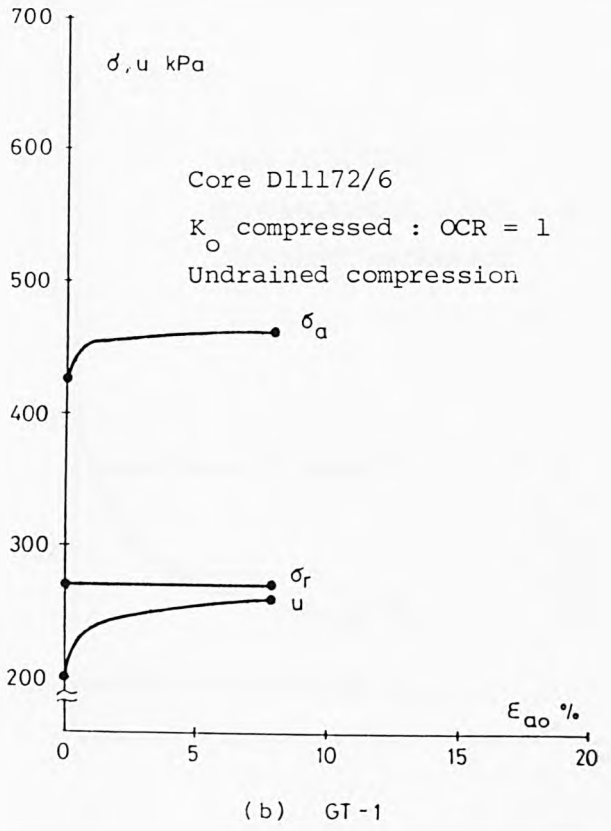

(b) GT - 1

Fig. 8.10 The basic shearing test results of the GME tubed specimens.

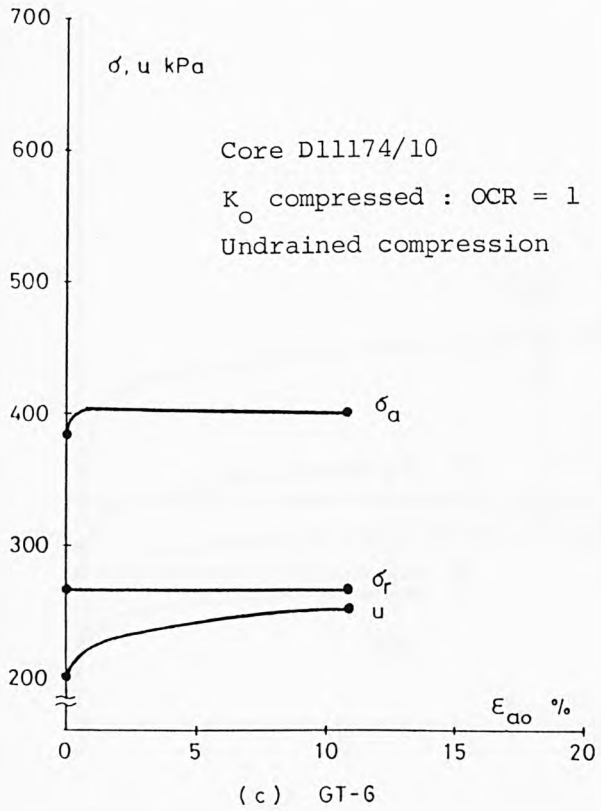

(c) GT-6

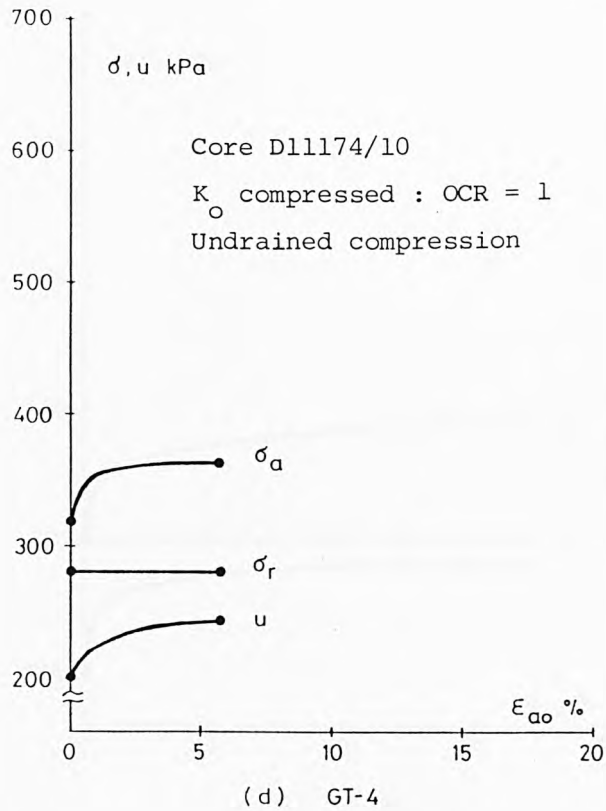

(d) GT-4

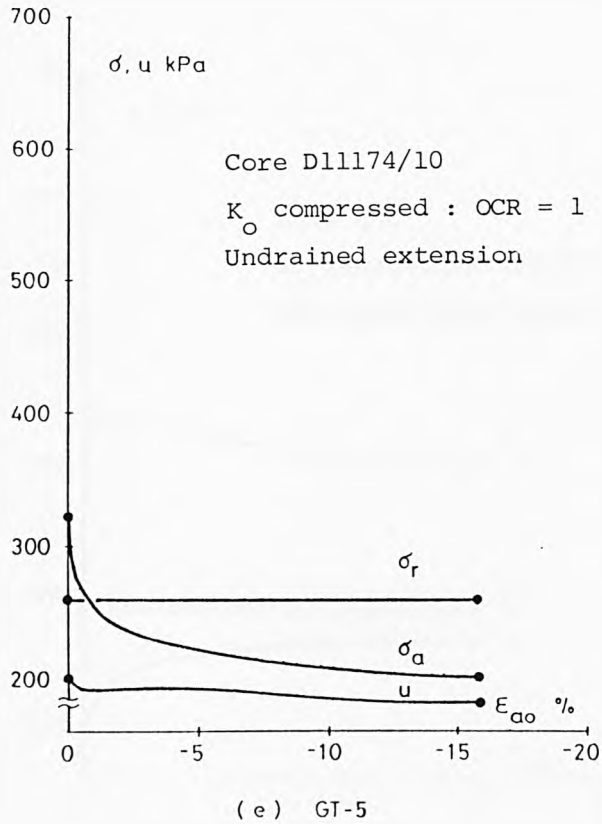

(e) GT-5

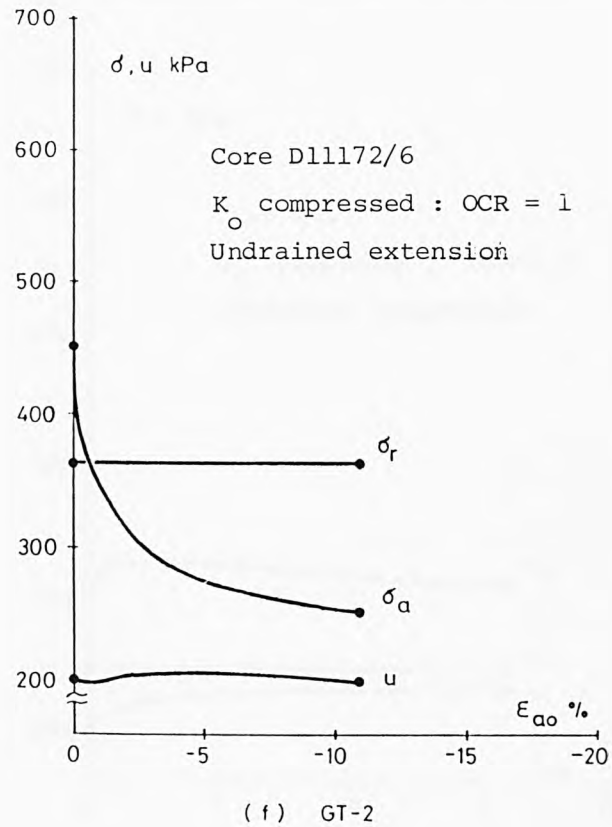

(f) GT-2

Fig. 8.10 The basic shearing test results of the GME tubed specimens.

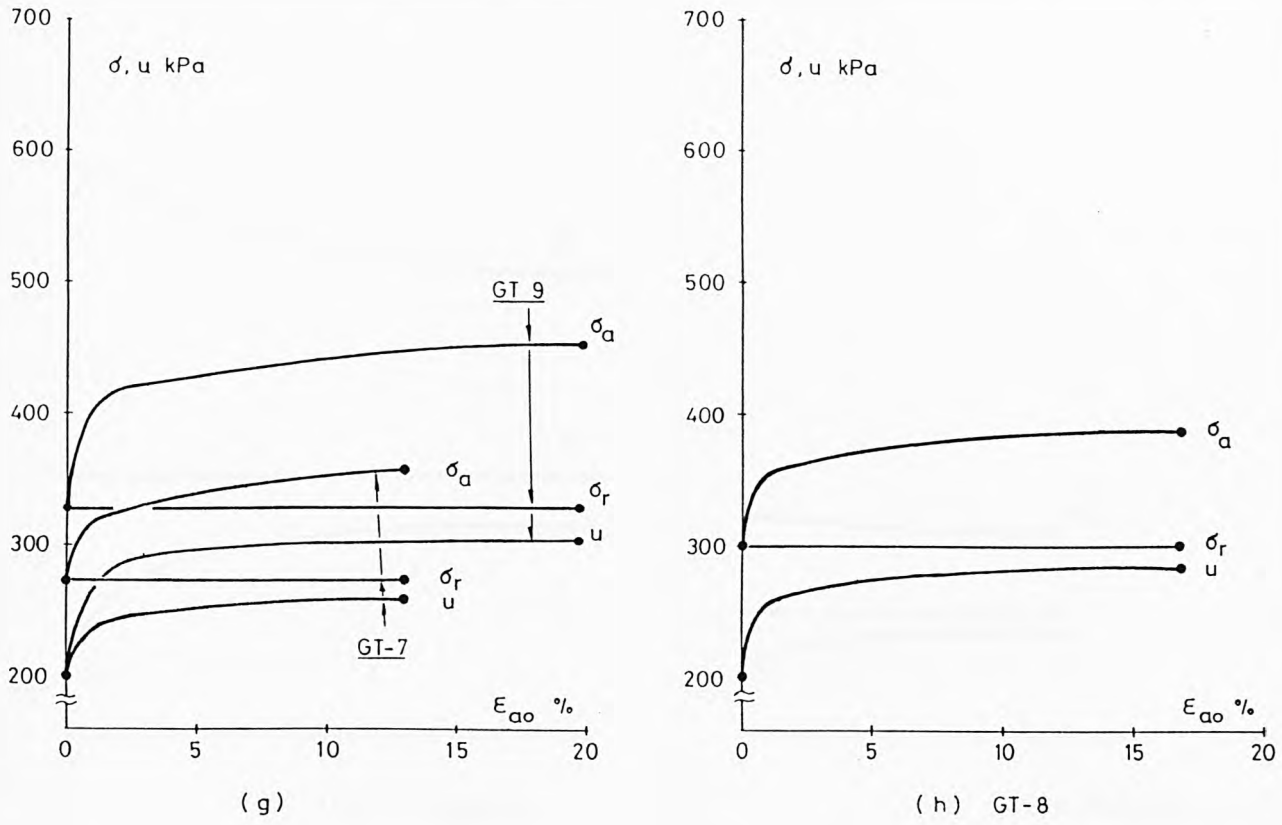

Fig. 8.10 The basic shearing test results of the GME tubed Specimens.
(Isotropic compressed : OCR=1 , Undrained compression)

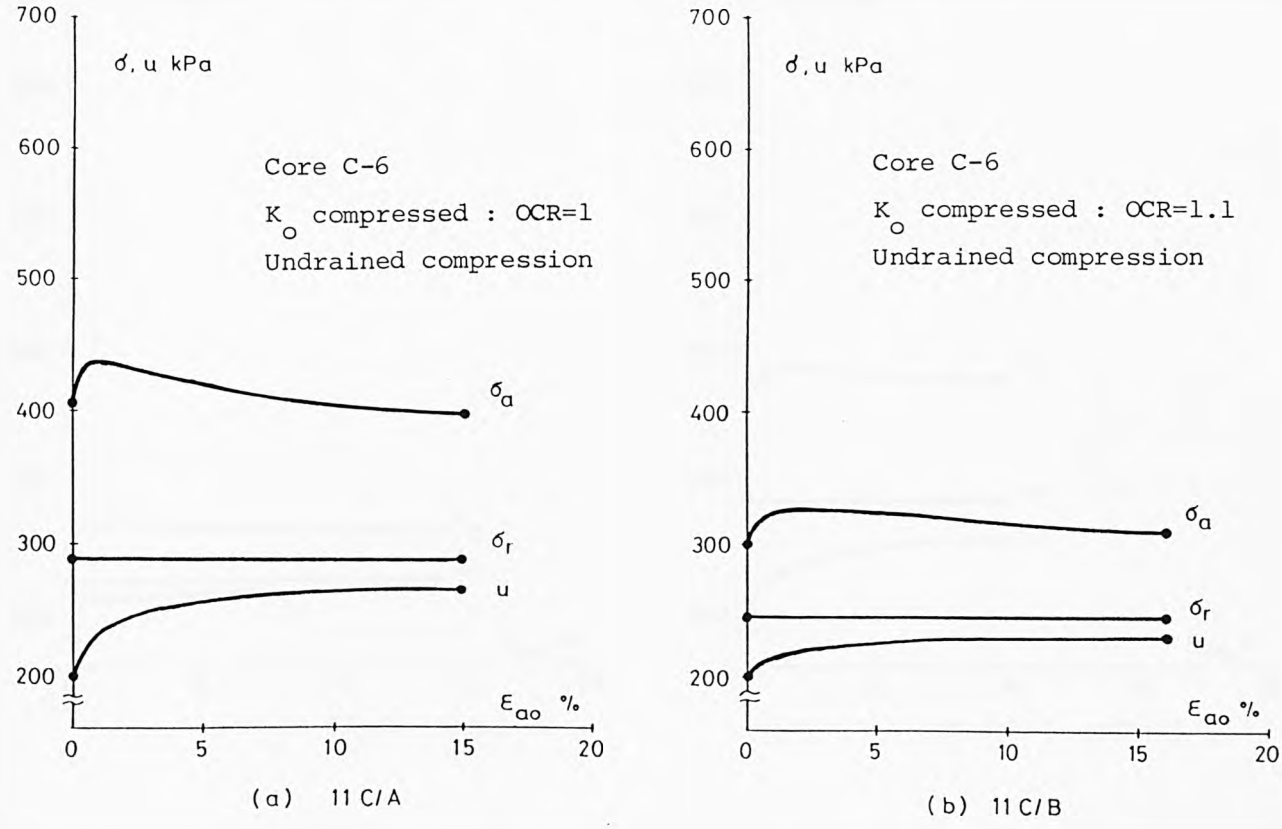

Fig. 8.11 The basic shearing test results of the GME C-6 tubed specimens.

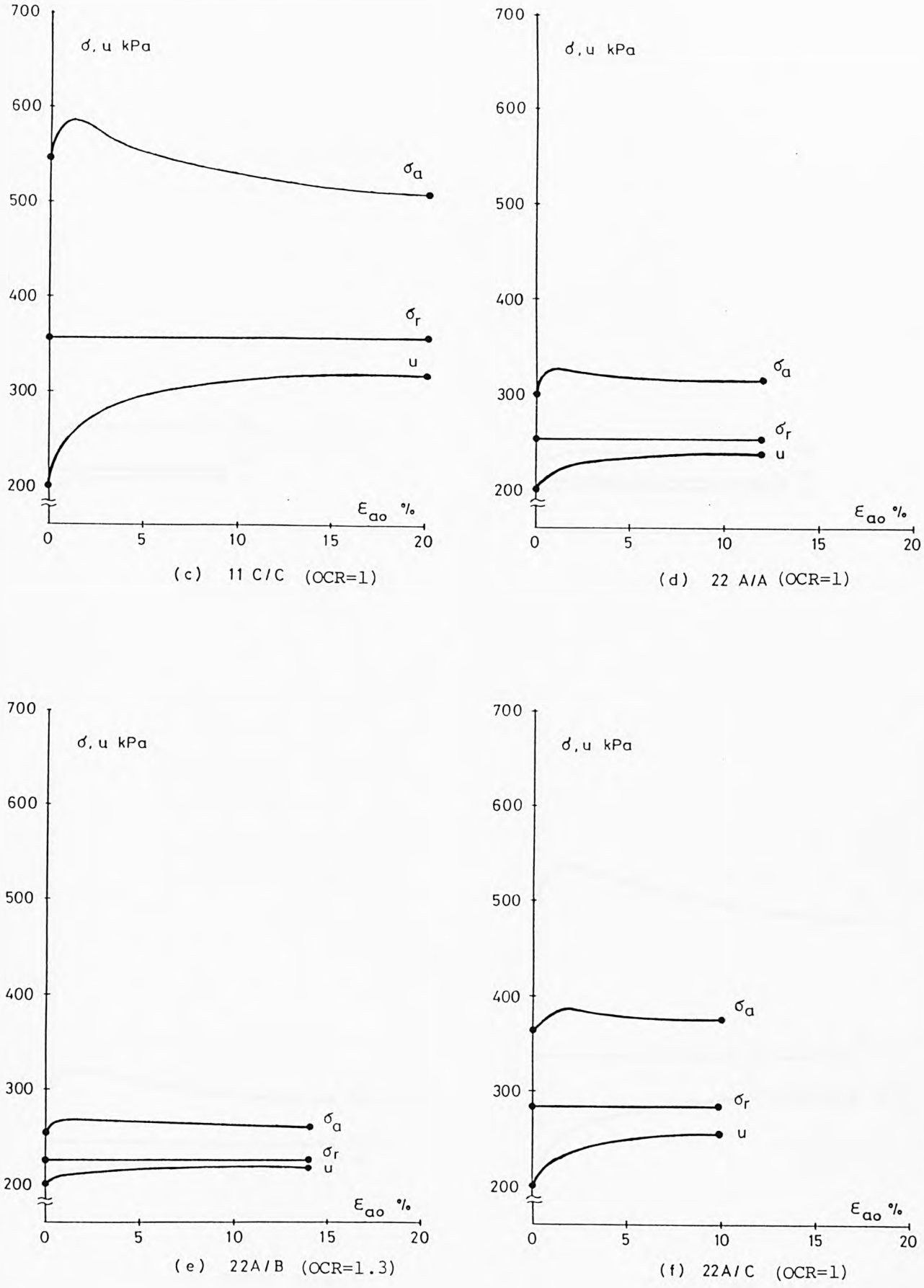

Fig. 8.11 The basic shearing test results of the GME C-6 tubed specimens.

(Core C-6, K_o compressed undrained compression)

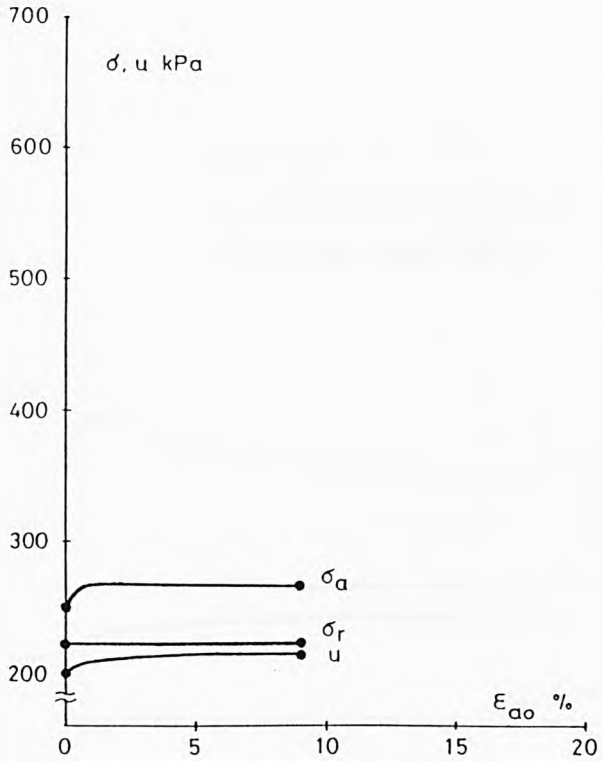

(g) 30A/A (OCR=1.1)

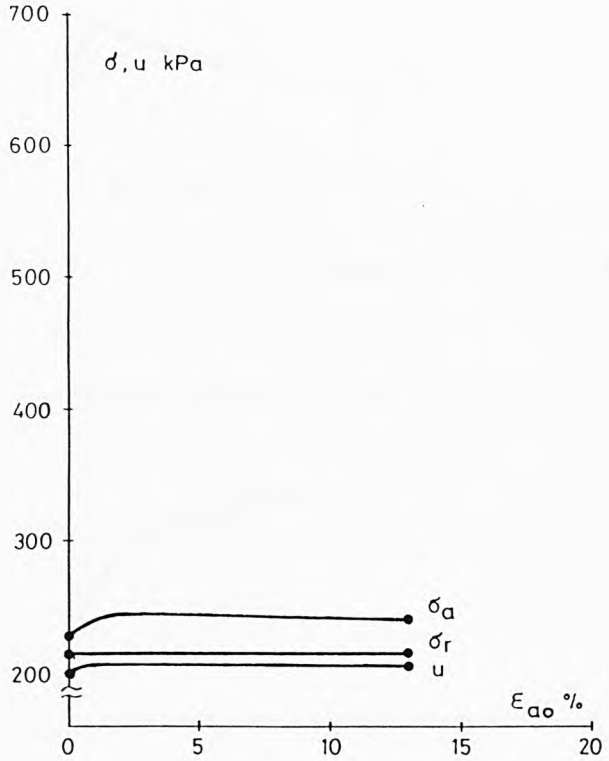

(h) 30A/B (OCR=2.1)

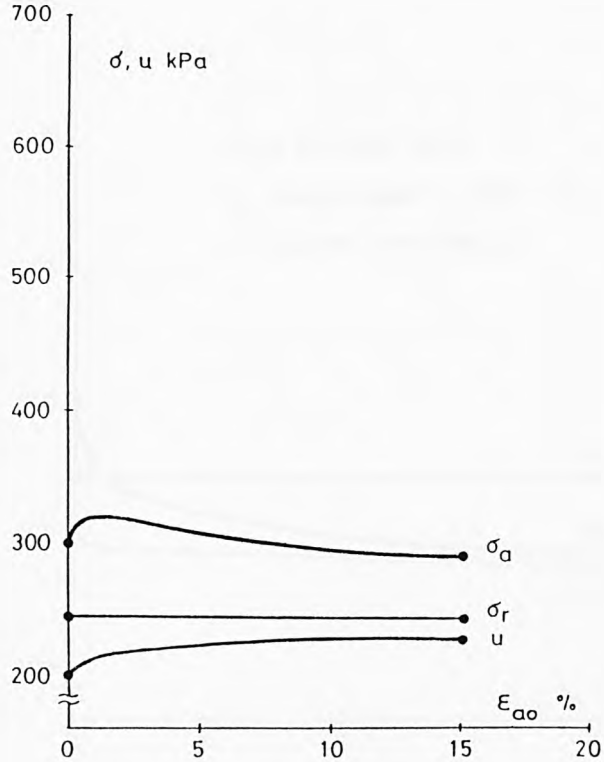

(i) 30A/C (OCR=1)

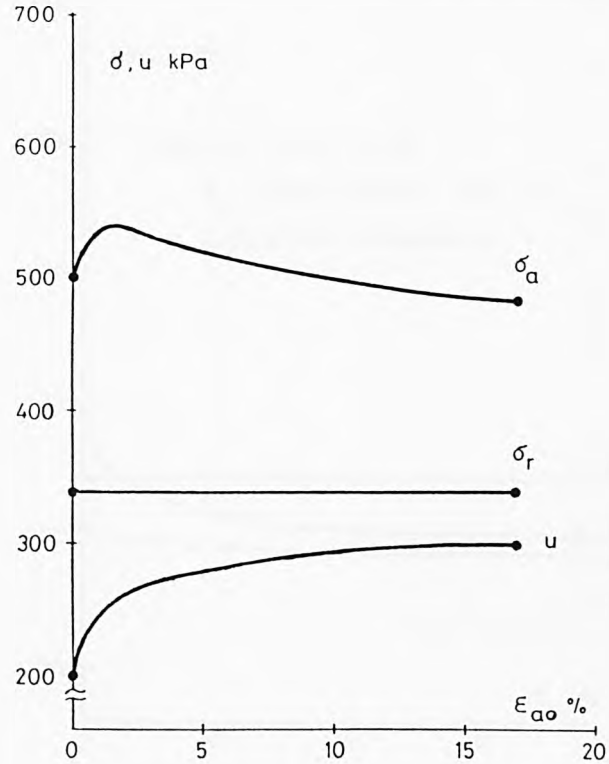

(j) 1B/A (OCR=1)

Fig. 8.11 The basic shearing test results of the GME C-6 tubed specimens.

(Core C-6 , K_o compressed undrained compression)

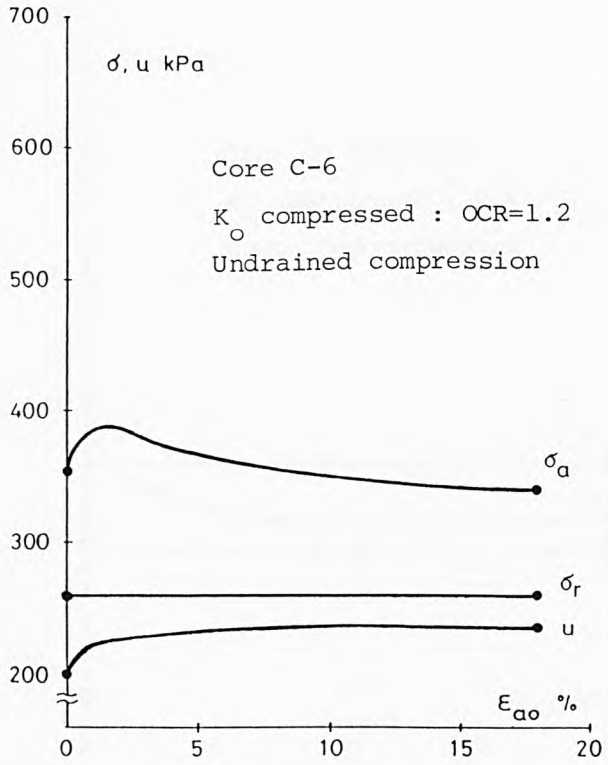

Fig. 8.11 (k) 1B/B

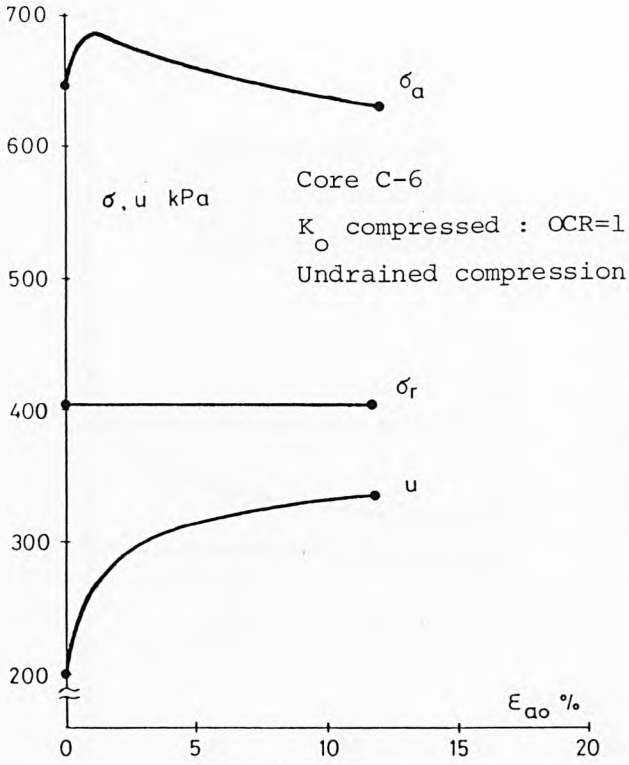

Fig. 8.11 (l) 1B/C

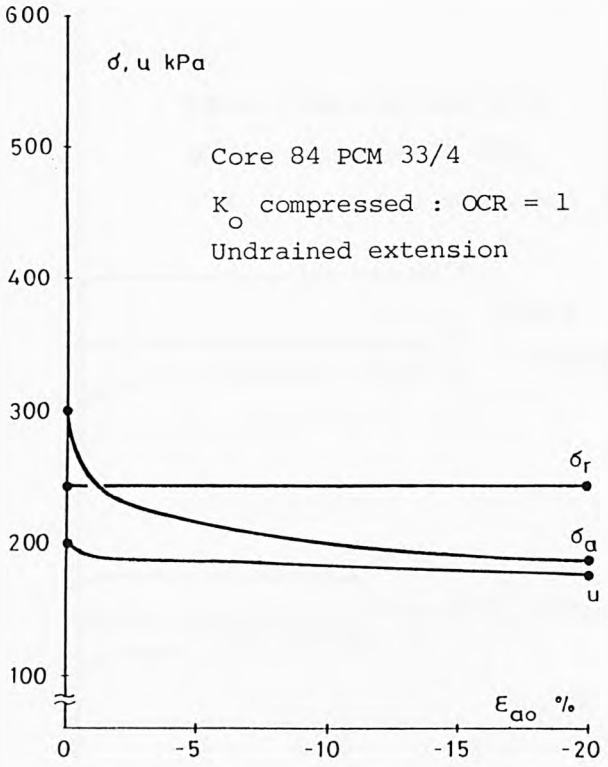

(a) NT-1

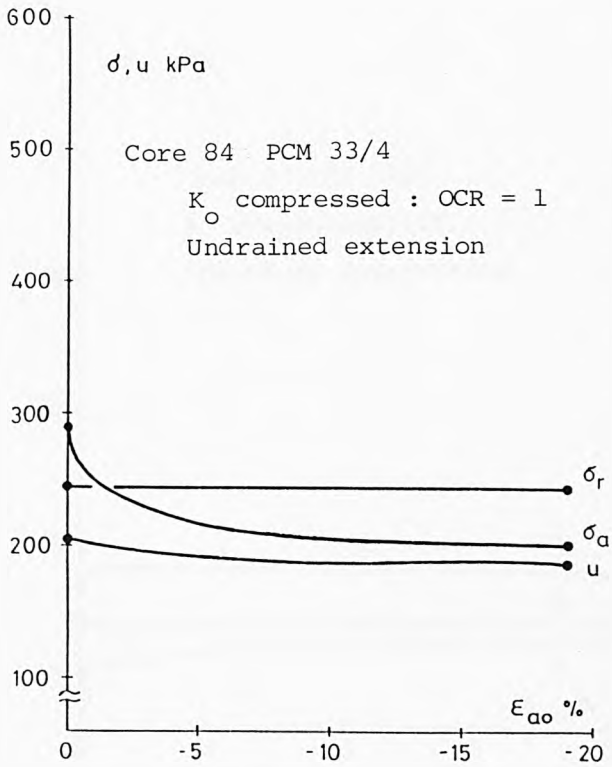

(b) NT-2

Fig. 8.12 The basic shearing test results of the NAP tubed specimens.

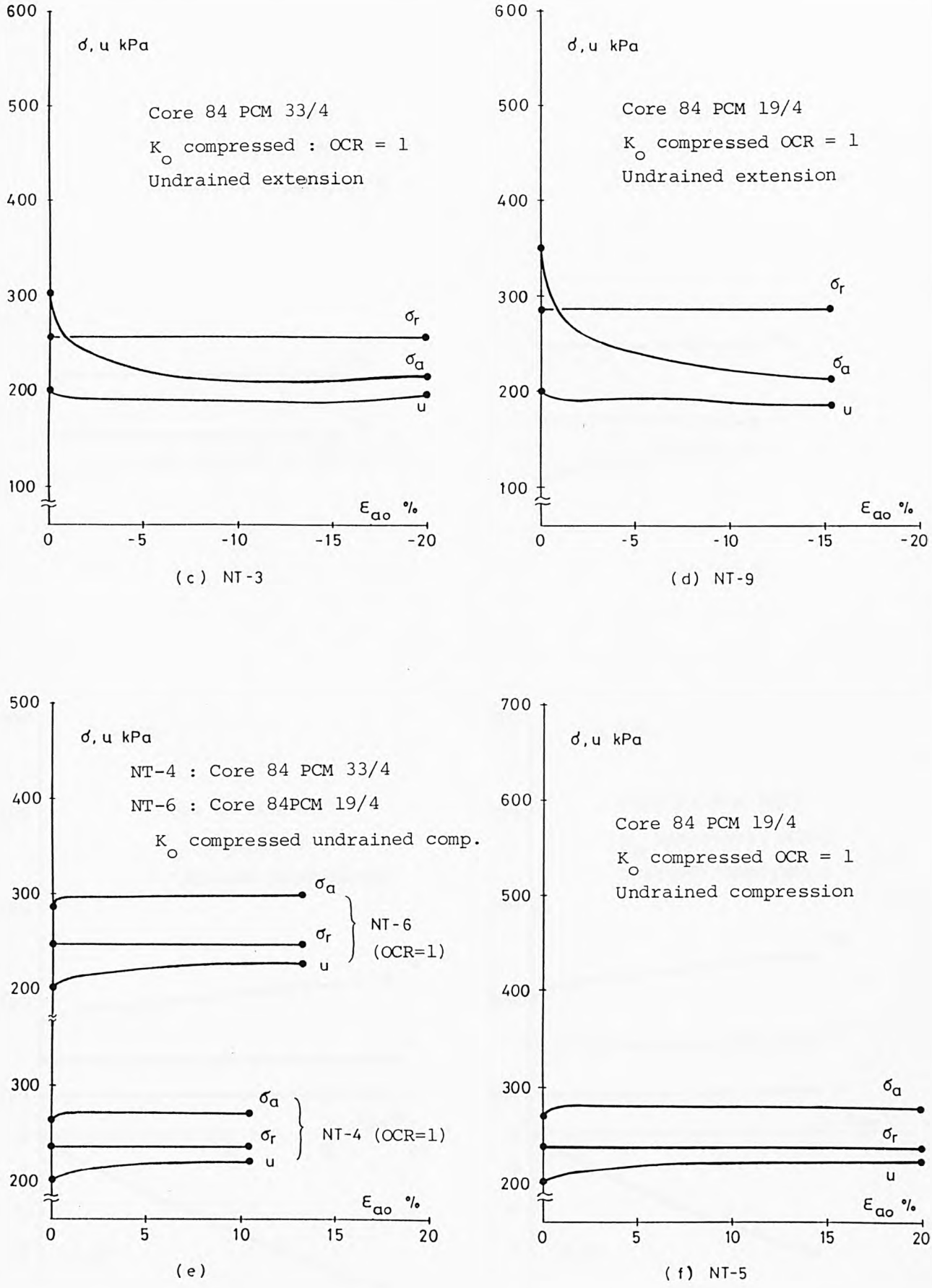

Fig. 8.12 The basic shearing test results of the NAP tubed specimens.

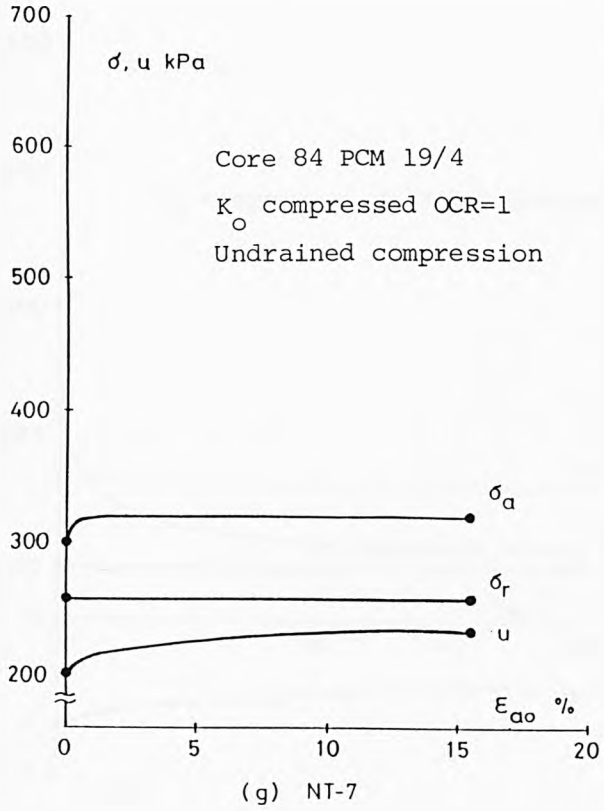

(g) NT-7

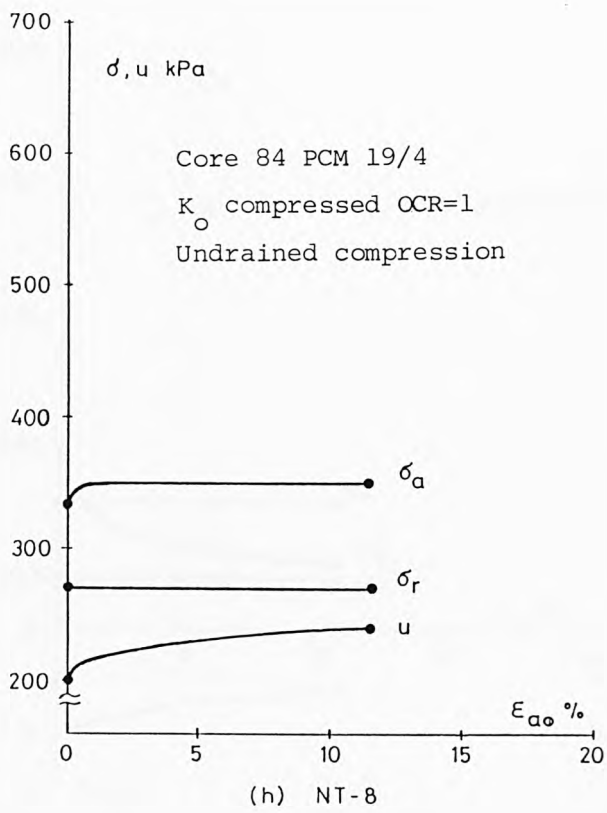

(h) NT-8

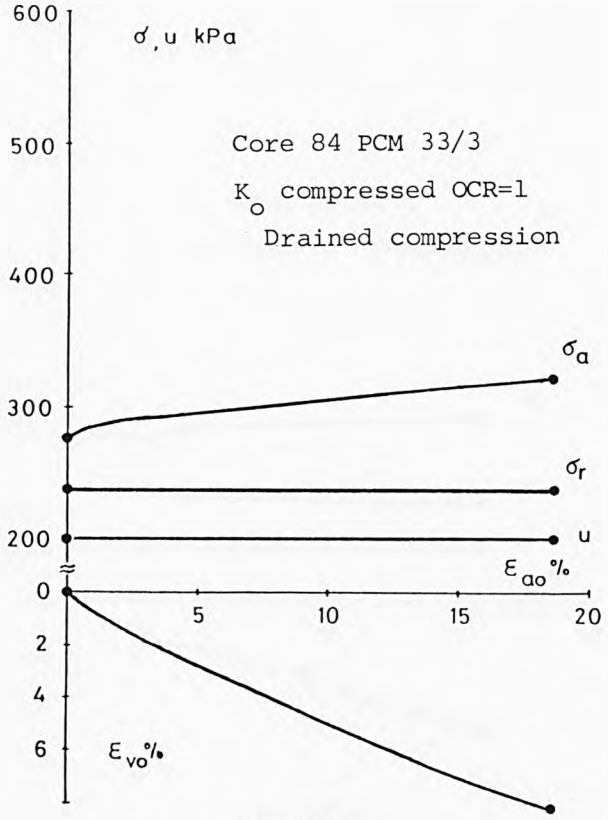

(i) NT-11

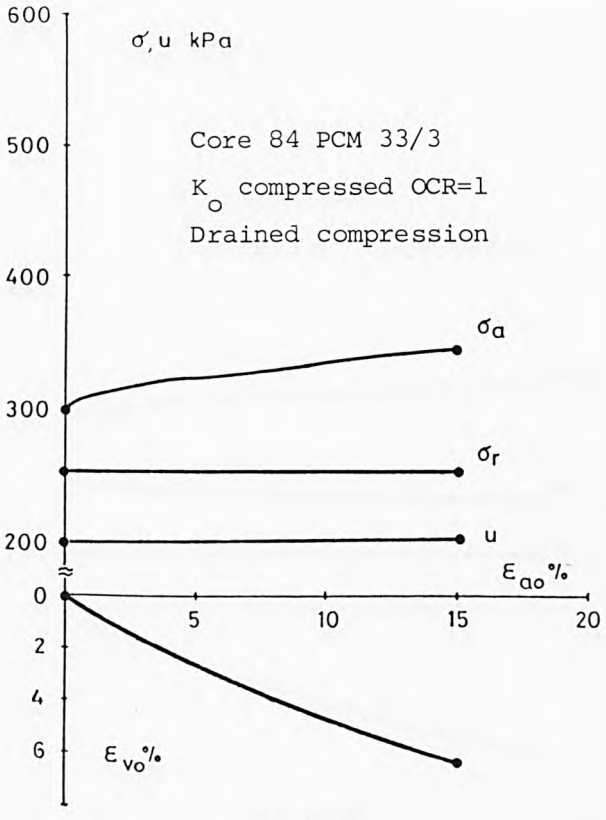

(j) NT-13

Fig. 8.12 The basic shearing test results of the NAP tubed specimens.

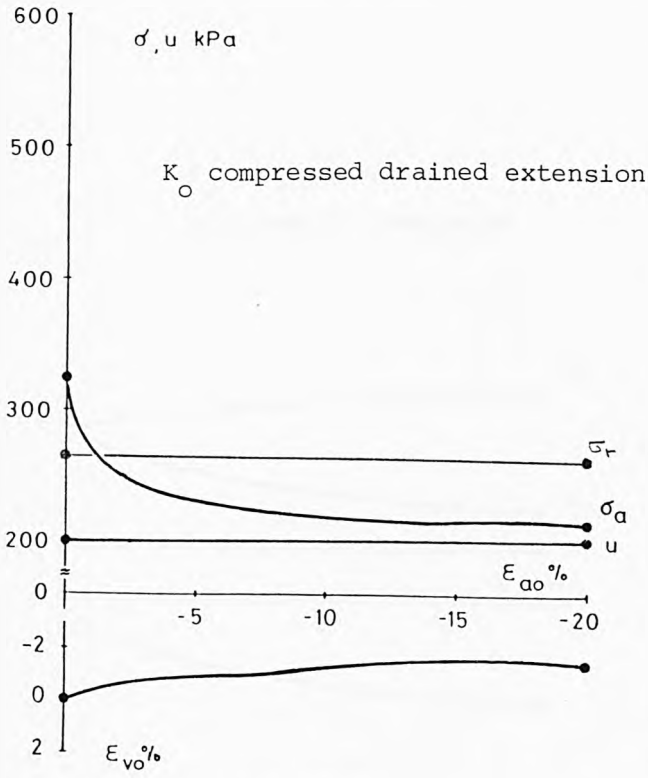

(k) NT-10

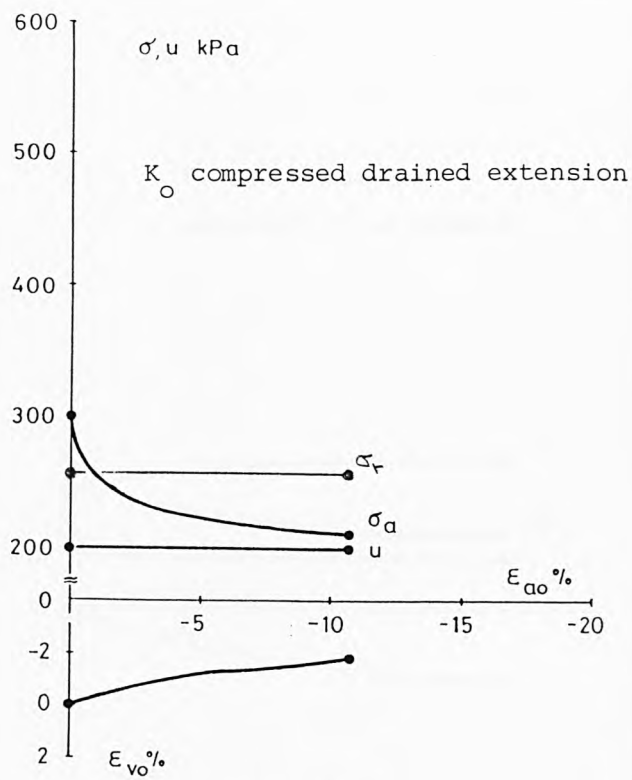

(l) NT-12

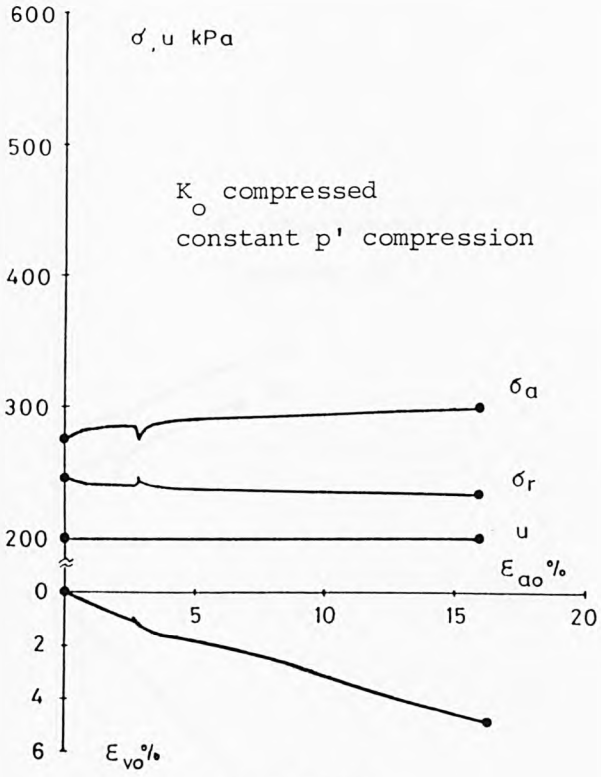

(m) NT-15

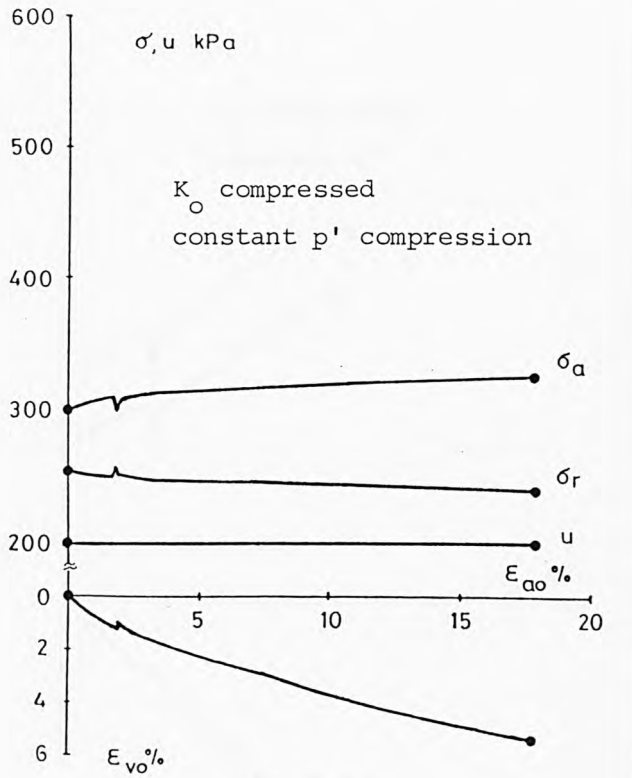

(n) NT-18

Fig. 8.12 The basic shearing test results of the NAP tubed specimens.

(Core 84 PCM 33/1 : OCR=1)

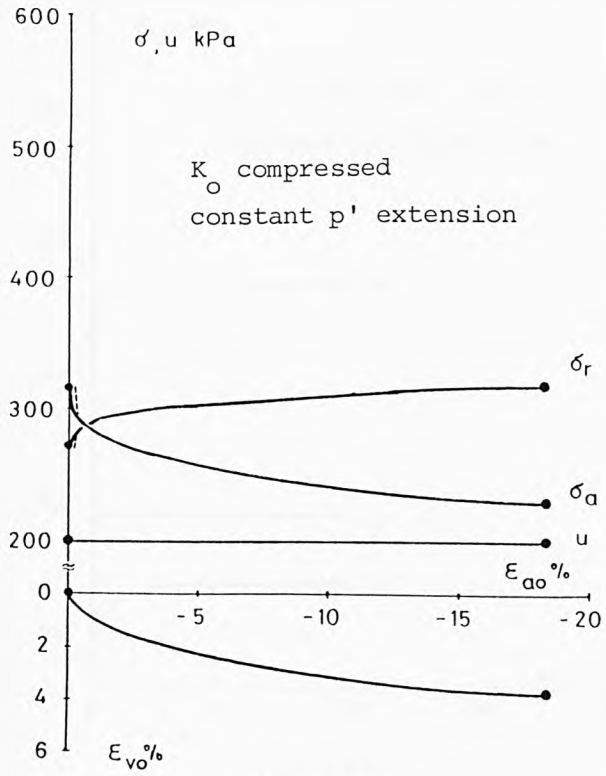

(o) NT-16

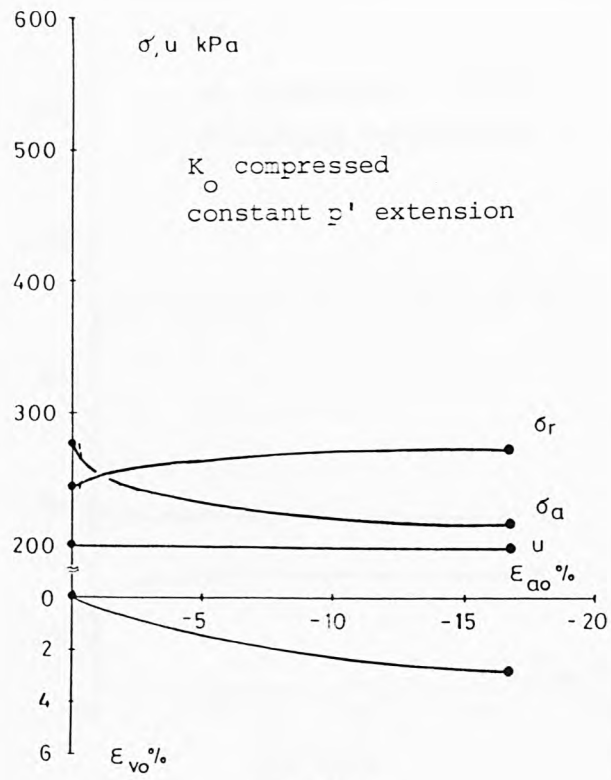

(p) NT-19

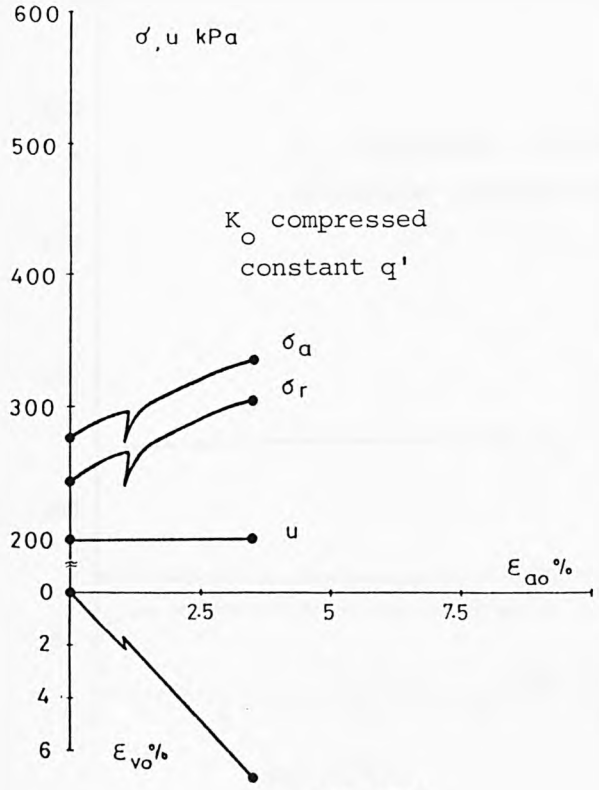

(q) NT-14

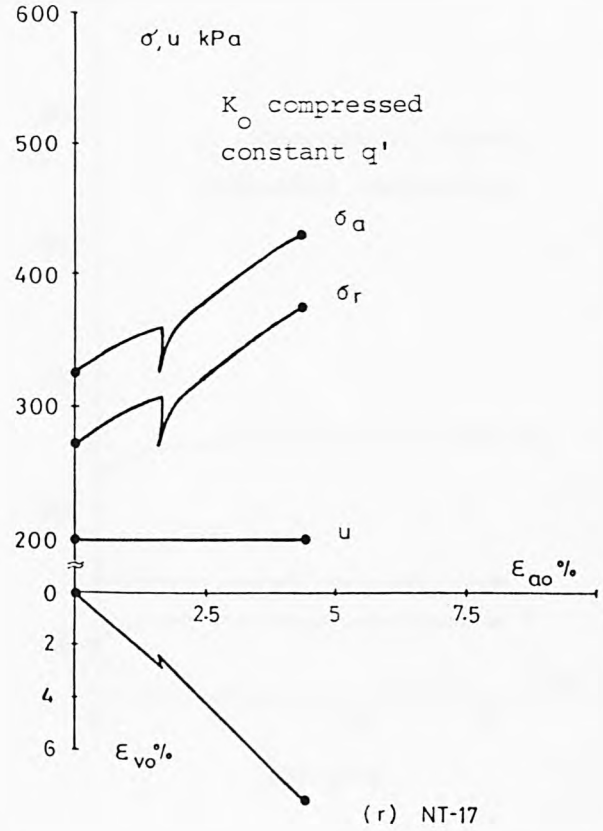

(r) NT-17

Fig. 8.12 The basic shearing test results of the NAP tubed specimens.
(Core 84 PCM 33/1 : OCR=1)

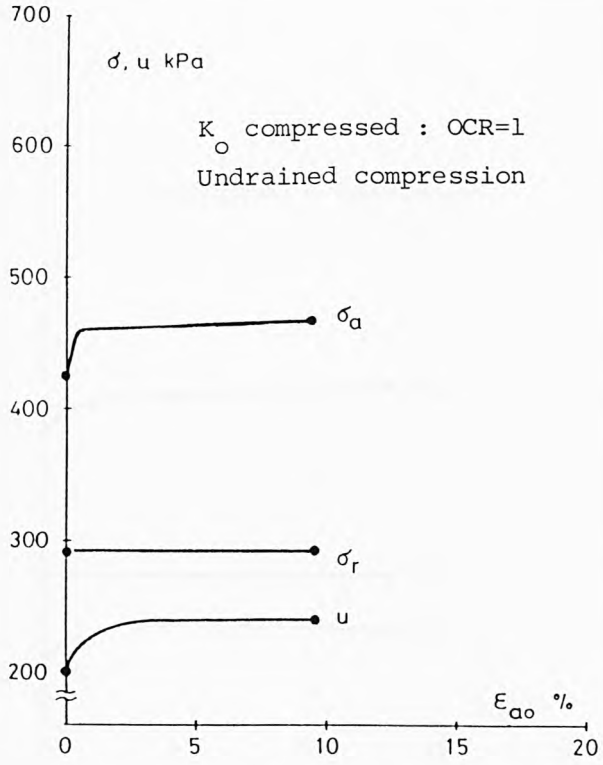

(a) GR-1

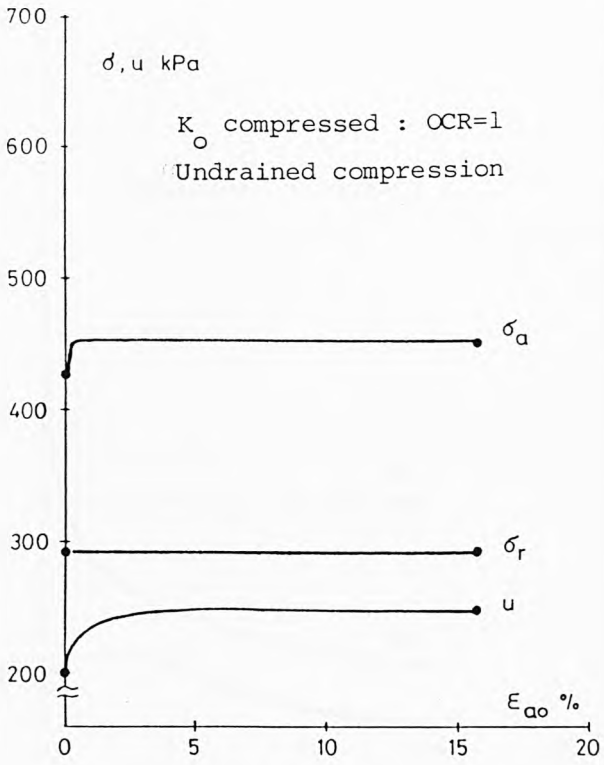

(b) GR-3

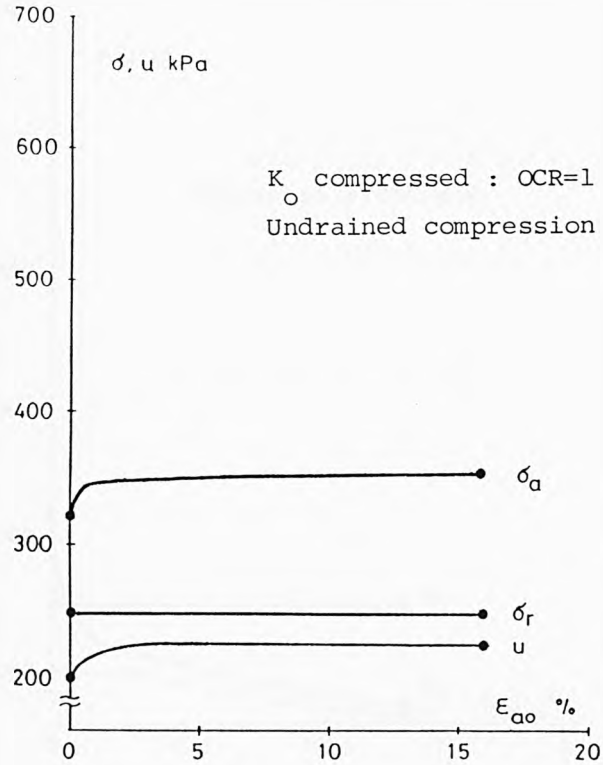

(c) GR-4

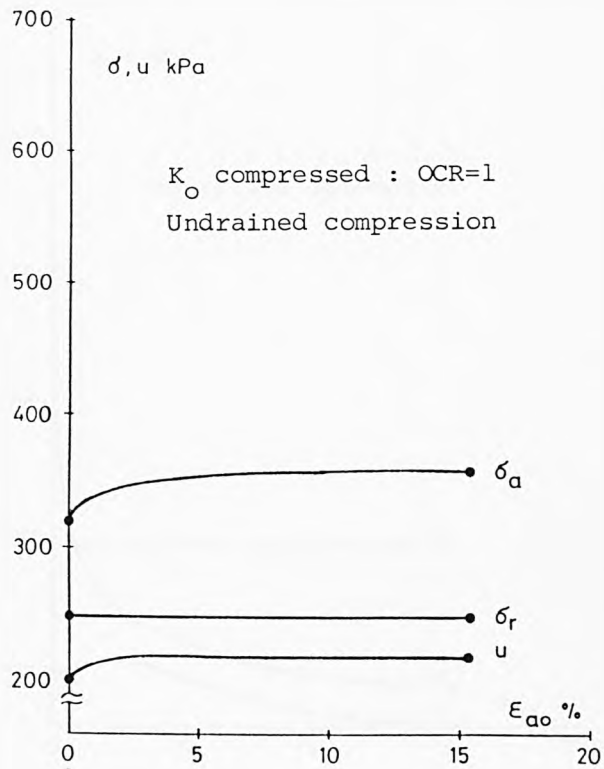

(d) GR-6

Fig. 8.13 The basic shearing test results of the GME reconstituted specimens.

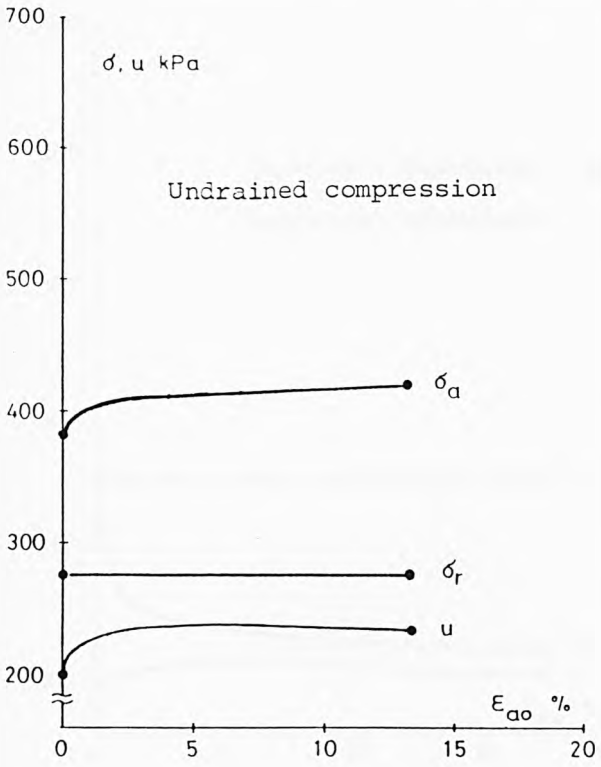

(e) GR-7

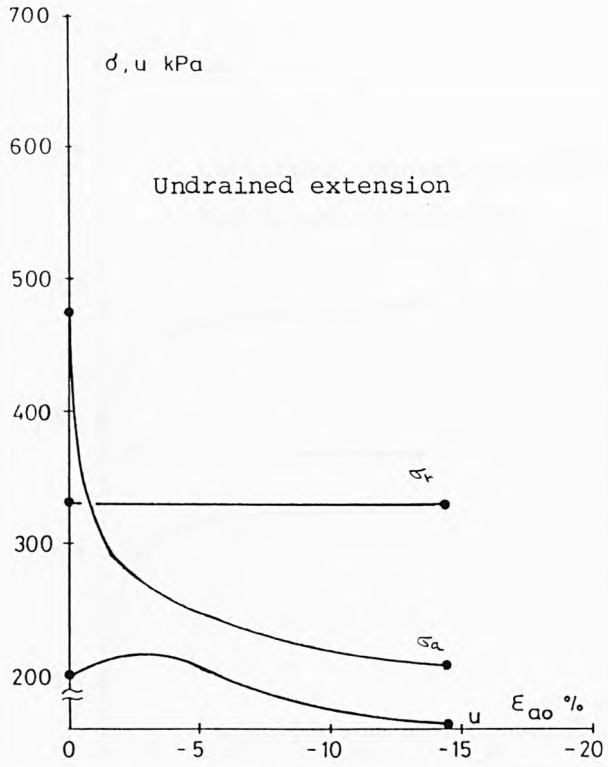

(f) GR-2

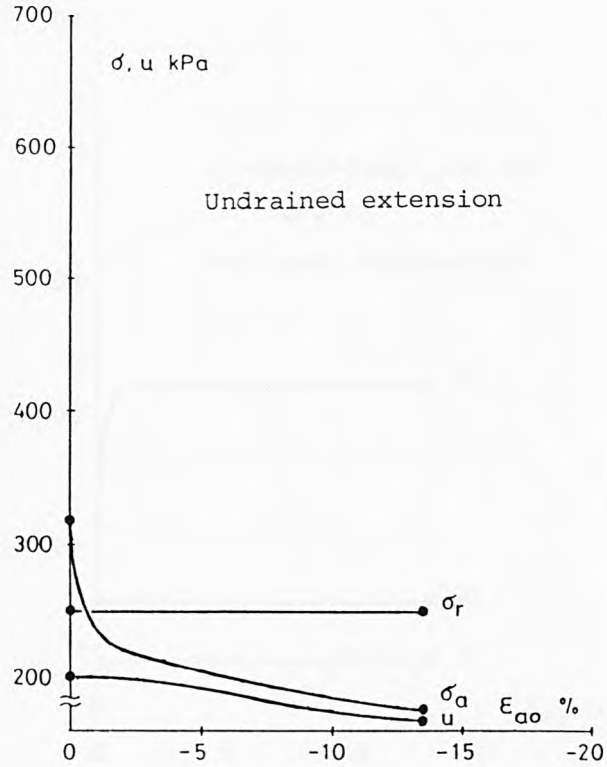

(g) GR-5

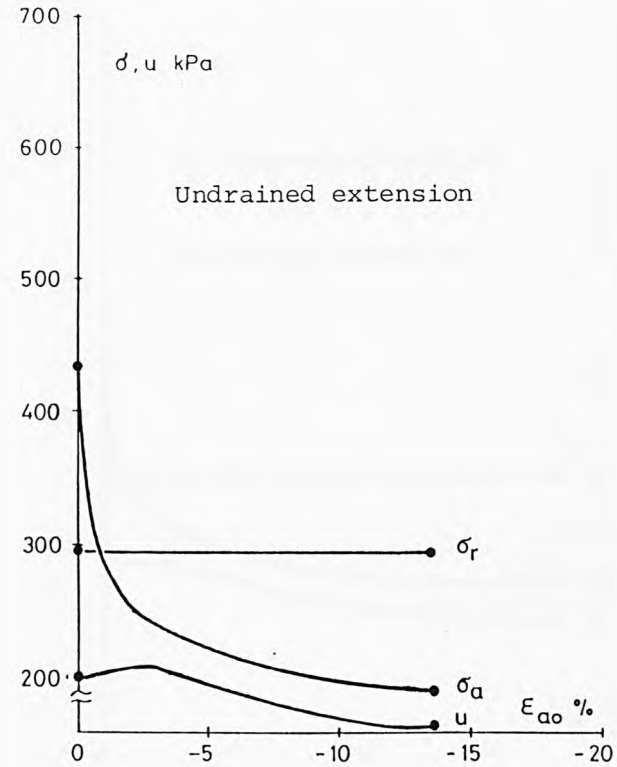

(h) GR- 8

Fig. 8.13 The basic shearing test results of the GME reconstituted specimens.
(K_o compressed : OCR=1)

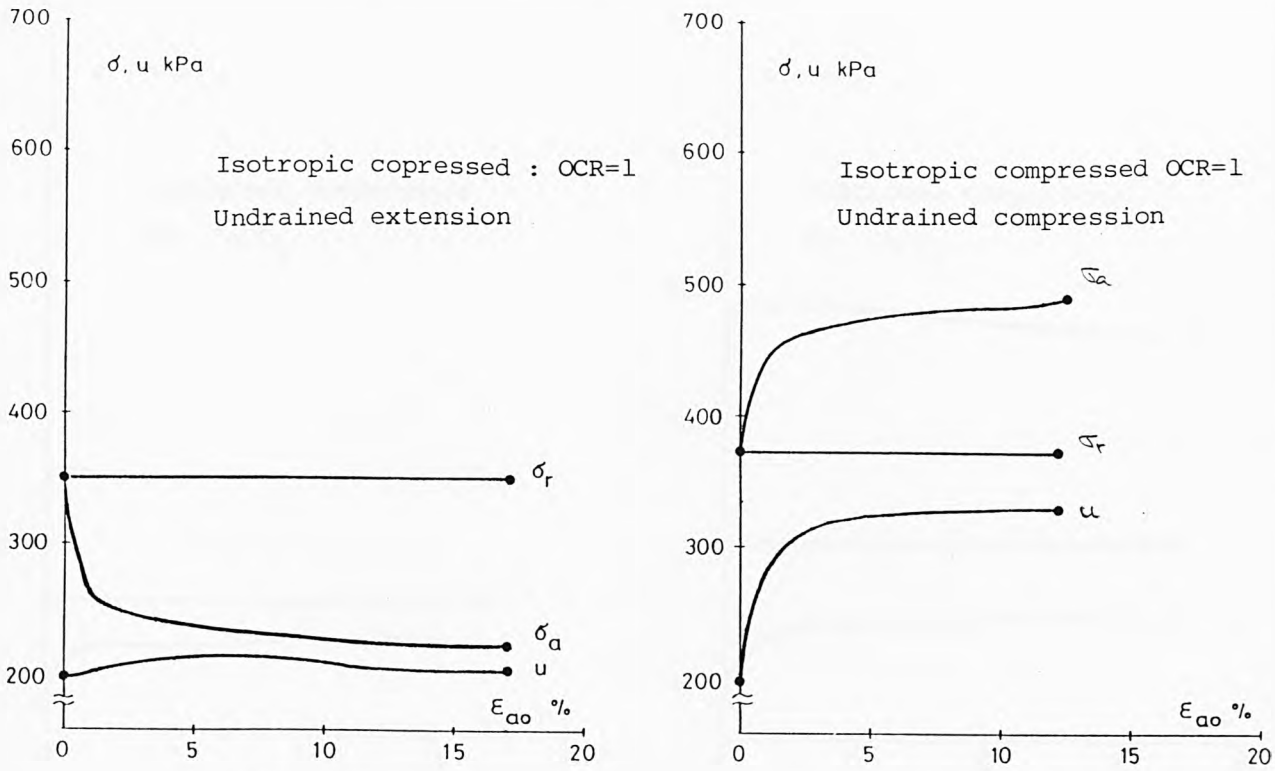

(i) GR-9

(j) GR-10

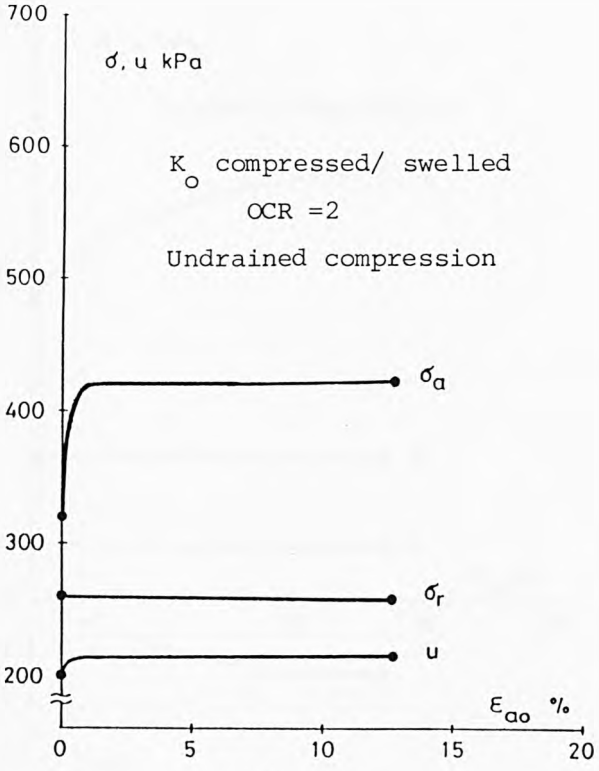

(k) GR-11

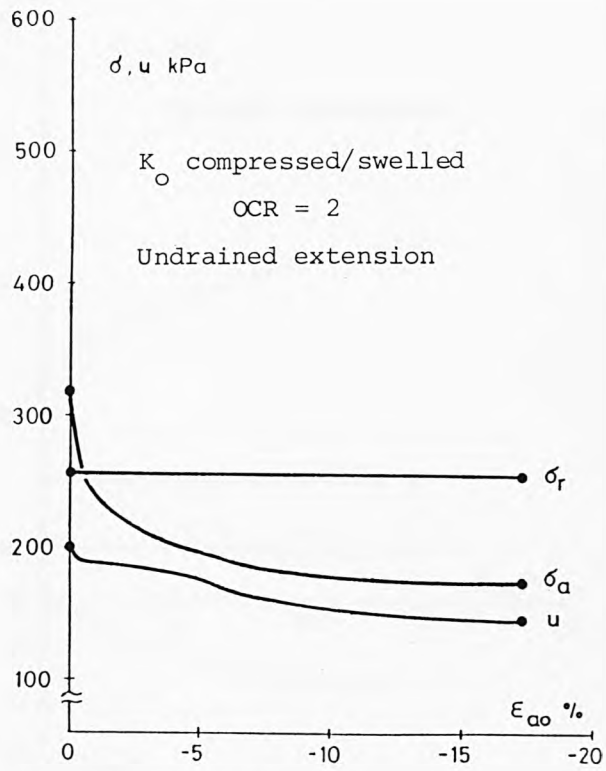

(l) GR-12

Fig. 8.13 The basic shearing test results of the GME reconstituted specimens.

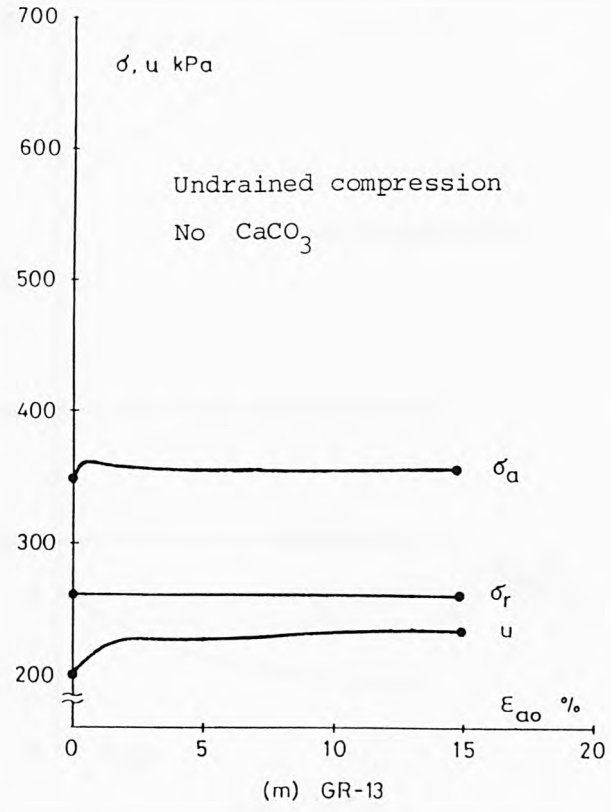

(m) GR-13

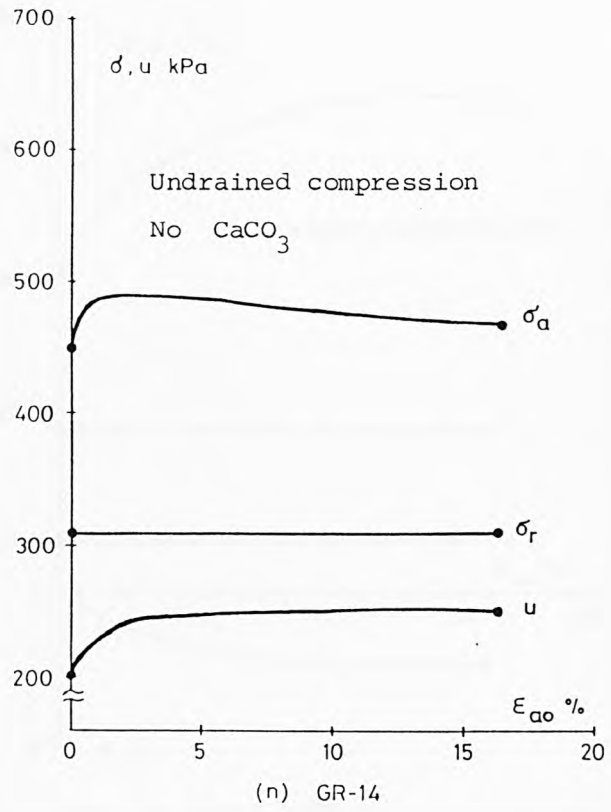

(n) GR-14

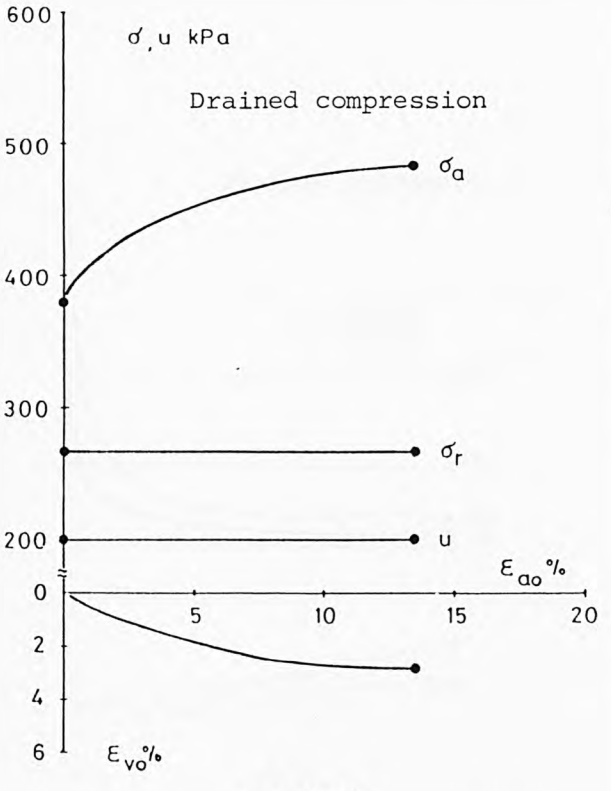

(o) GR-15

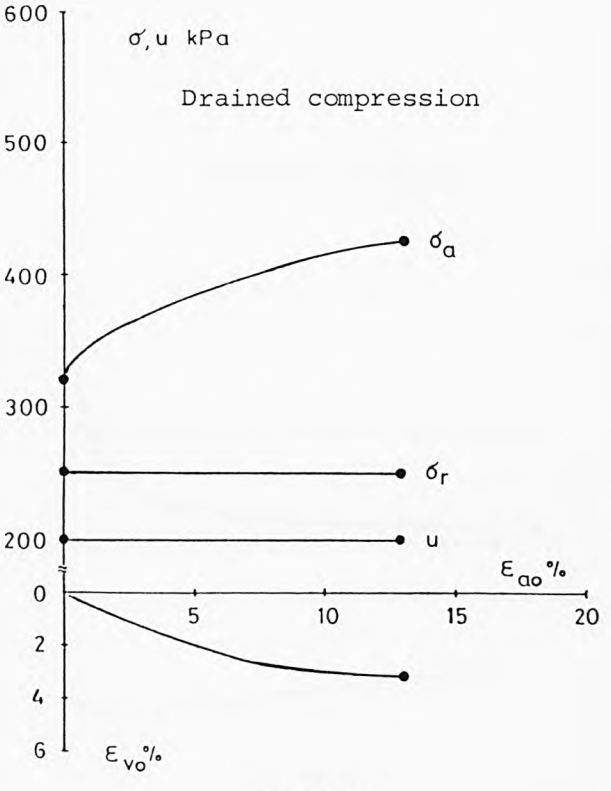

(p) GR-17

Fig. 8.13 The basic shearing test results of the GME reconstituted specimens.

(K_o compressed : OCR=1)

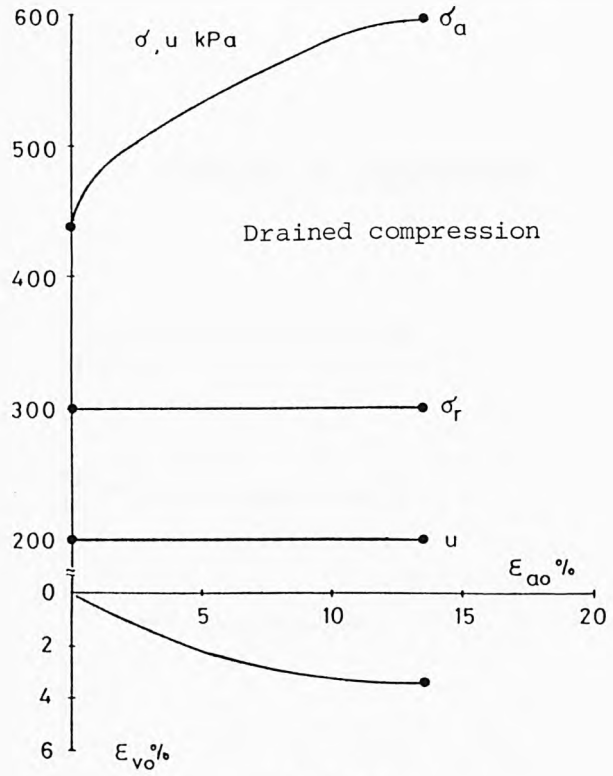

(q) GR-18

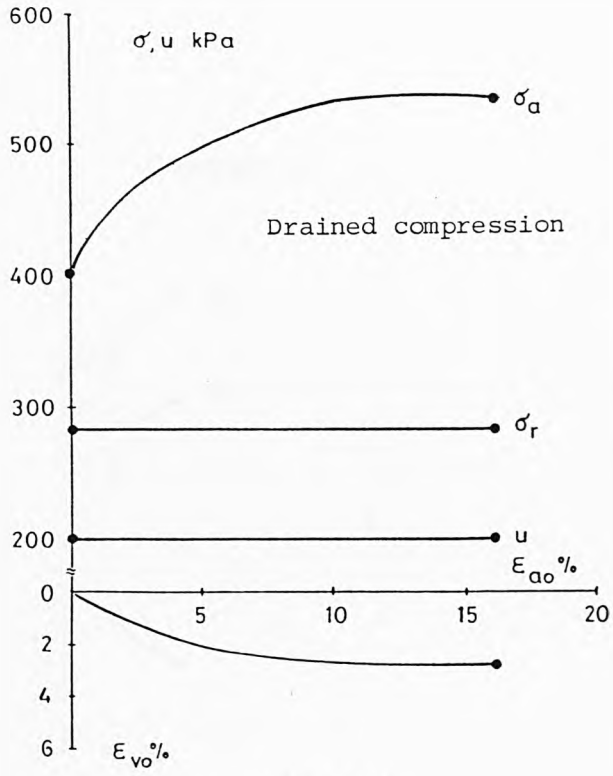

(r) GR-21

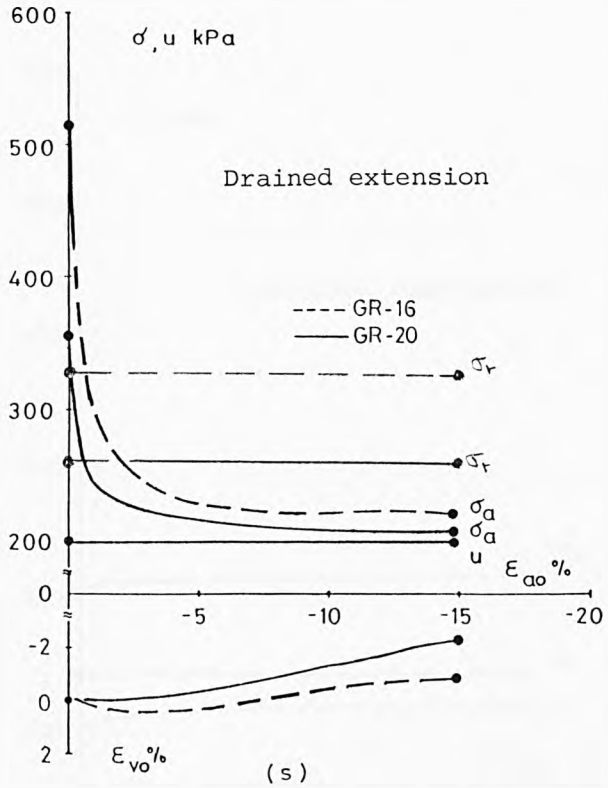

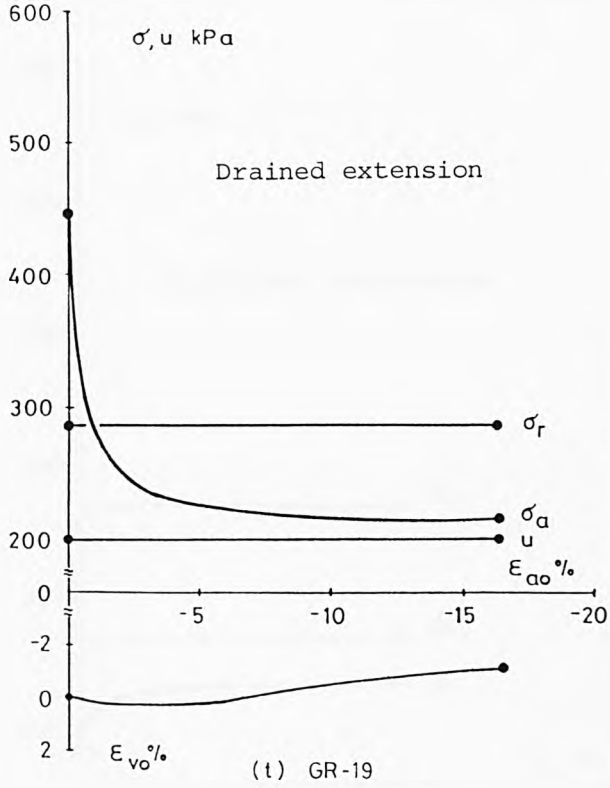

Fig. 8.13 The basic shearing test results of the GME reconstituted specimens.
(K_o compressed : OCR=1)

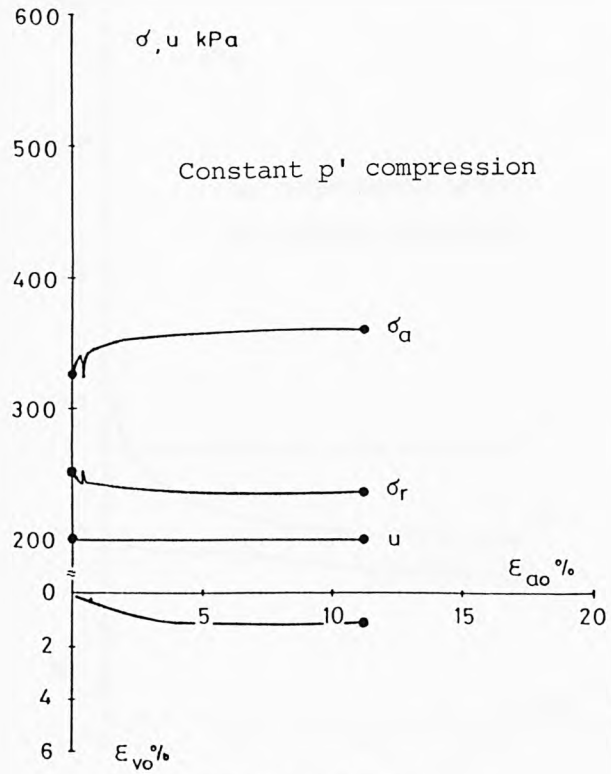

Fig. 8.13 (u) GR-23

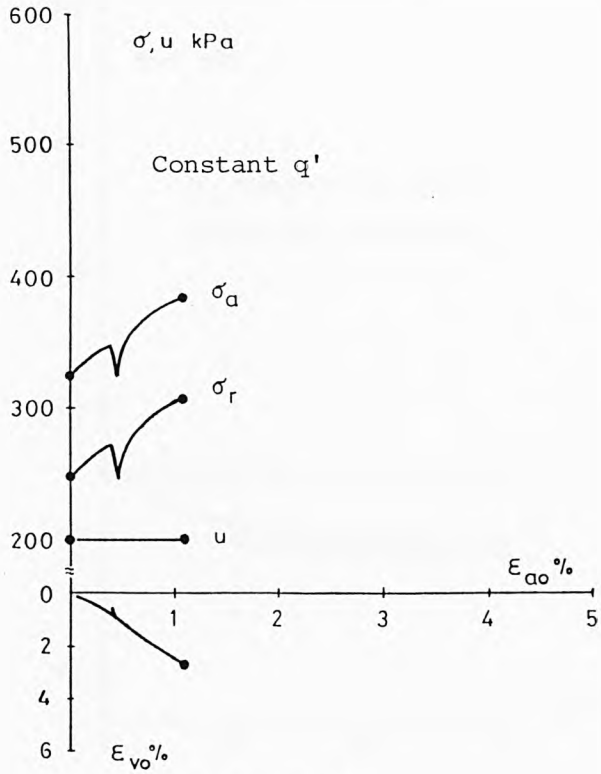

Fig. 8.13 (v) GR-22

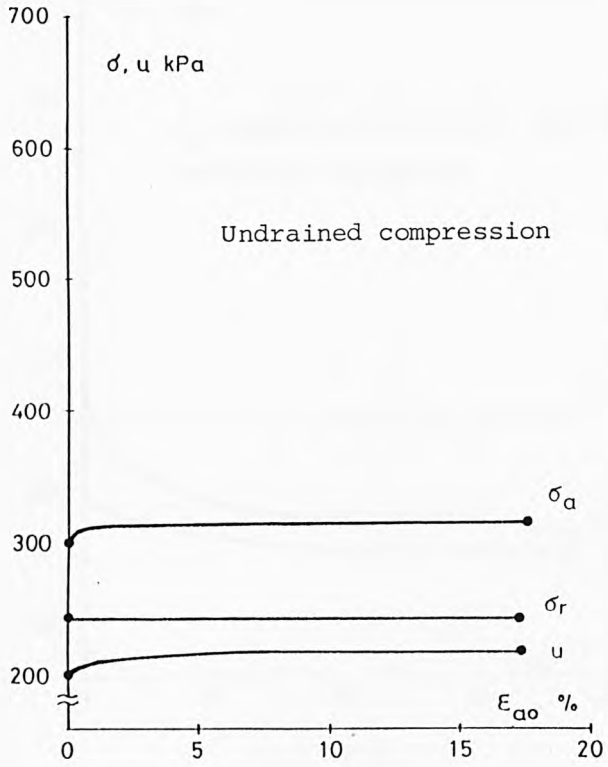

(a) NR-1

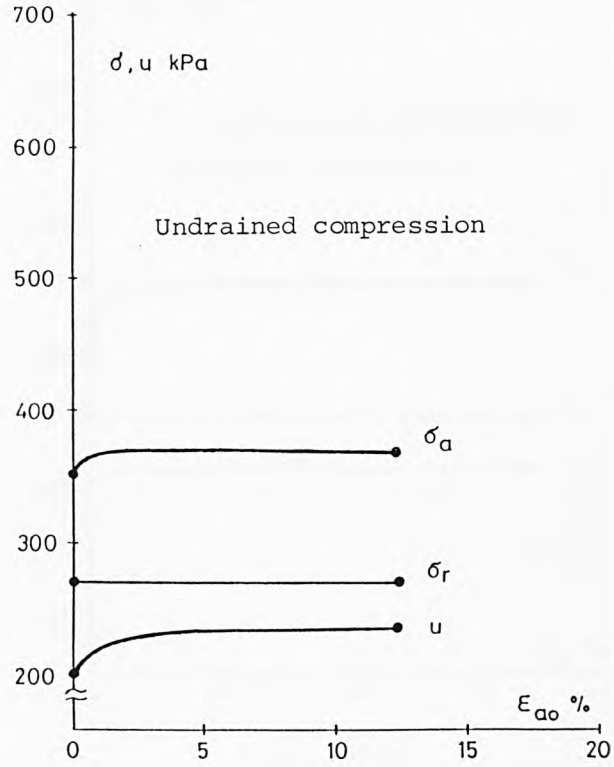

(b) NR-2

Fig. 8.14 The basic shearing test results of the NAP reconstituted specimens.
(K_o compressed : OCR=1)

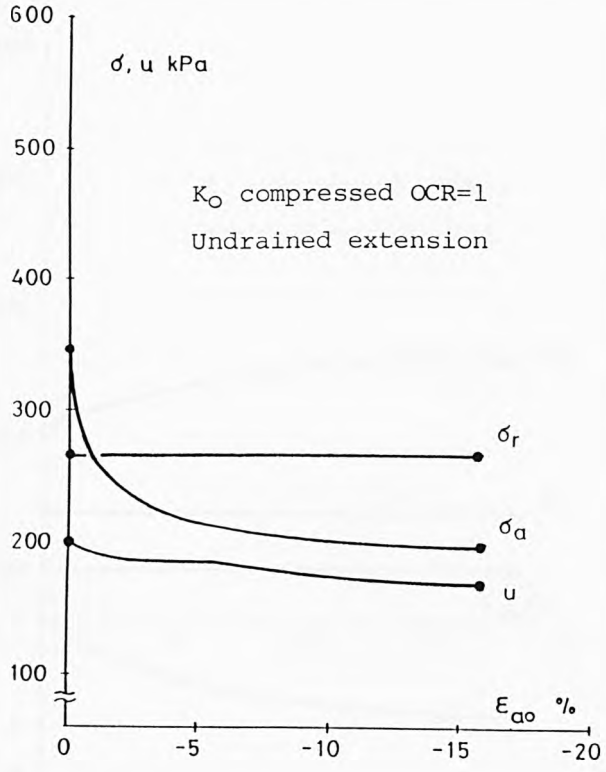

(c) NR-3

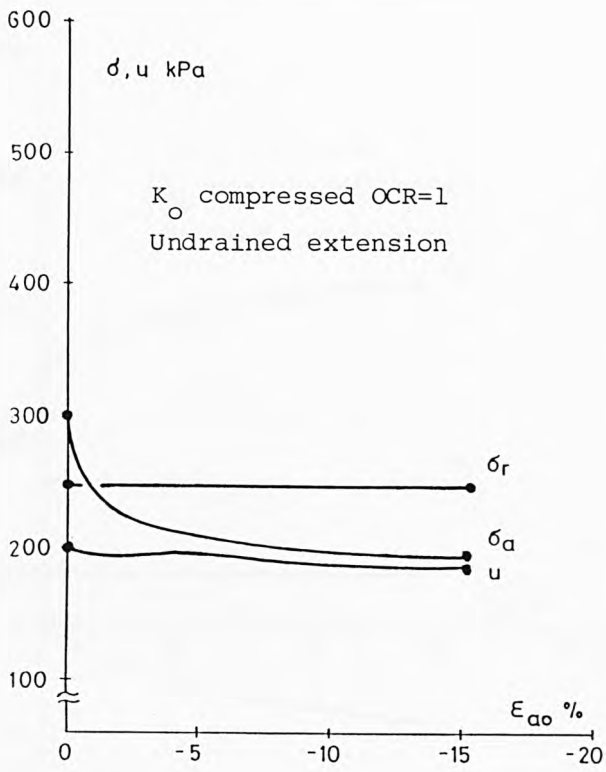

(d) NR-4

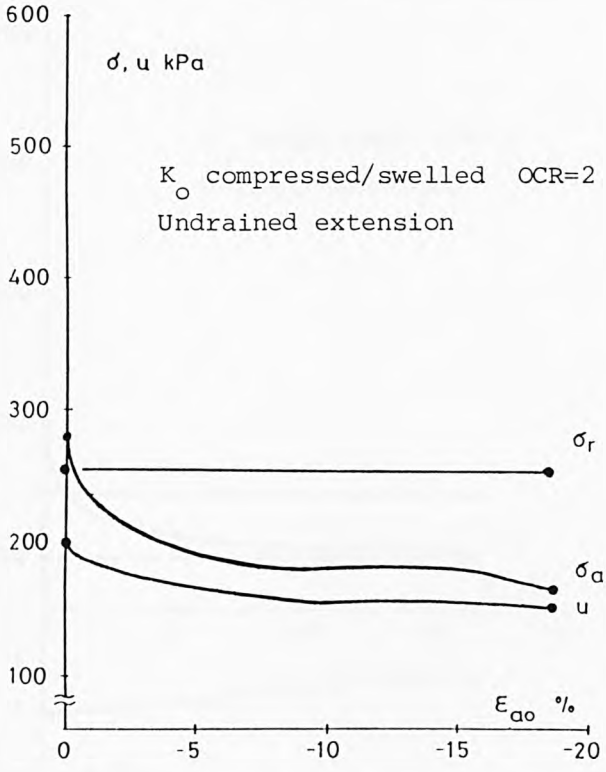

(e) NR-5

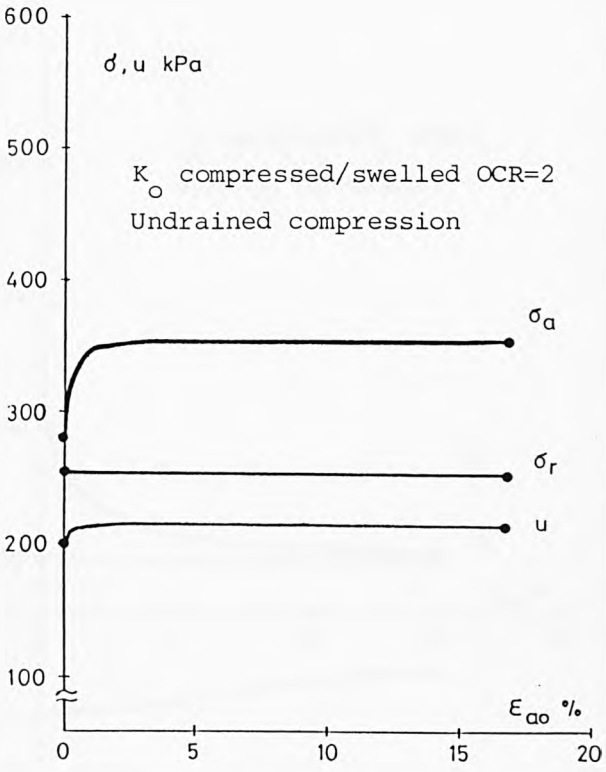

(f) NR-6

Fig. 8.14 The basic shearing test results of the NAP reconstituted specimens.

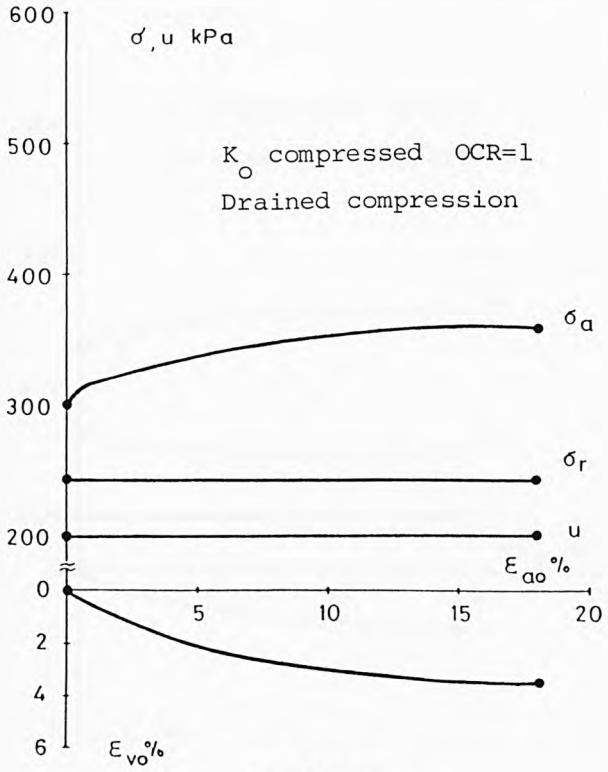

(g) NR-7

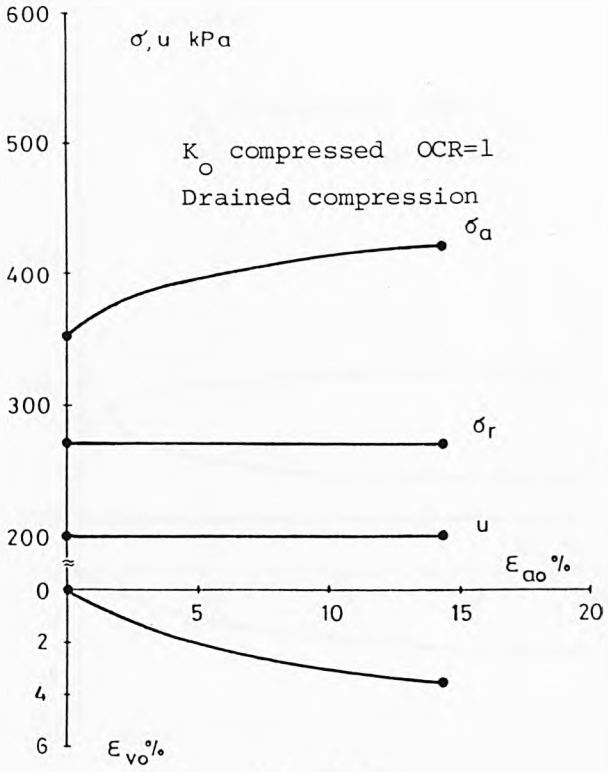

(h) NR-8

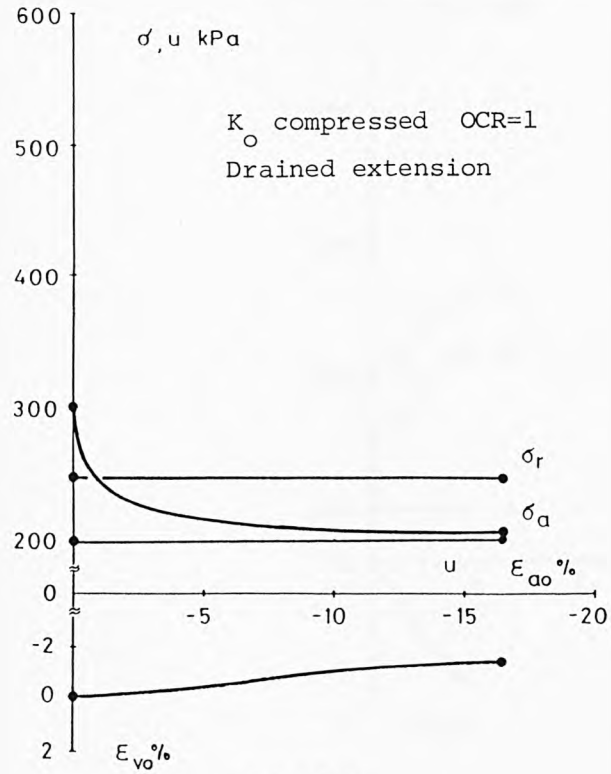

(i) NR-9

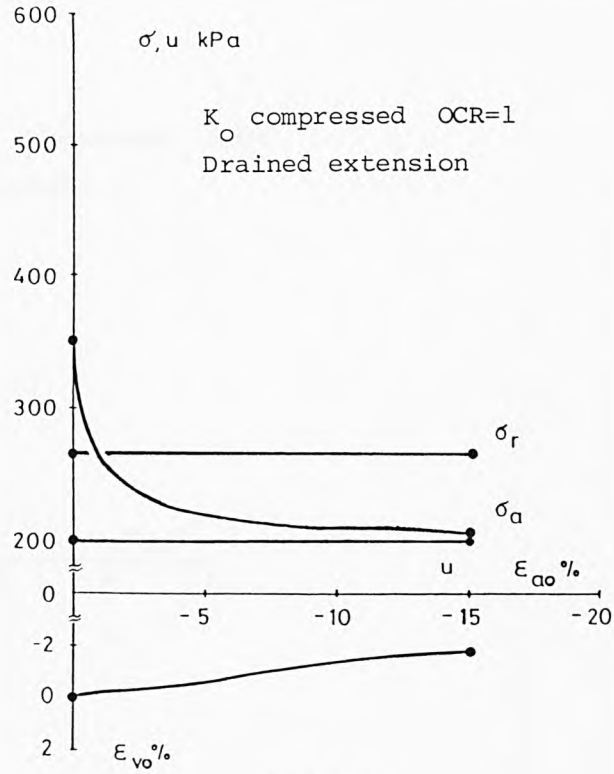

(j) NR-10

Fig. 8.14 The basic shearing test results of the NAP reconstituted specimens.

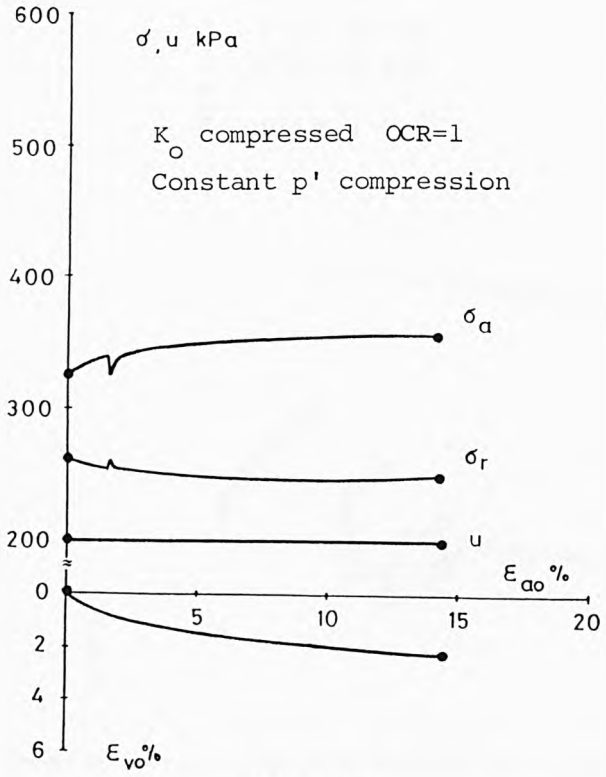

(k) NR-12

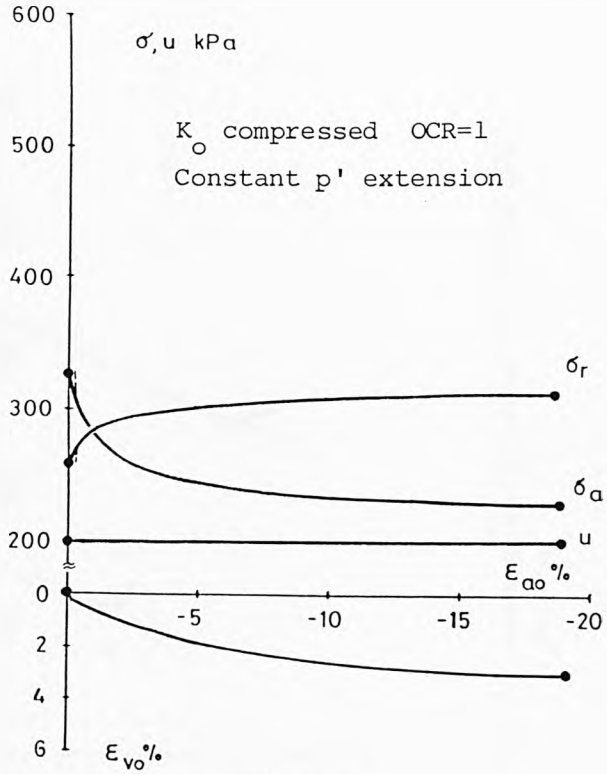

(l) NR-13

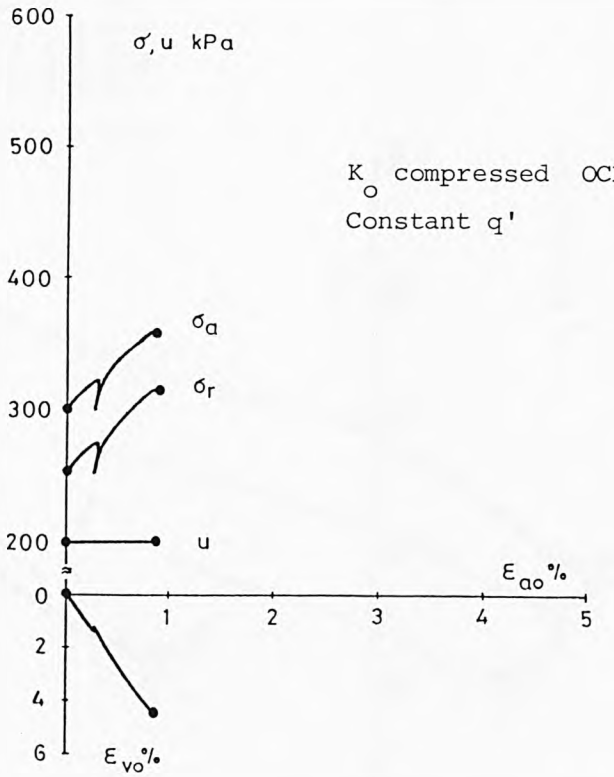

(m) NT-11

Fig. 8.14 The basic shearing test results of the NAP reconstituted specimens.

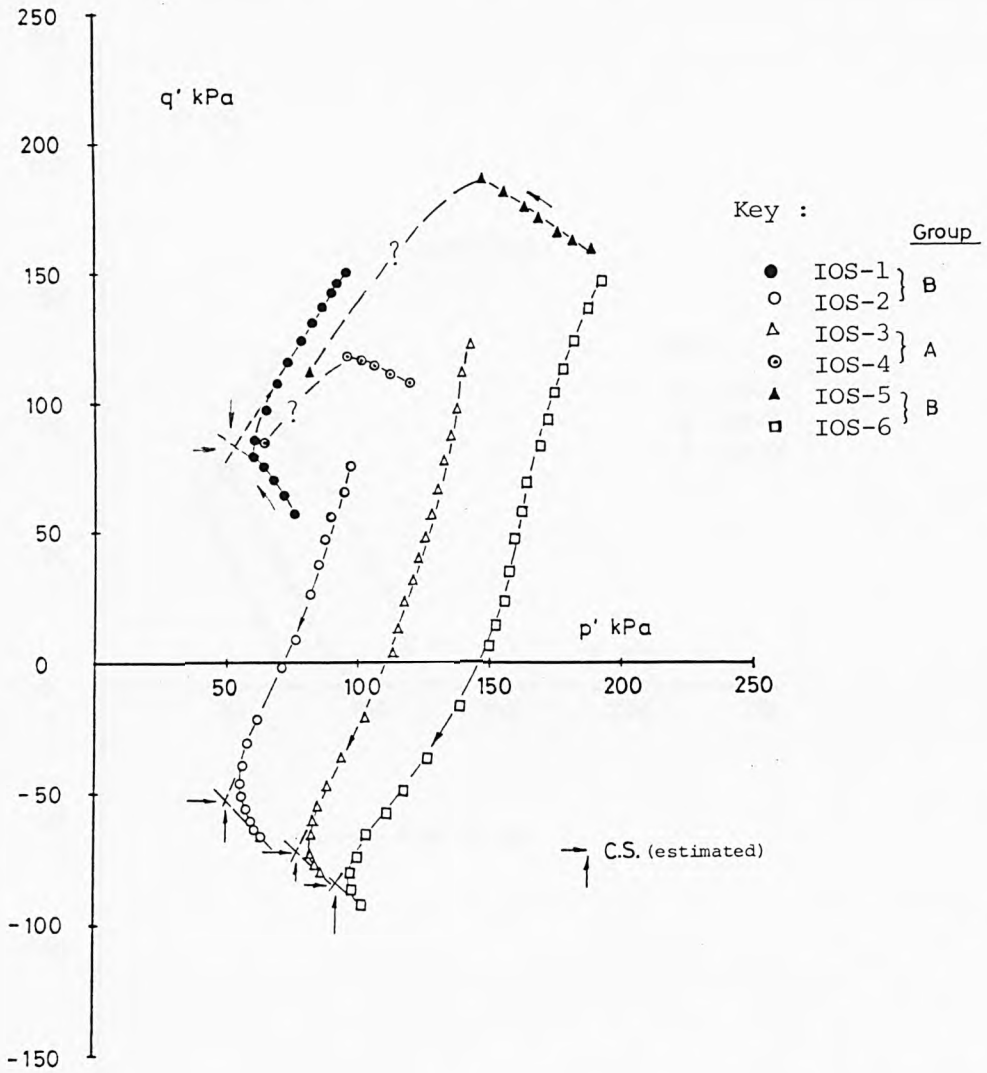

Fig. 8.15 Undrained effective stress paths for IOS tubed specimens.

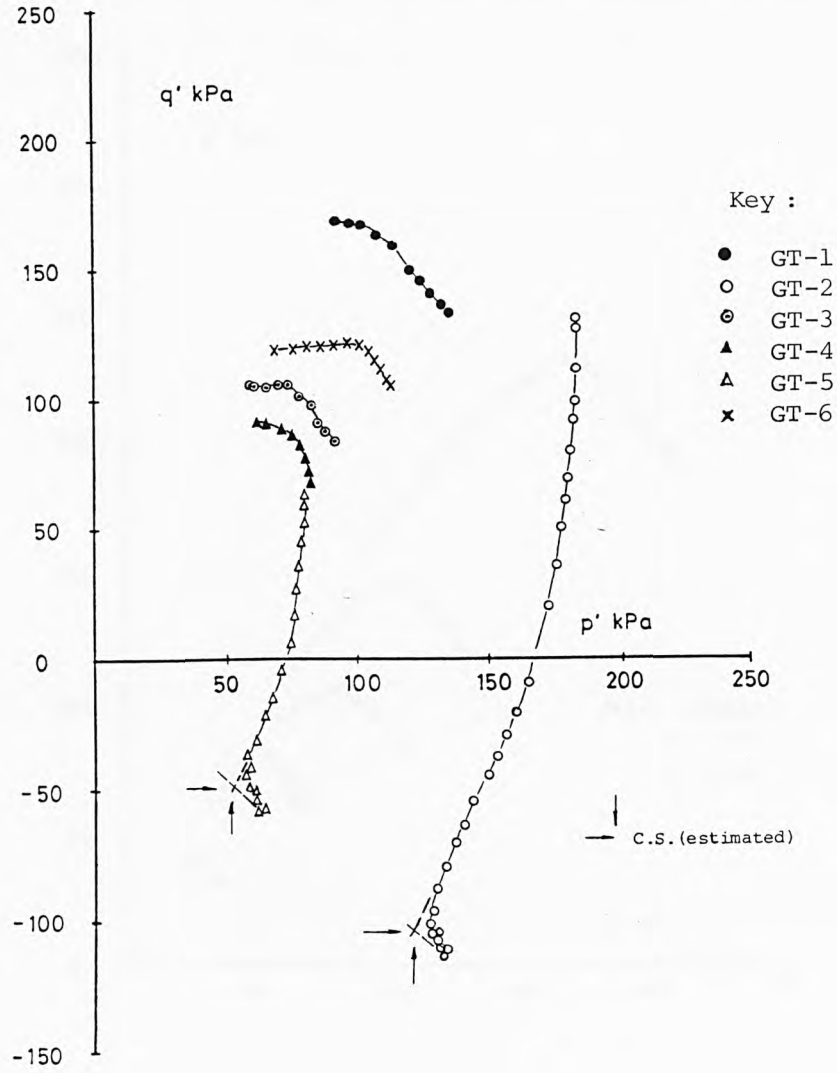

Fig. 8.16a Undrained effective stress paths for GME tubed specimens.

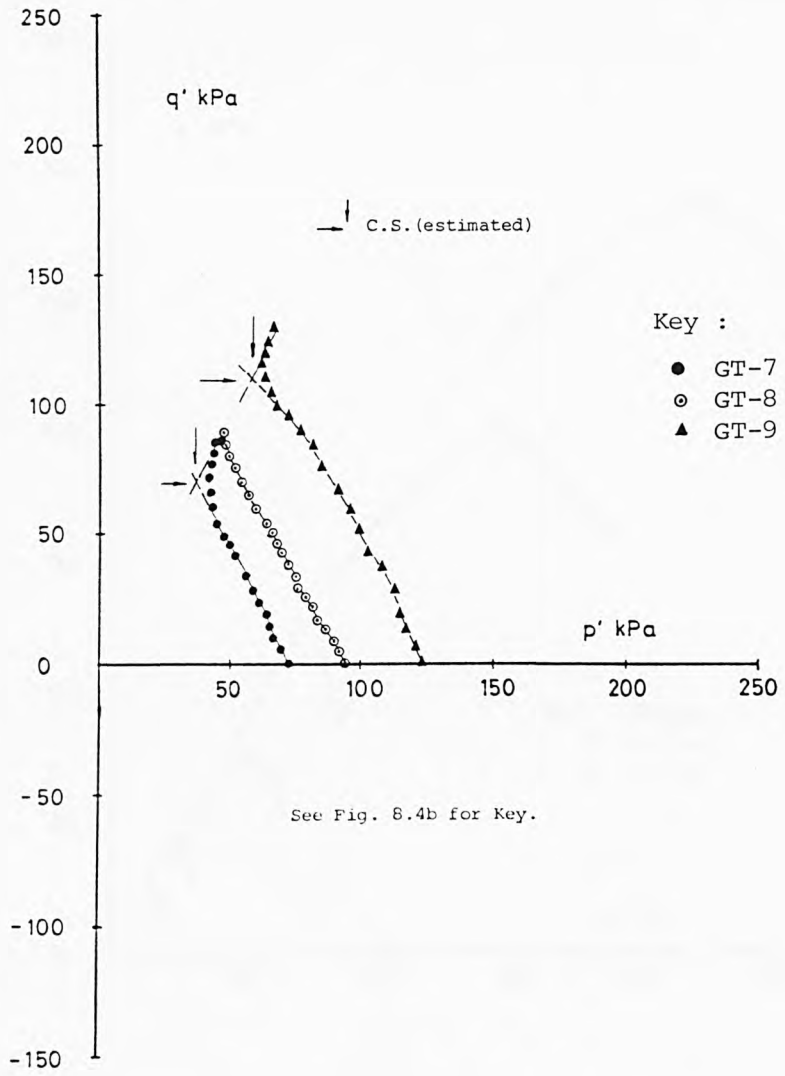

Fig. 8.16b Undrained effective stress paths for GME tubed specimens.

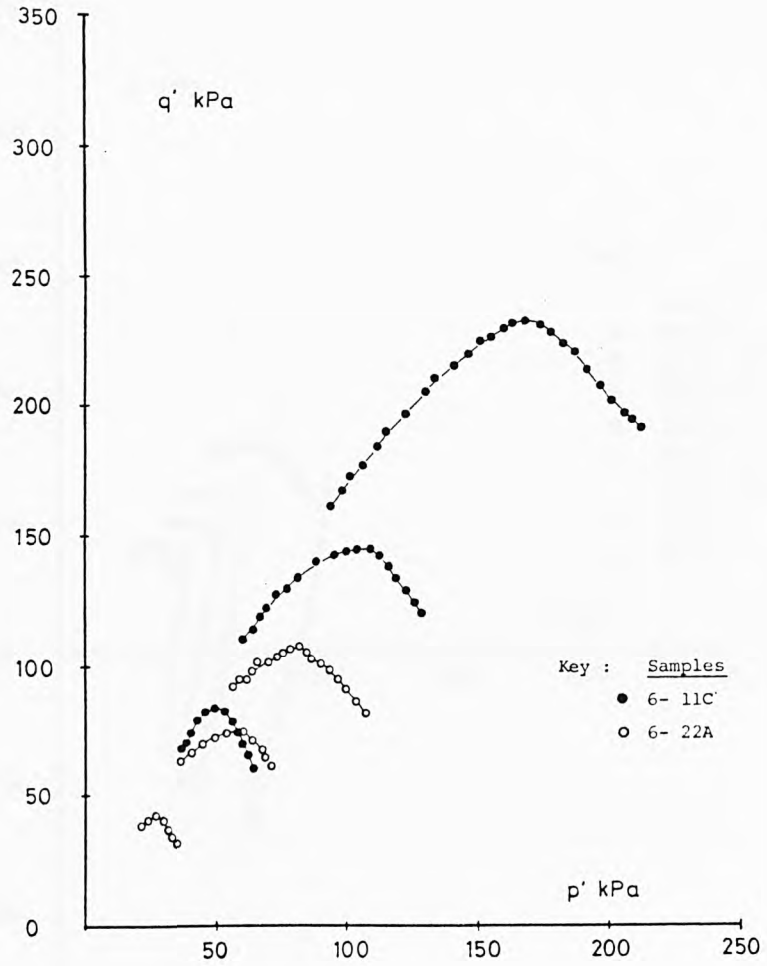

Fig.8.17a Undrained effective stress paths for GME C-6 tubed specimens.

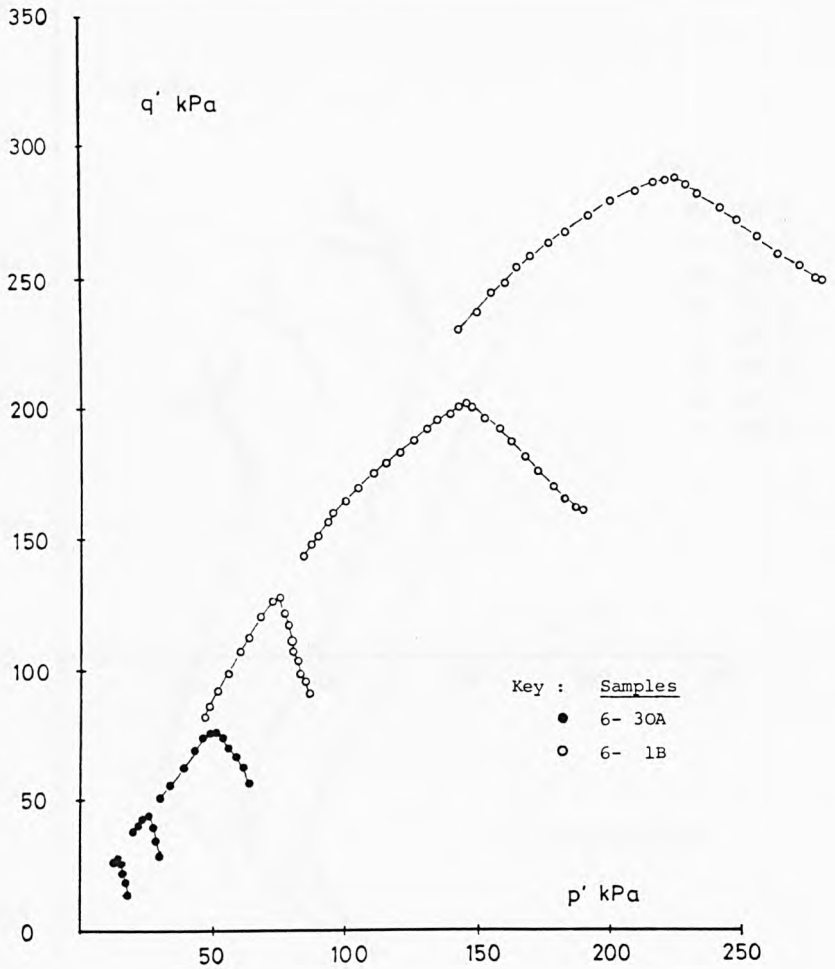

Fig.8.17b Undrained effective stress paths for GME C-6 tubed specimens.

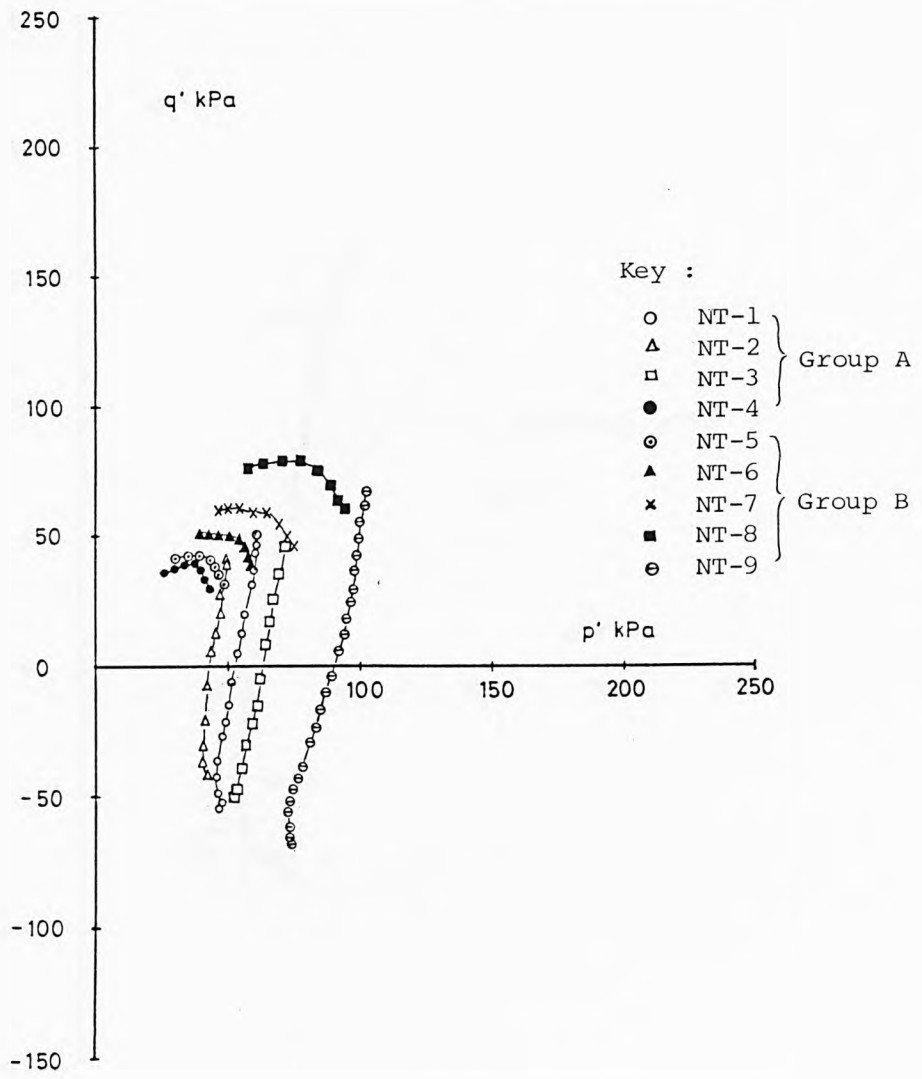

Fig.8.18 Undrained effective stress paths for NAP tubed specimens.

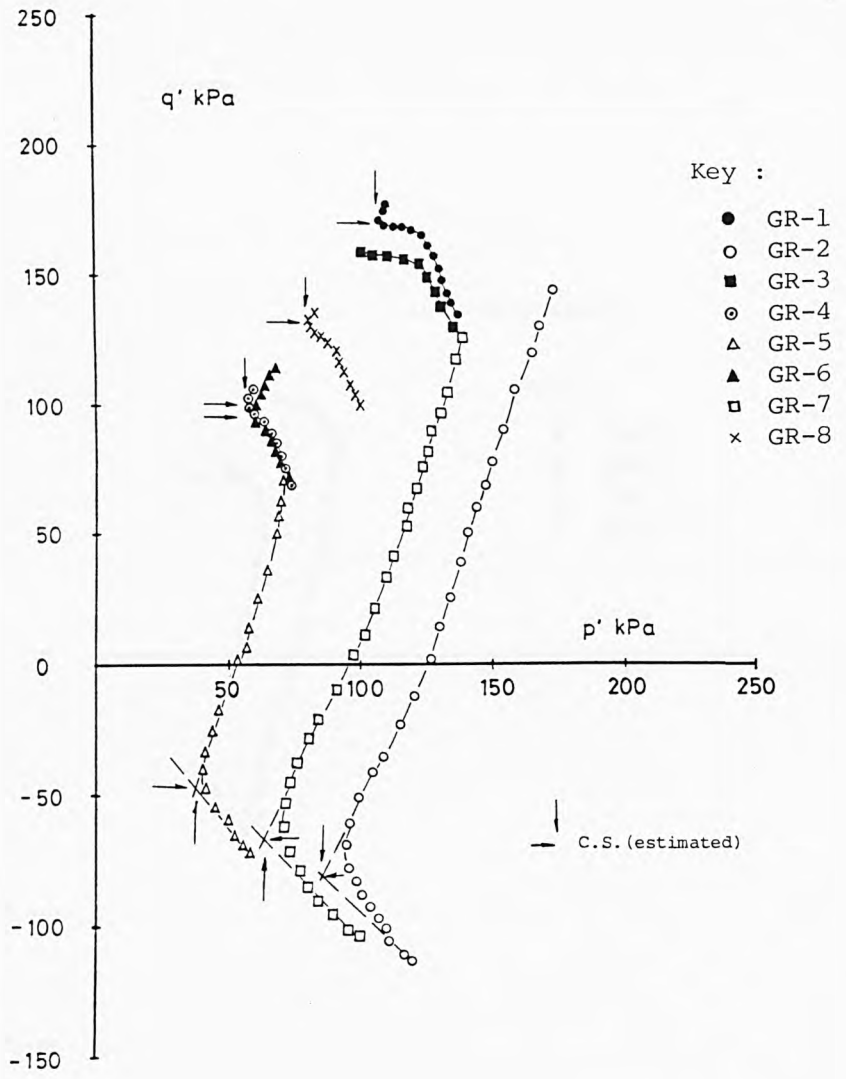

Fig. 8.19a Undrained effective stress paths for GME reconstituted specimens.

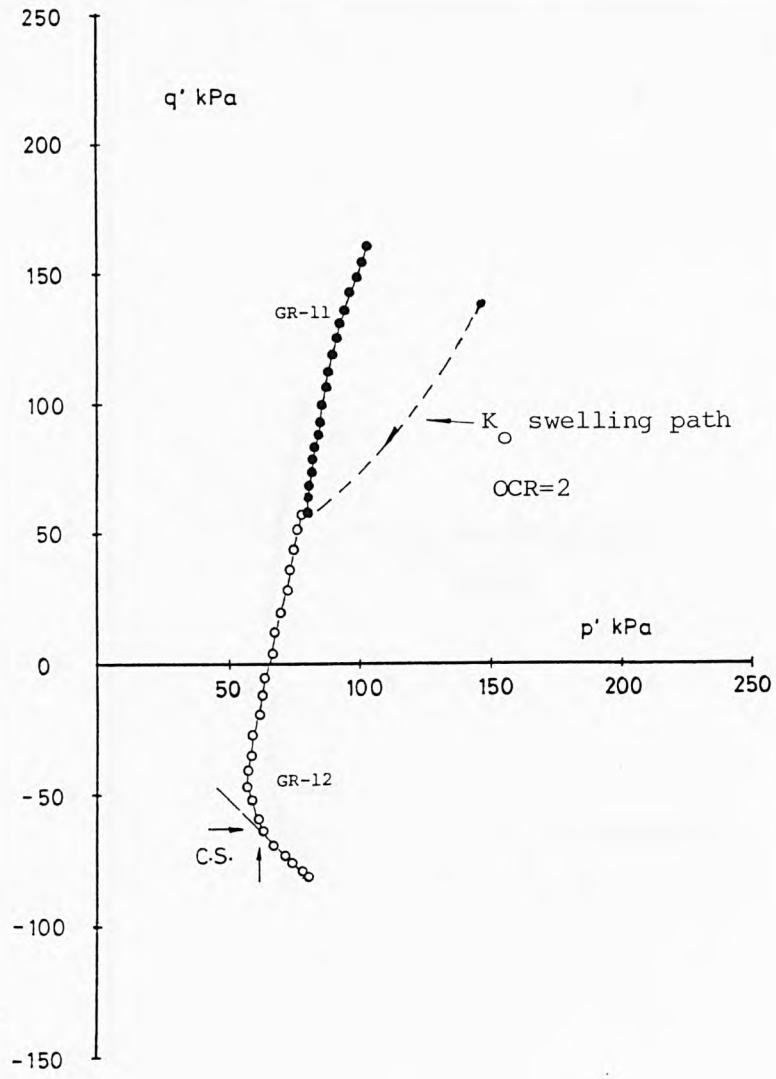

Fig. 8.19b Undrained effective stress paths for GME reconstituted specimens.

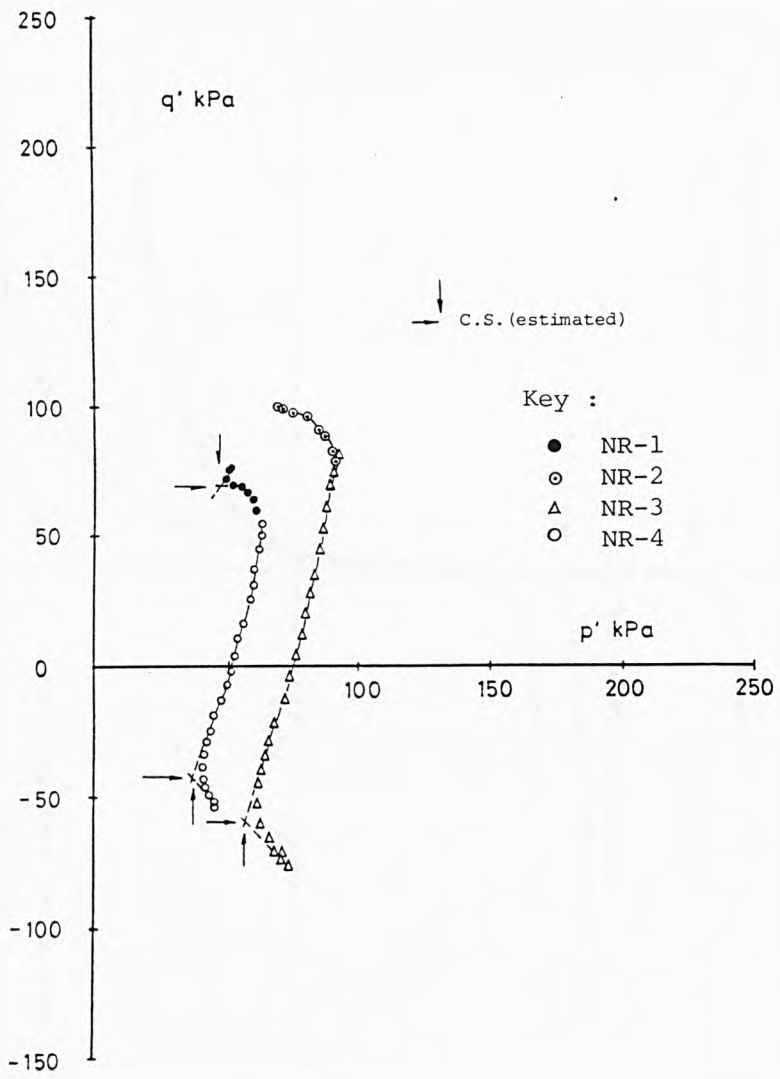

Fig. 8.20a Undrained effective stress paths for NAP reconstituted specimens.

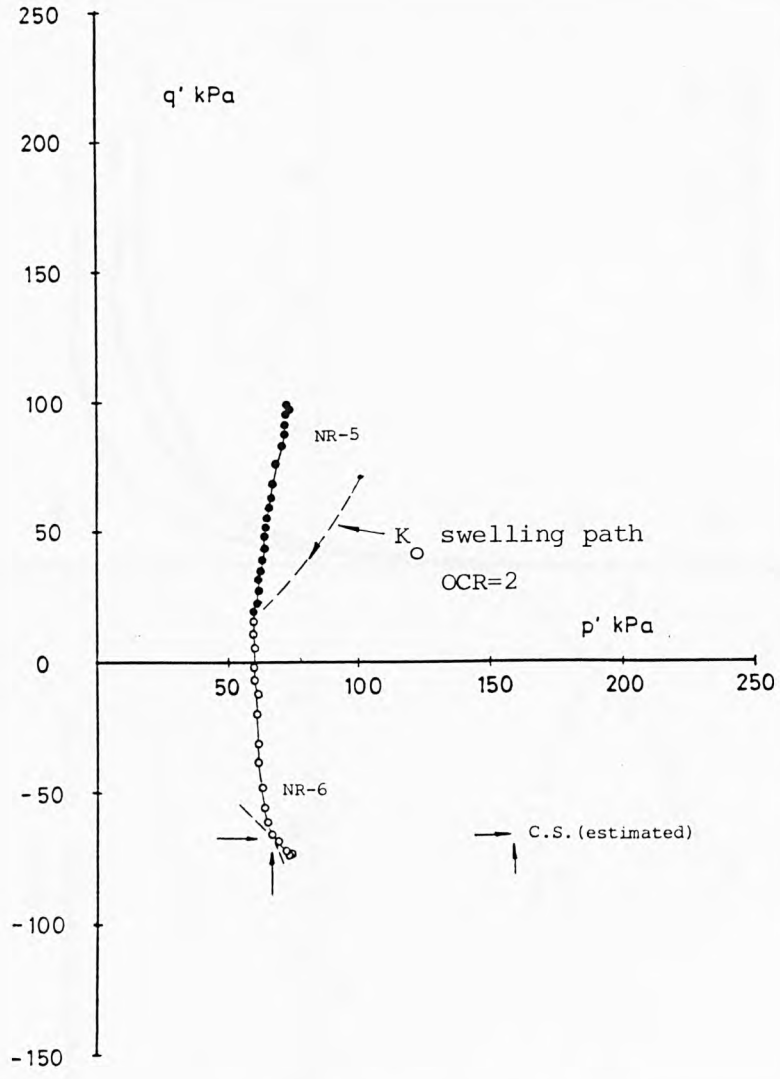

Fig. 8.20b Undrained effective stress paths for NAP reconstituted specimens.

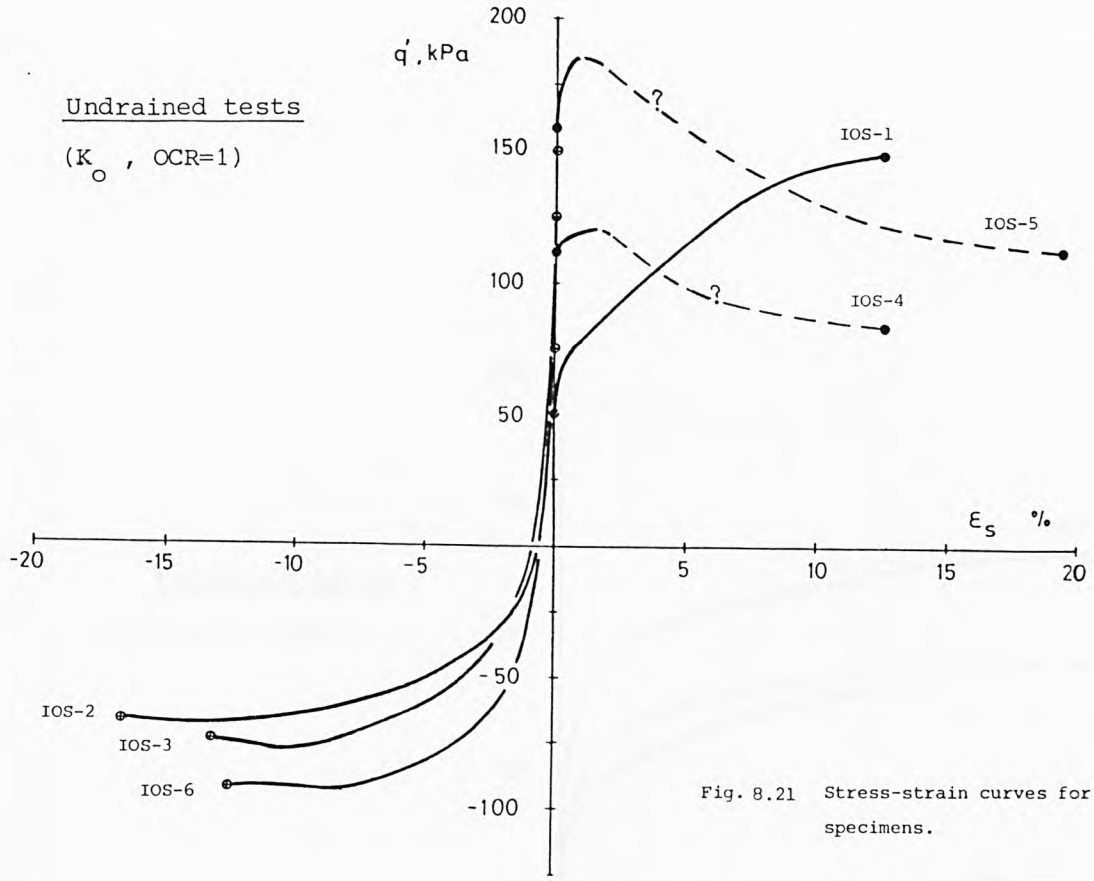

Fig. 8.21 Stress-strain curves for IOS tubed specimens.

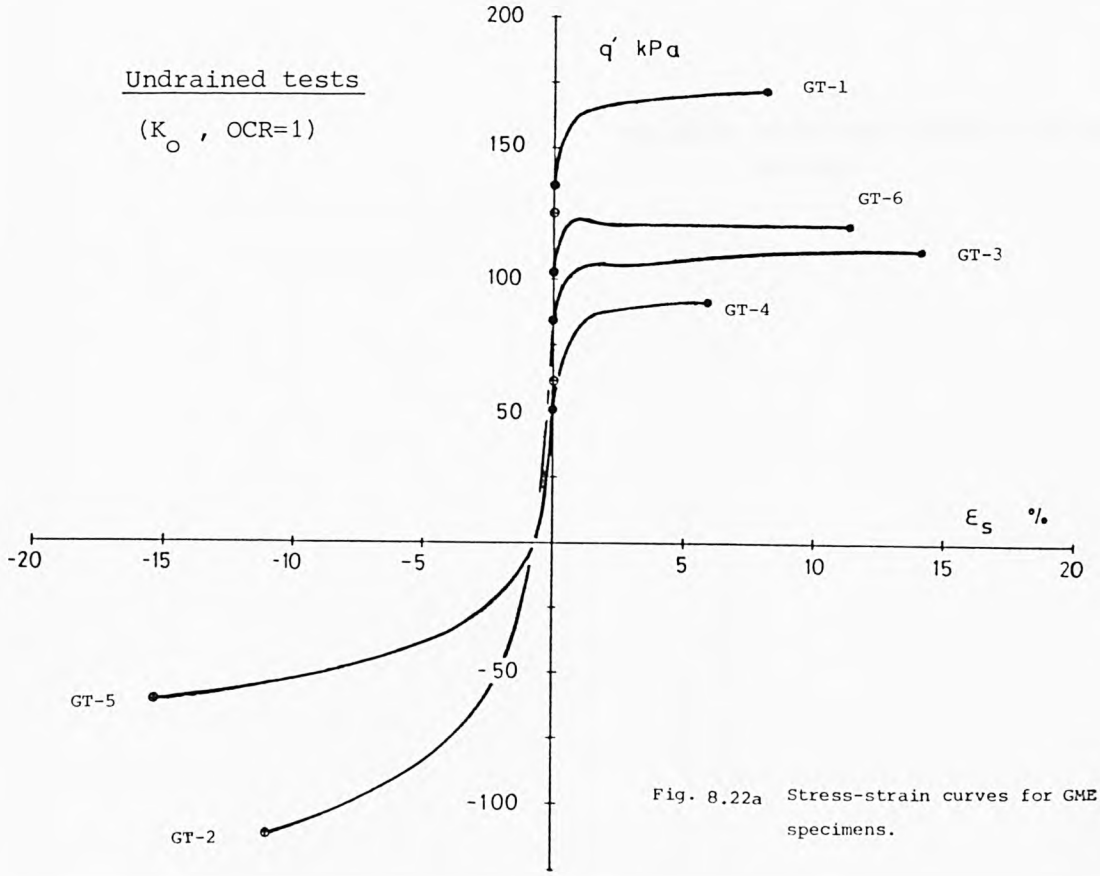

Fig. 8.22a Stress-strain curves for GME tubed specimens.

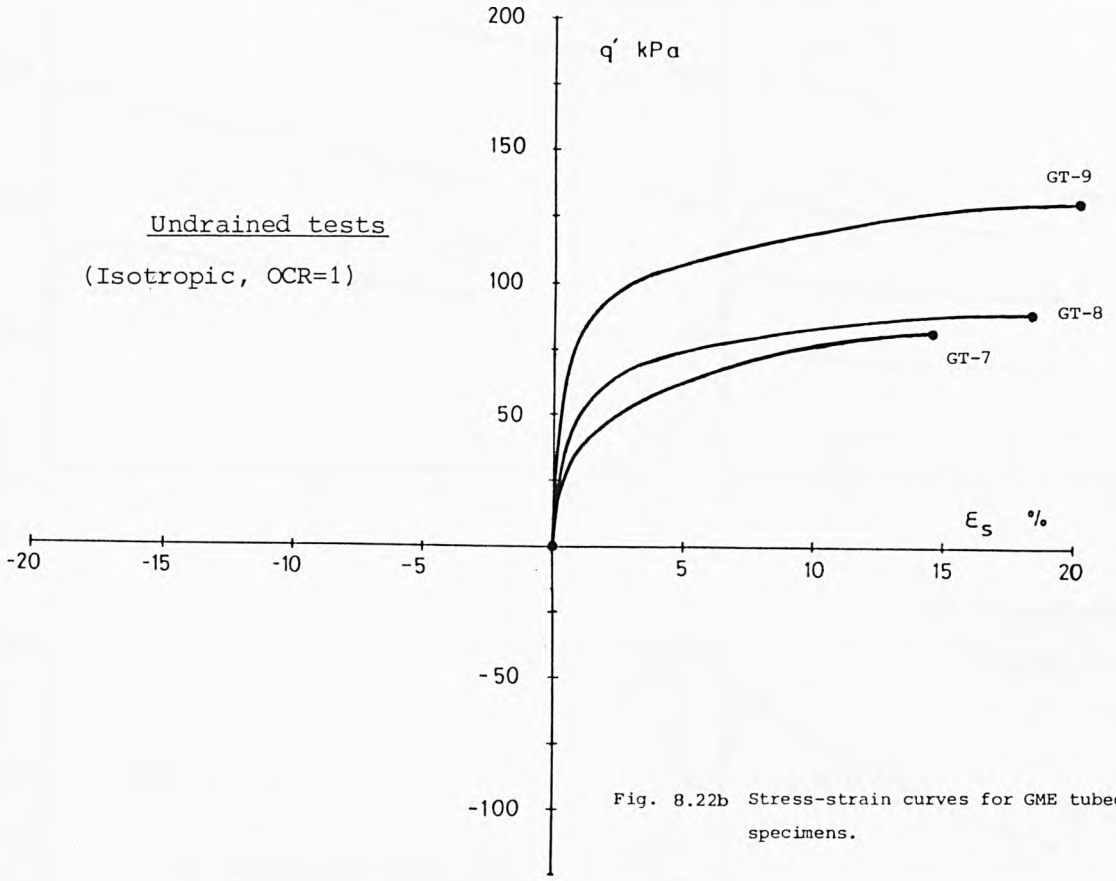

Fig. 8.22b Stress-strain curves for GME tubed specimens.

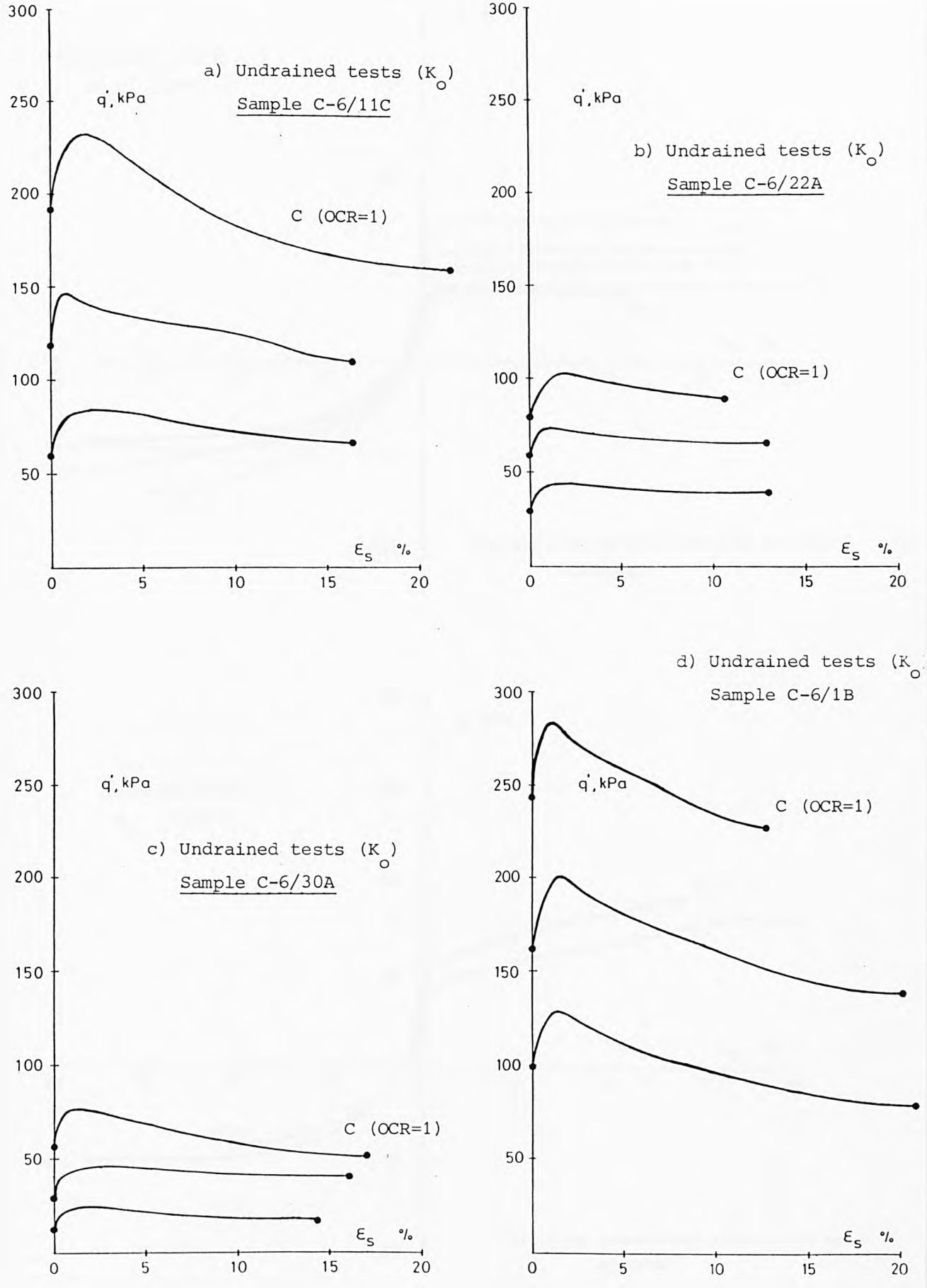

Fig. 8.23 Stress-strain curves for the GME C-6 tubed specimens.

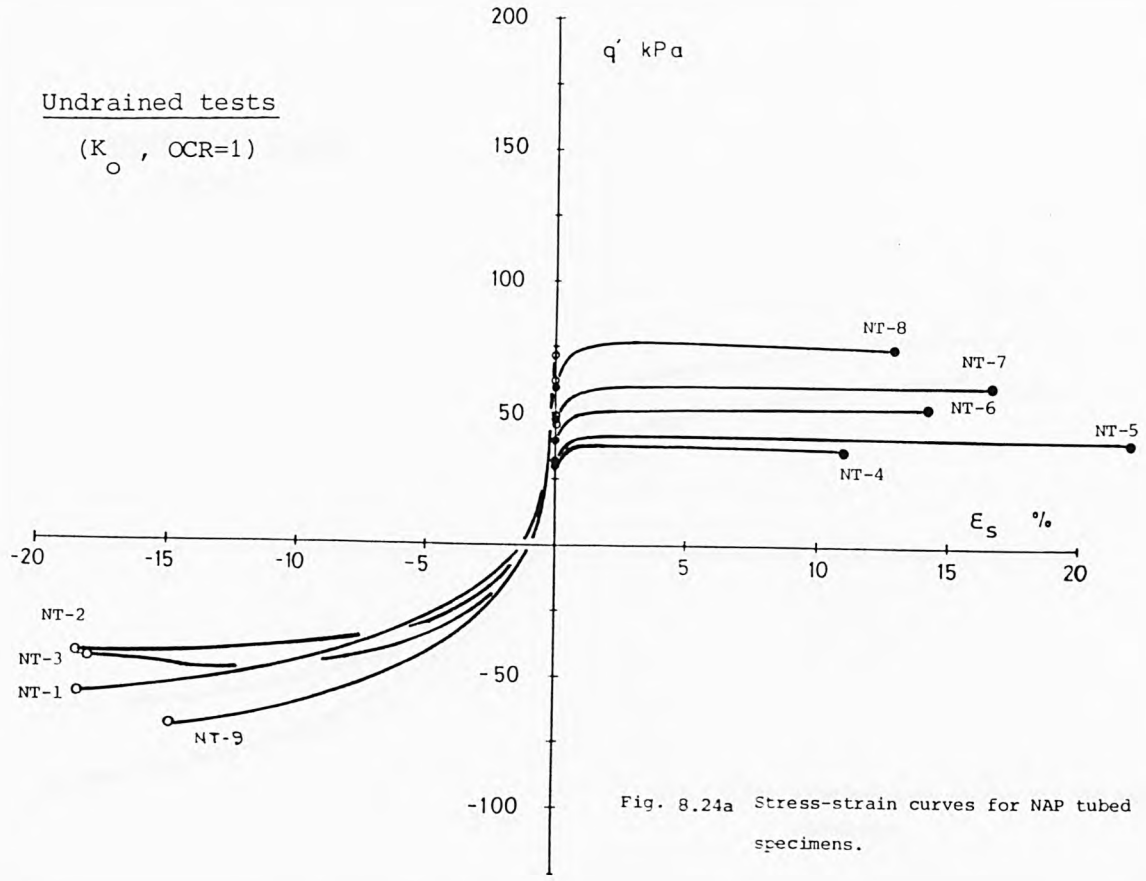

Fig. 8.24a Stress-strain curves for NAP tubed specimens.

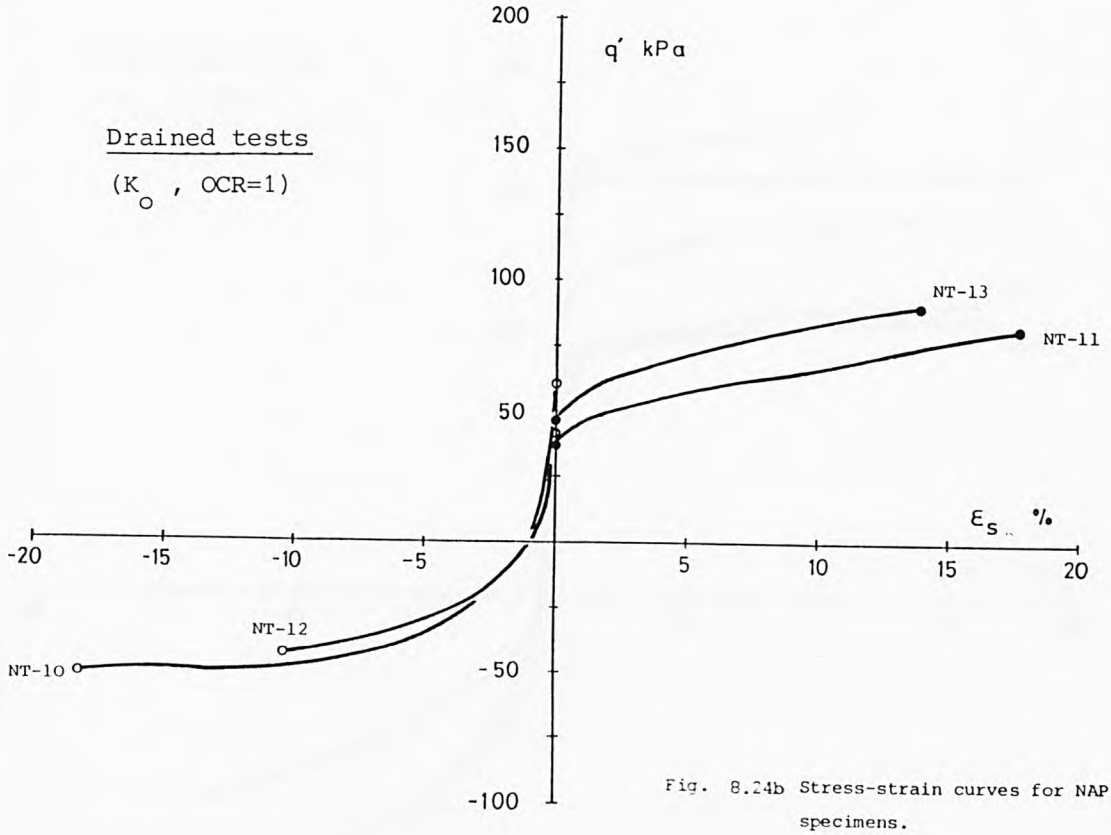

Fig. 8.24b Stress-strain curves for NAP tubed specimens.

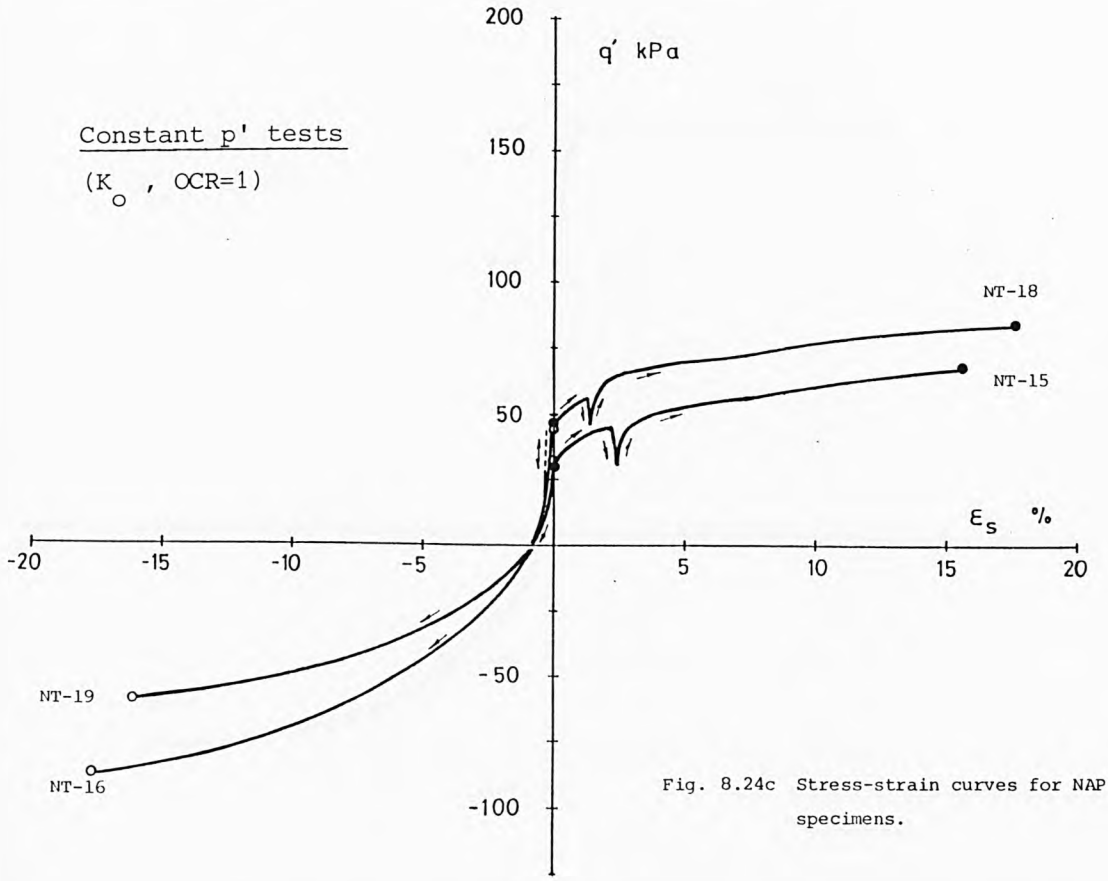

Fig. 8.24c Stress-strain curves for NAP tubed specimens.

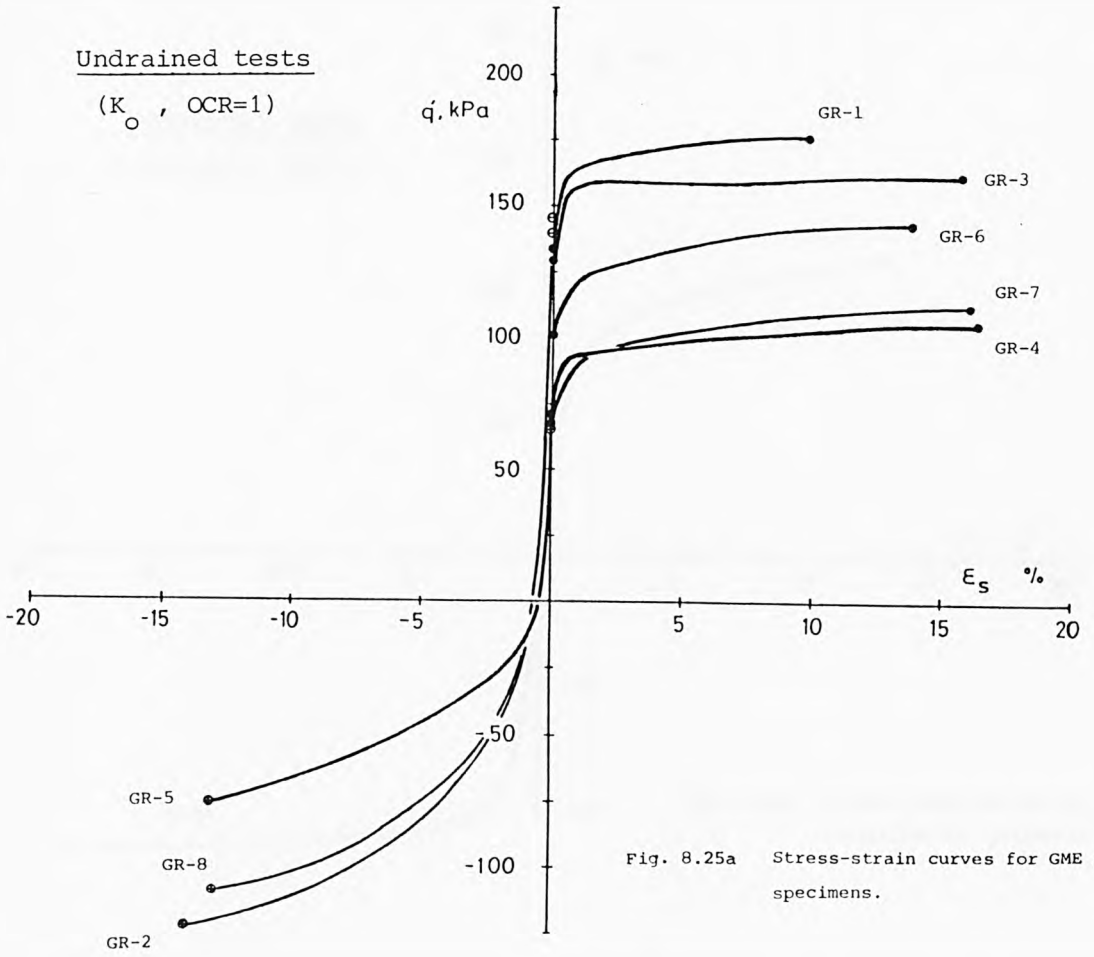

Fig. 8.25a Stress-strain curves for GME reconstituted specimens.

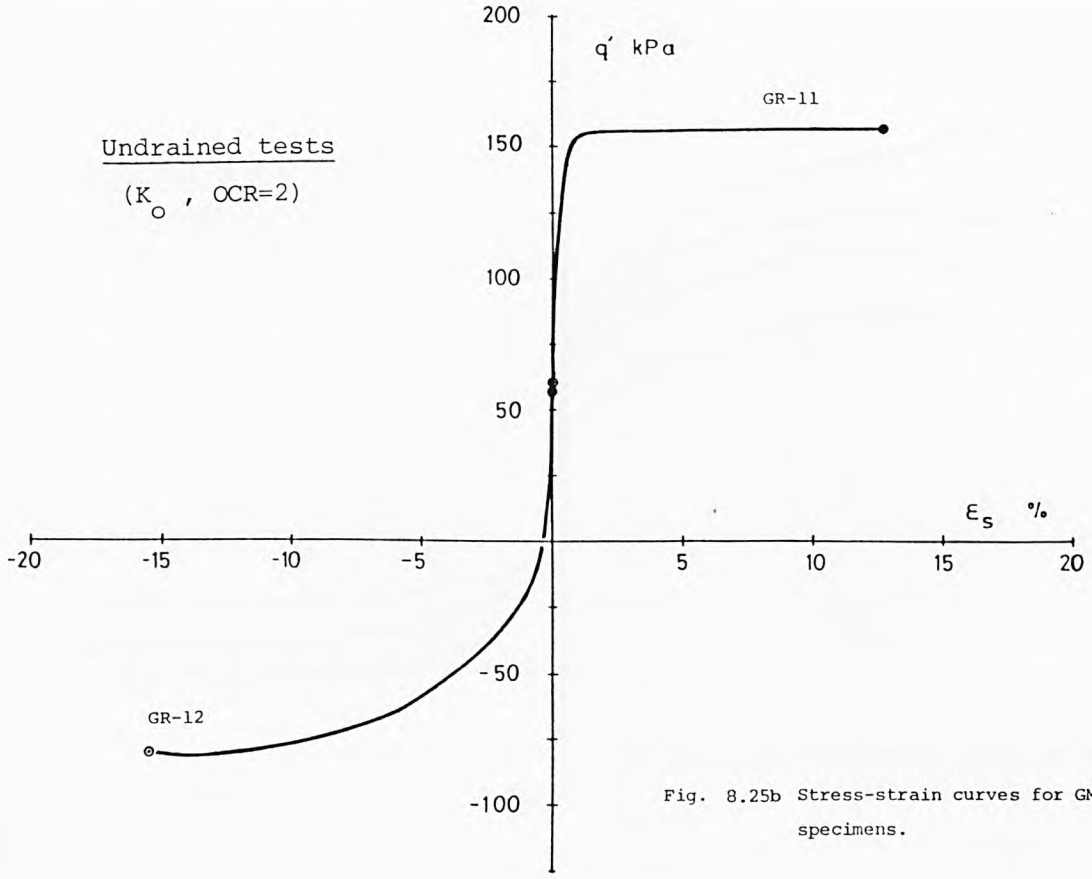

Fig. 8.25b Stress-strain curves for GME reconstituted specimens.

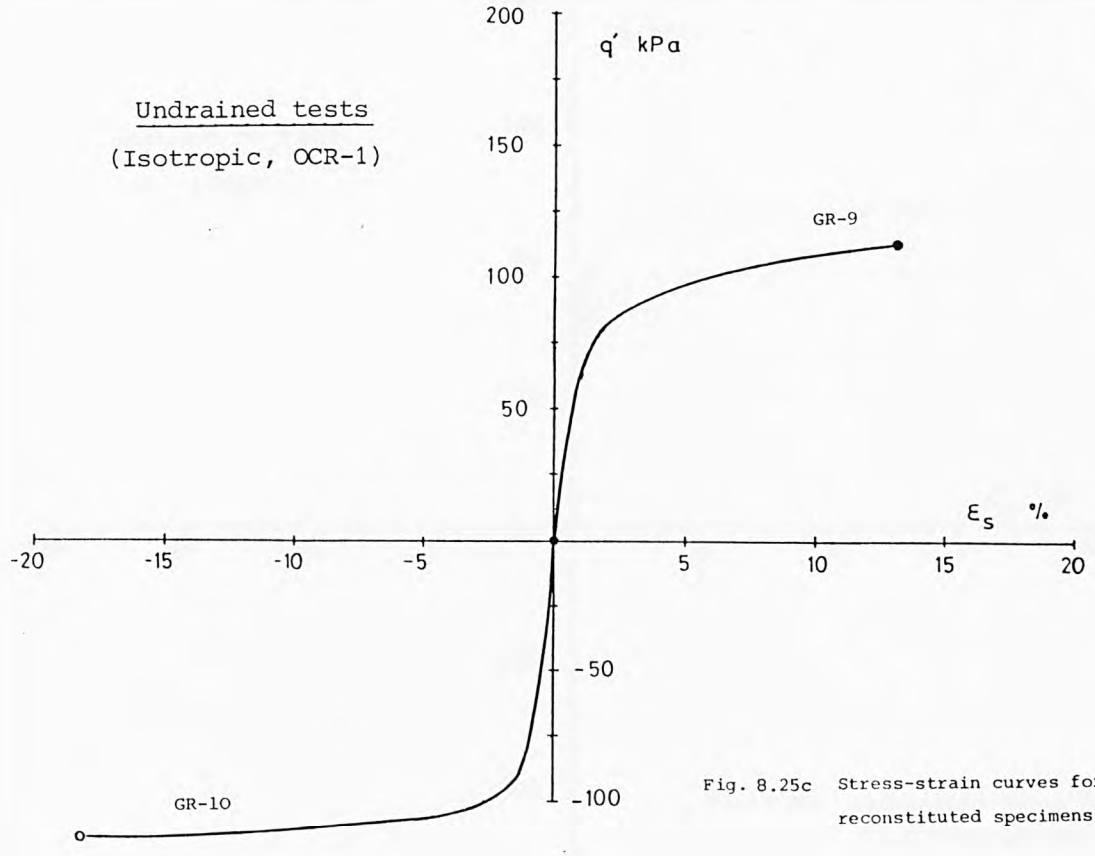

Fig. 8.25c Stress-strain curves for GME reconstituted specimens.

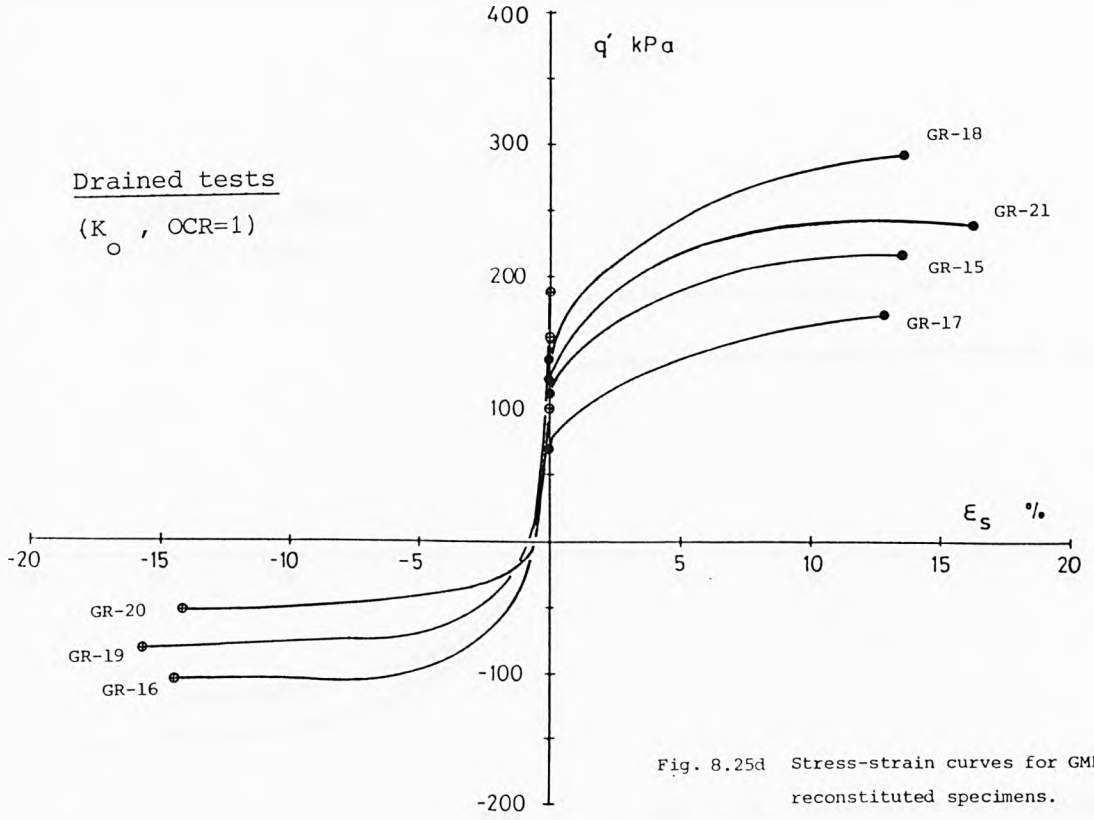

Fig. 8.25d Stress-strain curves for GME reconstituted specimens.

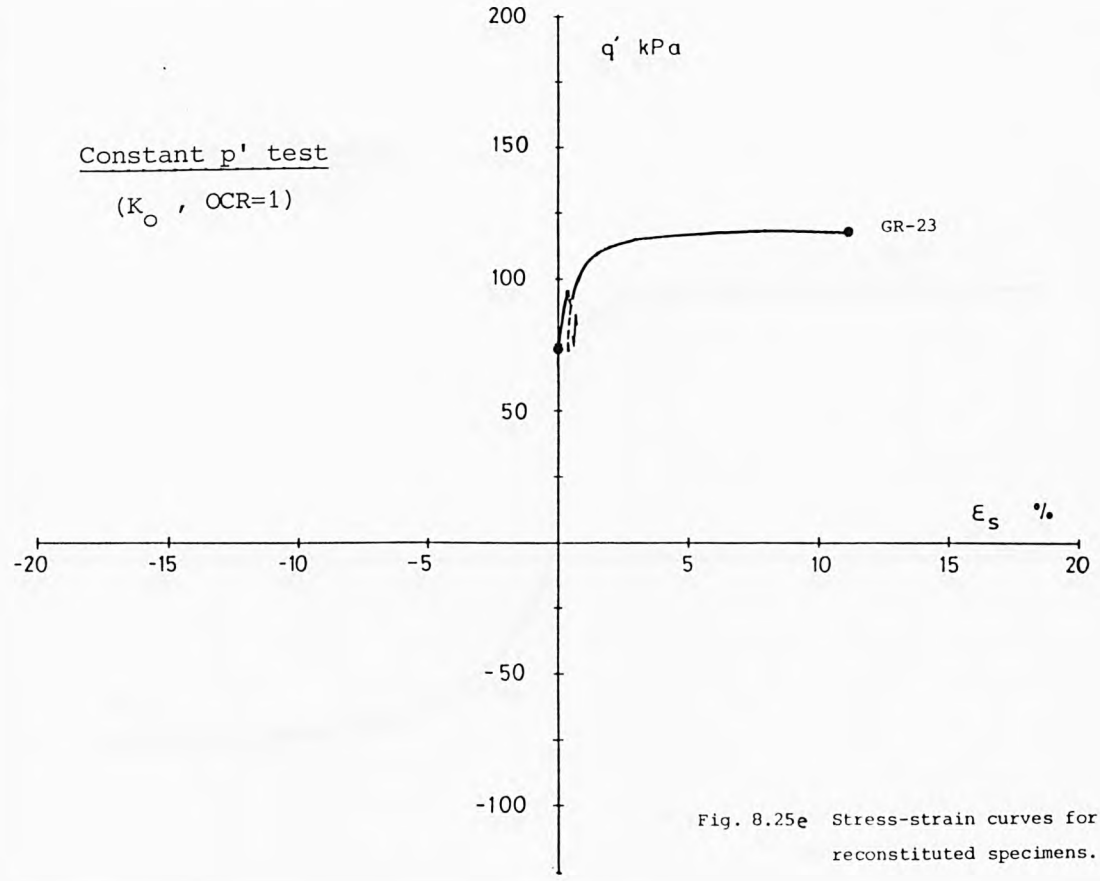

Fig. 8.25e Stress-strain curves for GME reconstituted specimens.

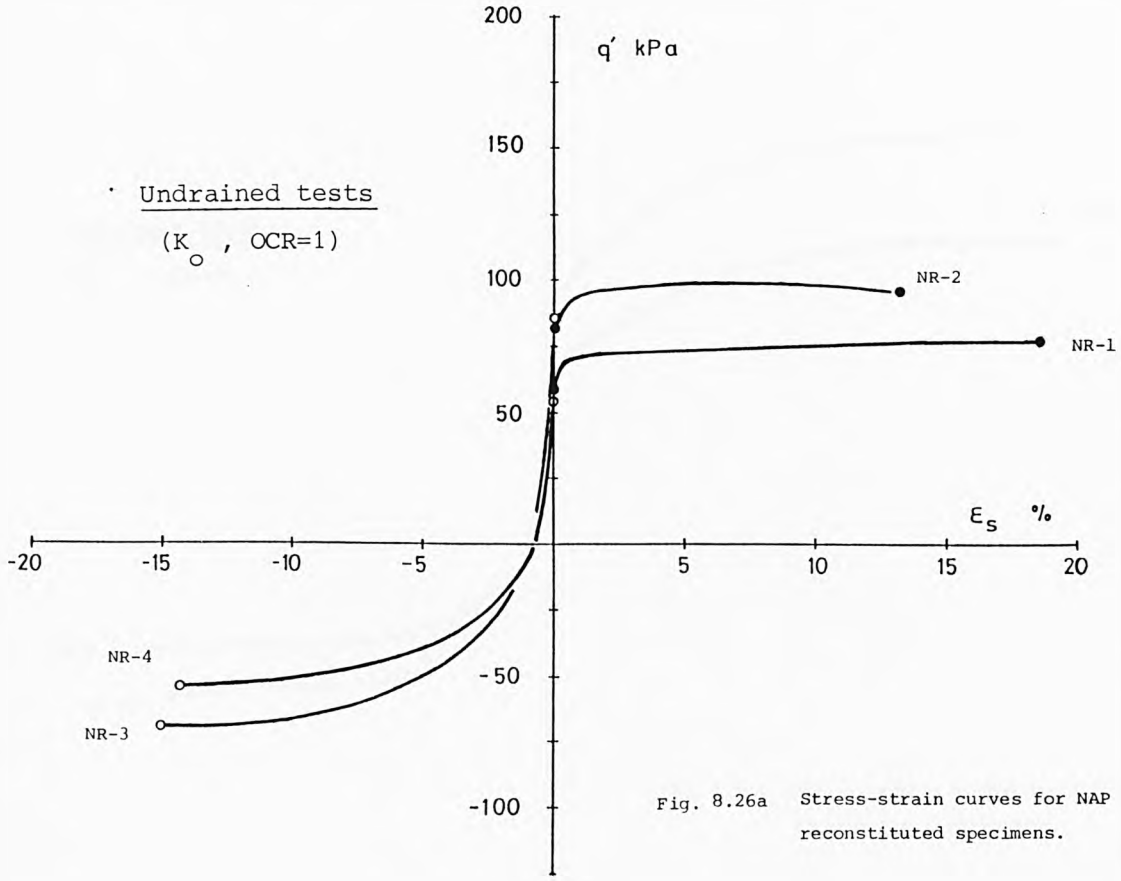

Fig. 8.26a Stress-strain curves for NAP reconstituted specimens.

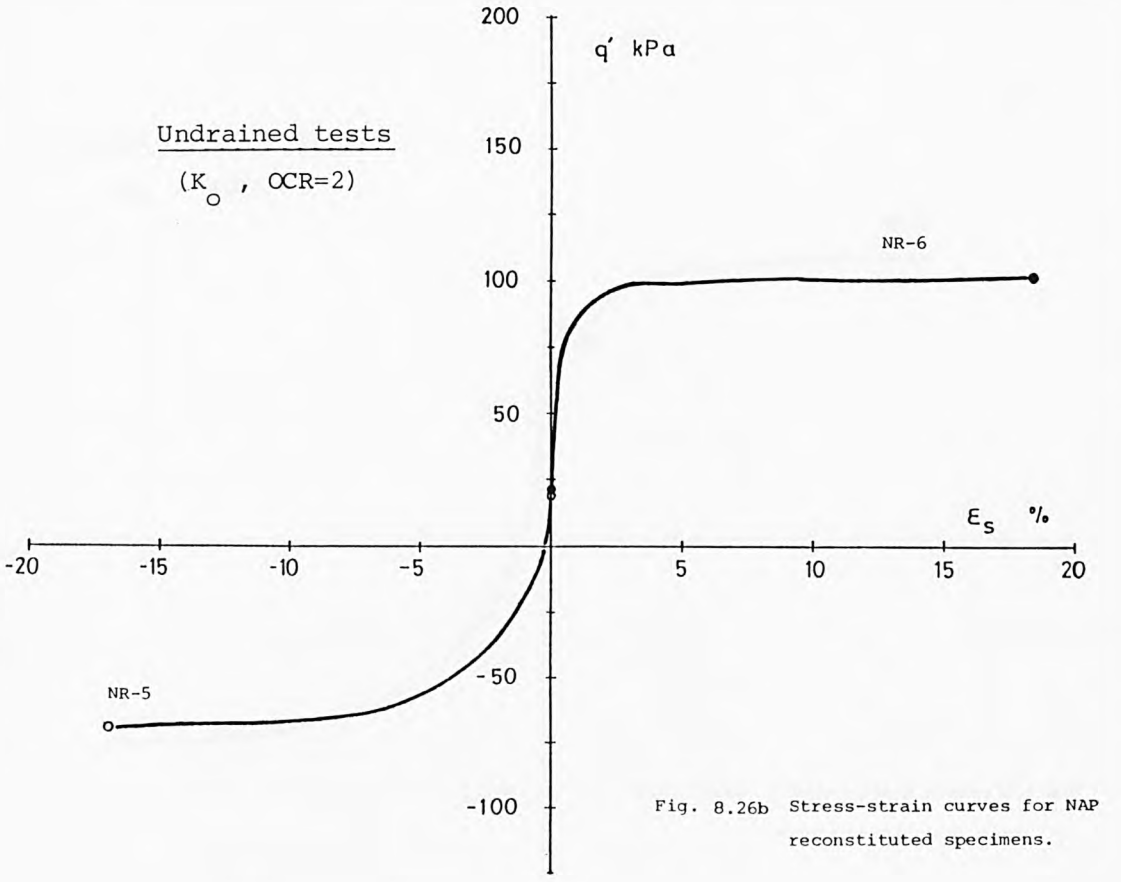

Fig. 8.26b Stress-strain curves for NAP reconstituted specimens.

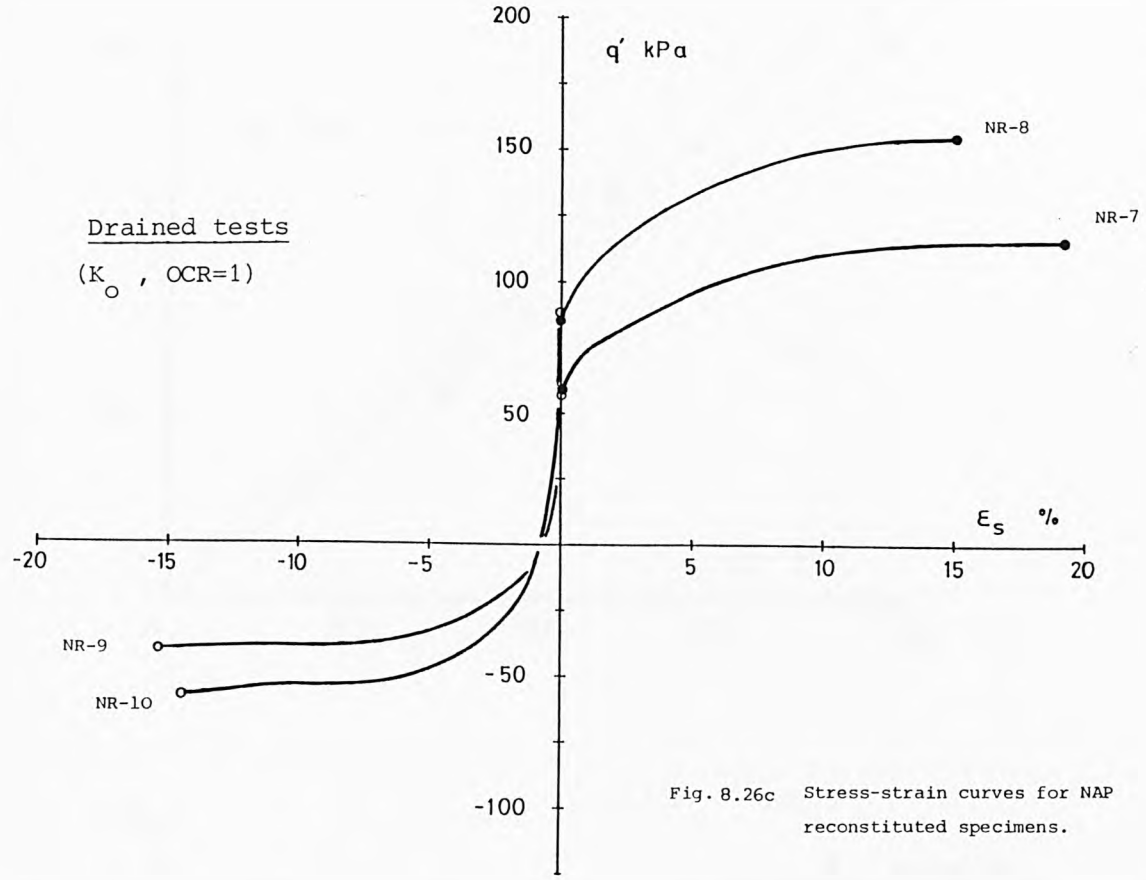

Fig. 8.26c Stress-strain curves for NAP reconstituted specimens.

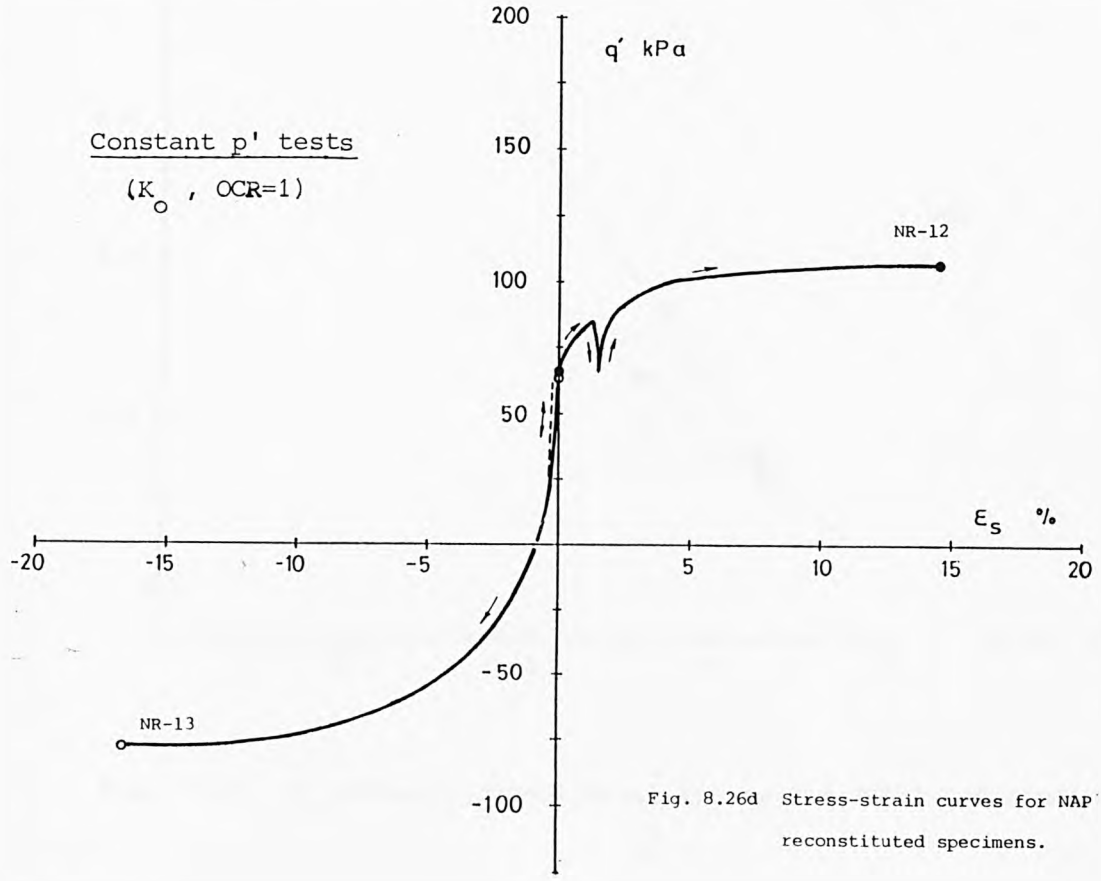

Fig. 8.26d Stress-strain curves for NAP reconstituted specimens.

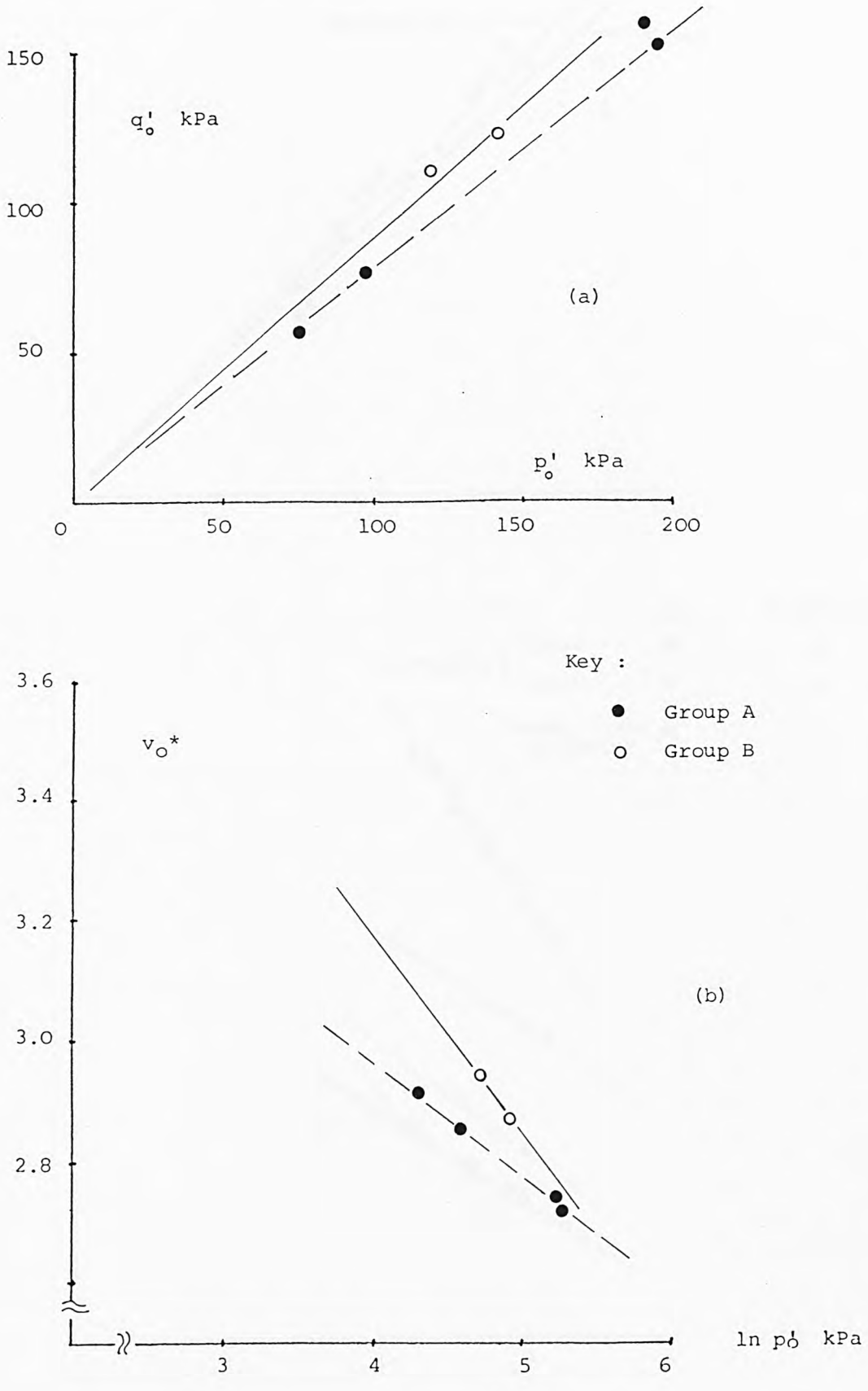

Fig. 9.1 K_o normally consolidated states for IOS tubed specimens.

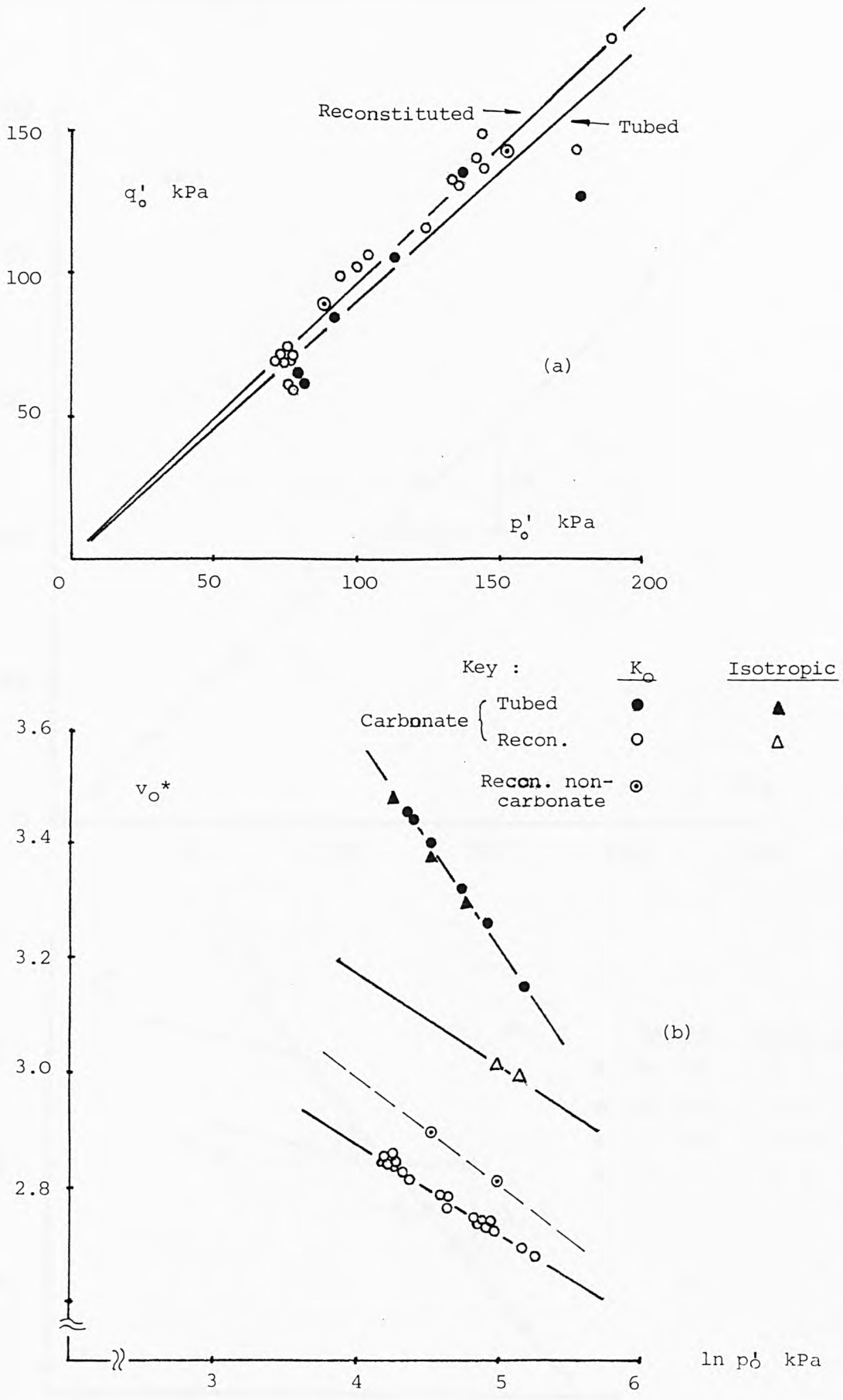

Fig. 9.2 K_o and isotropic normally consolidated states for GME tubed and reconstituted specimens.

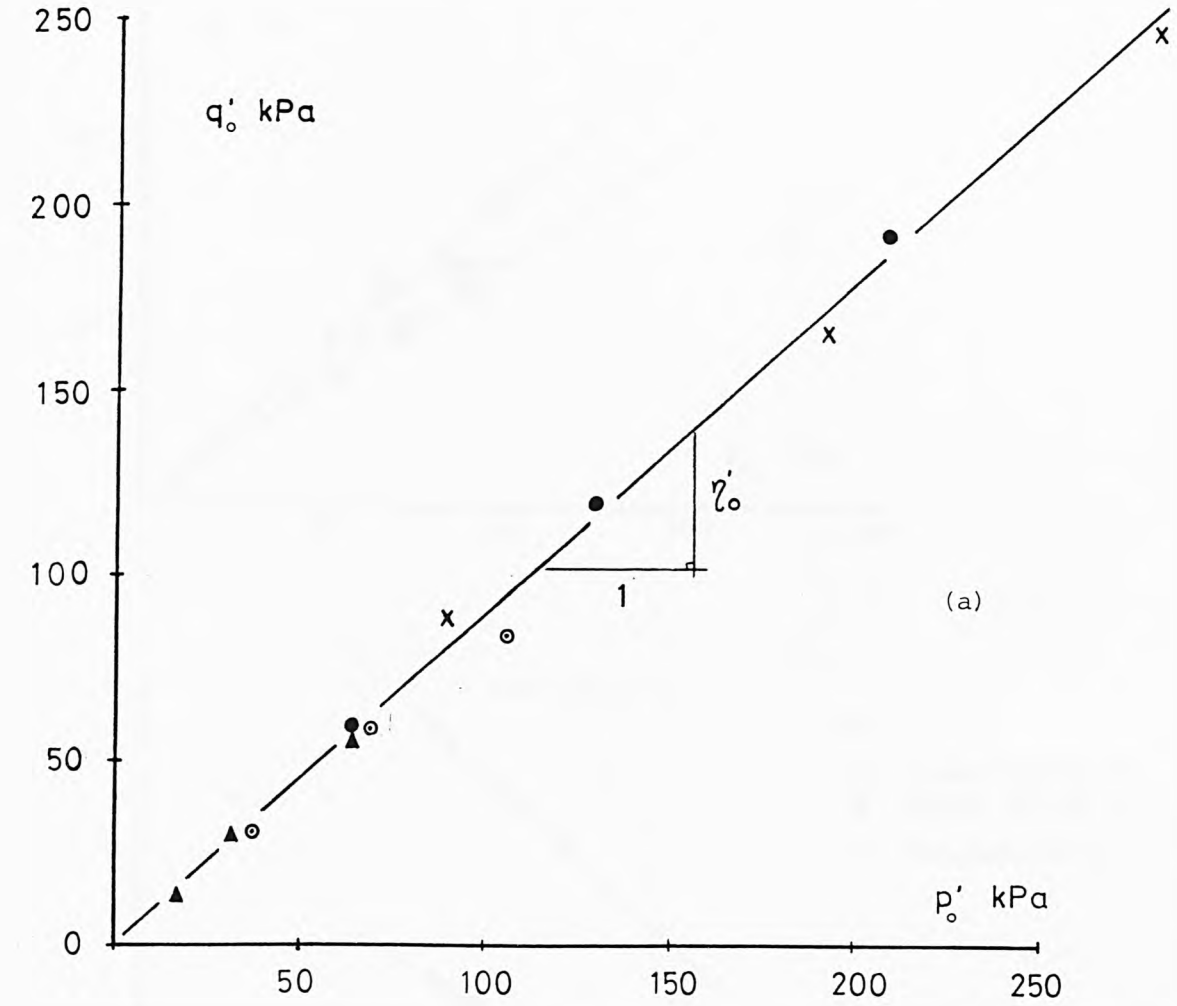

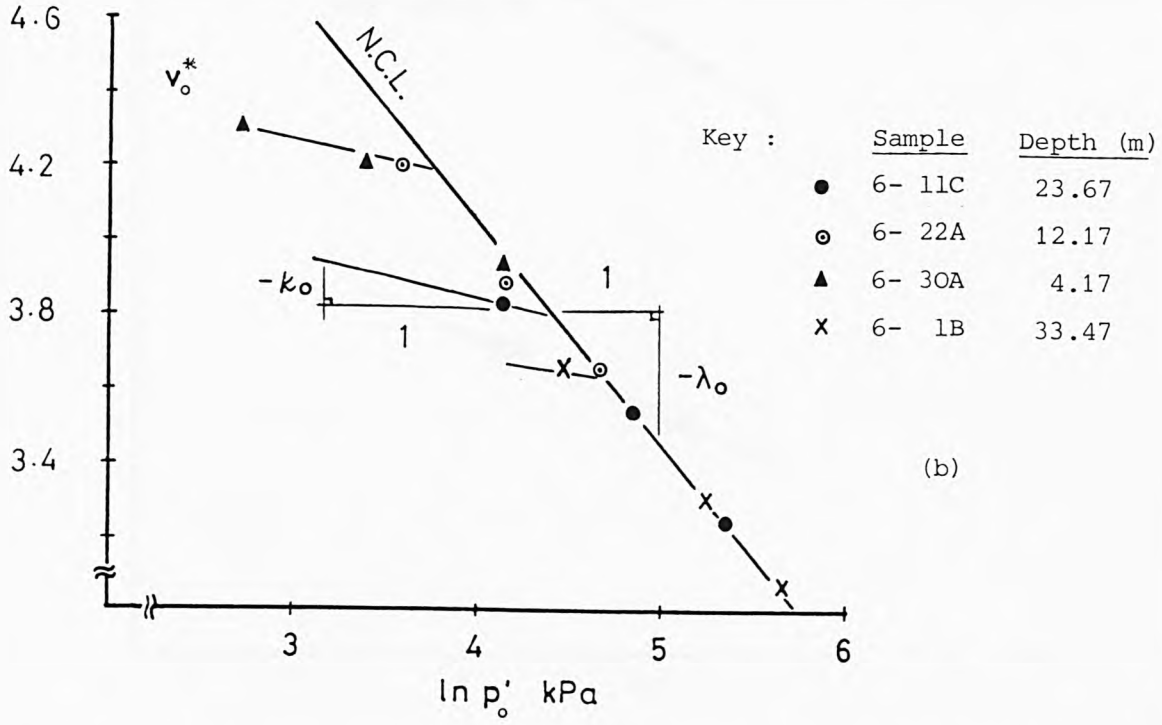

Fig. 9.3 K_o normally and over-consolidated states for GME C-6 tubed specimens.

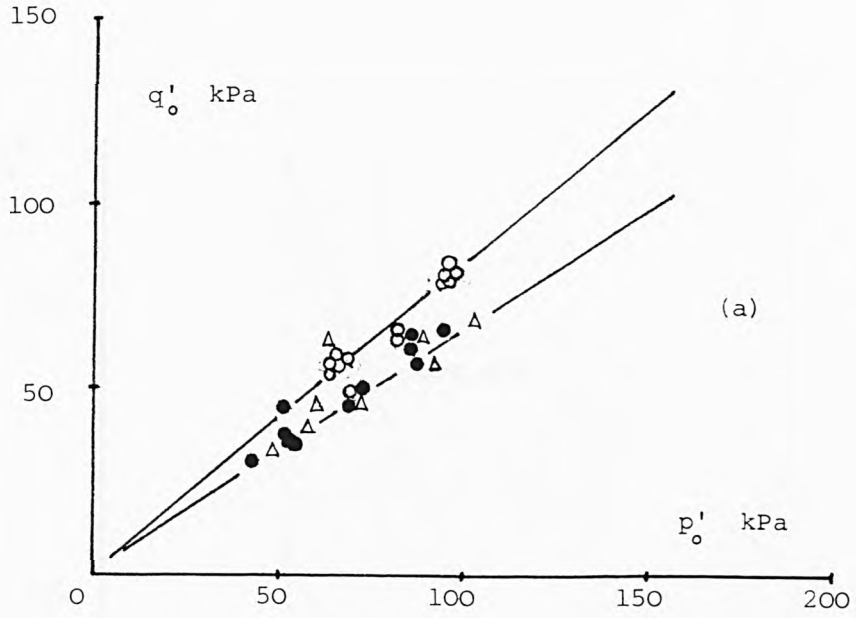

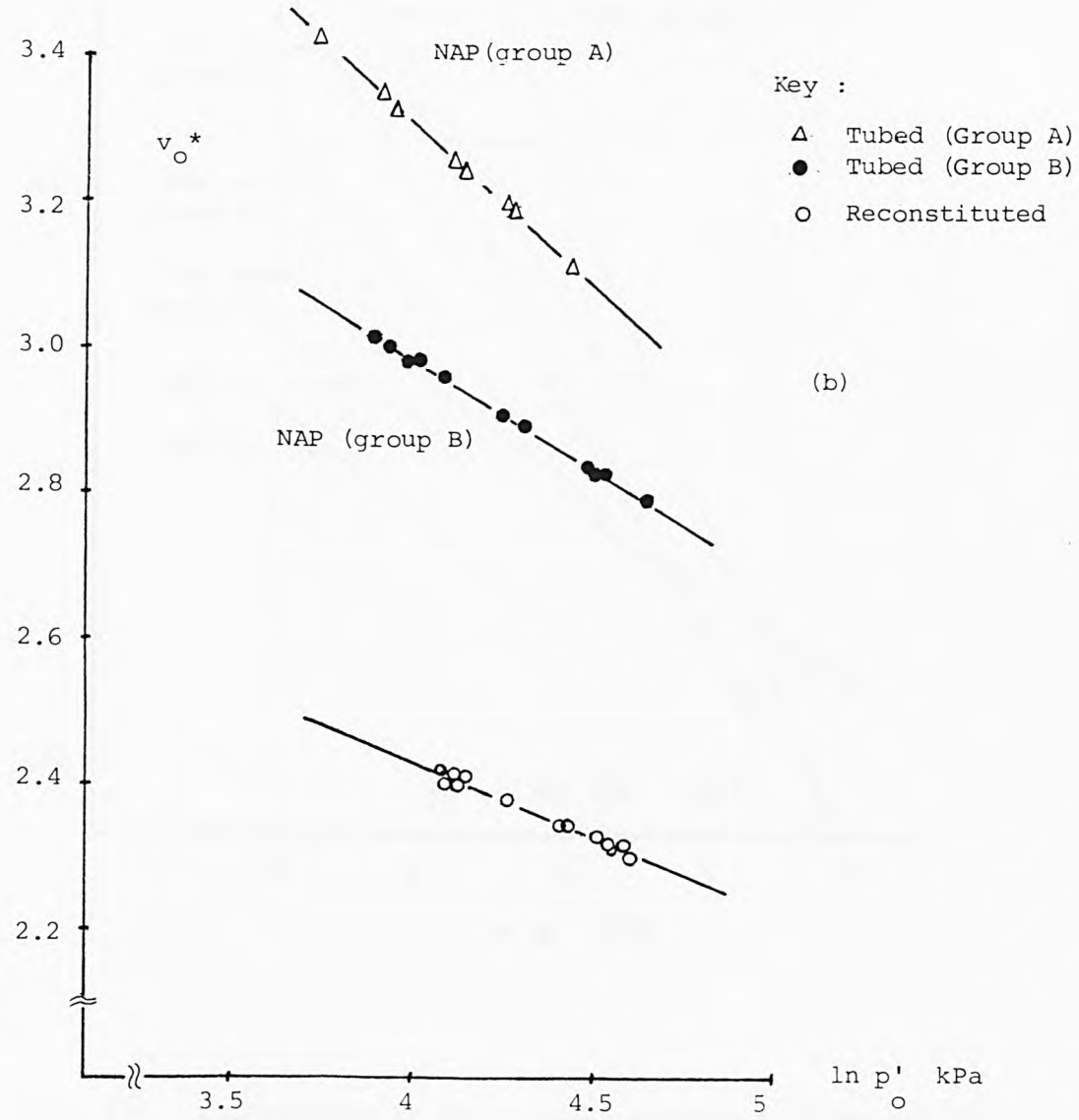

Fig. 9.4 K_o normally consolidated states for NAP tubed and reconstituted specimens.

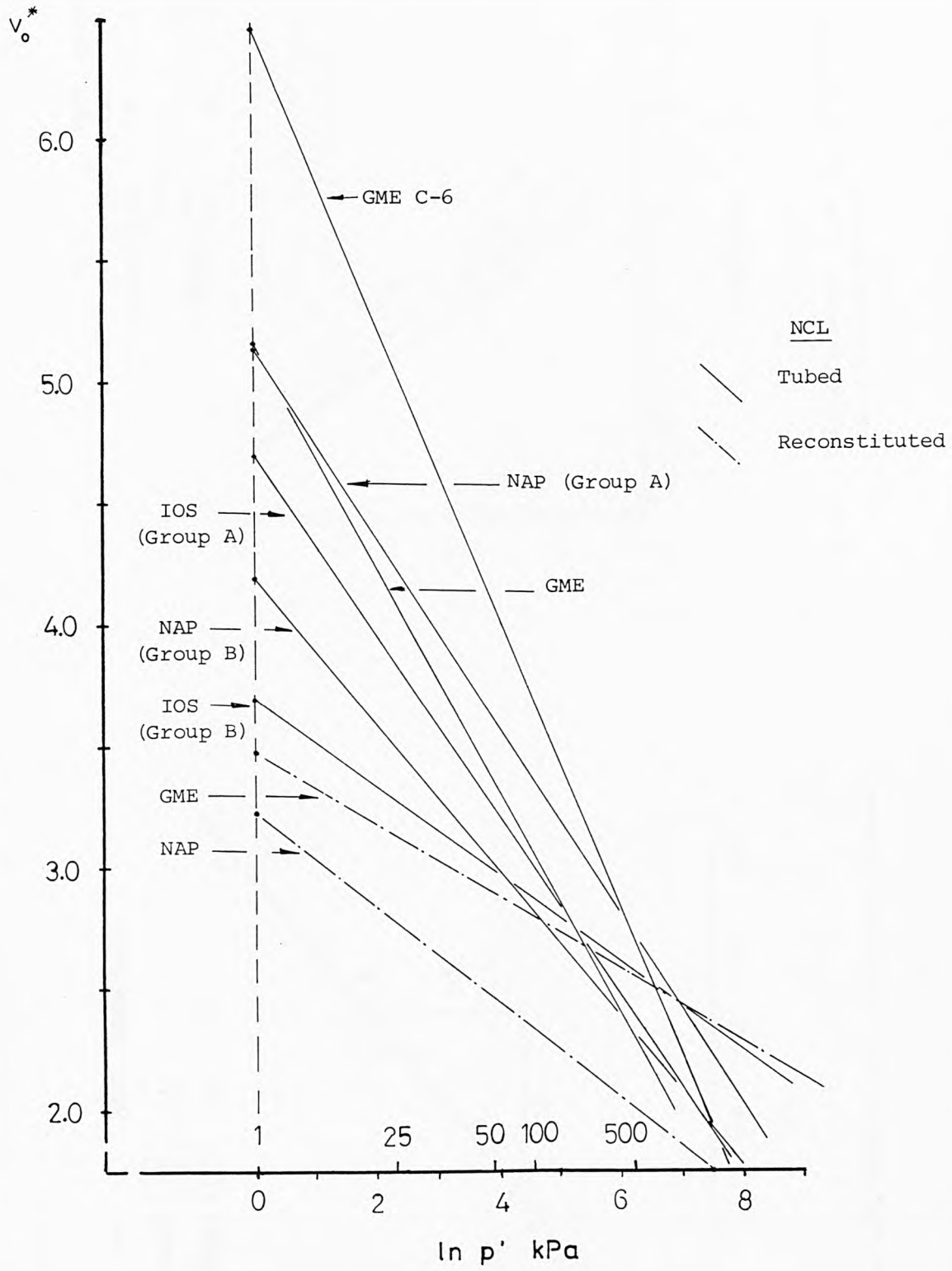

Fig. 9.5 A comparison of the normal compression lines between tubed and reconstitiuted specinems.

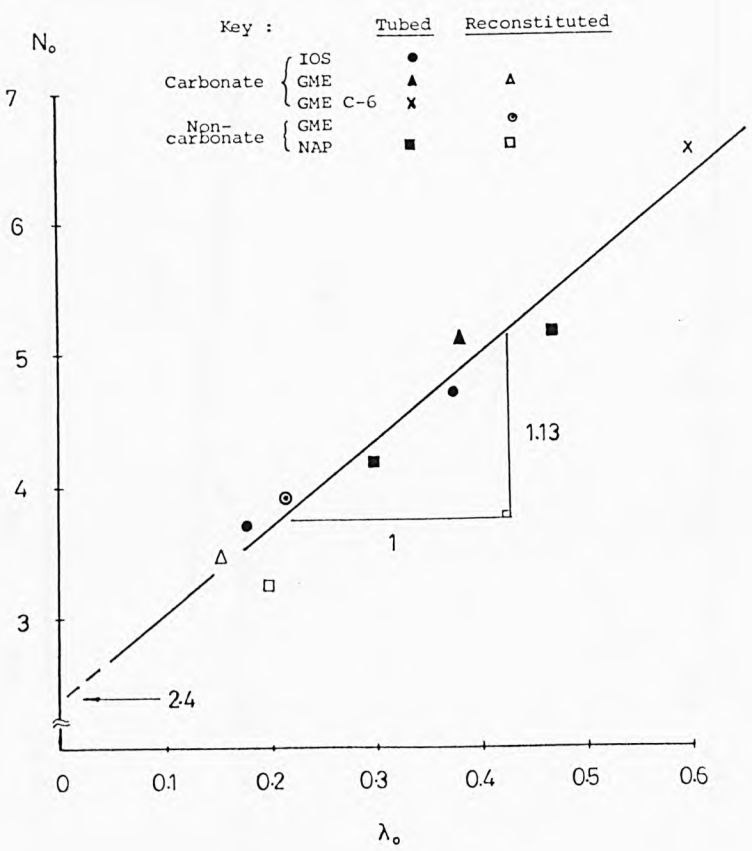

Fig. 9.6 Relationship between N_o and λ_o for deep-ocean sediments.

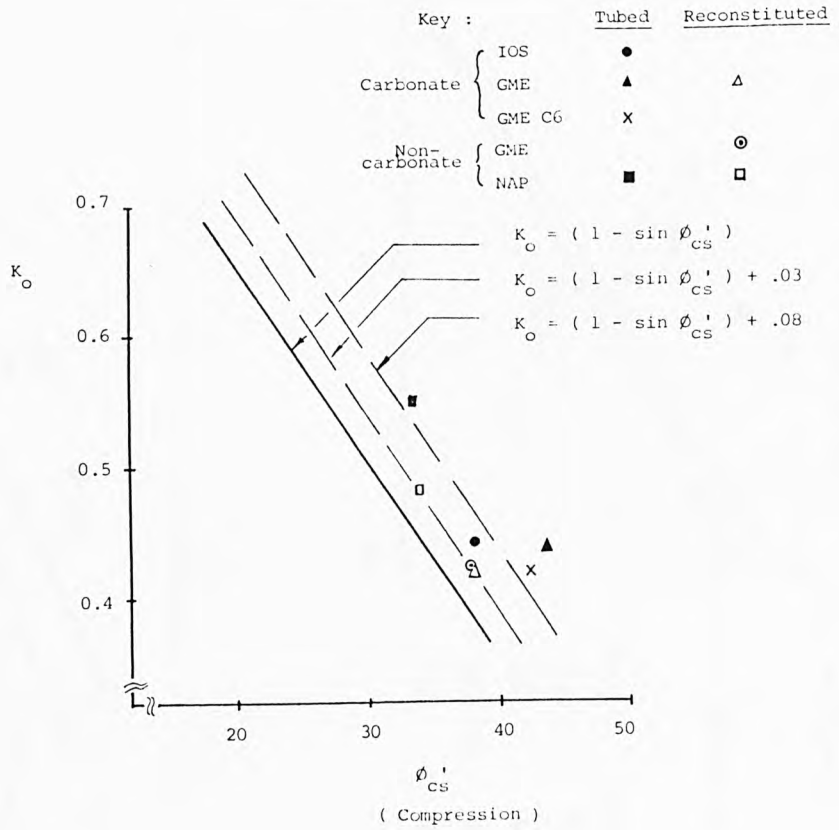

Fig. 9.7 Relationship between K_o and ϕ_{cs}' for the North Atlantic deep-ocean sediments.

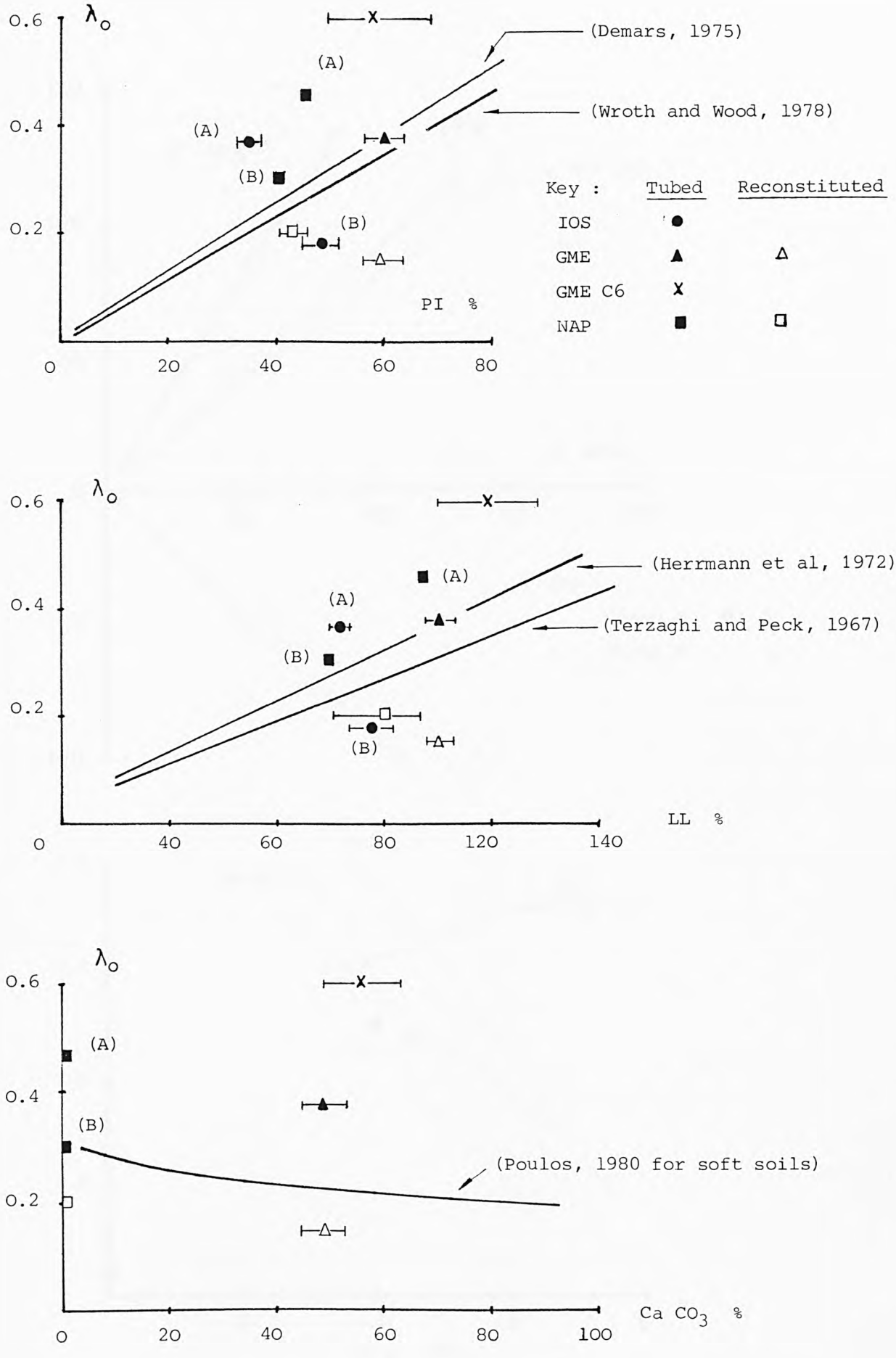

Fig. 9.8 Relationships between λ_o and index properties.

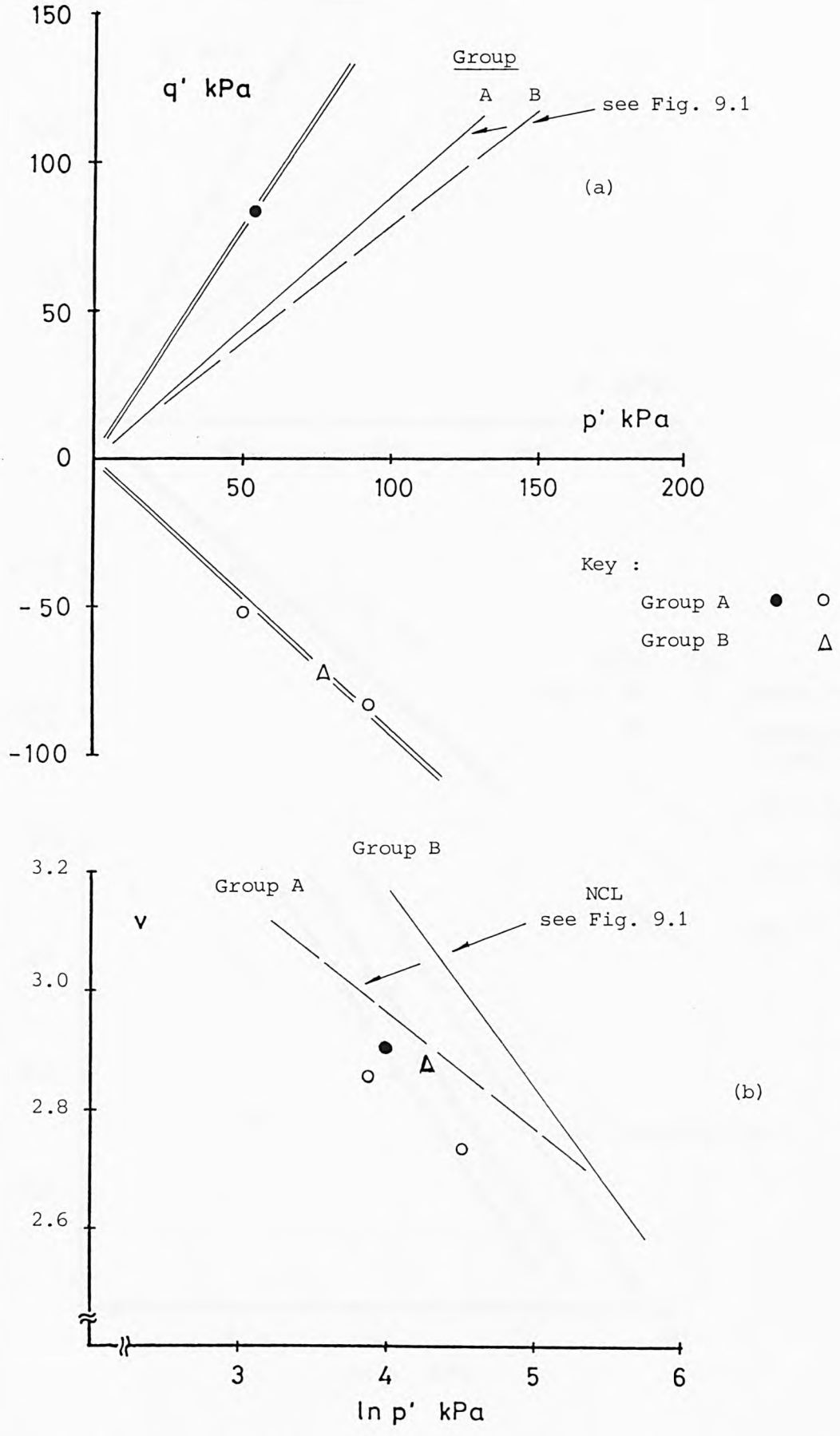

Fig. 9.9 Critical states for IOS tubed specimens.

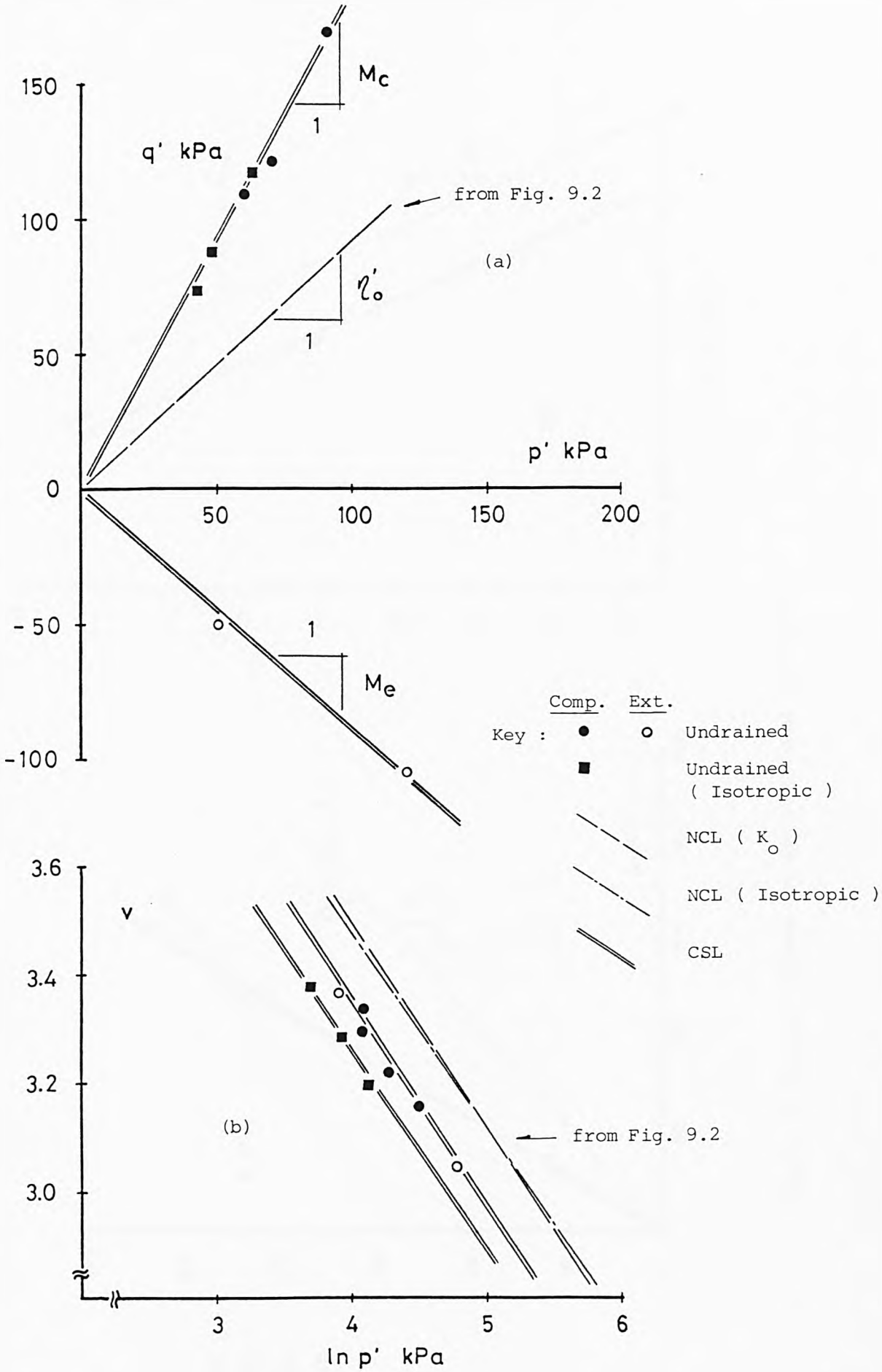

Fig. 9.10 Critical states for GME tubed specimens.

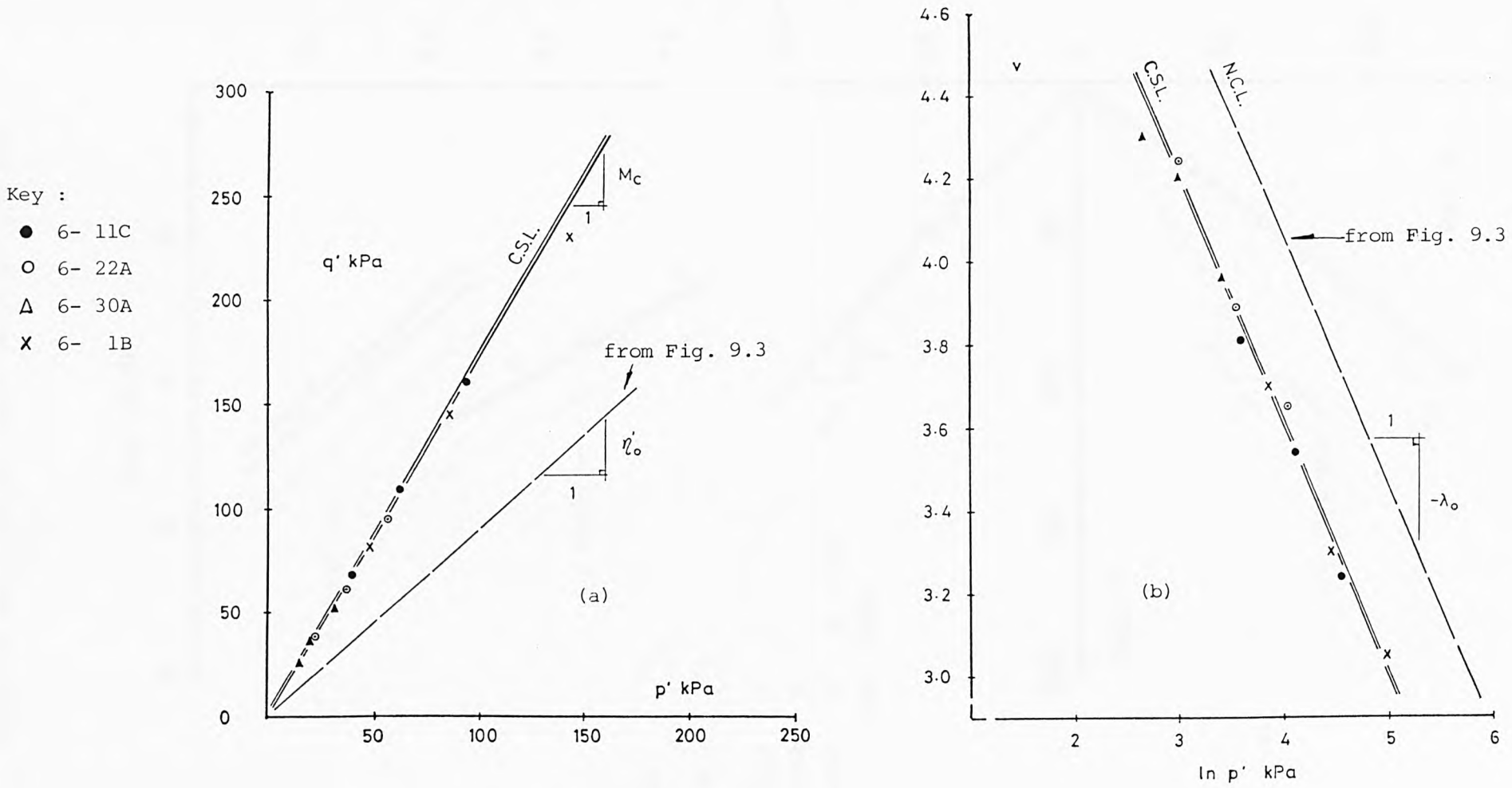

Fig.9.11 Critical states for GME C-6 tubed specimens.

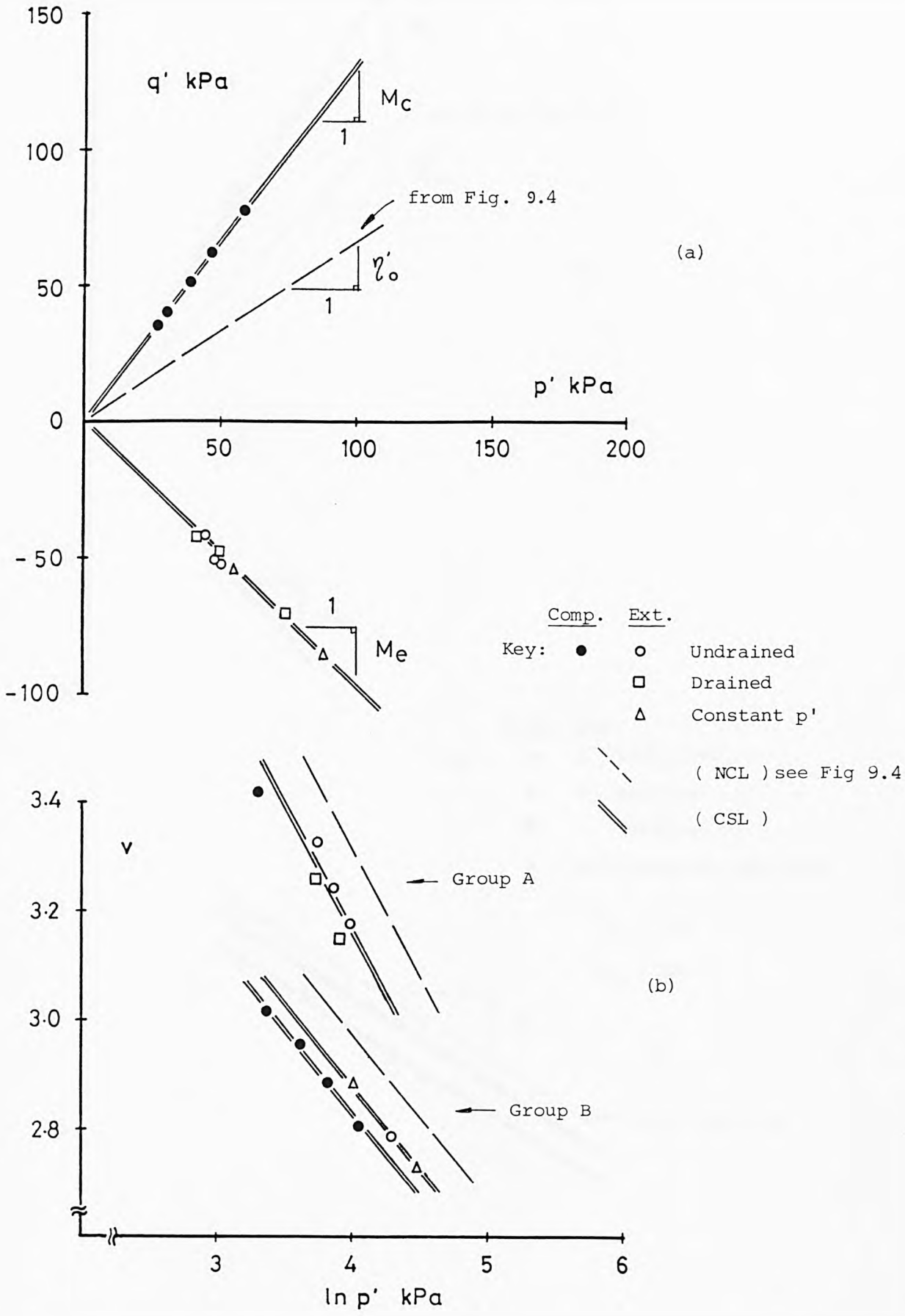

Fig 9.12 Critical states for NAP tubed specimens.

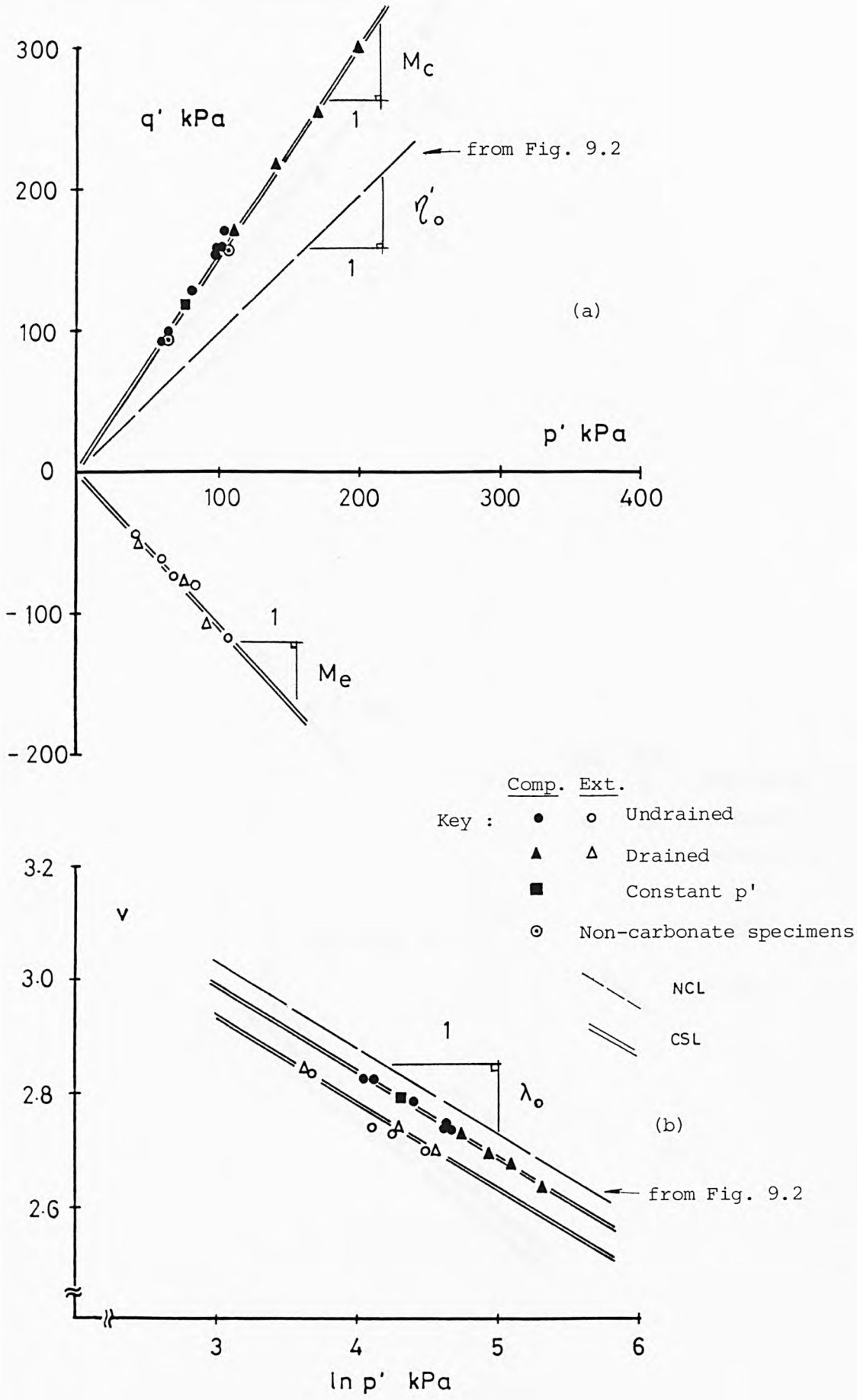

Fig. 9.13 Critical states for GME reconstituted specimens.

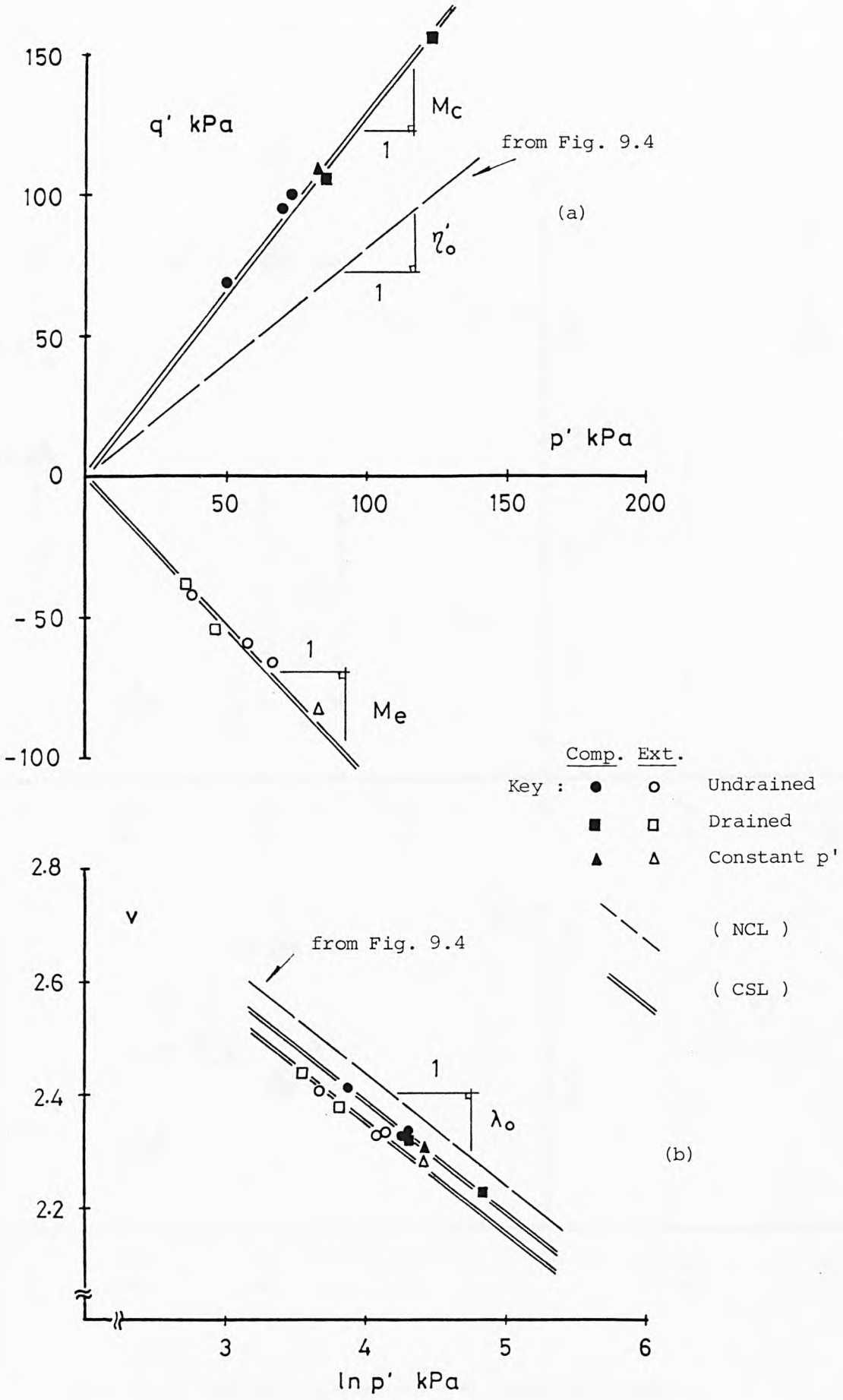

Fig. 9.14 Critical states for NAP reconstituted specimens.

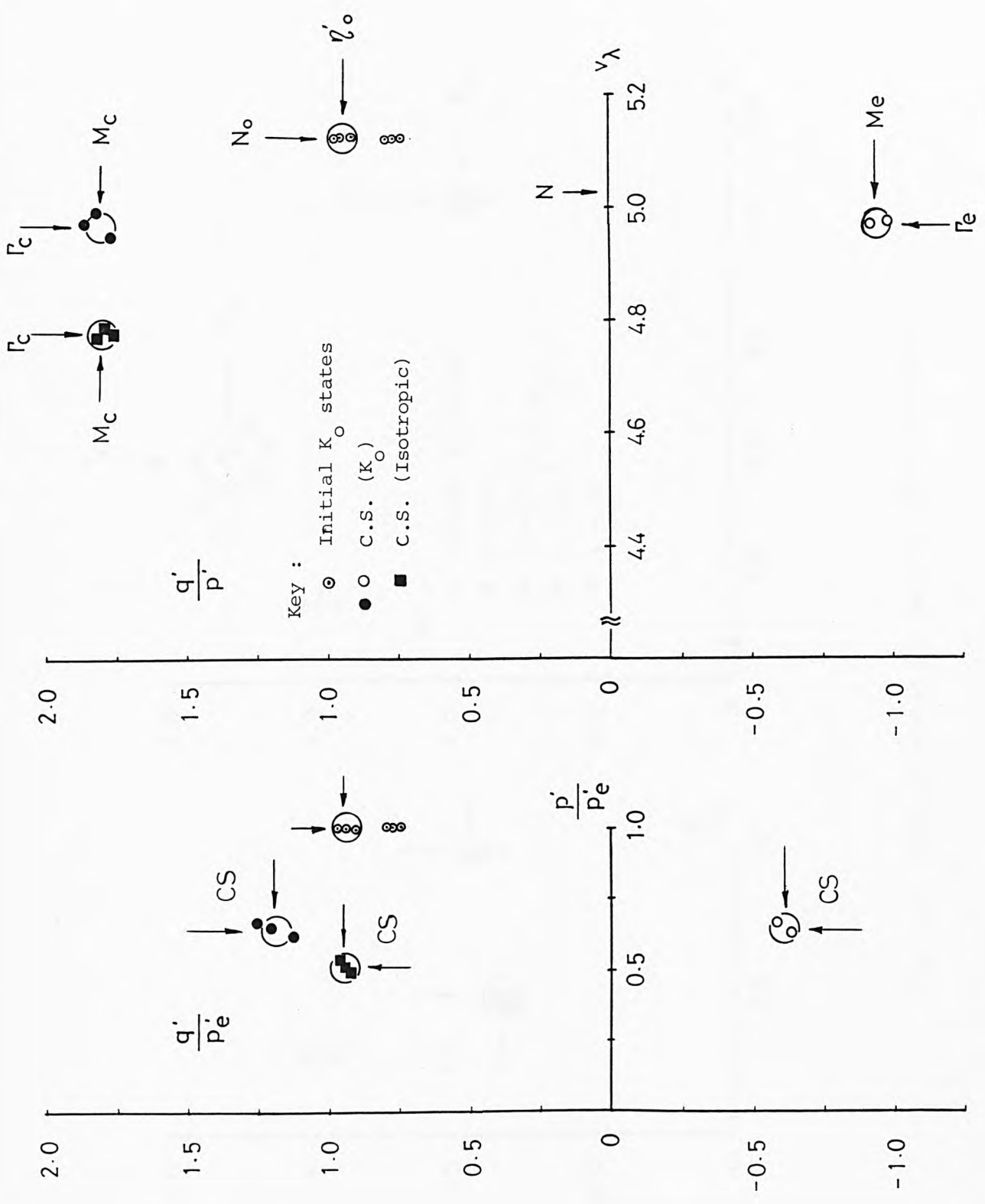

Fig. 9.15 Critical states for GME tubed specimens.

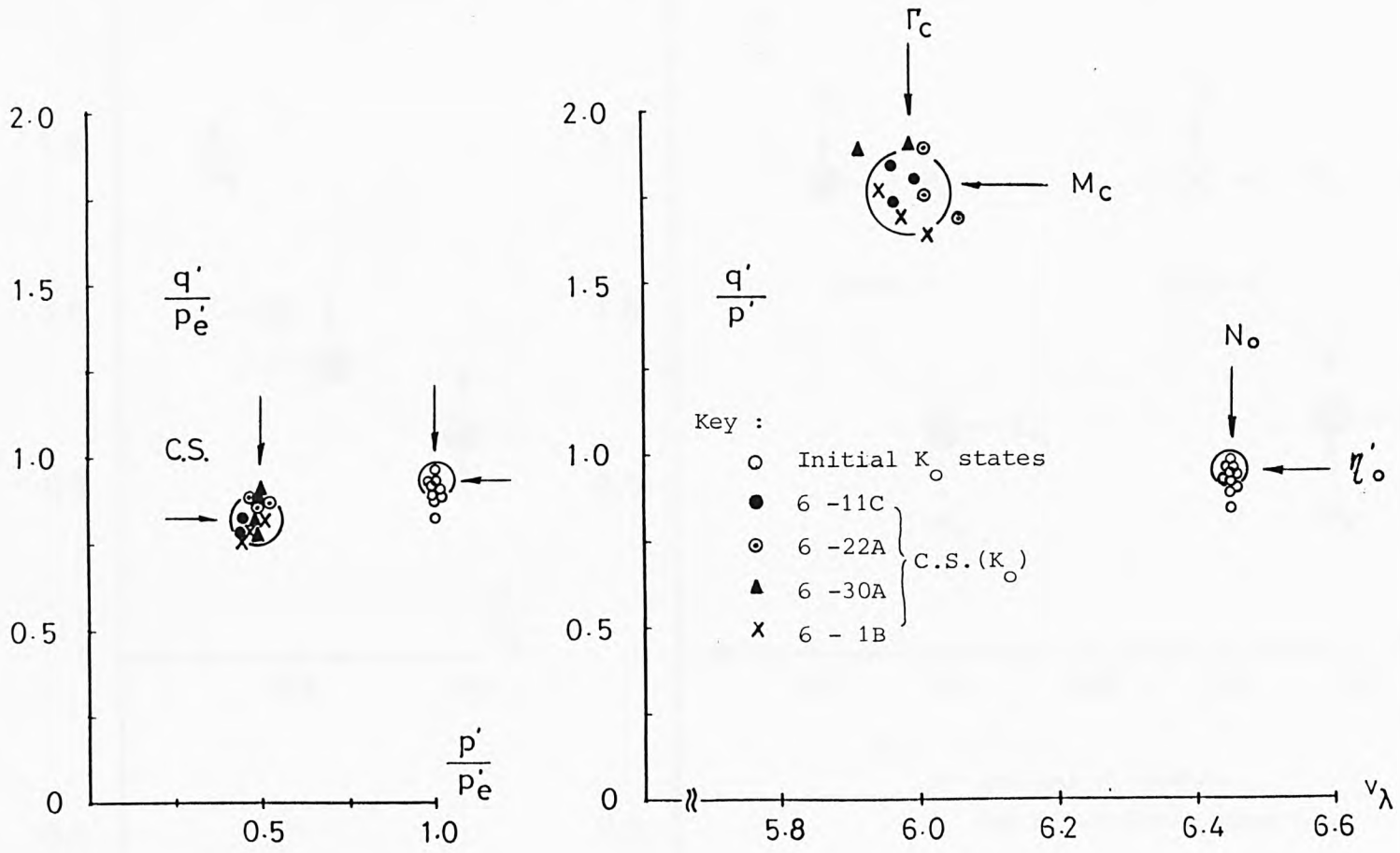

Fig. 9.16 Critical states for GME C-6 tubed specimens.

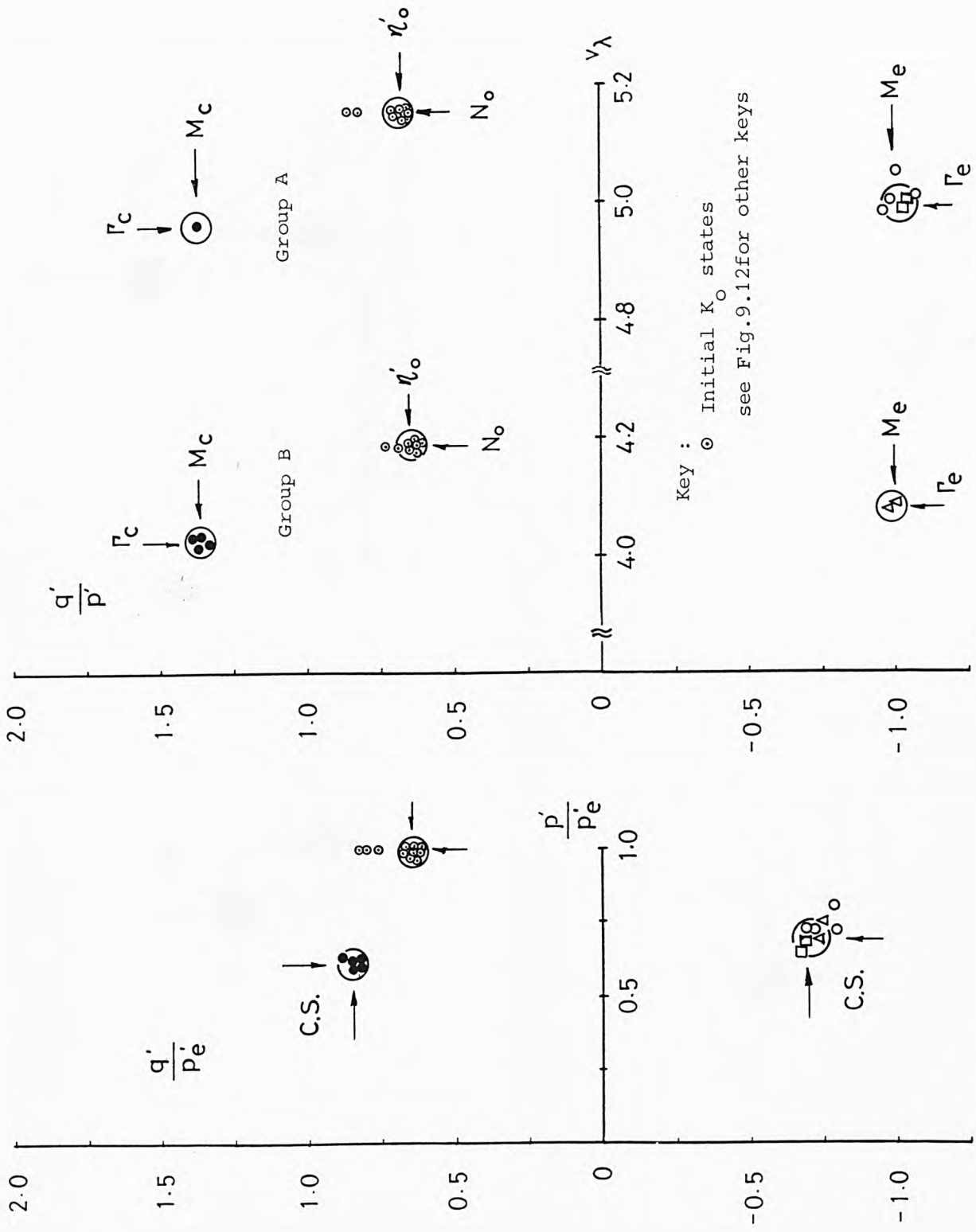

Fig. 9.17 Critical states for NAP tubed specimens.

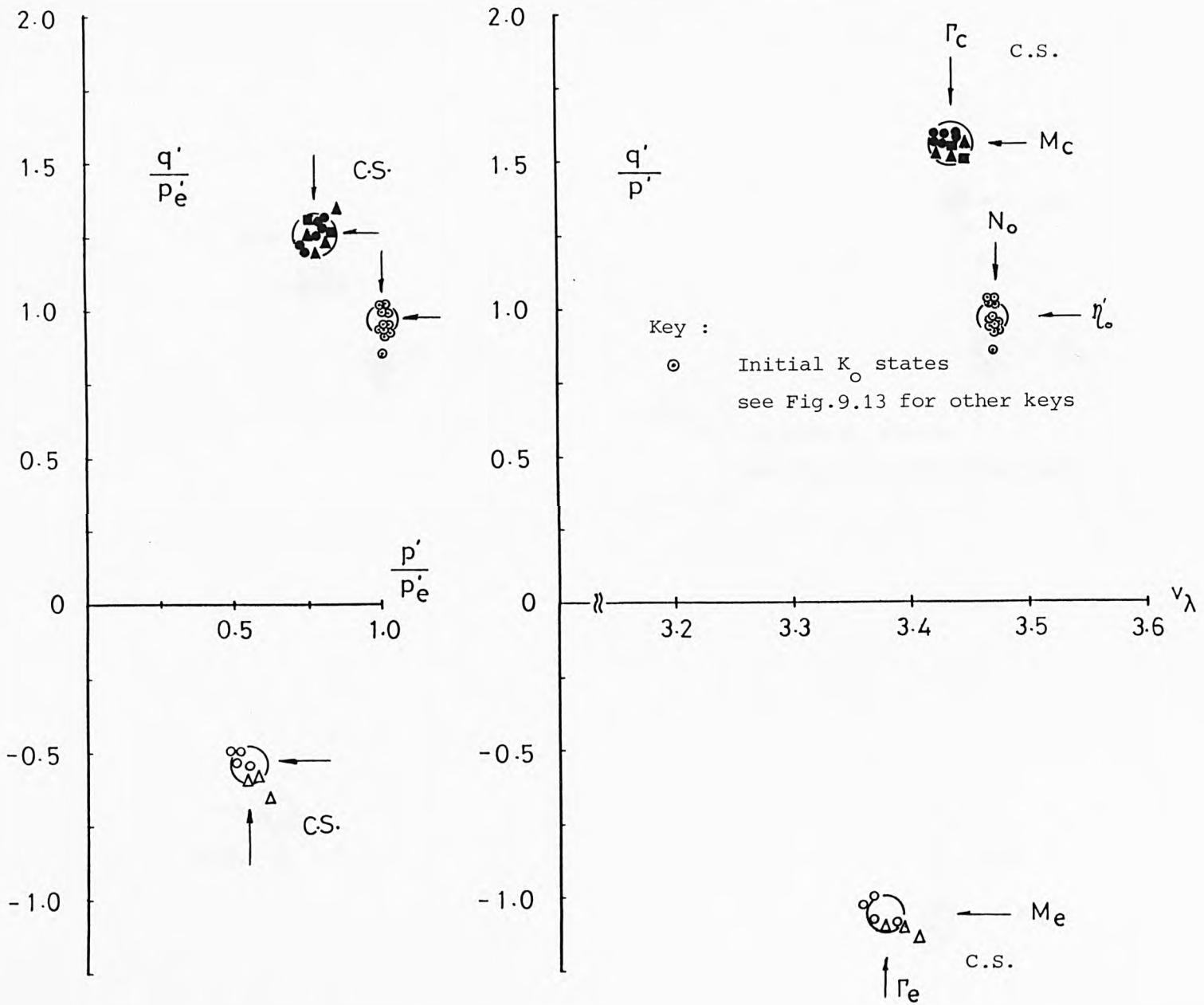

Fig. 9.18 Critical states for GME reconstituted specimens.

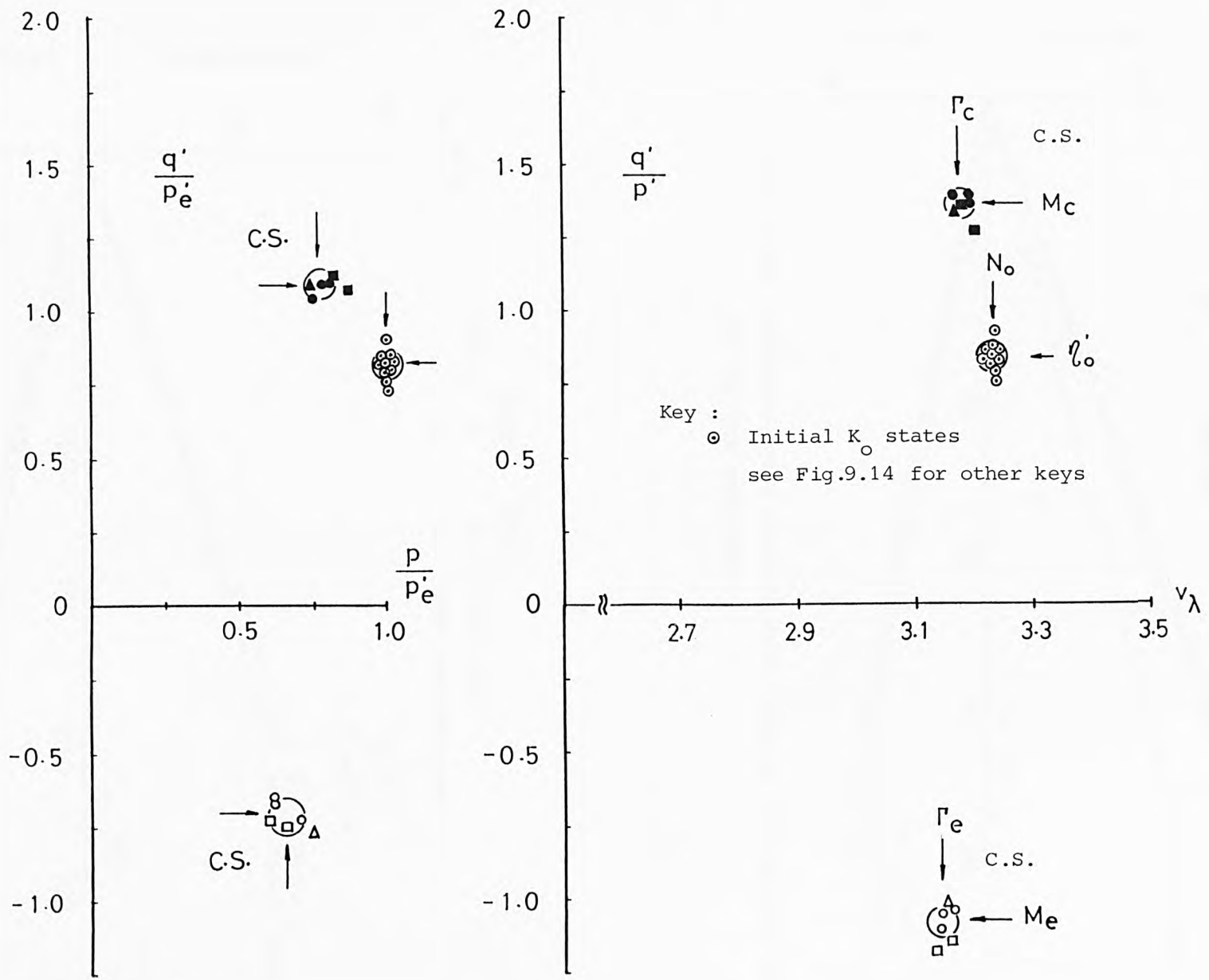

Fig. 9.19 Critical states for NAP reconstituted specimens.

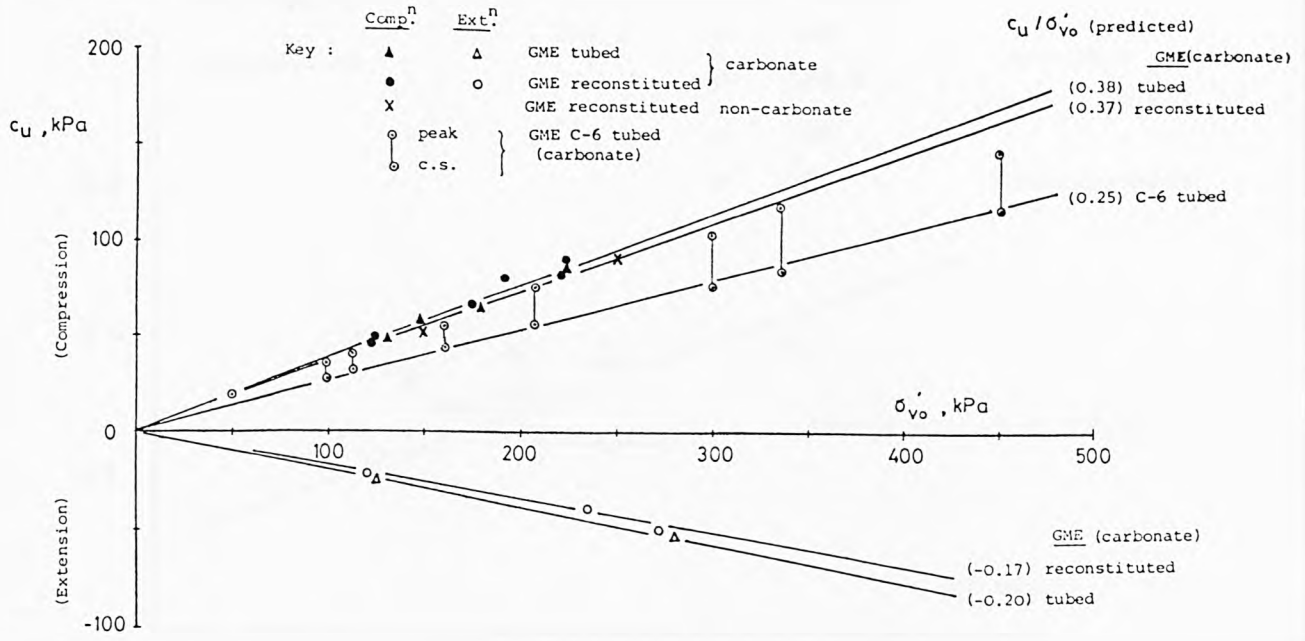

Fig. 9.20a Undrained shear strength with vertical effective stress for the GME specimens.

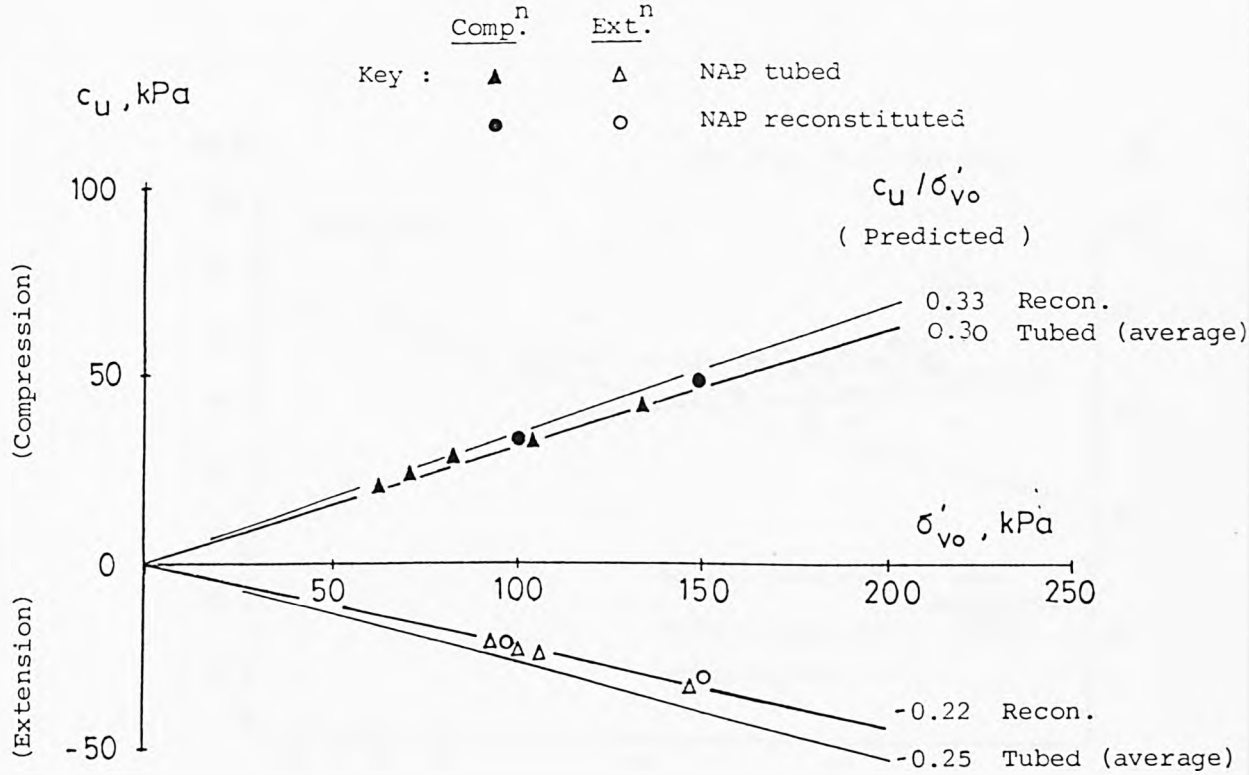

Fig. 9.20b Undrained shear strength with vertical effective stress for the NAP specimens.

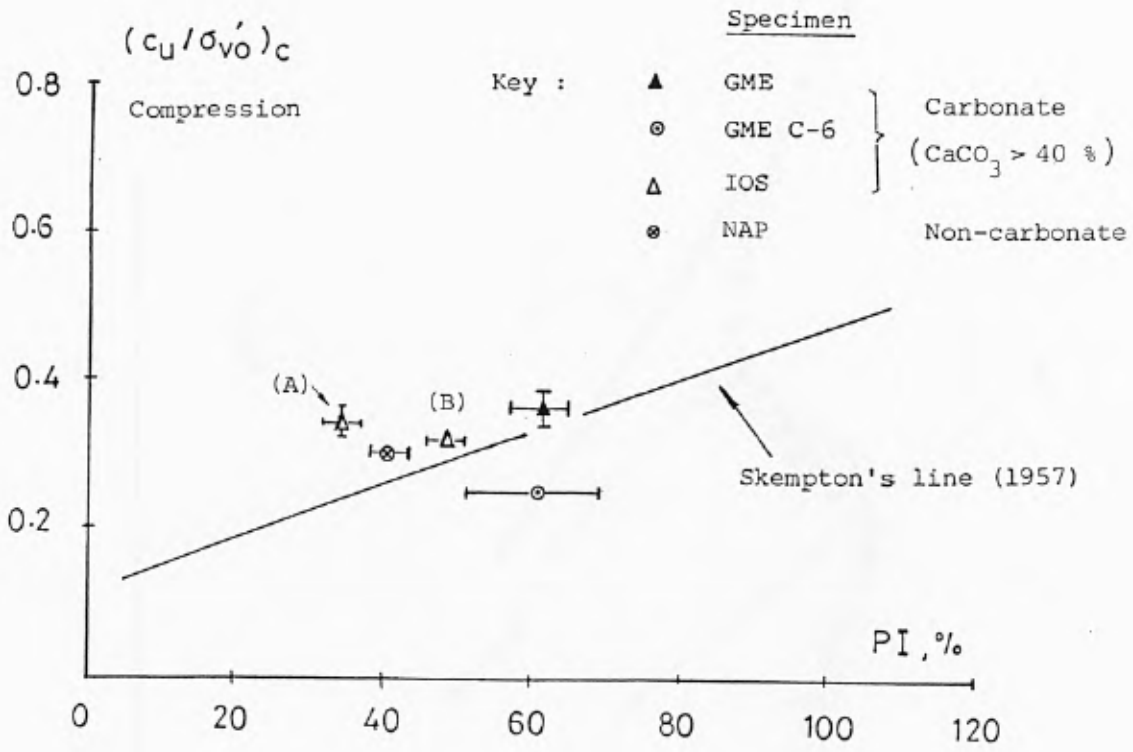

Fig. 9.21 Relationships between the undrained shear strength ratio and plasticity index for deep-ocean sediments.

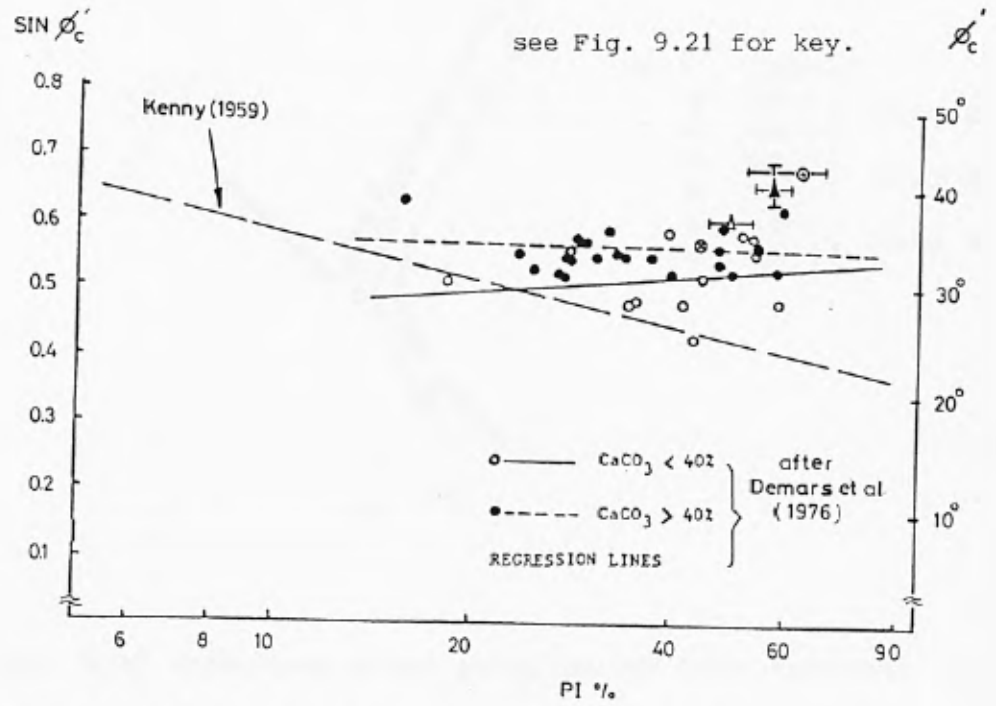

Fig. 9.22 Relationship between SIN ϕ'_c and Plasticity Index

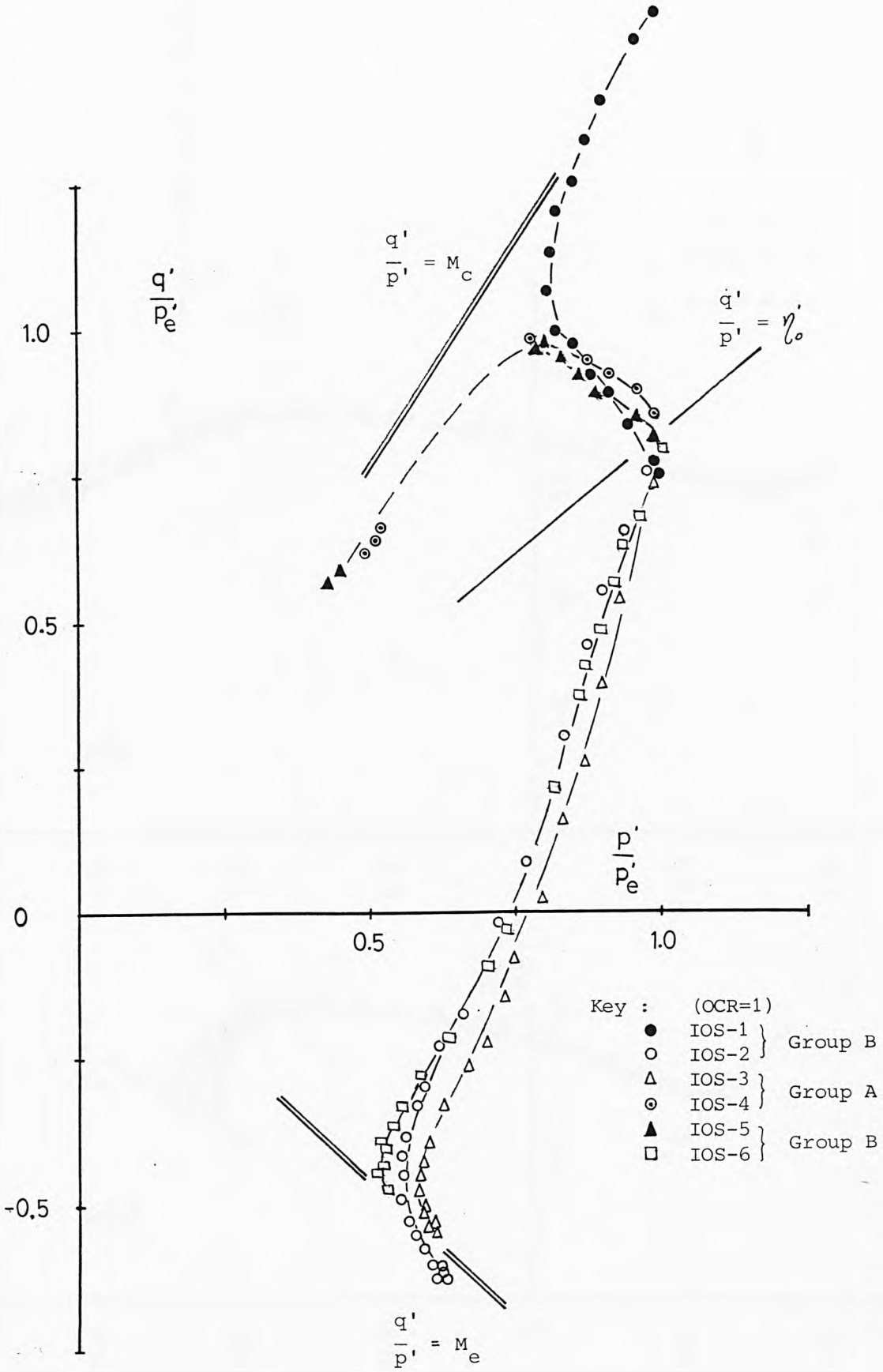

Fig. 9.23 Normalised stress paths for IOS tubed specimens.

Fig. 9.24 Normalised state paths for GME tubed specimens.

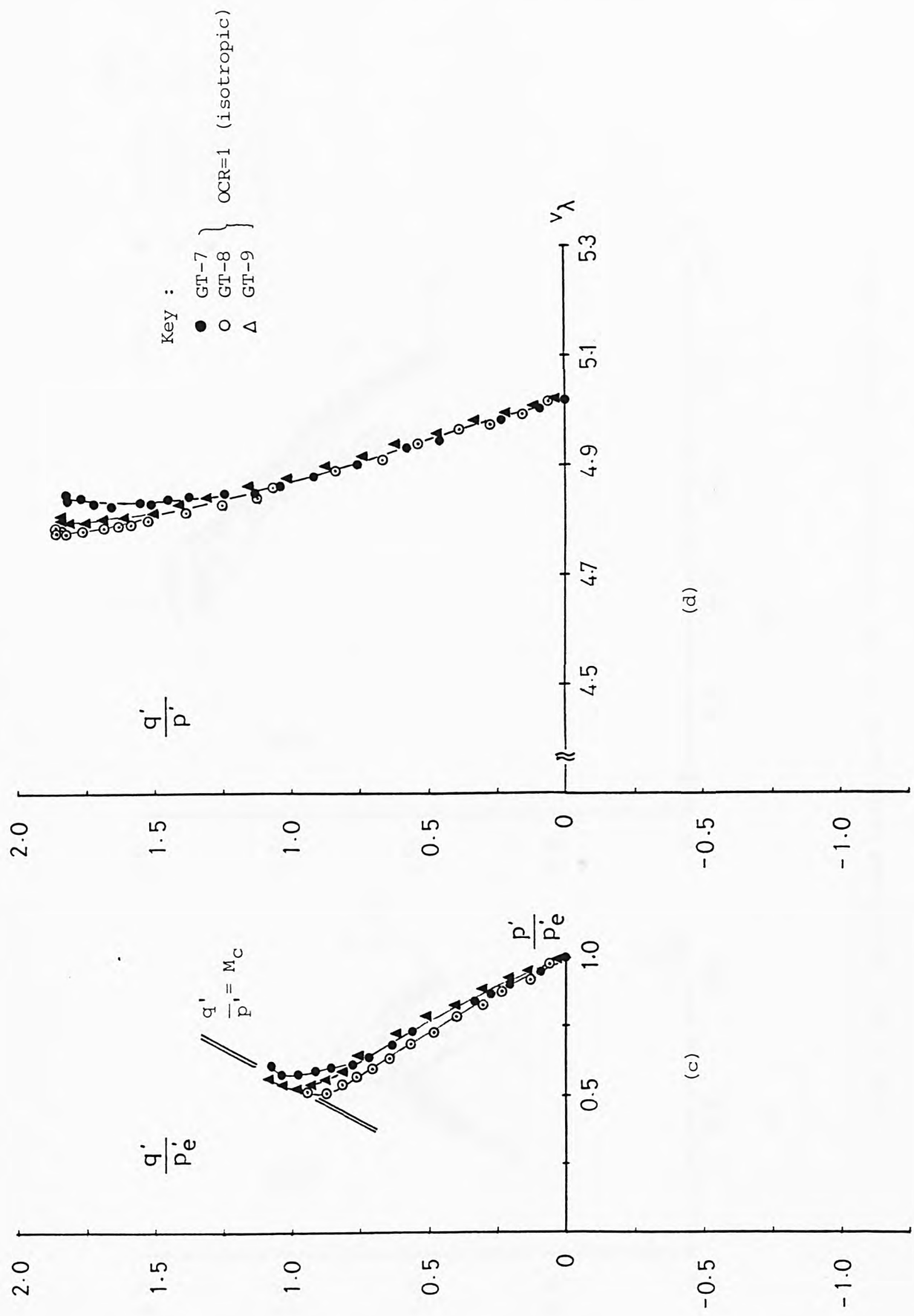

Fig. 9.24 Normalised state paths for GME tubed specimens.

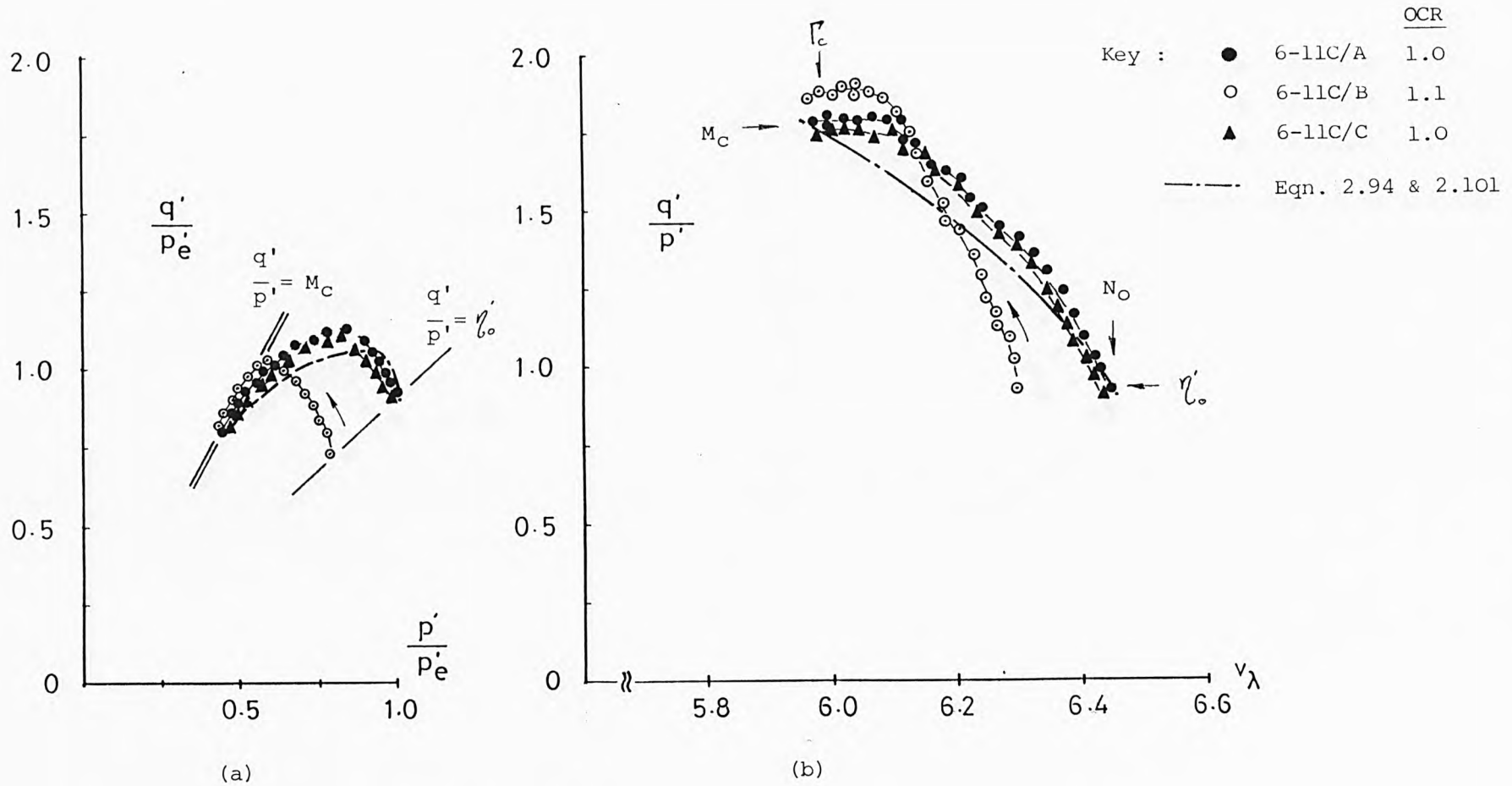

Fig. 9.25 Normalised state paths for GME C-6 specimens. (Sample 6-11C)

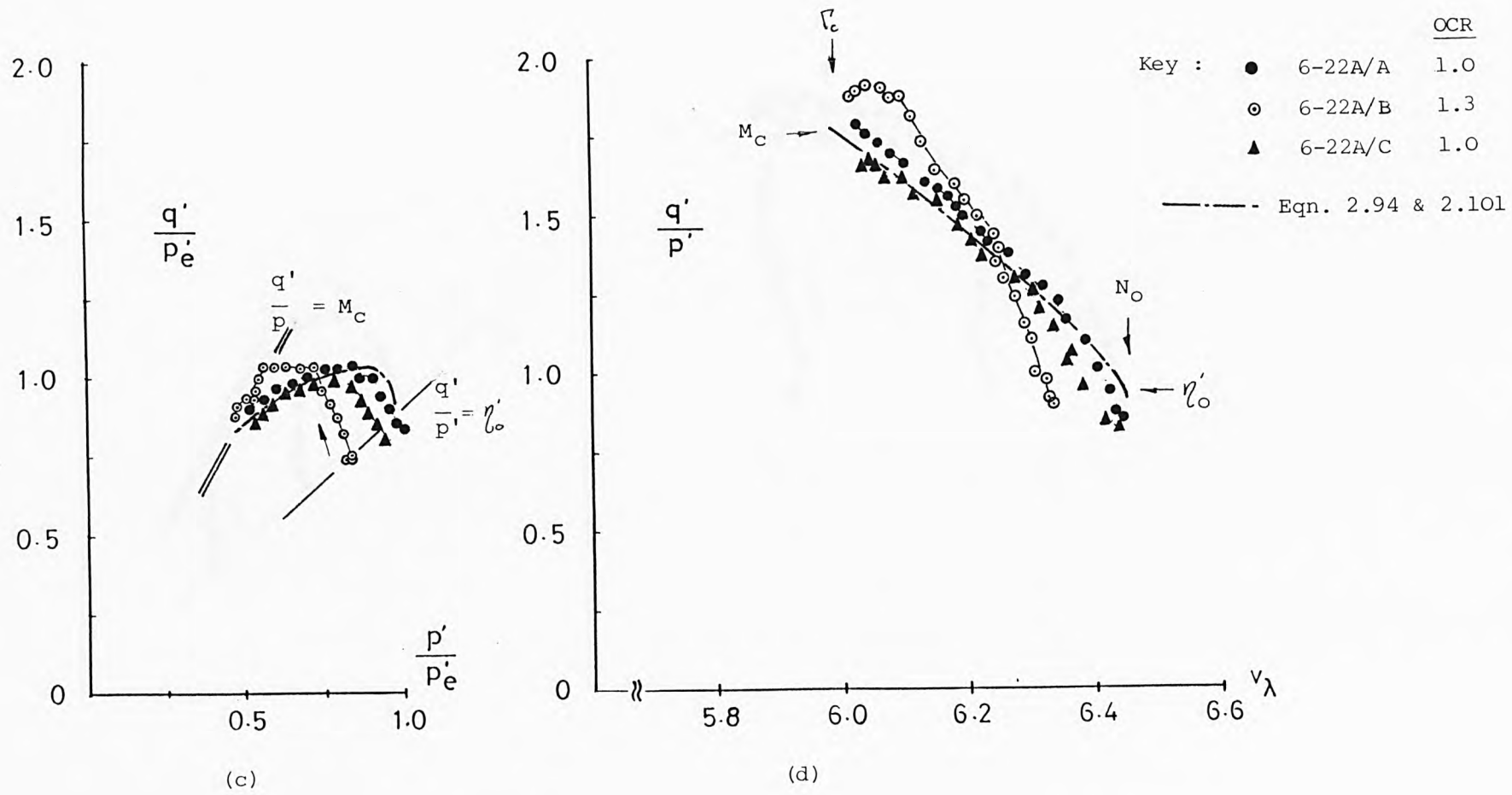

Fig. 9.25 Normalised state paths for GME C-6 specimens. (Sample 6-22A)

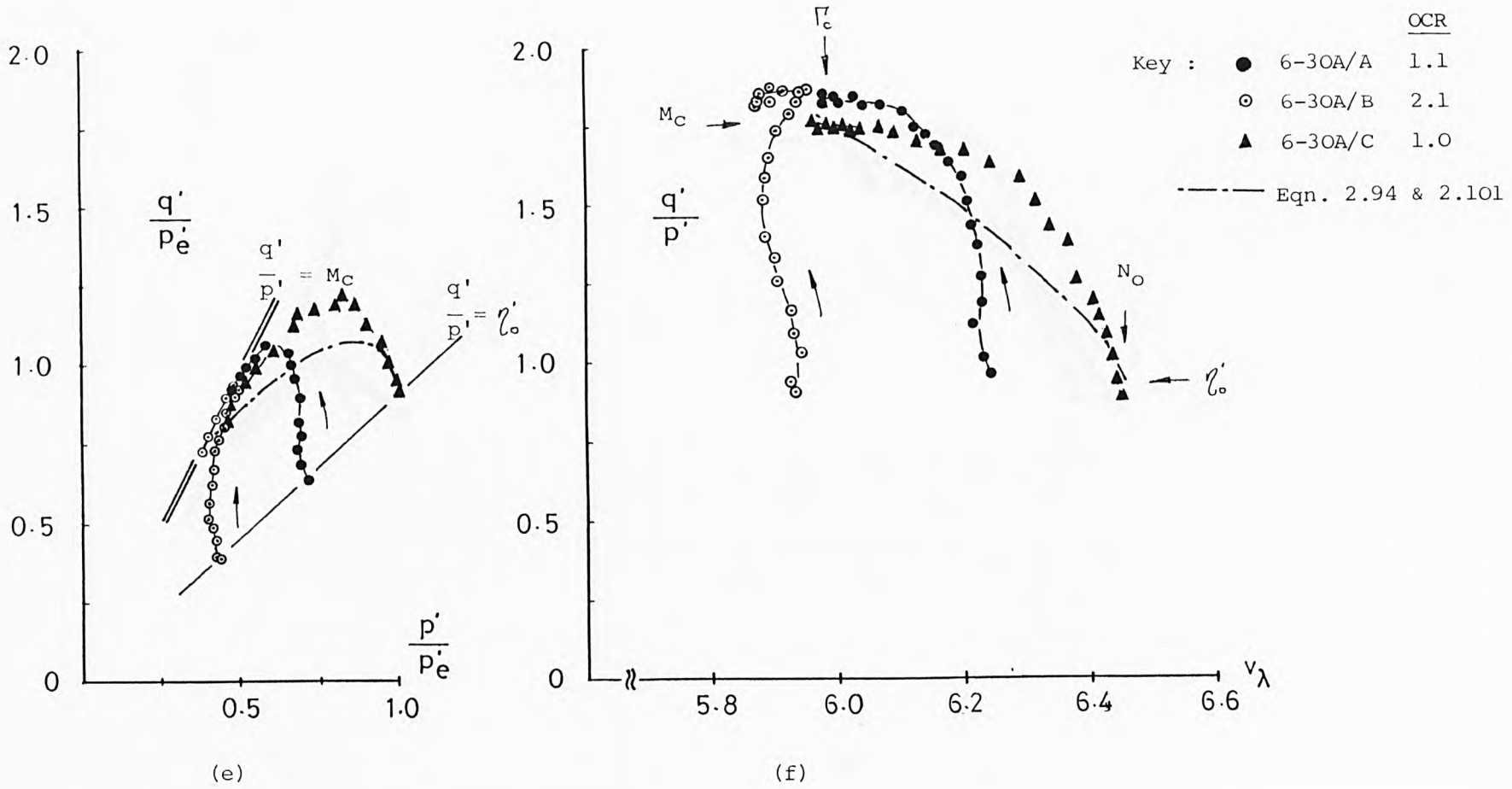

Fig. 9.25 Normalised state paths for GME C-6 specimens. (Sample 6-30A)

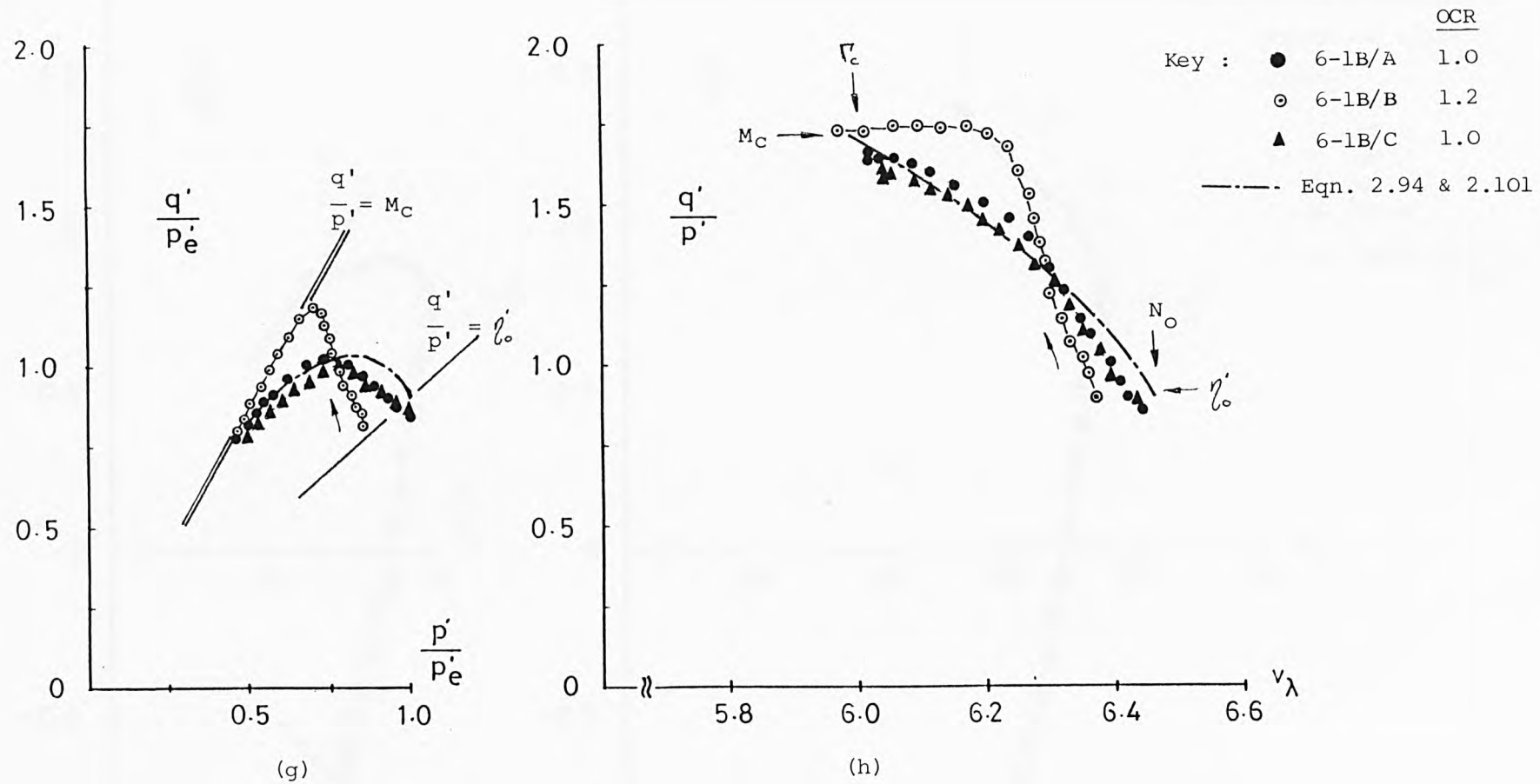

Fig. 9.25 Normalised state paths for GME C-6 specimens. (Sample 6-1B)

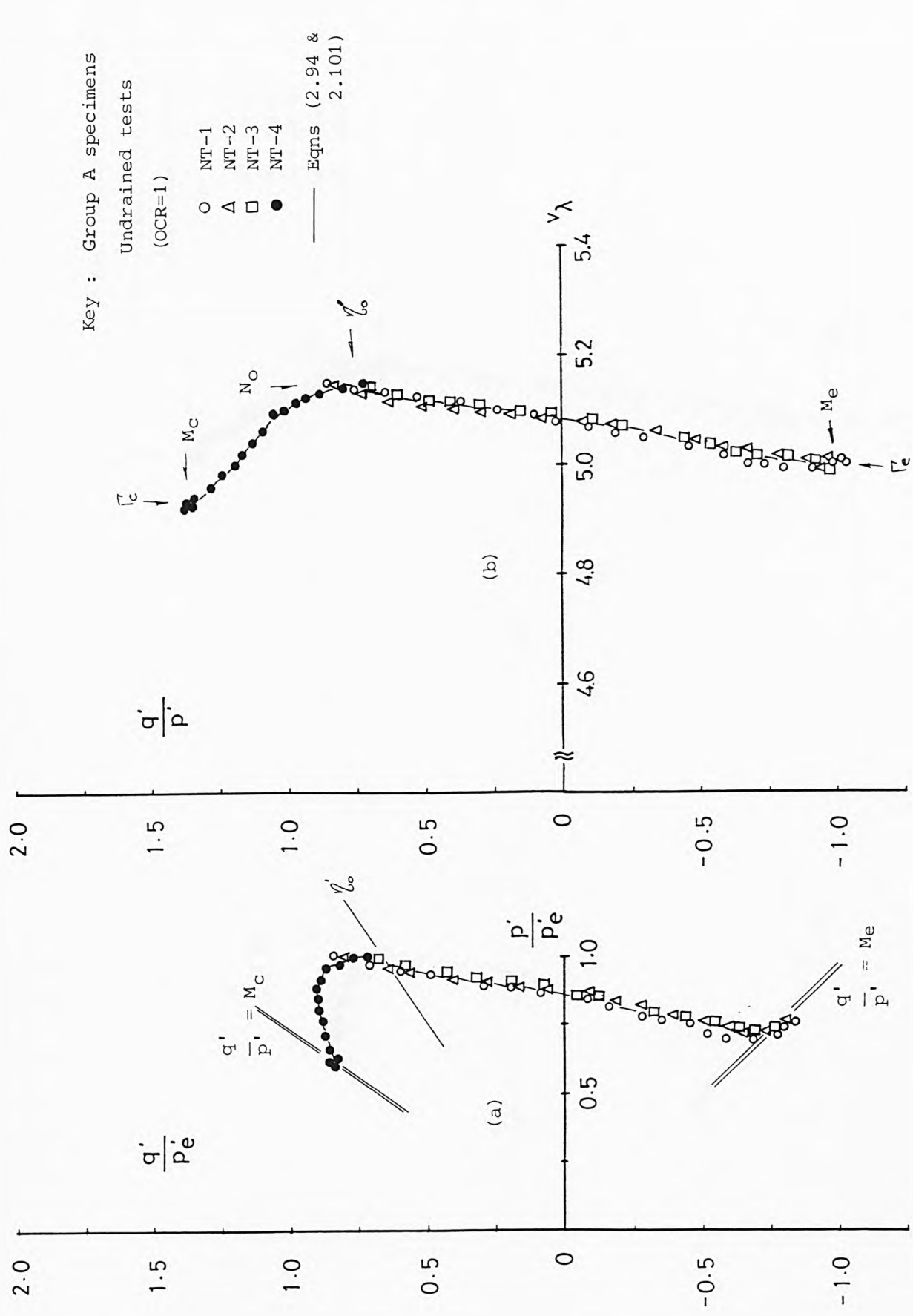

Fig. 9.26 Normalised state paths for NAP tubed specimens.

(Sample group A)

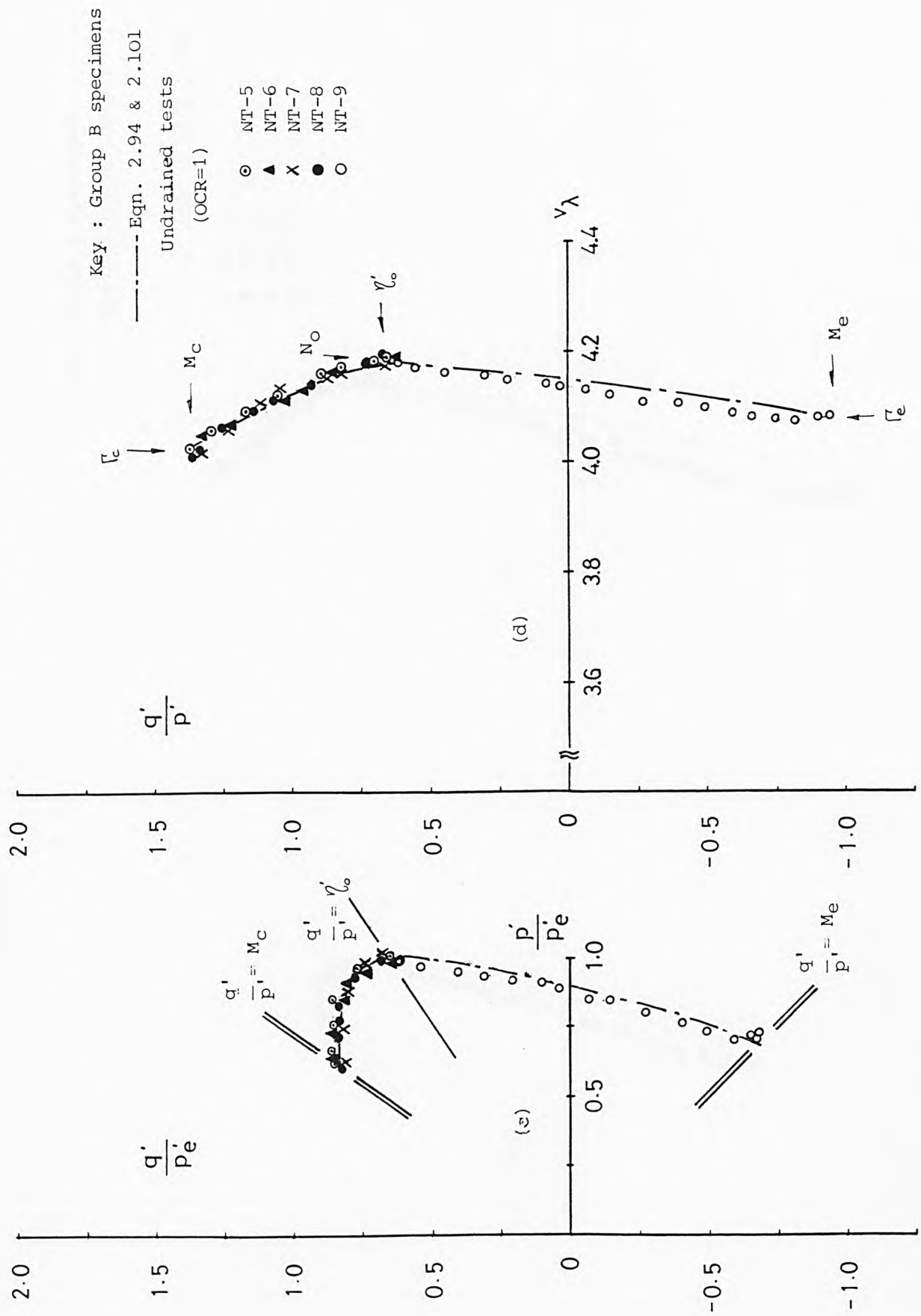

Fig. 9.26 Normalised state paths for NAP tubed specimens.

(Sample group B)

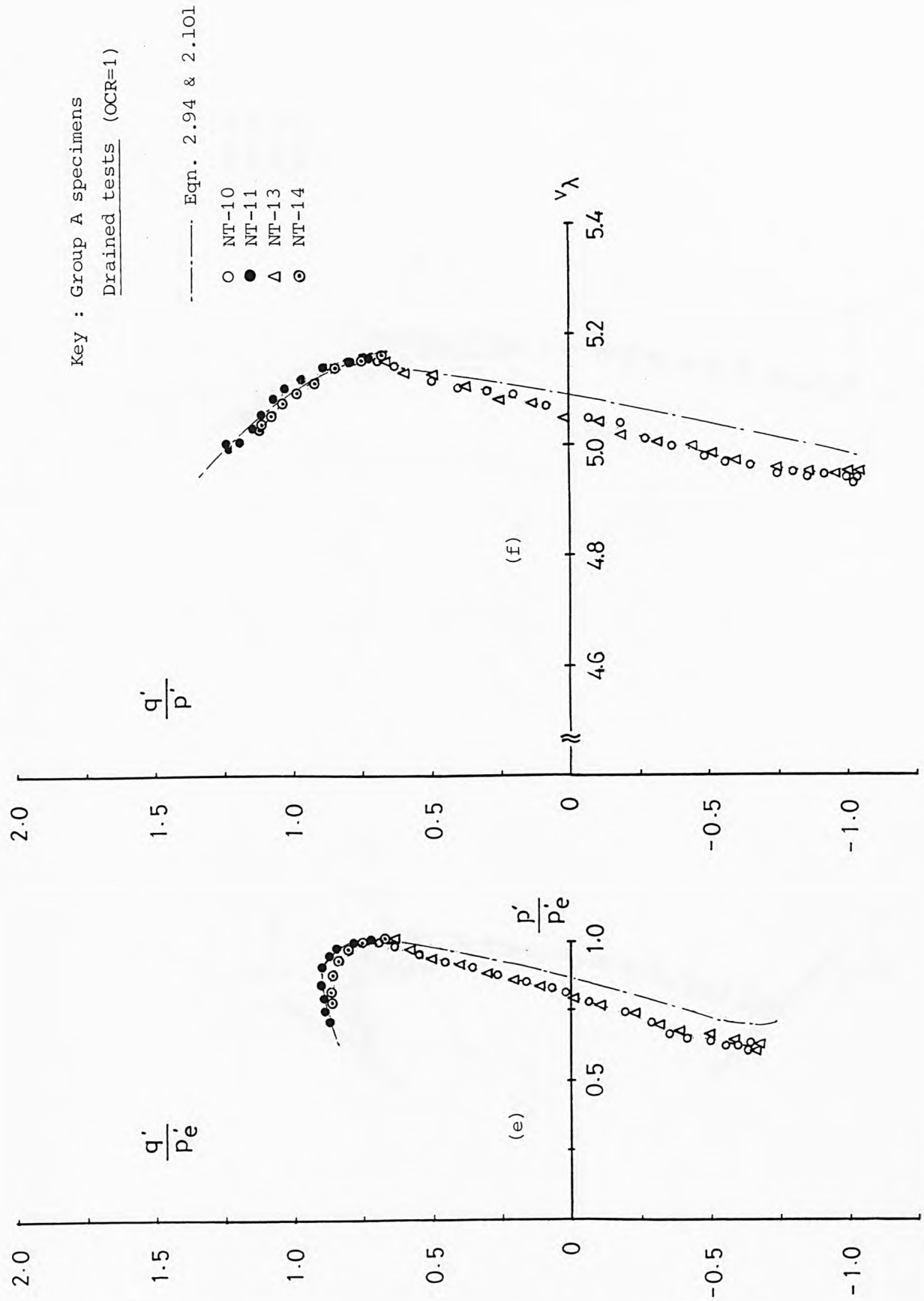

Fig. 9.26 Normalised state paths for NAP tubed specimens.

(Group A samples)

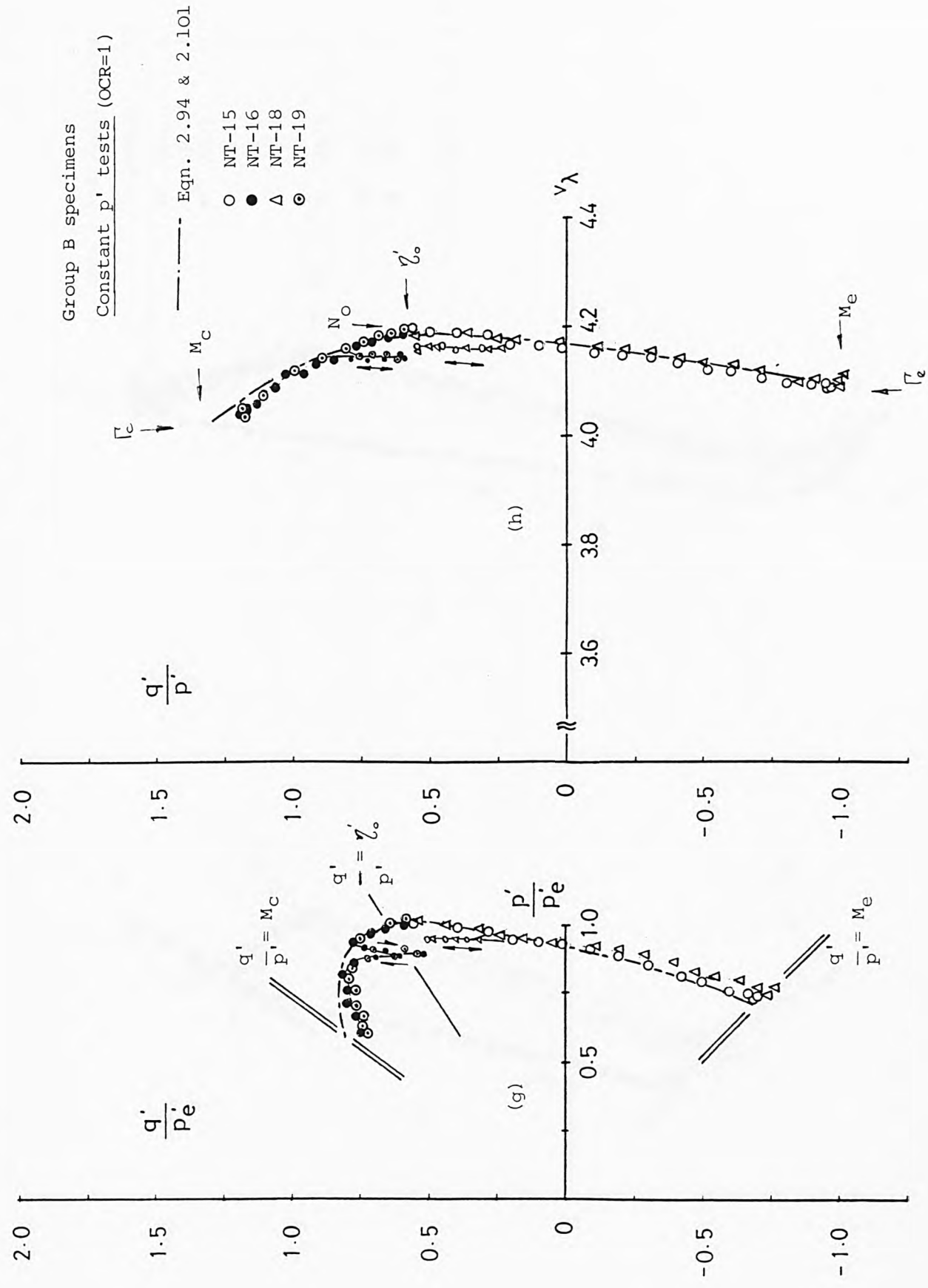

Fig. 9.26 Normalised state paths for NAP tubed specimens.

(Group B samples)

Fig. 9.27 Normalised state paths for GME reconstituted specimens.

Fig. 9.27 Normalised state paths for GME reconstituted specimens.

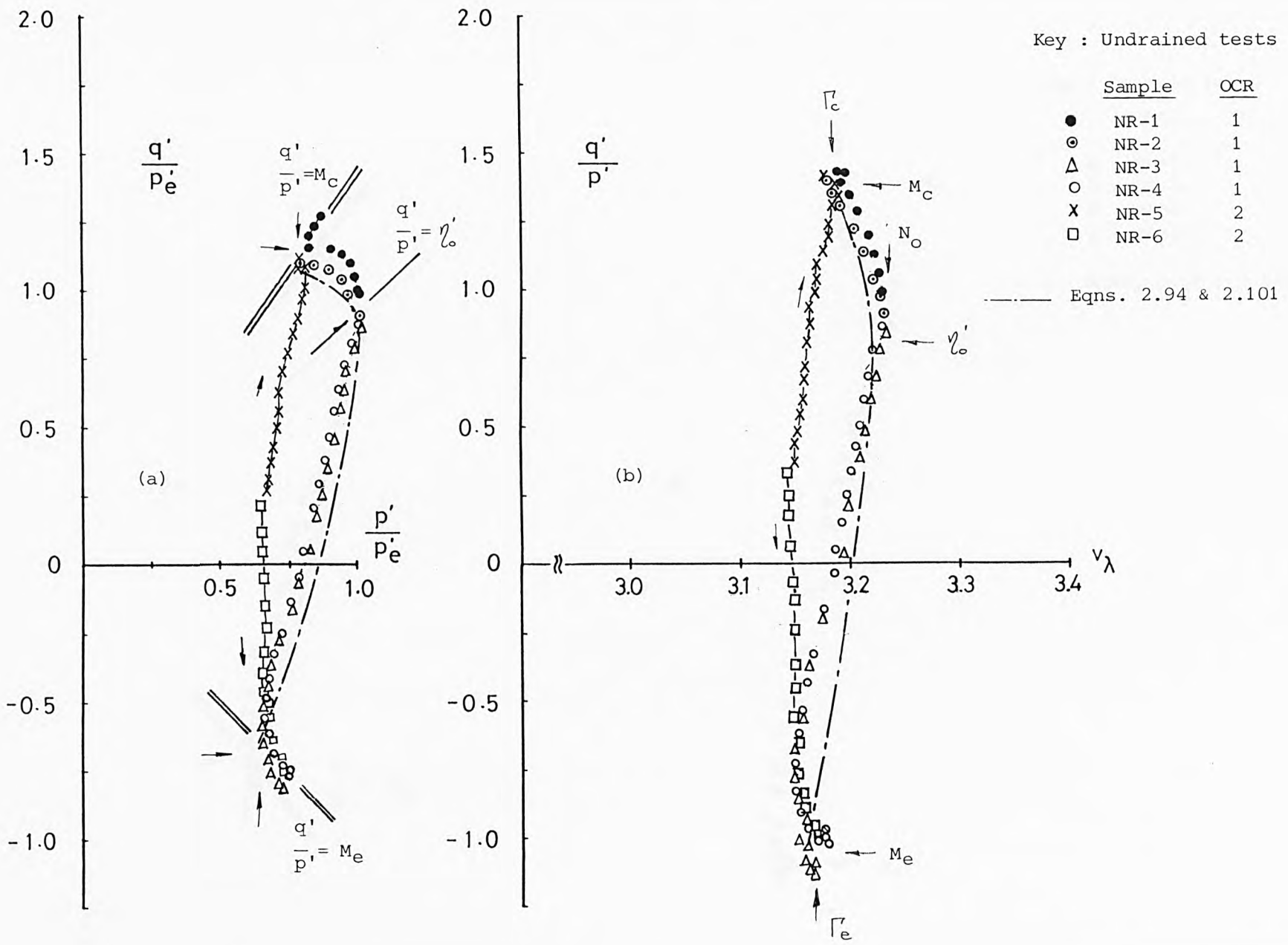

Fig. 9.28. Normalised state paths for NAP reconstituted specimens.

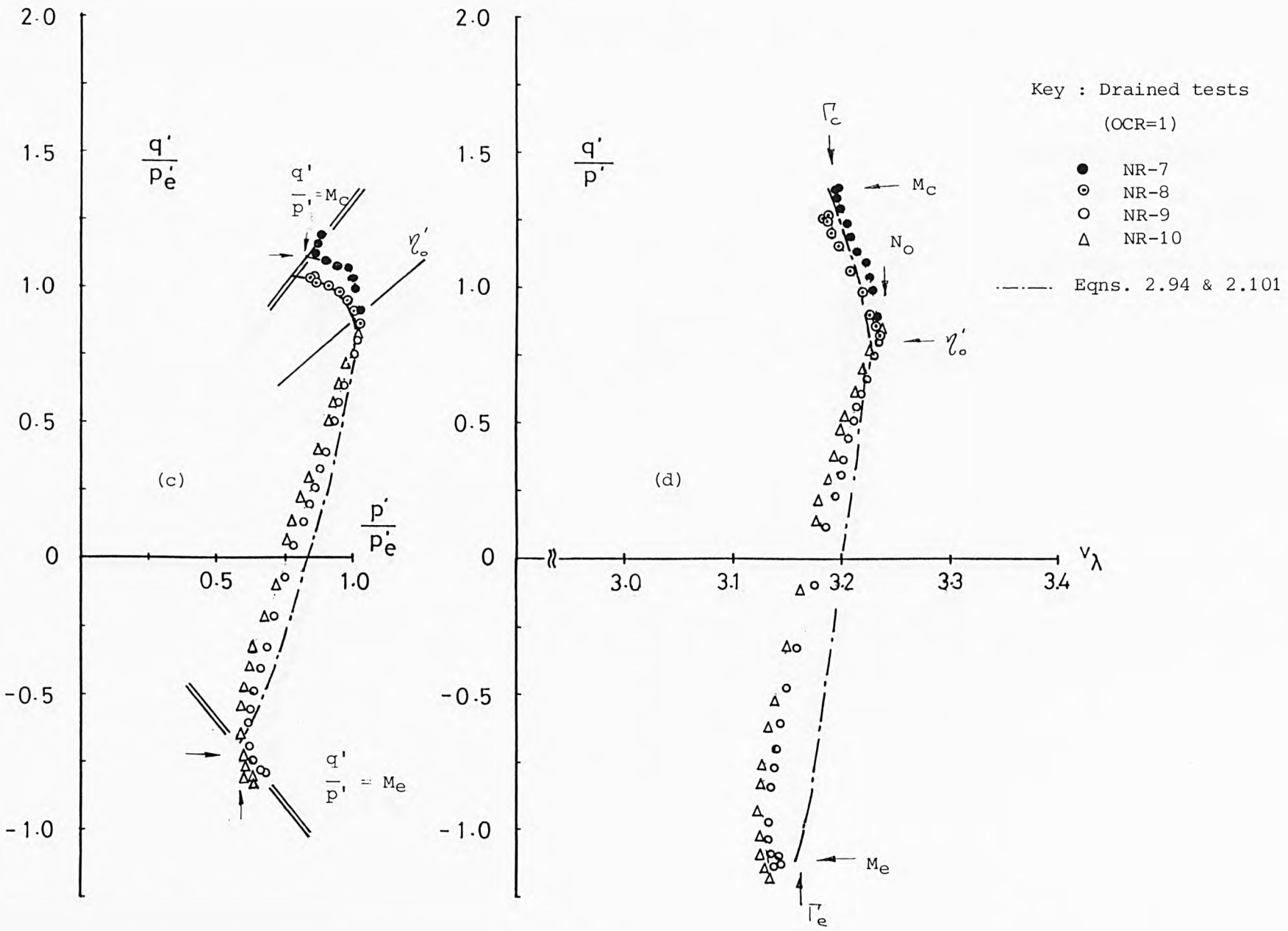

Fig. 9.28 Normalised state paths for NAP reconstituted specimens.

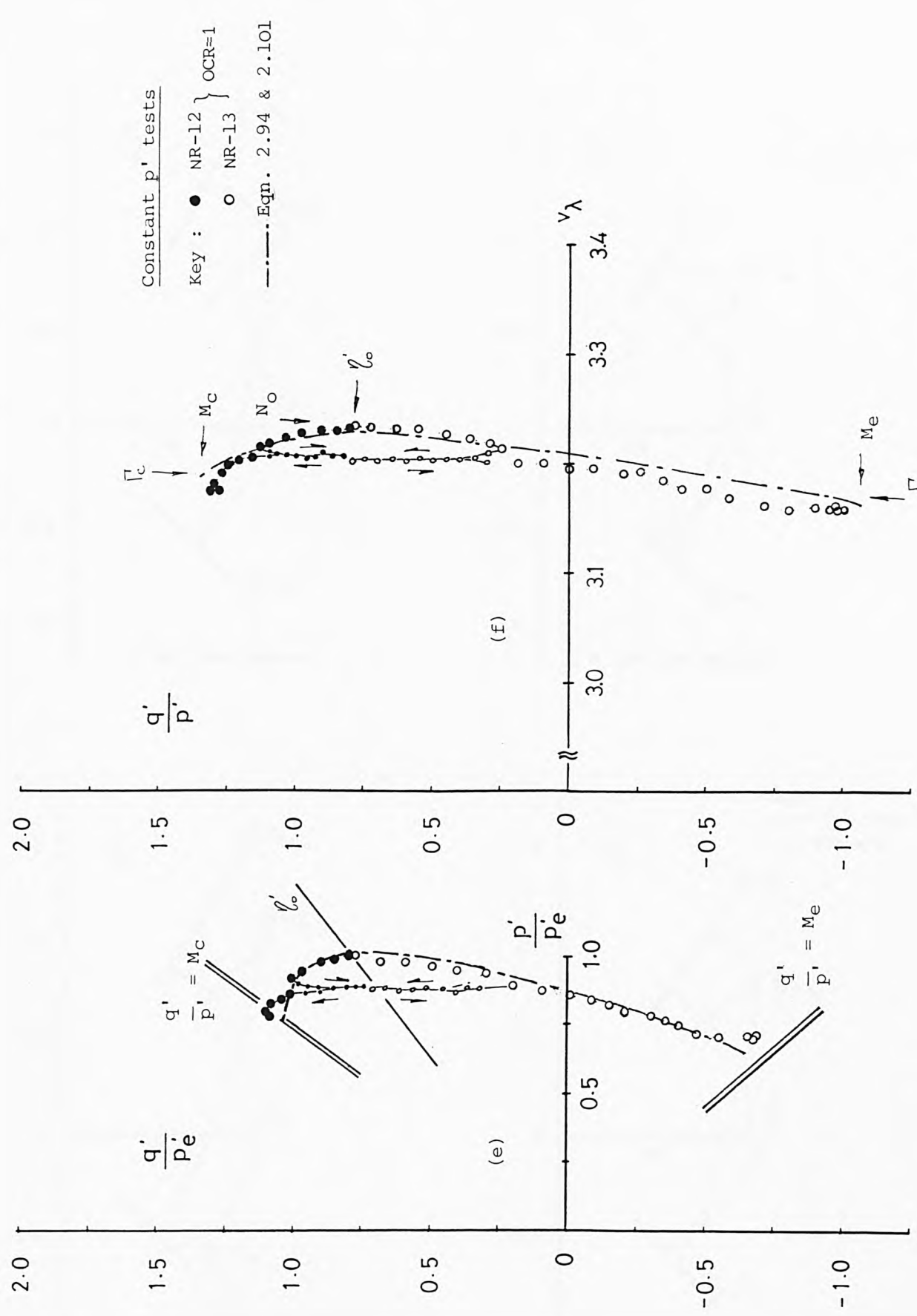

Fig. 9.28 Normalised state paths for NAP reconstituted specimens.

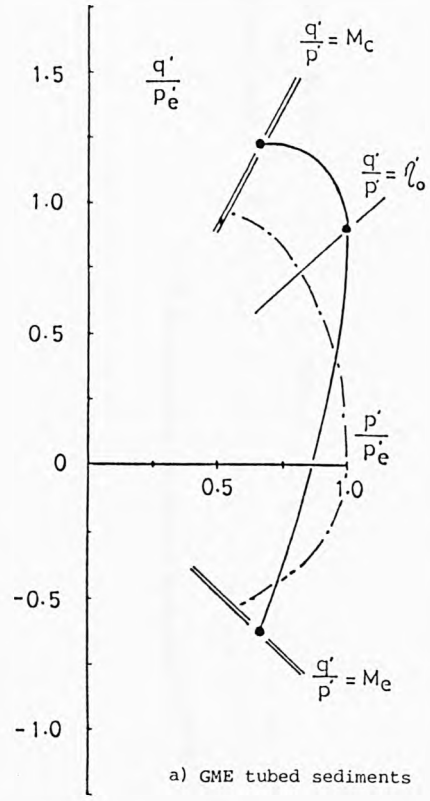

a) GME tubed sediments

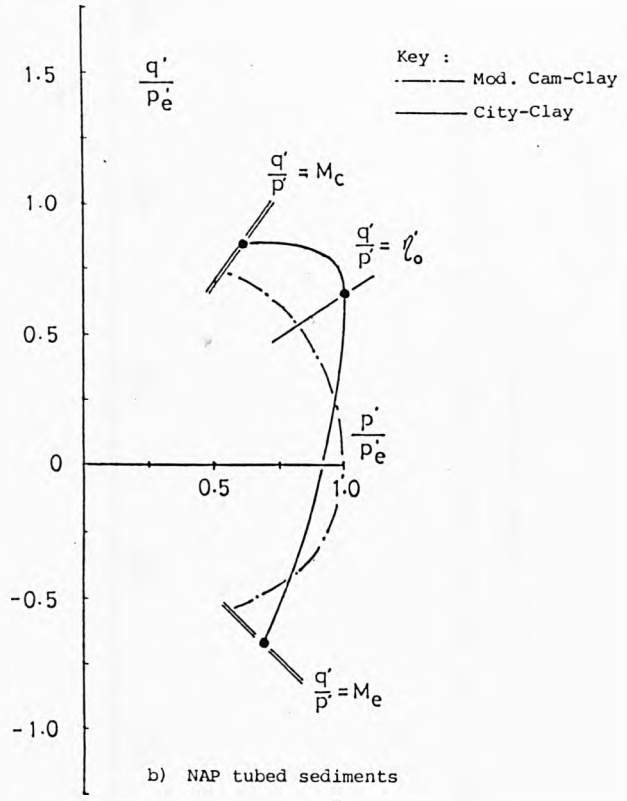

b) NAP tubed sediments

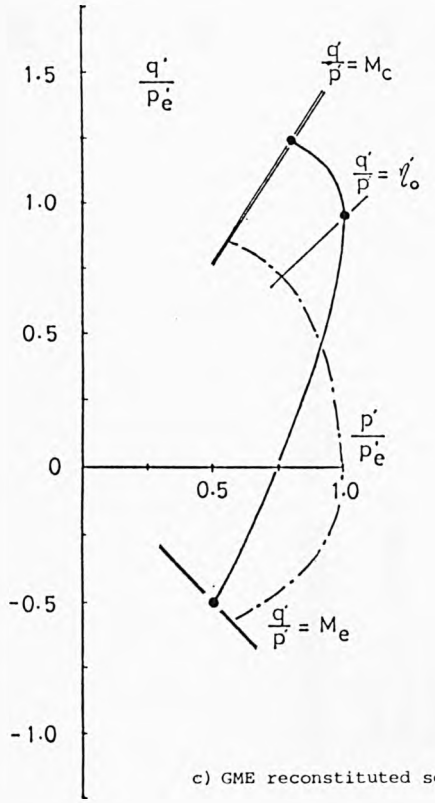

c) GME reconstituted sediments

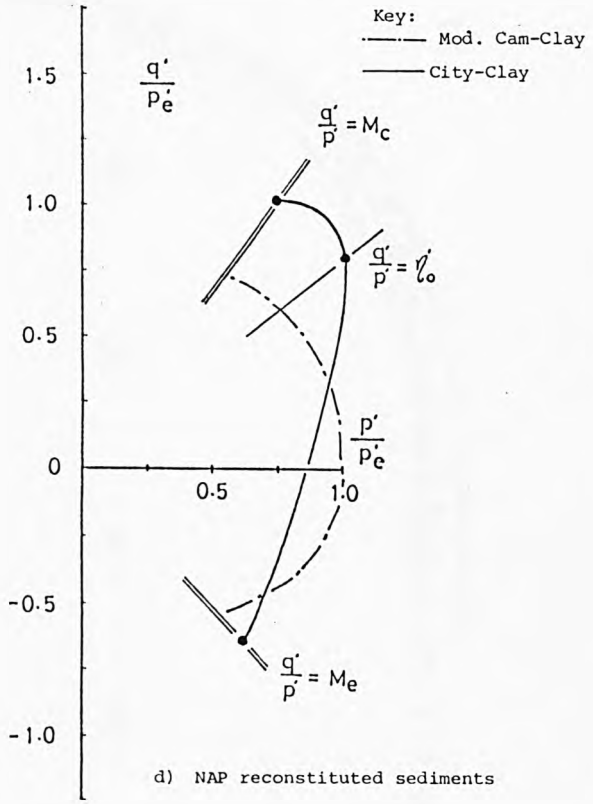

d) NAP reconstituted sediments

Fig. 9.29 State boundary surfaces for deep-ocean sediments.

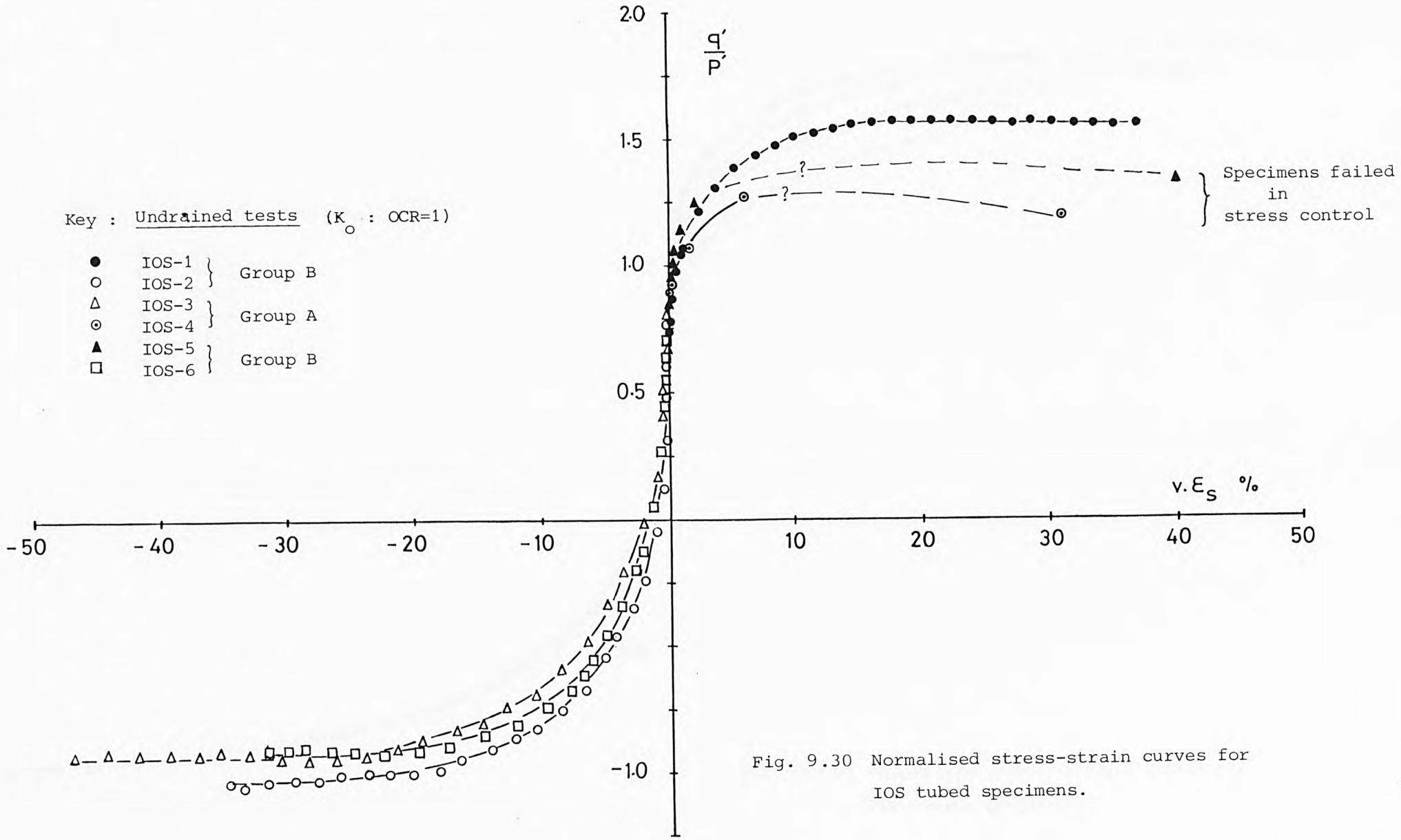

Fig. 9.30 Normalised stress-strain curves for IOS tubed specimens.

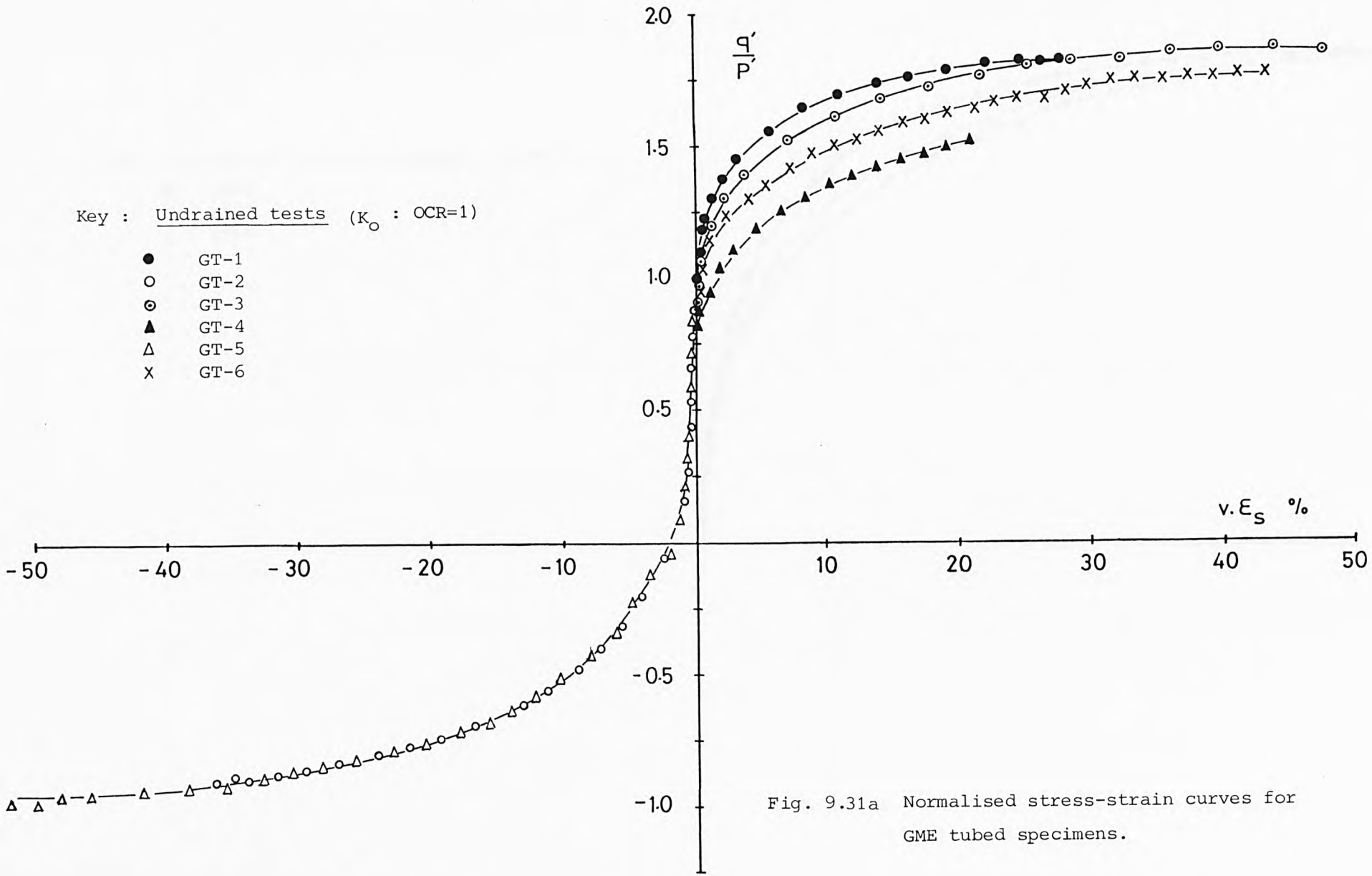

Fig. 9.31a Normalised stress-strain curves for GME tubed specimens.

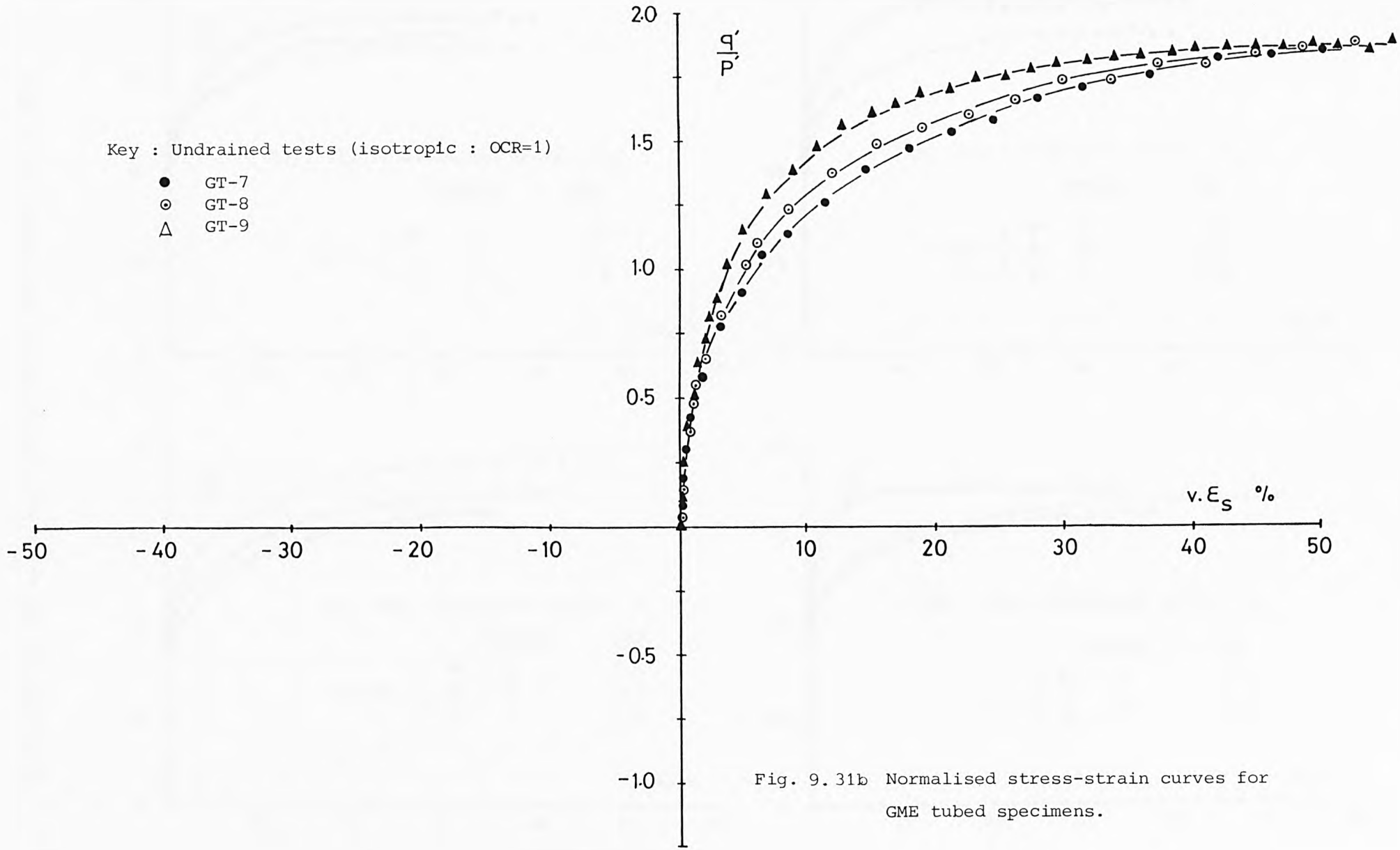

Fig. 9.31b Normalised stress-strain curves for GME tubed specimens.

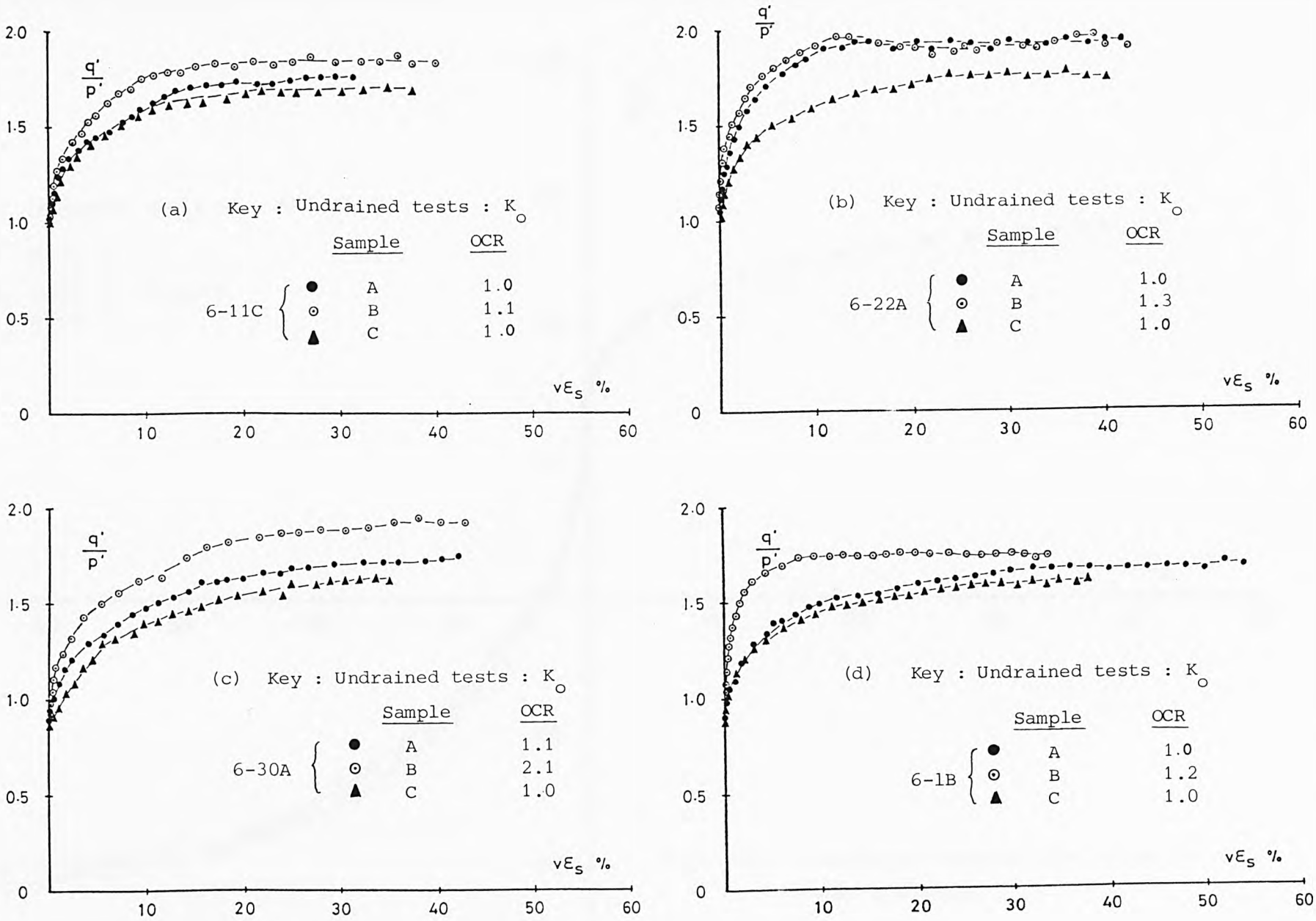

Fig. 9.32 Normalised stress-strain curves for GME C-6 specimens.

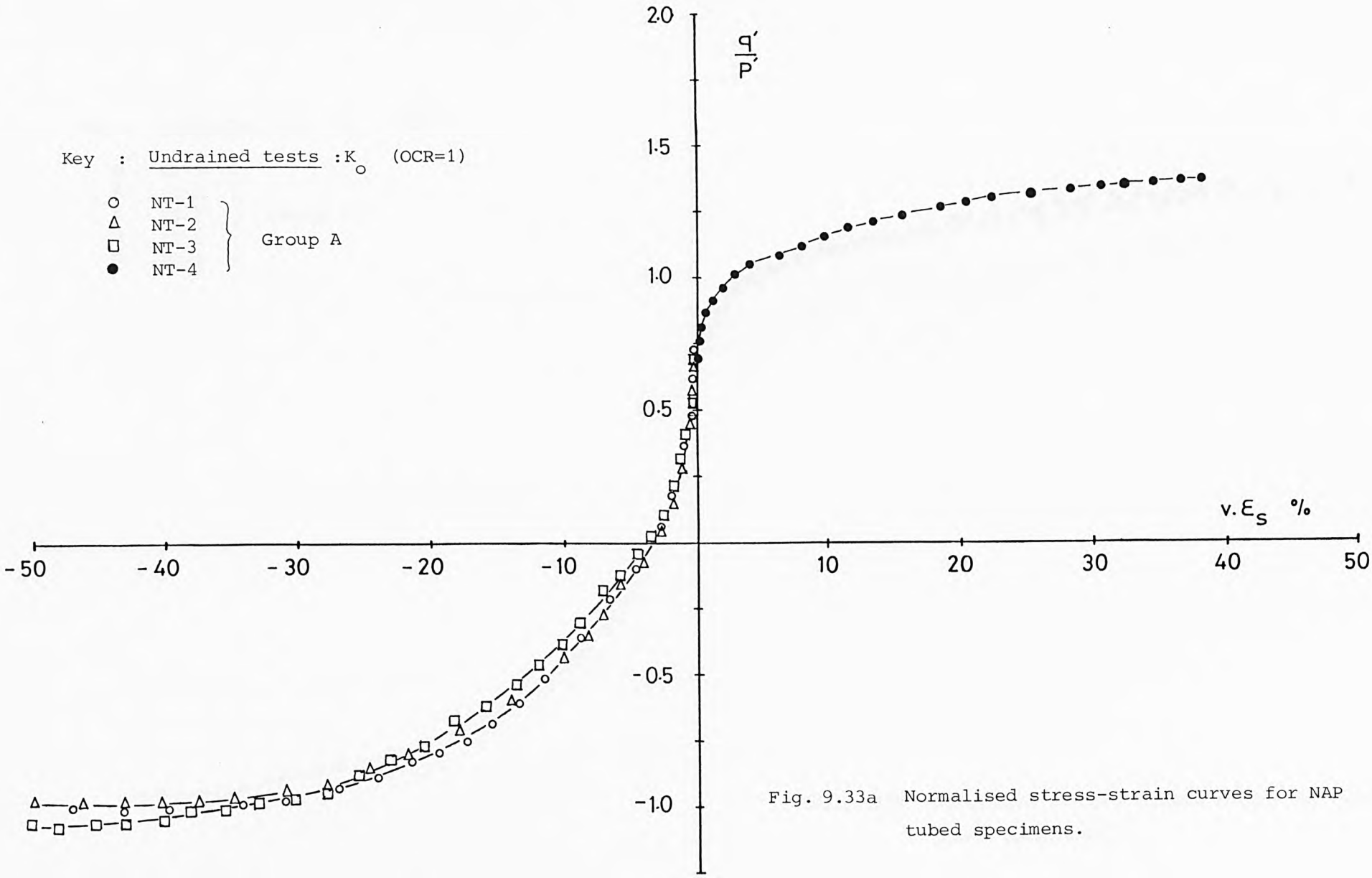

Fig. 9.33a Normalised stress-strain curves for NAP tubed specimens.

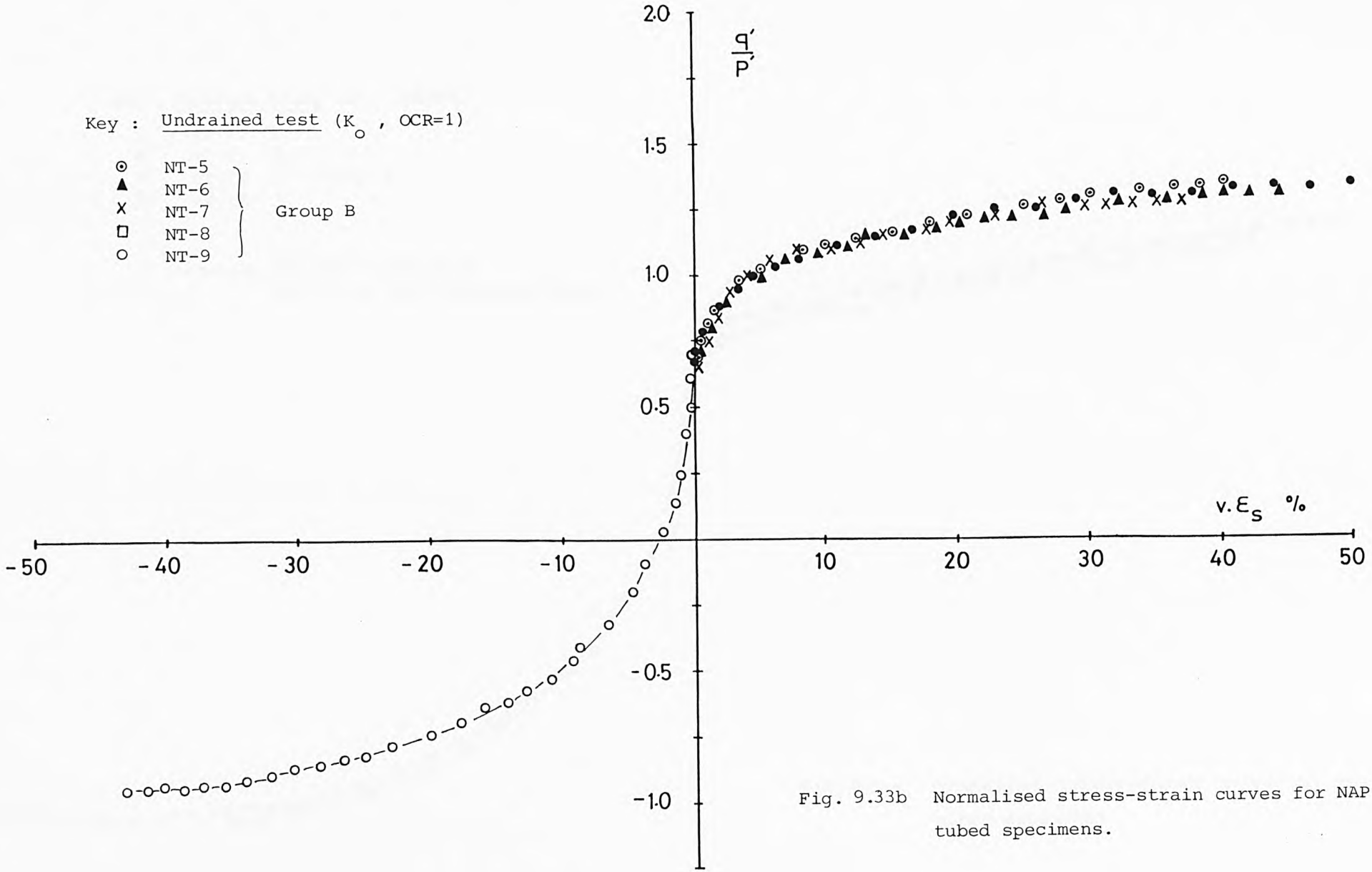

Fig. 9.33b Normalised stress-strain curves for NAP tubed specimens.

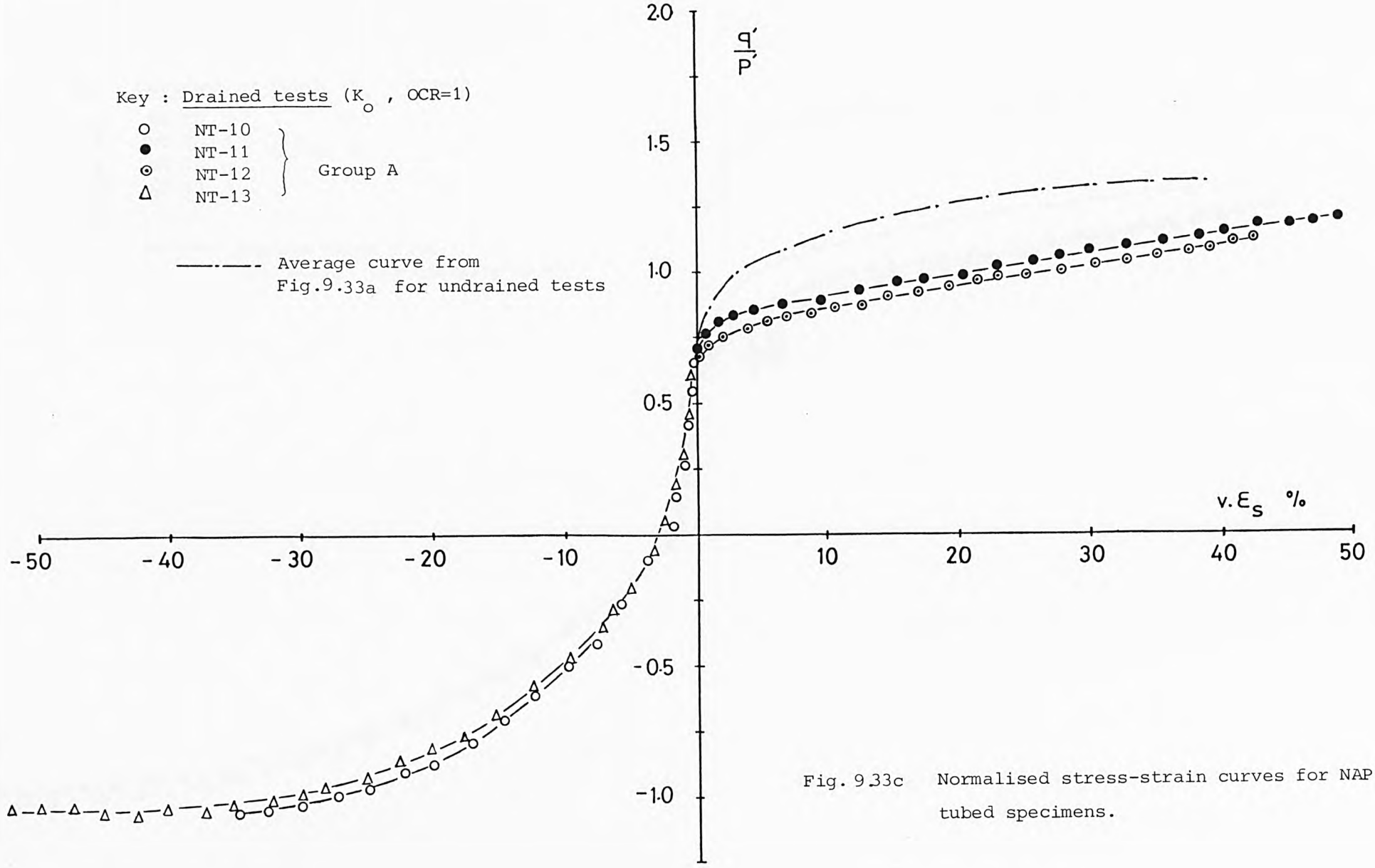

Fig. 9.33c Normalised stress-strain curves for NAP tubed specimens.

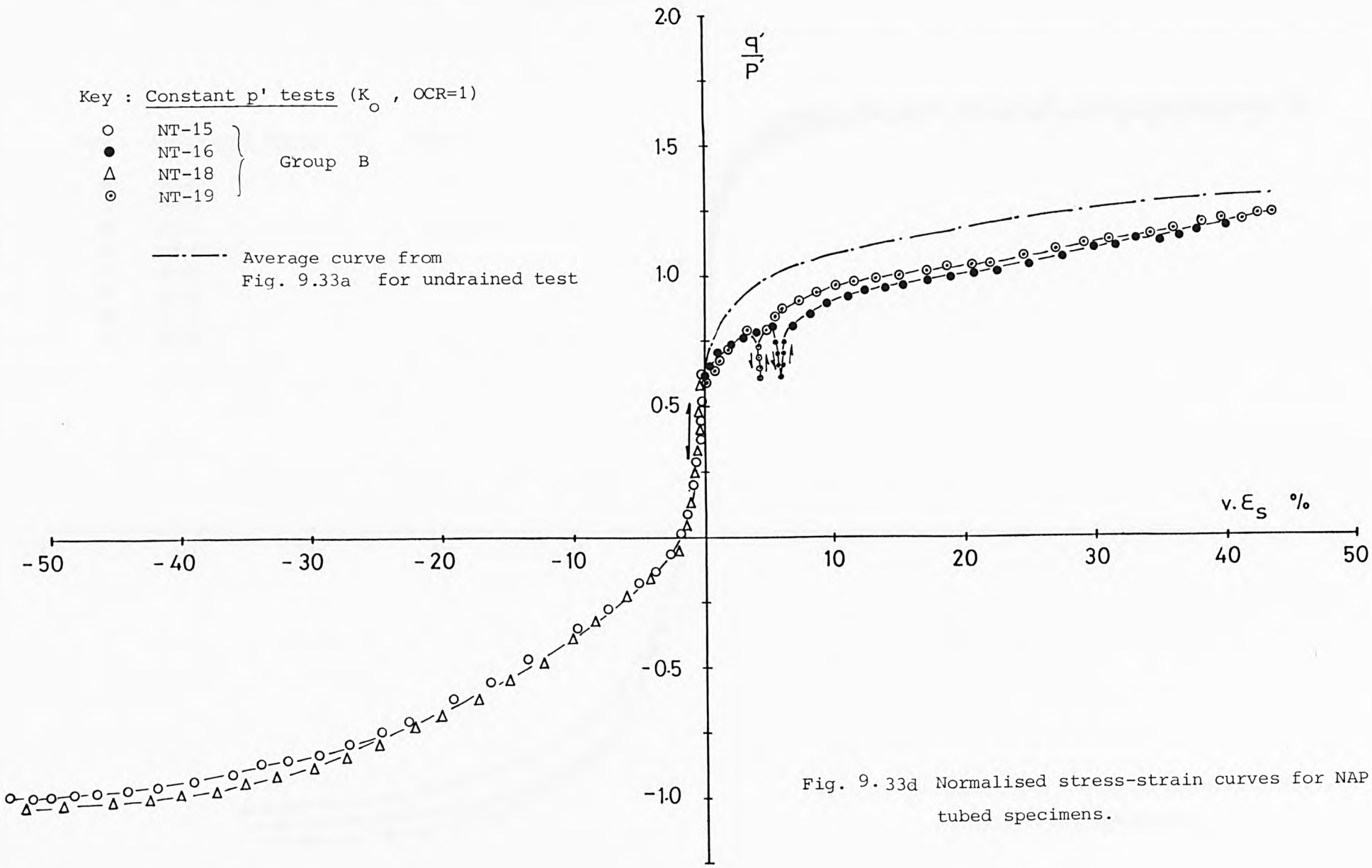

Fig. 9.33d Normalised stress-strain curves for NAP tubed specimens.

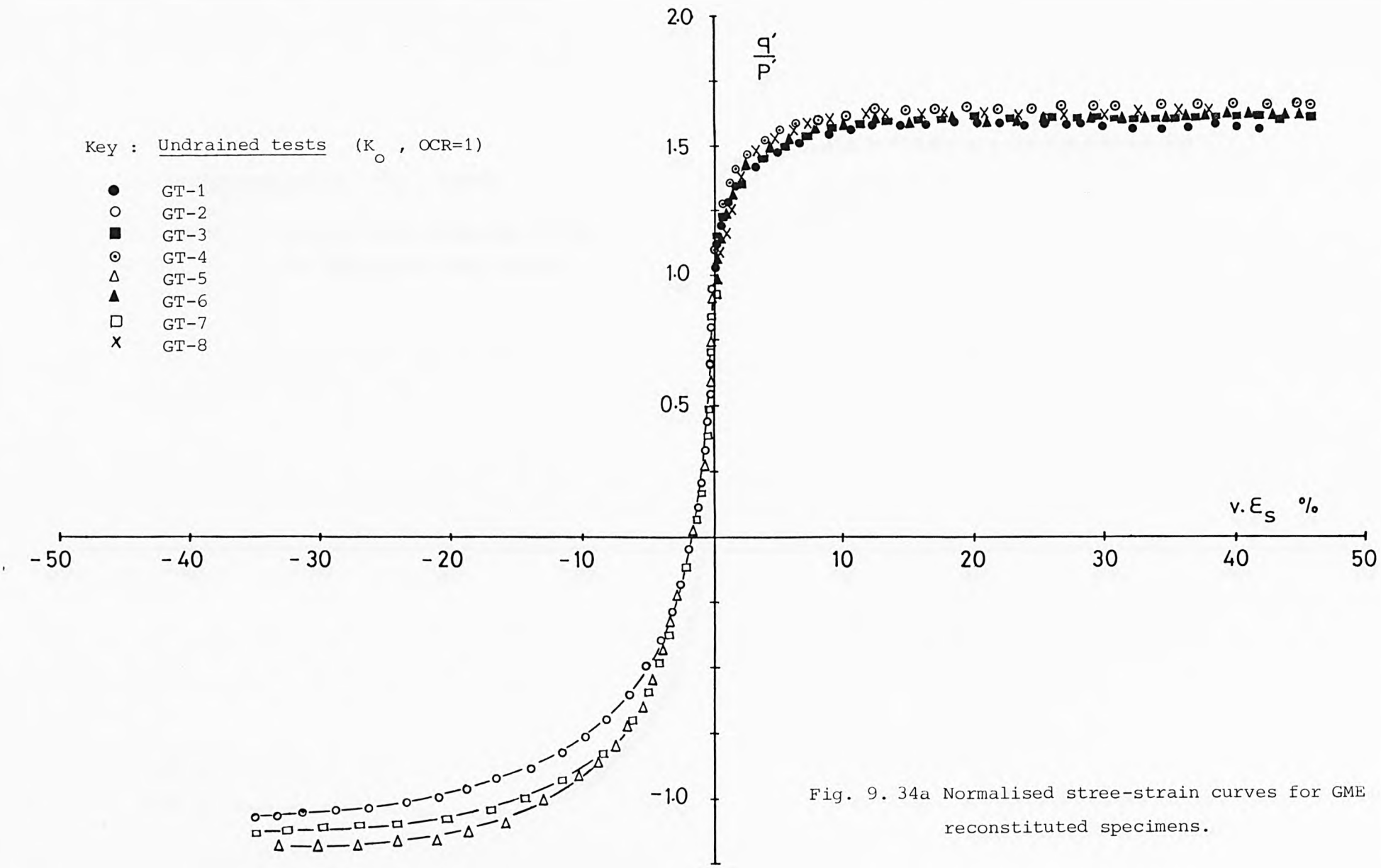

Fig. 9. 34a Normalised stree-strain curves for GME reconstituted specimens.

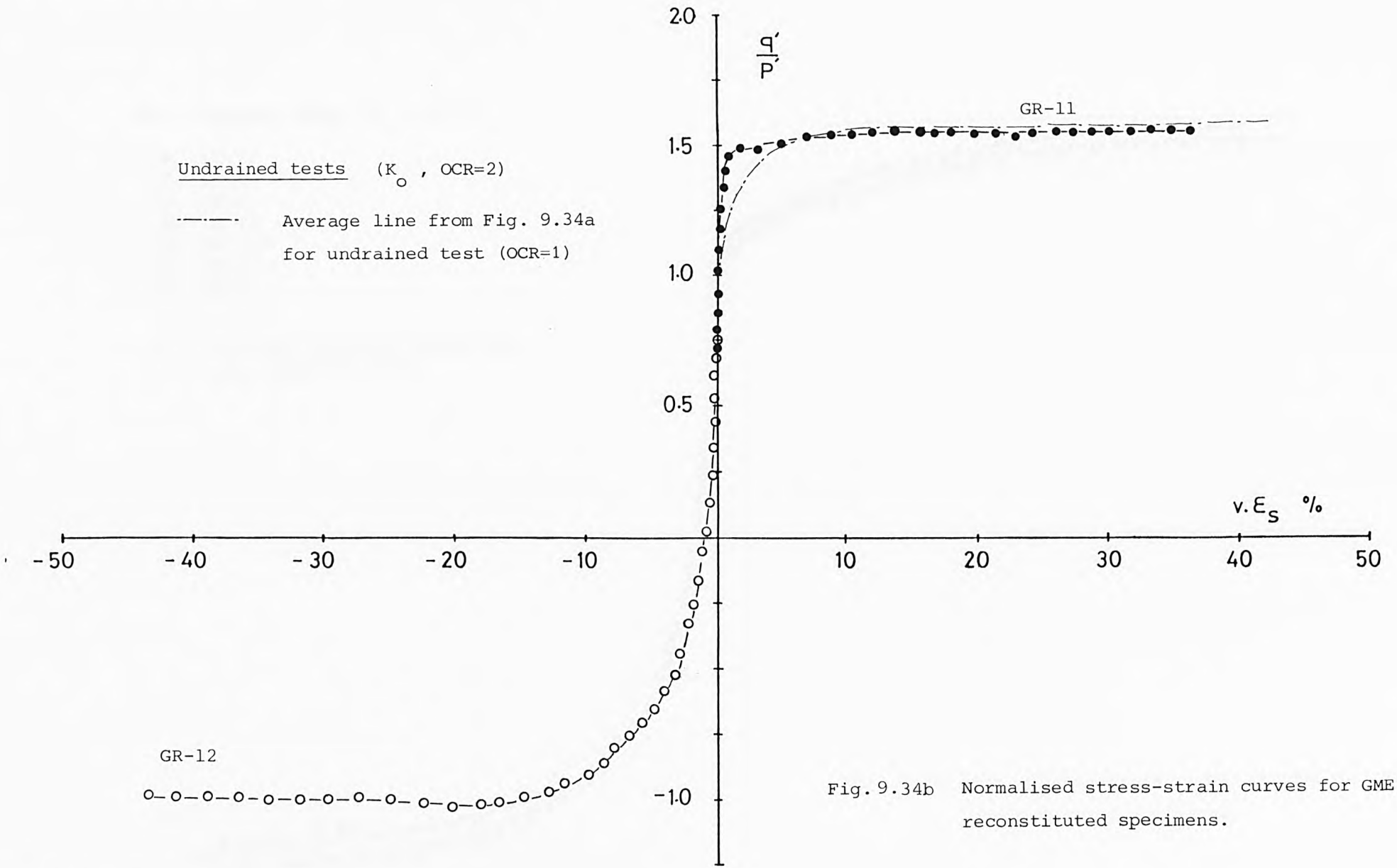

Fig. 9.34b Normalised stress-strain curves for GME reconstituted specimens.

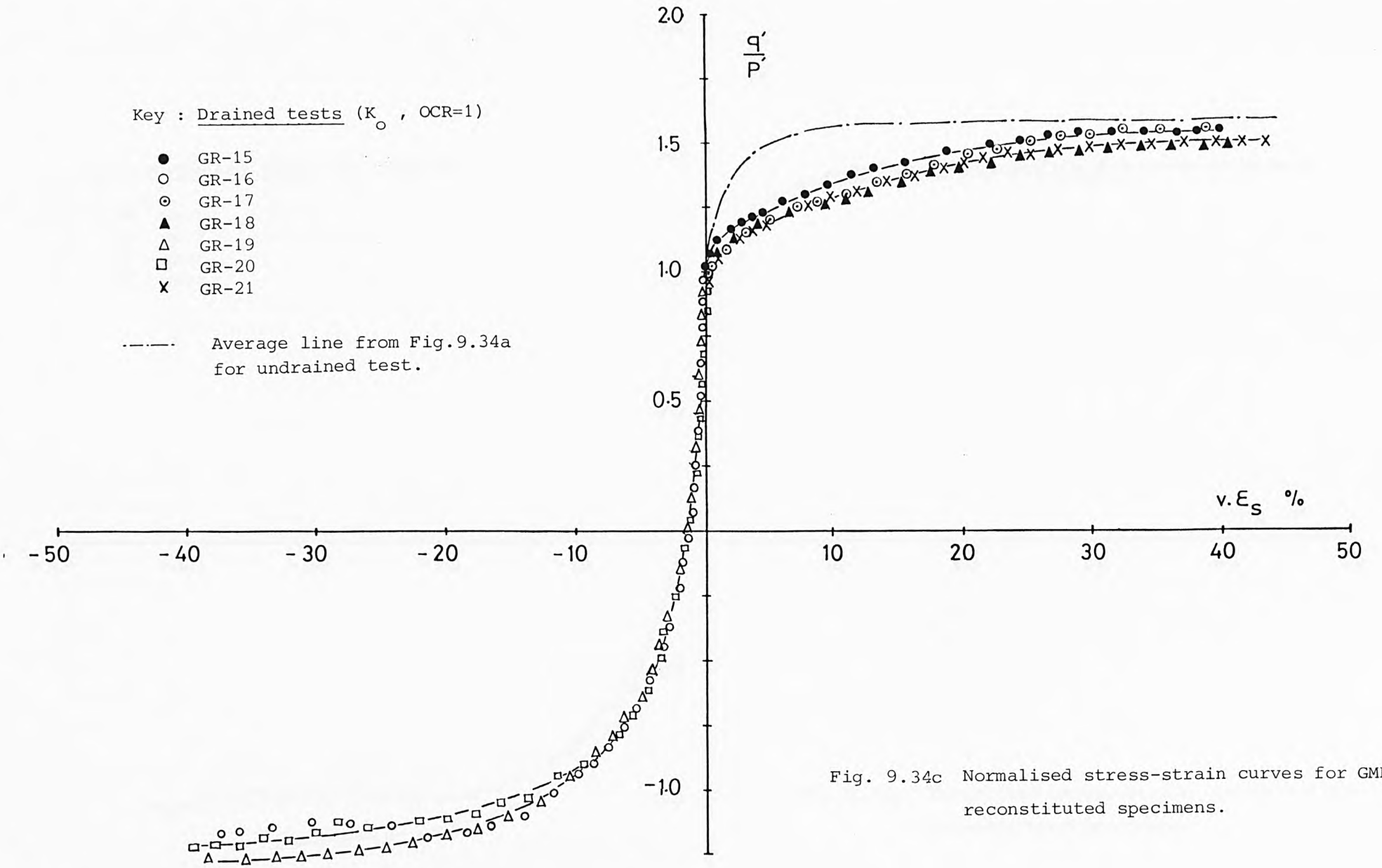

Fig. 9.34c Normalised stress-strain curves for GME reconstituted specimens.

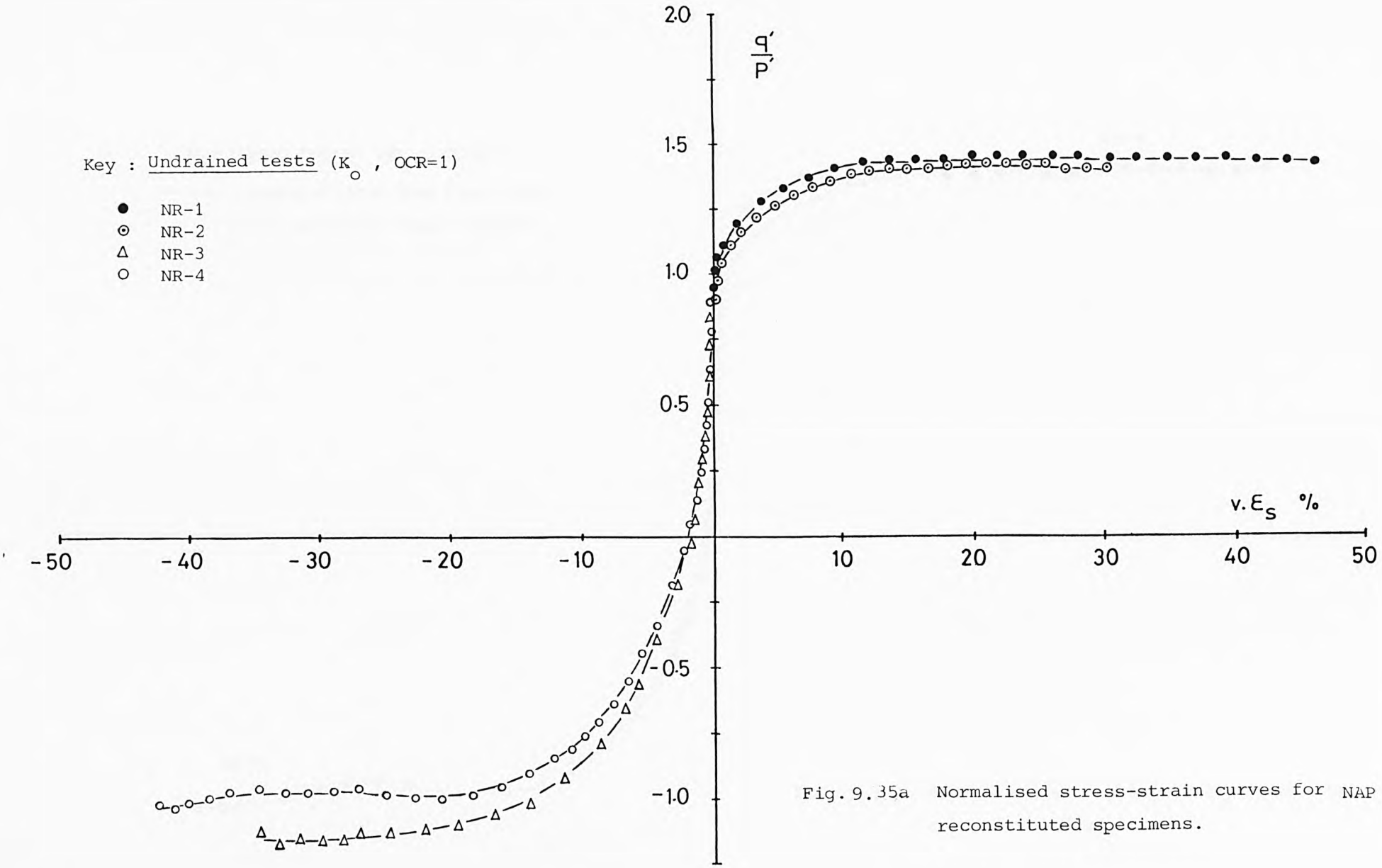

Fig. 9.35a Normalised stress-strain curves for NAP reconstituted specimens.

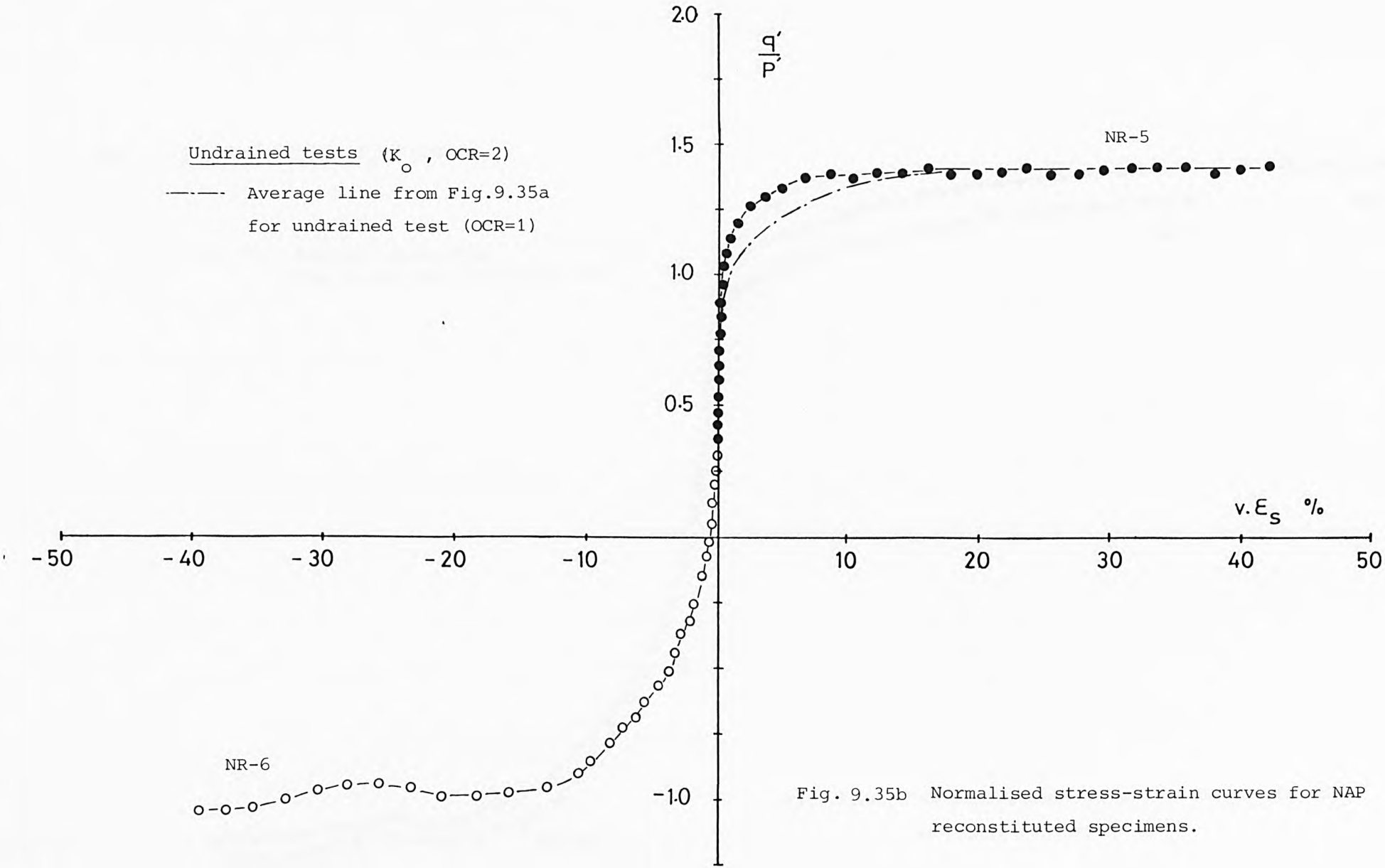

Fig. 9.35b Normalised stress-strain curves for NAP reconstituted specimens.

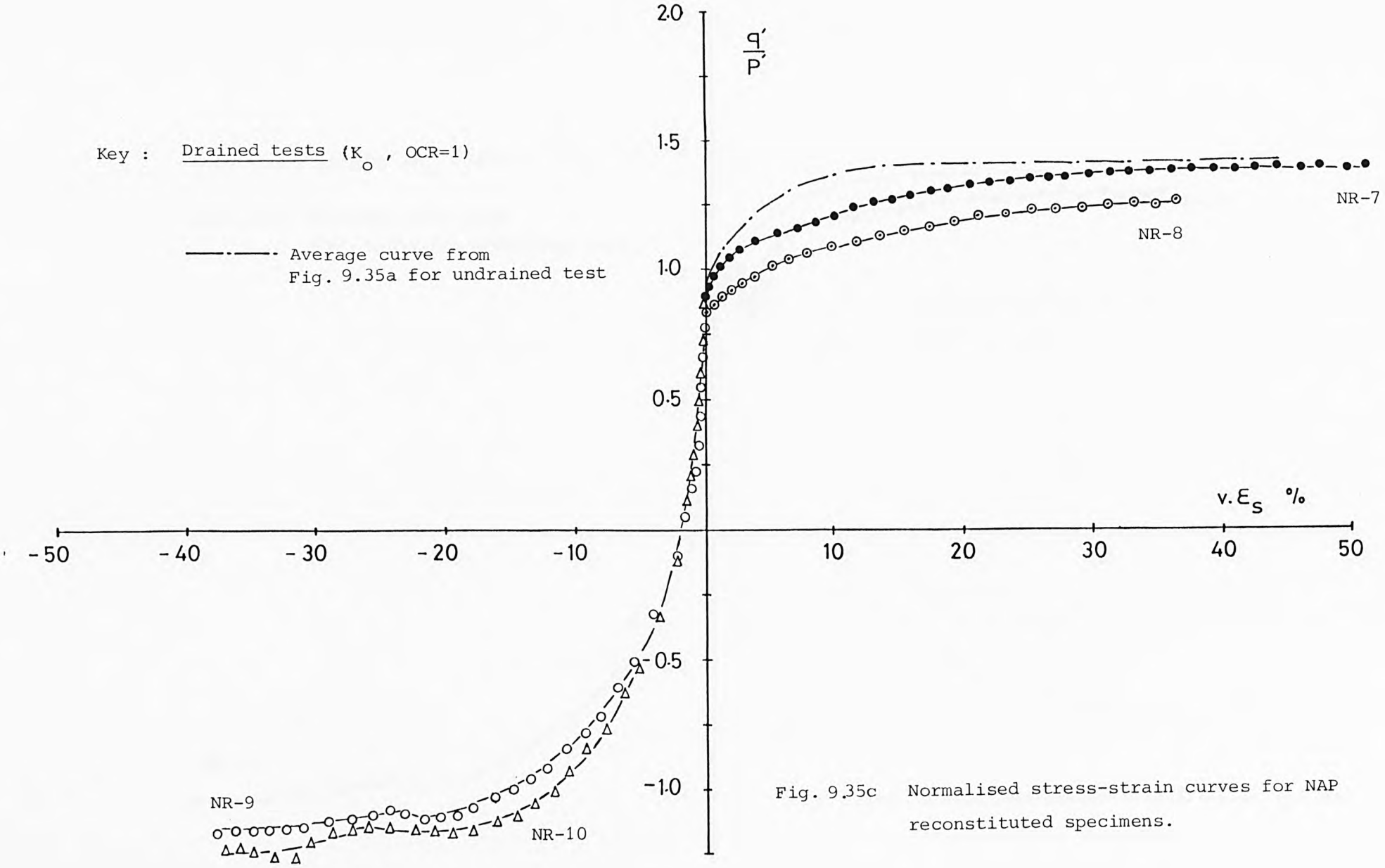

Fig. 9.35c Normalised stress-strain curves for NAP reconstituted specimens.

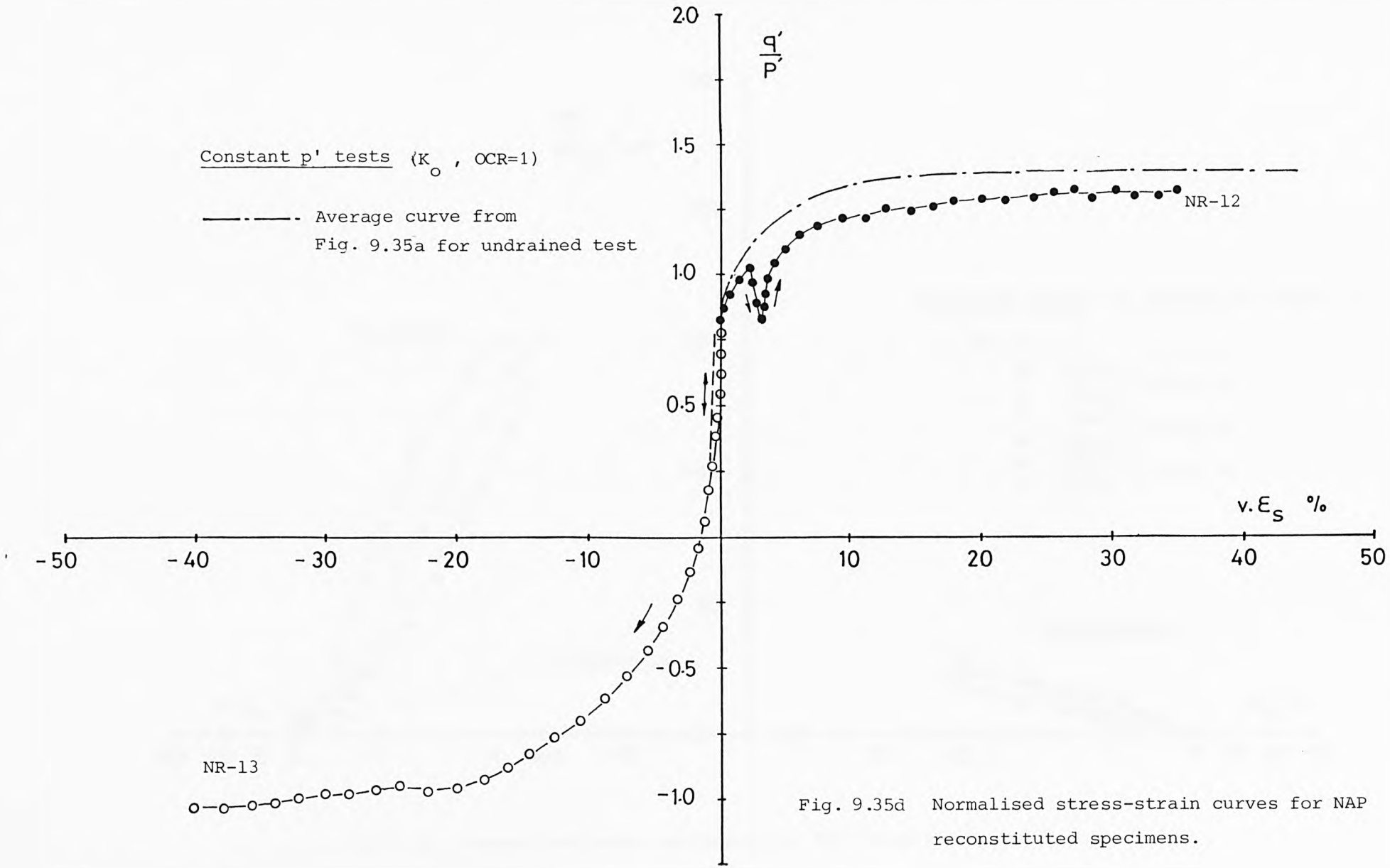

Fig. 9.35d Normalised stress-strain curves for NAP reconstituted specimens.

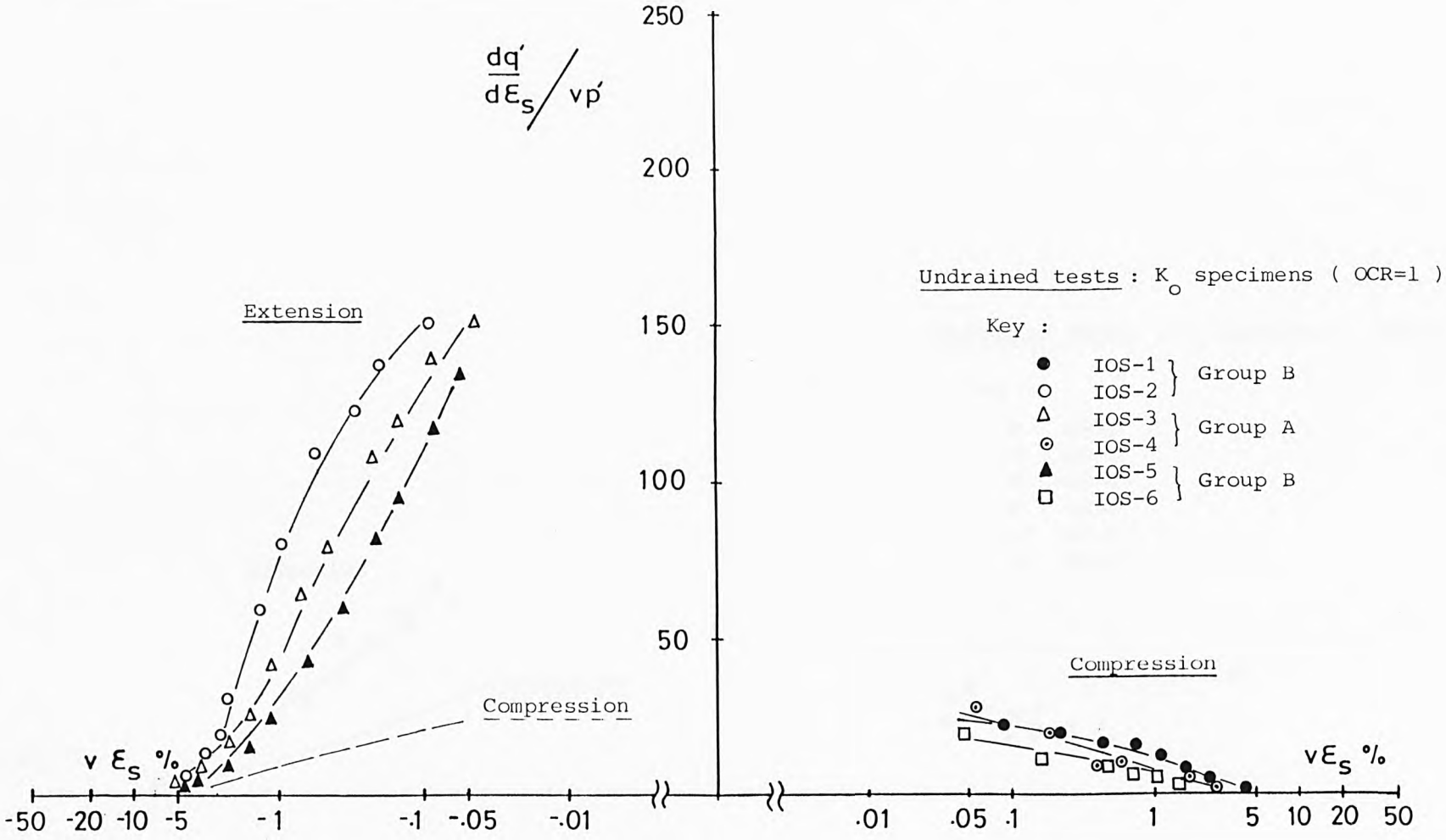

Fig. 9.36 Normalised shear stiffness for IOS tubed specimens.

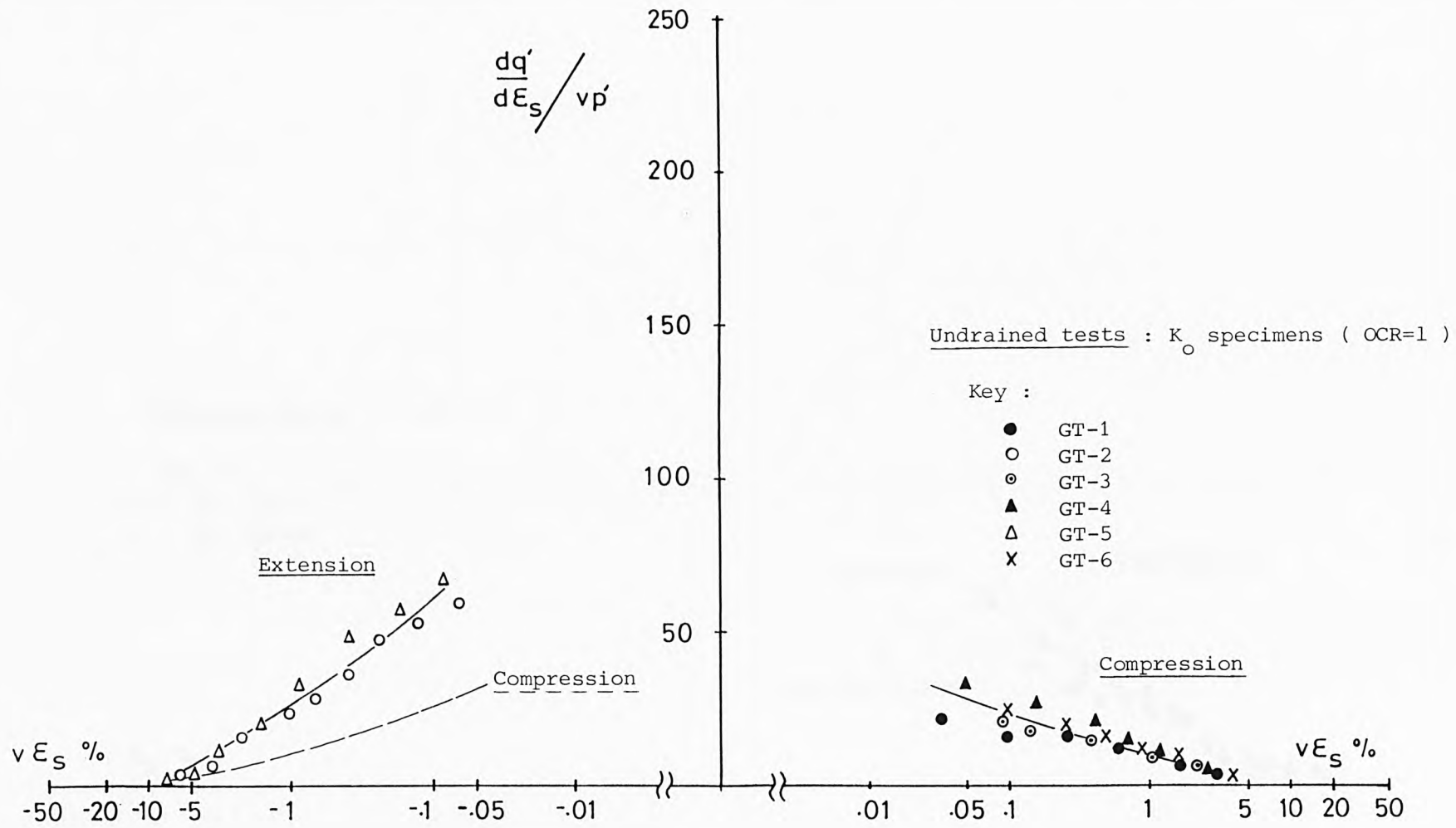

Fig. 9.37a Normalised shear stiffness for GME tubed specimens.

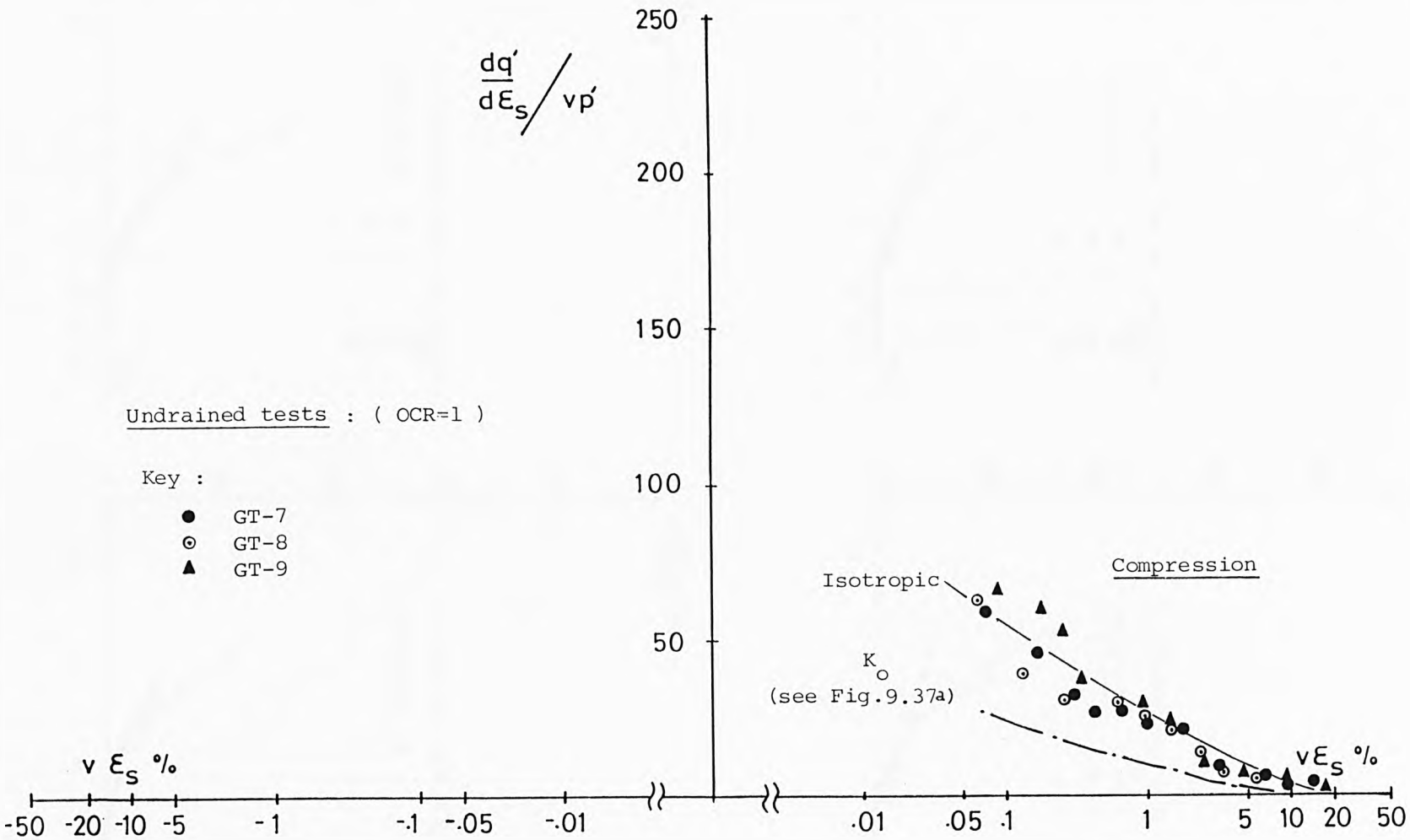

Fig. 9.37b Normalised shear stiffness for GME tubed specimens.

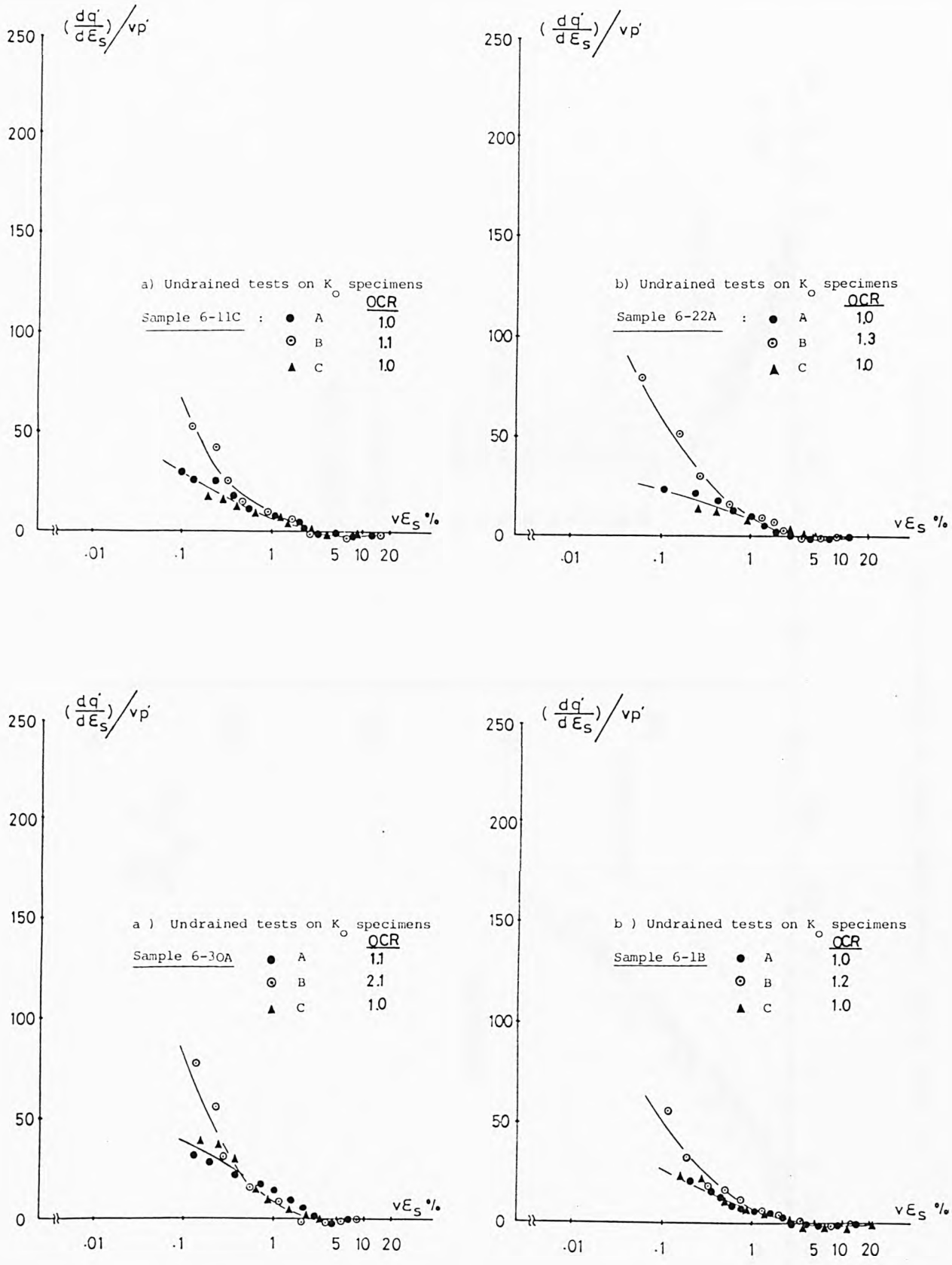

Fig.9.38 Normalised shear stiffness for GME C-6 tubed specimens.

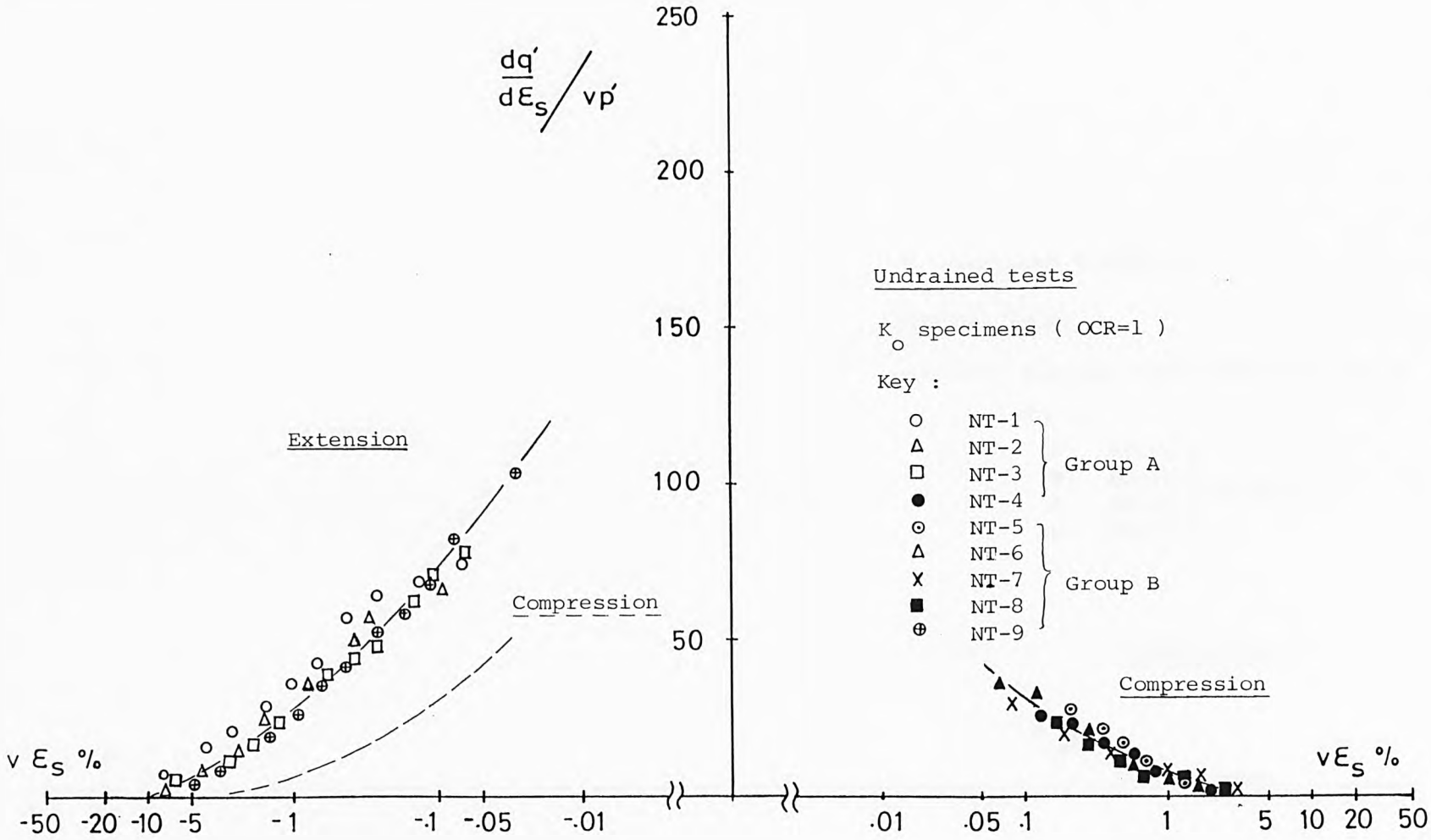

Fig. 9.39a Normalised shear stiffness for NAP tubed specimens.

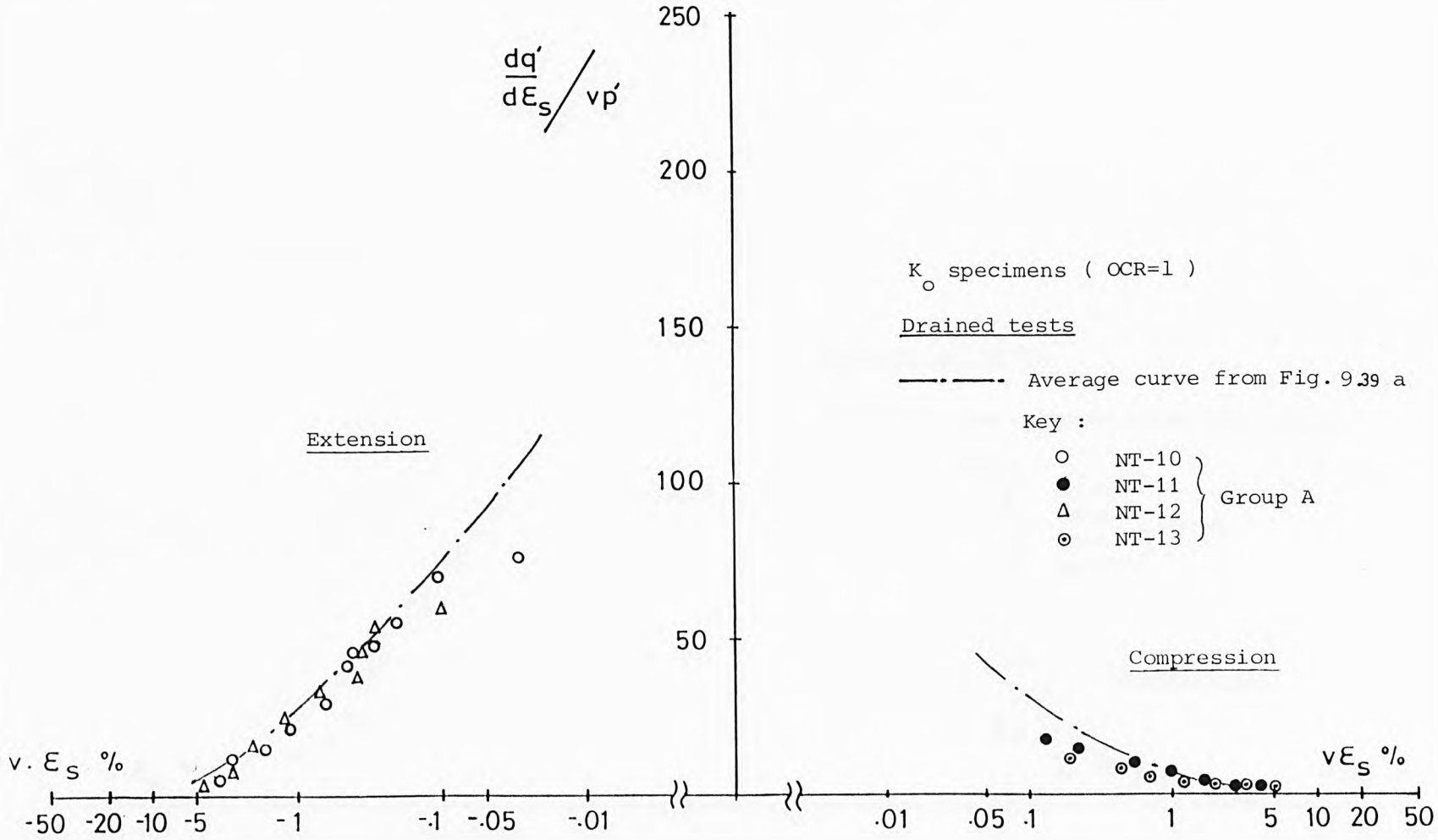

Fig. 9.39b Normalised shear stiffness for NAP tubed specimens.

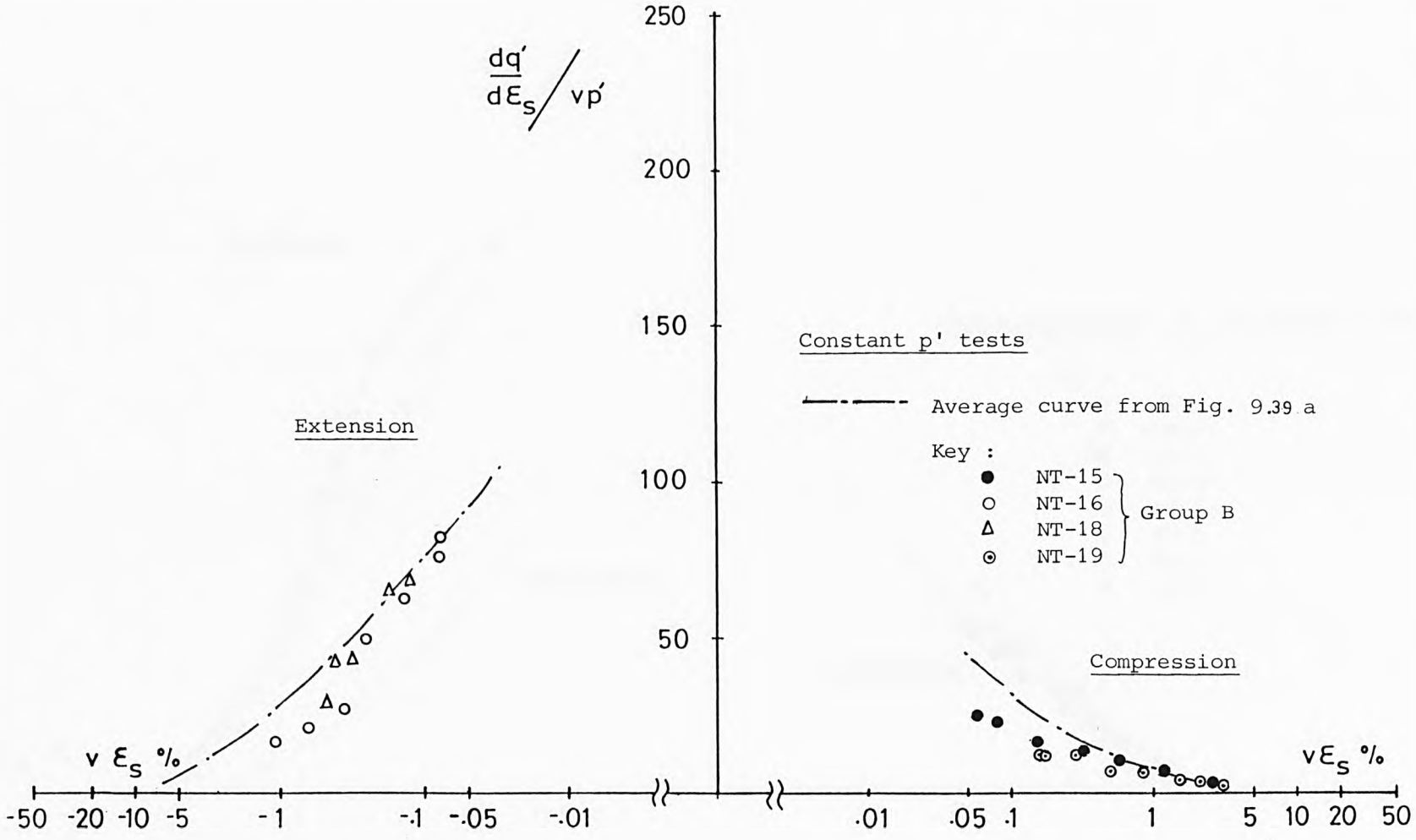

Fig. 9.39c Normalised shear stiffness for NAP tubed specimens.

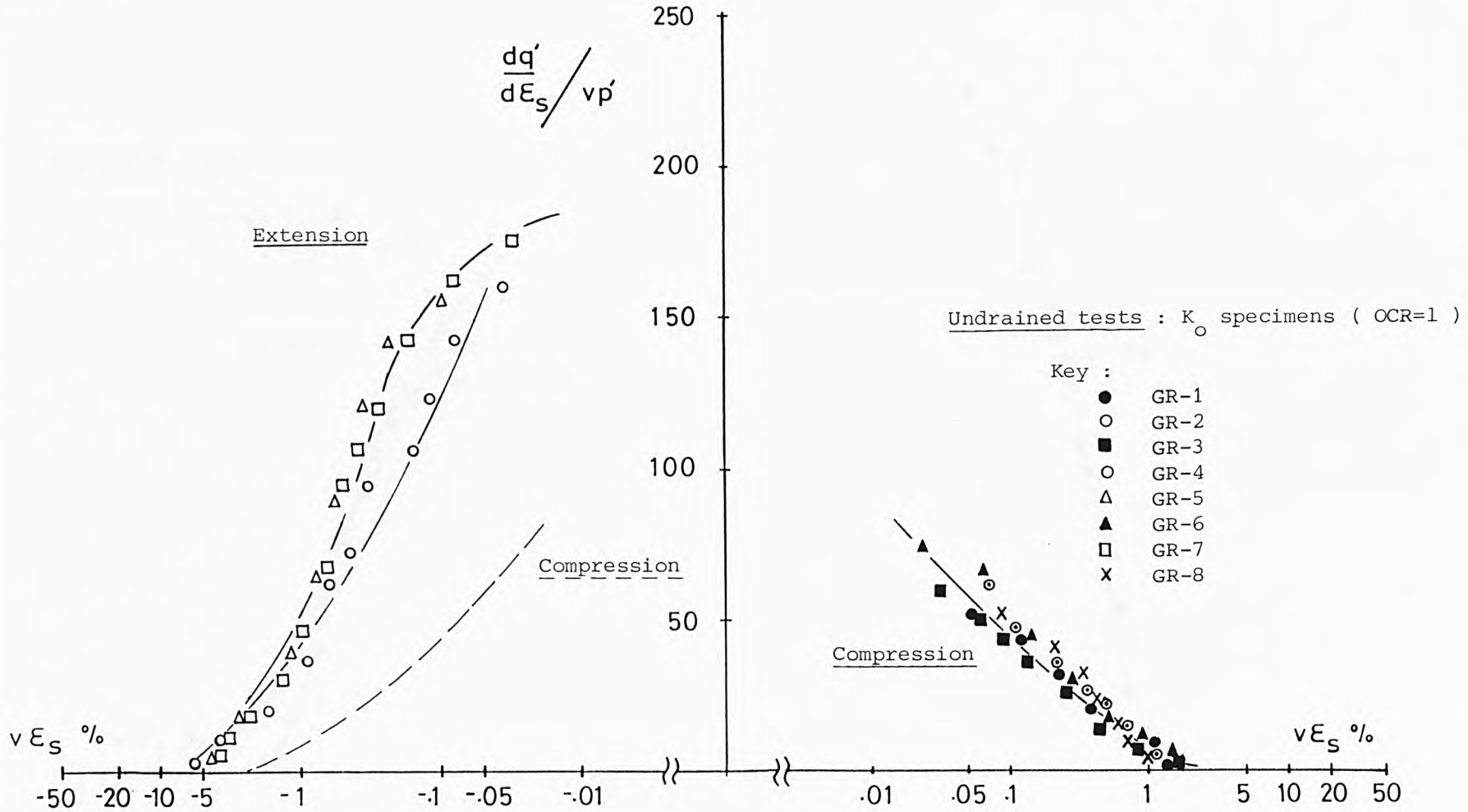

Fig. 9.40a Normalised shear stiffness for GME reconstituted specimens.

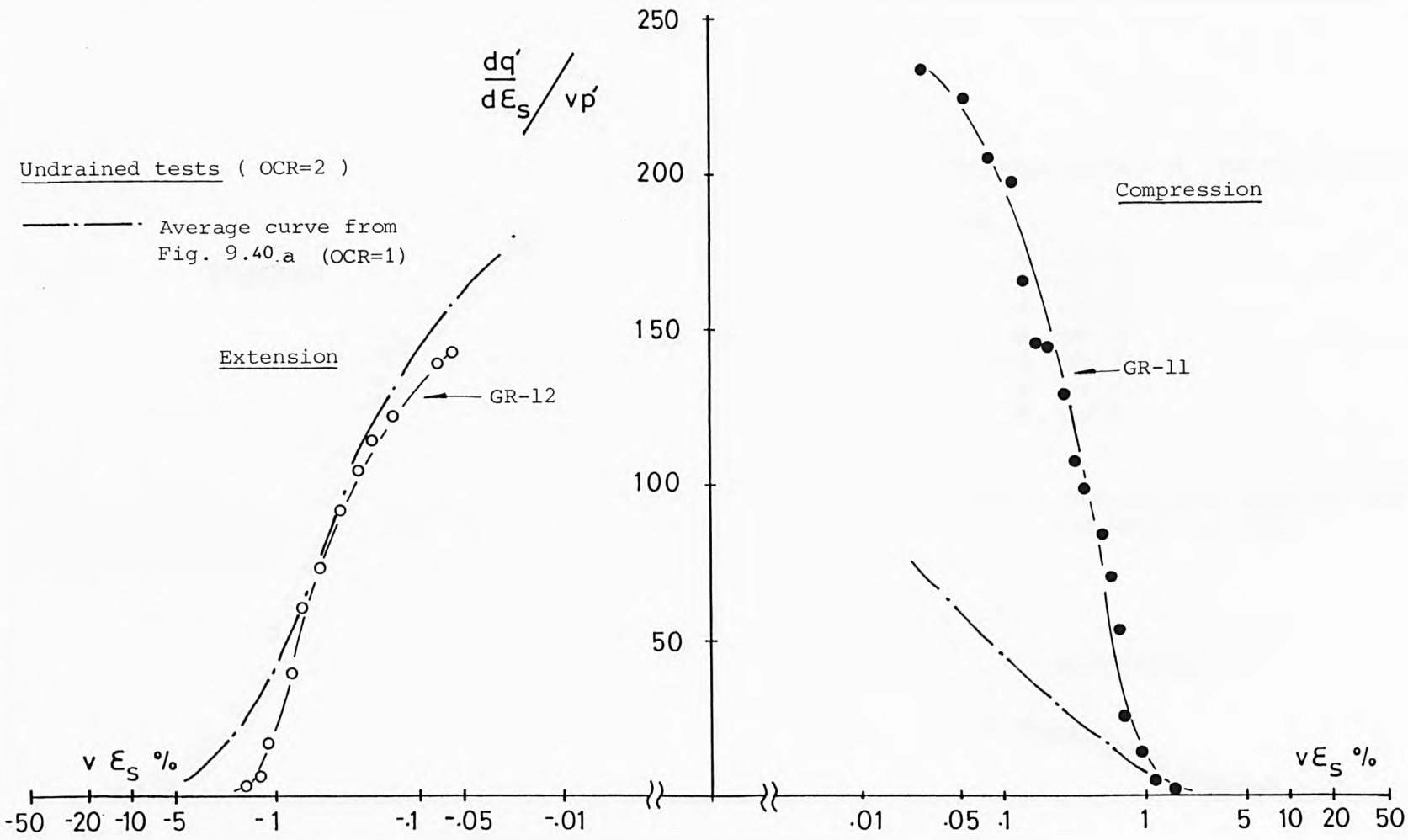

Fig. 9.40b Normalised shear stiffnesses for GME reconstituted specimens.

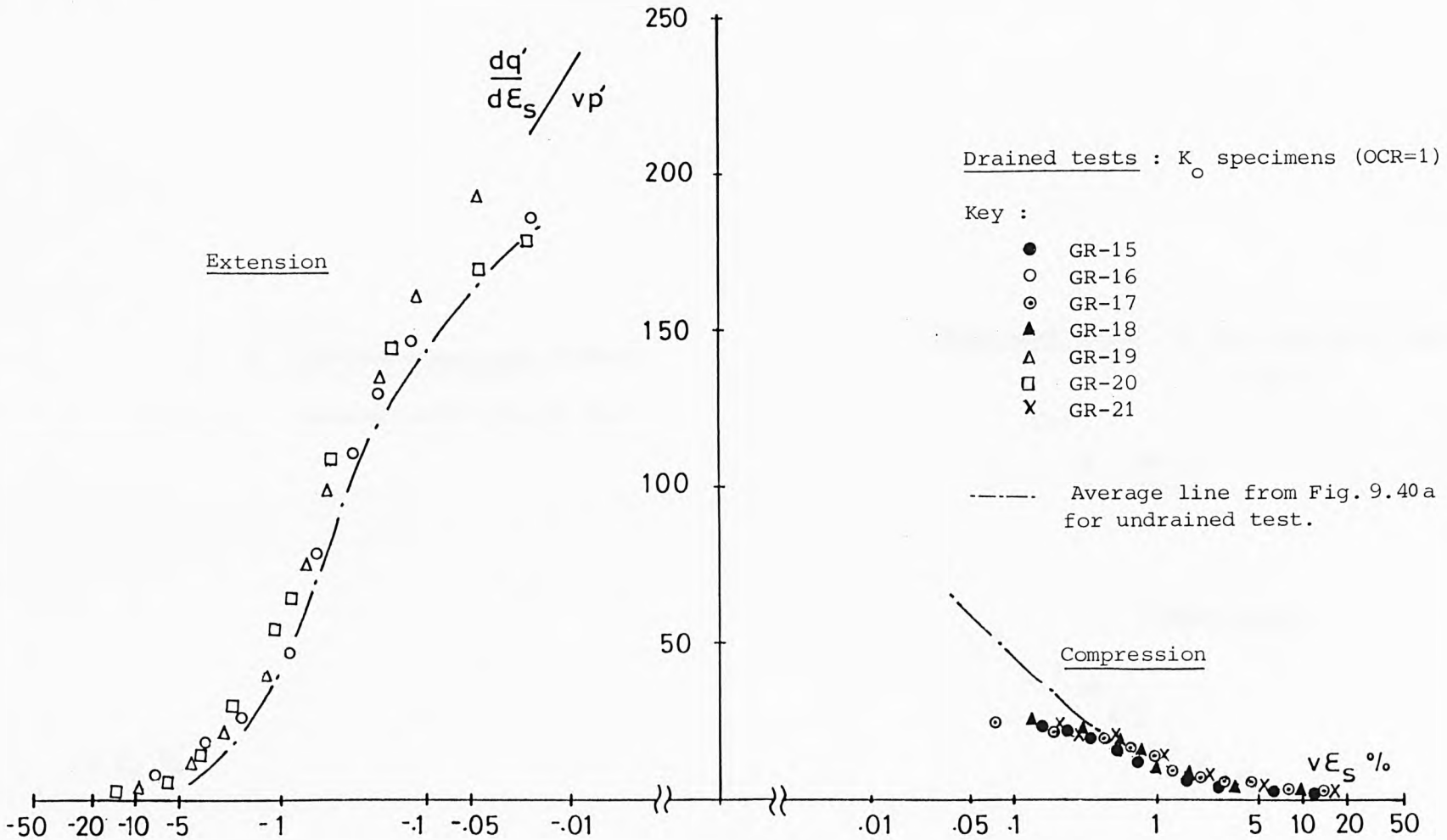

Fig. 9.40c Normalised shear stiffness for GME reconstituted specimens.

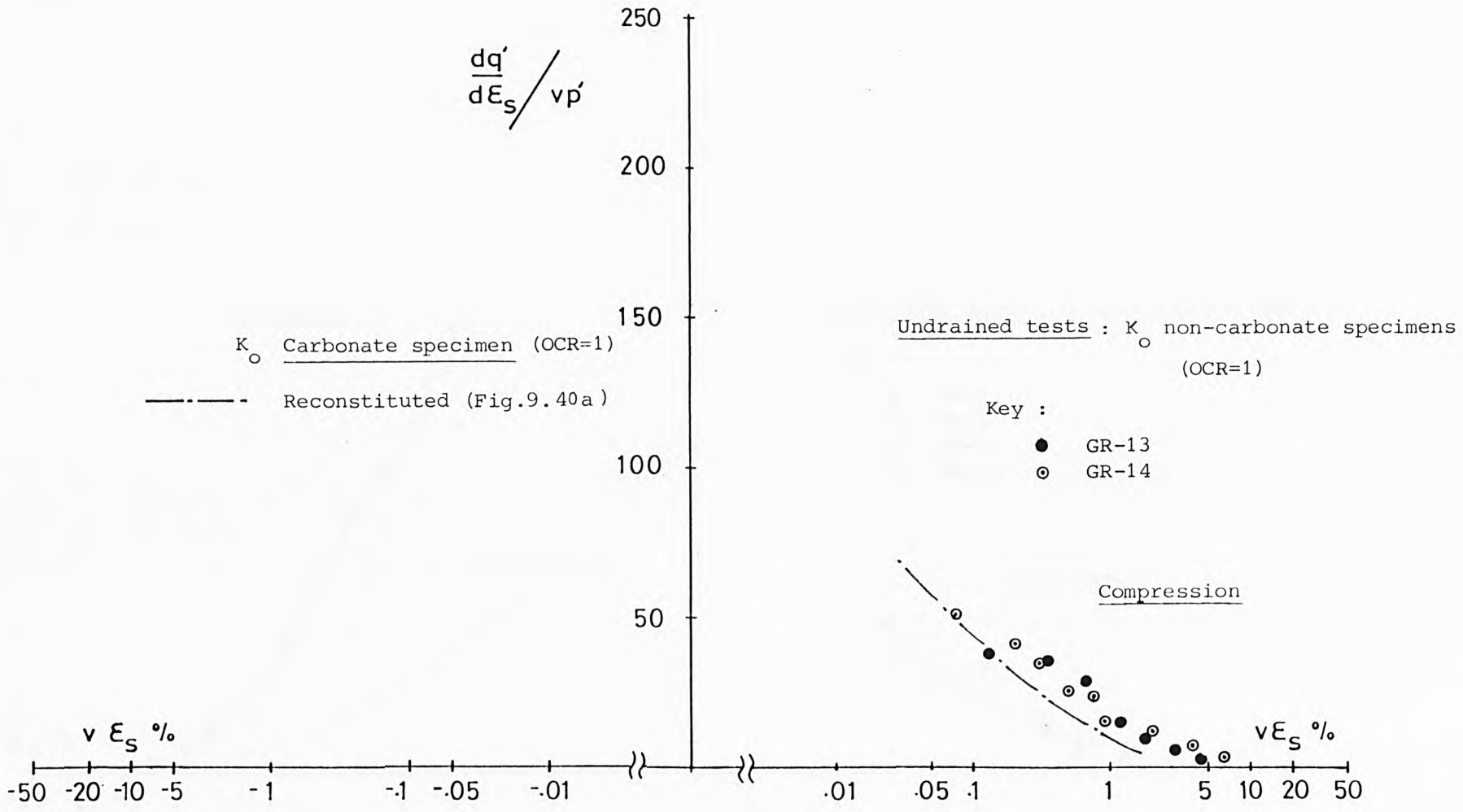

Fig. 9.40d Normalised shear stiffness for GME reconstituted specimens.

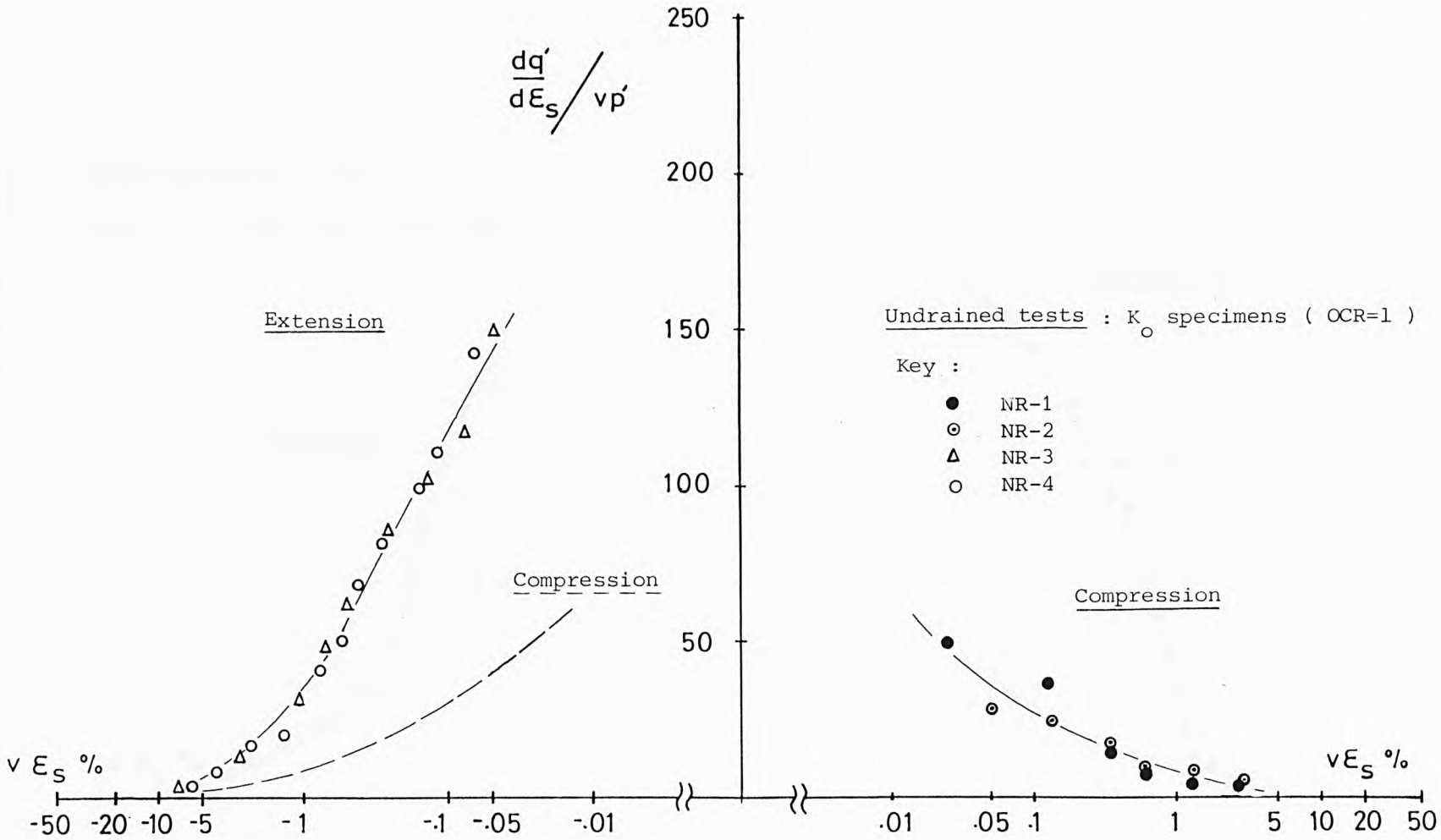

Fig. 9.41a Normalised shear stiffness for NAP reconstituted specimens.

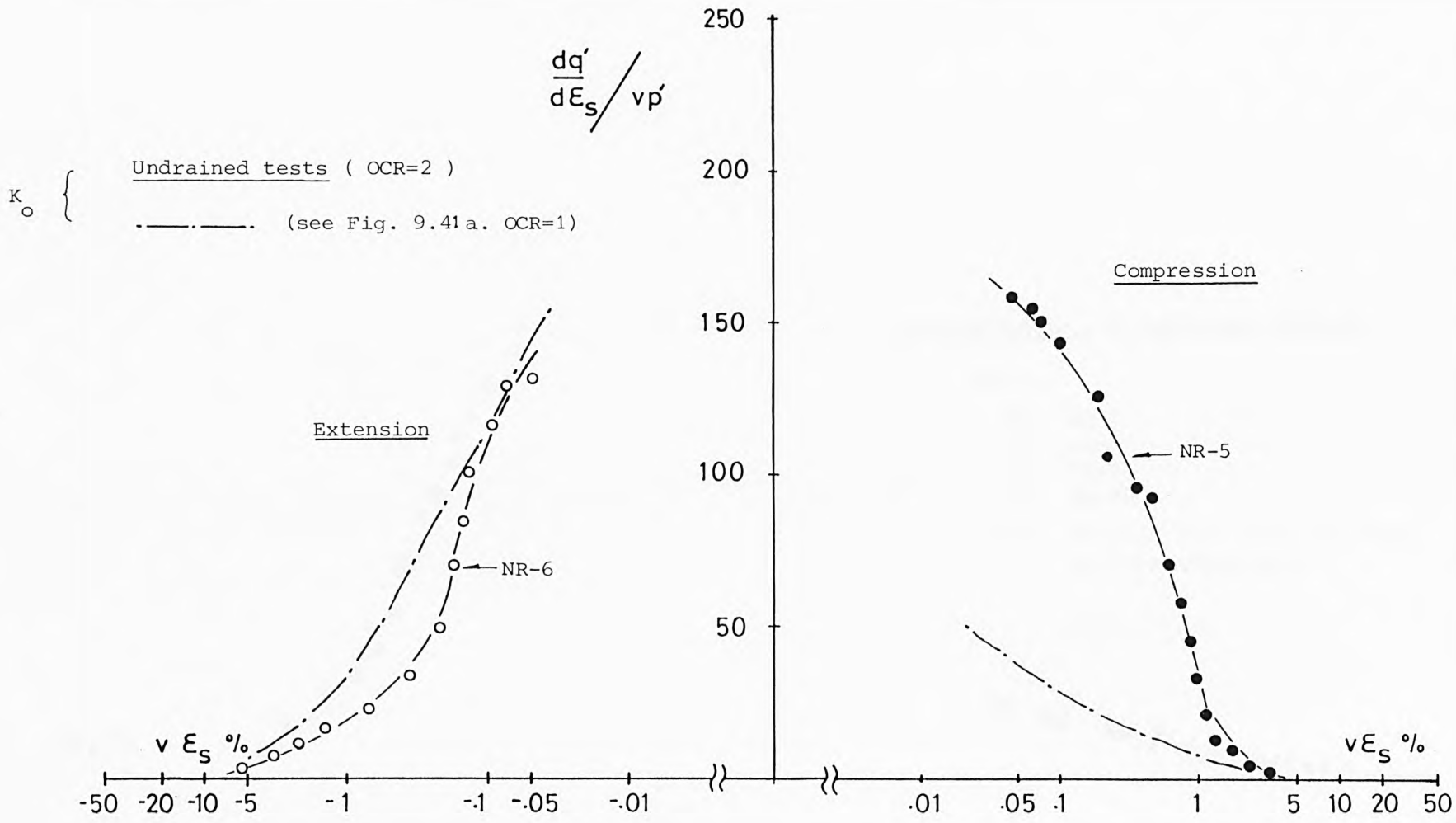

Fig. 9.41b Normalised shear stiffness for NAP reconstituted specimens.

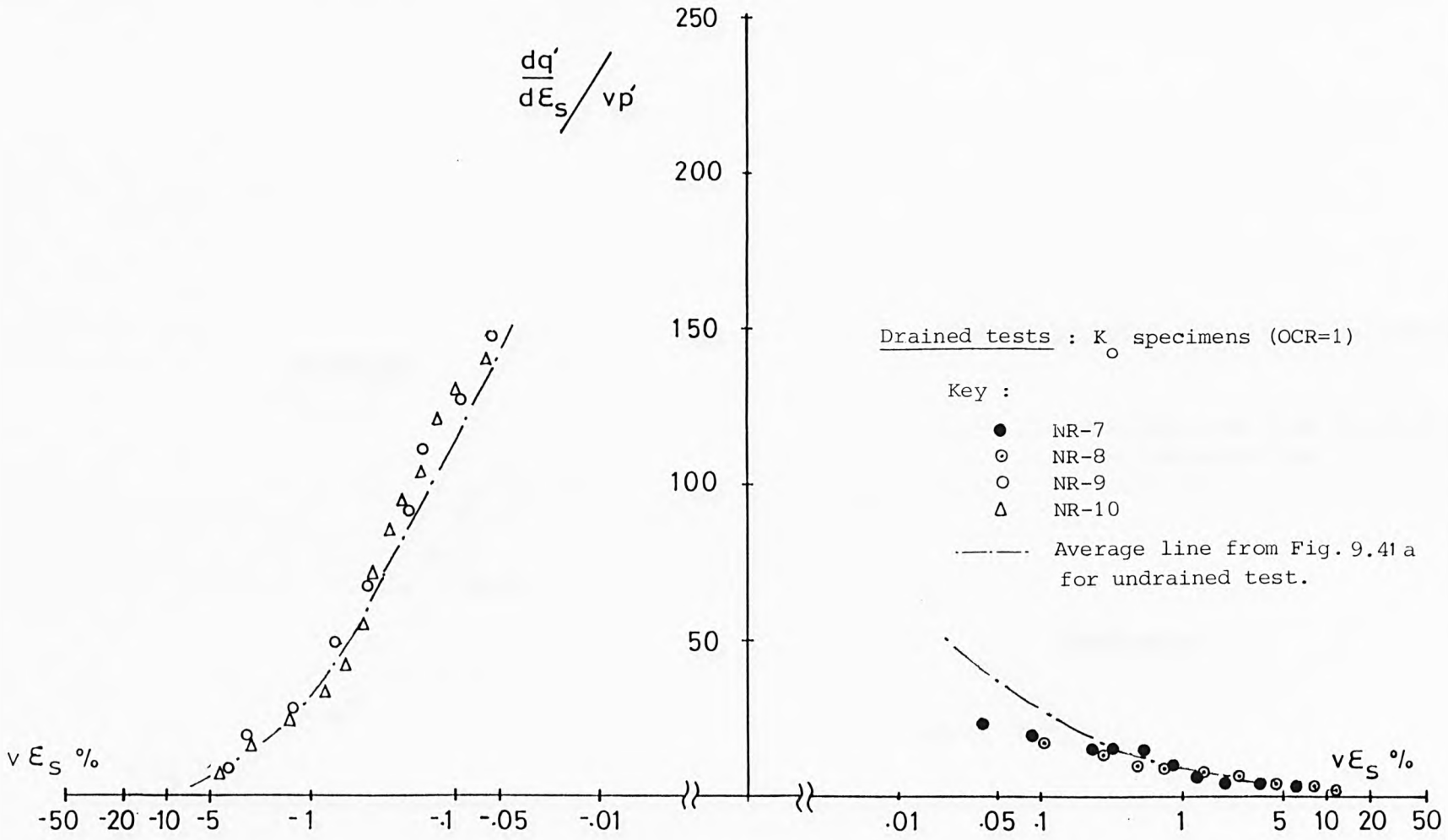

Fig. 9.41c Normalised shear stiffness for NAP reconstituted specimens.

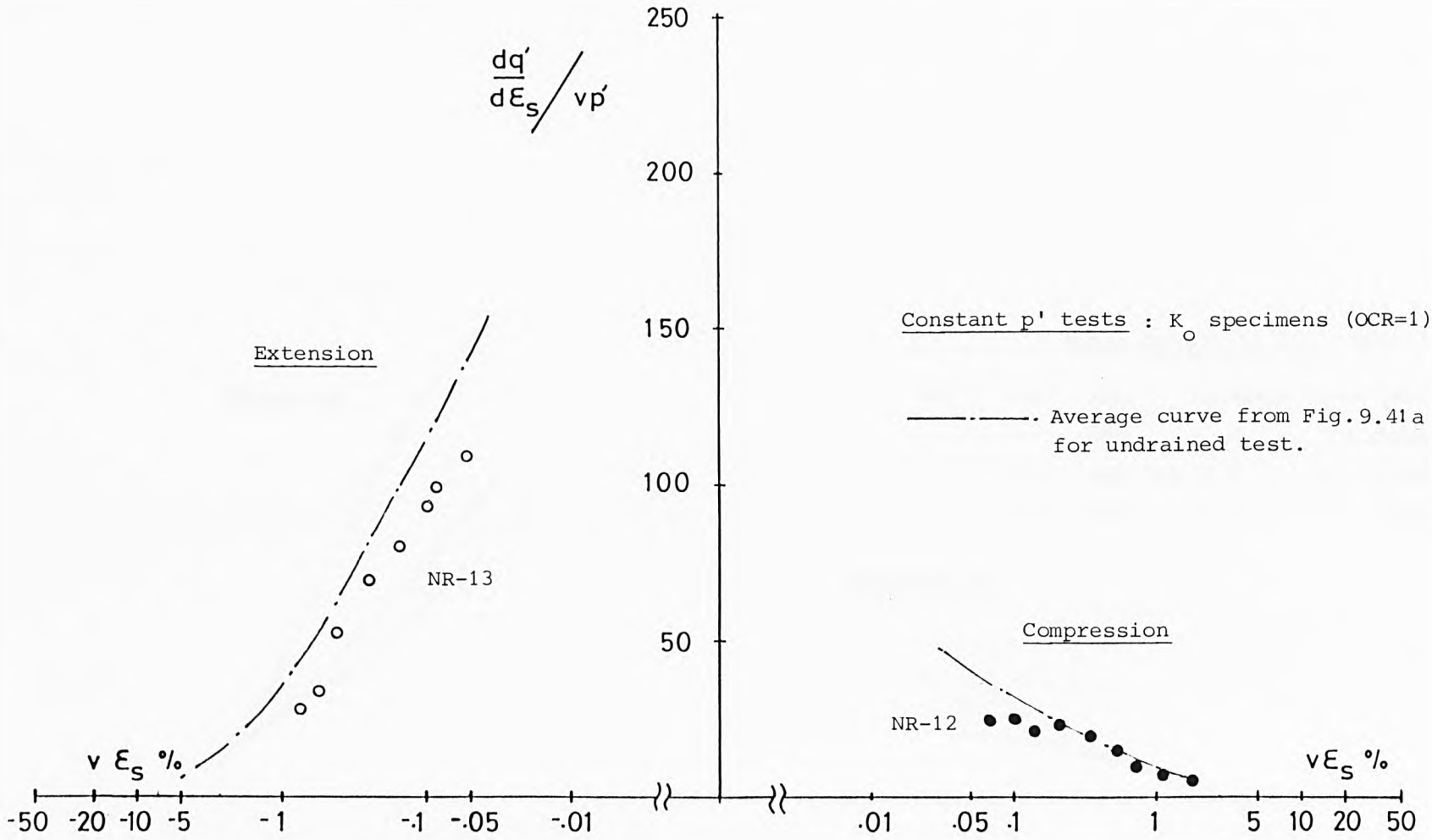

Fig. 9.41d Normalised shear stiffness for NAP reconstituted specimens.

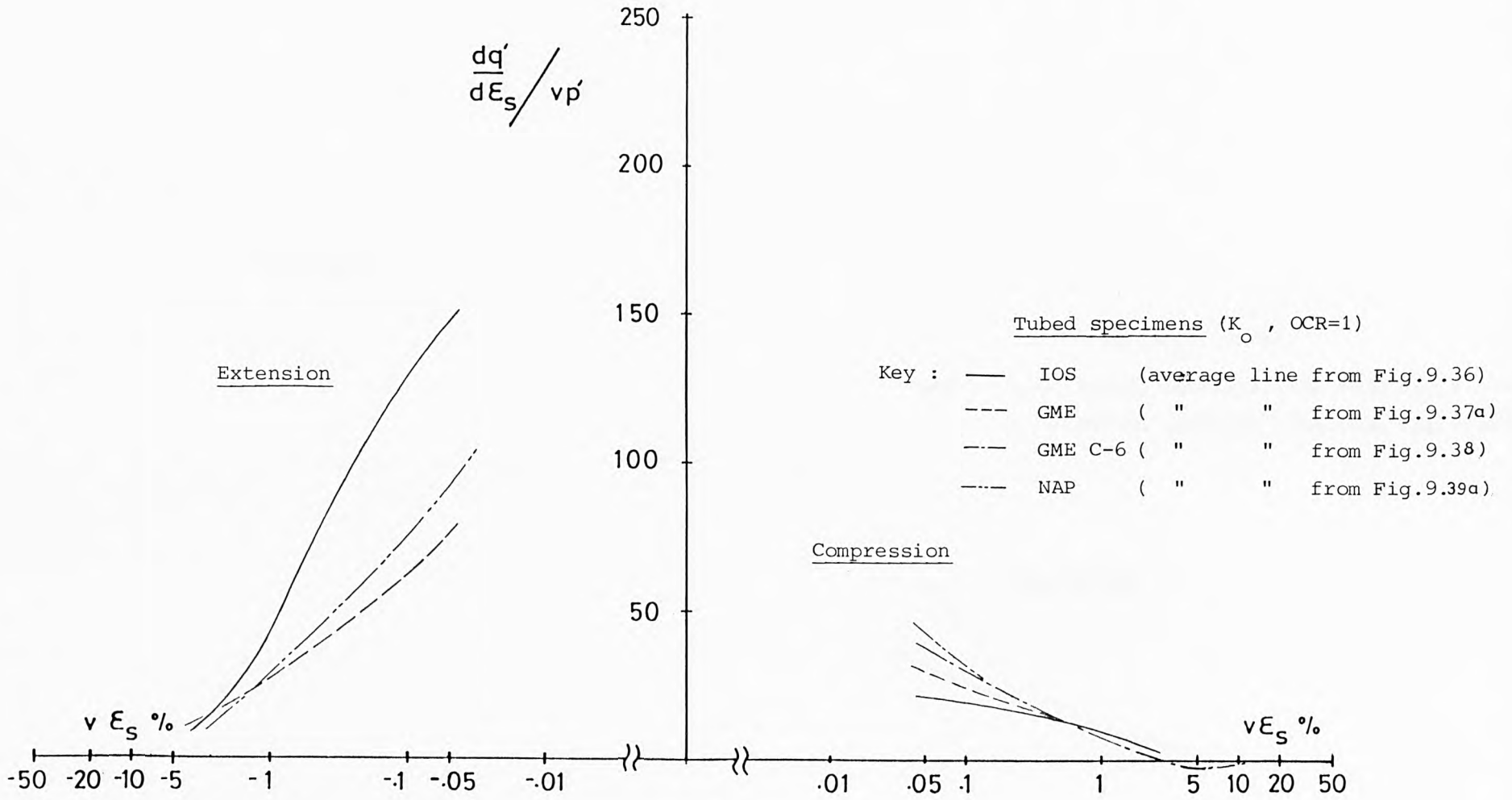

Fig. 9.42 A comparison of the undrained shear stiffnesses between different tubed sediments.

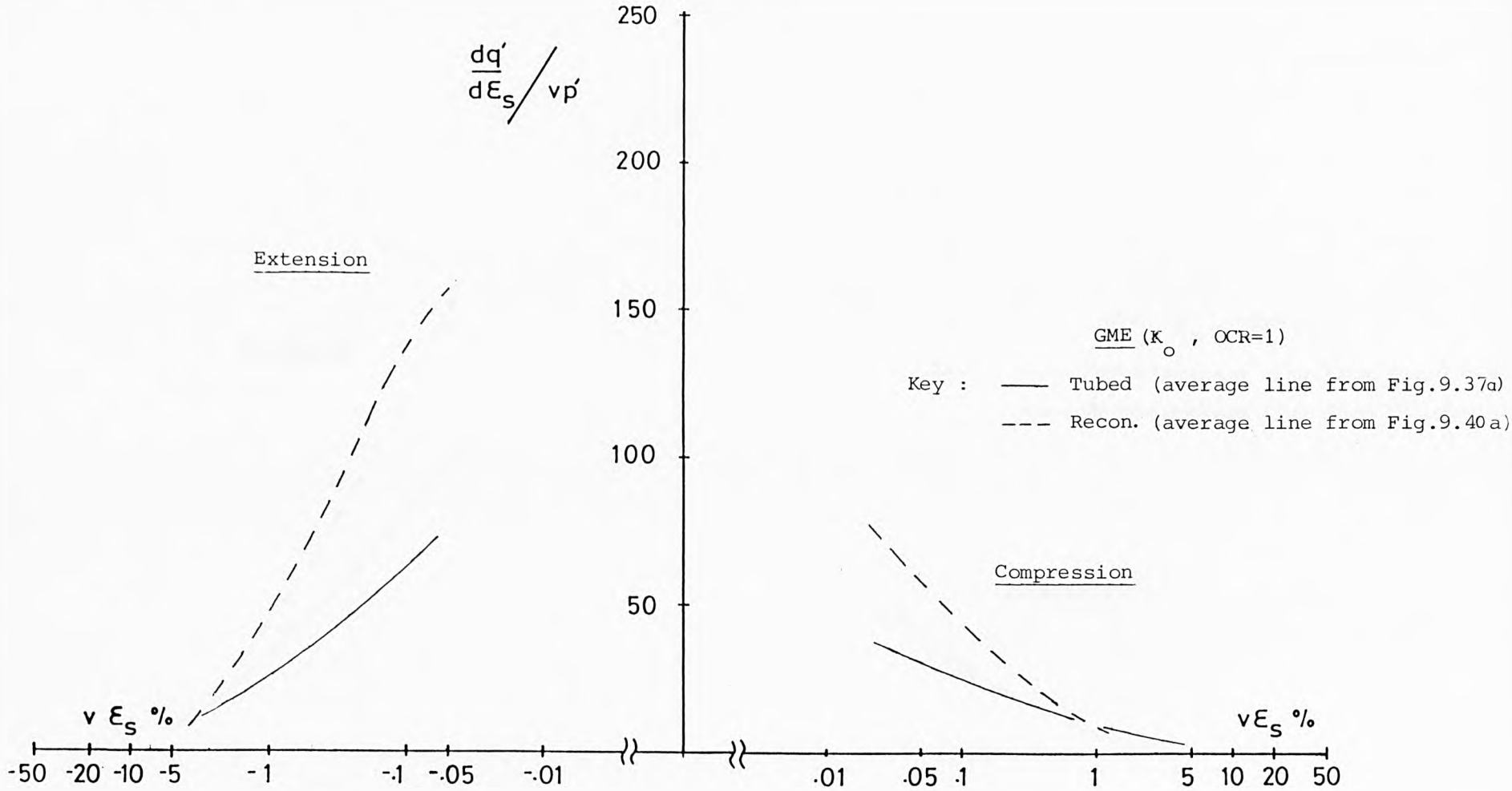

Fig. 9.43 A comparison of the undrained shear stiffnesses between tubed and reconstituted GME sediments.

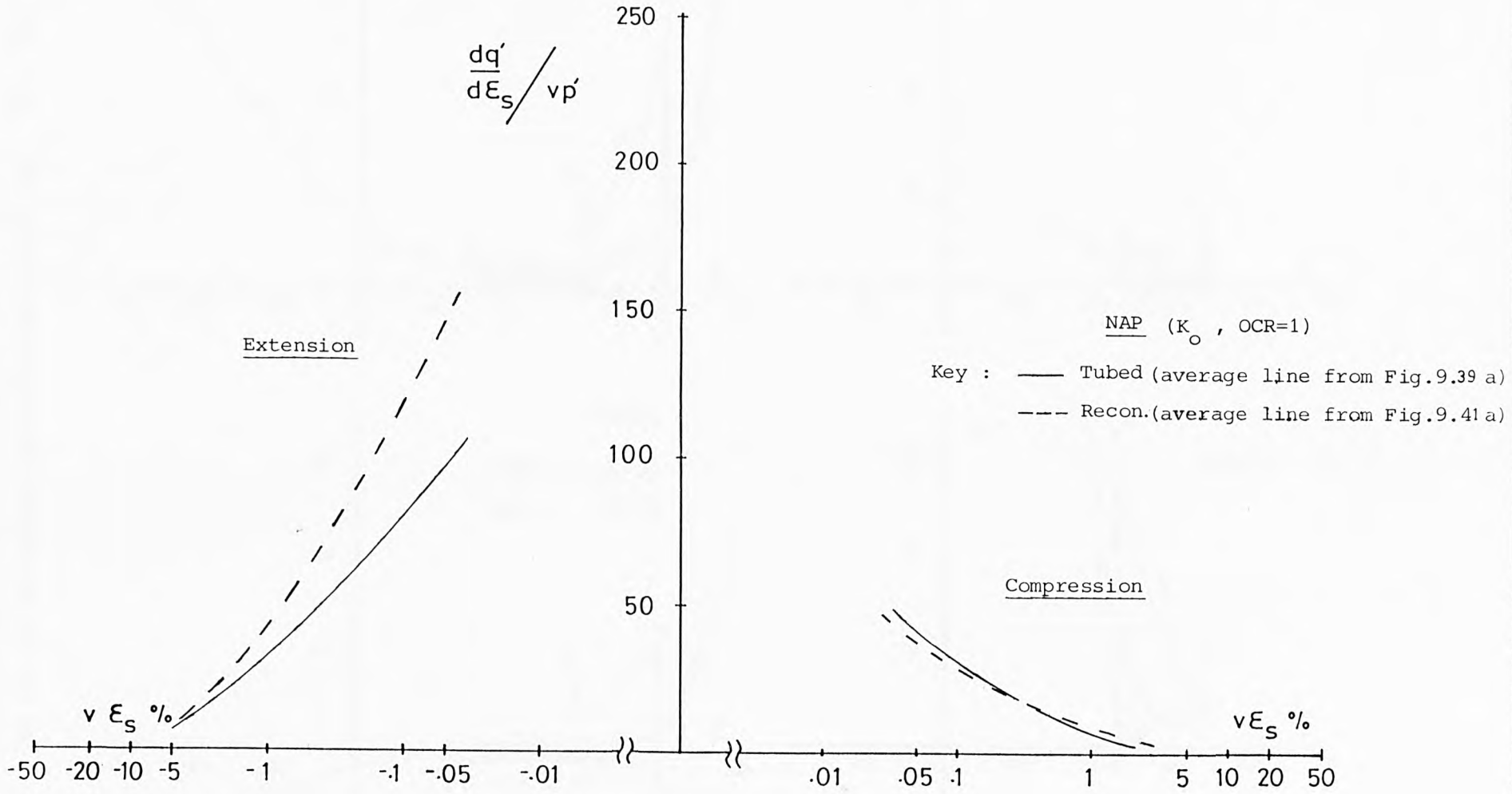

Fig. 9. 44 A comparison of the undrained shear stiffnesses between tubed and reconstituted NAP sediments.

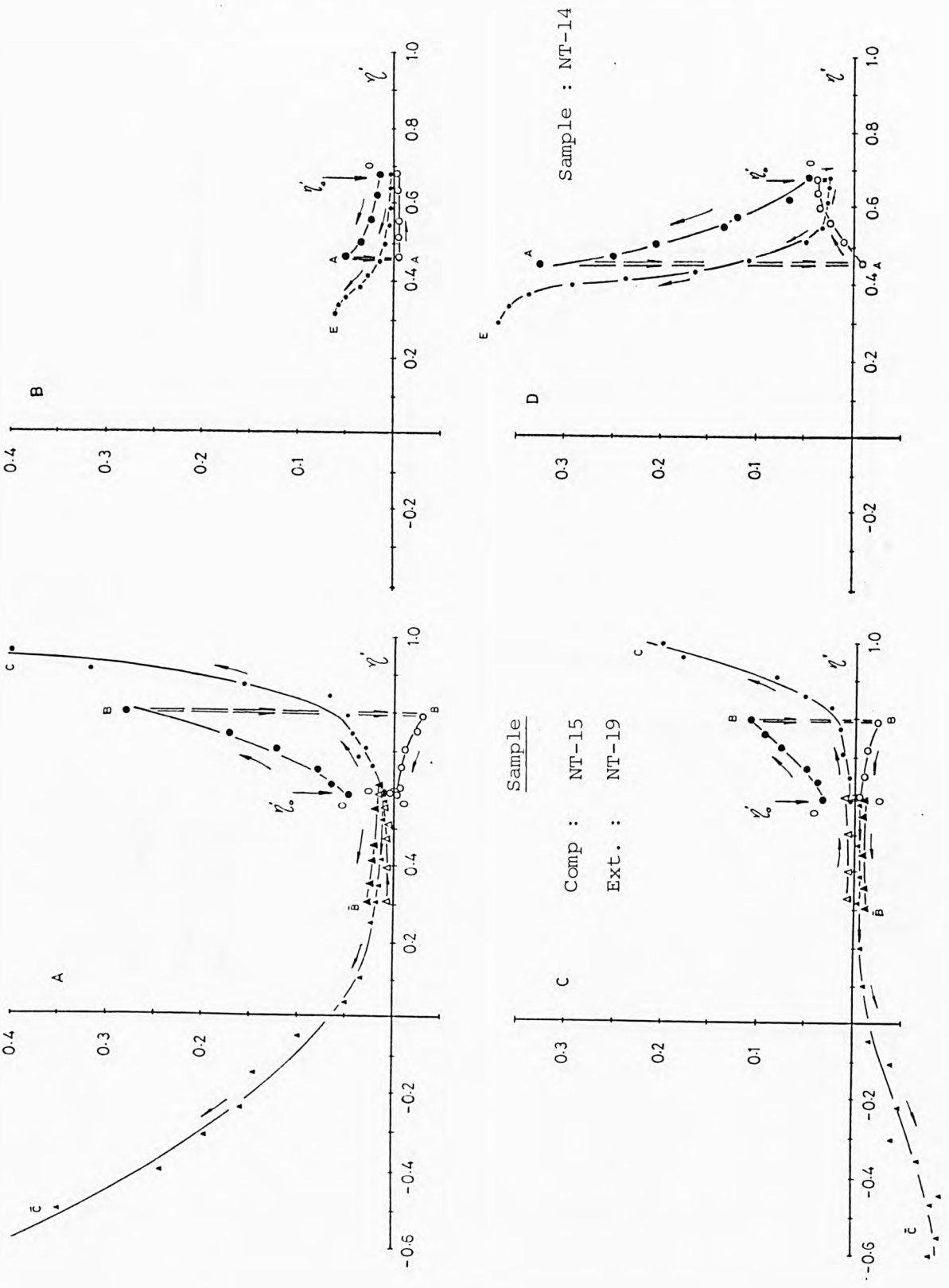

Fig. 9.45 The normalised compliance parameters for the NAP tubed specimens. (Compliances A and C from constant p' tests , compliances B and D from constant q' test)

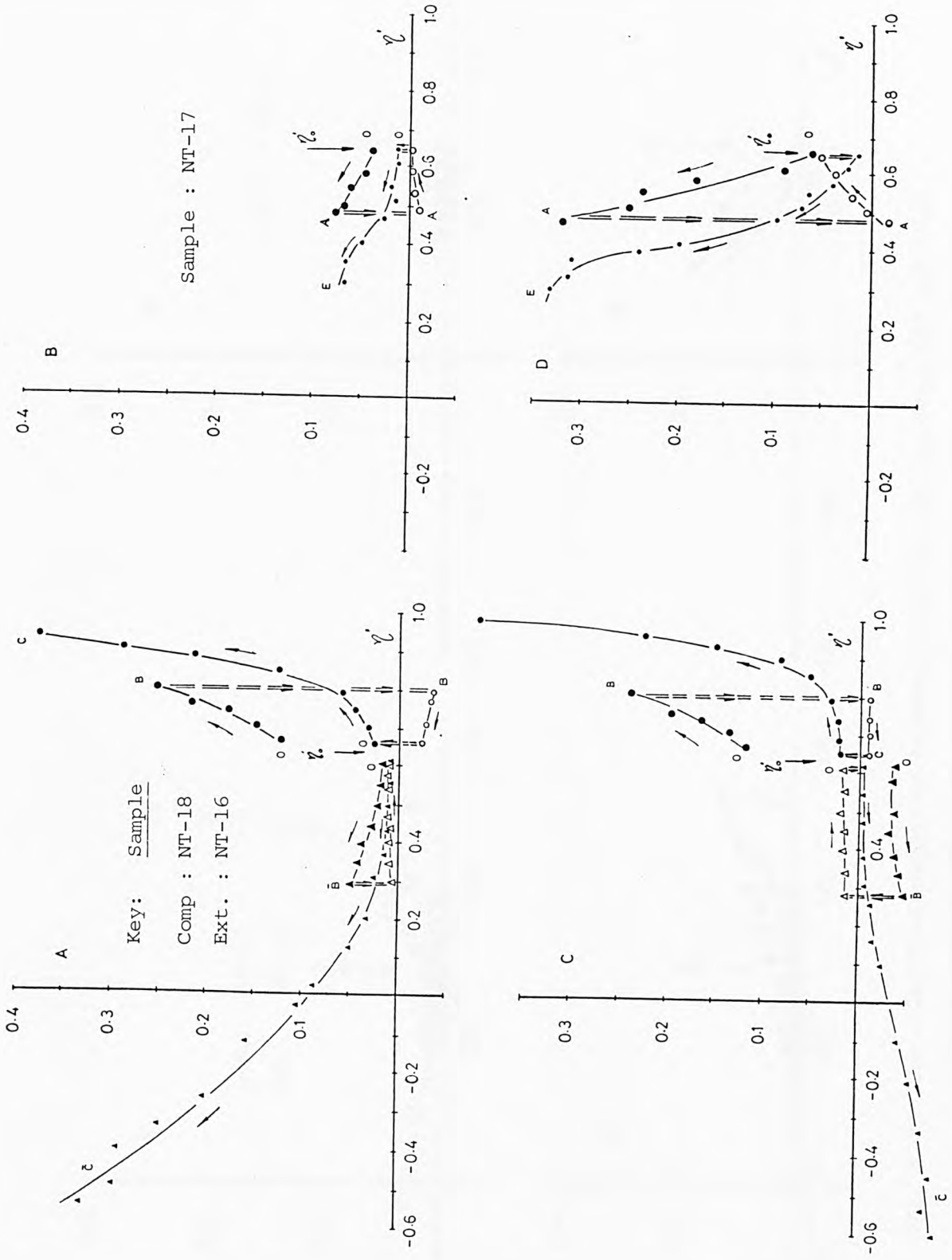

Fig. 9.46 The normalised compliance parameters for the NAP tubed specimens. (Compliances A and C from constant p' tests, compliances B and D from constant q' test)

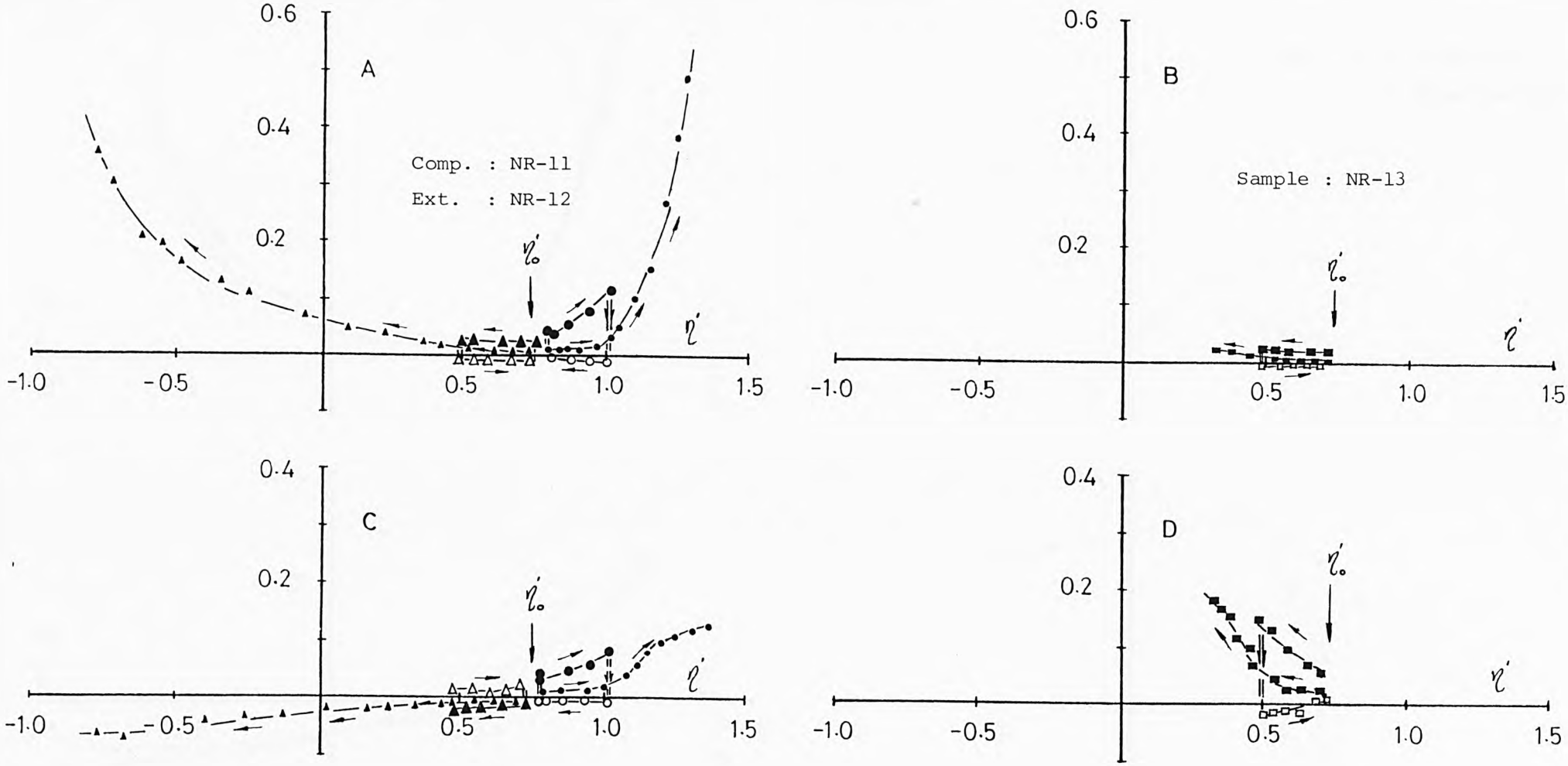

Fig. 9.47 The normalised compliance parameters for the NAP reconstituted specimens. (Compliances A and C from constant p' tests , compliances B and D from constant q' test)

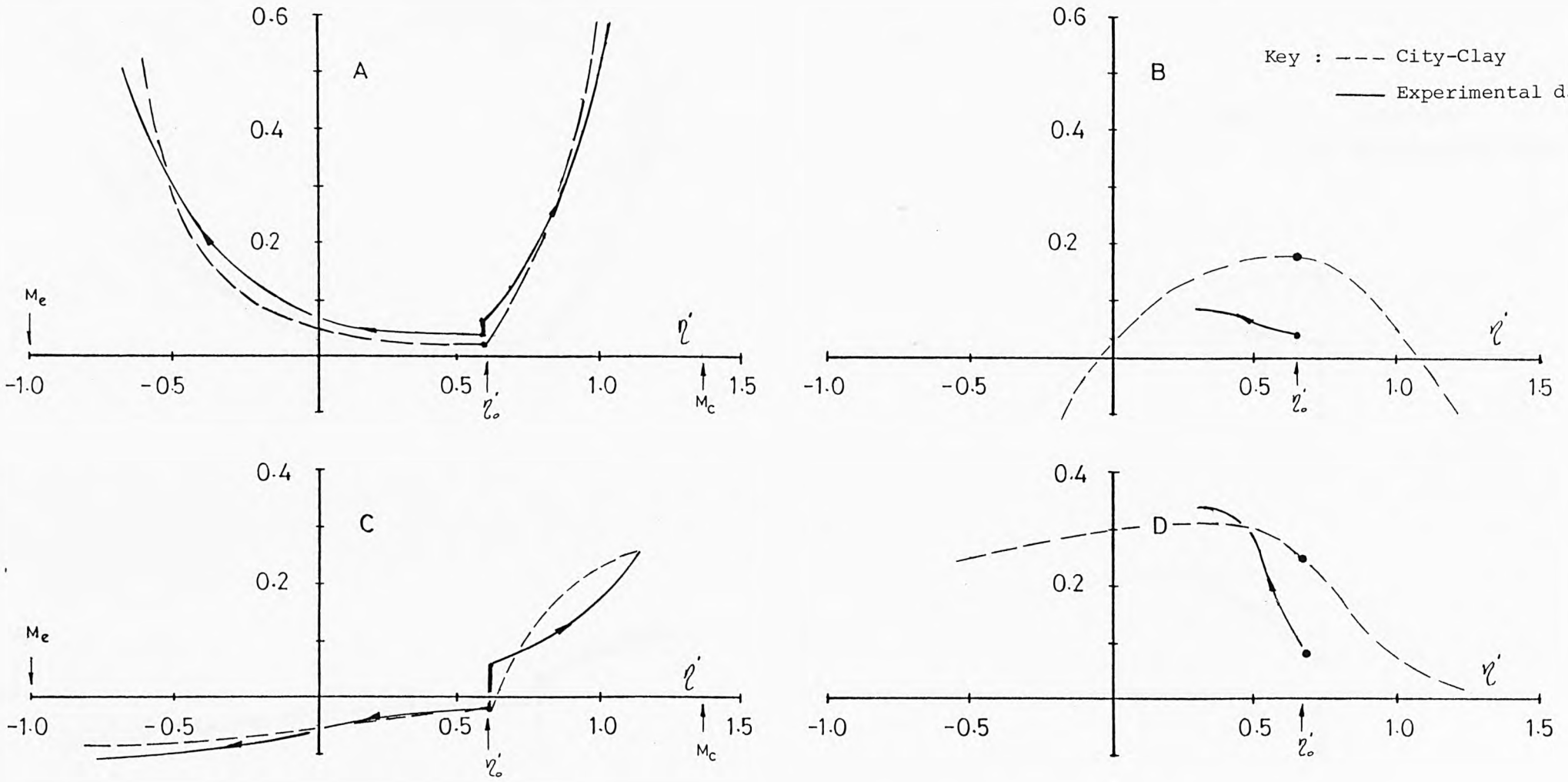

Fig. 9.48 A comparison of the normalised compliance parameters between theoretical and experimental results for NAP tubed specimens.

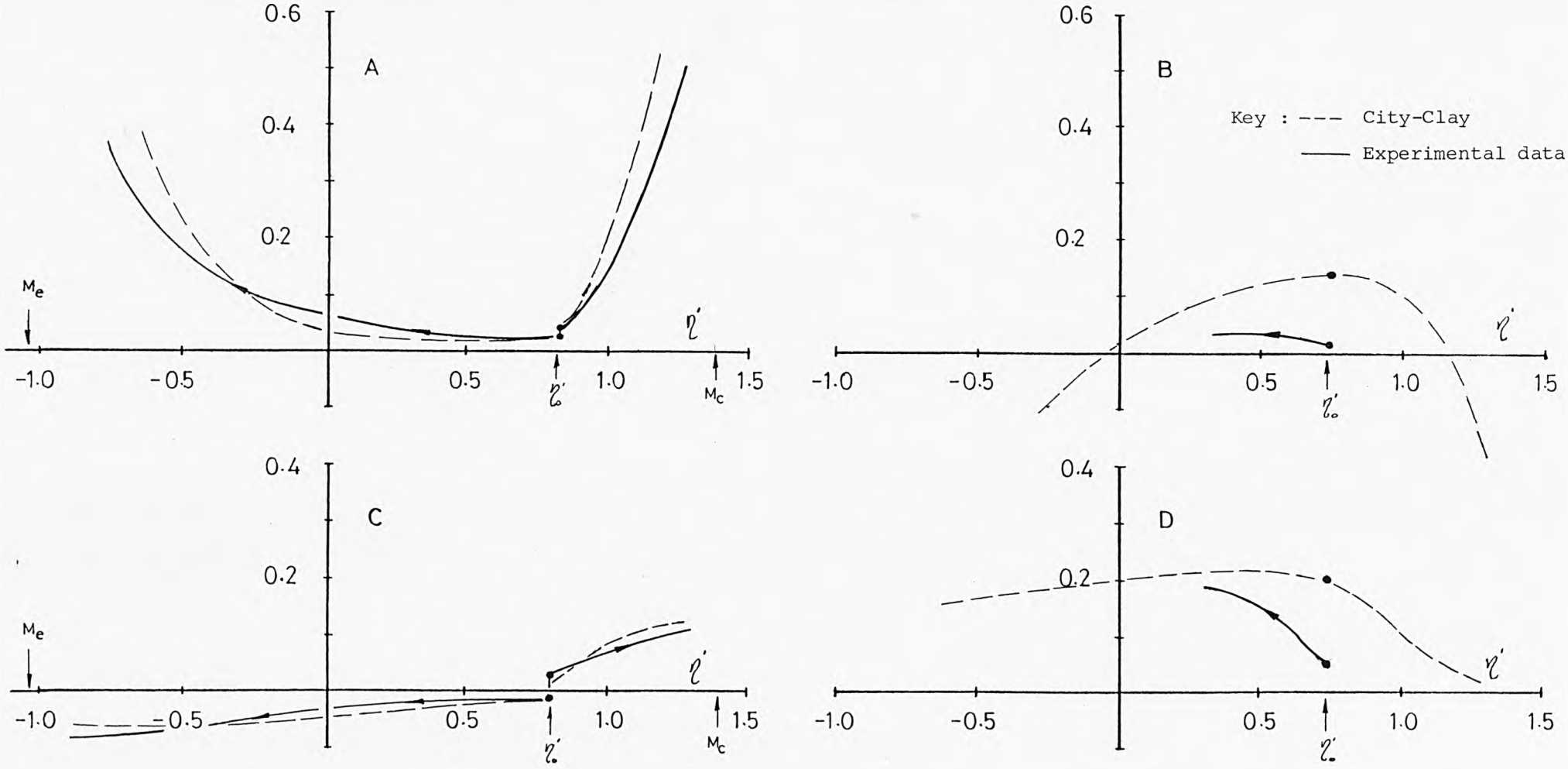

Fig. 9.49 A comparison of the normalised compliance parameters between theoretical and experimental results for NAP reconstituted specimens.